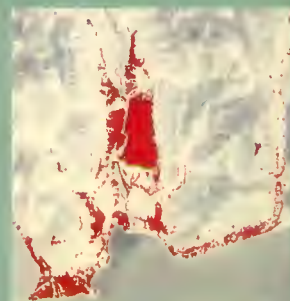
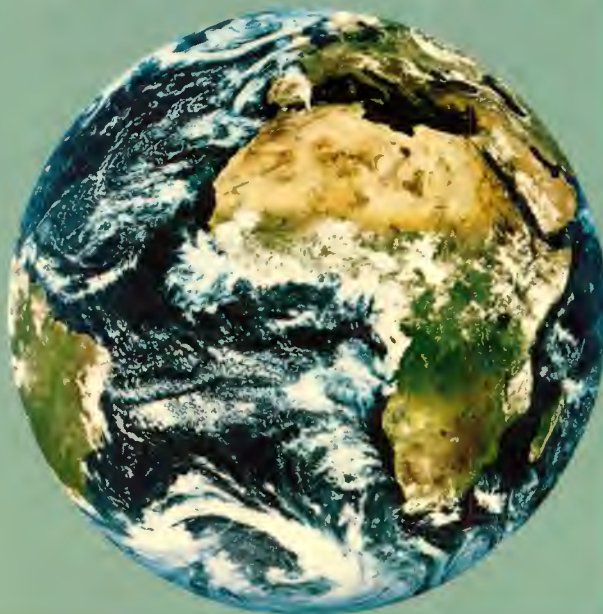


3RDPARTY002E

*European
Coordinated
Effort for*

Monitoring the Earth's Environment





esa SP-1102

ISBN 92-9092-000-9

May 1989

E U R O P E A N C O O R D I N A T E D E F F O R T F O R

Monitoring the Earth's Environment

*A Pilot Project Campaign on Landsat
Thematic Mapper Applications (1985 – 87)*

Editors : T.-D. Guyenne & G. Calabresi

ESA SP-1102 — ISBN 92-9092-000-9

Workshop organised by: Earthnet Programme Office
ESRIN, Frascati, Italy

Report published by: ESA Publications Division
ESTEC, Noordwijk, The Netherlands

Cover: Carel Haakman — *Layout:* Mario van Voorst

Copyright © 1989 European Space Agency

Price: 80 Dfl (or 40 \$) postage included.

Printed in The Netherlands (May 1989).

CONTENTS

1. SNOW

- IMPROVED SNOW AND GLACIER MONITORING BY THE LANDSAT THEMATIC MAPPER 3
H. Rott & G. Markl, Institut für Meteorologie & Geophysik, Universität Innsbruck, Austria
- MULTITEMPORAL SNOW CLASSIFICATION WITH TM DATA 13
U. Gangkofner, Gesellschaft für Angewandte Fernerkundung, München, FR Germany

2. HYDROLOGY

- UTILITY OF THEMATIC MAPPER DATA FOR NATIONAL SURVEY OF IRISH LAKES 25
B.C. Reardon, University College, Dublin, & M.L. McGarrigle, An Foras Forbartha, Ireland
- APPLICATION OF LANDSAT DATA TO HYDROLOGIC MAPPING 33
L. Paus & U. Streit, Department of Geography, University of Münster, FR Germany
- IRRIGATION WATER MANAGEMENT IN TWO ITALIAN IRRIGATION DISTRICTS 41
S. Azzali & M. Menenti, Inst. for Land & Water Management Research, Wageningen, Netherlands
- REMOTE SENSING OF LIMNOLOGICAL PARAMETERS IN RESERVOIRS 49
J.L. Ortiz Casas & R. Peña Martínez, Centro Estudios y Exper. de Obras Públ., Madrid, Spain
- COLOUR ANALYSIS OF INLAND WATERS USING LANDSAT TM DATA 57
J.-M. Jaquet, Department of Geology, Univ. of Geneva & B. Zand, UNEP, Geneva, Switzerland

3. COASTAL WATERS

- INVESTIGATION OF POLLUTION-RELATED CHARACTERISTICS OF DUBLIN BAY, IRELAND 71
B. Masterson & D. Conry-McDermott, Biochemistry Dept., University College, Dublin, Ireland
- TM STUDY OF SUSPENDED SEDIMENTS IN A FJORD SYSTEM IN WESTERN NORWAY 77
J. Nilsen & I. Selseth, Norwegian Hydrotechn. Lab., Trondheim & V. Nilsen, Forut/Statoil, Norway

4. GEOLOGY

- PEATLAND MAPPING AND MINERAL EXPLORATION IN IRELAND 91
G.W. Horgan & M.F. Critchley, Trinity College, Dublin, Ireland
- STUDY OF SABKHA SURFACES IN THE QATTARA DEPRESSION, NW EGYPT 99
F. K. List & D. Linne, Inst. of Applied Geology & B. Meissner, Laboratory of Map Design, Berlin
- IMAGE PROCESSING STRATEGIES FOR MINERAL EXPLORATION IN ARID AREAS 111
H. Kaufmann, Dept. of Photogrammetry & Remote Sensing, University of Karlsruhe, FR Germany

APPLICABILITY OF LANDSAT-TM DATA FOR GEOSCIENTIFIC PURPOSES IN ICELAND	127
<i>F. Jaskolla & K. Arnason, Inst. f. Allgem. & Angewandte Geologie, Univ. München, FR Germany</i>	
KARST DRAINAGE IN THE PELOPONNESUS: APPLICATION OF TM IN HYDROGEOLOGY	141
<i>B. Reichert & H. Hötzl, Lehrstuhl für Angewandte Geologie & H. Kaufmann, Univ. Karlsruhe</i>	
DETECTION OF SHORT-TERM CHANGES IN TIDAL FLAT GEOMORPHOLOGY	149
<i>J. Ehlers, Geolog. Landesamt, Hamburg & F. Böker, Geowiss. & Rohstoffe, Hannover, Germany</i>	
METHODICAL AND STRUCTURAL MSS AND TM INVESTIGATIONS IN THE SWABIAN ALB	161
<i>R. Stellrecht & A. Hoydem, Geol. Inst., H. Kaufmann & W. Weisbrich, Karlsruhe, FR Germany</i>	
GEOLOGICAL STRUCTURES IN COASTAL AREAS OF TRØNDELAG, NORWAY	169
<i>B. Rindstad & A. Grønlie, Geological Survey of Norway, Trondheim, Norway</i>	

5. LAND USE

LES POTENTIALITES DE LANDSAT TM EN MILIEU URBAIN – LE CAS DE BRUXELLES	185
<i>M.L. De Keersmaecker, UCL, Laboratoire de Télédétection, Louvain-la-Neuve, Belgique.</i>	
LAND-USE CLASSIFICATION IN UPPER RHINE VALLEY WITH MULTITEMPORAL TM DATA	191
<i>W. Mauser, Inst. for Physical Geography, Dept. of Hydrology, University Freiburg, FR Germany</i>	
MAPPING WINTER GRAZING AREAS FOR REINDEER ON SVALBARD USING TM DATA	199
<i>S. Spjelkavik & A. Elvebakk, Institute of Biology & Geology, University of Tromsø, Norway</i>	
REMOTE SENSING OF THE MADRID AREA ECOSYSTEMS	207
<i>J. L. Labrandero Sanz, Instituto de Edafología y Biología Vegetal, Madrid, Spain</i>	
COMPARISON OF THE CLASSIFICATION RESULTS OBTAINED WITH TM AND MSS DATA IN THE LAND USES IDENTIFICATION OF THE 'COMUNIDAD AUTONOMA DE CANTABRIA'	213
<i>F. Gonzalez Alonso, Proyecto de Teledetección, Sección de Proceso de Datos INIA, Madrid, Spain</i> <i>J. M. Ureña Francés, Depart. de Urbanismo y Medio Natural, Univ. de Cantabria, Santander</i>	

6. FORESTRY

FOREST DAMAGE MAPPING IN AUSTRIA USING LANDSAT TM IMAGE DATA	223
<i>W. Schneider, Institut für Vermessungswesen & Fernerkundung, Universität für Bodenkultur, Vienna, Austria</i>	
DISCRIMINATION OF GEOBOTANICAL ANOMALIES IN CONIFEROUS FROM TM DATA	233
<i>C. Banninger, Institute for Image Processing & Computer Graphics, Graz Research Centre, Austria</i>	
CLASSIFICATION OF SMALL-SCALE FORESTS IN FLANDERS USING TM DIGITAL DATA	241
<i>R. R. De Wulf & R. E. Goossens, Rem. Sens. & Forest Managt. Lab., Gent State Univ., Belgium</i>	
FOREST CLASSIFICATION WITH TM DATA IN THE AREA OF FREIBURG, FR GERMANY	251
<i>M. Schardt, DFVLR, Oberpfaffenhofen and Albert-Ludwigs-Universität, Freiburg, FR Germany</i>	
USE OF LANDSAT-TM DATA FOR FOREST DAMAGE INVENTORY	261
<i>A. Kadro, Abt. Luftbildmessung & Fernerkundung der Universität Freiburg, FR Germany</i>	
MAPPING OF VEGETATION IN THE DIVIDALEN AREA, CENTRAL TROMS, N. NORWAY	271
<i>H. Tømmervik, University of Tromsø, Norway</i>	

APPLICATION OF TM IMAGES TO FOREST FIRE MAPPING IN MEDITERRANEAN AREA	279
<i>E. Chuvieco, Department of Geography, University of Alcalá de Henares, Madrid</i>	
LARGE-SCALE FOREST MANAGEMENT USING LANDSAT THEMATIC MAPPER DATA	287
<i>R. Caloz, Inst. of Rural Engineering & T. Blaser, Fed. Inst. of Technology, Lausanne, Switzerland</i>	
MULTITEMPORAL ANALYSIS OF FOREST AREAS IN THE SURROUNDINGS OF INNSBRUCK	293
<i>F. H. Berger, Institut für Meteorologie, Freie Universität Berlin, FR Germany</i>	
7. CARTOGRAPHY	
COMPARAISON DES DONNEES MSS ET TM POUR LA CARTOGRAPHIE EN ZONE ARIDE	301
<i>R. Escadafal & J. Pouget, Atelier de Télédétection, Centre ORSTOM, Bondy, France</i>	
PROCESSING AND INTERPRETATION OF TM IMAGES IN PIACENZA PROVINCE	309
<i>A. Annoni & E. Zini, RSDE, Milan & R. Arcozzi, Ufficio Cartografico, Bologna, Italy</i>	
PRODUCTION OF SATELLITE IMAGE MAPS FROM TM DATA	315
<i>J. Albertz & A. Mehlbreuer, TU Berlin, Fachgebiet Photogrammetrie & Kartographie</i>	
INTEGRATING TM AND CARTOGRAPHIC DATA	323
<i>P. Mogorovich, CNUCE Institute, CNR, Pisa, Italy</i>	
TESTS OF TOPOGRAPHIC MAPPING WITH THEMATIC MAPPER IMAGES	333
<i>G. Togliatti, G. Lechi & A. Moriondo, Ist. Topogr., Fotogram. e Geofisica, Politec. Milano, Italy</i>	
LIST OF KEYWORDS	339

Introduction

Earthnet operations within the framework of the European Space Agency's Earth Observation Programme started in early 1977. The main role of the Earthnet programme over the past decade has been the acquisition, pre-processing, archiving and distribution of data from the major US remote-sensing satellite missions.

The experience gained in handling data from different platforms and payloads – such as Landsat MSS (Multispectral Scanner), Seasat SAR (Synthetic Aperture Radar), HCMM (Heat-Capacity Mapping Mission), Nimbus-7 CZCS (Coastal Zone Colour Scanner), NOAA/Tiros AVHRR (Advanced Very-High Resolution Radiometer), TOVS (Tiros Operational Vertical Sounder), MOS (Japanese Marine Observation Satellite) and the Metric Camera onboard ESA's Spacelab – has been most valuable; but a new dimension was added to Earthnet's work when the Thematic Mapper (TM) was flown in 1984.

The direct read-out of the TM payload started with Landsat-4 and continued with Landsat-5. The use of TM 30-m ground-resolution power and its seven different channels including the thermal band ensured multitemporal analysis and Earth resources monitoring.

It was in 1985 that Earthnet decided to promote the use of the Thematic Mapper in Europe with the so-called 'Pilot Project Campaign'. The considerable volume of data received was then made available to the user community at particularly favourable conditions. The campaign stimulated a wide range of projects and studies in almost all European countries. The role of Earthnet's National Points of Contact (NPOC) in selecting, among many requests for data allocation, the most interesting application projects was fundamental.

Over a hundred projects covering different application fields were carried out during the two-year campaign and each one was described in a technical report. The authors were given the opportunity to present the results of their studies at a Workshop entitled 'Landsat Thematic Mapper Applications' organised by Earthnet at ESRIN, Frascati, Italy, in December 1987. As a record of the Workshop, thirty-six authors representing Austria, Belgium, France, Ireland, Italy, Germany, The Netherlands, Norway, Spain and Switzerland have expressed their wish to publish their contributions in the present document.

Most of the application fields have been covered by the Pilot Project Campaign and resulted in a number of reports as follows:

– Snow cover	2
– Hydrology	5
– Coastal waters	2
– Geology	8
– Land use	5
– Forestry	9
– Cartography	5

It is hoped that this document will be a valuable tool for further research and studies, and new step towards a coordinated European remote-sensing programme. Within this framework the forthcoming European Earth Remote-Sensing (ERS-1) satellite to be launched in the Summer of 1990 and the Columbus Polar Platform to be in orbit by the middle of the next decade are expected to play a significant role in the Agency's overall Earth Observation Programme.

The editors would like to convey their gratitude to all authors and the National Points of Contact for their full cooperation throughout the preparation of this document.

Gianna Calabresi
Earthnet Programme Office
ESRIN, Frascati, Italy

Duc Guyenne
ESA Publications Division
ESTEC, Noordwijk, The Netherlands

1. Snow Cover

Improved Snow and Glacier Monitoring by the Landsat Thematic Mapper

H. Rott and G. Markl

*Institut für Meteorologie und Geophysik
Universität Innsbruck, A-6020 Innsbruck, Austria*

The significance of the improved spectral and spatial capabilities of the Landsat Thematic Mapper (TM) were investigated in a pilot project within the framework of the ESA/Earthnet Programme. Digital methods were applied for snow mapping in two drainage basins of the Austrian Alps using spectral ratioing of the TM bands 3 and 5 for the compensation of topographic effects. An algorithm was developed for estimating the snow extent in partly cloud covered scenes, based on the altitude distribution of the different surface classes in the cloud-free areas. The accumulation and ablation area of glaciers in the Ötztal Alps, Austria, were derived from TM images at the end of the ablation seasons 1985 and 1986. These data were compared with field measurements of glacier mass balance and with aerial photography. Landsat TM was found an excellent tool for snow mapping in Alpine drainage basins and for investigations of snow and ice areas on Alpine glaciers.

Keywords: Landsat, Thematic Mapper, Snow Cover, Glaciers.

1. Introduction

More efficient management of the water resources from Alpine regions requires improved information on the snow cover and on glaciers. Also for flood warning and for climatological purposes improved data on snow and glaciers are of great interest. Even in the Alpine countries the number of snow measurement stations and the number of glaciers under continuous survey are very limited. Satellite sensors are able to provide areal data on snow and ice which are valuable supplements to in situ measurements. In remote areas satellite data may even be the only information source.

The potential of Landsat for snow and glacier monitoring has been early realised. The main drawback for snow mapping is the weather dependence of the system. In many mountain areas, such as the Alps, the cloudiness during the snowmelt season is high. Improvements in this respect were expected from the Thematic Mapper (TM), because the enhanced spectral capability enables better discrimination of snow and clouds and consequently more accurate snow mapping in partly cloud covered scenes. Another improvement of TM, the higher spatial resolution compared to the MSS, is of particular interest for monitoring the small Alpine glaciers as well as for snow mapping in areas with complex terrain and complex land use pattern.

The significance of the improved spectral and spatial capabilities of TM for snow mapping and for glacier ap-

plications were investigated in a pilot project sponsored by ESA/Earthnet.

2. The Signatures of Snow in TM Bands

Snow shows a wide range of reflectivities in the visible and infrared part of the spectrum, depending on various parameters. The visible albedo of clean snow is very high; small amounts of impurities, such as dust or soot, reduce the albedo significantly. In the near infrared snow reflectance decreases strongly with increasing wavelength and is mainly sensitive to the size of the snow grains (Warren, 1982). At wavelengths $> 1.5 \mu\text{m}$ the albedo is the order of a few percent. The liquid water content of snow has little direct effect on the albedo. In general, however, wet or refrozen snow has a lower near infrared reflectivity than fresh dry snow, because the melt metamorphism results in increased size of the snow grains.

Figure 1 shows the results of measurements of the spectral reflectivity of snow, which were carried out during the spring season with an albedometer in 10 narrow spectral intervals between 500 nm and 1600 nm (Rott and Sogaard, 1987). The measurements were made at solar elevation angles around 40° . The spectral reflectivities for 3 different snow types are shown: (1) clean wet snow, dry; (2) clean snow, wet and frozen, with grain diameters around 0.5 mm; (3) old snow, polluted by dust from glacier moraines. The impurities result in strong

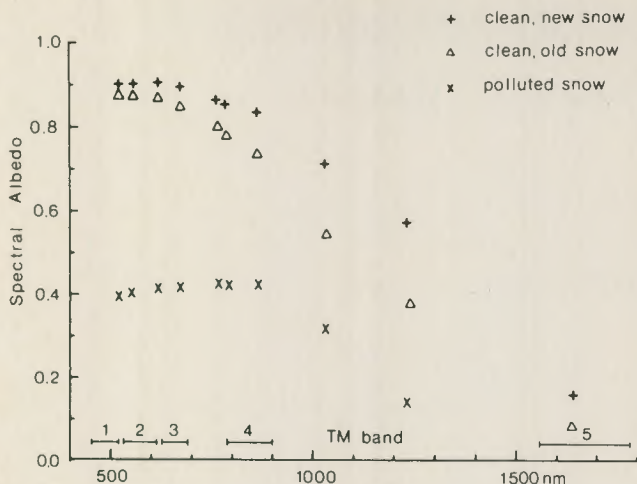


Figure 1. Albedo of snow measured in 10 narrow spectral intervals at solar elevation angles near 40° . The bars show the spectral ranges of the TM bands 1 to 5.

decrease of snow albedo, in particular in the visible part of the spectrum. On glaciers in summer solar albedo values as low as 0.25 were measured for polluted firn snow in extreme cases (Wagner, 1979). The visible albedo is an important quantity for discriminating snow areas from different years on the glaciers.

In the measurements of Figure 1 the snow albedo decreases for clean snow at frequencies above 700 nm and for polluted snow above 900 nm. In the wavelength interval of TM band 5 the reflectivity is only a few per cent. This enables the clear discrimination against clouds, which show high reflectivity. The albedo of most other natural surfaces, with the exception of water, is in the TM bands 5 and 7 higher than the albedo of snow.

The use of TM for quantitative studies of snow reflectance is limited by the low saturation radiances of the visible bands. According to Dozier and Marks (1987) the saturation radiances in per cent of the exo-atmospheric solar irradiance are for the various TM bands:

TM band 1	24.4	} Saturation, per cent of extraterr. irradiance
TM band 2	51.0	
TM band 3	41.2	
TM band 4	61.9	
TM band 5	39.0	
TM band 7	60.6	

Table 1 shows as an example the percentages of saturated pixels for the snow covered areas of an Alpine drainage basin.

The differences in the saturation percentages of the TM bands 1, 2, and 3 are primarily effects of the different gain settings, because the snow reflectivity is similar in these 3 bands. In band 4 the reflectivity of snow is reduced. In the example of the Fotsch basin, the decrease in

saturation between 20 April and 6 May is a result of aging of the snow cover and related decrease of reflectance. New snow fall occurred during the days before 20 April, but no snow fall was observed after this period till 6 May.

Table 1: Percentage of saturated pixels in 2 TM scenes for the snow-covered area of the Fotsch basin.

TM band	Saturated pixels in %	
	20 April 1984	6 May 1984
1	73.8	66.0
2	33.5	16.1
3	40.8	27.3
4	14.8	0.3
5	0.0	0.0

3. Snow Mapping in Mountainous Basins

Key problems for satellite snow mapping in mountainous basins are related to:

- (1) varying solar illumination due to topography;
- (2) obscuration of the earth surface by clouds;
- (3) obscuration of the surface in forests.

Various algorithms with different degrees of complexity have been developed to compensate for these effects (Salomonson, 1983). Manual as well as digital analysis techniques have their particular merits, depending on the application; an outstanding method for all purposes is not available. Digital elevation data might be considered the optimum data base for compensating illumination effects. However, classification methods, which require registration of TM data to digital elevation data, may produce poor results, if the elevation data are not of high quality (Dozier, 1987; Dozier and Marks, 1987). Moreover, if classification is carried out for cloudy scenes, the digital elevation data are of little use for calculations of illumination in the areas shadowed by clouds.

Recognising these difficulties, as well as the fact that no adequate comparative data were available for independent verification of complex classification methods, we applied the band ratio technique to remove the topographic effects. This method is well suited for snow mapping, because the spectral reflectance of snow differs clearly from the reflectance of other surfaces.

The radiance L measured at the satellite can be described by the simplified equation:

$$L = (E/\pi) \tau r + L_a \quad [\text{W m}^{-2} \text{ nm}^{-1} \text{ sr}^{-1}] \quad (1)$$

where E ($\text{W m}^{-2} \text{ nm}^{-1}$) is the solar irradiance at the reflecting surface, r is the surface reflectivity, τ is the total atmospheric transmittance and L_a is the atmospheric radiance in the sensor's field of view due to

scattering. For a given sun position, E and L vary with the local solar incidence angle θ within the TM image: $L=L(\theta)$, $E=E(\theta)$. The ratio of two channels is:

$$\frac{L(1)}{L(2)} = \frac{E(1) \tau(1) r(1) + L_a(1)}{E(2) \tau(2) r(2) + L_a(2)} \quad (2)$$

The additive term L_a can be neglected, if the contribution of the diffuse skylight L_a is significantly smaller than the reflective contribution. This is the case in red and near infrared wavelengths in the clear Alpine atmosphere, if reflection from snow in the direct sunlight is considered. However, in shadow zones diffuse skylight may represent a considerable contribution to the measured signal. Another simplification is possible if two adjacent spectral channels are taken: $\tau(1) \approx \tau(2)$. If the diffuse irradiance at the surface is small compared to the direct irradiance, the ratio of incoming solar radiation in the two channels $E(1, \theta)/E(2, \theta)$ depends only weakly on the local incidence angle of the solar beam θ and the simplification is possible:

$$\frac{L(1, \theta)}{L(2, \theta)} \approx \text{const.} \frac{r(1)}{r(2)} \quad (3)$$

Considering the selection of channels for ratioing, it is evident that the method works best for spectrally adjacent channels and for spectral regions in which atmospheric scattering is weak (Holben and Justice, 1981).

3.1 Snow depletion in an Alpine basin

Digital snow mapping was carried out for an Alpine basin near Innsbruck which is covered by two adjoining Landsat paths. TM data are available for the following 4 dates of the snowmelt season 1984: 20 April, 6 May, 9 July (scene 193/027, quarter 4), 3 August (scene 192/027, quarter 3). On two of these days, 6 May and 9 July, the basin was partly covered by clouds, on the other two days the image is cloud-free.

Figure 2 shows a sketch map of the Fotsch basin, which covers 40.6 km² and rises from 938 m to 3087 m a.s.l. The main part of the basin is lying above the timberline, 20% of the total area are covered by predominantly coniferous forests. The main valley is south-north oriented, which results in significant differences of illumination for the slopes to the right and to the left of the river.

Figure 3 shows a false colour of the Fotsch basin based on the TM bands 5, 4, and 3. The clouds can be easily discriminated from the snow cover, because the cloud reflectance is high in all 3 bands. In TM band 5 the snow-free surfaces show higher reflectivity than the snow areas.

Due to its high reflectance, snow cover can be clearly separated from snow-free areas in the TM bands 1 to 4. TM band 5 is required for snow/cloud discrimination. Various combinations of TM bands were tested for snow

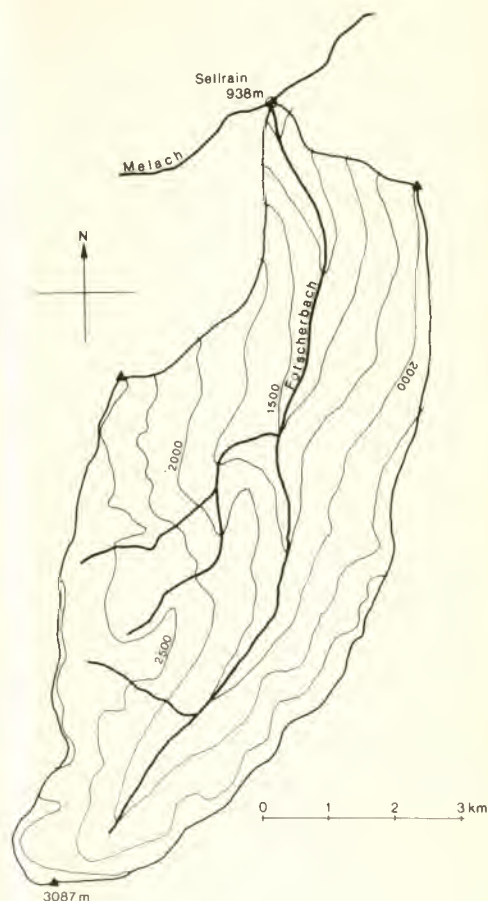


Figure 2. Sketch map of the drainage basin Fotsch (Stubai Alps, Austria) with topographic contour lines of 250 m altitude.



Figure 3. Landsat TM false colour image composite of band 5 (shown in red), band 4 (green), band 3 (blue). Part of scene 193/027, 5 May 1984, Stubai Alps, Austria. The boundaries of the Fotsch basin are shown.

mapping. Ratios of the TM bands 1/5 and 2/5 do not adequately compensate topographic effects. The reason is that contributions by atmospheric scattering are much larger in the bands 1 and 2 than in band 5.

The ratios of the TM bands 3/5 as well as of the bands 4/5 were found useful for reducing topographic effects and for snow discrimination. The ratio 3/5 showed better performance in the shadow zones. The ratio 4/5 enables more accurate snow mapping on sun-facing slopes with patchy snow-cover, because the percentage of saturated pixels is lower in band 4 than in band 3. However, ambiguities between snow and vegetation were found with the ratio 4/5, because some pixels of vegetated areas showed comparatively high values of this ratio. As a whole, the ratio 3/5 showed better results and was finally used for snow classification.

The first step in the snow mapping algorithm is the cloud detection, which is based on the measured radiances in the TM bands 3 and 5. A pixel was allocated to the cloud cover class, if

$$R(TM3) + R(TM5) \geq b_1 \quad (4)$$

R is the planetary albedo in the respective TM band

$$R = \pi L / (\cos \theta_s S_0) \quad (5)$$

where L is the nadir radiance measured at the satellite, θ_s is the solar zenith angle, and S_0 [$\text{W m}^{-2} \text{nm}^{-1}$] is the irradiance on a surface perpendicular to the solar beam at the top of the atmosphere. The threshold value $b_1=0.6$ was found valid for the available TM scenes, in which scattered cumulus clouds had to be distinguished from snow. This value seems to be rather low, but in case of a higher threshold value those parts of the clouds, which are in the shadow of the cloud tops, would not be correctly classified. Confusion between snow and clouds did not occur, because the sum $[R(TM3)+R(TM5)]$ for snow is clearly lower than 0.6 due to the low saturation radiance in TM band 3 and the low snow reflectance in band 5.

Finally, the cloud-free pixels are allocated to the snow cover class if

$$R(TM3) \geq b_2(TM5) \quad (6)$$

The threshold value $b_2=2.7$ was determined by comparing the classification results and the original images. In order to fully assess the accuracy of the snow mapping algorithm, comparison with completely independent data, such as aerial photography, would be required. Independent verification was possible for the glacier studies, described in section 4 of this paper.

Figure 4 shows the results of snow classification for the Fotsch basin on 6 May 1984, based on the TM bands 3



Figure 4. Results of classification based on the TM data of Figure 3. Key to colours: Blue - clouds; White - snow; Green - snow-free.

and 5. The comparison with Figure 3 confirms that the snow surfaces, in the shadow and in the sun, are correctly classified. The scattered cumulus clouds, which are typical for the late morning hours on sunny days in spring, are also accurately shown.

Table 2: Snow cover classification for the drainage basin Fotsch

Classes	Coverage (in per cent of total area)			
	20 Apr.	6 May	9 July	3 Aug. 84
snow cover	98	66	7	1
clouds	0	12	18	0
snow-free	2	22	75	99

The classification results for the Fotsch basin are listed in Table 2 for the 4 TM scenes available in 1984. On 4 May clouds obscured 12% of the area, on 9 July 18%. The main decrease of the snow covered area occurred during the months of May and June, which showed also the peak snowmelt contribution to runoff.

3.2 Snow distribution in a high Alpine basin

The described algorithm was also applied to snow mapping in a high Alpine drainage basin, for which digital elevation data are available in a 30 m grid. The TM data of 9 July 1984 have been geometrically rectified and matched to the elevation data.

Figure 5 shows a false colour display from the rectified TM image of the Ötztal Alps in Tyrol, based on the bands 4, 5, and 7. The boundaries of the basin of the Niederjochbach are plotted. The basin, which has a size of



Figure 5. Landsat TM false colour image composite of band 4 (shown in red), band 5 (green), band 7 (blue). Part ($8 \times 8 \text{ km}^2$) of scene 193/O27, 9 July 1984, Ötztal Alps. Yellow: Boundaries of the Niederjoch basin.

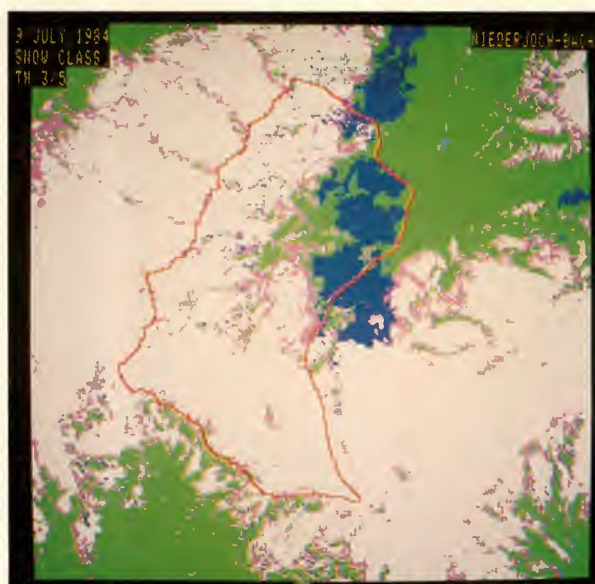


Figure 6. Results of classification based on TM data in bands 3 and 5, corresponding to Fig. 5. Key to colours: Blue - clouds; White - full snow cover; Pink - patchy snow cover; Green - snow-free.

11.5 km^2 and extends over altitudes from 2400 to 3600 m a.s.l., is partly covered by glaciers. Snowmelt starts late in spring, on 9 July 1984 the main part of the basin was still covered by snow. Scattered cumulus clouds developed over the lower parts of the basin, which can easily be separated from the snow areas in the false colour image.

Snow mapping was carried out using the algorithm described in paragraph 3.1. The results are shown in Figure 6. In addition to the classes 'snow-free surfaces', 'clouds', and 'snow cover', a separate class was introduced for the areas near the snow boundary, which show reduced reflectivity in the visible TM bands. This class represents broken snow cover, as concluded from the signatures and from the typical snow patterns in this area in early summer (Rott and Domik, 1985). For full snow cover the threshold value $b_2=4.3$ was selected, for broken snow cover $b_2=2.7$ (in equation 6).

The classification results for the Niederjoch basin are:

clouds	11.9%
snow-free	16.4%
broken snow cover	7.0%
full snow cover	64.7%

The clouds were not equally distributed over the altitude zones of the basin. In order to estimate the snow extent for the cloudy parts of the basin, an algorithm was developed which takes into account the altitude distribution of the snow extent. Matching of the classification

results with the digital elevation data is required. The total area A of the basin was divided in N elevation zones:

$$A = \sum_{i=1}^N a_i \quad (7)$$

For each elevation zone a_i the areal extent of each class was determined:

$$a_i = as_i + ac_i + af_i \quad (8)$$

where as is the areal extent (in per cent of the basin area) of the snow cover, ac of the clouds, and af of the snow-free surfaces. The broken snow cover class was split up equally between the full snow cover and the snow-free class, to reduce the number of parameters. Finally, the cloud area is divided between the snow cover and snow-free classes according to the ratio of the two classes in each altitude zone. This results in the corrected snow extent for altitude zone i :

$$as_i(\text{corr.}) = as_i + ac_i as_i / (as_i + af_i) \quad (9)$$

Altitude steps of 50 m were used for the calculations in the Niederjoch basin. The altitude distribution of the different classes and the corrected values for the snow are shown in Figure 7. Applying equation 9, about one third of the cloud area was allocated to the snow cover, two thirds to the snow-free surfaces. Quantitative assessment of the accuracy of the cloud correction algorithm is difficult, but the visual impression confirms that the convective clouds were located mainly over the snow-free surfaces.

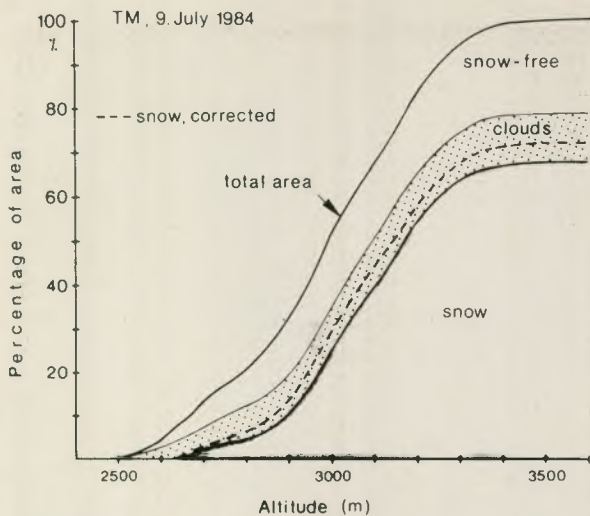


Figure 7. Altitude distribution of the area and of classification results (based on TM data of 9 July 1984) for the Niederjoch basin, Ötztal Alps. Grey - snow cover, stippled - clouds. The hatched line shows the percentage of snow-covered area after correction for the cloud-covered area.

4. Glacier Monitoring

4.1 Glacier investigations in Alpine countries

The Alpine glaciers play an important role as water resource. Many of the annual reservoirs are located at high elevations and are filled by glacier streams. Scientific investigations are carried out on the Alpine glaciers since more than hundred years. Presently, emphasis of these activities is in the field of physical glaciology, on the hydrology of glacierised basins, and on the relation between glaciers and climate. High-resolution satellite images are able to provide valuable support information for these investigations.

Topographic maps of glaciers are the basis for all glaciological work. Due to the dynamic nature of glaciers, repetition of the surveys is required in more or less frequent intervals, depending on a glacier's flow behaviour and mass variations. In the Alpine countries glacier mapping is based on aerial photogrammetry. In Austria the standard repetition period for aerial surveys of glaciers is 7 years, in Switzerland 5 years. These data are used for updating glacier boundaries. Topographic evaluations of the glacier surfaces involve considerable costs and efforts, and are carried out less frequently. Accurate mapping of surface topography of mountain glaciers is not possible with satellite imagery, because very high spatial resolution is required to carry out stereoscopic analysis for snow areas. Imagery from earth observation satellites is used to derive base maps on glacier extent. For many glacier regions outside the Alps satellite imagery is the main data source on the extent of glaciers (Williams, 1983).

The glaciers of the Alps are small in size. The Austrian Alps comprise 925 glaciers with a total area of 542 km²; five of the glaciers are larger than 10 km², 25 glaciers are larger than 4 km². Typically, the annual variations of the glaciers' termini are in the order of a few meters to tens of meters. Consequently, the repetition rate of the aerial surveys is in most cases adequate for monitoring glacier extent. For some of the larger glaciers high-resolution satellite imagery may be of interest for determining areal changes in shorter time intervals. Another advantage of satellite imagery is the synoptic coverage of large areas, enabling quick overview on the glacier areas of whole mountain groups. Regarding the size of the Alpine glaciers, the improved resolution of TM is of key importance for glacier monitoring in the Alps.

The main glaciological application of Landsat imagery in Alpine countries is monitoring of snow and ice areas on glaciers, the extent of which shows much more variations than the extent of the glacier areas. During the summer season the retreat of the snowline on the glaciers is of interest for hydrological and climatological investigations. The extent of the accumulation and ablation areas at the end of the ablation season may provide – at least qualitatively – information on a glacier's mass balance, a basic quantity for glacier studies. The annual mass balance B of a glacier is derived by integrating the specific mass balance b at any point of the glacier over the total glacier area S :

$$B = \int_S b dS = \int_{S_c} b dS + \int_{S_a} b dS \quad (10)$$

For Alpine glaciers the annual mass balance is usually determined for the period 1 October to 30 September. The glacier area S can be divided in an area of net accumulation S_c and of net ablation S_a for the mass balance year: $S = S_c + S_a$.

The determination of the annual mass balance requires extensive field measurements. Consequently, mass balance investigations are carried out only on few glaciers all over the world. One of the longest mass balance records exists for Hintereisferner in the Ötztal Alps (Austria). Figure 8 shows the mass balance analysis for Hintereisferner for the budget year 1984/85. The hatched areas represent the areas with net loss of mass during this year (S_a), the white areas correspond to the accumulation zone S_c . For the period 1 October 1984 to 30 September 1985 the mass balance was negative, which means that the total mass of the glacier decreased. Due to the strong ablation in the summer a complicated pattern of accumulation and ablation was observed in the high parts of the glacier. The analysis was compiled from many point measurements of accumulation and ablation, and from photography of the ablation patterns. The ratio of the accumulation area to the glacier area (S_c/S) was 0.48 for the 1984/85 balance year, the mean specific mass balance \bar{b} ($=B/S$) was -580 kg/m^2 .

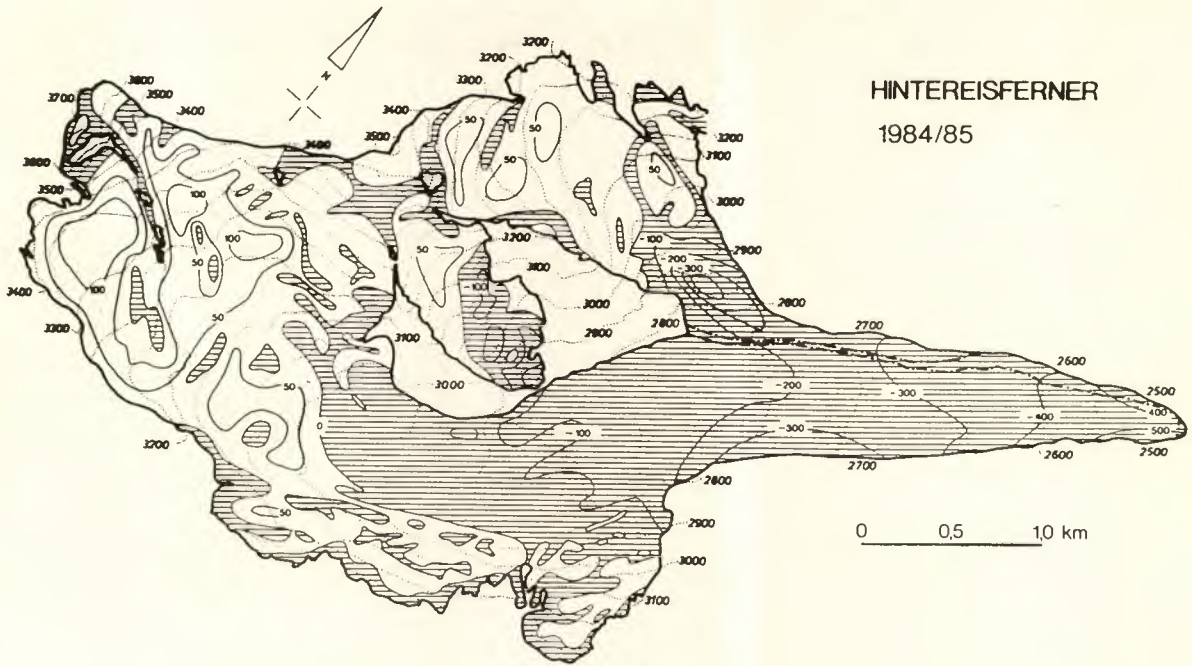


Figure 8. Mass balance analysis for Hintereisferner (Örtal Alps, Austria) for the balance year 1 October 1984 to 30 September 1985. The ablation area S_a is hatched. Contour lines of the specific mass balance b in g/cm^2 .

In Figure 9 the values of \bar{b} for Hintereisferner are plotted versus the mean altitude of the equilibrium line ELA, resp. the ratio S_c/S , for the balance years 1952/53 to 1985/86. The equilibrium line represents the boundary between accumulation and ablation area on a glacier. A clear relation exists between \bar{b} and S_c/S , respectively ELA. Consequently the ratio S_c/S offers a possibility to estimate the mass balance of a glacier.

The relation between S_c/S and \bar{b} shows some variability from one glacier to another, even in the same mountain group (Kuhn *et al.*, 1985; Rott, 1976). Therefore \bar{b} can be estimated only qualitatively for glaciers, on which no mass balance studies have been carried out. For East Alpine glaciers, for example, the ratio $S_c/S=0.7$ is a typical value for balanced mass budget ($b=0$).

Under certain conditions S_c/S can be derived from high-resolution satellite imagery. The first condition is the availability of an image at the end of the ablation season. This has to be the case before the equilibrium line is covered by new snow. On the average over several years the equilibrium line corresponds to the boundary between snow and ice areas at the end of the ablation season (Rott, 1976). In years with positive mass balance accumulation and ablation areas can usually be clearly identified in aircraft or satellite imagery. In negative mass balance years the equilibrium line may be located within the firn area of the glacier and may show complicated patterns as evident from Figure 8. But also in this case accumulation and ablation areas can be frequently discriminated in multispectral satellite imagery, because the albedo is different for snow from the current year and for older firn snow.

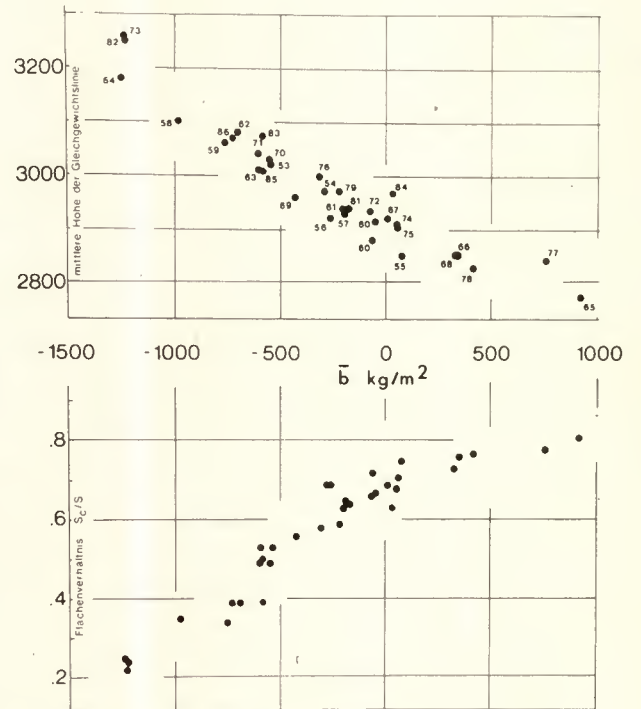


Figure 9. Mean specific mass balance \bar{b} (kg/m^2) versus the mean altitude of the equilibrium line (top) and versus the accumulation area ratio S_c/S (bottom) for Hintereisferner; for the balance years 1952/53 to 1985/86.

Table 3: Mass balance data derived from in situ measurements and accumulation area ratios S_c/S derived from TM images for 3 glaciers in the Ötztal Alps.

Glacier	area S [km ²]	from field measurements		based on TM
		S_c/S	\bar{b} [kg/m ²]	S_c/S
mass balance year 1984/85				
Hintereisferner	9.1	0.48	-580	0.48
Kesselwandferner	4.2	0.75	- 8	0.74
Vernagtferner	9.6	0.60	-112	0.61
mass balance year 1985/86				
Hintereisferner	9.1	0.39	-732	0.39
Kesselwandferner	4.2	0.52	-494	0.59
Vernagtferner	9.6	not available		0.19

4.2 Analysis of East Alpine glaciers by means of TM

TM images have been acquired over the Ötztal Alps (scene 193/027) on 30 September 1985 and 3 October 1986, the end of the ablation season. Parts of these scenes, composed of the bands 4, 3, and 2, are shown in the Figures 10 and 11. In both years the mass balance of the East Alpine glaciers was in general negative. For the 1985/86 balance year the losses in mass were larger than for 1984/85. On Kesselwandferner the glacier boundaries and the boundaries between the snow areas with high albedo and the areas with lower reflectivity (polluted firn and glacier ice) are delineated in Figure 10. On Hintereisferner an area with very low reflectivity is visible between the accumulation area with snow from the year 1984/85 and the ice area. This low reflectance zone represents polluted firn from previous mass balance years and appears also very clearly in the aerial photography (Figure 12). At the end of the balance year 1984/85 the accumulation and ablation areas could be well identified in the TM image because of significant differences in albedo. This is confirmed by the comparison of the TM-derived ratios S_c/S with the ratios from the mass balance studies in Table 3. Hintereisferner, Kesselwandferner, and Vernagtferner are the glaciers of the Ötztal Alps on which mass balance studies are carried out regularly.

Table 4: Average accumulation area ratios S_c/S derived from the TM image of 30 September 1985 for glaciers of different size in the Ötztal Alps

Glacier size [km ²]	No. of analysed glaciers	mean S_c/S	range of S_c/S
5.0 to 17.7	8	0.55	0.44 to 0.68
1.0 to 4.9	9	0.58	0.34 to 0.74
0.2 to 1.0	10	0.63	0.44 to 0.83

In September/October 1986 the separation of accumulation and ablation areas was not so clear. Even on aerial

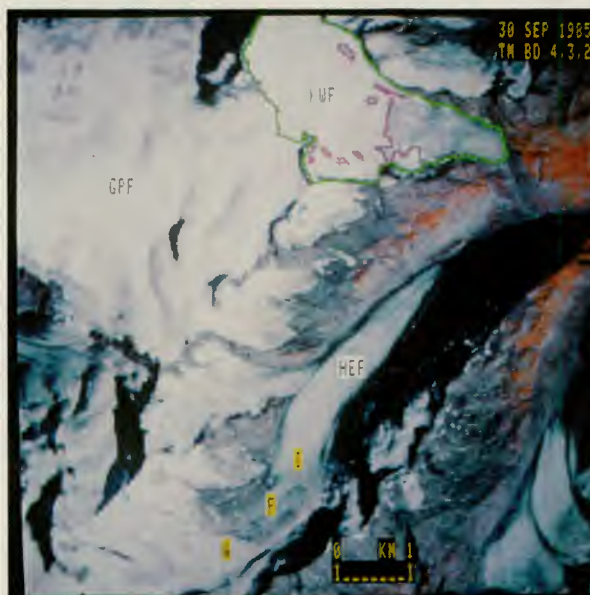
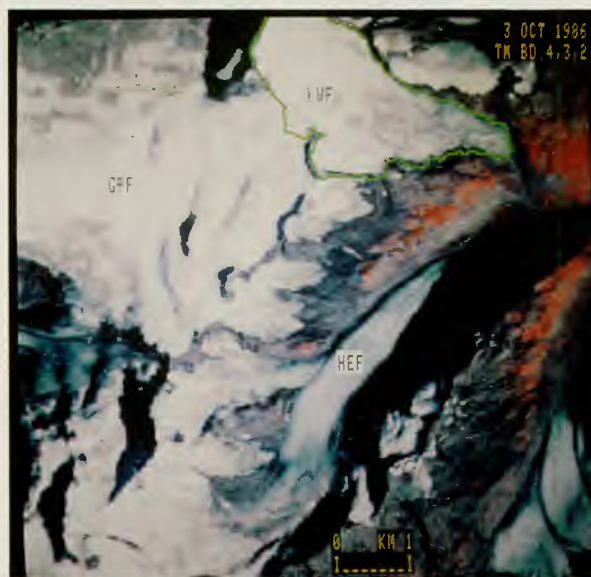


Figure 10. Landsat TM false colour image composite of band 4 (shown in red), band 3 (green), band 2 (blue). Part of scene 193/027, Ötztal Alps. Glaciers: GPF - Gepatschferner, HEF - Hintereisferner, KWF - Kesselwandferner. Green line: glacier boundary of KWF; purple line: equilibrium line. Key to characters on HEF: A - accumulation area, F - polluted firn, I - glacier ice. 30 September 1985.

Figure 11. As Figure 10, 3 October 1986.



photography it is hardly possible to define the equilibrium line, as evident from Figure 13 showing the firn area of the Vernagtferner. Several snow layers with different reflectivities appear at the surface. In situ measurements are required to identify the boundaries between accumulation and ablation areas. In the analysis of the TM image of 3 October 1986 it was assumed that the snow area with the highest reflectivity is the accumulation zone. The TM derived ratio S_c/S for the balance



Figure 12. Oblique photograph of the upper part of Hintereisferner, Ötztal Alps, taken on 13 September 1985. Upper left corner: Weißkogel peak, 3738 m.

year 1985/86 is in agreement with in situ measurements at Hintereisferner (see Table 3). For Kesselwandferner the accumulation area is overestimated in the TM-analysis, because the equilibrium line was located within the snow area of high reflectivity. This is a typical source of errors in years with strong ablation, as realised also in earlier analyses of Landsat MSS images (Rott, 1976).

Mapping of accumulation and ablation areas was carried out for a number of glaciers in the Ötztal Alps based on the TM image of 30 September 1985; some results are summarised in Table 4. Similar investigations are going on with the 1986 TM data. The S_c/S ratios show significant variability from one glacier to another. This is due to various effects, including differences in topography and dynamic response (Kuhn *et al.*, 1985). TM data can help to decide on the representativeness of the mass balance investigations and to draw conclusions on the behaviour of all glaciers of a mountain group.

Various methods were tested for mapping the accumulation and ablation areas in TM images. Pattern recognition techniques on a pixel-by-pixel basis did not prove useful because the reflectivities of the snow surfaces show significant variability from one glacier to another or even



Figure 13. Oblique photograph of part of the firn area of Vernagtferner, Ötztal Alps, taken on 16 October 1986.

on a single glacier. Further difficulties result from the illumination effects due to topography, as evident in Figures 10 and 11. Also photointerpretation methods based on rectified photographic prints of TM data in scale 1 : 50 000 were not useful, because the limited dynamic range of the prints did not allow the separation of snow and ice areas in shadow zones or on slopes with slanting incidence of the solar beam.

The analysis was finally carried out interactively using an image processing system. TM bands 4, 3 and 2 were the basis for the analysis of glacier areas in the sunlight, bands 3, 2, and 1 were used for the shadow zones. Interactive contrast enhancement was carried out separately for each glacier or part of a glacier in dependence of the illumination. Finally, snow and ice areas were tracked with a cursor, and digital data were extracted for the calculation of the area and for statistical investigations. A critical point in the analysis is the selection of the boundary snow/ice, resp. accumulation/ablation area. In order to learn about variations in subjective interpretation, several glaciers were analysed independently by various persons. The results showed good agreement, indicating that the possible range for the definition of the boundaries is limited. The comparison of methods showed for this particular application that a specialist, by implicitly using spectral, textural, and contextual image information, can come to more accurate results than automatic techniques.

5. Conclusions

Landsat Thematic Mapper is an excellent tool for monitoring the seasonal snow cover and glaciers. Digital analysis techniques, based on multispectral signatures of TM data, can be effectively used for snow mapping in mountain basins. TM band 5 enables clear discrimination

of snow and clouds. The high spatial resolution of TM is of great value for snow mapping in Alpine drainage basins because of the rugged topography and the complex land-use pattern. The main drawback of TM for operational snow mapping is the weather dependence of the sensor; this problem can only be overcome with microwave techniques (Rott and Mätzler, 1987).

Due to the limited size of the glaciers, the improved spatial resolution of TM is important for monitoring glaciers in the Alps. TM imagery is a valuable data source for deriving base maps on glacier extent in regions, where no regular airborne surveys are carried out. The main glaciological application of TM in the Alps is monitoring the retreat of the snowline on glaciers during the summer season and mapping the extent of accumulation and ablation areas at the end of the mass balance year.

6. Acknowledgements

This work was supported by the Austrian Fonds zur Förderung der Wissenschaftlichen Forschung, Projekt Nr. S3800, and the Geophysical Commission of the Austrian Academy of Sciences. Landsat data was made available for this study in part by ESA/Earthnet Programme Office within the Landsat TM Pilot Projects. Mass balance data of Vernagtferner were kindly supplied by Dipl.-Met. O. Reinwarth, Glaciological Commission of the Bavarian Academy of Sciences.

7. References

- Dozier J 1987, Remote sensing of snow characteristics in the southern Sierra Nevada, *Proc. of Symp. on Large Scale Effects of Seasonal Snow Cover*, IAHS Publ. No. 166, 305-314.
- Dozier J & Marks D 1987, Snow mapping and classification from Landsat Thematic Mapper data, *Proc. of 2nd Symp. on Remote Sens. in Glaciology*, *Annals of Glaciol.* 9, 97-103.
- Holben B & Justice C 1981, An examination of spectral band ratioing to reduce the topographic effect on remotely sensed data, *Int. J. Remote Sensing* Vol 2, 115-133.
- Kuhn M et al 1985, Fluctuations of climate and mass balance; different responses to two adjacent glaciers, *Zeitschr. f. Gletscherkunde und Glazialgeol.* Bd. 21, 409-416.
- Rott H 1976, Analyse der Schneeflächen auf Gletschern der Tiroler Zentralalpen aus Landsat Bildern, *Zeitschr. f. Gletscherkunde und Glazialgeol.* Bd 12, 1-28.
- Rott H & Domik G 1985, The SAR-580 Experiment on snow and glaciers at the Austrian test site, Final Report of the European SAR-580 Campaign Vol. 2, SA/I.04,E2.85, Ispra, Italy, 217-231.
- Rott H & Mätzler C 1987, Possibilities and limits of synthetic aperture radar for snow mapping and glacier surveying, *Proc. of the Symp. on Remote Sens. in Glaciology*, Cambridge, *Annals of Glac.* Vol. 9, 195-199.
- Rott H & Sogaard H 1987, Spectral reflectance of snow-covered and snow-free terrain in Western Greenland. Manuscript.
- Salomonson V V 1983, Water resources assessment, in: Colwell R N (Ed), *Manual of Remote Sensing*, 2nd Edition, Am. Soc. for Photogrammetry and Remote Sensing, Falls Church, VA, 1497-1570.
- Wagner H P 1979, Strahlungshaushaltsuntersuchungen an einem Ostalpengletscher während der Hauptablationsperiode, I. Kurzwellige Strahlung, *Arch. Met. Geoph. Biokl.* Ser. B 27, 297-324.
- Warren S G 1982, Optical properties of snow, *Reviews of Geophysics and Space Physics* Vol. 20(1), 67-89.
- Williams R S 1983, Remote sensing of glacier, in: Colwell R N (Ed), *Manual of Remote Sensing*, 2nd Edition, Am. Soc. of Photogrammetry and Remote Sensing, 1852-1866.

Multitemporal Snow Classification with TM Data

Ute Gangkofner

Ges. f. Angewandte Fernerkundung, Leonrodstr. 68, 8000 München 19, FR Germany

The areal extent of snow-cover in a part of the Ötztaler Alpen, Austria, is determined on TM images from 20 April, 6 May and 9 July, 1984 by means of supervised maximum likelihood classification. The delineation of the snow-covered area is unambiguous in the July image due to relatively uniform illumination conditions. Besides that, the snowline is completely above the treeline on that date. The earlier images are more difficult to interpret on shady slopes and in forests with uncertain snowcover. The April and especially the May image contain considerably more variance in snow reflection than the July image, and only the April image shows substantial differences in thermal radiation within the snow-covered area. Interpretation is severely restricted by saturation: TM1 totally saturates over snow, TM2 and especially TM3 largely, and even TM4 saturates to some extent. Besides snow-mapping, the major vegetation types in the July image were classified. Classes for alpine meadows, alpine tundra, forest and the manured meadows in the valley floors were established.

TM band 5 proved to be of major importance not only for snow-cloud discrimination, but also for differentiation within the snow-covered area and the vegetation types.

1. Introduction

Since the launch of the first weather satellites in the 1960's snow-mapping from satellite images has been broadly developed. Especially the Landsat and the NOAA satellite systems with improved spatial and spectral resolution caused a tremendous increase of snow-mapping investigations. A variety of techniques was applied to snow-mapping including optical-mechanical, optical-electronical and digital interpretation methods⁽¹⁶⁾. Digital methods are indispensable when small reflectance differences within the snow surface are to be detected and mapped consistently. Most research was carried out in mountainous regions, where the retreat of the snowline, variable snow surface conditions and the changing areal extent of snow-cover are of scientific and in many places also of economic interest.

The major practical application of areal snow-cover information is its implementation in snowmelt-runoff models for water management purposes. This is of special significance in areas with snow as a major contributor to the water demand. So the USA, Canada, Japan, New Zealand, USSR, Austria and Switzerland belong to the earliest applicants of snow-mapping techniques⁽¹⁶⁾. Especially the USA, Norway and Switzerland contributed largely to the publications in this field^(1,4,8,10,11,12,14).

Among the variety of snowmelt-runoff models the SRM developed by Martinec (Martinec-Model) is frequently cited and was successfully tested under a broad range of geographical and hydrological conditions^(6,9,10).

2. Objective

The objective of this study is the multitemporal analysis of spectral reflectance and mapping of the areal extent of snow-cover by means of digital image interpretation techniques. The July image was additionally used for classifying major vegetation types and for demonstrating TM's spectral ability to separate clouds from snow.

3. Image Data

Landsat-5 TM data from 20 April, 6 May, and 9 July 1984 were evaluated (P193, R24, quarter 3 and 4). Since TM band 1 was almost completely saturated over snow, it was not used. The April image is cloud-free, the May image contains a few clouds and from the July image about 10% are cloud-covered.

4. Study Area

The study area belongs to the Ötztaler Alpen, Austria, which in turn are part of the relatively dry Central Alps (Fig. 1). The area comprises a 512 by 512 pixel subimage covering about 236 km². Elevation ranges from about 1300 m a.s.l. up to 3400 m. The area is mainly composed of metamorphic rocks building up a relatively smooth alpine relief. Vegetation zones comprise forests (spruce, larch, cembra pine), alpine tundra, alpine meadows and small stands of riparian vegetation. The meadows on the valley floors and on the lower slopes are being cultivated and the upper slopes are widely used for pasture.

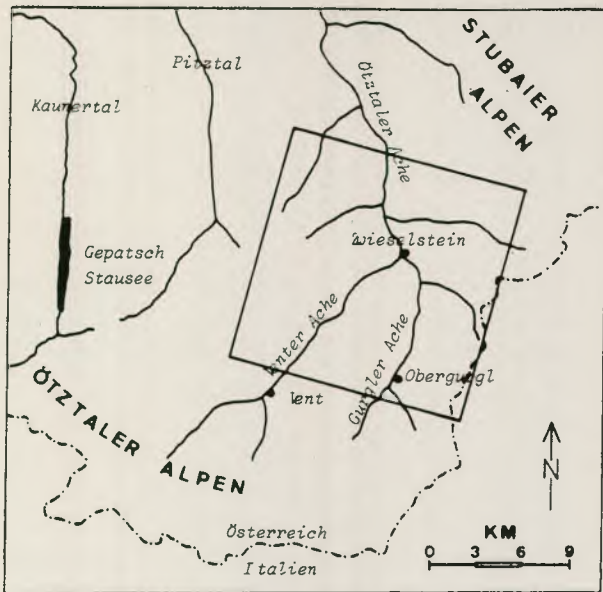


Figure 1. Study area

5. Reflection Properties of Snow

According to Häfner⁽⁵⁾, snow reflectance is affected by the underground up to 30 cm depth of snow. Muri⁽¹²⁾ considers the upper 10 cm most significant for snow reflection. In laboratory measurements O'Bryan and Munis⁽¹³⁾ found that a snowpack of 5–6 cm was enough to prevent underground reflection.

Figure 2 shows laboratory snow reflectance curves and the effect of snow aging. Both snow samples reflect more than 95% in the visible part regardless of their physical condition. Reflectance is decreasing all over the near IR, but in this part of the spectrum the nearly fresh snow reflects more strongly than the older snow. Generally snow reflectance decreases in the near IR during snow aging, which doesn't affect the reflection in the visible part. There only snow pollution and snow surface morphology are important. From the single processes of snow aging, the increase of grain size is considered the most important for the decreasing reflection in the near IR⁽²⁾. O'Bryan and Munis also found that the reflectance of snow with a thin ice crust stays about constant from 1.4 μm toward longer wavelengths.

From Figure 2 it can be seen that TM bands 4 (0.74–0.90 μm), 5 (1.55–2.75 μm) and 7 (2.08–2.35 μm) are spectrally suited to discriminate various snow surface conditions while the visible bands serve for delineation of the snow-covered area.

In reality, snow reflection on satellite images is modified by topographic and atmospheric factors, geometric and radiometric sensor restrictions, and interpretation is complicated in areas covered by clouds, forests, mountain shadows and on weakly illuminated slopes.

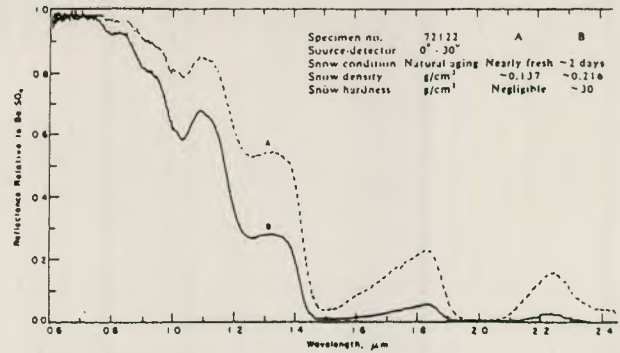


Figure 2. Snow reflectance. O'Bryan and Munis 1975, p 351

6. Image Analysis

The image processing was performed with the DIBIAS system (Digital interactive Image Analysis System) at DFVLR, Oberpfaffenhofen (near Munich).

The subimage analysed was selected based on the snow-coverage on 20 April when snow-free areas reached about 1500 m a.s.l.

Spectral Reflection of the Snow-covered Areas

In the first step, the images were statistically analysed and several enhancement products were derived, allowing optimised differentiation of specific image features. The enhanced images were used for the definition of training areas. Figure 3 shows a band 4-3-5 (RGB) composite of the May image. It was maximally stretched within the snow-covered area, thus leaving no gray-values for differentiation in the snow-free area. In sun-facing slopes, snow appears yellow due to saturation in band 3 and band 4. By contrast, all green pixels indicate dominance of band 3. This happens on shady slopes, in the lower parts of sun-facing slopes and along rock outcrops or otherwise exposed places of sunny slopes. The white areas (not to be confused with the clouds in light blue) on top of the mountains in the left (Weißkamm, some are also on the middle ridge, the Ramolkamm) coincide largely with glaciers which were snow-covered on all imaging dates. White means saturation in band 3 and band 4 and relatively high reflection in band 5. This may be due to a thin ice crust (Firnspiegel) which causes reflection to stay constant from 1.4 μm on, as was mentioned above.

The same phenomenon was encountered in the April image, but there the high reflectance in band 5 (relatively high, absolute gray values were around 50 to 60 at most over snow) extended considerably more downslope. Therefore, one could argue that surface-snowmelt on 20 April did not reach as far upward as on 6 May. This is supported by the reflection in band 4 which saturates all over the upper sunny slopes in the April image but shows less saturation in the May image and almost none

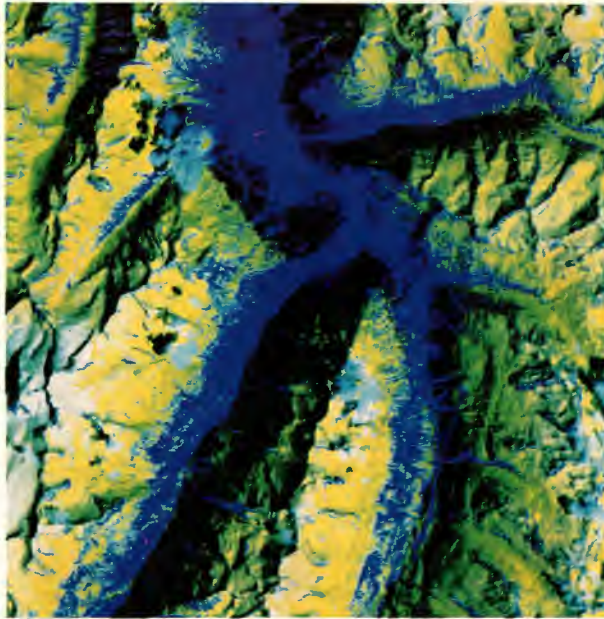


Figure 3. Enhanced colour composite 4-3-5. (6 May 1984)

in the July image. In the latter the reflection in band 5 is low (around 10 gray values) everywhere.

In general, a downslope decrease of snow-reflection was observed in TM band 2, 3, and 4 on all imaging dates. Unfortunately, no reliable conclusion can be drawn out the image data alone, since they were not radiometrically corrected and are therefore not absolutely comparable. However, the temporal and spatial differences of the snow reflectance conform to the expected snow-conditions and spatial changes of snow depth.

Table 1 shows the percentages of saturated snow-pixels in the complete image (1a) and relative to the snow-covered area (1b), determined by means of the multispectral classification (not including snow-boundary areas and snow-covered forests). Saturation is most severe in TM3, followed by band 2, but band 4 is also affected to a high degree. This means that the differentiation of various snow surface conditions with the TM is radiometrically somewhat limited, unless the saturated areas really do not show any variation. The saturation percentages differ substantially from Dozier's⁽²⁾ results with Landsat 4 TM-Dates from the Sierra Nevada, California. Dozier obtained 48.5% saturation in band 1, 0.18% in band 2, 1.55% in band 3 and 0.002% in band 4.

Table 1a. Proportion of saturated pixels in the total study area

Date	TM 2	TM 3	TM 4
20-4-84	41.7	52.3	19.2
6-5-84	30.7	42.2	6.1
9-7-84	4.1	9.4	—

Table 1b. Proportion of saturated pixels in relation to snow-covered area

Date	TM 2	TM 3	TM 4
20-4-84	60.7	76.1	27.9
6-5-84	54.7	75.2	10.9
9-7-84	26.1	59.9	—

Snow-boundary Zone, Snow-covered Forests

Owing to the relatively fine radiometric and geometric resolution of the TM the variance of gray values in the snow-boundary areas is very high. This is especially true for the May image, where the snow-boundary zone covers all kinds of different surface types. On the July image, on the other hand, the snow-boundary zone lies completely in the alpine meadows, rocks and debris. Also illumination conditions are by far more uniform by that time. Thus the identification of the snow-boundary zone is unambiguous on the complete July image and on the sun-facing slopes of the earlier images. On the opposite slopes however, even though cast shadows are largely lacking, it is more difficult to visually separate snow from snow-free areas in steep and rocky terrain. The same applies to snow-covered forest. In many places, mainly on shady slopes, it can only be visually associated to snow-covered areas by comparison with clear-cut or unforested areas nearby. However, the ratio TM 3/4 seems to be a good means to separate snow-covered forest from snow-free forest, because the ratio values are distinctly higher in the snow-covered forests.

Vegetation on the July Image

For vegetation interpretation the colour composite 5-4-3 (5-4-2) was used and specifically contrast-enhanced (Fig. 13). Only major vegetation types were tried to be separated. The visually most distinct vegetation elements are the manured meadows on the valley floors and on the lower slopes due to their outstanding reflection in TM4. Also the riparian vegetation along small creeks and moist depressions is visible in spite of its limited areal extent. The zonal aspect (in terms of elevation) of vegetation patterns is indicated by an upslope transition from the greenish areas with relatively high reflection in TM4 (alpine tundra, pasture areas, meadows) to the red zone (relatively high gray-values in TM5) consisting of alpine meadows with upward increasing proportions of rocks and debris.

Principal Component Analysis

Form the eigenvalues of the principal components the proportion of total variance contributed by the single components was computed (Table 2). The variance contribution of the first component decreases with increasing proportion of the snow-free area, because the first principal component represents the major brightness differences between snow and snow-free areas. In the first principal component image, contrast between snow and

snow-free areas is enhanced on sunny slopes, but reduced on shady slopes and within the snow-covered area. The second principal component represents largely TM5. But like the first and also the third component, it shows little contrast between snow and snow-free areas on shady slopes.

Table 2. Variance contribution of the principal components

PC	20-4-84	6-5-84	9-7-84
1	94.5	92.0	79.3
1 + 2	97.9	97.6	97.5
1 + 2 + 3	99.4	99.5	99.2

7. Maximum Likelihood Classification

Training Statistics

The major differences between the reflection of the snow classes are caused by the varying illumination angles. Figures 4 through 6 show the arithmetic means of the training signatures for snow and snow-boundary classes. As mentioned above, only the April and especially the May snow classes vary in band 5 and in band 7 respectively. In the July image only snow 6 deviates in band 5 (and 7) because of its thin cloud cover. In the thermal band (TM6), the April snow classes vary remarkably as compared to the very small differences in the May image and the almost negligible variations in the July image. High mean values in band 5 (snow in the highest elevations) are paired with relatively low means in band 6 in the April and May snow classes. This probably reflects the increasingly uniform snow-surface temperatures from April to July, but may also be partly due to the increasing water-vapour content (indicated by the meteorological records) and increasingly uniform illumination conditions.

Standard deviations (SD) of the snow classes and especially of the snow-line classes are very high: TM3 has the highest SDs (between 10 and 20), followed by TM2 and TM4. In bands 5, 6 and 7, SDs range from 2 to 6 with TM5 having the highest and TM6 the lowest SDs. For the snow-line classes, SDs up to 40 (TM3) were obtained.

Figure 7 shows signature plots of the cloud classes. Curve 1 represents a big cloud with the thinner edges included, curve 2 a thin cloud over snow, curve 3 is typical for pure cloud pixels and curve 4 shows a mixed cloud/vegetation signature.

Figure 8 contains the vegetation signatures of the July image. They represent the reflection characteristics of the major vegetation formations described earlier. The classes veg.1, veg.2, veg.3 contain mainly alpine tundra, but also some meadows and riparian vegetation.

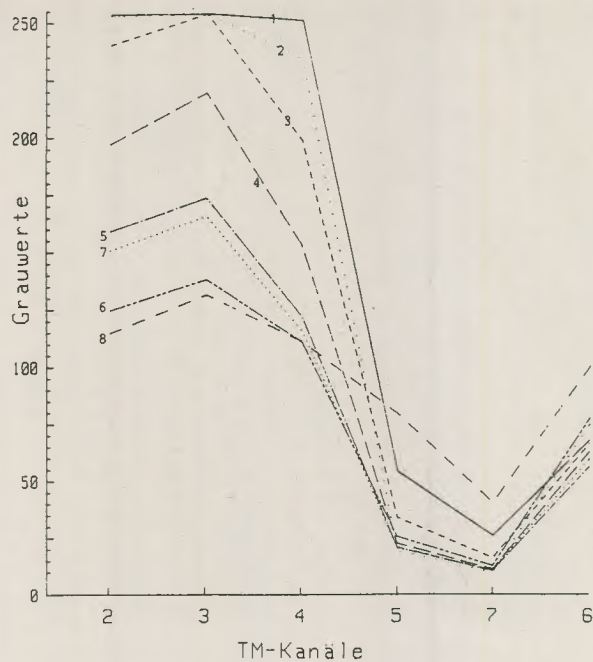


Figure 4. Signatures of the snow and snow-boundary (sb) classes. (20 April 1984)

1-5 = snow 1 - snow 5
6 = snow-covered forest
7, 8 = sb 7, sb 8

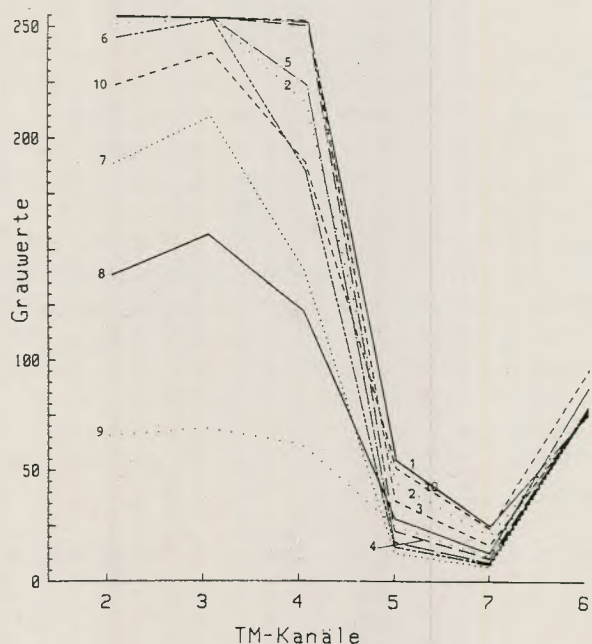


Figure 5. Signatures of the snow and snow-boundary (sb) classes. (6 May 1984)

1-7 = snow 1 - snow 7
8-10 = sb 1 - sb 3

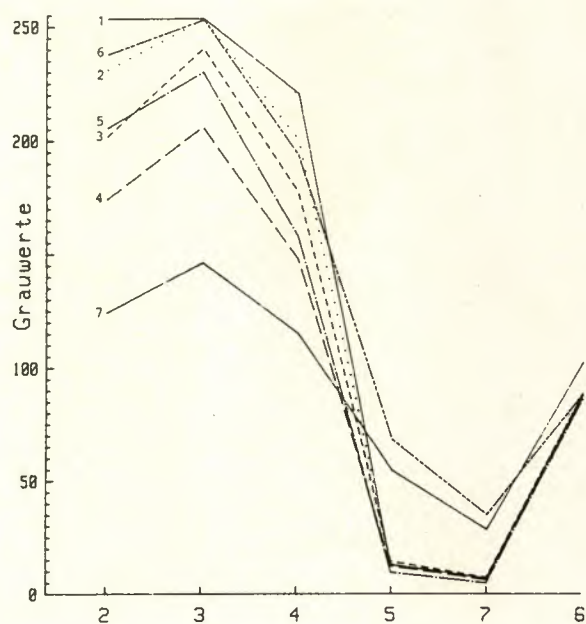


Figure 6. Signatures of the snow and snow-boundary (sb) classes. (9 July 1984)
 1-6 = snow 1 - snow 6
 7 = sb

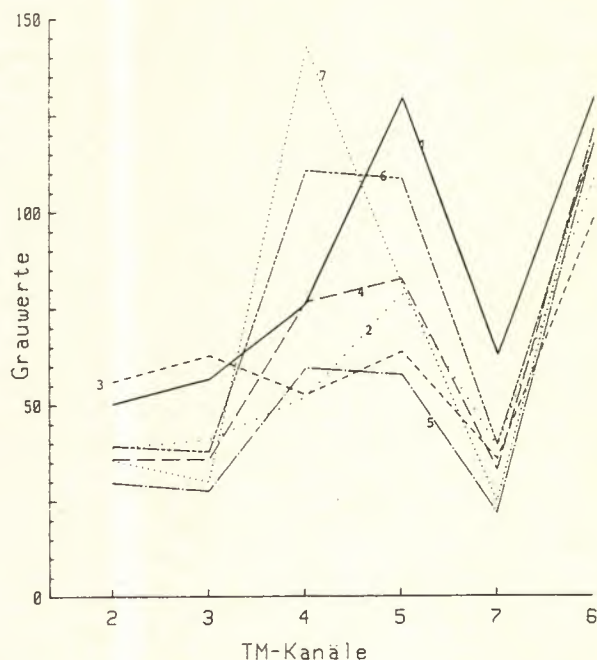


Figure 8. Signatures of the vegetation classes (9 July 1984)

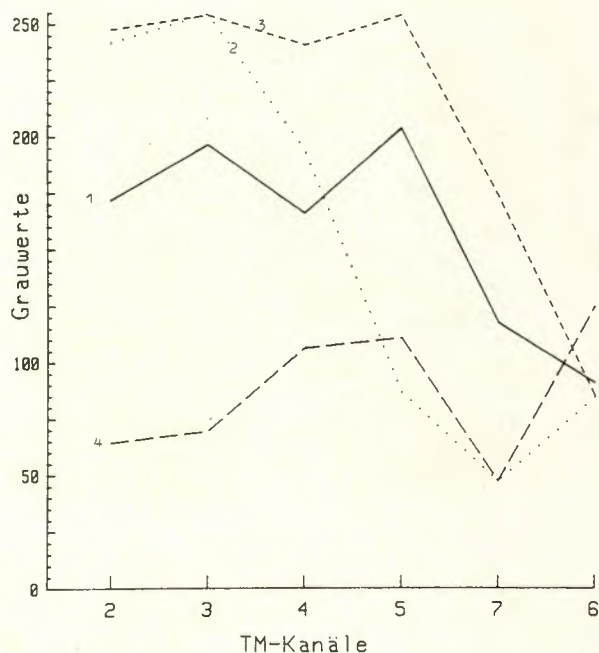


Figure 7. Signatures of clouds (9 July 1984)

Confusion Matrices

The classification results for the training fields are based on classifications using TM band 2, 3, 4, 5 and rejection thresholds of 2.5 SD. Tables 3 through 5 show the confusion matrices. While misclassifications among the snow classes are of no concern to the snow-covered area, there are problems with one snow-line class in the April and in

the May image. Only very few snow- or snowline-pixels were classified into snow-free areas. In the May and the July image, the rock- and shadow-classes should be better defined.

Classification Results

Figure 10, 12 and 14 show the classified images. Five classes were used for the snow-free areas in the May image and two for the April image, not including forest. When comparing the valleys of the Gurgler Ache and the Venter Ache, the retreat of the snow-covered area is clearly more advanced in the latter in the April and May image. Actually Vent (in the Venter valley south of the study area) has about 100 mm less precipitation than Obergurgl in the Gurgler valley (840 mm) and is covered by snow 157 days a year in the average whereas Obergurgl has a 184-day statistical snow-cover period^(7,3).

For the snow-boundary area, the actual snow cover must be estimated. Assuming an average snow cover of 50% for those areas, the following figures result:

- 20/4/84: 84.3 snow-covered
- 6/5/84: 60.7 snow-covered
- 9/7/84: 28.1 snow-covered

In Figure 15 a small portion of the TM snow-boundary pattern is compared with a detailed snow-boundary presentation resulting from large-scale aerial photographs from 4 July 1977. The TM-derived map renders the major characteristics of the snow pattern in spite of the reduced resolution.

	snow1	snow2	snow3	snow4	snow5	snow/forest	sb1	sb2	rock	forest	snowfree	not class.
snow1	96.0	2.0	1.0				0.5	0.5				
snow2		95.0	2.0	1.0				2.0				
snow3			96.0	2.0	1.0		0.5	0.5				
snow4				85.0	14.0			1.0				
snow5					14.0	71.0		14.0	1.0			
snow/forest						99.0	4.0	6.0				
sb1				6.0	39.0	2.0	50.0	3.0				
sb2						4.0	94.0					2.0
rock				0.5	1.0	2.0	96.5					
forest									99.0	1.0		
snowfree								1.3			98.7	

Table 3 Confusion matrix, April 20, 1984

	snow1	snow2	snow3	snow4	snow5	snow6	snow7	sb1	sb2	sb3	clouds	shadow	rock	forest	snowfree
snow1	97.5	2.0													0.5
snow2	8.0	86.0													4.0
snow3			99.0	0.5											0.5
snow4	0.5	2.0	90.5	7.0											
snow5				8.0	85.0	6.0									1.0
snow6					7.0	89.0	3.0								1.0
snow7							99.0	0.5							0.5
sb1								92.0	6.0	2.0					
sb2									3.0	96.0					1.0
sb3	1.0	14.0	8.0	13.0	2.0		5.0	47.0							
clouds											2.5	93.3	4.3		
shadow								4.5				90.0	5.5		
rock				0.3	2.0		0.6	1.8	1.8	0.7	4.0	88.8			
forest								0.6	3.4					96.0	
snowfree								0.2	0.1					0.2	99.5

Table 4 Confusion matrix, May 6, 1984

	snow1	snow2	snow3	snow4	snow5	snow6	sb	clouds	shadow1	shadow2	rock	alp. meadow	Vegl/2/3	forest	cut. meadow
snow1	96.6				2.9	0.5									
snow2	6.8	86.6	5.1			1.5									
snow3		8.5	77.5	11.5		2.5									
snow4			3.5	93.1	0.4	3.0									
snow5	3.4				95.6		1.0								
snow6	1.0	1.0			1.0	95.5	1.5								
sb		0.8	0.7		0.5	96.3					1.7				
clouds						0.3	98.5							1.2	
shadow1								97.0		3.0					
shadow2									1.0	82.0	7.0			10.0	
rock						7.0				11.0	79.0	3.0			
alp. meadow											3.0	97.0			
Vegl/2/3							0.3				1.2	91.8	6.4	0.3	
forest									2.2	0.1		1.8	95.9		
cut. meadow												1.5	0.5	98.0	

Table 5 Confusion matrix, July 9, 1984

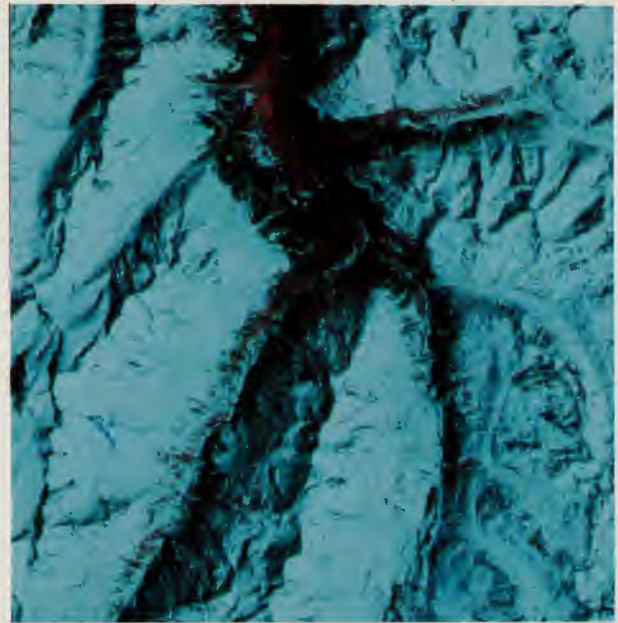


Figure 9. Colour composite 5-4-3 (20 April 1984)

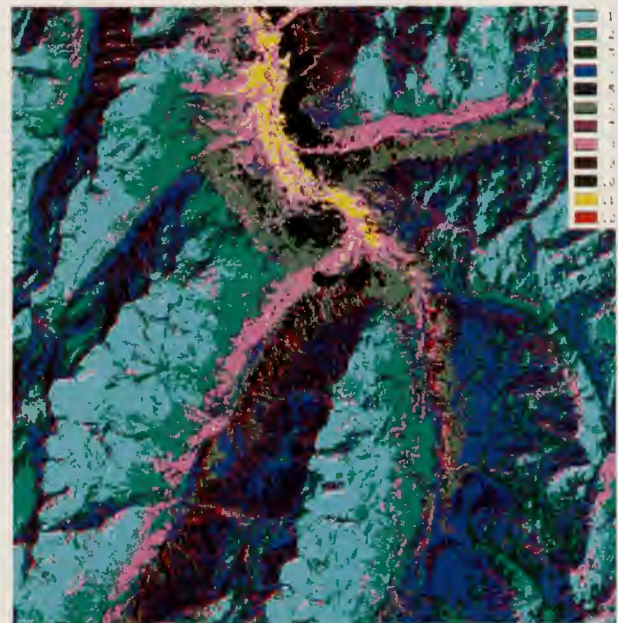


Figure 10. Classified image (20 April 1984)

- 1 = snow1
- 2 = snow2
- 3 = snow3
- 4 = snow4
- 5 = snow5
- 6 = snow/forest
- 7 = sb1
- 8 = sb2
- 9 = rocks
- 10 = forest
- 11 = snow-free
- 12 = not classified



Figure 11. Colour composite 5-4-3 (6 May 1984)

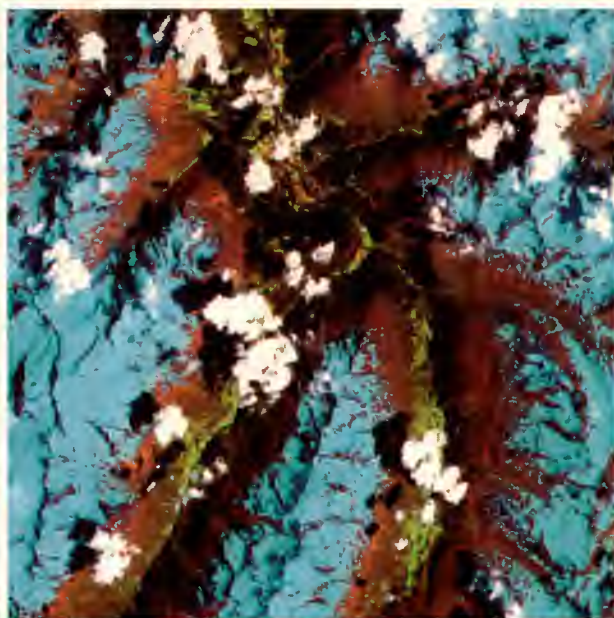


Figure 13. Colour composite 5-4-3 (9 July 1984)



Figure 12. Classified image (6 May 1984)

1 = snow1	5 = snow5	9 = sb2
2 = snow2	6 = snow6	10 = clouds
3 = snow3	7 = snow7	11 = cloud-shadows
4 = snow4	8 = sb1, sb3	12 = rocks

13 = forest
 14 = snow-free
 15 = not class.

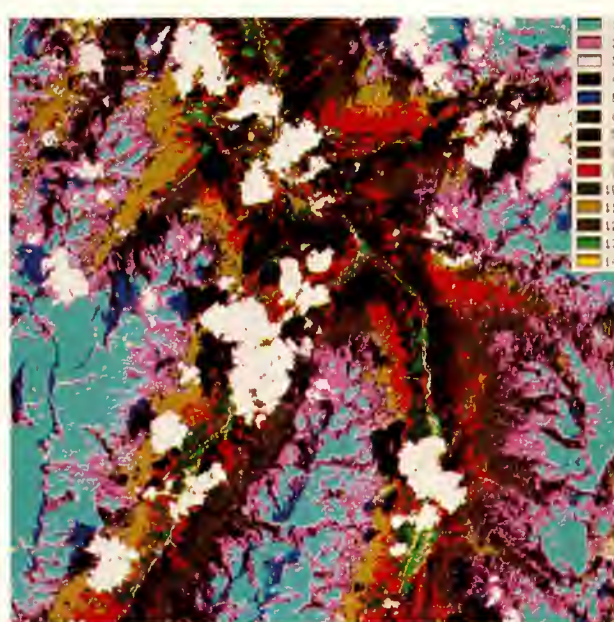


Figure 14. Classified image (9 July 1984)

1 = snow	6 = rocks
2 = sb	7 = forest
3 = clouds	8 = Veg.2
4 = cloud-shadows2	9 = Veg.1
5 = cloud-shadows1	10 = Veg.3

11 = alp. meadow1
 12 = alp. meadow2
 13 = cultivated meadows
 14 = not classified

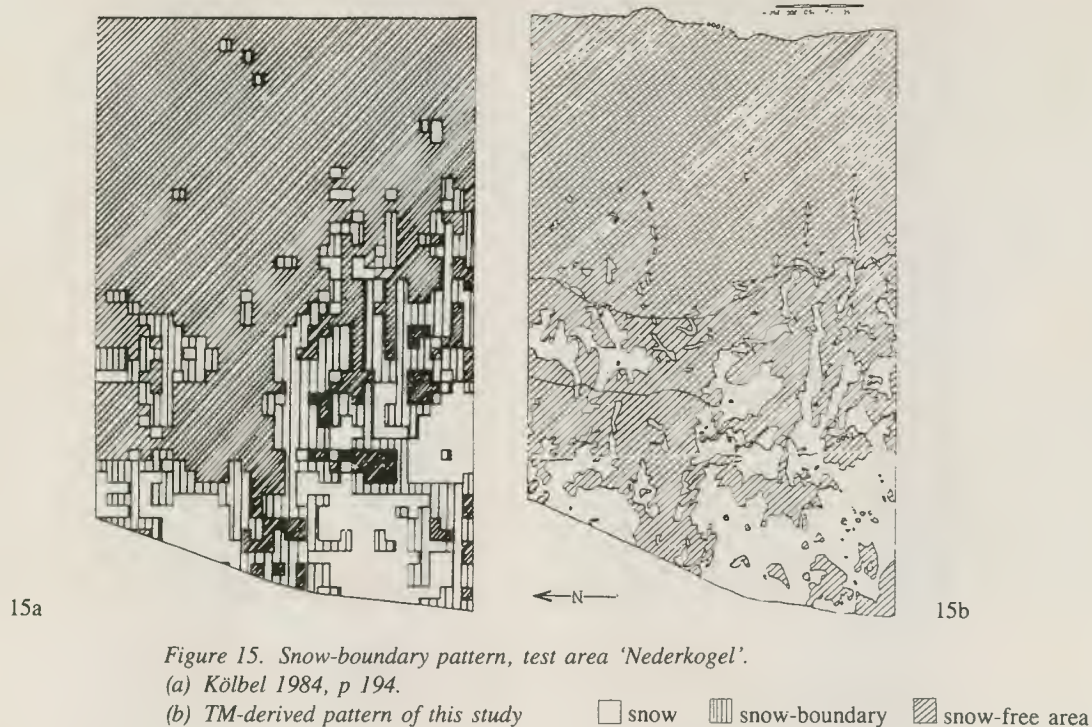


Figure 15. Snow-boundary pattern, test area 'Nederkogel'.

(a) Kölbl 1984, p 194.

(b) TM-derived pattern of this study

□ snow ▨ snow-boundary ▩ snow-free area

8. Discussion and Conclusion

This study was only a demonstration of the TM capability for snow mapping. To take full advantage of the TM sensor and the digital method of snow mapping, the images had to be registered to a map and digitally combined with topographic and additional information. Then, for example, cloud-covered areas could be digitally associated to snow or any appropriate class depending on the elevation, slope aspect or other known properties of the cloud-covered areas.

In practice, many factors have to be taken into consideration when selecting an appropriate sensor/interpretation method for snow mapping. For drainage areas down to 10 km² size, the much cheaper Landsat MSS data may be sufficient⁽¹⁵⁾. For large areas (in Norway from 500 km² on) NOAA AVHRR, formerly VHRR data, have been applied successfully⁽¹⁴⁾. The latter have the advantage of daily coverage which compensates for the lacking 1.6 μm band for cloud snow discrimination. Missing spectral separability of snow and clouds can also be compensated for by visual interpretation and mechanical snow mapping since the human interpreter uses shape, texture and distribution patterns in addition to spectral criteria.

Concerning ground resolution, TM data may be even disadvantageous in snow-boundary areas or otherwise inhomogeneous areas, because in comparison to lower-resolution sensors, they have higher variances which are difficult to handle in classifications (at least as long as only spectral criteria are applied).

Scientific Applications

If not for detailed ecological studies such as⁽⁴⁾, the TM ground resolution of 30 m should be enough to correlate snow-retreat patterns with topography and vegetation patterns on a somewhat more generalised level. For vegetation classification it seems that the major vegetation formations like alpine meadows, tundra, meadowed meadows and forest can be separated by means of supervised ML-classification.

References

1. Bowley C.J., Barnes J.C. and Rango A., Application Systems Verification and Transfer Project. Vol. III: *Satellite Snow Mapping and Runoff Prediction Handbook*. NASA Technical Paper 1829 (1981).
2. Dozier J., Snow reflectance from Landsat 4 Thematic Mapper. *IEEE Transactions on Geoscience and Remote Sensing*, Vol. GE-22, No. 3 (1984), p 323-328.
3. Fliri F., Ein Beitrag zur Kenntnis des Jahresganges der Schneehöhe im Alpenraum von Tirol. *Zeitschrift für Gletscherkunde und Glazialgeologie*, Bd. 16 (1980), H. 1, p 1-9.
4. Häfner H., *Bibliography of Snow Mapping with Remote Sensing Techniques*. Remote Sensing Series, Vol. 2, Department of Geography, University of Zürich, 1979.
5. Häfner H., *Snow Surveys from Earth Resources Satellites in the Swiss Alps*. Remote Sensing Series, Vol. 1, Department of Geography, University of Zürich, 1980.

6. Herrmann A., Ablation der temporären Schneedecke unter besonderer Berücksichtigung des Schmelzwasserabflusses. II. Schneedecke eines randalpinen Niederschlagsgebiets. *Deutsche Gewässerkundliche Mitt.* 19 (1975), H. 6, p 158-167.
7. Kölbl H., *Die Schnee-Ausaperung im Gurgler Tal (Ötztal/Tirol). Ihre Erfassung, Darstellung und ökologische Aussage.* Dissertation, Universität München, 1982. Salzburger Geographische Arbeiten, Band 12, Institut für Geographie der Universität Salzburg, 1984.
8. Lichtenegger J., Seidel K., Keller M. and Häfner H., Snow Surface Measurements from Digital Landsat MSS Data. *Nordic Hydrology* 12 (1981), p 275-288.
9. Martinec J., Rango A. and Major E., *The Snowmelt-Runoff Modell (SRM) User's Manual.* NASA Reference Publication 1100 (1983).
10. Martinec J., Modelling the Snow Accumulation and Snowmelt Runoff. In: *Schneehydrologische Forschung in Mitteleuropa.* DVWK Mitteilungen, Deutscher Verband für Wasserwirtschaft und Kulturbau, Bonn, 1984, p 59-76.
11. Meier E., Unterscheidung verschiedener Schneetypen im Multispektralscannerbild. *Remote Sensing Series*, Vol. 6, Dept. of Geography, Univ. of Zürich, 1982.
12. Muri R., *Verfahren zur großräumigen, automatisierten Klassifikation von Schnee; ein Beitrag zur Auswertung multispektraler Fernerkundungsdaten.* Dissertation, Universität Zürich, 1981.
13. O'Brien H.W. and Munis R.H., Red and Near-Infrared Spectral Reflectance of Snow. In: *Operational Applications of Satellite Snowcover Observations*, NASA SP-391 (1975), p. 345-360.
14. Odegaard H.A., Andersen T. and Ostrem G., Application of Satellite Data for Snow Mapping in Norway. In: *Proc. of the Final Workshop on the Operational Applications of Satellite Snowcover Observations*, Nevada, 1979, p 93-106.
15. Rango A., Martinec J., Foster J. and Marks D., Resolution in Operational Remote Sensing of Snowcover. In: *Proc. Symp. on Hydrological Applications of Remote Sensing and Remote Data Transmission*, IUGG General Assembly, IAHS Publ. No. 145 (1983), p 371-382.
16. *Snow Survey from Earth Satellites. A Technical Review of Methods*, Report on WMO/IHP Projects, WMO No. 353, Genf, Schweiz, 1973.
17. Guck U., *Auswertung von digitalen, multitemporalen Landsat-5 Thematic-Mapper Daten zur Erfassung der Schneefläche und anderer Oberflächenarten im hinteren Ötztal unter besonderer Berücksichtigung der wasserwirtschaftlichen Bedeutung von Schneeflächendaten.* DFVLR-FB 86-46 (1986).

2. *Hydrology*

Utility of Thematic Mapper Data for National Survey of Irish Lakes

B.C. Reardon

*Department of Computer Science,
University College, Belfield, Dublin 4, Ireland*

M.L. McGarrigle

An Foras Forbartha, Regional Water Laboratory, Castlebar, Co. Mayo, Ireland

Ireland, in which lakes abound in a far greater concentration than in any other country of the European Economic Community, is unable to devote sufficient resources to mount an ongoing ground-based survey to monitor all these lakes adequately. Currently, out a total of more than 4000 lakes, about 40 are monitored on a regular basis. As in the USA, Canada, and the Scandinavian countries, remote sensing techniques have been applied in Ireland to estimate water quality parameters, such as chlorophyll and Secchi disc values. The authors of this paper published a report in July 1986, in which they examined the problems arising in the use of such techniques, and, for MSS data, showed that there was significant correlation between the image data and ground-based measurements, as shown by regression analysis.

The aim of the current paper is to investigate the utility of TM data, with its increased number of narrower spectral bands and better spatial resolution, to see whether this data is more suitable for water quality monitoring purposes. Modifications to the software system used to extract lake statistics from the TM data are described, and a number of problems discussed. Since, due to lack of ground truth closely coincident with the Landsat passes, statistical regression techniques could not be applied, cluster analysis techniques were used to group lakes, and Monte Carlo simulation, involving randomisation of the input data, was used to show that the groups obtained were significant. A study of a number of TM scenes, relating the clusters to the known general characteristics of the lakes involved, showed that, in general, clusters corresponded to various lake trophic states, and so indicated that the TM data is capable of separating such characteristics. Some anomalies were noted, indicating that, as expected, factors other than trophic state were affecting the clustering process. The principal factors are probably lake water clarity, affected by the amount of humic substances present, and water depth, yielding bottom reflectance in shallow lakes, and it is surmised that different regression curves should be used for such different lake types, with clustering being used to aid in determining these groups.

This study has given added impetus to a campaign during the Summer and Autumn of 1987 to collect ground data, closely coincident with Landsat-5 passes, so that work can proceed on establishing the necessary regression curves, so leading towards the implementation of a national monitoring system for Irish lakes.

Introduction

Ireland's lakes are a major resource from the economic, aesthetic and scientific point of view. They are of value for water supply, angling, and general amenity purposes, and they encourage tourism traffic to those areas of the country where lakes are plentiful. Lake monitoring by normal ground-based methods is an expensive and time-consuming process, and it is effectively impossible to

monitor more than a small fraction of Irish lakes, which exceed 4000 in number (for those lakes which exceed approximately 100 meters in their largest dimension). Currently, approximately 40 lakes have been studied in any detail and possibly only 150 have been even cursorily examined. Whereas most European countries have relatively few lakes to manage, lake monitoring problems in Ireland are more similar to those of the Scandinavian countries, Canada and some of the northern states of the

...the ... of ...

Application of Landsat Data to Hydrologic Mapping

Ludger Paus and Ulrich Streit

Department of Geography, University of Münster, FR Germany

Based on a spatial disaggregation approach, a hydrological model for estimating flood hydrographs in all sub-catchments of a larger river basin is developed. The spatial reference system of sub-catchments, grid cells etc. can be defined in accordance with the underlying practical problem. The hydrological model itself consists of several modules, simulating the various sub-processes such as areal rainfall, snow melt, infiltration or flood routing. The global estimation errors are eliminated by means of an adjusting algorithm.

Landsat-5 TM data are used for a spatially detailed land use classification as an essential input of the module, which transforms rainfall to direct runoff. After aggregating the original information to $100 \times 100 \text{ m}^2$ pixels to fit into an 1-ha grid system, 19 training samples are chosen, to establish reliable discrimination and classification functions on the basis of the TM bands 1, 3, 4, 5, and 6, selected in this study. For the special purpose of hydrological mapping, the land use classification does not intend to uncover the variety of all individual kinds of land use in the study area. Instead, a rough distinction between coniferous, mixed and deciduous forests, arable land and grassland, impervious and water areas is sufficient for runoff estimation. The methods used for sample and image classification as well as spatial filtering are discussed briefly. In spite of some problems with delimiting adjacent areas of similar spectral characteristics, the results of land use classification at a level of $100 \times 100 \text{ m}^2$ pixels satisfy the requirements of rainfall-runoff modeling.

The final results of this study are represented as chorological runoff maps for several hydrologic components and different levels of spatial resolution in the upper Lenne basin, located in the Rhinian Slate Mountains (FRG). This kind of spatially detailed runoff maps can be used for regional hydrologic studies and the planning of flood protection measures.

1. Introduction

In hydrology there is a number of spatial variates which are measured at single points but really refer (or are referred) to an areal information unit. A concrete example is the discharge of a river catchment, which is measured locally at the outlet of the basin but is referred to the entire catchment area. Strictly speaking, the measured value is the result of a superposition of individual hydrographs from various parts of the catchment, thus comprising information on the spatial and temporal variation of the runoff process as a whole. The decoding of these hidden elements of information may give support to a deeper understanding of the spatial individuality and variation of hydrologic processes. This concept of spatial disaggregation must naturally be based on hydrologic models and has to take into consideration spatially detailed information on the physiographical conditions underlying the hydrologic processes in each sub-catchment. In comparison to building up special networks of hydrologic measuring stations with a sufficient spatial density, this concept is more flexible and less ex-

pensive. It can be used to improve and update spatial databases and to construct large-scaled digital maps for regional studies as well as for water management.

In this paper, the spatial disaggregation approach is outlined by the example of flood discharge. The spatial reference system consists of one or more gauged river catchments with measured runoff data (called 'adjusting' region) on the one hand and a number of ungauged sub-catchments (or grid cells etc.) on the other hand — the latter representing a higher level of spatial resolution in accordance with the underlying problem. The rainfall-runoff model used for estimating discharge for all ungauged sub-catchments in the sense of regionalisation consists of several sub-models, which shall not be described here in full detail. Within the phase of runoff-formation, a hypsometrically modified grid procedure computes areal rainfall depths from point measurements. During winter months a snow compaction-model (Knauf, 1974) is used to simulate the conditions of snow cover

and to calculate meltwater amounts. To model that part of rainfall or meltwater which becomes effective for runoff, each sub-basin is subdivided again into a set of partial areas, being approximately homogeneous with respect to soil cover and land use.

In this central part of the rainfall-runoff model, Landsat data are used for a spatially detailed land use classification, which will be discussed below in more detail.

Using a combination of the well-known SCS-method (Chow, 1964) and a soil moisture capacity model (Anderl, 1975), the effective rainfall (= direct runoff) is estimated for each partial area. Subsequently, the individual hydrographs of direct runoff are computed for each sub-catchment by routing the runoff amounts through a parallel system of linear reservoirs in series. The baseflow rates of the sub-catchments are estimated from measured flow rates of groundwater recharge areas (Streit & Paus, 1987). A simple translation model performs flood routing of the waves in the channel between the individual sub-catchments and the outlet of the gauged basin. The parameters of this complex rainfall-runoff model are bound to physiographic characteristics by means of calibration values, which can be optimised by the Marquardt-method (Marquardt, 1963).

Rough estimates of the flood hydrographs for all sub-catchments result from these computations. In a second step the regional estimation error, which is the difference between the measured hydrograph at the basin outlet and the superposition of the locally estimated waves, has to be eliminated. Taking into account the individual times of translation in the drainage system, the 'adjusting' algorithm (Streit, 1984) with an antecedent precipitation index (winter: temperature index) for controlling the compensation of local estimation errors, gives an acceptable solution of this problem.

This disaggregation approach has been tested with rainfall-runoff data in the upper Lenne basin upstream Bamenohl-gauge (Rhianian Slate Mountains, FRG), which is 451 km² in size and is divided into four separate adjusting regions (= spatial level A) by four gauging stations. Several sets of sub-catchments have been used as spatial reference systems for disaggregation, for instance 16 sub-catchments with an average size of 28.2 km² (level B) and 81 small sub-catchments with a mean size of 5.57 km² (level C).

To carry out a complete analysis of transformation of rainfall into runoff, the computer program needs a lot of input data: rainfall depths, air temperatures, snow cover data, measured runoff etc. for the flood under consideration, but also geologic, morphometric, hydraulic and pedologic data. Of special importance are spatially detailed land use data, being a necessary basis for estimating the rainfall-runoff ratio as well as the spatial distribution

and water equivalent of snow cover. Landsat-TM data have been used to give a spatially detailed and actual survey of land use. In the following parts of the paper the numerical analysis of these data shall be discussed in more detail.

2. Numerical analysis of Landsat data

The large-scaled computer-aided classification and mapping of land use in the upper Lenne basin is based on the Landsat-5 TM scene no. 196/24 dating from 30-7-1984.

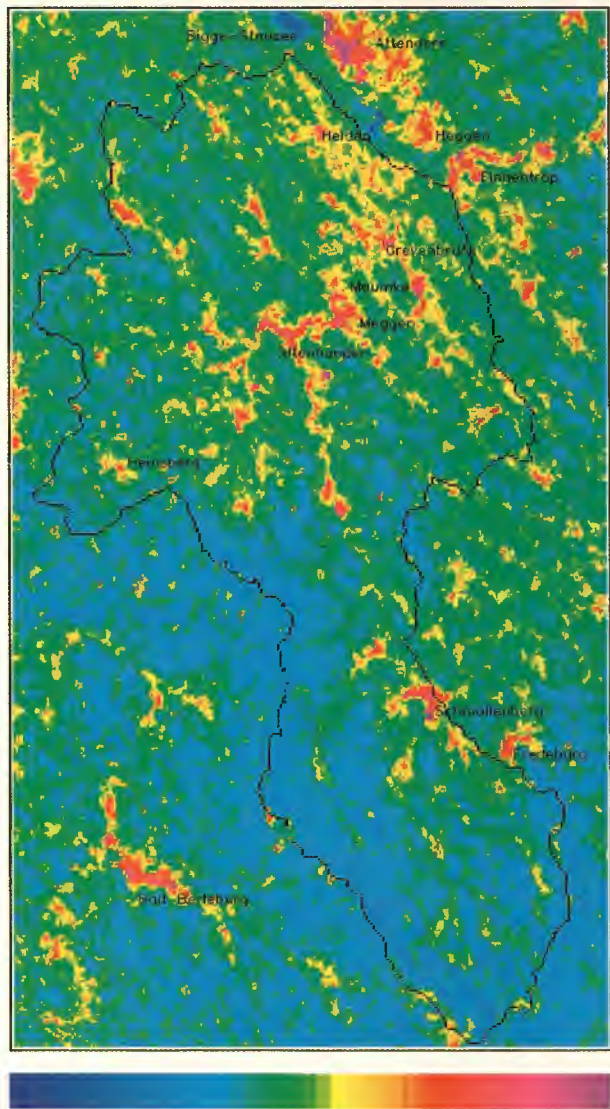
2.1. Preparation of raw data

After a geometric restoration and correction of the video data according to the backstep procedure (Steiner, 1974), the original values have to be aggregated to new pixels of 100 × 100 m² in order to become compatible with a spatial database, already existing on a 1-ha grid basis. This is done by linear interpolation with moving averages (Kirchhoff et al., 1985). The classification of large datasets, comprising the total available spectrum, is very expensive; moreover, a large number of wavebands may result in misclassification and in difficulties with regard to statistical interpretation (Itten, 1979). Therefore, a selection of suitable wavebands seems to be useful, paying special attention to poor correlation, large dynamic range and suitability for vegetation survey purposes (Curran, 1985). So the TM bands 1, 3, 5, 6 and especially 4 are selected.

2.2. Training data analysis

For the special purpose of hydrologic mapping, land use classification does not intend to uncover the variety of all individual kinds of land use in the study area. Instead, a rough distinction between coniferous, mixed and deciduous forests, arable land and grassland, impervious (settled) and water areas is thought to be sufficient for runoff estimation. At first, each of these six types of land use has to be defined by a separate class of sample elements, paying special attention to an adequate representation in the statistical as well as spatial context (large samples, no local singularities).

The aggregation of the original TM data mentioned above results in difficulties when attempting to delimit these samples in the satellite image visually: instead of a sharp boundary a transition zone may exist between two classes, being dependent on the actual waveband. Only the samples for impervious areas and lakes can easily be localised, using the thermal band 6 (see Map 1). Therefore, the following procedure is used for the topographical assigning of the training samples: according to the existing 100 × 100 m² grid, the related topographic maps scaled 1 : 25 000 are partitioned into pixels of the same size. Using clearly identifiable control points on the topographic map as well as in the satellite image, the spatial relation between both datasets can be



110 (cold) 125 139 (warm) 154
 Mean: 131.40 Standard deviation: 9.76 N→

Map 1: Colour plot of video data for the Landsat-5 TM band no. 6 (10.4–12.4 μm). (Scene no. 196/24; 30-7-1984)

established. In this way, the borders of the 19 training areas used for this study are transformed into image coordinates.

In order to obtain a reliable database for the image classification, these samples have to meet some requirements. In a first step, each sample is visually investigated for homogeneity in every selected waveband; if necessary, alien elements are removed. In a second step, arithmetic means and standard deviations of the roughly refined samples are computed. Table 1 shows that in some cases relatively high standard deviations may result. To reduce such large sample variations, single pixels of very extreme value are eliminated. Thresholds, defined as multiples of standard deviations plus/minus the corresponding mean, have proved to give acceptable solutions. After numerous empirical tests with

various multipliers, a value of 1.9 was found to be suitable. This elimination of outliers has to be repeated for several samples to obtain a satisfying level of accuracy in all selected TM bands.

2.3. Sample classification

After the elimination of outliers the 19 training samples have to be checked for the discriminating power of the selected wavebands. To handle this multivariate statistical problem, discriminance analysis is used, resulting in discrimination equations and coefficients to judge the separability of samples and as well in classification functions to assign the sample elements to the predefined types of land use. The cross-table (Table 2) shows the results of this re-classification, listing the percentages of assigned elements within each training sample: the elements of the principle diagonal represents an exact re-classification, e.g. 71.2% in sample S1. But the remaining 28.8% is not a real mis-classification, because the adjacent samples S2 and S3 belong to the same type of land use. Therefore, real mis-classifications are found outside the diagonal boxes only, e.g. 6.7% of M3-elements (mixed woodland) are wrongly assigned to the sample N3 (coniferous forest). Altogether, 567 pixels within the 19 training samples are assigned to six different types of land use; only 0.53% of these are mis-classified. This low percentage indicates a good separability on the basis of the five TM bands selected here.

2.4. Image classification

The classification of the total scene means an extrapolation of this assigning procedure. The more or less subjective choice of training samples may cause a poor representation within the larger study area. Therefore, it is useful to limit the range of internal variation of each class: a pixel is assigned to a particular type of land use, if it falls into an interval around the corresponding sample mean, the limits of which are defined by multiples of the sample standard deviation (Paus, 1987). The optimal multiplier is found by trial and error, testing values between 1 and 10 (Table 3): the value 8.5 gives an acceptable accuracy of pixel assignment. The percentage of non-assigned pixels is only 1.4% in this case of a supervised classification.

2.5. Spatial filtering

The intention of spatial filtering is to improve the image by modifying the assignment of certain pixels to obtain a more coherent and less diffuse structure. Each pixel (including the unclassified ones) is compared to its neighbours and subject to a revised evaluation with regard to its most probable class membership. For this task, a logical filter operation, developed by Blum (1982) and tested with success several times, is applied. This filter examines a 3×3 -window of pixels and decides on the classification of the central element by taking into account the information of the neighbouring pixels. Its

Table 1: Arithmetic means (M) and standard deviations (S) for some training samples

Water (W1)					Coniferous forest (N3)				
band	M	S	M*	S*	band	M	S	M*	S*
1	74.4	2.13	74.0	0.68	1	69.9	1.00	69.6	0.71
3	23.5	0.50	23.6	0.50	3	22.1	0.94	22.3	0.87
4	24.9	0.19	25.0	0.01	4	39.5	2.11	40.1	1.96
5	24.2	1.53	24.2	0.84	5	29.2	8.18	25.6	3.04
6	126.2	0.47	126.4	0.34	6	127.1	3.81	126.0	0.50

Arable land (A1)					Arable land (A2)				
band	M	S	M*	S*	band	M	S	M*	S*
1	83.0	3.97	82.7	3.48	1	79.7	2.61	79.7	1.92
3	34.4	4.10	32.4	2.83	3	33.1	3.21	32.4	1.88
4	94.7	9.99	98.3	5.85	4	85.1	12.5	78.0	7.83
5	75.9	3.36	76.7	2.60	5	79.2	5.82	79.8	6.45
6	135.0	1.23	135.0	0.87	6	1.32	1.64	133.0	1.00

Before and after (M* resp. S*) outlier elimination

Table 2: Results of training sample classification

Land use class	Water		Grassland			Coniferous forest			Mixed an deciduous forest				Arable land				Impervious areas			
	W1	W2	G1	G2	G3	N1	N2	N3	M1	M2	M3	M4	A1	A2	A3	A4	S1	S2	S3	
W1	96.3	3.40																		
W2	0.00	98.0							2.0*	0.00	0.00	0.00								
G1			90.0	10.0	0.00															
G2			0.00	100.	0.00															
G3			3.20	4.80	92.0															
N1						95.0	0.00	5.00												
N2						0.00	100.	0.00												
N3						0.00	0.00	100.												
M1									100.	0.00	0.00	0.00								
M2						0.00	5.3*	0.00	0.00	94.7	0.00	0.00								
M3						0.00	0.00	6.7*	0.00	0.00	93.3	0.00								
M4									0.00	0.00	0.00	100.								
A1													61.4	27.3	9.10	2.30				
A2													10.0	83.3	0.00	6.70				
A3													0.00	14.3	66.7	19.0				
A4													0.00	0.00	7.10	92.9				
S1																	71.2	1.70	27.1	
S2																	0.00	93.3	6.70	
S3																	3.30	0.00	96.7	

All frequencies in percent (%); * means real mis-classification

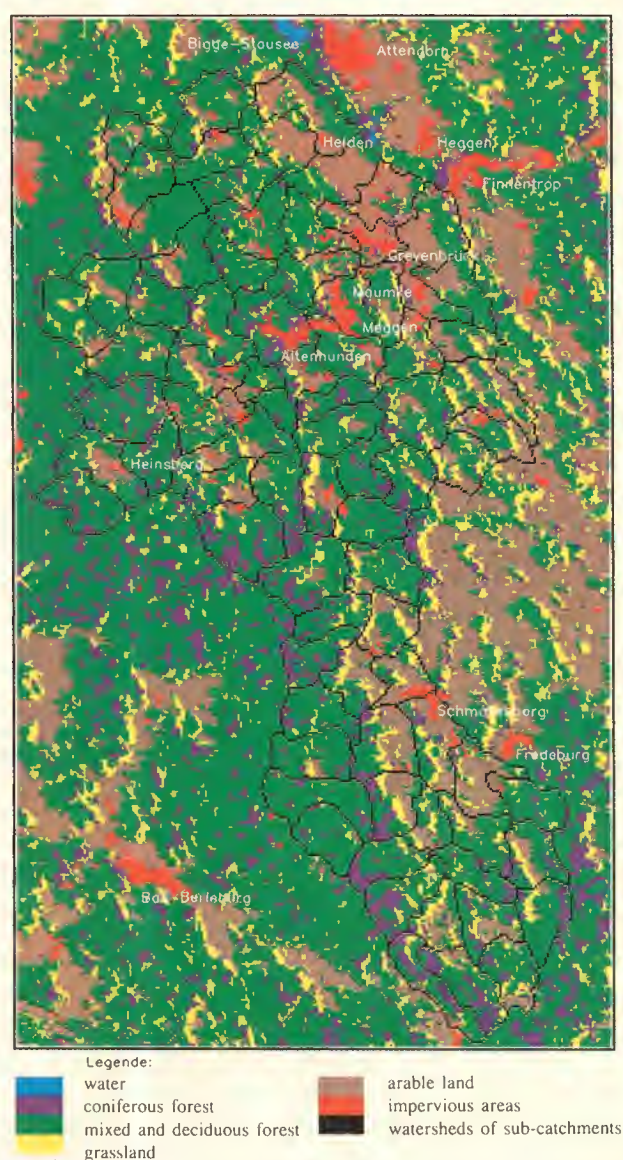
Table 3: Results of image classification (scene no. 196/24; 30/7/1984) for different multipliers m of standard deviation and for the spatially filtered data (*)

No.	Land use class	$m = 1.5$	$m = 3.0$	$m = 5.5$	$m = 8.5$	$m = 8.5^*$
1	water	0.07	0.08	0.09	0.09	0.09
2	grassland	5.89	8.05	11.0	12.1	11.2
3	coniferous forest	4.76	7.89	9.41	9.73	9.49
4	mixed & deciduous forest	29.9	44.2	52.1	52.5	54.5
5	arable land	10.2	15.4	21.0	21.2	21.7
6	impervious areas	1.29	2.04	2.91	2.98	2.87
	classified	52.14	77.62	96.51	98.60	99.85
	non-classified	47.86	22.38	3.490	1.400	0.250

generalising effect is not extremely strong. The last column of Table 3 shows the magnitude of changes induced by this spatial filtering: there is only a slight shifting of the areal ratio of land use, and the amount of unclassified pixels is reduced to a very small number.

2.6. Results of classification

Randomly chosen test areas with field surveys, as well as the above-mentioned 19 training samples serve as a basis for the evaluation of the results. Whereas the reclassification of the training samples is successful in all cases, the test areas exhibit some typical classification problems, resulting mainly from the reduced spatial resolution of $100 \times 100 \text{ m}^2$ pixels in contrast to the original data and from local variations in the spectral characteristics of a land use type, too: small plots of land use tend to become smaller or they even can disappear; errors predominantly occur in transitional zones between different types of land use which are similar with respect to their spectral characteristics. Map 2 shows the classification results combined with the watersheds of the spatial system C with 81 sub-catchments. Clearly to be seen is the morphologic structure induced by the geologic conditions and the tectonic key lines in the study area. The uplands in the southern and eastern parts (maximum elevation 839 m above sea level) are predominantly covered with coniferous forests and mixed woodland. The lower altitudes in the north-western parts (minimum elevation 235 m) are mainly used as arable land. The river plains of the upper Lenne east of Altenhudem form a small, well recognisable, almost straight-lined strip and are used as grassland. The lower parts of the valley contain some larger settlements, whereas the other parts of the study area show sparse population only. Noticeable is the stripy pattern of grassland along the southern borders of arable land: this may be interpreted as an effect of 'illuminating' the relatively small strips of grassland by the larger areas of arable land immediately following, or as a modification of the spectral characteristics of arable land at exposed sites. A clear analysis of this 'shadow-



Map 2: Land use classification after spatial filtering for the upper Lenne basin and adjacent areas, based on Landsat-5 TM data

effect' is not possible on the basis of the available data; therefore, the land use classification in these parts should be judged with caution. All in all, the coarse-grained land use classification of TM data in a $100 \times 100 \text{ m}^2$ grid gives acceptable results for hydrologic applications.

3. Chorologic runoff maps

The rainfall-runoff computations, following the principle of spatial disaggregation, can easily be represented in chorologic maps for total runoff or runoff components like direct runoff or baseflow. An essential advantage of this kind of hydrologic map is its higher spatial resolution in comparison to the originally measured discharge. This shall be demonstrated by the example of a rainfall-runoff event between 7/9 and 24/9/1984.

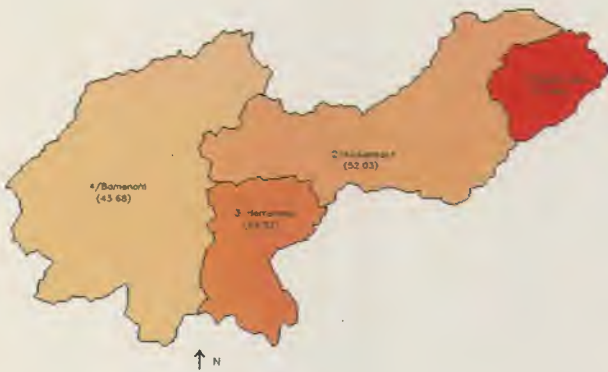
During the second week of September 1984 an area of low pressure led to heavy rainfalls which resulted in a very high flood. Map 3 shows the measured direct runoff

in the 4 gauged 'adjusting regions' of level A after separation of baseflow from total runoff. In the eastern part (Oberkirchen - gauge) a direct runoff depth of 78 mm has been measured, whereas in the lower western parts only 44 mm have been recorded.

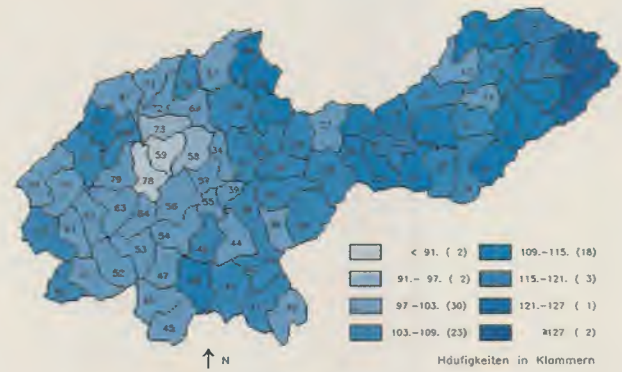
An important basis for the estimation of spatially detailed runoff depths is areal rainfall. Its spatial variation shows a certain concordance with the orographic conditions: the rainfall amounts slowly increase with altitude from west to east. The spatial pattern of direct runoff, computed for the 16 sub-catchments of level B principally varies in the same manner (sub-catchment 14 with 33.4 mm, sub-catchment 1 with 78 mm), but shows some modifications, too, induced by land use inter alia (Map 4).

Looking at the highest disaggregation level C with 81 sub-catchments, these statements can be refined still further (Map 5): the highest rainfall amounts of more than 120 mm occur on the western side of the highest mountain (Kahler Asten). The lowest rainfall depths of under

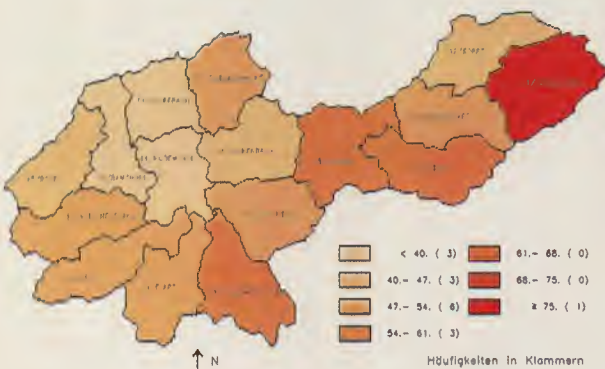
Map 3: Upper Lenne basin: 4 gauged adjusting regions (level A). Direct runoff depths (mm) for the flood 8–21 Sept. 1984



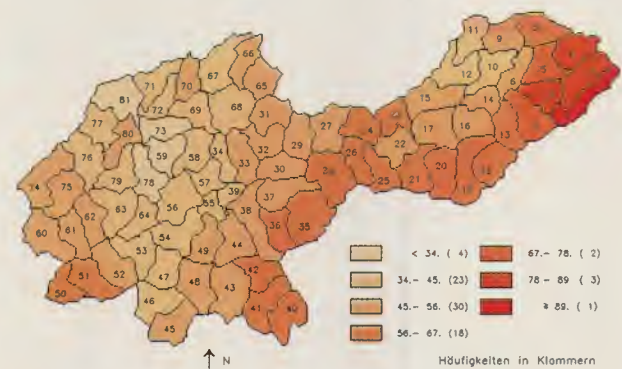
Map 5: Upper Lenne basin: 81 ungauged sub-catchments (level C). Areal rainfall depths (mm) for the flood 8–21 Sept. 1984



Map 4: Upper Lenne basin: 16 ungauged sub-catchments (level B). Direct runoff depths (mm) for the flood 8–21 Sept. 1984



Map 6: Upper Lenne basin: 81 ungauged sub-catchments (level C). Direct runoff depths (mm) for the flood 8–21 Sept. 1984



90 mm can be found in the inner parts of the western Lenne valley. The spatial distribution of computed direct runoff for level C (Map 6) generally follows the rainfall pattern, but there are some interesting local peculiarities: for instance, comparing sub-catchments 1 and 2 in the eastern part of the study area, the spatial unit 2 produces less direct runoff than number 1, but has more rainfall input. Similar differences between the local ratios of runoff and rainfall can be found in many other parts. The colourful spatial pattern of these runoff coefficients is a combined effect of different land use, antecedent soil moisture and morphometric conditions.

Spatially detailed runoff maps, like those presented here, may give interesting information for regional hydrologic studies or water management measures and can help to improve local and regional flood protection. As the resulting chorologic runoff maps have a pure digital basis, they may become part of a hydrologic or more general spatial information and planning system.

4. Research problems

One of our current research problems concerns the spatial distribution of snow cover and its characteristic values, especially water equivalent. Up to now we have to rely on point measurements only and on their spatial transfer by the aid of a digital terrain model. We are trying to obtain better information by including Landsat images into the spatial analysis of snow cover.

But the most severe hydrologic problem is the lack of data concerning the spatial distribution of depth, texture and potential infiltration capacity of soils. With such basic data of soil physics with high spatial resolution for complete river catchments, the temporal and spatial variation of soil moisture can be simulated, being very important for a more realistic runoff modeling. We place our hopes in the development of remote sensing techniques, which will allow to put these data at the hydrologist's disposal in near future.

5. References

- Anderl B 1975, Vorhersage von Hochwasserganglinien aus radargemessenen Regen. *Mitteilungen des Institutes Wasserbau III der Univ. Karlsruhe*, Heft 7.
- Blum E 1982, Ein interaktives Verfahren zur Klassifikation von multispektralen Fernerkundungs-Bilddaten. *Zuercher Geograph. Schriften*, Heft 6.
- Chow VT 1964, *Handbook of applied hydrology*. McGraw-Hill, New York.
- Curran JL 1985, *Principles of remote sensing*. Longman, London.
- Itten KI 1979, *Grossräumige Inventuren mit Landsat - Erderkundungs satelliten in der Schweiz*. Habil.Schrift; Univ. Zürich.
- Kirchhof W, Mauser W & Stiebig HJ 1985, *Untersuchungen des Informationsgehaltes von Landsat-Thematic-Mapper und Spot-Multiband Bilddaten mit simulierten multispektralen Bilddaten des Gebietes Freiburg*. Wiss. Berichtsw. DFVLR (FB85 - 49).
- Knauf D 1974, *Abfluß aus Regen und Schneeschmelze*. 6. Fortbildungslehrgang für Hydrologie des DVWW, Bad Herrenalb.
- Marquardt DW 1963, An algorithm for least-squares estimation of non-linear parameters. *Jl. Soc. Industr. Appl. Math.*, Vol. 2/2; 431-441.
- Paus L 1987, CMVD - Ein Programmsystem zur Entzerrung, Klassifikation und Filterung multivariater, digitaler Bilddaten. Inst. f. Geographie, Univ. Münster; unpubl. paper.
- Steiner D 1974, Digital geometric picture correction using a piecewise zero-order transformation. *Remote Sensing of Environment*, 74/3; 261-283.
- Streit U 1984, Adjusting rough estimates of subregional data to a regional mean of known size. *Proc. Intl. Symp. 'Spatial data handling'*, Zürich, Vol. 1; 289-298.
- Streit U & Paus L 1987, Construction of runoff-maps derived from basin characteristics. *Geolog. Jahrbuch* (in print).

Application of Remote Sensing to Irrigation Water Management in two Italian Irrigation Districts

S.Azzali and M.Menenti

Institute for Land and Water Management Research (ICW), Wageningen, The Netherlands

The feasibility of a remote sensing method to determine quantity, type and water shortage (water stress) of crops by means of Landsat-TM images is demonstrated in two irrigation districts in the Po valley, Italy. Individual crops have been mapped with Landsat-TM multitemporal data by applying different vegetation indices. It is shown that an accurate crop calendar applying for each area is required for the multitemporal analysis to be successful.

Reflectance measurements in TM-bands 3, 4, 5 and 7 were more reliable than estimates of surface temperature with TM-band 6 measurements in detecting shortage of water availability in crops.

Three practical applications, described in this paper, dealt with: 1) estimation of actual crop cultivated area; 2) the occurrence of water stress in the main cultivated crops; 3) detection of water depth in rice fields.

1. Introduction

During the past fifteen years remote sensing methods have been proposed to obtain:

1. Inventories of crop types and acreages in various crops (Hall and McDonald, 1983; Johnson, 1981; Crist and Malila, 1981).
2. Crop yield estimate (Curran, 1981; Heileman & al., 1977).
3. Detection of crop yield decrement caused by:
 - a. diseases or insect infestation (Nilsson, 1984).
 - b. disuniformity of application of fertiliser and irrigation (Jackson, 1986; Jackson et al., 1986).

Only few practical applications have been actually performed dealing mainly with land inventories, updating of agricultural statistics and assessment of crop production (Price, 1986; Anderson, 1985). The purpose of the present research was to assess the feasibility of monitoring quality, quantity, type of crops and their occurring water stress. The approach was tested in two irrigation districts located in the Po valley, Italy, namely: East Sesia (210 000 ha) and Grande Bonifica Ferrarese (56 150 ha) (Fig. 1).

The general idea was to test the procedure under operational conditions:

- (i) the analysis had to involve only that number of suitable images that can be reliably acquired during a growing season;
- (ii) the results of the analysis had to be delivered in due time to the end-users (the two irrigation districts) to be applicable the next growing season.

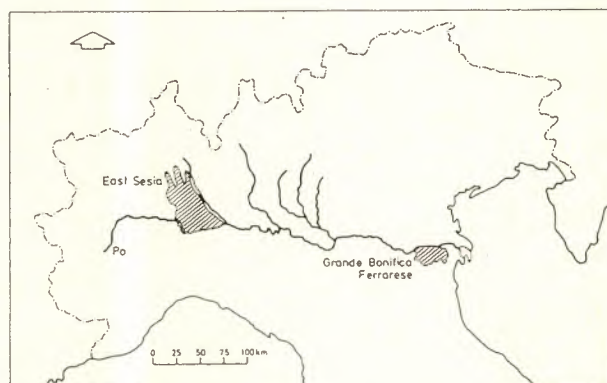


Figure 1. Sketch map of the Po valley, with the two irrigation districts studied in this report.

2. Methods and materials

2.1. Method approach

A method has been developed to map crops through the interrelation between crop phenology and spectral signature. To establish this method, values of different vegetation indices have been calculated and statistically compared. It has been found that even when the values of one index were not statistically different, values of another index were. So an univocal relationship can be established between each crop and a particular combination of vegetation indices values at characteristic growth stages. This approach has been termed 'multi-index, multi-temporal' (Azzali 1985a,b; 1986; 1987).

Such approach requires, at first, detailed information regarding the phenological cycle of the main crops cultivated in the study-areas in the considered years (average crop calendars).

By collecting the crop phenological data and combining them with the crop signatures we are able to obtain the temporal variations of crop spectral signatures. To evidence the different signatures between crops, the following vegetation indices were utilised: Greenness, Brightness and Transformed Vegetation Index (TVI).

A particular important application of remote sensing to irrigation water management is the assessment of crop water stress. Crop water stress by means of spectral measurements has been studied through about a decade.

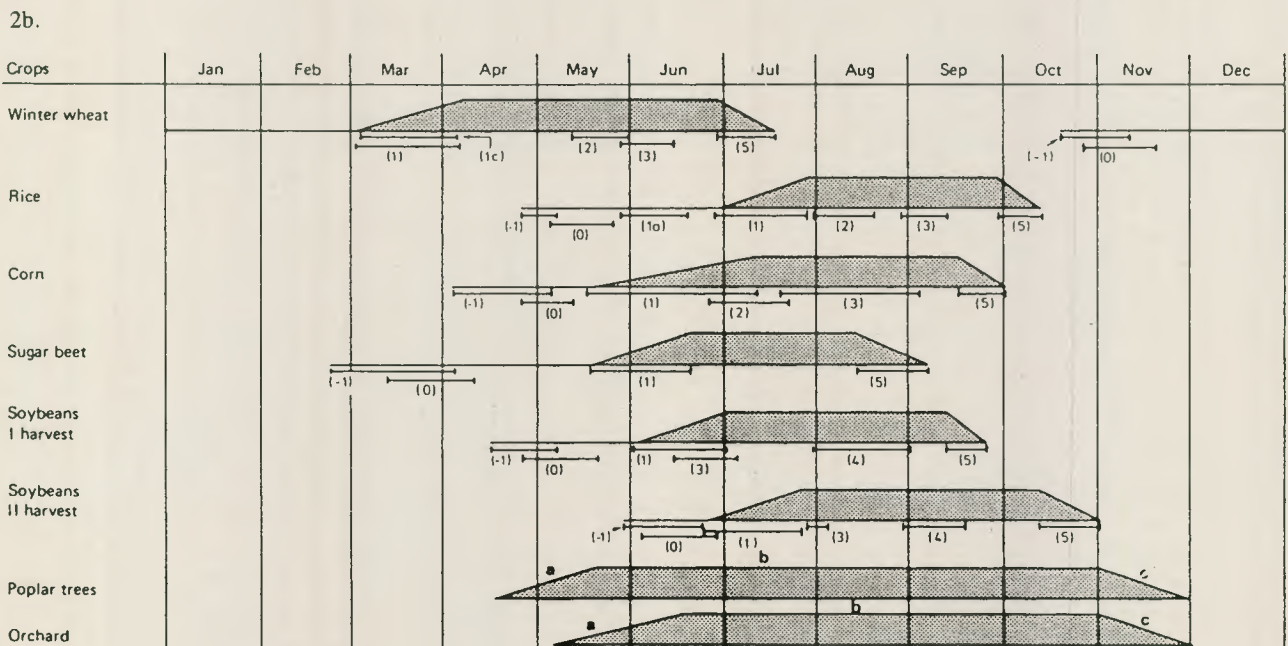
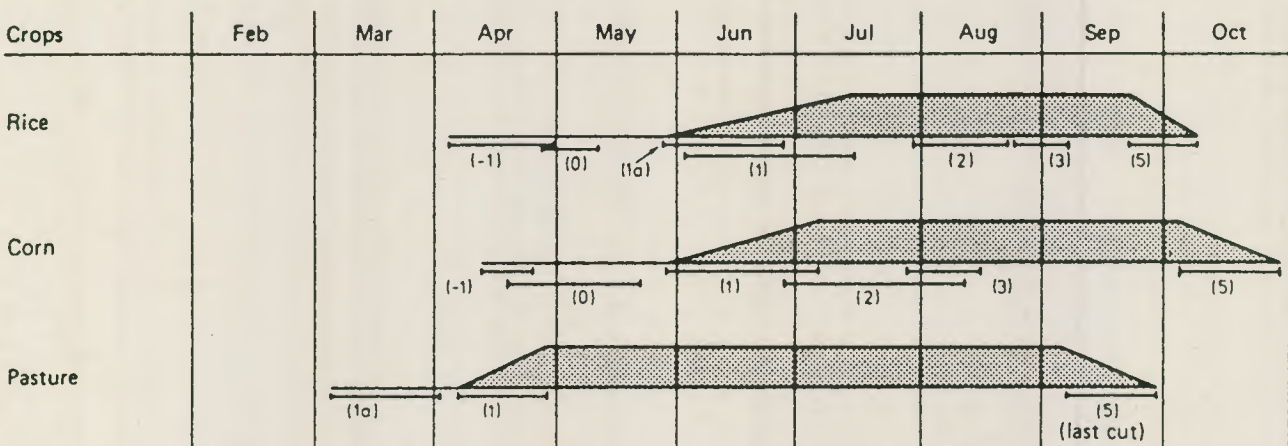
Near infrared and red wavelengths for the detection of water content in the vegetation and the ratio, near infrared over red, have been used for the detection of drought stress.

Another approach to assess crop water stress is by measuring canopy temperature by means of thermal infrared thermometry. Such research development was pointed out by a number of literature reviews, of which the most important remain: Jackson, 1986; Pinter, 1982; and Hatfield, 1983.

Both approaches require crop identification as first step, e.g. by means of different vegetation indices. Then, combining the information extracted by spectral measurements of near infrared and red wavelengths with

Figures 2a, b. Average crop calendars for the year 1985 of the main crops cultivated respectively in East Sesia and in Grande Bonifica Ferrarese. Symbols and numbers refer to:

(-1) seeding stage; (0) emergence; (1) full cover; (1a) tillering, only for rice; (1c) head development; (2) flowering; (3) yield formation; (3) milk ripening, only for grains; (4) full ripening; (5) harvest; (a) leaves development; (b) full vegetative cover; (c) leaves loss.



temperature measurements, we can try to assess occurred water stress in crops. In conclusion, the practical steps to apply the multi-temporal multi-index method for crop discrimination are:

- assessment of average crop calendar for the study area;
- calculation of vegetation index values for the main crops from the available images;
- assessment of crop characteristic interval of applied vegetation indices;
- crop discrimination.

2.2. Crop calendars 1985

During the crop year 1984-85 in both the irrigation districts several field plots have been selected and agronomic informations have been recorded on the actual cultivated crops (Azzali, 1987). By using the method illustrated by Menenti et al. (1986), we were able to calculate the average duration of each phenological stage. Then the average crop calendar was set on for East Sesia (Fig. 2a) respectively Grande Bonifica Ferrarese (Fig. 2b) irrigation districts.

2.3. Applied vegetation indices

The Thematic Mapper sensor on board the Landsat satellite measures radiance data in arbitrary units. The raw data in digital counts should be converted to scientific units such as reflectance in order to compare data between images taken on different dates. Reflectance values were used in this research and three vegetation index formulae (Greenness, Brightness and TVI) were applied.

The greenness and brightness formulae coefficients are strictly correlated with the type of soil present in the study area (Kauth and Thomas, 1979; Hall, 1984). Therefore, we have computed a new soil line for the most representative soil associations present in the two irrigation districts (Azzali, 1985 b) and the new coefficients in vegetation index formulae are:

$$\text{Greenness} = 0.144 \cdot R1 - 0.173 \cdot R2 - 0.262 \cdot R3 + 0.214 \cdot R4 - 0.159 \cdot R5 - 0.339 \cdot R7$$

$$\text{Brightness} = 0.151 \cdot R1 + 0.264 \cdot R2 + 0.354 \cdot R3 + 0.415 \cdot R4 + 0.601 \cdot R5 + 0.499 \cdot R7$$

$$\text{TVI} = \left(\frac{R4 - R3}{R4 + R3} \right)^{1/2} \cdot 100$$

The following Landsat-TM images were acquired and analysed:

	Frame/Row	Dates
East Sesia	194/28	30 April 1985
		3 July 1985
		20 August 1985

Grande Bonifica	192/29	2 May 1985
Ferrarese		3 June 1985
		22 August 1985

3. Method results

3.1. Crop discrimination with TM images

Reflectance and vegetation index values for each crop in the three available images have been obtained for every ground control plot. To consider the variability of each crop due to different seeding date, varieties, management, etc., we calculated an interval of vegetation index characteristic values for each crop. Following the method described by Menenti et al. (1986), crop classification was performed assigning a characteristic interval for each crop and for the considered vegetation indices (TVI, greenness and brightness) having as two limits (upper and lower limits) the mean vegetation index value for each crop (mean value calculated from vegetation indices measurements extracted from several ground control areas) respectively +1.5 and -1.5 of its standard deviation. Such characteristic interval, which for better understanding will be called 'method a' was calculated for each available image.

The vegetation index characteristic intervals for each crop were then compared with the vegetation index values applying to the other crops to establish which vegetation index on which date gave statistically significant differences between that particular crop and the other ones.

3.1.1. Crop discrimination in East Sesia

With just one image (30 April 1985) crop classification was performed by means of vegetation index TVI in East Sesia irrigation district. That date is the best one to discriminate rice from corn and from grass because these crops have achieved three different stages (flooded field for rice, seeding stage for corn and full ground cover for grass).

Nevertheless, the crop classification with the image of April using the characteristic interval 'method a' leaves unclassified part of the cultivated areas of the main considered crops. The best classification was achieved when the characteristic interval for each crop is calculated following this procedure ('method b'):

- 1) lower limit = the lowest mean value of TVI for a certain crop extracted by the ground control plots minus $0.75 \cdot \text{standard deviation}$;
- 2) upper limit = the maximum mean value of TVI for a certain crop extracted by the ground control areas plus $0.75 \cdot \text{standard deviation}$.

Results of crop classification according to the characteristic interval 'method b' is shown in Table 1.

Table 1. TVI characteristic crop interval 'method b' (a, b); crop cultivated area (as percentage of TM-subimage area) estimated by means of TVI; East Sesia, April 1985

Crops	TVI	Area
	(/)	(%)
Rice	(50-67)	37.3
Haygrass pasture	(102-112)	7.2
Corn	(71-81)	31.8

Table 2. Discrimination scheme of crops cultivated in Grande Bonifica Ferrarese

Crops	2 May	3 June	22 August
Rice		BR rice	
Winter wheat	TVI w.wheat		
Trees	TVI trees		
Corn			BR corn + trees
Sugar beet		TVI sugar beet + trees + w. wheat	
Soybeans I harvest		GR soybeans I harv. + corn + soybeans	
		II harvest	
Soybeans II harvest			TVI soybeans II harvest

Table 3. Characteristic crop interval 'method a' (a, b) of greenness (GR), brightness (BR) and Transformed Vegetation Index (TVI) for winter wheat, rice and trees; smaller characteristic crop interval (a, b) of greenness, brightness and TVI for corn, soybeans and sugar beet; crop cultivated area (as percentage of TM-subimage area) estimated by means of the multi-temporal multi-index method; Grande Bonifica Ferrarese, year 1985

Crops	2 May		3 June			22 August	
	TVI	GR	TVI	BR	GR	TVI	BR
Rice			(17-31) 5.5				
W. wheat	(105-1087)	12.8					
Corn						(30-32) 23.1 23.1-15=8.1	
Sugar beet			(98-107) 43.8 43.8-15.9-15=12.9				
Trees	(91-101)	15					
Soybeans I harvest			(119-124) 35.6 35.6-8.1-0.1=27.4				
Soybenans II harvest						(108-110) 0.1	

3.1.2. Crop discrimination in Grande Bonifica Ferrarese

Winter wheat, tree and rice were discriminated by applying the crop characteristic intervals 'method a'. The spring crops can be discriminated by means of the multi-

temporal multi-index method assigning the characteristic interval calculated with 'method a' where the standard deviation is multiplied by 0.75 instead than 1.5.

Table 2 shows the discrimination scheme for the main crops in Grande Bonifica Ferrarese, while Table 3 shows the results of crop classification.

4. Practical applications

4.1. Declared versus actual crop cultivated area

By applying the multi-temporal multi-index method, discrimination of crops in the considered irrigation districts gave good results. Yearly crop maps are basic informations for the irrigation district board in order to

Photo 1. Colour-coded TVI image of East Sesia where rice is shown in blue, corn in green, pasture and haygrass in red, natural vegetation and poplar trees in yellow. (30 April 1985).

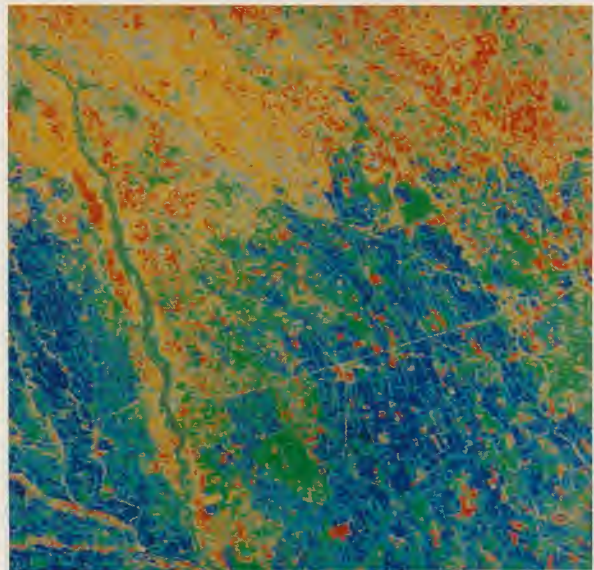


Photo 2. Colour-coded (bands 4/3/2) TM-image of Grande Bonifica Ferrarese, where full green winter wheat is red, paddy rice fields are black and emerging vegetation plus bare soil is gray-blue. (2 May 1985).



forecast total crop water requirements. In East Sesia and Grande Bonifica Ferrarese irrigation districts, water is allocated on fixed rotational intervals on the basis of the crop area. The irrigation districts control only the actual hectares of paddy rice fields while for the other crops irrigation water is delivered according to the hectareage declared by farmers. Photo 1 shows the crop map of the growing season 1984-85 of part of East Sesia irrigation district. From such map the irrigation district board can extract the actual extension of the declared irrigated areas.

Photo 2 shows part of the territory of Grande Bonifica Ferrarese of a colour-coded Landsat-TM image on 2 May 1985. Winter wheat, green at that time of the year, is indicated by red colour. Paddy rice fields are black, while gray-blue colour indicates bare soil and cultivated fields in which soil vegetation cover is lower than 25%. According to the interviews to the farmers done in September 1985, the black framed field in Photo 3 should have been cultivated with winter wheat. However, the colour of the black framed field (greyish-blue) denotes that the cultivated crop there is not winter wheat. Further support to such conclusion is given by a colour-coded TM-image (Photo 3) of the same area four months later (22 August 1985).

In Photo 3 the so-called wheat field should appear in greyish-blue colour which denoted, at that time, the field where wheat was previously grown without a second crop. Nevertheless, the so-called wheat field is orange which denotes the presence of a spring-summer crop as it happened to the surrounding fields (soybeans cultivations).

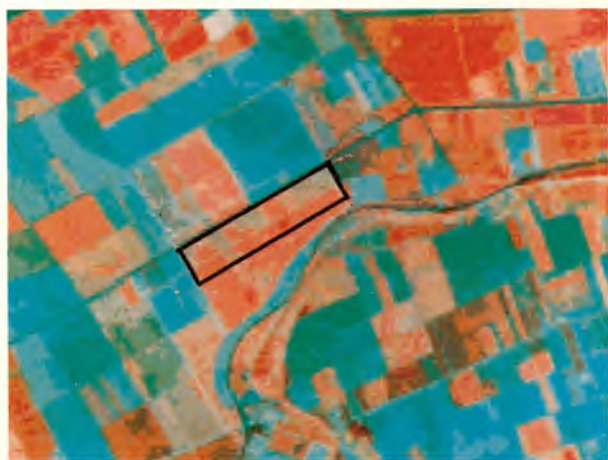


Photo 3. Colour-coded (bands 4/3/2) TM-image of Grande Bonifica Ferrarese, where full green corn, soybeans, rice, sugar beet are red-orange, stubble plus bare soil are dark blue to blue. (22 August 1985).

The irrigation charges of the Grande Bonifica Ferrarese to the farmers are depending on the type of cultivated crops, and winter wheat belongs to the category of non-

irrigated crops while soybeans to the irrigated ones. So, that farm has cultivated in the year 1985 more hectares with irrigated crops than declared to the irrigation district, with the consequence of paying less than due. In the Grande Bonifica Ferrarese irrigation district, probably, other mispayments on irrigation charges are occurring because the irrigation district itself does not check out the actual hectareage of irrigated crops taking for granted what the farmers declare. Consequently, in this case, a very useful application is the discrimination of crops by means of satellite images, in order to establish the hectares of irrigated crops.

4.2. Water stress detection

The assessment of occurring crop water stress was done by means of the Landsat-TM images acquired in 1985 and by observing TVI, reflectances in bands 5 and 7 and temperature values. Details of such procedure have been explained by Azzali, 1987. The results confirmed that reflectances in band 5 and 7 were more accurate in water stress detection than the temperature measurements.

Water stress was only localised with satellite images of East Sesia in a very small part of the total area cultivated with grass while for the other crops evidences of water stress were not found in July and August. In order to cross-check the results extracted by satellite images, a numerical simulation model of water flow in unsaturated soil (Swatre; Belmans et al., 1983) has been applied to obtain the water balance in different parts of the East Sesia territory. The model, however, did not detect any water shortage for rice and corn in July and August 1985.

Then the results of Swatre model confirm and support the validity of the method which was used with the satellite images. Also in Grande Bonifica Ferrarese during August 1985 the main crops did not suffer of any lack of water according to the reflectance measurements of bands 3, 4, 5 and 7. Nevertheless during the interviews conducted in September 1985 in both irrigation districts, farmers complained about water shortage caused by a very dry and exceptional hot summer.

On the other side, the board of the Grande Bonifica Ferrarese irrigation district rose complaints on the huge quantity of water that had to be pumped out from the district territory (which is in part under sea level) during the 1985 irrigation season, in order to prevent waterlogging. So the results of satellite data analysis have been confirmed by the water management applied in 1985.

4.3. Water depth detection in paddy rice fields

Rice is cultivated in both study areas but in East Sesia such crop is the main one. The possibility of the assessment of water level in the rice basins by means of satellite images can be useful to check the occurrence of rice field flooding and possibly the quantity of water delivered to the rice farms.

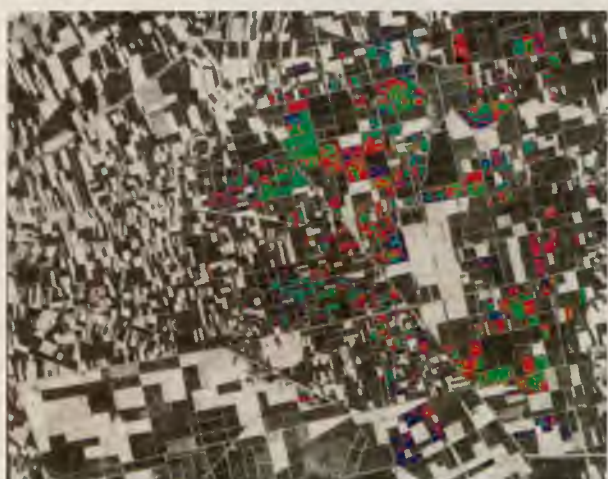


Photo 4. False-colour Landsat-TM image of TVI of Grande Bonifica Ferrarese on May 2, 1985, where paddy rice fields are classified by the TVI interval values 55-60 (green colour) when 10-cm water or more are applied to the field, by the interval values 61-65 (red colour) when 5-cm water or less are applied to the field, by the interval values 66-67 (blue colour) when flooding process in rice basins.



Photo 5. False-colour Landsat-TM image of TVI of East Sesia on April 30, 1985, where paddy rice fields are classified by TVI interval values 50-55 with blue colour, by TVI interval values 56-60 with green colour, by TVI interval values 61-67 (red colour). White circle frames a rice farm.

The attempt of assessing water level in the rice basins by means of satellite images was performed by Azzali, 1987. The vegetation index TVI was found to be rather sensitive to different water depths for a given soil type. Two relationships have been applied between type of soils and water depth in the two irrigation districts. The first relationship in Grande Bonifica Ferrarese was established between dark textured soils (peat podzol) and different water depths in the rice fields. The second relationship was established in East Sesia between light and dark (podzol) soils at different water depths in the rice fields.

Photo 4 shows the different water depths recorded for the flooded rice fields in Grande Bonifica Ferrarese by means of vegetation index TVI (Azzali, 1987). Photo 5 shows different spectral signatures (TVI) according to the main soil characteristics present in East Sesia territory (Fig.3). As we can see, higher TVI values are recorded from a lighter texture soil (sandy soil), while a heavy dark soil (podzol) shows low TVI values. The farm framed in white circle is located in podzol soil.

The established relationship between TVI and water depth in the irrigated fields did help in finding some contradictions between the estimated water depth (through TVI) and the water depth that has been declared by the farmers. For example, in the framed area of the East Sesia (white circle) the water depth measured in the farm shows different result from that one expected by the declaration of the rice field owner.

In addition, the relationship found between TVI and water depth in rice field was confirmed by the measurements and the declaration of applied water in other farms located in the Grande Bonifica Ferrarese and East Sesia irrigation districts. Therefore, considering that water charges for rice fields are related to the declared water quantity supplied in the field, the owner of the farm has paid less than the right amount which should have been paid during the seeding time in 1985.

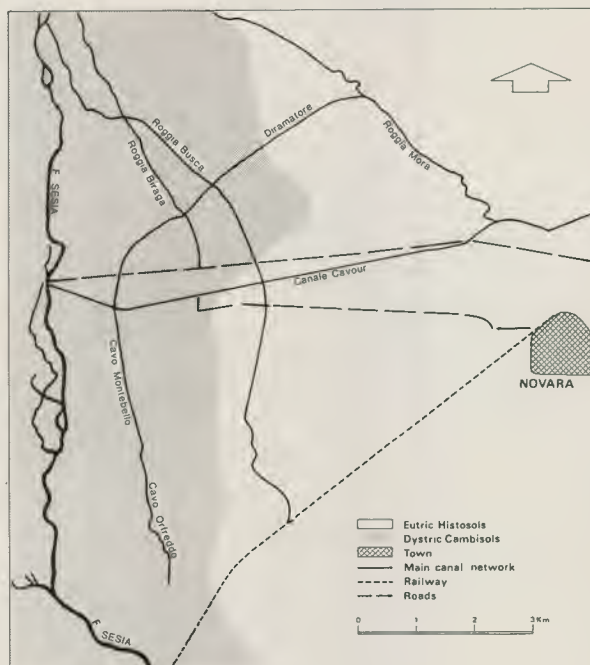


Figure 3. Sketch map of part of East Sesia irrigation district.

5. Conclusions

Crop identification and classification performed by the multi-index multi-temporal method with Landsat-TM images show how useful accurate reference data are.

The procedure shows that it is essential to have a rather consistent amount of ground truth plots and a detailed crop calendar applying to the current year in order to interpret properly the satellite images. Moreover, the application of different vegetation indices in a combined manner enhance the opportunities for classification of crops which present similar growth cycle. The achieved crop discrimination by the Landsat images gives the possibility to produce crop maps of the study areas, useful for statistical studies. On the other hand, location of the cropped area can be usefully utilised for estimation of the actual cultivated area when crop cultivation is subsidised.

The application described in this paper allows for a straightforward comparison between the cost of applying satellite data with the resulting benefit.

The here described application would probably cost 20 KAU (thousand accounting units) per year per district when operational. Since the irrigation water charges amount to some 80 AU per hectare per year, the identification of only 250 ha of erroneous declaration would pay the cost of the application. The subject 'detection of water stress' deserves special attention. The used method by means of TM-images shows good results to detect water stress in the main cultivated crops of East Sesia and in two crops of Grande Bonifica Ferrarese. These results, obtained by satellite images, were checked via a mathematical model (Swatre), by simulating the soil water balance for the whole 1985 in the two study districts. This type of research can also help to estimate how much water, delivered in the main district network, is not utilised for irrigation. Furthermore, the quantity of water delivered during the seeding stage of rice fields is detected by means of TVI for different soil types. Such results can assess the uniformity of water application by the irrigation districts.

References

- Anderson JW 1985, Remote sensing finds down-to-earth application. Commercial Space. *EARSeL News*, 28: 36-39.
- Azzali S 1985a, *A multi-index multi-temporal approach to map crops in the early growing season. An application to two Italian irrigation districts: East Sesia and Grande Bonifica Ferrarese*. Nota 1611. Inst. for Land and Water Management Research, Wageningen. 39 p.
- Azzali S 1985b, *Greenness and brightness formulae applicable to East Sesia and Grande Bonifica Ferrarese*. Nota 1673. Inst. for Land & Water Managt. Res., Wageningen. 32 p.
- Azzali S 1986, *Matching the analysis of Landsat data to users' requirements*. Nota 1711. Inst. for Land & Water Managt. Res., Wageningen. 15 p.
- Azzali S 1987, *The contribution of Landsat data to water management in two Italian irrigation districts*. Nota 1764. Inst. for Land & Water Managt., Wageningen. 47 p.
- Belmans C, J.G. Wesseling & R.A. Feddes 1983, Simulation model of the water balance of a cropped soil: Swatre. *J. Hydrol.*, 63: 271-286.
- Crist E & W Malila 1981, A technique for automatic labeling of Landsat agricultural scene elements by analysis of temporal-spectral patterns. *Proc. 15th Intl. Symp. remote sensing of environment*. Ann Arbor, 11-15 May, 1981. Vol. II: 1227-1236
- Curran PJ 1981, Multispectral remote sensing for estimating biomass and productivity. In: H. Smith (ed.), *Plants and the daylight spectrum*, Academic Press, 65-99.
- Hall FG & RB MacDonald 1983, A survey of automated remote sensing for agriculture. *Proc. IGARSS*, San Francisco, Aug. 31-Sept. 2, 1983. Vol. II, FA-5: 1.1-1.12.
- Hall K 1984, *Studies on the qualitative influence of various biological and physical parameters on Landsat-MSS data*. Rapport och Notiser 59. Lunds Universitets Naturgeografiska Institution, Lund. 49 p.
- Hatfield J.L. 1983, Evapotranspiration obtained from remote sensing methods. In: D. Hillel (ed.). *Advances in Irrigation*, Vol. 2. Academic Press: 395-416.
- Heilman JL, ET Kanemasu, JO Bagley & VP Rasmussen 1977, Evaluating soil moisture and yield of winter wheat in the Great Plains using Landsat data. *Remote Sens. Environt.* 6: 315-326.
- Jackson RD 1986, Remote sensing of biotic and abiotic plant stress. *Ann. Rev. Phitopatol.* 24: 265-287.
- Jackson RD, PJ Pinter jr., RJ Reginato & SB Idso 1986, Detection and evaluation of plant stresses for crop management decisions. *IEEE Trans. geoscience and remote sensing*, vol. GE-24 1: 99-106.
- Johnson WR 1981, A temporal/spectral analysis in small grain crops and confusion crops. In: *Agristars*. NASA, Houston. 61 p.
- Kauth RJ & GS Thomas 1976, The tasseled cap - a graphic description of the spectral-temporal development of agricultural crops as seen by Landsat. *Proc. Symp. machine processing remote sensed data, LARS*, Vol. 4b: 41-50.
- Menenti M., S. Azzali, S. Leguizamon & D.A. Collado 1986, Multitemporal analysis of Landsat Multispectral Scanner and Thematic Mapper data to map crops in the Po valley (Italy) and in Mendoza (Argentina). *Proc. 7th Intern. Symp. on remote sensing for resource development and environmental management*, Enschede, 25-29 August, 1986. Vol. 1: 293-299.
- Nilsson HE 1984, Remote sensing of plant stress and diseases. *Proc. integrated approach of remote sensing*. Guilford, 8-11 April, 1984: 115-125.
- Pinter PJ jr 1982, Remote sensing of microclimatic

stress. In: *Biometeorology in Integrated Pest Management*. Academic Press: 101-145.

Price JC 1986, Applications of remote sensing in the U.S. Department of Agriculture. *Proc. IGARSS Symp.*, Zurich 8-11 September, 1986: 739-742.

Remote Sensing of Limnological Parameters in Reservoirs

J.L. Ortiz Casas and R. Peña Martínez

Centro de Estudios y Experimentación de Obras Públicas, Madrid, Spain

Evaluation and mapping of surface limnological variables in reservoirs has been made, on a single-date basis, by making use of Landsat-5 TM imagery. The variables used were water temperature, chlorophyll a concentration, and Secchi depth transparency. Surface-water sampling and Secchi disk measurements were carried out concurrently with Landsat satellite data acquisition dates, covering 2-4 reservoirs in each quarter of TM scene under study, and providing ten sampling sites per water-body. In total, eight images/dates were included in the study, involving up to eleven reservoirs, distributed in three different quarters of TM scene. Single-date empirical relationships were developed by multiple stepwise regression analysis, making use of the TM spectral band counting values as independent variables. Colour-coded reservoir thematic maps were developed from those relationships which actually proved to be significant.

While surface-water temperature did not provide significant relationships, it was possible to develop reliable maps for chlorophyll and Secchi depth transparency in most instances, whereas combinations of spectral TM bands turned out to be different in all the equations obtained.

1. Introduction

The incorporation of the new sensor Thematic Mapper in the Landsat satellites since the launch of Landsat-4, and the consequently higher resolution power (i.e., smaller pixel size) and more refined spectral discrimination, as compared to the multispectral scanner features, make satellite remote sensing more promising for inland water studies. This project aims at the application of TM digital imagery to the indirect evaluation of surface limnological variables related to reservoir trophic status, such as chlorophyll concentration and Secchi disk water transparency, as well as water temperature.

There are in the literature a number of studies about Landsat imagery application to the evaluation of limnological variables in lakes, reservoirs and estuaries, but most of the efforts carried out so far involved the MSS sensor, since this was first used in Landsat satellites. Some of these study programmes were focused on the classification of water bodies within a regional or State area according to the trophic condition as deduced from some eutrophication index based on a set of limnological parameters. Other studies have provided specific relationships for some given reservoirs, either on a specific date or on a multirate basis. The evaluation of the different limnological variables within each of the pixels covered by the reservoir surface image results in the preparation of thematic mapping for the variable and date of concern.

No previous experience has been developed in Spain on this type of satellite remote-sensing application, in spite of the special interest given to this approach by the large amount (near to 900) of dams spread out all over the country. The study referred to in this report is focused on a small number of Spanish reservoirs, gathered in a few quarters of TM imagery scenes, which are being analysed for a set of dates throughout 1985.

2. Overall Approach and Methods

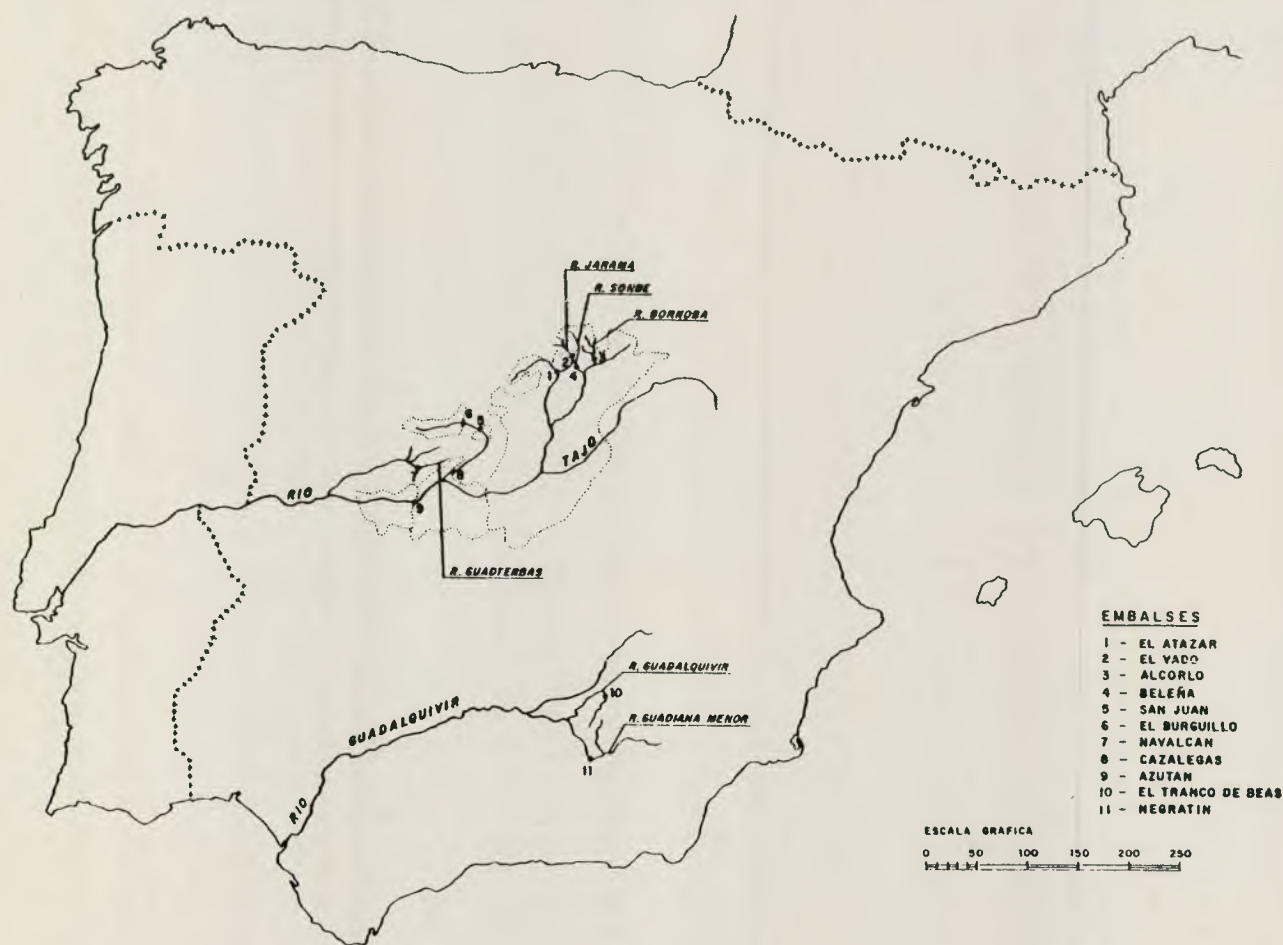
In order to achieve single-date empirical relationships between spectral bands and true values of limnological variables, and to develop further thematic mapping for the groups of reservoirs under study, ten sampling stations per reservoir were provided. At each of these points, water sampling and field measurements concurrent with remote sensing data acquisition dates have been carried out for determination of surface-water temperature, surface-chlorophyll concentration and Secchi disk transparency. Reservoirs and dates selected for this purpose are listed in Table 1 where image identification data are included as well as storage capacity and water surface area at full pool conditions.

The selection of reservoirs has been made in such a way that the largest possible number of waterbodies, up to

Table 1. Reservoirs studied and sampling/image dates

Reservoir	Storage capacity hm ³	Water surface ha	Image			Landsat-5 Image Dates
			Path	Row	Quarter	
El Atazar	468	1200	201	032	II	4 July 85 6 Sept 85.
El Vado	57	264	201	032	II	
Alcorlo	180	595	201	032	II	
Beleña	56	287	201	032	II	
San Juan	162	650	202	032	II	15 Oct 85.
El Burguillo	208	680	202	032	II	
Navalcán	34	746	202	032	IV	9 Jun 85
Cazalegas	11	150	202	032	IV	12 Aug 85
Azután	113	1250	202	032	IV	13 Sept 85.
Tranco de Beas	500	1800	200	034	II	27 Jun 85.
Negratín	546	2170	200	034	II	

Figure 1. Reservoirs location map



four as a maximum, are gathered in a single quarter scene, in order to draw the greatest possible advantage of the information acquired in each CCT. Each group of reservoirs has been treated as one single statistical data

population, for every date and variable of concern. Consequently, each population is made up by 40 data at the most, for every limnological variable and sampling date, even though this population size has rarely been reached.

It would have been helpful to have big contrasts in trophic conditions within a single group of reservoirs, in order to widen the spectrum, but this was not actually feasible, since geographic proximity proved to be associated to limnological similarity. The map in Figure 1 shows the location of the reservoirs under study.

As for the choice of image and sampling dates, it has been limited to summer season for several reasons:

- 1) Summer time is the period which brings about the highest water quality concern from a water management viewpoint, since recreation and water supply uses of reservoirs gain more relevancy during this season.
- 2) It is in summer when not only more critical and continued reservoir eutrophication symptoms occur, but also when a higher probability for significant gradients or contrasts along waterbodies are actually offered.
- 3) It is likewise in summer when there is a higher likelihood of cloud-free imagery availability. The reiteration of sampling days in group 202-032-IV is just a consequence of higher occurrence of sunny days experienced in that area.

The work steps following field and laboratory determination were performed by means of the digital image analysis and display system NUMELEC 'Pericolor 1000', owned by the Spanish NPOC (CONIE by the time during which the collaboration took place, presently INTA). The operations carried out with this equipment can be summarised as follows:

- a) Location of subscenes where the reservoirs of concern are included, within each quarter of scene, and identification of the image coordinates taken as subscenes origins.
- b) Delimitation of reservoir shorelines, by replacing land- water separation pixels by blanks.
- c) Screen pixel identification of sampling sites. For this purpose, reservoir map transparencies were superimposed on the image displayed on the screen. Maps had first to be reduced by photography to the same scale in the display system.
- d) Land masking, by automatic removal of all those pixel digital values over threshold used for reservoir shoreline delimitation and, in general, of all those located off the area enclosed by the reservoir shoreline.
- e) Direct video console extraction of digital data corresponding to the sampling sites and all their eight surrounding pixels, for each one of the seven TM bands. Once the statistical data work-up was completed as referred to above, another task was also accomplished with CONIE's equipment.
- f) Spectral band combination, according to the statistical relationships thus obtained for reservoirs within each quarter of scene, and display of these combinations,

by attributing subsequent digital ranges with a set of colours. In some instances, it was found appropriate to make a slight filtering treatment of the image, by applying a numerical convolution procedure to every image pixel. Such filtering has no other goal but just to improve its general outlook, aiming at further over-view interpretation.

The remainder of the work was performed as summarised below, by using the facilities of the Centre for Hydrographic Studies, namely a personal computer Sharp MZ-80B:

- a) Background data storage, including digital radiance counts as drawn from the Pericolor system.
- b) Calculation of chlorophyll *a* concentrations, and computer storage of the corresponding results.
- c) Statistical data work-up through multiple correlation and multiple linear regression analysis.

As dependent variables, surface water temperature, inverse Secchi depth, and surface chlorophyll *a* were taken. As independent variables, radiance count values for each of all seven TM bands were taken into account. The procedure used was the buildup of multiple linear regression equations through selective accumulation of independent variables. The first variable to be chosen is the one showing the highest simple correlation coefficient with the dependent variable as well as the smallest standard error of estimate. In each subsequent stage, the next variable to be chosen is the one showing a higher multiple correlation coefficient and smaller standard error after accumulation to the previous variable(s). This process is ended as soon as the improvement trend either is reversed or becomes non-significant.

3. Goals Achievement

As pointed out above, the immediate goals fixed in this Project were the development of a set of empirical relationships, for each one of the dates previously scheduled, and for the three limnological variables referred to above (water temperature, chlorophyll, inverse Secchi transparency), thus permitting to assess the variable values occurring on the corresponding date at any site of any reservoir included within the same image (i.e. quarter of Landsat TM scene).

As a consequence of the above achievement, it was intended to develop thematic maps, for each of the reservoirs and dates of concern, showing the surface value distribution for each of the three limnological variables.

After completion of this study, it was found that surface water temperature data did not turn out to offer, by far, significant regression fits with band 6 counting data, unlike what might be expected, bearing in mind that this band is the thermal infrared spectrum section. In con-

trast, chlorophyll concentration and inverse Secchi disk transparency did result in significant regression and mapping, except for some cases which will be a subject for further discussion below. Even so, a possibility remains open for an improvement of this technique to be attempted by making use of various approaches:

- 1) Optimization of the iterative multiple regression procedure.
- 2) Expansion of the monitoring sampling program, including depth-integrated water samples.
- 3) Incorporation of atmospheric, solar and radiometric corrections.
- 4) Temperature is taken into account for the time of direct field measurements, as compared to the time of satellite imagery acquisition.
- 5) Improvement of sampling site and pixel identification system.

4. Significant Results

In order to present correctly the statistical results appearing to be more significant, these will be discussed separately, according to the limnological variable of concern. Some of the equations involving chlorophyll and transparency have been selected to prepare colour-coded thematic maps, which are shown in Figures 2 through 5.

4.1. Water temperature

As previously pointed out, surface water temperature did not provide the results which might be expected, since band 6 (thermal infrared), did not appear in half of the equations developed for this variable. It did not either provide at least moderately high values for simple correlation coefficients.

However, for images dated 25/6/85 (Navalcán) and 27/6/85 (Tranco de Beas/Negratín), the resulting determination coefficients were very high (0.99 and 0.84 respectively), band 6 data being among the independent variables chosen by the statistical procedures referred to above. Simple correlation coefficients for temperature and band 6 data were instead as low as 0.30 and 0.24 respectively.

In general, the standard error of estimate is low, sometimes very low, but these results are misleading if no account is given to the narrow ranges. In fact, differences between extreme values are usually as small as 2°C and this limitation does not permit to develop valuable predictive equations.

It should also be pointed out that Azután Reservoir data were excluded from regressions, because they happened to impair very much the statistical correlations for all images where it was included. This can be due, on one hand, to the fact that its short water residence time (about fifteen days) makes it possible for the time gap between

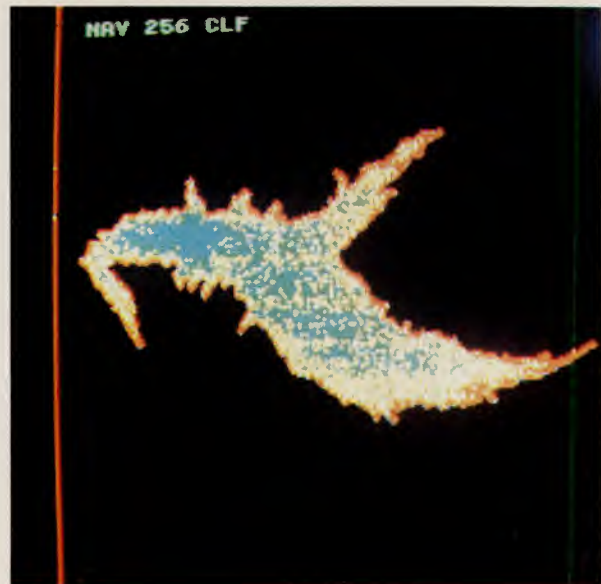


Figure 2. Surface chlorophyll concentration (mg/m^3) of Navalcán Reservoir derived from Landsat-5 TM image of 25/6/85. Red >80 ; yellow 60-80; green 40-60; light blue 20-40; dark blue <20 .

sampling and Landsat overpass to account for significant water temperature differences caused by the overall downstream flow within the waterbody. It should be emphasised that surface water temperature changes in day time much more remarkably than transparency and chlorophyll concentration do.

4.2. Chlorophyll

The results of the multiple lineal regression analysis performed on every image for surface chlorophyll concen-

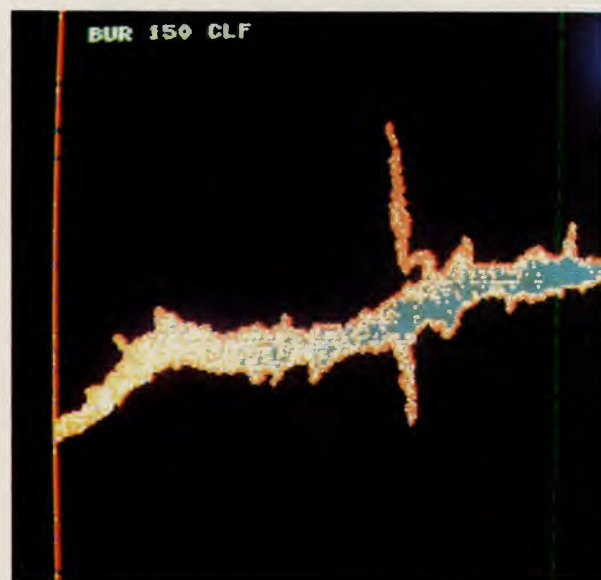


Figure 3. Surface chlorophyll concentration (mg/m^3) of El Burguillo Reservoir derived from Landsat-5 TM image of 15/10/85. Red >20 ; yellow 15-20; green 10-15; blue <10 .

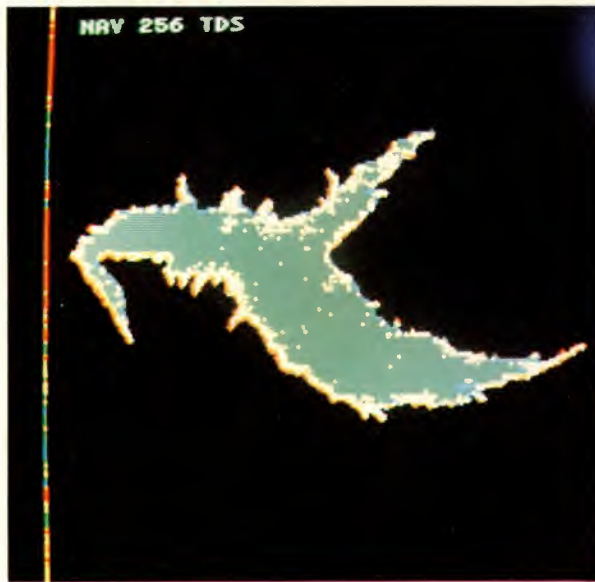


Figure 4. Secchi depth (m) of Navalcán Reservoir, derived from Landsat-5 TM image of 25/6/85. Red < 0.5; yellow 0.5-0.6; green 0.6-0.7; blue > 0.7.

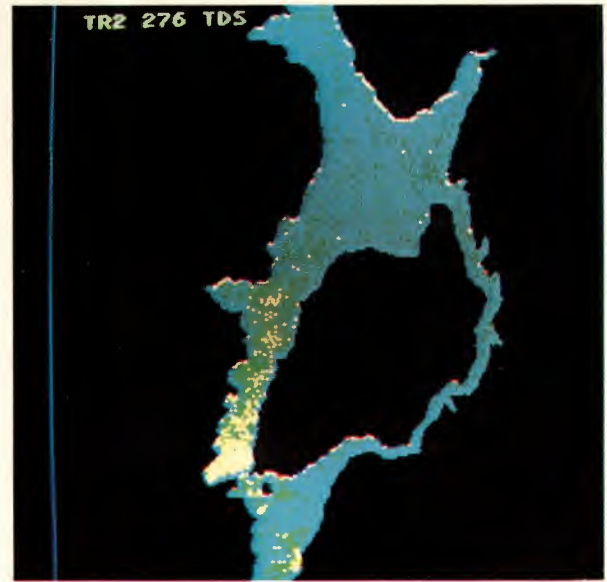


Figure 5. Secchi depth (m) of El Tranco Reservoir, derived from Landsat-5 TM image of 27/6/85. Red < 1; yellow 1-2; green 2-3; blue > 3.

tration are shown in Table 2. Even though the multiple determination coefficient generally showed fairly good values, remarkable exceptions were found on 4 July (Atazar/Vado/Alcorlo/Beleña) and 6 September (same group of reservoirs), especially those of the first date mentioned, which resulted in a R^2 value as low as 0.07. In both cases, the reason for such a poor result seems to be the occurrence of slight remainings of cloudiness, which could not be even noticed at a first glance on the 'quick-look' prints.

On the other hand, the standard error of the estimate turns out to be around 25% in most instances, except for

images dated 25 June (Navalcán) and 13 September (Navalcán/Cazalegas), where the standard error went down to 13.3% and 11.4% respectively. Both equations bring about the best correlations, as well, resulting in 0.86 and 0.96 as respective R^2 values. It is worth emphasising that the equations obtained from these two latter images, although offering very satisfactory regressions, involve totally different combinations of bands (bands 1 and 4, on 25/6/85; bands 2, 7 and 5, on 13/9/85), which is not a promising finding with regard to further development of 'multidate' equations.

Unlike temperature, chlorophyll range for each date was

Table 2. Results of multiple lineal regressions for surface chlorophyll concentration

Date	Image	Reservoirs	Excl.	Bands	N	R^2	SE: %mY	Range(*)
090685	202/32/4	CAZ-NAV-AZU	AZU	1-7-4	20	0.74	25.1	9.4-48.8
		CHL-a = 200.612 - 3.016* TM1 + 2.953* TM7 + 2.662* TM4						
250685	202/32/4	NAV-AZU	AZU	1-4	10	0.86	13.3	24.0-84.9
		CHL-a = 371.291 - 6.815* TM1 + 13.153* TM4						
270685	200/34/2	TRB-NEG	-	1-7-5	20	0.85	28.0	0.1- 1.0
		CHL-a = 5.094 + 0.069* TM1 - 0.253* TM7 + 0.085* TM5						
040785	201/32/2	ATZ-VAD-ALC-BEL	-	6-3	39	0.07	54.1	1.1- 6.4
120885	202/32/4	CAZ-NAV-AZU	AZU	3-4-7	20	0.81	25.7	19.7-98.5
		CHL-a = 117.376 - 7.238* TM3 + 8.233* TM4 + 3.890* TM7						
060985	201/32/2	VAD-ATZ-ALC-BEL	-	5-6-7	39	0.53	51.5	0.2- 6.4
130985	202/32/4	NAV-CAZ-AZU	AZU	2-7-5	18	0.96	11.4	14.2-69.9
		CHL-a = 227.363 - 6.196* TM2 - 2.067* TM7 - 2.007* TM5						
151085	202/32/2	SJN-BUR	-	3-4-6	19	0.80	30.1	6.1-41.6
		CHL-a = 64.831 + 5.446* TM3 + 3.237* TM4 - 1.319* TM6						

(*) Chlorophyll a, mg/m^3

CHL-a = chlorophyll a concentration

Table 3. Results of multiple lineal regressions for Secchi disk transparency

Date	Image	Reservoirs	Excl.	Bands	N	R ²	SE: %mY	Range(*)
090685	202/32/4	CAZ-NAV-AZU	AZU	1-2-7	20	0.75	14.8	0.55–1.05
		1/SDT = 5.261 - 0.097* TM1 + 0.102* TM2 + 0.49* TM7						
250685	202/32/4	NAV-AZU	AZU	5-4-1-6	10	0.87	1.1	0.59–0.64
		1/SDT = 1.567 + 0.018* TM5 - 0.036* TM4 + 0.015* TM1 + 0.018* TM6						
270685	200/34/2	TRB-NEG	—	7-3-1-2	20	0.79	10.6	1.64–3.85
		1/SDT = 0.538 - 0.054* TM7 + 0.042* TM3 - 0.010* TM1 - 0.002* TM2						
040785	201/32/2	ATZ-VAD-ALC-BEL	—	1-3-2-4	39	0.49	25.0	2.43–7.14
120885	202/32/4	CAZ-NAV-AZU	AZU	1-2	20	0.22	10.1	0.35–0.55
060985	201/32/2	VAD-ATZ-ALC-BEL	—	2-6-3-5	39	0.78	19.5	1.50–9.40
		1/SDT = - 2.050 + 0.016* TM2 + 0.014* TM6 + 0.014* TM3 - 0.010* TM5						
130985	202/32/4	NAV-CAZ-AZU	AZU	2-6	19	0.88	7.7	0.40–0.75
		1/SDT = - 4.371 - 0.083* TM2 + 0.074* TM6						
151085	202/32/2	SJN-BUR	—	5-1-3	19	0.73	18.3	1.60–4.40
		1/SDT = 0.816 + 0.061* TM5 - 0.024* TM1 + 0.032* TM3						

(*) Transparency, m 1/SDT = inverse Secchi disk transparency

very wide for most images, reaching high values of 40 mg/m³ in five from the eight images under study. This makes the equations more valuable as predictive tools and it results in more reliable thematic mapping. By looking at the photographs of the thematic chlorophyll maps developed (see examples in Figs. 2 and 3), it can be noted a distribution pattern from tail to dam. Based on the colour distribution, a higher concentration often appears along the reservoir shorelines. This must be due, in fact, to a higher accumulation of algae near the shore, and so was actually checked in a number of cases. Yet it can not be discarded that sometimes the resulting red colour is due to either the influence of shallow sandy beds, or bottom sediment disturbance by the waves' action.

4.3 Secchi disk transparency

As previously indicated, the reverse of Secchi disk depth, rather than Secchi transparency, was taken as the dependent variable, in order to handle values positively correlated with the satellite radiance count data. All pertinent statistical data are reported in Table 3, while two of the resulting Secchi depth maps are shown in Figures 4 and 5. Significant results obtained from all the above data are largely similar to those stated in 4.2. for chlorophyll concentration. Namely:

- 1) Fairly good determination coefficients, except for images dated 4 July and 12 August. On 4 July, as pointed out in 4.2. there were slight remainings of cloudiness on the area, while on 12 August, the Secchi depth range turned out to be very narrow, covering only from 0.35 to 0.55 m.
- 2) Rather low values for standard errors of estimate, even lower than those for chlorophyll regressions.
- 3) Different band combinations in all equations, band 2 (green) being the one appearing in more equations (four from six valid equations).

- 4) Distribution pattern of Secchi depth values according to the expected general pattern, that is, normally showing higher transparency values from tail to dam.
- 5) Need of excluding Azután data, in order to get significant regressions from all images where this waterbody was included.

5. Publications

During the period covered by this study, a paper was presented in the 1st Scientific Meeting of the Remote Sensing Working Group, organised by the Instituto Jaume Almera (CSIC) in Barcelona, 10-11 December 1986, under the title 'Cartografía temática de embalses' by R. Peña and J.L. Ortiz. This paper has been published in the Proceedings of the above Meeting. Also in press is a summary reporting this study programme in the Boletín Bibliográfico de Ingeniería Civil issued by the CEDEX.

Within two years, a Final Report is planned to be published by the CEDEX accounting for a four-year cooperative US-Spanish Project, as a follow-up to these studies.

6. Difficulties Encountered

Some of the operational difficulties arisen during this study have nothing to do with remote sensing, as they have been indirectly referred to in precedent pages. Thus, chlorophyll concentration measurement is, by itself, a question to be tackled cautiously, since not all of the analytical methods proposed in the literature yield the same results. It should be stressed that surface

chlorophyll concentration at a given pixel site was actually represented by one single water sample, which involves the assumption that chlorophyll is evenly distributed all over the pixel area. While generally this is practically the case in reality, some significant differences in chlorophyll might occur whenever patchy algal growth or blooms take place.

Sampling point references in the field and further identification of corresponding pixels in the video console is a task subject to some uncertainty, particularly in large, wide waterbodies, or in basins presenting gentle slopes or in areas lacking conspicuous landmarks. The use of nearby geodesic survey points for this purpose has often proven to be neither feasible nor helpful. Usually, point identification by means of pairs of crossing sight lines is an approach reliable enough. In some cases, it was necessary for sampling points to be located on the image to superpose on the display screen transparencies taken from previously available maps.

The desirability to sample water at the same time of the satellite overpass (half an hour past noon, official summer time) can not be met thoroughly, due to operational reasons. Many of the limnological determinations have often been made with a 5-hour gap in relation to the satellite passtime. Normally, this is not important, but in those reservoirs undertaking a high turnover rate, like Azután (water retention time, 15 days), there is the possibility for a significant downstream water movement, with a consequent displacement of plankton biomass.

Operational troubles typically associated to this kind of studies are those related to the weather conditions, i.e., the occurrence of waves, whether or not with foam formation, haze, cloudiness, etc. Particularly, whenever the absence of clouds are nearly total, but no absolute, there is a chance of partial interferences caused by very light remains of clouds in process of disappearance, even though the 'quick look' prints do not clearly show such an interference.

Troubles may also arise when dealing with clean, shallow waters lying over sandy bottoms as well as in very narrow reaches, wherever the distance to the shoreline turns out to be shorter than the pixel size. Another type of interferences in water can be due to high mineral turbidity and colour caused by factors other than algal growth.

7. Data Quality and Delivery

As a whole, the quality of the digital CCT data received from the Fucino station was excellent. Exception should be made, however, for the 202/032-2 image, dated 15 October 1985, where some black pixels lines appeared on San Juan reservoir, probably because of some malfunc-

tion in the TM operating system. Fortunately, the pixels affected were not coincident with sampling sites, and therefore they did not disturb the statistical regression analysis, while for thematic mapping purposes they will call for some further correction.

More important was the omission of information derived from the data 'cutting out' regularly operated at Fucino station on the image scene edges. This omission, justified by the necessity for satellite information size to fit the standard capability of 1600 bpi CCT, may be irrelevant for those users who, needing, for some reason, to handle adjoining scenes imagery, are provided with a wide overlapping of data. In contrast, for some applications like the one dealt with in the present project, where the study area is greatly restricted and clearly specified, the information thus lost for this reason becomes irretrievable though it may involve the area of concern. In fact, this was the case for San Juan and Alcorlo reservoirs, which happened to be partially 'mutilated' because of the image cutting referred to above.

As far as data delivery is concerned, no delay has been experienced in relation to terms previously announced by the Spanish NPOC, neither for the 'quick-look' prints nor for the CCTs.

8. Recommendations

In view of the experience gained so far, it should be recommended either to modify the CCT data format, or to increase the number of tapes per quarter of scene in order to provide entire room for the whole information ordered and thus avoid the data omission discussed above.

It is unquestionable that for those users concerned with specific and reduced imagery areas, it would be very advantageous to be given the possibility to acquire smaller image sections, say, a ninth or a sixteenth of scene. Taking into account the high cost involved in satellite digital imagery acquisition, up to levels potentially dissuasive for some project, the utility of Landsat satellites would be significantly increased by somehow making more feasible the acquisition of this type of digital information, specially for those study programmes focused on very small surface areas. In this respect, it was a very valuable initiative to permit this and other research groups to benefit, during the annual period covered by this project, from a symbolic price, as compared to the nominal price set for the year 1985.

As for the need for technical improvements, the guidelines have been already mentioned in section 3.

Acknowledgement

The authors of this report wish to express their gratitude to the Spanish NPOC, for its valuable cooperation in the progress of the study, which could not otherwise have been achieved. Particular acknowledge is indebted to

José M^a de la Cruz, for all the support and facilities he provided throughout the study period, as well as to Rufino Barco, for his efficient and continued technical assistance and to ESA/Earthnet for the provision of TM data.

Colour Analysis of Inland Waters Using Landsat TM Data

J.-M. Jaquet

Dept. of Geology, University, 13 rue des Maraîchers, CH-1211 Geneva

B. Zand

GRID-Processor, UNEP, 8 rue de la Gabelle, CH-1227 Geneva

Chromaticity transforms based on TM bands 1, 2 and 3 have been computed for over 50 inland water bodies located in western Switzerland and south-eastern France. They include large, deep subalpine lakes, Jura and alpine mountain lakes, reservoirs, ponds and rivers. Their trophic state varies between oligotrophic and eutrophic.

In chromaticity space, hue range from green-blue, moderately saturated (clear water) to green, less saturated (high chlorophyll). A third pole is located towards isoradiance point (high mineral turbidity). Targets with bottom signal influence plot in between.

It is shown that colour transforms yield more information on water bodies typology and features than principal component analysis based on band radiances.

Keywords: Landsat, TM, inland waters, chromaticity, water colour, classification

1. Introduction

The classification of water into 'types', based on optical properties (Jerlov 1976), has been widely applied to oceans. Colour studies of sea water were given a significant impetus by the advent of Nimbus CZCS, and numerous algorithms are now available to link the spectral signature of water to its chlorophyll or suspended solid content.

The relatively small size of many inland water bodies has not favoured the use of CZCS in limnology. To date, most of the applications of remote sensing to coastal or inland waters studies have been based on Landsat MSS data. The approaches taken are:

- 1) *Classifying water bodies on the basis of multiband intensity data into types related to the trophic spectrum (oligotrophic to eutrophic). Examples include the work of Wezernak et al. (1976), Blackwell and Boland (1976), Lillesand et al. (1983) and McGarrigle and Reardon (1986).*
- 2) *Statistically relating single-band intensities (as DN values) or band ratio to usual limnological parameters such as turbidity (Piech et al. 1978, Shimoda et al. 1984, Lindell et al. 1985), Secchi depth SD (Smith and Addington 1978), or chlorophyll (Lemoalle 1979).*
- 3) *Computing water colour by chromaticity analysis and relating chromaticity coordinates to turbidity and*

other water quality parameters (Alfoldi and Munday 1978, Munday et al. 1979). The MSS of Landsat being devoid of a blue band, this transform results in a 'false colour' description: the information from intensity is eliminated, leaving only hue and saturation.

The advent of the Thematic Mapper affords the limnologist the following a priori advantages over MSS:

- (i) presence of a near-blue band;
- (ii) better spatial resolution (30 m vs. 80 m);
- (iii) availability of a thermal IR band.

According to Tassan (1984), the chlorophyll and sediment (sm) retrieval performance of TM approximately matches that of CZCS in marine situations (where sm is correlated to chlorophyll). So far, only a few applications of TM to limnology have been published (see for example Lathrop and Lillesand 1986, 1987).

Taking advantage of these features, we present here (a) a colour analysis of inland water bodies, (b) compare it with the results of a classical unsupervised classification and (c) relate it to known limnological parameters such as trophic status, bottom effects, and presence of submerged aquatic vegetation (SAV).

To keep variability sources to a minimum, the analysis was conducted on a single date and a single frame. Work

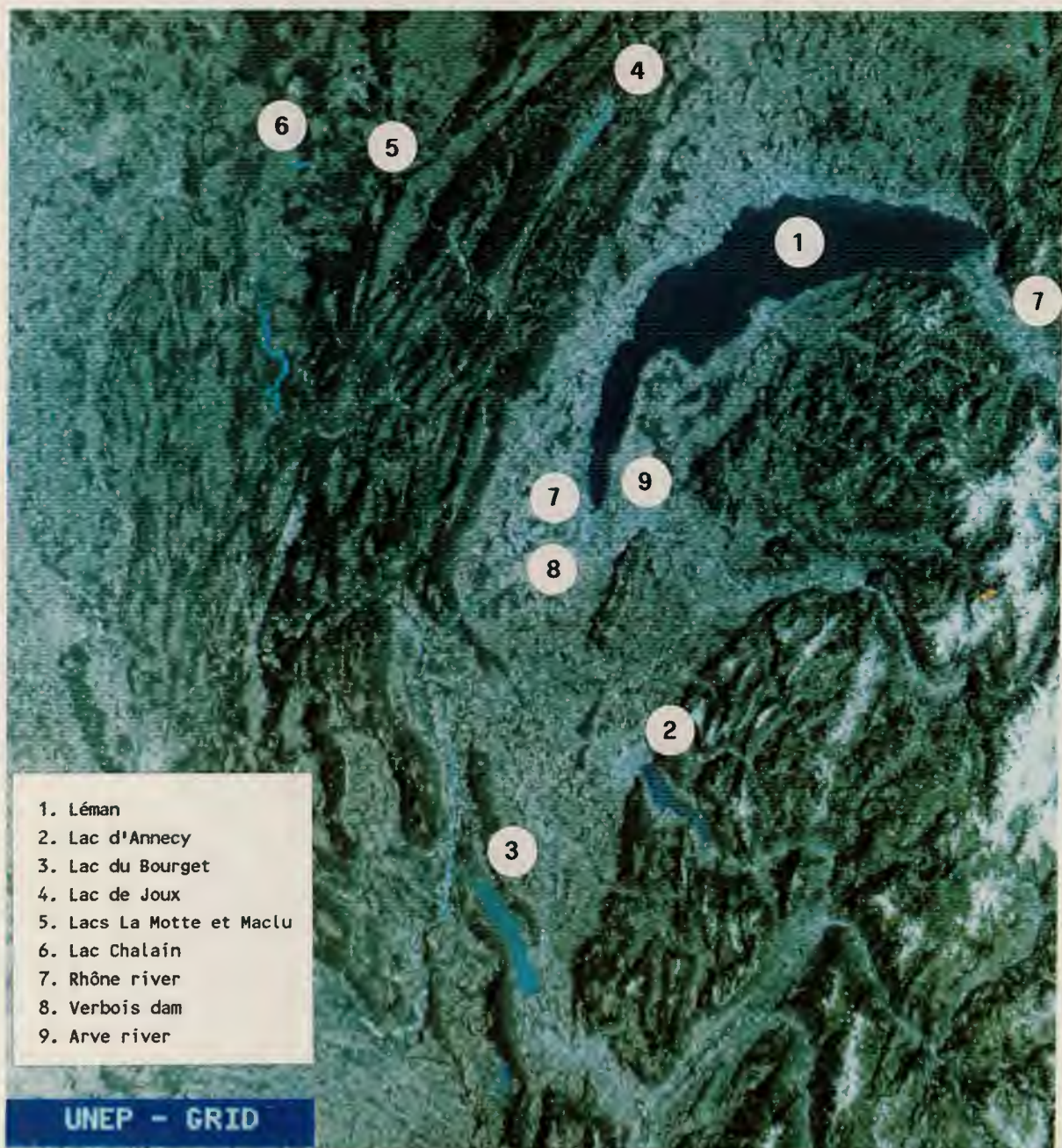


Figure 1. True colour image of Landsat TM frame 196/028 (30.07.84) showing some of the water bodies mentioned in the text. Length of Léman is approximately 100 km.

is in progress to extend it to a broader scale, temporally and geographically.

2. Material and Methods

2.1. Scene

Within the framework of the TM Pilot Studies, three adjacent frames were provided by ESA/Earthnet through the Swiss NPOC: 195/028, 196/027 and 196/028. Only the last one, taken on 30 July 1984, will be considered here. The Earthnet acquisition station is Fucino, and the data are system-corrected (radiometric preflight and

geometric correction). There is no cloud cover and the visibility vote equals 3.

Frame 196/028 covers the Jura mountains, the Plateau and part of the Alps in Western Switzerland and SE France (Fig. 1). Over 50 water bodies ranging in size from the large, deep subalpine lakes (Léman, Annecy, Bourget) to small Jura or alpine lakes or rivers have been studied. The span of their trophic status is rather large, and they are either natural or man-controlled.

2.2. Image handling and calculations

Polygons were drawn (a) at the limit between land and water by displaying band-4 images, thus including the

Table 1 - LANDSAT-5 TM RADIANCE CONVERSION PARAMETERS FOR SCENE 196/028 (30.07.84)

Band	Spread		A0	A1
	Min	Max		
1	45	255	-.067	.042
			-.117	.064
2	1	255	-.157	.104
			-.215	.127
3	10	255	-.113	.065
			-.185	.098
4	6	255	-.233	.117
			-.207	.092
5	2	255	-.086	.027
			-.042	.013
7	1	255	-.051	.017
			-.022	.007

A0: $mW\ cm^{-2}\ sr^{-1}\ \mu m^{-1}$ A1: $mW\ cm^{-2}\ sr^{-1}\ \mu m^{-1}\ DN^{-1}$

For each band:: first line = in-flight values
2nd line = preflight values
(SLATER et al. 1987)

whole water body (labelled Zbat=0 in Table 2) and (b) between inshore and pelagic zones (depth greater than 5-10 m depending on the water body; Zbat=P). This was done on the basis of bathymetric charts when available (Delebecque 1898 and large-scale Swiss and French topo maps), or by exclusion of areas with obvious bottom signal (see Fig. 2a). In some instances, they were specifically sampled and are labelled Zbat=F in Table 2.

Band statistics were computed for each polygon and chromaticity values calculated after transformation of the DN's into radiance L_i ($mW.cm^{-2}.sr.\mu m$) by means of the A0 and A1 coefficients found in the CCT radiometric calibration ancillary record (Table 1). The formulae are:

$$X = L1/\Sigma Li, \quad Y = L2/\Sigma Li \quad \text{and} \quad Z = L3/\Sigma Li.$$

Initially, an approximate atmospheric correction was applied to the data by 'dark pixel subtraction' (Rochon 1975). Since all the shadows used for correction were on land, the subtracted radiance would be too high (Piech and Walker 1971) and result in some negative values for water. Pending the application of a formal atmospheric correction, chromaticities were computed on uncorrected radiances. This does not affect the relative position of water bodies in the XYZ chromaticity space, but shifts them all towards the blue pole.

To preserve spatial resolution which is a prerequisite for the study of small lakes and narrow rivers, no filtering was applied to eliminate the various banding types present in the data (Poros and Peteron 1985). However, an

estimate of total variability due to various noise sources was obtained by computing band coefficient of variation for a seemingly homogeneous area (250×250 pixels) in Lac Léman (Fig. 1) with the following results: band 1: 2.1%; band 2: 3.0%; band 3: 5.1% and band 4: 6.7%. The differences in odd and even 16-line band mean values were 0.3, 0.5, 1.5 and 5% respectively. As a rule, we considered that differences between water bodies in terms of DN's had to be $>10\%$ to be considered as significant.

Data handling and image processing were done at the GRID-processor in Geneva using ELAS and ERDAS systems. Multiband classification of water bodies was performed on principal component scores by the modules PRINCE and CLUSTER (ERDAS). This last system was also applied when digitising bathymetric maps and setting up a GIS, in order to superimpose contours over satellite imagery (Fig. 2).

3. Results

3.1. Penetration depth of imagery

In order to assess the true signal from lake water, the influence of bottom reflection must be eliminated. According to Gordon and McCluney (1975), the penetration depth $Z_{90} < 1/a$, where a is the absorption coefficient of water for given wavelength. Since the values of a are not available for our dataset, a safe estimate of maximum penetration depth can be computed from Scherz and Van Domelen's (1974) Figure 5, whereby $Z_{90max} < SD$ for white light (see also Jaquet 1987).

From the population of water bodies listed in Table 2, we have selected clear lakes La Motte and Maclu (Fig. 1), which have a rather low reflectance in each band and white chalk banks along their western shore (Fig. 2). In band 1, the bottom signal is perceived approximately down to the 10 m contour. This value is close to the maximum SD readings known in these lakes (Verneaux et al. 1987). It is therefore safe to use $Z_{90}=10$ m as a maximum penetration depth or limit for the pelagic zone, since all the other lakes studied have $SD < 10$ m, or bottom less reflective than chalk.

3.2. Colour analysis

3.2.1. Poles and loci

The various water targets considered are plotted on colour diagrams shown in Figure 3, both as XY and triangular diagrams. Owing to the position and width of the TM bands, chromaticity coordinates do not represent 'pure' blue, green or red, but rather blue-green centered at 480 nm (X), green-yellow centered at 560 nm (Y) and red centered at 650 nm (Z). It should also be kept in mind that the swarm of points represent radiances not corrected for atmospheric influence.

Figure 2. Influence of bottom signal from Chalk Banks in TM bands 1 (strong) and 4 (weak) for lakes La Motte and Maclu.



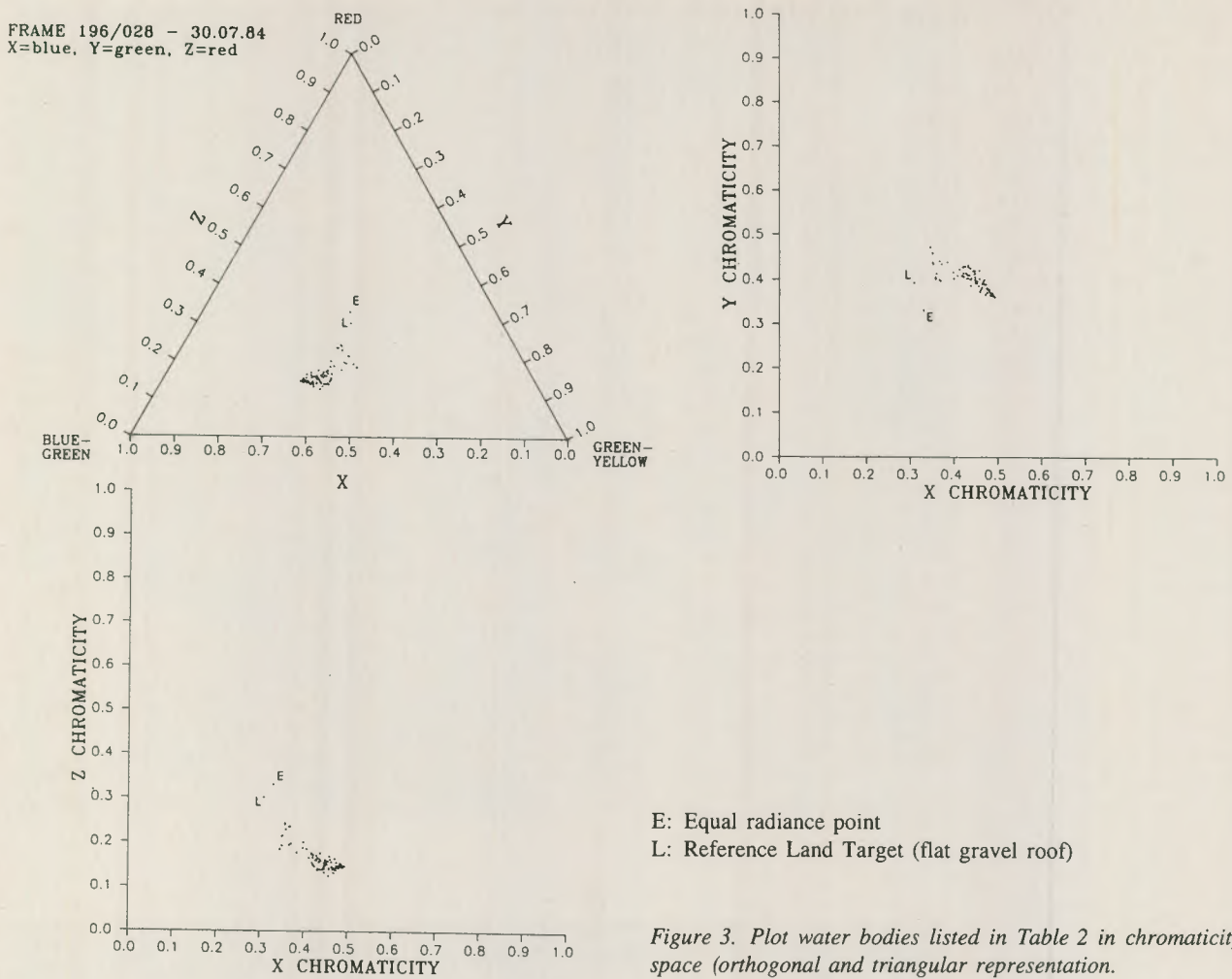


Figure 3. Plot water bodies listed in Table 2 in chromaticity space (orthogonal and triangular representation).

bidity gradient. These loci generally point towards a few attraction points (AP) also shown on the diagrams.

The water bodies located at maximum X values represent the clearest lakes of our dataset, seen as green-blue from the satellite (W). The pole of clearest known lake water would be at higher saturation towards the blue (Crater lake, Smith et al. 1973).

A second AP (C), located at maximum Y values is occupied by eutrophic lac de Joux and lac Brenet, characterised by high chlorophyll content and small SD (1.5 m at end of July 1984). Turbid alpine rivers (Arve, Rhône) cluster (M) towards the equal radiance point E, and chalky bottom sediments more or less covered with aquatic macrophytes (SAV) plot at B. The remaining water bodies are located between these attraction points, and some of them plot along well-defined loci. They are:

1) *Pelagic zone - total lake - chalky bottom*. As already mentioned, the whole lake includes signals from shallow-water banks. In most cases, they consist of white lacustrine chalk more or less covered with SAV, resulting in the intermediate position of B between C and M. This first trend type (Fig. 4), however short, consistently points towards B.

- 2) *Pelagic zone - total lake - sandy bottom*. In the large subalpine lac Léman, shallows are sandy (Vernet et al. 1972) and the SAV cover is dense (Lachavanne and Wattenhoffer 1975). They plot along a curvilinear locus among 'normal' water bodies from which they cannot be discriminated. This is in agreement with Ackleson and Klemas' (1987) results in Chesapeake Bay, where the signature from dense SAV cannot be isolated from that of deep water.
- 3) *Clear water - turbid water (mineral turbidity)*. The relatively clear water of Léman ($1-2 \text{ g/m}^3$ in Summer, Jaquet et al. 1983) empties into the Rhône river in Geneva, which receives the highly turbid alpine Arve river ($>100 \text{ g/m}^3\text{sm}$). The mixed waters are then retained behind Verbois dam (Fig. 1). The locus is curvilinear, going from lac Léman - mixture Rhône+Arve - Arve with increasing turbidity. It is similar in shape and orientation to loci shown in Munday et al. (1979) and Alfoldi and Munday (1978). It points towards the land target (T) and the iso-radiance point E.

3.2.2. Interpretation

Bukata et al. (1983) have generated subsurface irradiance spectra for lake Ontario modelled as a 4-component

Table 3 - MEAN DIGITAL REFLECTANCE FOR TM BANDS 1, 2, 3, 4, 6 AND CHROMATICITY VALUES

Name	No	CH1M	CH2M	CH3M	CH4M	CH6M	X	Y	Z	Name	No	CH1M	CH2M	CH3M	CH4M	CH6M	X	Y	Z
CHALAIN_0	1	92.14	35.77	19.17	12.14	127.16	0.447	0.419	0.133	SARINE_P	49	78.11	31.38	20.20	12.75	113.88	0.427	0.413	0.160
CHALAIN_5	2	90.65	34.51	17.43	10.09	126.26	0.457	0.419	0.125	BRET_P	52	67.46	26.26	18.10	11.85	126.37	0.432	0.402	0.166
NARLAY_P	3	60.10	18.89	12.92	9.73	124.39	0.492	0.362	0.146	BRET_0	53	67.71	26.45	18.74	15.13	127.33	0.429	0.401	0.171
GD_MACLU_P	4	57.83	18.10	12.58	9.14	125.13	0.493	0.360	0.147	EMOSSON	54	101.57	43.65	32.02	10.77	109.50	0.398	0.415	0.187
LA_MOTTE_P	6	64.10	22.25	13.53	9.44	124.46	0.473	0.389	0.138	SALANFE	55	83.44	32.54	20.76	9.84	110.75	0.435	0.408	0.156
CHAMBLY_NP	7	65.52	21.72	14.23	10.58	127.20	0.480	0.375	0.145	MONTRION_P	56	61.68	21.60	13.36	9.91	121.23	0.470	0.389	0.141
CHAMBLY_SP	8	66.92	23.64	14.84	10.56	126.13	0.465	0.390	0.144	ANTERNE_P	57	62.55	20.66	13.79	8.62	109.00	0.480	0.373	0.147
BONLIEU_P	9	63.46	22.69	13.62	9.16	124.48	0.466	0.395	0.139	NOIR	58	54.92	18.19	13.77	18.12	118.96	0.471	0.365	0.164
MOTTE_1	9	84.07	41.57	30.00	14.79	127.21	0.366	0.440	0.194	DIVONNE_P	59	70.32	25.68	17.65	11.67	130.01	0.449	0.391	0.161
ABBAYE_P	10	57.25	18.46	13.11	9.45	123.85	0.483	0.364	0.153	VERBOIS	60	90.78	36.68	26.08	12.93	126.29	0.417	0.407	0.176
CLAIRV_NO	11	94.14	39.74	25.88	13.91	128.25	0.412	0.422	0.166	MACHILLY_P	61	73.22	30.61	24.94	18.03	132.69	0.399	0.401	0.200
CLAIRV_NP	12	87.31	34.22	19.10	10.51	126.78	0.443	0.418	0.139	LEMAN_P	62	66.36	21.20	14.49	8.57	124.59	0.486	0.366	0.148
CLAIRV_SP	13	79.60	29.05	17.42	11.02	126.79	0.458	0.400	0.142	LEMAN VIDY	63	68.40	21.90	14.79	8.53	123.25	0.486	0.367	0.147
ROUSSSES_P	14	57.97	19.24	13.66	9.96	121.39	0.475	0.370	0.155	LEMAN_ROLL	64	67.61	21.44	15.00	8.69	124.19	0.486	0.363	0.151
JOUX_0	15	82.05	45.73	29.52	11.76	122.42	0.345	0.470	0.185	LEMAN_DRAN	65	66.31	20.97	14.23	8.25	125.03	0.489	0.364	0.146
JOUX_P	16	82.36	46.08	29.33	11.18	121.44	0.345	0.472	0.183	LEMAN_EVIA	66	65.34	20.89	14.09	8.39	125.02	0.487	0.367	0.146
TER	17	61.60	22.87	17.27	12.60	129.13	0.438	0.386	0.176	LEMAN_LOCU	67	64.29	20.64	13.94	8.60	123.86	0.486	0.367	0.146
BRENET_P	24	78.38	42.08	28.92	14.13	123.41	0.350	0.458	0.192	LEMAN_RHON	68	66.12	21.50	14.54	9.01	124.01	0.482	0.370	0.148
BRENET_0	25	78.48	42.01	29.15	15.78	124.40	0.350	0.457	0.193	LEMAN_VILL	69	65.93	21.34	14.30	9.43	124.26	0.484	0.369	0.146
ANNECY_0	26	76.40	25.74	16.39	9.99	124.38	0.475	0.381	0.144	ARVE_MIN	70	99.00	46.00	44.00	27.00	132.00	0.357	0.404	0.240
ANNECY_P	27	75.66	25.01	15.93	9.78	123.88	0.480	0.377	0.142	ARVE_CONTA	71	102.00	45.00	43.00	20.00	126.00	0.369	0.396	0.235
GIROTTE_P	28	131.52	62.75	46.35	12.99	106.07	0.371	0.433	0.197	RHONEVS_A	72	102.00	48.00	43.00	22.00	117.00	0.359	0.412	0.229
GITTAZ_P	29	69.53	22.23	14.55	10.84	109.64	0.488	0.369	0.143	RHONEVS_B	73	102.00	47.00	46.00	21.00	117.00	0.357	0.400	0.243
ROSELEND_0	30	68.90	26.06	16.16	10.24	111.14	0.448	0.404	0.148	RHONE_GEA	74	81.00	33.00	22.00	14.00	130.00	0.421	0.413	0.166
ROSELEND_P	31	68.75	26.08	16.16	10.02	109.69	0.447	0.405	0.148	TANNAY_P	77	61.18	20.64	13.69	10.67	118.67	0.475	0.378	0.147
GUERIN_P	32	69.80	26.67	18.20	10.95	106.10	0.437	0.399	0.163	HONGRIN_P	78	63.56	22.17	15.21	11.23	117.51	0.463	0.382	0.156
BOURGET_0	33	79.32	30.40	17.77	9.66	127.22	0.446	0.411	0.143	GENIN	79	63.89	23.95	15.53	10.32	127.32	0.447	0.399	0.153
BOURGET_P	34	79.77	30.67	17.66	9.35	127.14	0.447	0.413	0.141	PALEXPO	80	181.24	93.86	115.29	98.95	171.43	0.308	0.392	0.301
AIGUEBEL_0	35	81.32	29.72	17.52	11.20	128.39	0.458	0.401	0.140	RHONE_BUTI	81	85.14	35.32	26.23	23.68	134.41	0.407	0.408	0.185
AIGUEBEL_P	36	80.40	28.55	16.08	9.32	127.75	0.469	0.399	0.132	RADE_GE	82	68.47	23.42	17.69	9.88	125.84	0.459	0.372	0.169
VOUGLANS_S	37	93.89	38.76	20.81	10.05	126.85	0.431	0.431	0.138	ARVE_BATIE	83	100.59	45.09	42.73	23.68	131.18	0.366	0.399	0.235
VOUGLANS_M	38	87.35	35.77	19.90	10.27	125.86	0.432	0.427	0.141	LEM_VENG	84	74.34	29.44	19.36	11.24	128.64	0.430	0.409	0.161
VOUGLANS_N	39	76.91	32.44	19.79	10.18	128.06	0.419	0.426	0.155	LEM_BIT	85	72.60	26.33	17.67	10.08	126.38	0.452	0.391	0.157
CONDES_P	40	66.05	24.11	16.48	10.15	126.65	0.450	0.391	0.159	LEM_TRAVER	86	71.59	26.22	17.50	9.56	125.72	0.450	0.393	0.157
NANTUA_0	41	66.57	23.67	16.30	10.83	126.34	0.456	0.385	0.158	LEM_BABYPL	87	69.42	25.52	17.07	9.42	124.57	0.449	0.394	0.157
NANTUA_P	42	66.89	23.78	16.35	10.56	125.03	0.456	0.385	0.158	LEM_NAUTIQ	88	70.79	25.97	16.69	9.97	126.17	0.453	0.396	0.151
SYLANS_P	43	77.33	32.72	19.14	10.30	127.04	0.421	0.429	0.150	LEM_GRANG1	89	70.16	26.91	17.81	10.09	122.93	0.439	0.402	0.159
REMORAY_CR	44	85.05	43.53	34.54	12.48	125.99	0.350	0.437	0.213	LEM_GRAN2	90	74.14	30.13	21.33	10.64	123.77	0.418	0.408	0.174
REMORAY_0	45	69.75	27.93	19.70	13.39	124.87	0.422	0.405	0.172	LEM_GRAN3	91	73.25	29.46	20.81	12.89	124.94	0.421	0.406	0.173
REMORAY_P	46	65.53	23.19	14.67	9.94	123.29	0.464	0.390	0.145	CLAIRV_1	93	108.86	54.86	44.14	27.33	130.00	0.352	0.433	0.215
GRUYERES_P	47	83.43	39.18	26.11	11.97	124.27	0.384	0.438	0.177	CLAIRV_2	94	96.12	39.97	22.79	11.27	128.70	0.425	0.428	0.146
MONTALVEN	48	63.85	22.05	15.87	12.18	118.36	0.461	0.377	0.162	CLAIRV_3	95	91.14	36.60	20.20	11.06	126.80	0.437	0.424	0.139

water mass [water, chlorophyll (ch), mineral suspensoids (sm) and dissolved organic carbon (doc)]. They also computed chromaticity coordinates (blue, green, red) for water with doc=0 or 2 g/m³, ch between 0.05-20 mg/m³ and sm between 0-20 g/m³ (their Figs. 9 and 10): chromaticity loci for ch and sm are practically coincident up to concentrations of 3 mg/m³ and 1 g/m³, respectively. Beyond, they separate to form a loop with maximum opening (0.02 Y units) for ch=20 mg/m³ and sm=20 g/m³. The loci in Figure 4. form a pattern quite similar, with even a better separation (0.07 units) between the chlorophyll AP and the alpine rivers AP, which is pulled towards desaturation point E. This favourable feature stems from the high sm concentration in Rhône and Arve rivers (≥ 100 g/m³). Whilst X chromaticity is inversely related to total suspensoid concentration, Y ('greenness') allows a certain discrimination between the AP B, C and M.

The variable curvature of the chlorophyll and sm loci is probably due to the combined influence of suspensoids on hue and saturation: the colourless mineral suspensions mainly act as desaturating agents with little influence on hue, whereas coloured plant pigments logically induce a larger hue shift. Work is in progress to test this hypothesis. The straightness of type 1 trend is due to a simple mixture between the colour of deep, more saturated water and that of AP B.

It should also be noted that, since the water bodies are all located below point E on Figure 4a, a lowering of saturation corresponds to an increase along the Z axis.

Another feature of interest visible on these diagrams is the spread along the Y axis (or towards green) between green-blue lakes (Léman, La Motte) and greener ones (Chalain): this could be an effect of qualitative rather

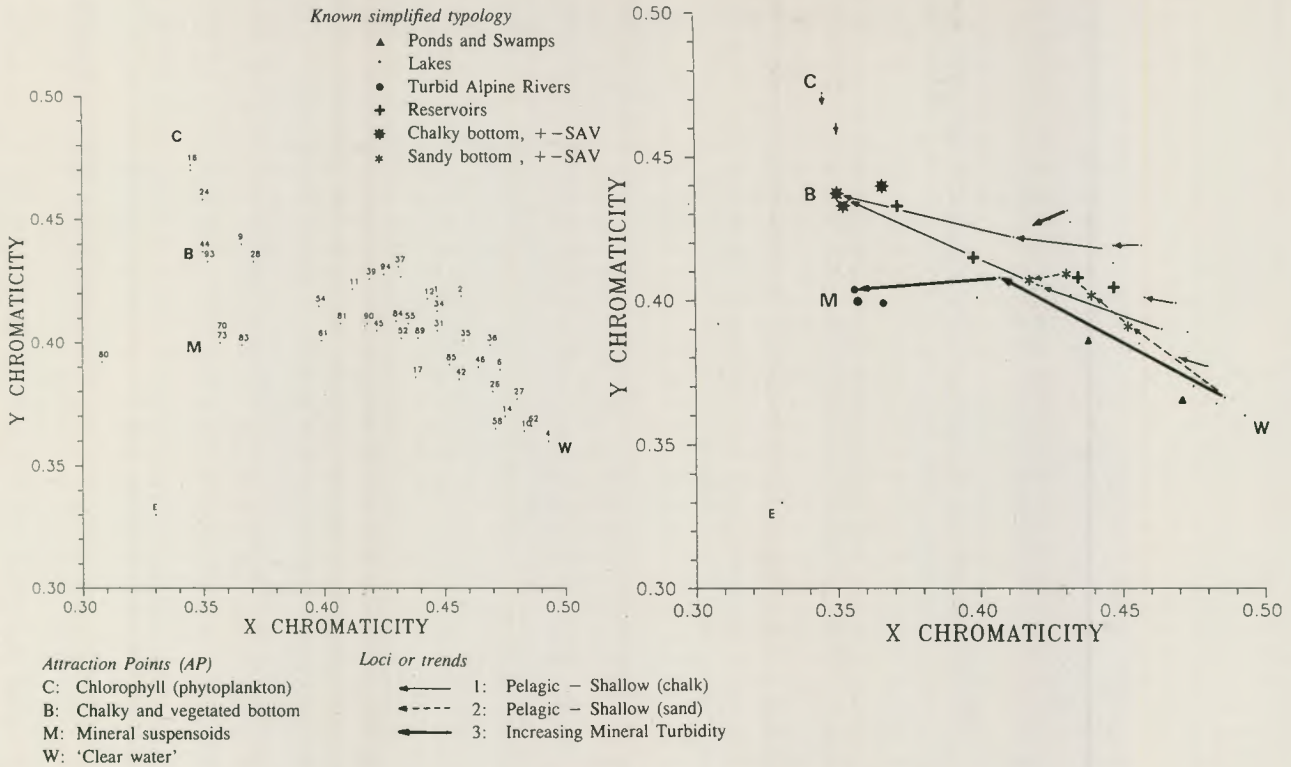


Figure 4a. Location of selected water targets in chromaticity space with typology and trends.

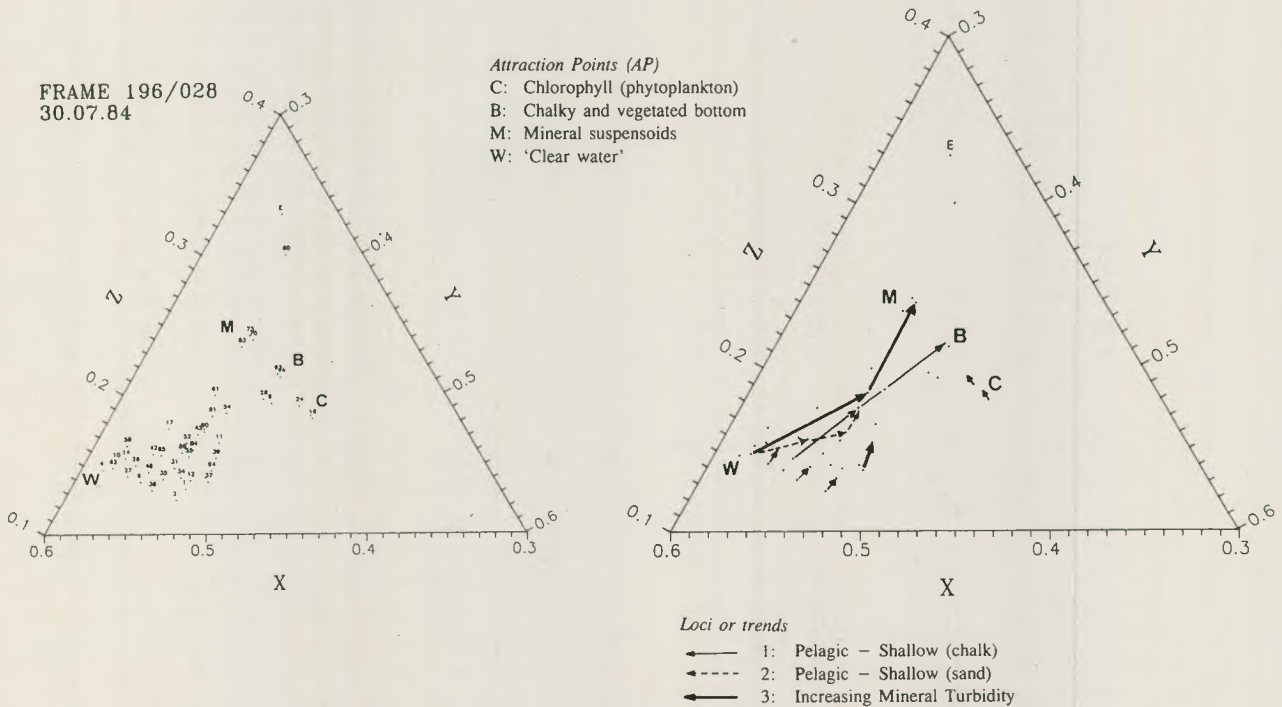


Figure 4b. Location of selected water targets in triangular chromaticity space with trends.

than quantitative changes in pigment (different phytoplanktonic species).

3.3. Four-band classification based on intensity

The information contained in the TM bands 1-4 was condensed by principal component analysis (PC) (Table 5). The results confirm the features of the correlation coefficient

matrix (Table 4): the first 3 bands are highly correlated, giving a PC allowing for more than 90% of the variance. The second PC expresses the influence of NIR1 and red bands.

A cluster analysis was performed on the PC's scores, resulting in the diagram of Figure 5. The groups are

Table 4 - CORRELATION BETWEEN TM BANDS FOR SELECTED WATER BODIES (PELAGIC ZONE).N = 45

Band	1	2	3	4	6
1		.94	.86	.31	-.11
2			.93	.34	-.09
3				.51	-.03
4					.31

Table 5 - PRINCIPAL COMPONENT ANALYSIS OF SELECTED WATERBODIES (PELAGIC ZONE) BASED ON DN's OF TM BANDS 1, 2, 3 AND 4. N = 45

PC	1	2	3	4
Variance %	91.3	5.4	2.6	0.7
Cum. var.	91.3	96.7	99.3	100.0

Eigenvectors

Band	1	2	3	4
Band 1	.79	-.39	-.46	-.15
Band 2	.49	.11	.53	-.68
Band 3	.37	.52	.40	-.66
Band 4	.09	.75	-.59	.28

represented in the PC1-PC2 space, and are discriminated essentially through intensities in bands 1, 2 and 3 (the vertical scale is blown up for clarity). Some of the trends defined above (3.2.1) are also shown. Although they are not consistent along PC1, the turbidity trends are proportional to PC2, which confirms the well-known correlation between turbidity and NIR1.

Ten groups are plotted on Figure 5, part of which can be related to the colour analysis results. Group 1 corresponds to 'dark lakes', with possibly some influence from peaty bottoms shown by relatively high values in PC2. Gr5 includes shallow, rather turbid lakes used for recreation and fishing (bottom resuspension?), and Gr6 productive 'green' lakes Joux and Brenet. Turbid rivers fall in Gr8 and 9, and alpine reservoirs in Gr7 and 10.

The relative difficulty in interpreting such a classification comes from the fact that intensity, as opposed to hue and saturation, often depends on transient, parasitic phenomena such as waves or white caps.

FRAME 196/028 - 30.07.84 - BANDS 1-4

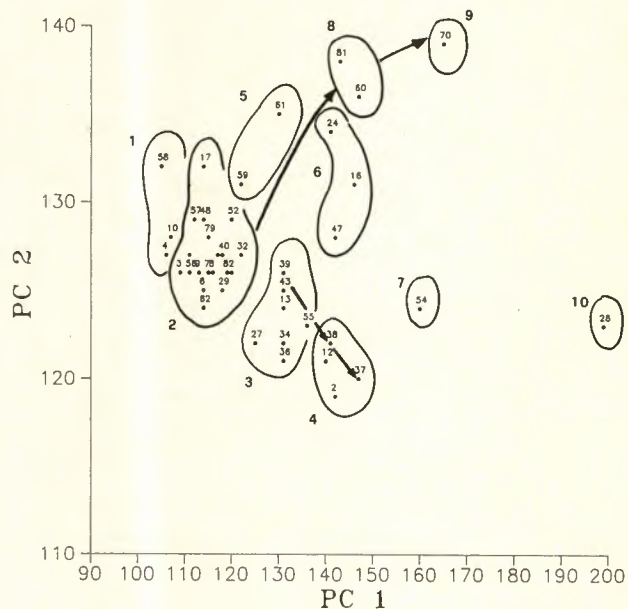


Figure 5. Classification of water bodies (Pelagic) by Cluster analysis in the two first principal components space. Group limits hand-drawn.

4. Discussion and Conclusions

The ground information available on the water bodies, not collected on the day of overpass, is very heterogeneous. Whereas some lakes such as Léman (Cipel 1984), Joux, Bourget and Jura lakes (Verneaux et al. 1987) are monitored more or less regularly, very little is known about the others (Table 2, column 6).

The notion of trophic state is a widely used, 'better-than-nothing' integrative descriptor for lakes. Discussing the merits of this notion is beyond our scope here. Suffice it to say that 'trophy' can be estimated via SD, total phosphorus or chlorophyll concentration (OECD 1982), and also from satellite data (Scarpace et al. 1979).

Chromaticity analysis, as shown on Figure 4 and restricted to pelagic data, allows a discrimination between oligo-mesotrophic lakes located around W (Maclu, La Motte, Léman, Annecy), meso-eutrophic (Bourget) and eutrophic ones (C: Joux, Brenet), following a trend of increasing pigment content. Moreover, the trend towards E separates water bodies chiefly on mineral turbidity, culminating at M (very turbid waters).

It is probable that water colour contains more information on other limnological parameters. For instance, within-lake hue and saturation heterogeneities are visible on the images, combined with thermal contrasts (TM band 6). This could help estimate spatial variability in lakes, almost impossible to measure with conventional methods.

In order to fully exploit colour information, the following should be undertaken:

- 1) *Ground colour measurements* conducted in situ and also on the organic and mineral suspensoids, so as to assess their bearing on hue and saturation.
- 2) Further *simulation of irradiance spectra* using a refined version of Bukata et al.'s (1983) model. In particular, the influence of phytoplankton type (pigment, size) should be estimated, as well as that of mineral particles (quartz, clay, autochthonous CaCO₃, Galat and Jacobsen 1985).
- 3) Application of *atmospheric correction* to allow for multirate colour analysis and a generalisation of the relationships found in this preliminary study.

At this stage, we can conclude that an excellent ground resolution and the presence of a 'blue' band make Landsat TM a valuable tool for the study of inland waters — superior in that to the much used MSS.

Acknowledgements

This report is a product of a continuing joint venture between UNEP-GRID and University of Geneva. The assistance and encouragements of D.W. Mooneyhan, director, and L. McGregor, both with GRID-P, are gratefully acknowledged, as well as that of J. Charollais, director of the Geology Department.

References

- Ackelson S.G. and Klemas V., 1987. Remote Sensing of Submerged Aquatic Vegetation in Lower Chesapeake Bay: A Comparison of Landsat MSS to TM Imagery. *Remote Sens. Envir.* 22: 235-238.
- Alföldi T.T. and Munday J.C., 1978. Water Quality Analysis by Digital Chromaticity Mapping of Landsat Data. *Can. Jour. Remote Sens.* 4(2): 108-126.
- Blackwell R.J. and Boland D.H., 1976. The Trophic Classification of Lakes Using ERTS Multispectral Scanner Data. *Proc. Amer. Soc. Photogram. 41st Ann. Meet.*, Falls Church, 393-414.
- Bukata R.P., Bruton J.E. and Jerome J.H., 1983. Use of Chromaticity in Remote Measurements of Water Quality. *Remote Sens. Envir.* 13: 161-177.
- Cipel, 1984. *Le Léman, synthèse 1957-1982*. Comm. Internat. Protection du Léman, Lausanne, 650 p.
- Delebecque A., 1898. *Les lacs français*. Béranger, Paris, 435 p.
- Galat D.L. and Jacobsen R.L. 1975. Recurrent aragonite precipitation in saline-alkaline Pyramid Lake, Nevada. *Arch. Hydrobiol.* 105(2): 137-159.
- Gordon H.R. and McCluney W.R., 1975. Estimation of the Depth of Sunlight Penetration in the Sea for Remote Sensing. *Applied Optics* 14(2): 413-416.
- Jaquet J.-M., Favarger P.-Y., Peter A. and Vernet J.-P., 1983. *Premières données sur la matière en suspension dans le Léman*. Internal Report, Institut Forel, University of Geneva, 83 p.
- Jaquet J.-M., 1987. *Remote Sensing Evaluation of Water Quality in the Gulf of Nicoya (Costa Rica)*. Annex to FAO Fisheries Technical Paper 287: 35-50.
- Jerlov N.G., 1976. *Marine Optics*. Elsevier Publ., Amsterdam, 231 p.
- Lachavanne J.-B. and Wattenhoffer R., 1975. *Les Macrophytes du Léman*. Comm. Internat. Protection du Léman, Lausanne, 147 p.
- Lathrop R.G. and Lillesand T.M., 1986. Use of Thematic Mapper Data to Assess Water Quality in Green Bay and Central Lake Michigan. *Photogr. Engin. Rem. Sens.* 52(5): 671-680.
- Lathrop R.G. and Lillesand T.M., 1987. Calibration of Thematic Mapper Thermal Data for Water Surface Temperature Mapping: Case Study on the Great Lakes. *Remote. Sens. Envir.* 22: 297-307.
- Lemoalle J., 1979. Application des données Landsat à l'estimation de la production du phytoplancton dans le lac Tchad. *Cah. ORSTOM, sér. Hydrobiol.*, 13(1-2): 35-46.
- Lindell L.T., Steinvall O., Jonsson M. and Claesson T., 1985. Mapping of coastal-water turbidity using Landsat imagery. *Int. J. Remote Sensing* 6(5): 629-642.
- Lillesand T.M., Johnson W.L., Deuell R.L., Lindstrom O.M. and Meisner D.E., 1983. Use of Landsat Data to Predict the Trophic State of Minnesota Lakes. *Photogr. Engin. Rem. Sens.* 49(2): 219-229.
- McGarrigle M.L. and Reardon B.C., 1986. *National Survey of Lakes by Remote Sensing*. Preliminary report, WR/L13, An Foras Forbartha, Dublin, 31 p.
- Munday J.C., Alföldi T.T. and Amos C.L., 1979. Verification and Application of a System for Automated Multirate Landsat Measurement of Suspended Sediment. *Satell. Hydrol., Amer. Water Res. Assoc.*, June 1979, 622-640.
- OCDE, 1982. *Eutrophication of waters: monitoring, assessment and control*. OCDE, Paris, 154 p.
- Piech K.R. and Walker J.E., 1971. Aerial Color Analyses of Water Quality. *Jour. Survey. Mapp. Div., Amer. Soc. Civil Engin.*, SU 2, Nov. 71: 185-197.
- Piech K.R., Schott J.R. and Stewart K.M., 1978. The Blue-to-Green Reflectance Ratio and Lake Water Quality. *Photogr. Engin. Rem. Sens.* 44(10): 1303-1310.
- Poros D. and Peterson C.J., 1985. Methods for Destriping Landsat Thematic Mapper Images - A Feasibility Study for an Online Destriping Process in the Thematic Mapper Image Processing System (TIPS). *Photogr. Engin. Rem. Sens.* 51(9): 1371-1378.
- Rochon G., 1975. *Etude méthodologique de l'évolution et de la classification des lacs par satellite*. CRE-75/06, Minist. Richesses Nat. du Québec, 90 p.
- Scarpace F.L., Holmquist K.W. and Fisher L.T., 1979. Landsat Analysis of Lake Quality. *Photogr. Engin. Rem. Sens.* 45(5): 623-633.

- Scherz J.P. and Van Domelen J.F., 1974. Water Quality Indicators Obtainable from Aircraft and Landsat Images and their Use in Classifying Lakes. *10th ERIM Symp.*: 447-460.
- Shimoda H., Etaya M., Sakata T., Goda L. and Stelczer K., 1984. Water Quality Monitoring of Lake Balaton using Landsat MSS Data. *18th ERIM Symp.*: 565-574.
- Slater P.N., Biggar S.F., Holm R.G., Jackson R.D., Mao Y., Moran M.S., Palmer J.H. and Yuan B., 1987. Reflectance- and Radiance-Based Methods for the In-Flight Absolute Calibration of Multispectral Sensors. *Rem. Sensing Envir.* 22: 11-37.
- Smith A.Y. and Addington J.D., 1978. Water Quality Monitoring of Lake Mead: a Practical Look at the Difficulties Encountered in the Application of Remotely Sensed Data to Analysis of Temporal Change. *5th Canad. Symp. on Remote Sens.* 174-186.
- Smith R.C., Tyler J.E. and Goldman C.R., 1973. Optical properties and color of lake Tahoe and Crater lake. *Limno. Oceano.* 18(2): 189-199.
- Tassan S., 1984. *Evaluation of the potential of the thematic mapper for chlorophyll and suspended matter determination in sea water.* Joint Research Centre, Ispra, Internal Rept., 21-25.
- Verneaux J., Remy F., Vidonne A. and Guyard A., 1987. Caractères généraux des sédiments de 10 lacs jurassiens. *Sciences de l'Eau*, 6: 107-128.
- Vernet J.-P., Thomas R.L., Jaquet J.-M. and Friedli R., 1972. Texture of the Sediments of the Petit Lac (Western Lake Geneva). *Eclogae Geol. Helv.* 65(3): 591-610.
- Wezernak C.T., Tanis F.J. and Bajza C.A., 1976. Trophic State Analysis of Inland Lakes. *Remote Sens. Envir.* 5: 147-165.

3. *Coastal Waters*

Use of Satellite Imagery for the Investigation of Pollution-Related Characteristics of Dublin Bay, Ireland

Bartholomew Masterson and Dymphna Conry-McDermott

Biochemistry Department, University College,
Belfield, Dublin 4, Ireland.

The use of satellite imagery in the context of a proposed water quality management plan for Dublin Bay Ireland is considered. In a preliminary assessment, using limited image processing techniques on a small number of available images, a unique synoptic appreciation of the heterogeneity of the Dublin Bay water-body has been obtained. The results, based on the reflectance patterns observed within the Bay, generally reinforce the limited published hydrological data and the known behaviour of point discharges, but suggest the complexity of the dispersion processes is greater than that hitherto observed. Other relevant questions are also stated and considered.

Dublin, the capital city of the Republic of Ireland, is fortunate in having the amenity of a large bay, which by European water quality standards, is only mildly polluted. There is cause for concern, however, about the maintenance of water quality (Clarke *et al.*, 1985), as well as an ambition to improve it in the spirit of the relevant European Commission directives and of the Irish Water Pollution Act (1977). The responsible government agency has commissioned the production of a water quality management plan for Dublin Bay, which has given rise to a requirement for a programme of broadly-based studies on a wide range of relevant aspects. Remote sensing techniques are expected to contribute to these studies, and the present report concerns a preliminary assessment of the potential usefulness of satellite imagery in this connection.

There has been some anxiety about the discharge of sewage into the Bay, in relation to its use for recreational and possible mariculture purposes. Although regular on-shore microbiological monitoring is carried out by Local Government agencies, there is relatively little information on the hydrology of the Bay apart from a limited study commissioned some years ago (Crisp, 1976). Thus the behaviour of point discharges under influence of tide and weather is poorly understood, and there is little information available upon which to plan a comprehensive hydrological study in the water quality context. Questions, for example, about the dispersion of sewage inputs, the assimilative capacity of the Bay, the residence time of inputs, the efflux and reflux characteristics of the Bay water with respect to the Irish Sea, remain unanswered. Of special significance here was the absence of a topographical appreciation of the water-body in respect of water quality determinants, covering the Bay

as a whole. The need for preliminary assessment of the heterogeneity of determinant values over the Bay, and of their dynamic ranges as a prerequisite for proper survey campaign design, has been adverted to by Stapleton (1986).

The objective of this study was to gain an understanding of the behaviour of the Dublin Bay water-body, in as far as such could be inferred from the reflectance topography viewed synoptically by satellite sensors, and using a number of images covering a range of tidal states and weather conditions. Satellite images of the Bay made available under the Pilot Project Scheme or obtained from archives, were processed to establish reflectance patterns representative of suspended solid levels, on the basis that these solids were associated with sewage discharges (Keenan, 1984; O'Donnell, 1987). A representative selection (Table 1) of the nine images considered by Masterson and Conry-McDermott (1987) are discussed here. There is a substantial basis in the literature for such use of satellite imagery; a selection of reports concerned with chemical, physical and biological water characteristics are cited below.

Table 1: Details of images considered in this report.

Sensor	Date	Path	Row	Quadrant
Landsat MSS	13-11-1976	222	23	—
Landsat TM	15-09-1984	205	23	1
Spot HRV	02-03-1986	18	242	—

Klemas *et al.* (1973, 1974) used Landsat MSS images in an early study of Delaware Bay, and found strong correlation of sediment content and Secchi disk

measurements with image radiance levels. Aranuvachapun and LeBlond (1981) produced quantitative maps of turbidity for the River Fraser estuary, useful in monitoring flow characteristics, and showing detailed features which they claimed were not observed in the images before removal of radiance due to atmospheric effects. Khorram (1981) found good correlation of turbidity levels with data from such images, although poorer correlation was obtained for suspended solid levels. Klemas and Philpot (1981) assessed the drift and dispersion of acid waste off the Delaware coast, using Landsat MSS data; visual estimates of plume width were made and plotted with time after dumping, the spatial and temporal resolution being insufficient to permit detailed interpretation. Mather (1981), using uncorrelated chromaticity coefficients (Munday *et al.*, 1979), examined Landsat MSS images of coastal waters around Britain, and derived contour maps of suspended solid concentrations at a number of locations; although no atmospheric corrections were made, explainable patterns of variation in suspended solid levels were seen. Landsat imagery was used by Ohlhorst (1981) to observe the plume produced by acid waste dumped off the entrance to New York harbour. Extensive work has been carried out on the Tay estuary (Cracknell *et al.*, 1982). Estuarine fronts were defined on the basis of differences in the suspended solid levels, agreeing well with *in situ* information; weather and tidal effects on the front movement and mixing were considered. Landsat MSS data were compared with Secchi disk depth measurements along the Swedish coast in a study by Lindell *et al.* (1985). The approach allowed the mapping of relative suspended solid loadings, rather than of absolute values, thereby obviating the need for extensive sea surface measurements and comprehensive correction techniques for atmospheric and other effects. Cheshire *et al.* (1986) used Landsat TM imagery together with near-simultaneously acquired sea surface data, to monitor the water quality of the River Neuse estuary; quantification of surface turbidity and total suspended solids was 'somewhat successful'. Radiometric problems with the TM sensor were encountered, explained as differences in forward and backward scans and time lag in the sensor response. SPOT-simulation data were used by Davies and Charlton (1986) in the absence of sea surface measurements, to detect and delineate effluent plumes at outfalls in the Firth of Forth. Image processing involved the use of contrast enhancement and principle component analysis techniques, and band combinations were presented as false-colour composites.

In the work reported here, a combined density slicing, colour coding technique of routine nature was used to produce qualitative information on relative amounts of suspended solids in the different parts of Dublin Bay. Digital numbers were not subjected to radiometric correction, nor corrected for atmospheric effects, and were uncalibrated in the absence of sea surface measurements.

This limited image processing approach was judged to be sufficient for the purposes of the work, which was focused on the detection of suspended solids. Having regard to these limitations, a number of questions were kept in mind during the study, as follows.

1. In as far as could be judged from the available imagery, processed as above, and having regard to local conditions, which satellite sensor features best met the study objectives?
2. For the sensors considered, which wavelength band or band combination was most informative?
3. Were suspended solids and patterns of sediment dispersion sufficiently discernible to allow their location with confidence? What was the influence of the time of year, and of the tide and weather conditions in the matter?
4. What discrimination of the levels of suspended solids was possible, and what was the influence of time of year and of weather conditions on this?
5. Which parts of the water-body were subject to bottom reflectance effects, and how did this change with reference to the state of tide?

Image Processing

Image processing of computer compatible tapes (CCTs) was carried out using a Gould 8500 system linked to a VAX 11/780 computer, operating ERDAS and LIPS software. A VICOM processor was used to access the CCT archive and to down-load the chosen CCTs, using a locally developed program (Quicklook).

The infrared bands (Landsat MSS - band 7; Landsat TM - band 4; SPOT HRV - band 3) were used to effect masking, so as to produce a sub-image with only the bay and estuary areas shown. Areas to be masked were specified using a maximum likelihood classifier, together with a recoding program (MASK). Statistics for the digital numbers (DN) arising from the water-body were computed, and a histogram generated; then the image location of the pixels for each DN was observed interactively by assigning an appropriate screen colour to the DN. Where such pixels were in small numbers and not grouped in any patch of significant size, the decision was made to combine these for further processing with those of similar small occurrence. The digital numbers were each assigned a unique colour to enable visual localisation on the monitor screen. Hardcopies of the processed images were produced with a Dunn 635 colour camera.

Results

The outcome of the above image processing approach is illustrated here with reference to red band images only; the results for other bands and band combinations have been considered more fully by Masterson and Conry-

McDermott (1987). Typical statistical results are shown in Table 2, and the basis of colour code assignment is given for one of the images.

Table 2: Digital number (DN) statistics and colour assignment for Landsat TM red band sub-image of 15-09-1984

Colour code	DN	No. pixels	Statistics
Yellow	11	6	
Yellow	12	39	
Dark aqua	13	1022	
Aqua	14	1745	Minimum DN: 11
Blue	15	826	Maximum DN: 27
Pink	16	445	
Purple	17	228	Mean DN: 14.7
Green	18	112	Median: 14
Orange	19	50	Mode: 14
Orange	20	34	
Orange	21	41	
Orange	22	26	Standard deviation: 1.9
Red	23	12	
Red	24	7	
Red	25	10	
Red	26	6	
Red	27	2	

A Landsat MSS red band (band 5, 600–700 nm) sub-image of 13-11-1976, processed as described above, is shown in Figure 1. The image shows sixth line banding, not much improvable by a destriping procedure. Geometric distortion is also evident. The major reflectance patterns are represented by a low DN range (1–12) coded at five levels (aqua, blue, pink, red and green). The image was acquired at low sun angle (09.53 GMT in mid-November) and global solar radiation level (75 J/cm²), and about one hour after low tide; weather conditions were a moderate westerly breeze, accompanied by continuous traces of rain for the 24 hours

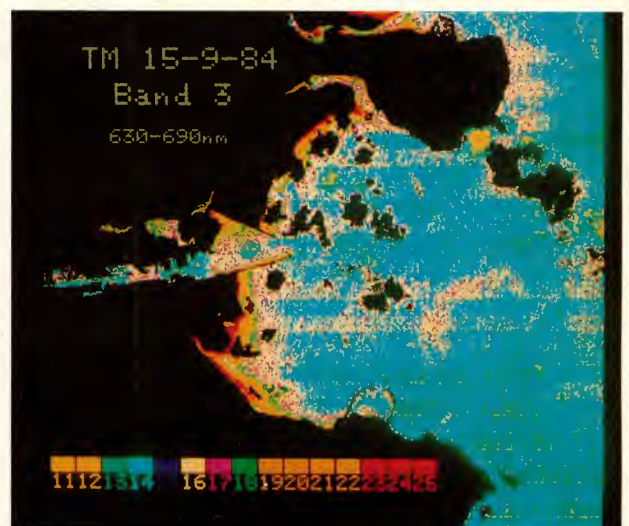
Figure 1: Landsat MSS red band sub-image of Dublin Bay.



before overpass. A plume-like pattern of high reflectance stretches eastwards from the River Liffey entering the Bay from the west. The Liffey at that time had a very high suspended solids level, associated in part with discharges from a paper mill no longer operational. Sewage solids, originating from overflow at a holding tank (White Banks) near the Liffey mouth, may have contributed to the apparent plume-like feature, and its easterly part is more likely to be associated with sludge and dredge-spoil dumping sites located in that area. There is an indication in the image that the northern section of the Bay, on the Howth headland side of the plume-like pattern, has surface water of lower reflectance, suggesting an influx of clearer water from the north during ebb tide. If so, this would be surprising, since it is generally held (Crisp, 1976) that the Bay currents maintain a clockwise gire at all states of tide. Nearshore reflectances are high, increasing shorewards from DN 7-12; this effect most likely represents the increasing influence of bottom reflectance, since the depth contours there decrease shorewards from four metres.

The Landsat TM red band (band 3, 630–690 nm) sub-image of 15-09-1984 (Fig. 2) was produced as described above. Sixteen line banding is evident; this radiometric defect has been ascribed by Fusco *et al.* (1986) to hysteresis in the response to large abrupt steps in the radiance levels during the sensor scan. The image digital number statistics showed a DN range 11-27, and the histogram showed the main numbers of pixels to have a DN range 13-18; the higher DN pixels were at nearshore locations. There was good sunshine (200 J/cm²), with a sun elevation angle of 37° and azimuth angle of 152° at image acquisition time (10.46 GMT). The tidal state was early ebb, at which all sewage outfalls, including discontinuous systems, would have been in operation. Weather conditions were a light north-westerly breeze with less than 0.6 mm rainfall in the 24 hours prior to overpass

Figure 2: Landsat TM red band sub-image of Dublin Bay.



time. The outer bay area has a DN range 13-15 (dark aqua, aqua and blue), representative of low reflectance, clear water. Patterns are produced by digital numbers in the range 16-17 (pink and purple), and probably represent patterns of sewage solids dispersion. There is a notable crescent-shaped feature in the centre of the outer Bay. As in the case of the MSS image above, nearshore digital numbers progress from 16 to 27 in line with a shorewards decrease in depth from 5 m. The presence of cloud reduces the usefulness of the image; reflectances from the Liffey estuary are obscured by cloud and cloud shadow.

In Figure 3 the processed SPOT HRV red band (band 2, 610–690 nm) sub-image of 02-03-1986 is shown. A vertical striping effect is clearly evident; methods to remove this noise effect have been described by Quarmby (1987), although not used here. Pixels are in the DN range 15-24; DN 22-24 are grouped and assigned the colour red, and each remaining DN was separately colour coded. Thus it is possible to discriminate radiance features at eight levels of intensity. The sun elevation angle was 28.1° and the azimuth angle was 164.4° , with good sunshine (182 J/cm^2) at the image acquisition time (11.42 GMT). The tide was in mid-flood; discontinuous sewage outfalls would not have been operating. Winds were fresh to moderate from the east with no rainfall in the previous 24 hours, and sea surface conditions were rough to moderate. As the image was acquired during flood tide an indication in the reflectance patterns of clockwise movement in the water-body would be expected (Crisp, 1976). Generally patterns can be explained on the basis of ebb tide loadings from point discharges taken clockwise and inwards by the returning tide prior to image acquisition time. A more detailed analysis of this image is given in Masterson and Conry-McDermott (1987).

Conclusion

The processed images demonstrate well the performance specifications of the sensors considered. The SPOT HRV images, having improved spatial resolution over Landsat MSS and TM images, showed water-body reflectance patterns in greater detail. In all the images the DN range was narrow however, so that the degree of discrimination of underlying turbidity or suspended solid levels would be quite coarse; the SPOT HRV sensor gave the best results in this respect though, which may relate to a comparatively lesser sensitivity of that sensor. In general the locations of the reflectance patterns are in accord with the limited published hydrological data for the Bay, its depth contours, and known behaviour of the point discharges. It is clearly evident from the images examined that there is a high degree of dispersive heterogeneity in the Bay, strongly linked to the tidal variations. It can be said that the examination of these images has produced an increased awareness on this latter point. Little variation in

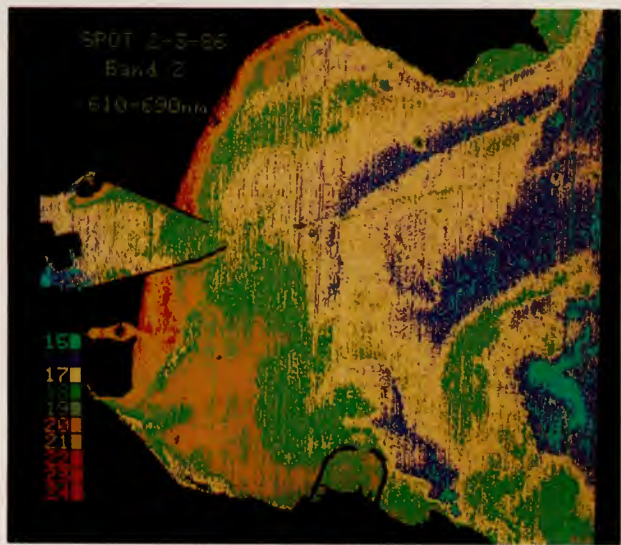


Figure 3: SPOT HRV red band sub-image of Dublin Bay.

weather conditions was encountered, which follows since good weather conditions are likely to be associated with image acquisitions which have the low cloud cover levels required. Although not illustrated here, the experience in general has been that winter images show less pattern-detail than summer images. Winter resuspension of bottom sediments tends to create a higher background sediment loading in the Bay, masking the effects of turbid point discharges on the reflectances. Also in general, DN ranges were higher in the southern part of the Bay and off the northern headland (Howth), where the major untreated sewage outfalls are located. Reflectances for the Liffey estuary were also high, but appeared to have decreased slightly in images acquired more recently; all effluent discharge into the Liffey since 1985 has received primary treatment to remove much of the suspended sediment load.

In this preliminary assessment then, using limited image processing techniques on a small number of available images, a unique synoptic appreciation of the heterogeneity of the Dublin Bay water-body has been obtained. The results, based on the reflectance patterns observed within the Bay, generally reinforce the limited published hydrological data and the known behaviour of point discharges, but suggest the complexity of the dispersion processes is greater than that apparently realised hitherto.

Acknowledgements

The authors wish to thank Dr. Brian O'Donnell (NPOC) for his support and encouragement, Martina O'Looney and John Nolan of the Computer Centre, Aidan Mulkeen of the Audio Visual Centre, and Dr. Bernard Reardon and other colleagues of the Remote Sensing and Image Analysis group at University College Dublin for invaluable help.

References

- Aranuvachapun S. and Le Blond P.H. 1981, *Remote Sensing of Environ.* **84**: 113-132. Turbidity of coastal waters determined from Landsat.
- Cheshire H.M., Khorram S. and Brockhaus J.A. 1986, in *Monitoring and Processing Global Environmental Data*. Remote Sensing Society, London. pp. 227-236. Monitoring estuarine water quality from Landsat TM.
- Clarke J., Masterson B., Max M. and O'Connor P.E. 1985, *A Study of the Impact of Sewage Discharges on the Recreational Quality of south Dublin Bay*. Irish Underwater Council, Dublin.
- Cracknell A.P., MacFarlane N., McMillan K., Chorlton J.A., McManus J. and Ulbricht K.A. 1982, *Int. J. Remote Sensing* **3**: 113-137. Remote sensing in Scotland using data from satellites. A study of the Tay Estuary region using Landsat scanning imagery.
- Crisp D.J. 1976, *Survey of Environmental Conditions in the Liffey Estuary and Dublin Bay*. Summary report. Dept. of Marine Biology, University College North Wales, Menai Bridge.
- Davies P.A. and Charlton J.A. 1986, *Int. J. Remote Sensing* **7**: 815-824. Remote sensing of coastal discharge sites using SPOT simulation data.
- Keenan T. 1984, in *Dublin Bay - an Outstanding Natural Resource at Risk?* Dublin Bay Environmental Group, Dublin. pp. 29-46. Sources of pollution in the Bay.
- Khorram S. 1981, *Int. J. Remote Sensing* **2**: 145-153. Water quality mapping from Landsat digital data.
- Klemas V., Borchardt J.F. and Treasure W.M. 1973, *Remote Sensing of Environ.* **2**: 205-221. Suspended sediment observations from ERTS-1.
- Klemas V., Otley M., Philpot W., Wethe C., Rogers, R. and Shah N. 1974, in *Proc. 9th Int. Symposium Remote Sensing of Environ.* Environmental Research Institute of Michigan, Ann Arbor. pp. 1287-1317. Correlation of coastal water turbidity and current circulation with ERTS-1 and Skylab imagery.
- Klemas V. and Philpot W.D. 1981, *Photogram. Engng. Remote Sensing* **47**: 533-542. Drift and dispersion studies of ocean-dumped waste using Landsat imagery and current drogues.
- Lindell L.T., Steinvall O., Jonsson M. and Claesson Th. 1985, *Int. J. Remote Sensing* **6**: 629-642. Mapping of coastal-water turbidity using Landsat imagery.
- Masterson B.F. and Conry-McDermott D. 1987, *Application of Satellite Imagery to the Study of the Water Quality of Irish Coastal Waters*. Report to the European Space Agency, July 1987. Biochemistry Dept., University College, Dublin.
- Mather P.M. 1981, *Computer Applications* **7**: 1051-1064. Use of digital Landsat MSS imagery to determine patterns of suspended sediment concentrations in coastal waters.
- Munday J.C., Alfondi T.T. and Amos C.L. 1979, in *5th W.T. Pecora Symposium on Satellite Hydrology*. Verification and application of a system for automated multirate Landsat measurement of suspended sediment.
- Ohlhorst C.W. 1981, *Environ. Monitor. Assess.* **1**: 143-153. The use of Landsat to monitor deep water dumpsite 106.
- O'Donnell K. 1987, in *Managing Dublin Bay* (Brunton M., Convery F.J. and Johnson A., eds.), REPC, University College, Dublin. pp. 71-78. Residential and industrial sources of pollution.
- Quarmby N.A. 1987, *Int. J. remote Sensing* **8**: 1229-1234. Noise removal from SPOT HRV imagery.
- Stapleton L. 1986, *Outfalls in the Context of Tidal Water Management*. An Foras Forbartha, Dublin.

Landsat-5 TM Study of Suspended Sediments in a Fjord System in Western Norway

J. Nilsen and I. Selseth

Norwegian Hydrotechnical Laboratory, Trondheim, Norway

V. Nilsen

Forut / Statoil, Norway

The spreading of suspended sediments discharged from the river Jostedøla into the Gaupne, Luster and Sogne fjords has been studied using visible and infrared TM data from Landsat-5. Four different methods have been used for presentation of the distribution of the surface turbidity and temperature. Of these, the colour coding of brightness levels from channels 1, 2 and 3 seemed to give the best resolution in the determination of the suspended sediment concentrations in the water masses. Supervised classification techniques were useful especially in determining the presence of classes defined in a nearby control area. Due to the non-conservative properties of temperature, the visible channels were found more useful for studying the spreading of the suspended sediments from Jostedøla the Gaupne Fjord.

1. Introduction

This report must be regarded as a first and limited attempt from our side to use TM data to find the distribution of suspended sediments discharged from a river into a fjord system. Our budgets were absolutely limited. Therefore no attempt was made in this project to measure ground-truth (in-situ optical information at the same time of the satellite passing). Earlier experiments in the same area (Nilsen 1981), where the concentrations of suspended sediments in the surface layer were measured and a near simultaneous satellite image processed, showed that sharp gradients might occur in the surface suspended sediment concentrations during late spring or early summer. High discharge in Jostedøla during this period is caused by the melting of snow in the mountains. The water transport was of the same magnitude in May 1984 as during the previous experiments in 1980.

We have embarked upon using and comparing (1) colour-coded brightness pixel levels in the visible TM channels, (2) classification techniques, (3) simple chromaticity transforms and (4) infrared TM channels, to find the surface distribution of suspended sediments in the Gaupne and Luster Fjords. Unfortunately the limited budget made it impossible to make more than brief comparisons between the different methods. Further development especially of the chromaticity transform technique and a more serious comparison of the different techniques may be of interest for future work.

2. The Thematic Mapper sensors

To some extent TM is closer in concept to the CZCS flown on Nimbus-7 which was designed specifically for marine science applications.

The TM sensor has seven channels in the visible, near-infrared, mean-infrared and thermal infrared part of the spectrum. The ground instantaneous fields of view (IFOV) of the sensors are 30 m × 30 m for channels 1–5 and 7 and 120 m × 120 m for channel 6.

3. TM scenes from Gaupne & Luster Fjords

To pick out the most suitable data set, a survey through available quick looks from the area was performed. This survey revealed that the data coverage was relatively good during late spring and summer 1984. During this period the water masses, transported by the Jostedal River, was rather larger due to snowmelt in the mountains and icemelt from the Jostedal Glacier. Table 1 shows a list of TM scenes which were possible to use.

Table 1. Available TM scenes from Gaupne and Luster Fjords from 23-05-84 to 27-08-84.

Orbit	Date	Orbit	Date
200/17	23-05	199/17	03-07
200/17	08-06	200/17	10-07
201/17	15-06	200/17	27-08

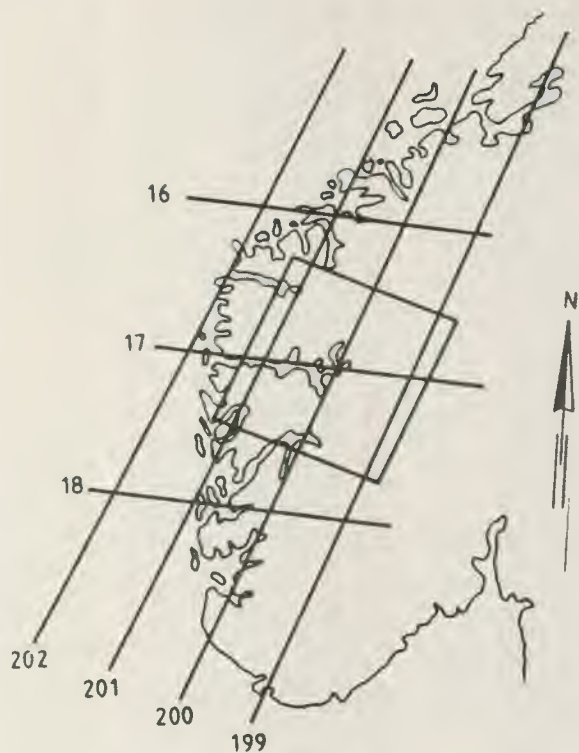


Figure 1. Approximately areal coverage of a full scene, Orbit 200/17.

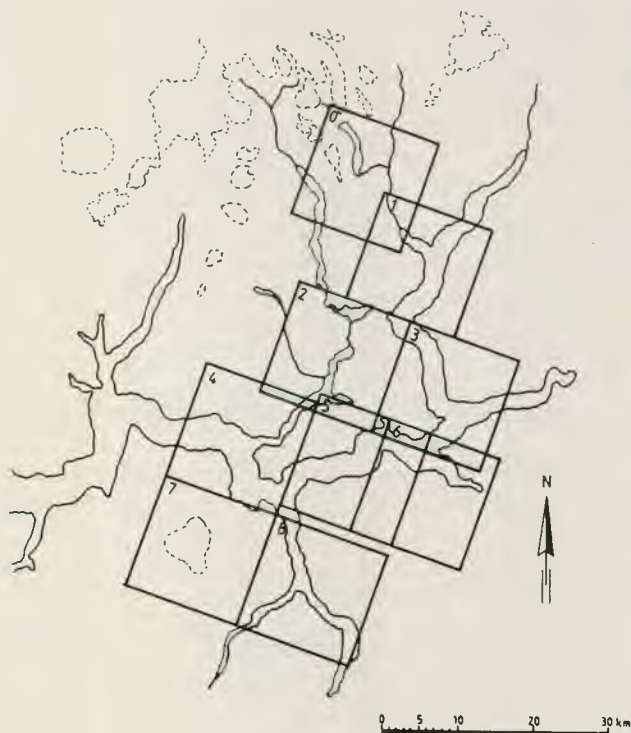


Figure 2. 512x512 pixel areas corresponding to the processed pictures.

- | | |
|------------------------|-----------------------|
| 0: Lake Tunsbergdal | 5: Outer Luster Fjord |
| 1: Gaupne Fjord | 6: Lærdal Fjord |
| 2: Inner Sogndal Fjord | 7: Fresvik Glacier |
| 3: Ardal Fjord | 8: Aurland Fjord |
| 4: Sogndal Fjord | |

The dataset from 08-06-84 was chosen, using orbit 200/17. The area covered by this full scene and the near orbit repeat cycle pattern of Landsat-5 are shown in Figure 1.

4. Results

4.1. Images processed from the visible TM channels

Figure 3 shows a very detailed and interesting colour coded picture of the surface distribution of suspended substances in the Gaupne and Luster Fjords and part of the Sogne Fjord. From the Jostedøla River, large amounts of suspended sediments are transported into the Gaupne Fjord. The main transport of suspended sediments (out of the Gaupne Fjord) is along the southern side of the fjord. Just outside the Gaupne Fjord sharp gradients between the turbid Gaupne Fjord water and the clean Luster Fjord water were formed. The circulation is affected by the Coriolis force which makes the water masses follow the shore to the right in the direction of the flow. This is seen in the figure in spite of relatively sharp right bends in the fjords.



Very small amounts of suspended sediments were transported north up the Luster Fjord. In the Luster Fjord

downstream of the Gaupne Fjord, the surface distribution of suspended sediments shows a rather complex feature, indicating that the surface circulation also was a result of different interesting hydrophysical processes. In some parts of the fjord small scale whirls were formed. This was especially seen in the horizontal shear layer between the Sogne Fjord and Lærdal Fjord waters. The suspended sediments coming from the Jostedøla River was transported far out in the Sogne Fjord.

As mentioned in Sections 1 and 2 water samples were collected the same day as the satellite passed the area. Earlier measurements of the suspended sediment concentrations in the surface layer in the Gaupne Fjord may have been 10–20 ppm. In the clear water in the Luster Fjord the suspended mass concentration may have been less than 0.5 ppm.

It is seen from Figure 3 that visible TM images from Landsat-5 are very useful in finding and studying the spreading of suspended sediments from the Jostedøla River into the fjord system. The areal resolution was fine enough for this large fjord and for understanding and revealing the hydrophysical processes at different scales occurring in the surface layer.

4.2. Calculations of chromaticity transforms

According to Munday and Alföldi (1975) the use of chromaticity transforms

$$x_i = TM_i \left/ \sum_{j=1}^3 TM_j \right.$$

where TM_i is the radiation of each TM channel, should eliminate atmospheric disturbances. Lindell (1981) used these transforms for correlation between the field data of

suspended sediments of chlorophyll and satellite data, in the Lake Malaren, Sweden.

Figure 4 shows the surface distribution in the fjords using two different sets of the simple chromaticity transforms:

$$y_{ij} = TM_i / TM_j \quad i, j, [1,3] \quad i \neq j$$

Some of the detailed information obtained in Figure 3 was not obtained in Figure 4. The main surface distribution may however be seen. No attempts were made to correlate the transforms with field data.

4.3. Mean vectors and correlation coefficients

Brightness level information from each of TM channels 1, 2 and 3 were obtained by defining training areas in the fjords and calculating the mean brightness vector of each of these areas. Information on the optical properties in the water masses were also found by calculating correlation coefficients between the brightness levels at the three visible TM channels for the pixel elements inside the training areas.

Tables 2 and 3 show mean vectors and correlation coefficients for different sets of training areas in the Gaupne and Luster Fjords shown in Figures 5a and b.

Table 2. Calculated mean vectors and correlation coefficients for the training areas shown in Figure 5a.

Test area	Correl. coeff.			Mean vector		
	G,B	R,G	R,B	R	G	B
: T1	0.60	0.62	0.62	33.8	46.5	111.0
: T2	0.55	0.42	0.35	25.0	38.2	100.2
: T3	0.51	0.26	0.29	21.0	31.9	87.3
: T4	0.04	0.06	0.08	18.5	27.5	76.6

Figure 4.

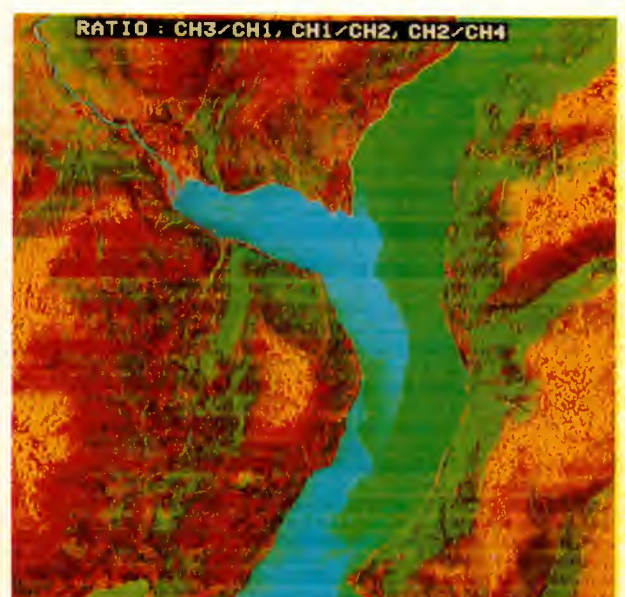
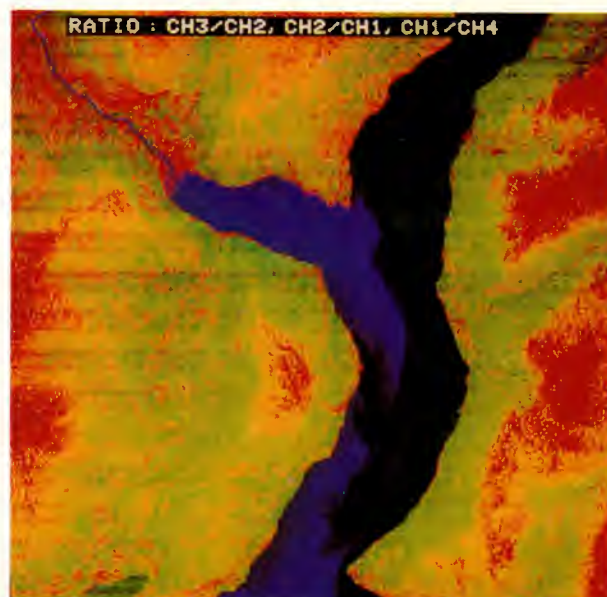




Figure 5a-b. Training areas in the Gaupne and Luster Fjords.

Table 3. Calculated mean vectors and correlation coefficients for the training areas shown in Figure 5b.

Test area	Correl. coeff.			Mean vector		
	G,B	R,G	R,B	R	G	B
: T1	0.62	0.66	0.50	31.4	45.0	108.7
: T2	0.41	0.21	0.27	25.1	38.5	101.2
: T3	0.01	0.26	0.02	24.8	38.5	99.9
: T4	0.12	0.11	0.03	19.7	32.0	87.8
: T5	0.56	0.35	0.32	21.0	31.9	86.9
: T6	0.05	0.04	0.04	19.0	27.8	79.4

It follows from Tables 2 and 3 that the highest brightness levels on the mean vector were obtained from channel 1 (in the blue part of the visible spectrum) in all test areas. The mean vector decreased towards increasing TM chan-

nel number of increasing visible wavelength also in all the selected training areas.

The correlation coefficients between pairs of the three different TM channels 1, 2 and 3 were usually found to be highest for areas in the fjords with the highest mean vectors or highest content of suspended sediments.

A major part of the suspended sediments supplied to the Gaupne Fjord runs through the Lake Tunsbergdal. This lake is located close to the Jostedal Glacier and usually has a high content of suspended sediments. Mean vectors and correlation coefficients from test areas in this lake (Fig. 6) have been calculated and are presented in Table 4.

Table 4. Calculated mean vectors and correlation coefficients from the training areas shown in Figure 6.

Test area	Correl. coeff.			Mean vector		
	G,B	R,G	R,B	R	G	B
5/03: T1	0.14	0.20	0.21	47.5	55.3	133.0
5/05: T2	0.64	0.23	0.14	42.9	53.2	128.0
5/06: T3	0.82	0.79	0.78	40.3	51.0	122.8
5/07: T4	0.84	0.80	0.84	33.3	45.1	110.8
5/08: T5	0.12	0.19	0.17	29.7	41.7	104.6



Figure 6. Training area T1-T5 in the Lake Tunsbergdalsvann.

It follows from Table 4 that the mean vectors in Lake Tunsbergdal were significantly higher than in the Gaupne and Luster Fjords. The brightness level decreased southwards in the lake. The correlation coefficients were significantly higher at T3 and T4. This may indicate inhomogenities in the water masses as e.g. the presence of ice in the northern part of the lake.

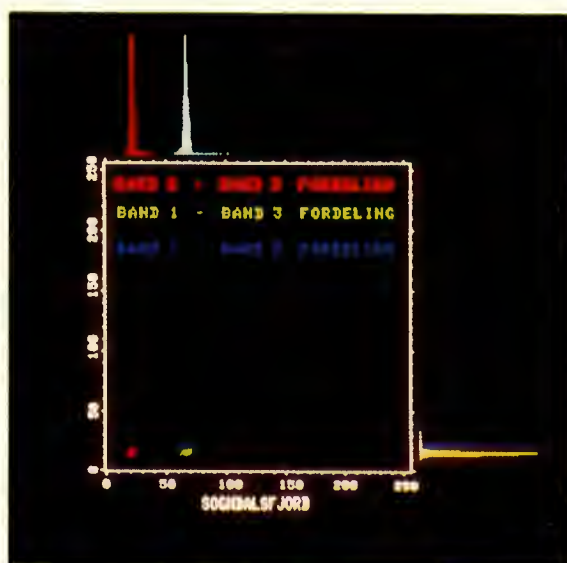
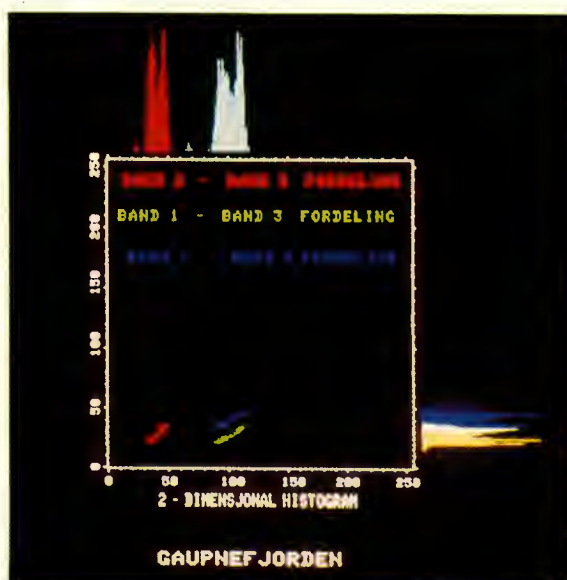
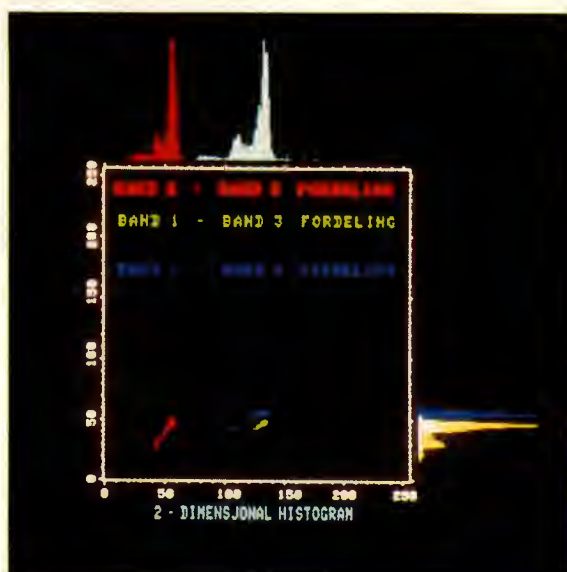
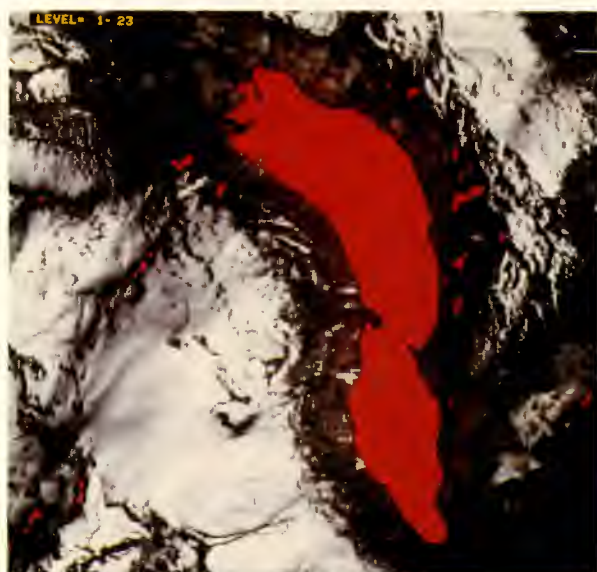


Figure 7.

4.4. Two-dimensional histograms

Figure 7 shows relations between brightness levels for the three pairs of channels 1, 2 and 3. The areas chosen are the Lake Tunsbergdal, the inner part of the Gaupne Fjord and parts of the Sogne Fjord and the Sundal Fjord. The distribution of the brightness levels are plotted out in two-dimensional histograms. Each pair of channels are colour-coded to avoid mixing of pairs. Clouds of points from each relation between channels 1–2 and 1–3 were derivable inclination coefficients. The largest spreading in the brightness levels found in the Gaupne Fjord indicates that the largest variations in the concentration of suspended sediments are to be found in this fjord.

Table 5. Mean vectors and correlation coefficients.

Test area	Correl. coeff.			Mean vector		
	G,B	R,G	R,B	R	G	B
Lake Tunsb. N	0.57	0.71	0.66	46.5	55.1	131.1
Lake Tunsb. S	0.46	0.70	0.42	31.1	42.9	108.8
Marifjøra	0.70	0.69	0.66	33.5	46.4	110.6
Stedje	0.25	0.37	0.31	15.1	21.0	66.9

Figure 8 shows the two-dimensional histogram of the channels 1–2 brightness level distribution from the three different areas given in Figure 7. The channel 1–2 distribution from the three different areas groups nicely along a straight line with a well defined inclination coefficient. These results show that it seems possible to use e.g. the brightness pixel levels from channel 1 directly to calculate the concentrations of suspended sediments in lakes and fjords.

4.5. Brightness pixel levels along cross-sections

Horizontal variations in the pixel brightness levels for

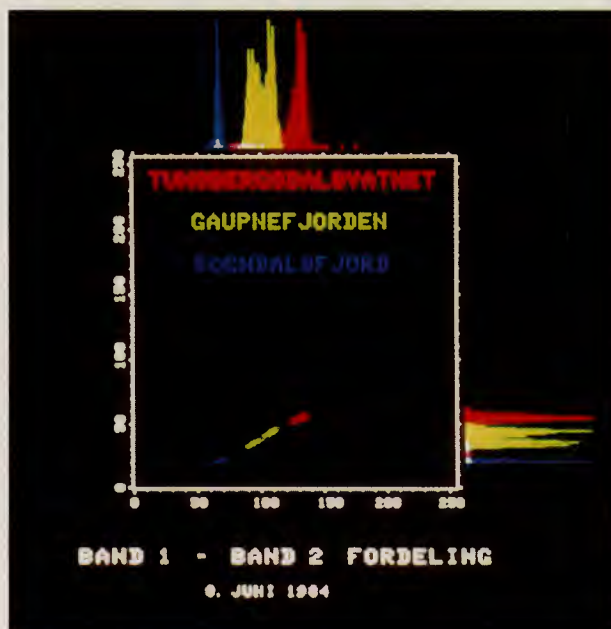


Figure 8.

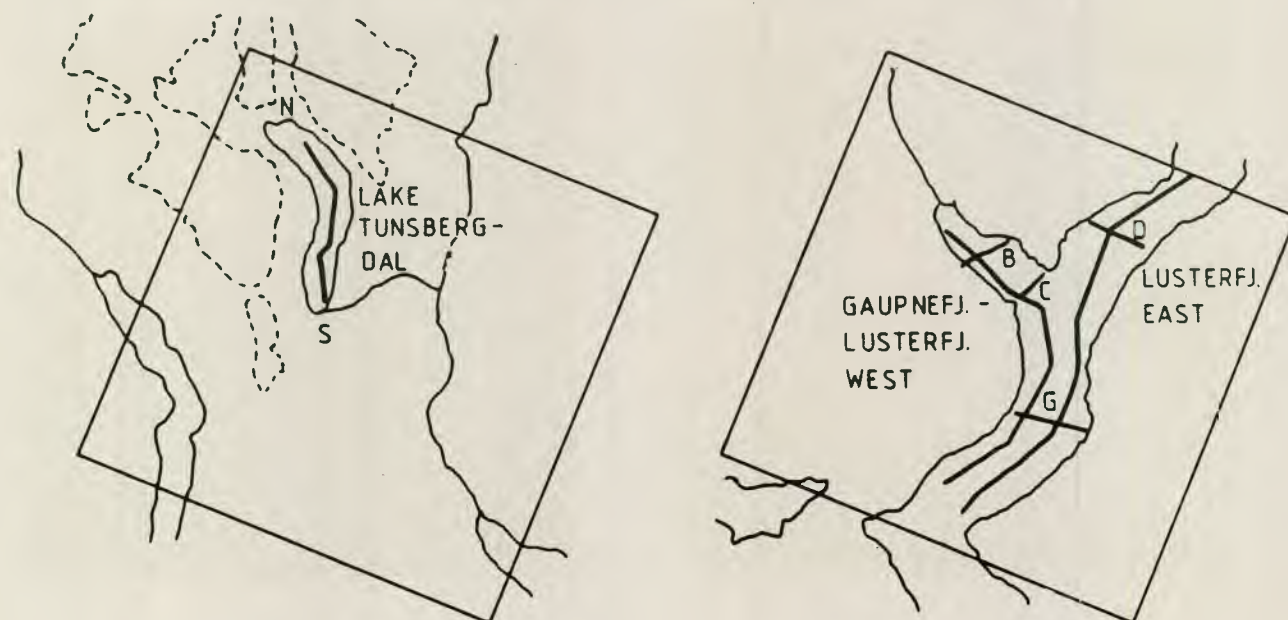
channels 1, 2 and 3 were presented along cross-sections in the lake Tunsbergdal and the Gaupne and Luster Fjords (Fig. 9).

It follows from Figure 10 that the largest gradients in the brightness levels were found in profile B which crosses the most turbid area in the inner part of the Gaupne Fjord.

4.6. Classification of water masses

Both supervised and unsupervised classical classification theory have been used in order to try to separate the water masses into defined classes (Fig. 11). Figure 12 shows the results of an unsupervised classification of the

Figure 9. Positions of cross-sections along which brightness levels are found from TM channels 1, 2 and 3.



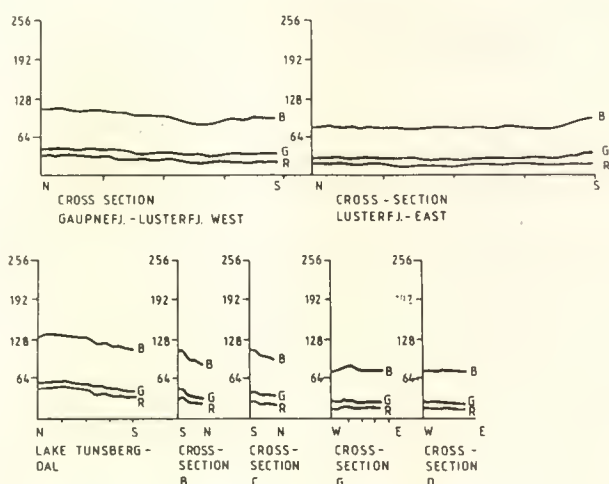


Figure 10. Variations in brightness levels in TM channels 1, 2 and 3 data along cross-sections defined in Figure 9.

surface water in the image. Information from all 'water' pixel elements have been used in the classification.

In Figure 13 pixel level information from selected training areas have been used in a supervised classification. The training areas used are defined in Figure 5a. It is seen from Figures 12 and 13 that using training areas covering mostly the turbid waters gives a higher resolution of classes in the turbid water masses than using the information from all pixel elements in the whole fjord.

Figure 14 shows how far out in the Sognefjord classes of water masses found in the Gaupne and Luster Fjords were observed. It seems that almost all classes found in these fjords have disappeared before reaching the Aurland Fjord.

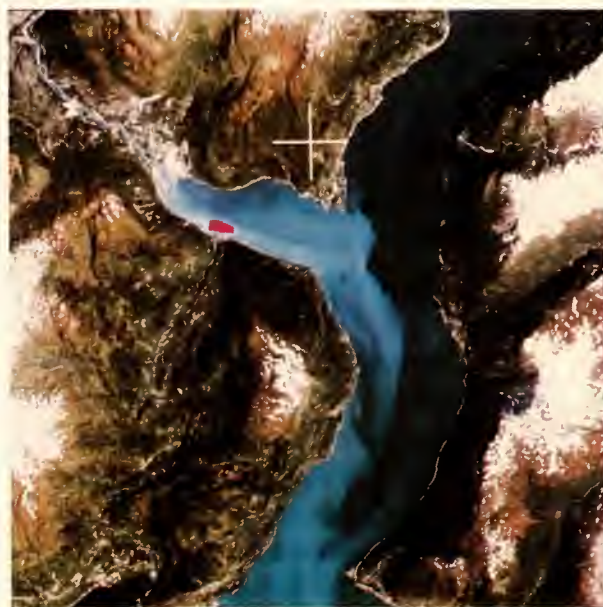


Figure 11.

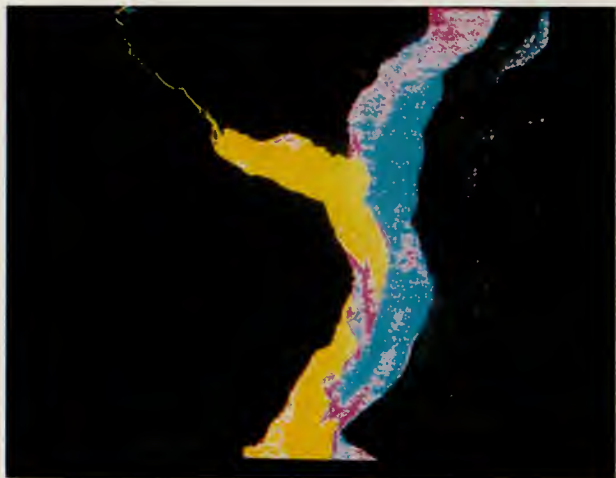


Figure 12.

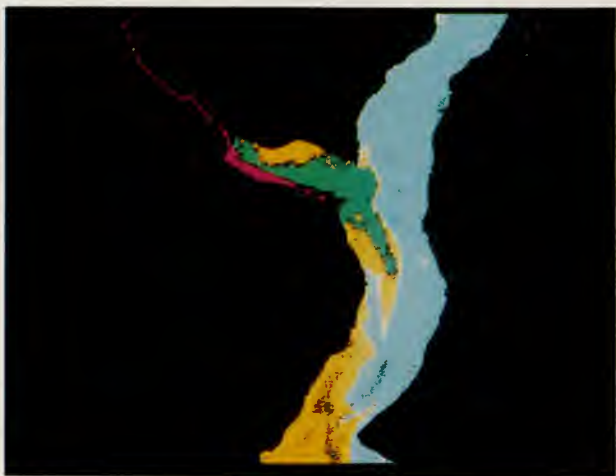


Figure 13.

Figure 15 shows an unsupervised classification of the Sogne, Aurland and Sogndal Fjords, colour-coded in a different way than for the classification of the Gaupne and Luster Fjords. It is seen that few classes occurred in this outer fjord system.

4.7. Thermal TM images

Figure 16 shows the temperature distribution in fjord systems given by TM channel 6 data. Ice and snow on land are coded dark blue, corresponding to a 0°C . The darkest red colour corresponds to the warmest parts of the Sogne Fjord. All warmer areas over land are defined white. The water temperature gradually increases outwards the Sogne Fjord. The cold river water from Jostedøla River into the Gaupne Fjord is seen, but the temperature differences disappear rather fast outside the Gaupne Fjord.

Training areas on both land and water are picked out and shown in Figure 17. Results of calculations of mean pixel level and standard deviation in pixel levels for the training areas are shown in Table 6 where the pixel level for ice/snow was ca. 80–81. The pixel level increased from



Figure 14.

Figure 15.



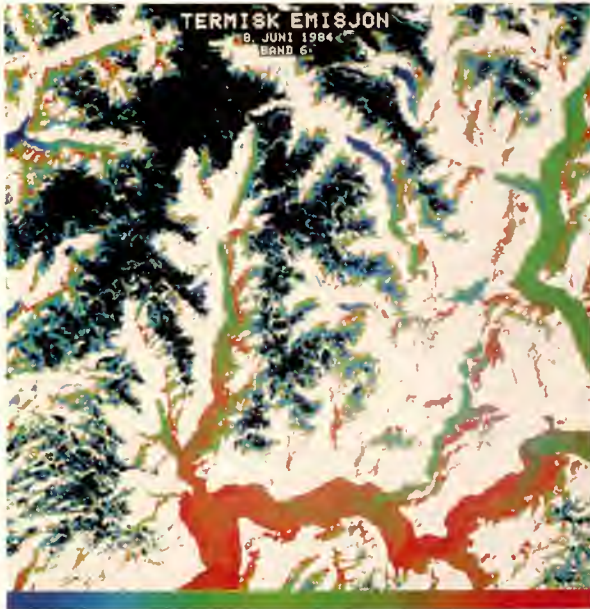


Figure 16.

80–81 to ca. 107 at Maalsnes in the Sogne Fjord. The temperature in the surface water at Maalsnes most probably was more than 10°C. If the temperature resolution is 0.5°C the mean temperature at Maalsnes was $(107.54 - 80.5) \cdot 0.5 \approx 14^\circ\text{C}$.

Table 6. Calculated mean vectors and standard deviations in pixel levels for training areas shown in Figure 17.

Location	standard deviation	mean vector
3/18: snow	1.531	80.50
3/19: Tunsb. Clacier	1.309	81.66
3/20: Lake Tunsb.	2.865	91.01
3/21: Gaupne Fjord	2.503	97.96
3/22: Solvorn	1.845	100.82
3/23: Sogndal	1.912	100.94
3/24: Leikanger	0.751	105.79
3/25: Maalsnes	0.865	107.54

Figure 18 shows the cross-section along which the pixel level for the TM channel 6 are presented.

Changes in the pixel level along the cross-sections, are presented in Figure 19. Relatively small gradients occurred in the cross-section, except for the land/sea calibration curve, representing both ice water and warmer land (see Figure 20). One must however bear in mind that a change in pixel value of 2 levels correspond to a change of 1°C.

5. Summary and Conclusions

The aim of this project was to use data from the visible Thematic Mapper channels 1–3 and the infrared channel 6 of Landsat-5 to study the spreading of both turbid and

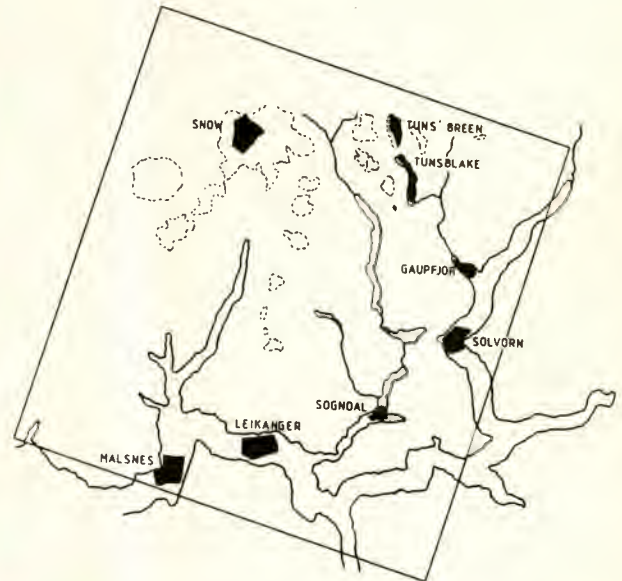


Figure 17. Training areas used for calculations of mean temperature pixel level vectors and standard deviations.

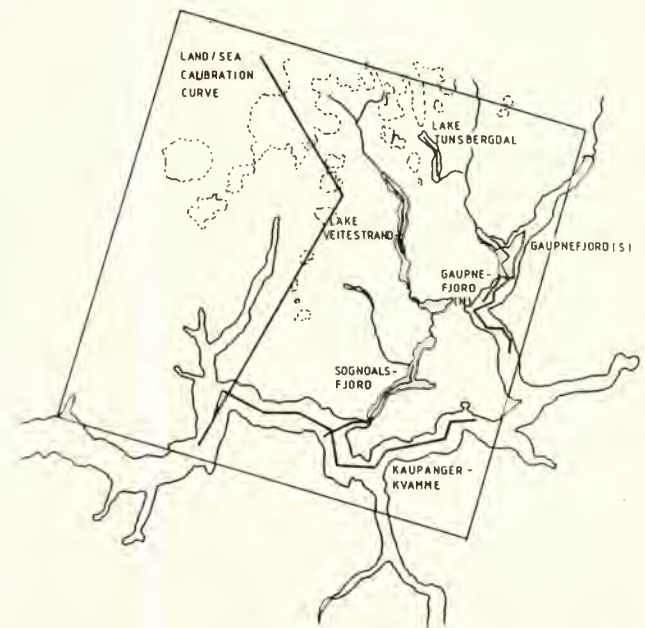


Figure 18. Cross-section along which the TM channel 6 pixel levels have been calculated.

cold Jostedøla river waters into the Gaupne-Luster-Sognefjord system in western Norway.

The TM scene chosen is from 08-06-1984. No in situ optical, or water sample measurements of the suspended sediment concentrations was available. Thus only the relative concentration distribution is obtained. No atmospheric corrections have been made on the system corrected data.

Three different techniques have been used on the visible data to find the distribution of the suspended sediments in the surface layer. The pixel brightness levels for each of the channels 1, 2 and 3 were colour-coded as near true

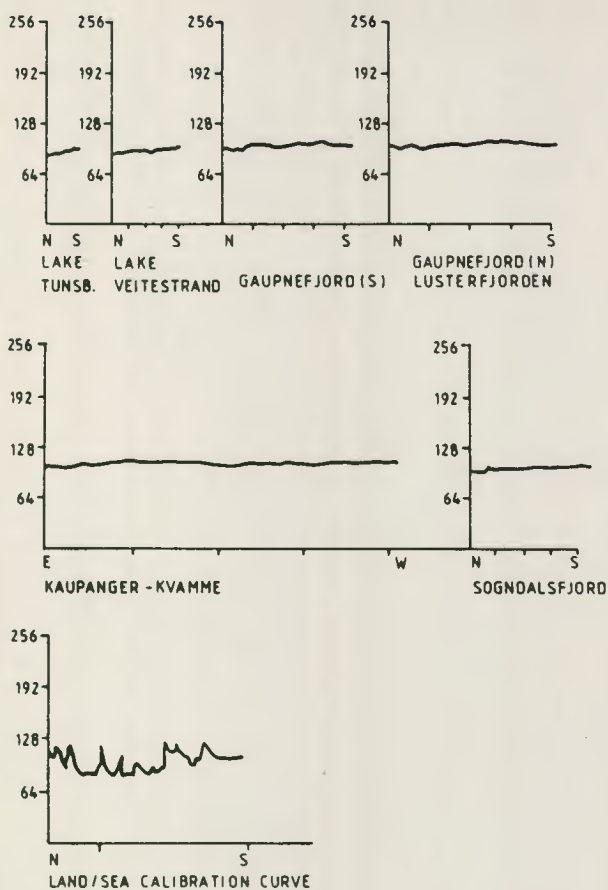


Figure 19. Changes in the pixel levels for TM channel 6 data along cross-sections defined in Figure 18.

colours, blue, green and red (RGB-images), resulting in an almost natural colour image of the areas. The results of this colour coding are good. It achieved a high resolution in the surface concentrations of suspended

Figure 20.



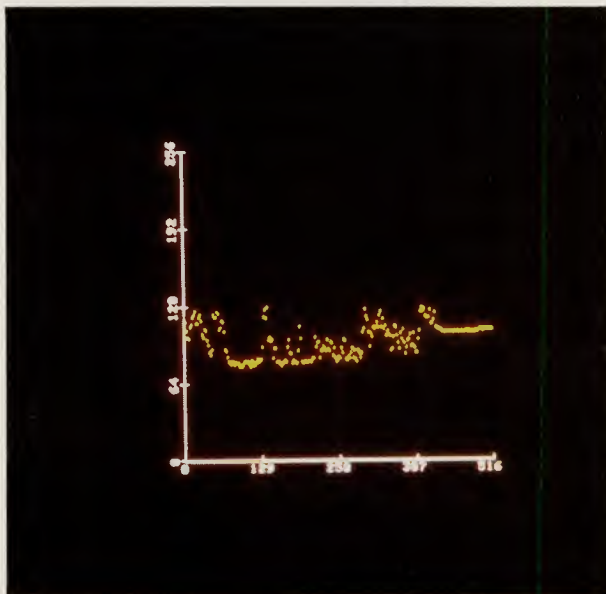
sediments, it revealed many interesting hydrophysical processes (e.g. whirls, upwelling areas, mixing) and it showed that suspended sediments was transported far out in the fjord system.

Simple chromaticity transforms were performed on the channel 1, 2 and 3 data, calculating ratios between pixel levels for pair of channels. The new indices calculated were colour-coded. The distribution of these indices in the water masses in the fjords showed well defined areas with suspended sediments.

Both supervised classification (minimum distance methods) used on selected training areas in the fjords and unsupervised classification (cluster analysis) used on the whole data from the fjords, were performed.

The results of the supervised classification showed that all classes defined in the Gaupne Fjord disappeared before the water masses reached the Aurland Fjord. The classification techniques were useful in revealing the optical homogeneity in an interesting area, but did not give much information about small-scale physical phenomena. Two-dimensional histograms showing the relation between brightness levels of pairs of visible TM channels (1, 2 and 3) seem useful for calculations of coefficients between brightness levels and field observations of suspended sediments.

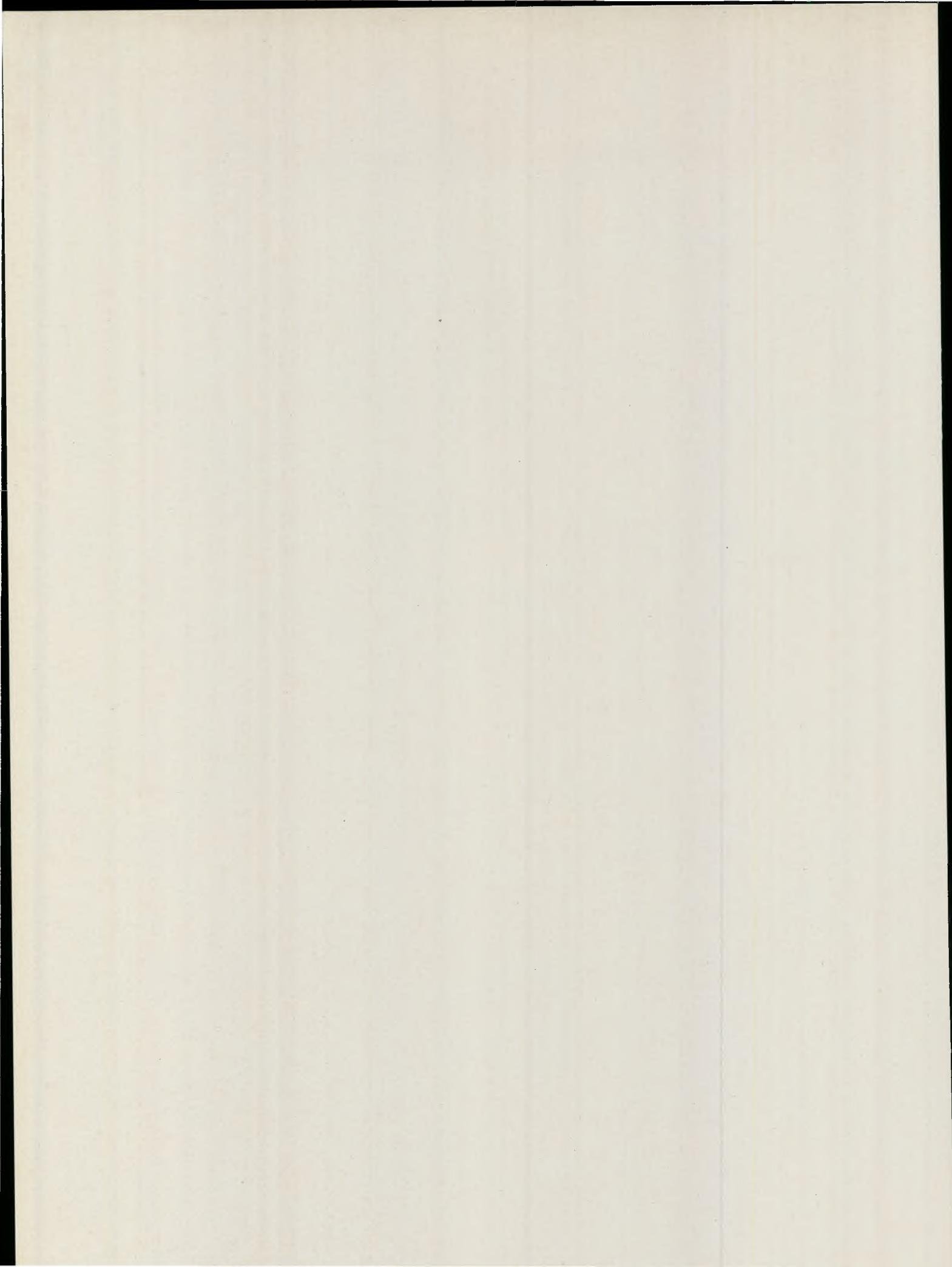
Along a cross-section in the Lake Tunsbergdal and in the fjords, the brightness level for each of the TM channels 1, 2 and 3 have been plotted. Such one-dimensional changes along straight lines, crossing e.g. fjords or other interesting areas, may be of interest for monitoring and for hydrophysical studies of phenomena in the water masses.



The present studies of the data from TM channel 6 showed that the temperature difference between the Jostedøla River water and the water masses in the Gaupne and Luster Fjords disappeared rather quickly outside the Gaupne Fjord. This was most probably caused by heating

of the surface water from the atmosphere and mixing processes in the water masses. The use of TM channel 6 data in studying the spreading of the Jostedøla River water into the fjord system was not very successful due to mixing and heat exchange with the atmosphere.

4. *Geology*



The use of Thematic Mapper Imagery for Peatland Mapping and Mineral Exploration in Ireland

G.W. Horgan and M.F. Critchley
Trinity College, Dublin, Ireland

Thematic Mapper imagery has been applied at Trinity College, Dublin to the mapping of Ireland's peat and mineral resources. Spectral bands 3, 4 and 5 have proved to be the most suitable channels for the mapping of peatlands. A two stage approach has been used in the mapping of peatlands. Firstly, techniques based upon mathematical morphology have been used to separate the peatlands from other types of land cover. Secondly, maximum likelihood methods were used to classify the different types of peatlands. Using these methods it has been possible to distinguish between areas of undisturbed, machine cut, hand cut and burnt peat.

Edge enhanced and directionally filtered TM band 4 imagery has been used in mineral exploration to map geological structures. Statistical pattern analysis has proved a useful method for treating the lineaments interpreted from the imagery. There are gross similarities in the lineament patterns observed on TM and MSS imagery. However, the TM lineaments tend to be shorter (possibly due to higher resolution) and interpretation of the TM imagery was hindered by agricultural features. MSS imagery tends to subdue agricultural features and hence large-scale geological features are generally more visible on the MSS imagery.

1. Introduction

During the period 1986-87, a series of studies were undertaken at Trinity College, Dublin to assess the use of TM imagery in the areas of peatland mapping and mineral exploration. Data for these projects was provided by the Earthnet Programme Office under the terms of its pilot application projects programme.

The availability of suitable TM imagery was a problem in nearly all the projects described below; either due to the available images being acquired from an unsuitable time of the year or due to a large percentage of cloud cover. In fact, cloud cover is the most restrictive factor when applied to satellite imagery in Ireland.

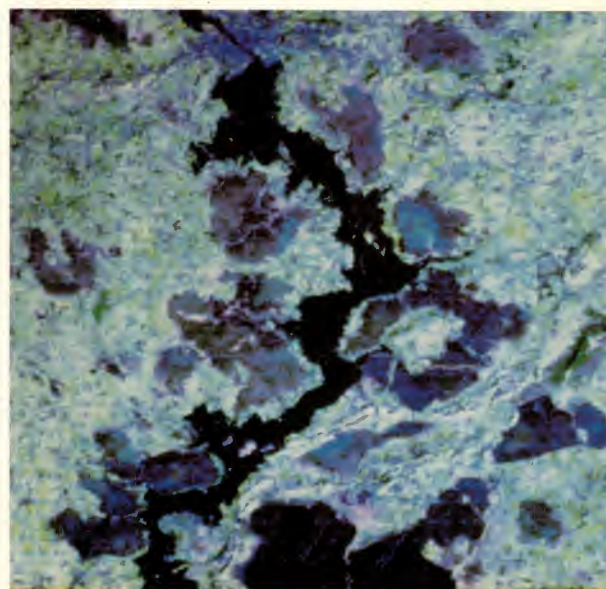
2. Mapping of raised peatland in Ireland

2.1. Aim of Project

The aim of the project was to use TM imagery to produce a map of peatland in Central Ireland, and, as far as is possible, to discriminate between different types of peatland and different types of peat exploitation. Peat occurs extensively in the Irish Midlands and is an important natural resource (Hammond, 1981). It is used predominantly as a supply of fuel. Peatlands are also of ecological importance, as they support a characteristic flora and fauna, which are rare elsewhere in Western Europe. For

this reason, it is important to know their distribution, and to be able to assess the type and degree of exploitation. The project was conducted in cooperation with the Forest and Wildlife Service of the Department of Fisheries and Forestry, as part of their study of peatlands in Ireland.

Figure 1. TM band 3, 4, 5 colour composite of bog test sites.



2.2 Imagery Used

The following TM imagery was used for this project: 206/23 (Q1; 17/3/85); 206/23 (Q1, Q3; 18/4/85); 207/23 (Full; 9/2/83). These scenes have no cloud cover over the area of interest. Visual examination of the imagery showed that peat could be distinguished clearly and that the presence of different types was apparent. A segment of a scene is shown in Figure 1.

2.3 Training Data

Training data for the classification were provided by the Forest and Wildlife Service. These came from two areas for which they had undertaken detailed ground surveys, one area near Athlone and another near Birr. For these areas the service gave examples of peat which had been machine cut, cut by hand, burnt and some which were undisturbed. They also classified each peatland as wet or dry depending on the amount of moisture present in the vegetation.

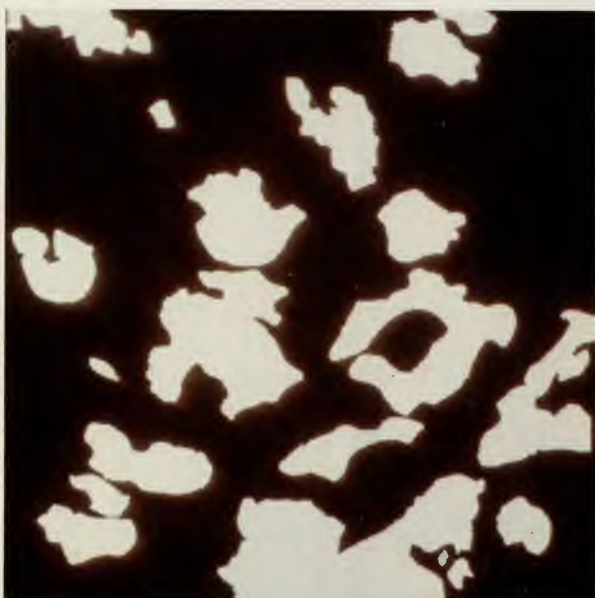


Figure 2. Bogs extracted manually from imagery shown in black.

A sample of reflectance values for different classes of peatlands was from the imagery. These data were analysed by the statistical package BMD FM, a stepwise variable selection routine for linear discriminant analysis (Dixon, 1981), to establish which classes could be distinguished and which bands should be used. From the analysis it was concluded that four types of peatland could be recognised. These were undisturbed peat, machine cut peat, hand cut peat and burnt peat. It was also possible to recognise peatland which had been planted with trees, and this was included in the classification. Recently cut peat could be distinguished from older cut peat, but as this was not of interest, these classes were combined.

It was found that spectral bands 3, 4 and 5 were sufficient to perform the classification, and that the other bands did not contribute significantly to the classification.

2.4 Classification

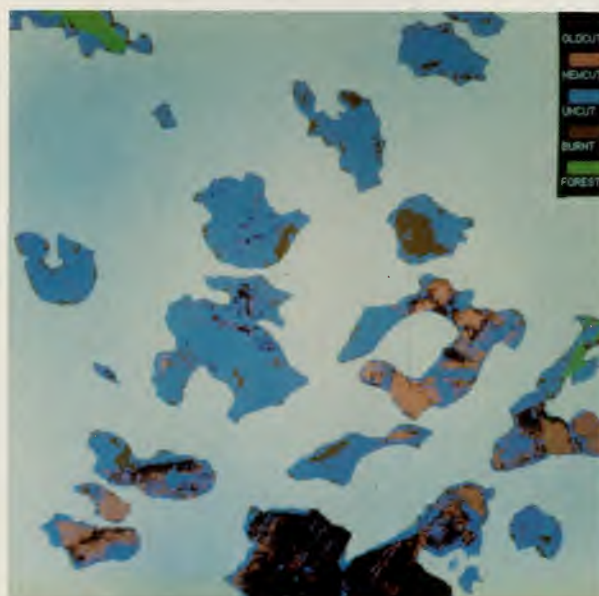
A classification of the image was first attempted by the parallelepiped method. It was found that this classification produced many areas classified as peatland that were not in fact peat. The reason for this is that the Irish Midlands contain, particularly in winter, many areas of wet pasture and flooded fields, which have the same spectral response, as peatland. Peatlands, however, were characterised by the fact that they occurred in large continuous regions, and were usually almost convex in shape. To map peat types it became clear that it would be necessary to first separate the peatlands from the background landscape. At the time of the study we did not have any technique available which would allow us to do this automatically, and so it had to be done manually by visual photo interpretation and digitisation. This was time-consuming and laborious, but successful (see Fig. 2).

After the peat had been successfully separated from the background, the second stage of the classification was to separate the peatland into the different types. This was done by the Gaussian Maximum Likelihood Allocation rule, using the output of the first stage as a mask. The parameters of the method were obtained from the training data. A smoothing (by the majority voting algorithm) was applied to the resulting classification. A segment of the classified image is shown in Figure 3.

2.5 Registration

The classified map produced was then geometrically cor-

Figure 3. Bogland classification for test sites.



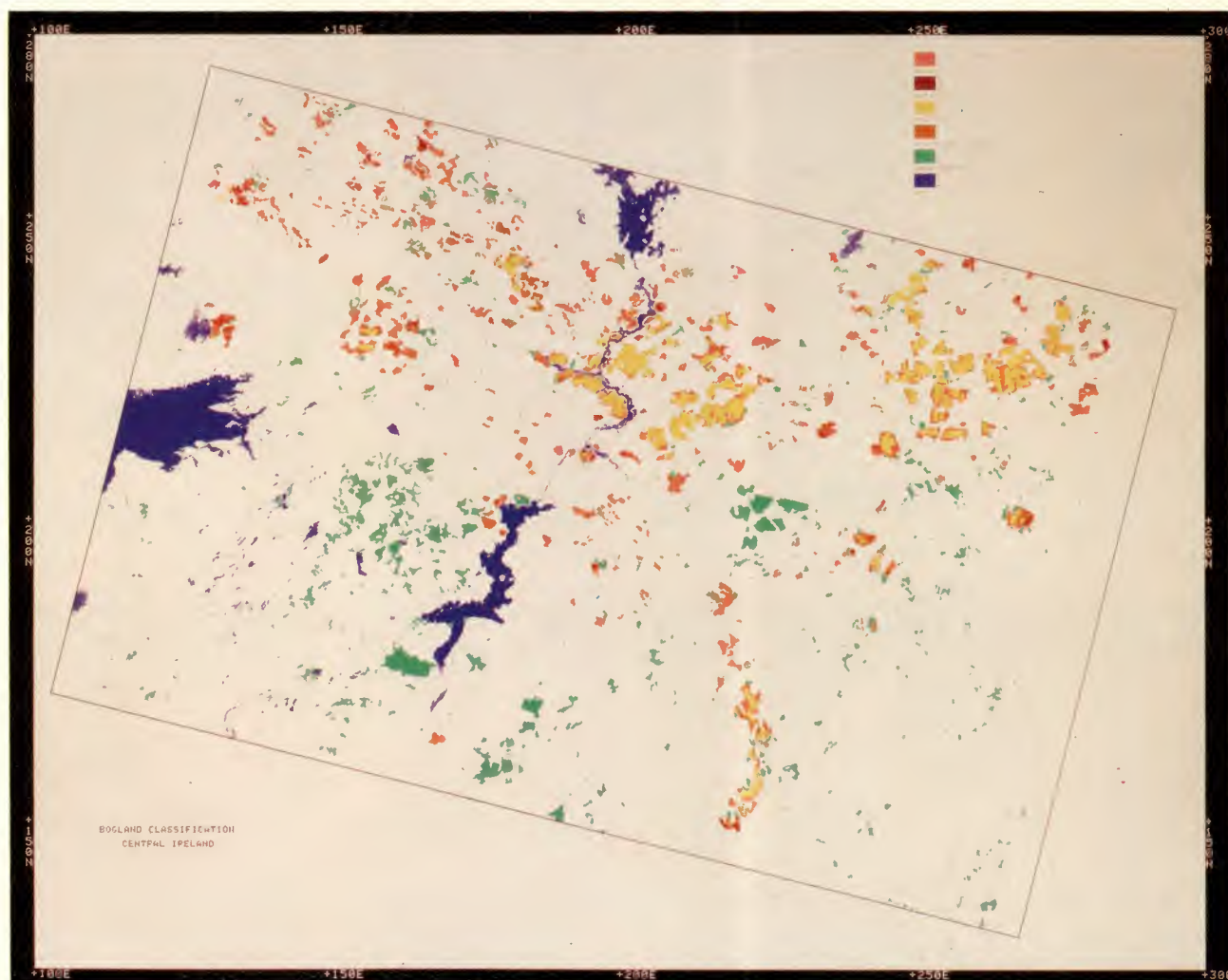


Figure 4. Bogland Classification for Central Ireland.

rected to the National Grid. This was accomplished by locating points (road intersections, bridges etc.) that had known grid locations and using cubic convolution resampling to a 50 m pixel. The decision to geometrically correct only the resultant classified image was made because of the reduced cost and because it was not necessary to relate to the raw unprocessed imagery to topographic maps.

2.6 Output

To produce a hardcopy map of the classified image, a colour was first chosen for each group. Three primary colour images (red, green, blue) were then generated from the classified image. The three primary colour images were then superimposed in plotting on an Optronics plotter. This plotter produces a photographic negative of the original images. This negative was then enlarged to give a 1 : 250 000 map of the study area, with the different classes shown as different colours (Fig. 4). A set of overlay maps were also produced, based on this classification.

2.7 Limitations

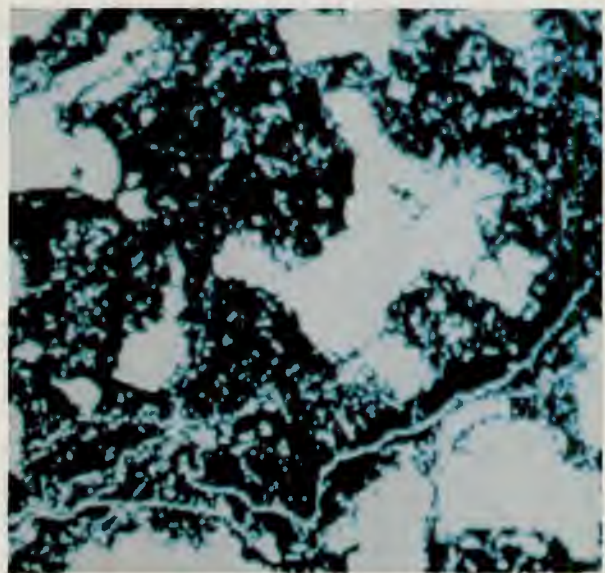
The main limitation discovered was that it was not possible to distinguish between wet and dry peatland. It was felt that this may have been due to our use of winter and spring images, in which the vegetation differences would be much less pronounced than in an image from summer or autumn. It was also found that the thermal band did not contribute to the distinguishing of peat types. It seemed that much of the landscape was of a uniform low (approx. 0°) temperature, as would be expected in the early morning during anticyclonic conditions in winter and spring. We felt that a summer image, either on its own or in combination with the winter and spring images, may allow greater possibilities for distinguishing peat types.

2.8 Additional Research

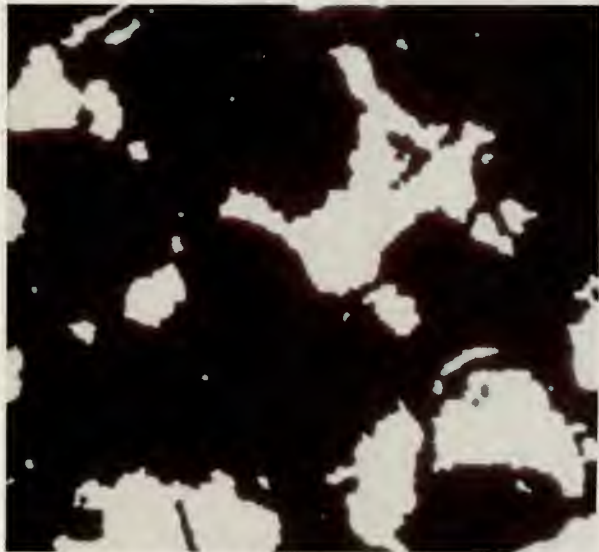
Although as pointed out above, it was not possible for us at the time of the study to separate peat from the background landscape in an automatic processing method, we have since been studying methods that would allow this type of processing to be done. The most relevant technique that we have found in this regard is Mathematical Morphology. This technique has been



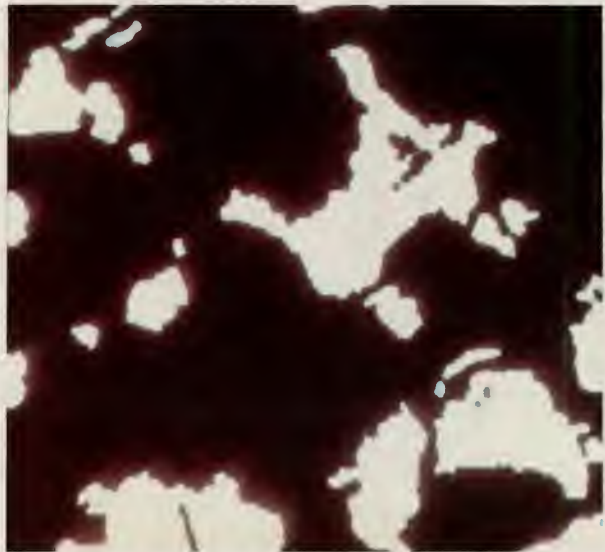
(a)



(b)



(c)



(d)



(e)

Figure 5. Application of mathematical morphology to bogland classification.

(a) Original Image of bogs.

(b) Simple Threshold.

(c) Erosion of size 2.

(d) Selection of particles with more than 10 pixels.

(e) Dilation of (d) conditional on (b).

developed at the Ecole des Mines at Fontainebleau, France, and is described by Serra (1982). The method is based on the ideas of topology and set algebra. Simple structuring elements are defined which can be found in an image by local transformations. By use of set algebra it is possible to build these simple structuring elements into more complex structures. The method is particularly

suiting to the analysis of images in which size and shape criteria are of importance, as was the case in recognising peat. We found that we could use the methods of mathematical morphology to extract the peatlands from the image. The stages of the processing applied to a test area are shown in Figure 5.

Since a visual photo interpretation had already been done, there was no cause to apply mathematical morphology to reprocess the entire scene. However, we hope that these methods can be applied to future land cover mapping projects.

3. Mapping of blanket peatland in the Slieve Aughty and Wicklow mountains

3.1 Aims

This work was undertaken as part of a larger project, being undertaken by Dr. Bradshaw in the Botany Department at Trinity College, Dublin, to study the causes and extent of blanket peat erosion in Ireland. This project was funded by the National Board for Science and Technology (NBST 99/84). An important part of this project was the mapping of different types of peatland, so that the patterns of disturbance can be studied (Bradshaw, 1987).

3.2 Location

The Slieve Aughty and Wicklow Mountains in central and eastern Ireland were chosen for an initial study of the

mapping potential of remotely sensed imagery. These mountains were chosen because of the availability of cloud-free Landsat-4 TM imagery for the area. The scenes used were: 206/23 (Q2, Q4; 17/3/85); 206/23 (Q2, Q3, Q4; 18/4/85); 207/23 (Q2; 26/1/85). The scenes were registered to the Irish National Coordinate Grid. All of the processing was performed on the VAX 11/780 computer of the Computer Science Department, Trinity College Dublin and the images were viewed on a Vicom digital image processor.

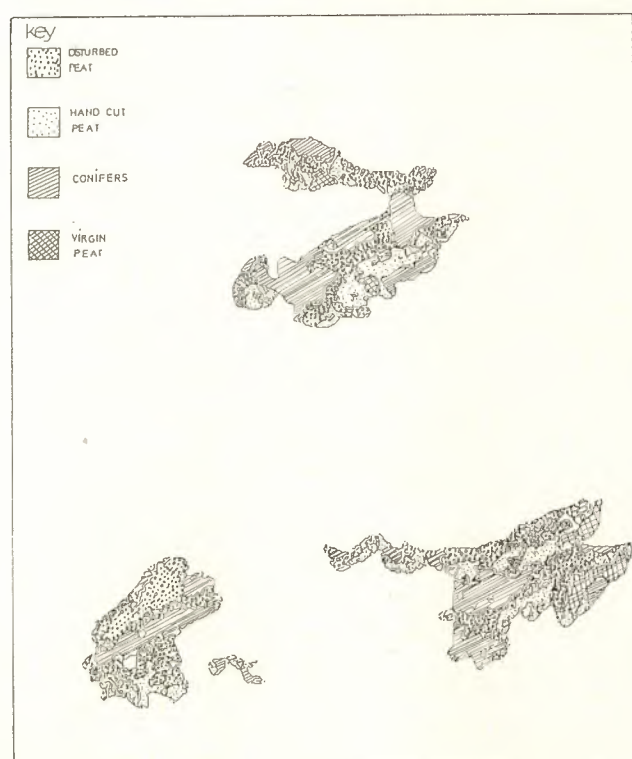
3.3 Classification method

It is known that the types of peatland of interest can only be found above about 250 m above sea level, and so it was decided to perform the mapping only above the 250 m contour. This contour was digitised from Ordnance Survey maps, and digitally overlaid on the TM image. This allowed the identification of all image pixels that were above 250 m.

After initial inspection of the imagery it was decided to attempt classification of each pixel into one of four classes, namely undisturbed peat, disturbed peat, cutaway peat and tree covered peat. Ground truth data were used to provide training samples for a statistical classification technique (maximum likelihood allocation) which assigned each pixel to one of 4 classes, according to which of these it most resembled in spectral intensity characteristics. This was based on the data bands 3, 4 and 5 of the Thematic Mapper imagery, which were found to contain all of the discriminating ability for the peatland types.

The resulting classified image was processed for map drawing by a pen plotter. A contouring program was used to generate instructions for the plotting, which was performed by a Calcomp pen plotter (Fig. 6). It was felt that the result was sufficiently successful to suggest that the use of TM imagery was a valuable aid in the study of peatland distribution and it is expected that the study will be extended to cover other TM scenes.

Figure 6. Upland bog classification, Slieve Aughty.



4. Application to mineral exploration

4.1 Aims

The aim of this project has been to assess the application of Landsat TM to the mapping of geological structures as an aid to mineral exploration in Ireland. This project was supported by an on-going research contract with the European Commission (Primary Raw Materials Programme) to develop remote-sensing and data integration methods for mineral exploration (Coller *et al.*, 1985; Critchley *et al.*, 1986). The test areas for the project comprised of the Lower Carboniferous limestones of the eastern and central midlands of Ireland. The rocks in this region are poorly exposed and it is not possible to directly map rock formations from satellite imagery. However,

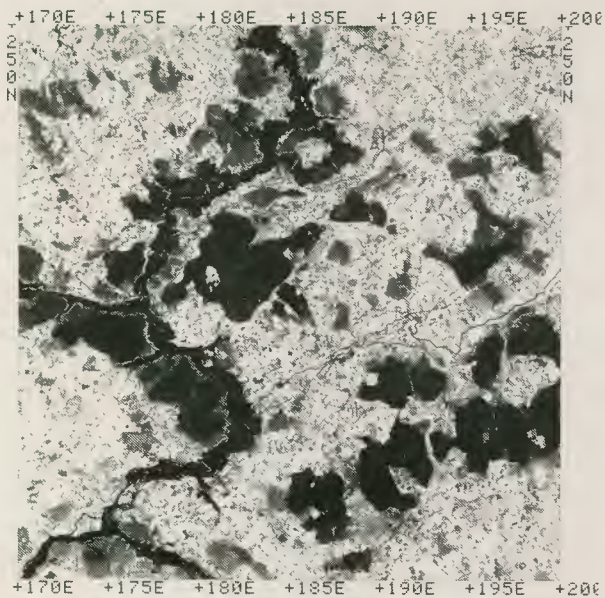


Figure 7. Hi-pass filtered TM band 4 image, Shannon Bridge area.

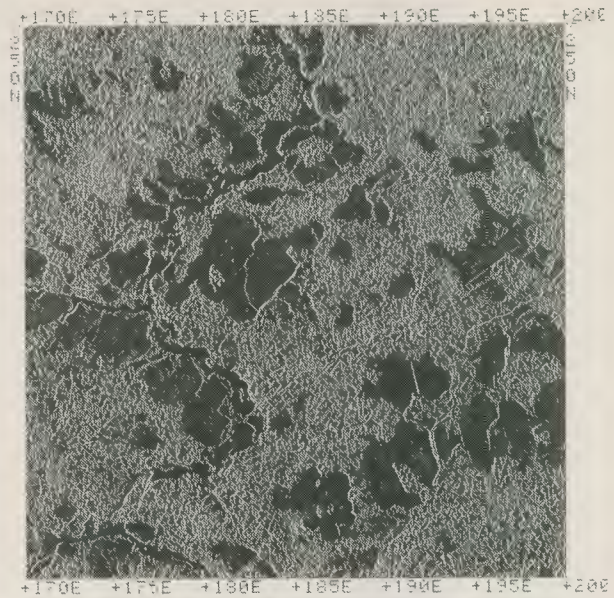


Figure 8. Directionally filtered TM band 4 image, Shannon Bridge area.

ground based studies have shown the close relationship between mineralisation and faulting within the limestones. It was therefore decided to test the ability of the TM imagery to map faults and compare these with fault structures identified on MSS imagery.

4.2 Image processing and interpretation

The imagery used for this study comprised of the following TM scenes: 207/22 (Q3; Q4; 8/5/84); 207/22 (Q1; 20/2/85); 208/22 (Q2, Q3, Q4; 26/1/85). After geometrically correcting the TM scenes a series of hard-copy images were produced of the enhanced band 4 data. A number of edge enhancement techniques were applied to the data, including hi-pass filtering and directional filtering on a 3-by-3 pixel basis (Figs. 7 and 8).

The hardcopy of the enhanced images were interpreted visually for linear features and after removing cultural features (such as roads and railways etc.) the lineaments were digitised and the digitised lines were further analysed using a series of statistical pattern analysis methods. These statistical methods involve sub-dividing the digitised lineaments into small grid cells (say 5 by 5 km) and calculating such measures as the total number of lines in a cell or their average orientation etc. Using both the major interpreted lineaments and the statistical 'pattern' analysis it was possible to compile a final map of some major fault zones. Using geological knowledge and other available data the location of mineralisation was predicted from this map.

4.3 Comparison of results with MSS imagery

However, when comparing the lineament interpretation from the TM imagery with that obtained from the MSS imagery it was apparent that although the gross pattern of

features seen were similar there were many differences in detail. In particular lineaments interpreted on the TM imagery tended to be shorter in length and less numerous. It is suggested that this is a function of the resolution of the TM imagery, whereby the higher resolution (as compared to MSS) allowed the identification of smaller scale geological features. In contrast the lower resolution of the MSS imagery seemed to enhance the recognition of the larger and more important geological structures. In addition the higher resolution of the TM imagery visually emphasised the agricultural patterns on a field size and tended to mask the larger scale features.

4.4 Conclusions and future work

Whilst the TM imagery was able to be used to map geological features in agricultural terrain of Ireland it was felt that MSS imagery was more suitable for this purpose. However, this project has not so far assessed the contribution of the spectral information from TM for geological mapping in agricultural areas and it is hoped that this will form a topic for future research. In addition research is also being directed at the automated computerised mapping of lineaments from TM imagery.

5. Acknowledgements

We wish to thank the Earthnet Programme Office for the supply of TM imagery and the National Board for Science and Technology for supporting the study of blanket peatlands. The contribution of the Forest and Wildlife Service of the Department of Fisheries and Forestry and the European Commission is gratefully acknowledged. Finally, we wish to record the invaluable assistance given by J. Cross, R. Bradshaw & A. Phillips.

6. References

- Bradshaw R. and McGee E. 1987. *The magnetic analysis of blanket peat erosion in Ireland*. Final report to the National Board for Science and Technology, ref. ST99/84.
- Coller D.W., Critchley M.F., Dolan J.M., MacDonaill C., Murphy C.J., Phillips W.E.A. & Sanderson D.J. 1986. Structural, remote sensing and multivariate correlation methods as aids to mineral exploration, Central Ireland. *Remote Sensing in mineral exploration (Resources Series)*, EUR 10334, 1-41.
- Critchley M.F., Coller D.W., Phillips W.E.A., Rowlands A.S. and Daly C.J. 1986. Structural, remote sensing and multivariate methods as aids to mineral exploration. *Proc. First European Workshop on Remote Sensing in Mineral Exploration. (Resources Series)*, EUR 10511, 34-84.
- Dixon W.J. et al, 1981. *BMDP Statistical Software*. Univ. California, Los Angeles.
- Hammond R.F. 1981. The peatlands of Ireland. *Soil Surv. Bull. (An Foras Taluntais)*, 35.
- Serra, J. 1982. *Image Analysis and Mathematical Morphology*. Academic Press.

Landsat-TM Study of Sabkha Surfaces in the Qattara Depression, Northwestern Egypt

Franz K. List, Doris Linne

Freie Universität Berlin, Institute of Applied Geology, Remote Sensing Group, W. Berlin

Bernd Meissner

Technische Fachhochschule Berlin, Laboratory of Map Design, W. Berlin

The Qattara Depression is situated in the northern part of the Western Desert of Egypt. It comprises an area of about 20 000 km² lying at or below sea level. About 5800 km² of it are covered by salt marsh, so-called 'sabkha' deposits consisting of a mixture of clay-like material and salt with varying water content. Preliminary multitemporal studies of Landsat-MSS data showed seasonal changes of the spectral signatures caused by differences in soil moisture.

A digital Landsat-TM scene of January 1986, was studied in detail for a better discrimination of the different types of sabkha surfaces. Several combinations of spectral bands were examined in order to find out what type of colour composite imagery would be best suited to visual interpretation. In addition, a digital classification of the scene was performed and the results compared. Two thematic maps, based on the results of the visual and the digital classification, were produced. In order to obtain more information on the significance of the spectral signatures observed in the TM imagery, ground truth measurements of the spectral reflectance of selected test sites were conducted, and soil samples were collected for laboratory analysis.

The digital classification by a maximum likelihood classifier proved superior to the visual interpretation. In both cases, the thermal channel is indispensable for the discrimination of sabkha deposits with different moisture content. The results of the spectroradiometric ground truth measurements showed that the spectral band from 1.15–1.30 μm that is provided on the Barnes spectroradiometer but not on Landsat-TM is very valuable for discrimination of soil classes.

The digital classification, though rendering more detailed discrimination of the sabkha surfaces than visual interpretation alone, nevertheless represents only an intermediary stage in the information extraction process. The results of the digital classification have to be reinterpreted and modified for the production of a thematic map.

1. Introduction

The Qattara Depression is situated in the northern part of the Western Desert of Egypt. It has the form of a huge bow opening toward the southeast, starting about 70 km south of El Alamein and continuing to the southwest for roughly 200 km. Its mean elevation is 60 m below sea level; the lowest point (–134 m) is found close to its southwestern end. To the north and west, the depression is confined by an escarpment of up to 250 m height that is formed by the limestone of the Marmarica Formation and, at its base, the marl and sandstone sequence of the Moghra Formation, both of Miocene age (Klitzsch, List, Pöhlmann *et al.*, 1986). The origin of this huge depres-

sion has been – and still is – a point of contention among geoscientists (Said, 1962). The most commonly held belief is that wind erosion was the major factor in its formation.

The area that lies at or below sea level is roughly 20 000 km². A major part of the depression, 5 800 km² according to Ball (1933), is covered by salt marshes, so-called 'sabkhas'. Sabkhas are 'characterized by evaporite-salt, tidal-flood, and eolian deposits' (Bates & Jackson, 1980: 550). In the present study, the term 'sabkha' is used in a slightly wider sense (Pertuisot,

1975). Within the Qattara Depression, obviously there are no tidal floods involved in the formation of the sabkhas; however, part of the salt present in the Depression probably constitutes the remnants of the regression of the Mediterranean sea during the Pliocene.

Preliminary multitemporal studies of Landsat-MSS data of the Qattara Depression were conducted in connection with field work for the preparation of a geological map of Egypt at a scale of 1 : 500 000 (List, Meissner & Pöhlmann, 1986). These studies (Linne & Meissner, 1983) showed that major parts of the Depression exhibit seasonal changes of the spectral reflection. Identical areas show different colours on satellite images taken at different seasons. This variation of the spectral signatures depends on changes in the moisture content of the soils. Using digital Landsat-MSS from 6 January and 12 February 1972, five different levels of moisture content could be recognized and mapped, using a combination of two colours for a kind of 'automatic' colour rendition of seasonal changes (Linne & Meissner, 1983).

When Landsat-TM imagery was made available through ESA and the German National Point of Contact (NPOC) at DFVLR, Oberpfaffenhofen, it was decided to conduct a pilot study of part of the Quattara depression with three objectives in mind:

- Evaluation of the improvement by the higher spatial and spectral resolution of Landsat-TM as compared to Landsat-MSS.
- Study of the variation in soil reflectance due to differences in soil composition and water content by spectral reflectance measurements in the field.
- Information on the seasonal variation of water influx and the ensuing soil moisture changes in the depression.

2. Methodology

For the present study, a part of the Depression was selected for more detailed investigation. This study area, of about 2500 km², is situated close to the western end of the Depression, east and northeast of the small oasis

Figure 1: Western part of the Quattara Depression, northwestern Egypt, showing the distribution of sabkha deposits (dark), dunes (stippled), and the study area.

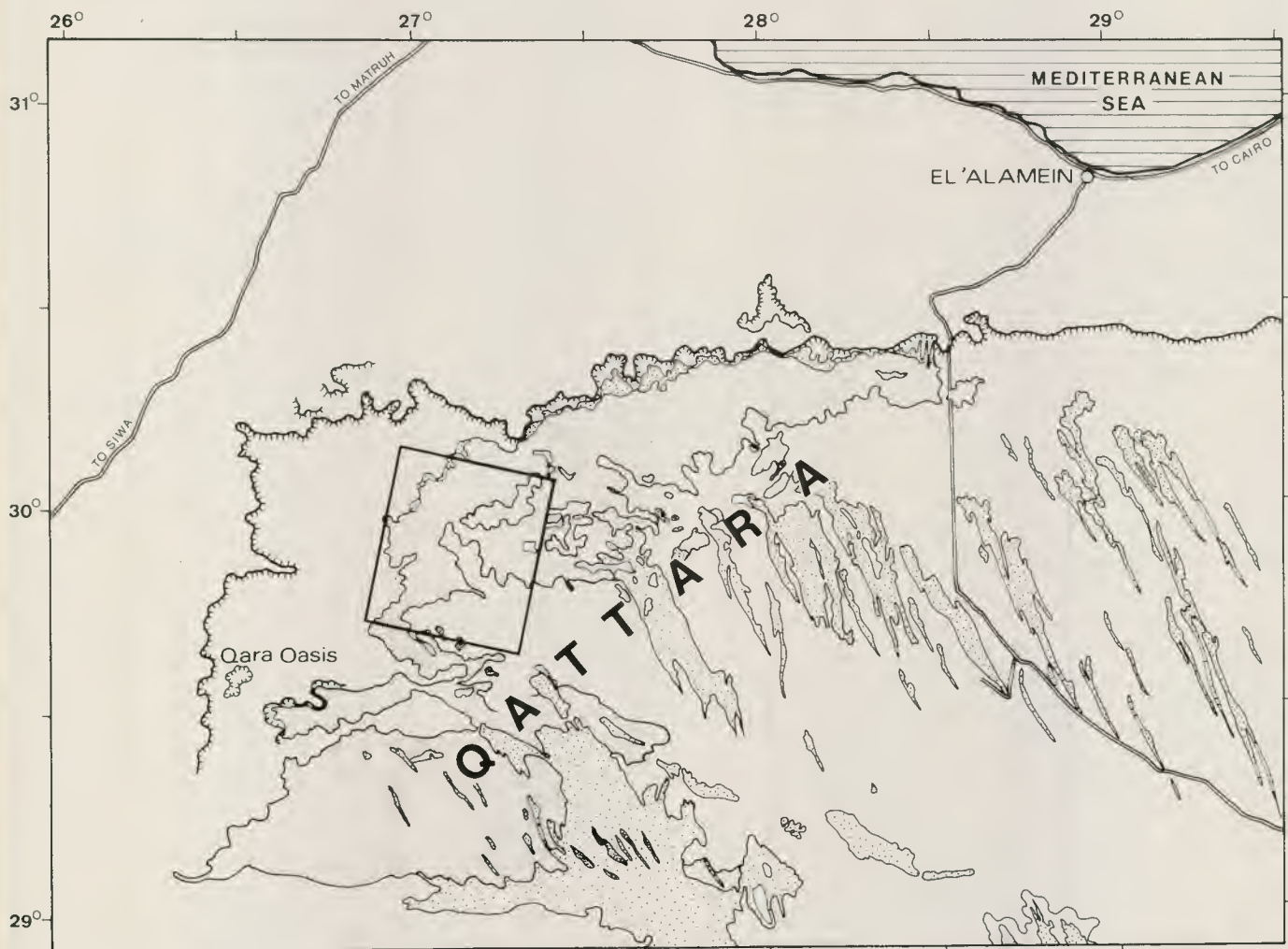




Figure 2: Landsat-1 MSS colour composite of spectral bands 4, 5, and 7. Scene recorded 6 January 1973.

of Qara (see Fig. 1). In this region, most of the different kinds of sabkhas occurring in the Qattara Depression are represented. Generally, the sabkha surfaces are extreme-

ly variable, ranging from very rough, dry, broken salt crusts to clay-like, moist soils with rather smooth surfaces. Details are given in Chapter 3.

2.1. Material used

While the present study concentrated on the use of Landsat-TM imagery, other additional data were also used, in particular field data, without which earth-oriented remote sensing cannot produce meaningful results.

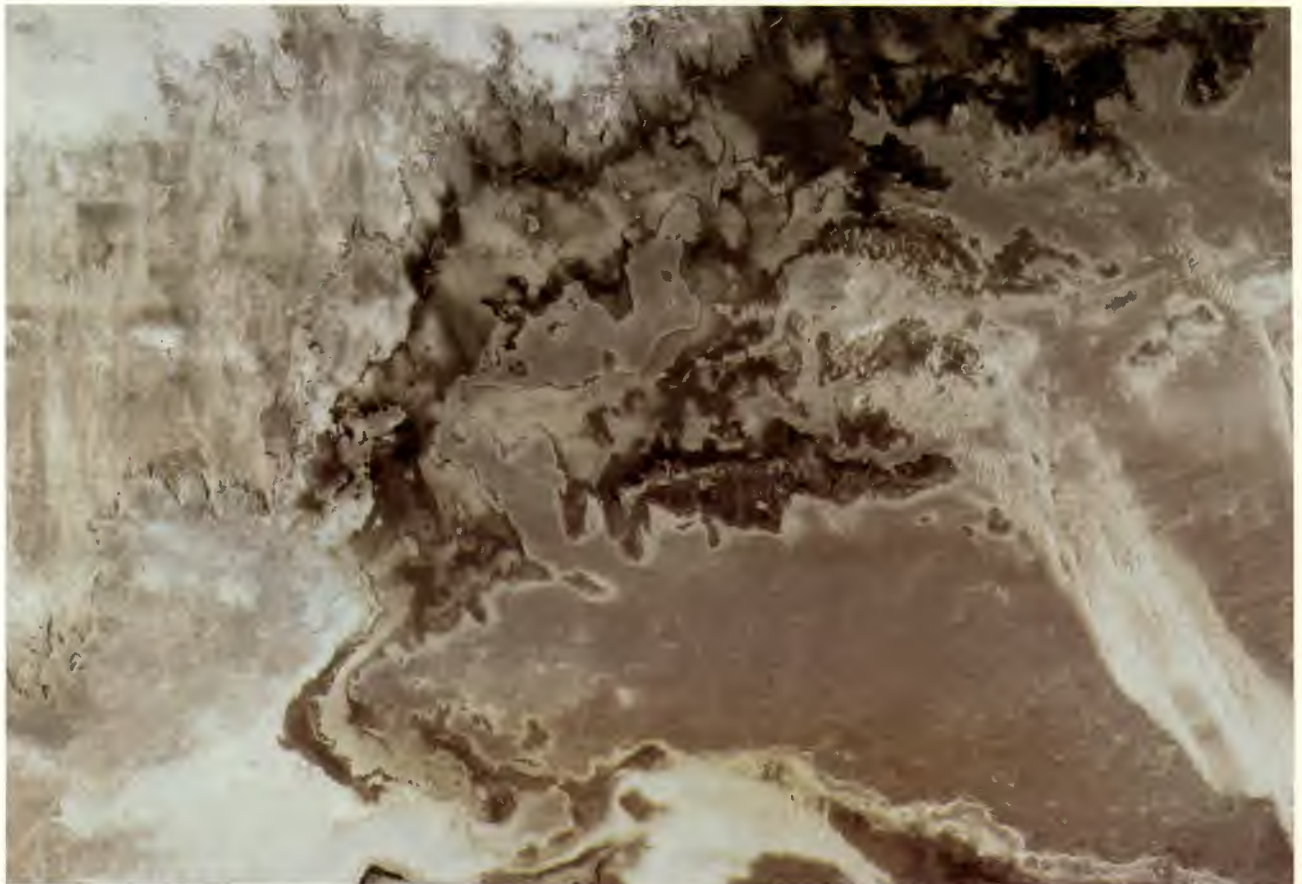
2.1.1. Maps

Due to the interest the Qattara region had already attracted in earlier years (Ball, 1933), more and better topographic maps are available of this area than of most of the rest of the Western Desert:

- Egypt 1 : 100 000 Western Desert, Sheet 12, Qattara; Sheet 13, El Qaneitra. Dept. of Survey and Mines, Cairo, 1939/40.
- Egypt 1 : 500 000, Sheet 1, Matruh; Sheet 4, Baharia. Survey of Egypt, Cairo, 1941/42.
- World 1 : 500 000, Sheet 448 A, Sallum; Sheet 448 B, Alexandria; Sheet 448 C, Bawiti; Sheet 448 D, Siwa. Dept. of Survey, War Office and War Ministry, London, 1971.

The 1 : 100 000 map of 1939 and 1940, on which the later smallscale maps are based, shows only one class of sabkha ('sabakha' on the map) surface. It does, however,

Figure 3: Landsat-5 TM colour composite of spectral bands 2, 3, and 4. Scene recorded 31 January 1986.



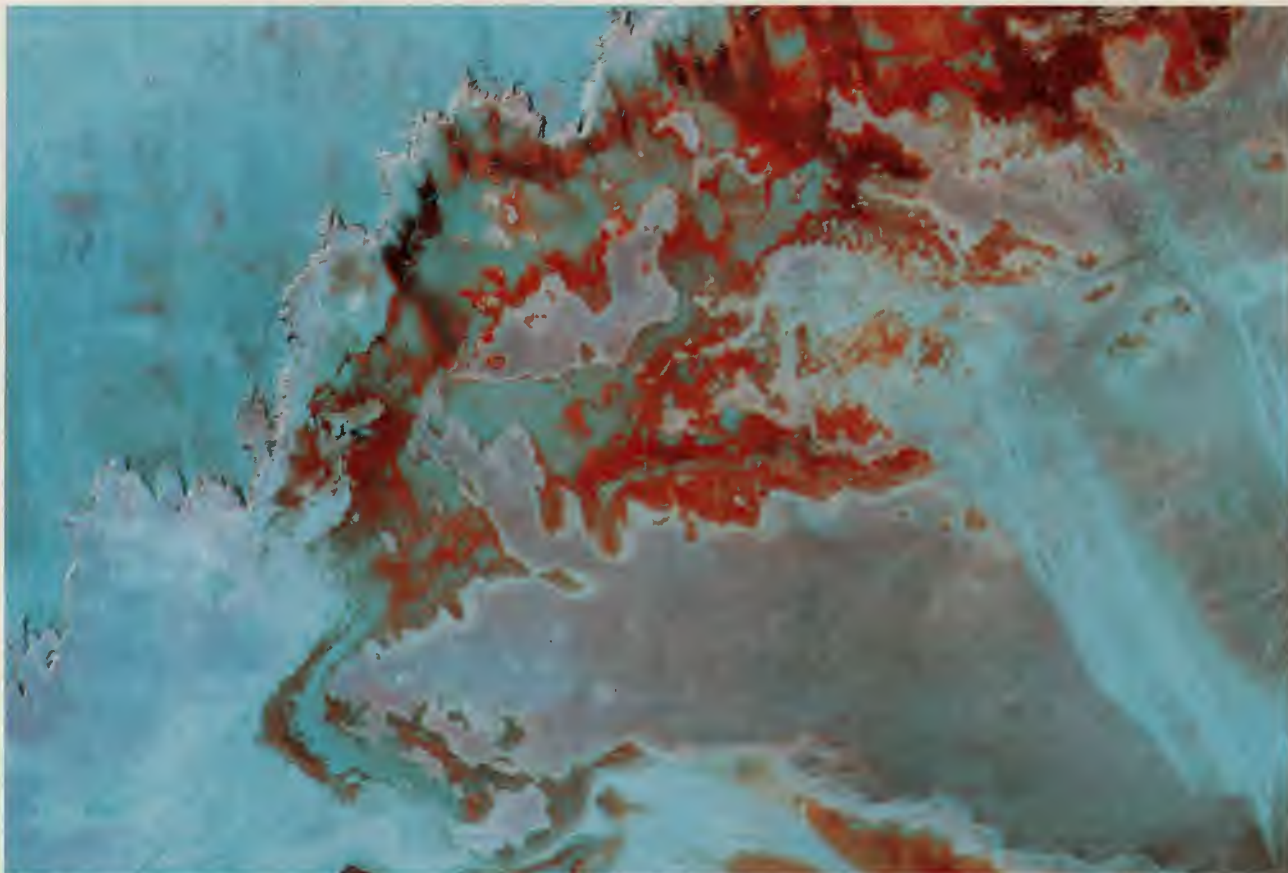


Figure 4: Landsat-5 TM colour composite of spectral bands 2, 4, and 6. Scene recorded 31 January 1986. Note improved separation of sabkha surfaces due to inclusion of thermal band.

Figure 5: Landsat-5 TM, same scene. Digital classification of bands 1, 5, 6, and 7 by the maximum likelihood method.



give additional information by terms like 'hard sabakha', 'wet sabakha', or 'very rough sabakha' printed on the map without actually separating these units.

In addition, the pertinent sheets of the new Geological Map of Egypt 1 : 500 000 (Klitzsch, List, Pöhlmann *et al.*, 1986) as well as data from the preceding preliminary Geological Interpretation Map of Egypt 1 : 500 000 (Klitzsch & List, 1979; List *et al.*, 1982) were used for this study.

2.1.2. Landsat data

Through the Landsat-TM pilot-study project of ESA, the Landsat-5 TM scene 179-39, recorded 31 January 1986, was made available through DFVLR, Oberpfaffenhofen. The data were delivered in digital form and processed by the Geomaps system at the Free University of Berlin (List, Richter & Schoele, 1987; Schoele, 1983). In addition to the TM data, digital Landsat-MSS data were used for this study. They were the only data available for the work of Linne & Meissner (1983). The frame used was 192-39, recorded 6 January 1973 (Fig. 2).

2.1.3. Aerial photography

Aerial photographs of the Qattara depression were also available as black-and-white paper prints. They were taken with a wide-angle camera in 1954 at a scale of 1 : 50 000. Although these photographs do not show the



Figure 6: Ground truth vehicle with extended hydraulic mast during field work.

Figure 7: View of the instrumentation on the ground truth vehicle.



actual state of the surfaces in the study area, they were very helpful as a kind of substitute for field data, whenever the scale and resolution of the Landsat imagery was insufficient.

2.2. Digital image processing

For visual interpretation of the Landsat-TM data, colour composites of various combinations of spectral bands (see Chapter 3.1.) were produced on the Geomaps system and plotted on an Optronics colour film plotter (Munier, 1983). The resulting transparencies (Fig. 3) were enlarged on colour film to a scale of 1 : 250 000 for visual interpretation. The interpretation was done on a light table, using transparent film and special inks for annotation of the interpreted units and their delimitations.

In the next step, a digital classification of the Landsat-TM data was performed. Based on the statistics of the data and the results of the various combinations of spectral bands studied by visual interpretation, the bands 1, 5, 6,

and 7 were selected as the ones with the least redundancy in information. The maximum-likelihood algorithm was used for classification, since in our experience it generally produces better results than the hyper-box or minimum-distance methods (Swain & Davis, 1978). The classified image was then geometrically corrected to control points determined in the field (List, Meissner & Pöhlmann, 1986) and plotted.

2.3. Field work and ground truth

The Qattara Depression was visited several times for field work in the course of the Special Research Project Sfb 69, funded by the German Research Foundation (Klitzsch & Schrank, 1987; List, Meissner & En-driszewits, 1987), and the CONOCO Mapping Project (List, Meissner & Pöhlmann, 1986). During these trips, interpretation and classification results were field-checked and samples of the different types of sabkha were taken for subsequent laboratory analysis.

In March 1987, a field party visited selected points of the study area for spectral reflectance field measurements of the various surface types. To this end, a four-wheel drive vehicle (Mercedes UNIMOG) with a hydraulic mast carrying several spectroradiometers and other instruments, specially equipped for desert work, was used (Figs. 6-7). This approach of collecting 'ground truth' on the spectral properties of natural surfaces, based on the work of Biniki *et al.* 1971a, 1971b), was developed during the last years at the Free University of Berlin (Köhler, 1982, 1983; List, Richter & Schoele, 1987; Richter, 1983a, 1983b).

3. Results

In the following, some of the results obtained so far are discussed. It must be emphasized, however, that they are of a preliminary nature. For final results, a comparison of the 1986 Landsat-TM data with those taken closest to the time of the radiometric ground truth acquisition (March 1987) is needed. Additionally, not all results of the mineralogical and moisture analyses of the soil samples collected during the last field trip are available as yet. The latter are essential before final conclusions can be drawn on how the soil composition and moisture content are reflected by their spectral signatures and to get a better understanding of the seasonal variations of soil moisture in the Qattara depression.

3.1. Visual interpretation

As a first stage and for obtaining preliminary data to be used for the planning of the field work, visual interpretation of various Landsat-TM colour composite images was performed. In the following, a short evaluation of the different spectral combinations used is given.

3.1.1. Combination of TM spectral bands 2, 3, 4

The spectral information content of this combination is

nearly equivalent to that of a usual Landsat-MSS colour composite image. Of course, with the significantly higher spatial resolution of Landsat-TM much more detail is shown. This fact alone represents a major improvement, rendering visual interpretation easier and more accurate (Figs. 2 and 3).

3.1.2. *Combination of TM spectral bands 3, 4, 7*

This type of colour composite imagery allows a very clear distinction between the rocks of the Moghra Formation and the sabkha deposits. Small areas consisting of bedrock that could not be identified on the Landsat-MSS image can be detected and located.

The differences between very bright sand sheets and highly reflecting salt crusts situated north of the Ghard el-Din dune are clearly visible. This could not be done on the MSS imagery, only on the aerial photographs. A similar phenomenon can be observed southwest of the Qara oasis. Light-coloured sand sheets can be separated from silty and calcareous beds of the Moghra Formation.

3.1.3. *Combination of TM spectral bands 1, 5, 7*

This combination produces good separation within the wetter areas, similar to the combination of bands 2, 3, and 4. The differences in soil moisture are represented by different shades of gray. The boundaries of the sabkha deposits to the Moghra Formation are not very distinct on this image.

A remarkable bright salt band outcrops along the main Qattara escarpment at a distance of two to five km. It is locally accompanied by open water and very wet soils. This salt band and the wet areas are most clearly visible with this combination; even drainage patterns show up. This spectral combination renders the best information on the wet areas; it does not however, offer additional distinction between the drier sabkha types with salt crusts.

3.1.4. *Combination of TM spectral bands 1, 5, 6*

The most impressive result of this combination is the extremely detailed differentiation within the areas with dry and rough salt crusts, comparable to the separation obtained by digital classification. Within one single 512 by 512 pixel subscene it was possible to differentiate up to twelve different types of salt-crust covered surfaces. Interestingly enough, the conspicuous bright salt band is not shown in this combination. The small outcrops of Moghra Formation within the sabkha soils as well as their boundary to the Moghra stand out very well, with differences in surface texture that show up as distinct colour changes in this image.

3.1.5. *Combination of TM spectral bands 2, 4, 6*

The combination of spectral bands 2, 4, and 6 enables the interpreter to carry out the most differentiated interpretation. Using the other spectral combinations mentioned

above or Landsat-MSS data, it was always difficult to obtain proper distinctions because the dry surfaces were represented by the same colours. The thermal channel is obviously less correlated with the others and therefore adds valuable additional information.

Since the data of channel 6 are superimposed on the images of bands 2 and 4, its lower spatial resolution is masked by the higher resolution of the other bands. The resulting image degradation is negligible for the requirements of the interpretation. This combination of spectral bands is generally the best for visual interpretation. Consequently, the visual interpretation map is based on the combination of bands 2, 4, and 6 (map 1).

3.2. Digital classification

As pointed out in Chapter 2.2., a maximum-likelihood classifier using spectral bands 1, 5, 6, and 7 was chosen for the digital classification of the sabkha surfaces. The resulting colour-coded classification is shown on Fig. 5. As compared to the result of the visual interpretation, the more detailed representation of a total of 13 spectral classes is obvious.

When working with the results of digital classifications, it always must be emphasized that a digital classification is not a map but only an intermediary step between the data and the final representation of the information extracted from the data in the form of a thematic map. This classification of part of the Qattara Depression is no exception. The number of classes differentiated by the computer on grounds of their spectral behaviour is determined by the selection of spectrally different test areas by the user. Generally, however, classes of sabkha deposits that are defined in a meaningful way on the basis of their physical and mineralogical parameters show a certain natural variation of their spectral reflectance properties. Therefore, the spectral classes have to be transformed into actual soil or rock classes. This can only be done by visual evaluation of the classification by a skilled interpreter, taking into account also all available ancillary information from field and laboratory. For this reason, the thematic map in its final form, though based on the digital classification, is significantly different from it.

As can be seen on the map derived from the digital classification, the number of actual surface types shown is smaller on the map than on the classification. This is due to the fact that the test areas for the classification were selected on grounds of their spectral features. Soil samples that were taken from these test sites showed that some spectrally different classes had to be lumped together on the map in order to obtain geologically meaningful subdivisions.

3.3. Ground truth

As mentioned earlier, final results of the ground truth

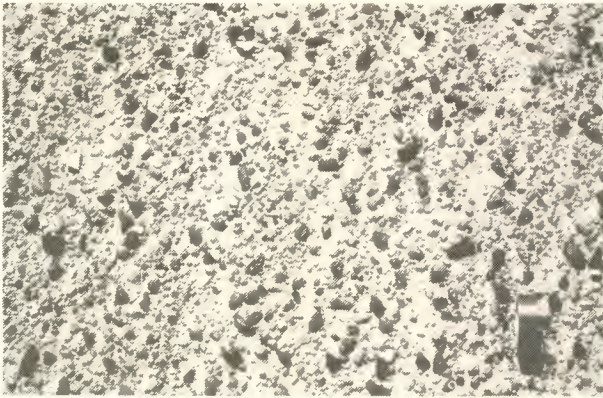


Figure 8: Typical surface of gravel-covered Moghra Formation.

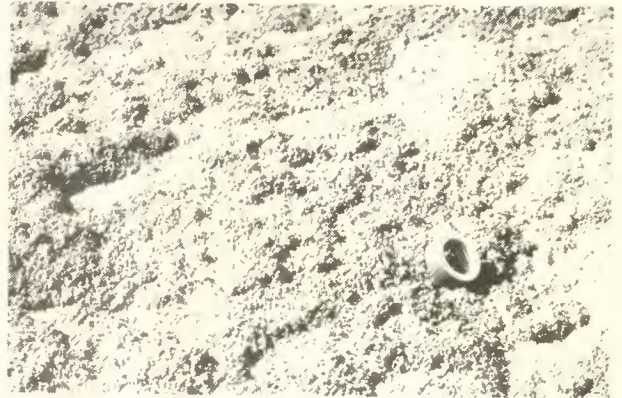


Figure 9: Typical surface of moist sabkha with fine-textured salt crusts.



Figure 10: Typical surface of moist sabkha, marginal to bed rock.



Figure 11: Typical surface of wet sabkha with white salt-covered polygons.

campaign cannot be given before the process of analyzing all samples taken, together with the spectral reflectance measurements, is finished. Nevertheless, some trends can already be deduced from the data presently available.

Figures 8 to 11 give an impression of four selected sabkha surface types. The corresponding spectral signatures are shown on Figures 12 to 15. On the histograms, the four spectral bands of the EXOTECH Mod. 100 A spectroradiometer are designated E1 to E4. They are shown on the left side. To the right follow seven out of the eight spectral bands of the Barnes Mod. 12000 spectroradiometer, B1 to B7, that correspond to the Landsat-TM bands. The only exception is band 5 of the Barnes radiometer (1.15 to 1.30 μm) that does not exist on Landsat-TM. The thermal TM band (band 6, 10.4 to 12.5 μm) is not represented due to calibration problems with that band on the Barnes; the surface radiation temperatures were measured by a Heimann KT 24 IR radiometer instead. The reflectance values, R%, are given as percentages relative to the sulphur standard used (List, Richter & Schoele, 1987).

The graphs show that the Landsat-TM data provide a much better spectral separation of the four sabkha types

than Landsat-MSS, even without the thermal channel. It can also be observed that the spectral band 5 (1.15 to 1.30 μm) of the Barnes radiometer provides a lot of additional information over the TM bands 4 and 5 (0.76 to 0.90 and 1.55 to 1.75 μm). It would be of great value for geology- or soil-oriented applications of multispectral remote sensing satellites if such a band were available on future earth-observing systems.

3.4. Subdivision of the mapped surface types

The results of the visual interpretation and the (modified) digital classification are shown as thematic maps (see maps 1 and 2). It has to be mentioned that the visual interpretation also profited somewhat from the digital classification: The visual interpretation showed some distinctions that were too slight to be taken as meaningful. When the same features showed up in the digital classification, these features were thought to be pertinent and put on the map.

The subdivisions of units on both thematic maps are the same since they refer to actual physico-mineralogical and not to spectral classes. However, classes 3.4.8. and 3.4.9. appear only on the map based on digital classification since they could not be identified by visual means. Class 3.4.7. is only found on the visual interpretation

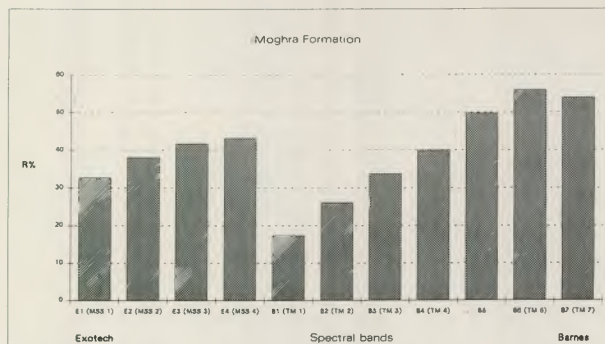


Figure 12: Spectral signature of gravel-covered Moghra Formation (see Fig. 8), measured in the field.

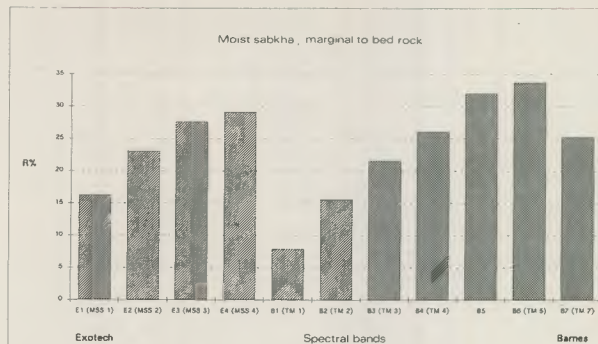


Figure 14: Spectral signature of moist sabkha close to bed rock (see Fig. 10), measured in the field.

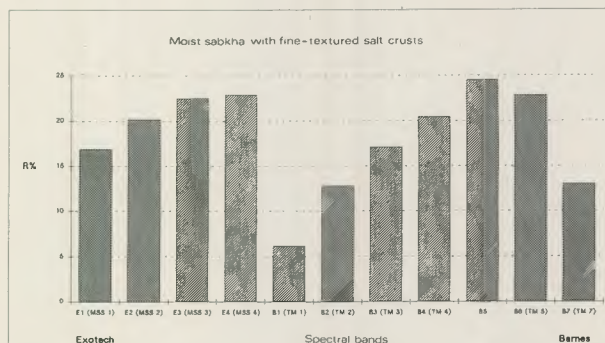


Figure 13: Spectral signature of moist sabkha with fine-textured salt crusts (see Fig. 9), measured in the field.

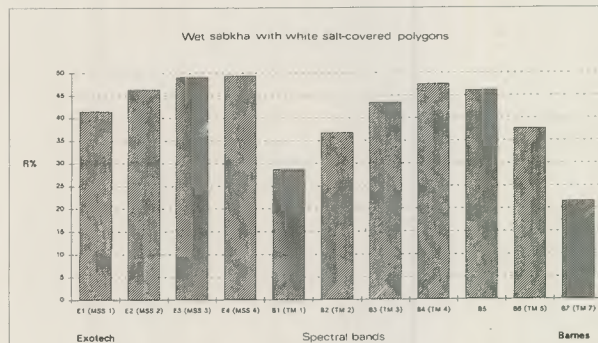


Figure 15: Spectral signature of wet sabkha with white salt-covered polygons (see Fig. 11), measured in the field.

map; it is a mixture of classes 3.4.2. and 3.4.3. that could not be separated visually in some areas. In the following, a short description of the different units is given.

3.4.1. Moghra Formation

The Moghra Formation forming the lower part of the Qattara escarpment predominantly consists of marl intercalated with siltstone and sandstone beds. It is also the source rock for most of the clay-like material constituting the sabkha deposits. It is covered by gravel beds that consist of about 50% gravel and 50% sand. The gravel contains 10% of dark, gray-to-black pebbles up to 3 cm in diameter; the rest ranges from 0.5 to 1.5 cm. The sand is mostly medium grained. The gravel beds locally are penetrated by small outcrops of silty limestone, partly ferruginated sandstone, and some spots of gypsum.

3.4.2. Dry, very rough salt crusts

This unit is characterized by a surface consisting of thick salt crusts that are typically broken up into an irregular tangle of salt slabs and floes with a relief up to 80 cm. This effect is caused by pressures originating from repeated crystallisation, solution, and recrystallisation. The capillary connection to the ground water is suppressed or interrupted. In spite of the very rough surface texture, the spectral reflectance in all channels is very high. This is probably due to the considerable amount of white salt crystals present in the dry and hence light-coloured clay-like matrix. The radiation temperature, in conse-

quence, is rather low. This surface type is the dominant one within the area studied.

3.4.3. Moist sabkha with fine-textured salt crusts

The unit consists of a gleyic solonchak soil that is covered by a porous, fine-textured saltcrust. This crust has capillary connection to the ground water; its relief of 1–1.5 cm is caused by the actual growth of salt crystals. The rate of reflection in all spectral bands decreases with the amount of moisture present in the soil. In the colour composite image (Fig. 4), this sabkha type is represented by light to dark red colours, depending on the water content.

3.4.4. Marginal sabkha, transitional to bed rock

The transition zone of sabkha soils to the bedrock, consisting of Moghra Formation more or less affected by salt weathering, was visually mapped as a separate unit only after the digital classification was available. Not surprisingly, in the colour composite images its characteristics are closely related to either the bedrock or the preceding type of moist sabkha. Close to the bedrock, it shows small polygons (20–30 cm) that become larger toward the interior of the salt marsh. Its surface consists of finegrained, loess-like material containing coarse sand grains, on top of a rather massive salt layer of about 10 cm thickness. Below that there are less dense salt soils. The ground water table is encountered at a depth of 70–80 cm.

In the colour composite image, this unit shows light brown, light turquoise, and faint reddish hues. The response of the thermal channel is the same for this unit and the Moghra Formation.

3.4.5. *Wet sabkha with rough surface*

This unit is similar to the surface type 3.4.2; the main difference is the fact that the ground water table is found only 30–50 cm below the surface, and the surface therefore is rather wet. It is characterized by broken, often tilted polygons of thick salt crust 30–50 cm in size which are partly bare and partly obscured by clay and sand.

The colour of this class in the composite image is a dark greyish green. The combination of the high moisture content with the rough surface texture is responsible for the thermal properties of this unit: The evaporation of the wet surface is increased by its roughness, resulting in low radiation temperatures. However, the relationship of soil moisture and radiation temperature is highly complex (Quiel, 1975; Schmugge, 1978); more detailed studies are needed before definite answers can be given. This unit could only be identified by the inclusion of channel 6 in the colour composite.

3.4.6. *Bright salt crusts*

A bright, white salt band runs parallel to the main scarp of the Qattara Depression. It is accompanied by open saltwater ponds that possibly mark the outcrop of a ground-water bearing layer. Similar salt crusts are also found around artificial ponds and lakes that originated from recently drilled water wells northwest of Minqar Abd el-Nabi.

In the colour composite image the salt band appears in strong light-blue to whitish colours; in the thermal channel it is shown as a black line.

3.4.7. *Mixture of dry, rough and moist, fine-textured sabkha*

This unit is a mixture of units 3.4.2. and 3.4.3. that cannot be separated visually on the colour composite images. The separation into two distinct classes by digital classification, on the other hand, presented no problem.

3.4.8. *Very dark, wet salt crusts*

Again, this class could only be discriminated by digital classification; it therefore does not appear on the map based on visual interpretation. It is characterized by a fine-textured, porous surface that is due to recent growth of salt crystals. Below it, a mixture of soft clay and salt or white salt crusts are found. It appears in the neighborhood of the white salt crusts described above.

3.4.9. *Clay-like to sandy surface topping porous salt crusts*

This unit could also be classified digitally. It comprises

surfaces consisting of a thin cover of clay-like mud and fine-grained sand over a porous and cavernous salt layer that is underlain by a hard, massive salt crust.

4. Conclusions

It is not surprising that for applications in geology and pedology, Landsat-TM data are markedly superior to Landsat-MSS. This is only partly due to the better spatial resolution of the TM data; the higher spectral resolution, especially the addition of the thermal band 6, seems even more important. In this context, it was found by radiometric ground truth studies that the spectral band from 1.15–1.30 μm that is provided on the Barnes spectro-radiometer but not on Landsat-TM renders valuable additional information. The inclusion of this spectral range on future remote sensing systems would be highly desirable.

Unlike the limited potential of digital classification when used for the lithologic discrimination of rocks, digital classification of sabkha surfaces proved superior to visual interpretation of colour composite images. Still, the result of any digital classification can only be considered as an intermediary stage in the process of information extraction from remote sensing data.

In order to produce a thematic map, the classification results have to be reinterpreted and modified.

By integrating data from spectral ground truth measurements, results of analyses of soil samples taken from selected test areas, and by digital analysis of multitemporal Landsat-TM data it is hoped that a better understanding of the significance of spectral signatures of sabkha surfaces and of the seasonal variations of water tables in the Qattara Depression will be obtained.

5. Acknowledgements

The authors gratefully acknowledge the contribution of ESA and DFVLR in that they made a full Landsat-TM scene available for this study at no cost. Dr. J. Pohlmann, FU Berlin, Institute of Applied Geology, kindly performed the digital classification of the TM data. We are also indebted to the German Research Foundation, DFG, that funded this work in the course of the Special Research Project on arid lands (Sfb 69). Last but by no means least, we wish to thank Conoco Coral Inc., Cairo, and its president, Mr. Coy H. Squyres, for providing the means for field work within the Conoco Mapping Project.

Sabkha Deposits of the Western Qattara Depression Visual Interpretation of Landsat-TM Color Composite (Bands 2, 4, 6)



- Moghra Formation (Miocene)
- Dry, very rough salt crusts
- Moist sabkha with fine-textured salt crusts
- Marginal sabkha, transitional to bed rock
- Wet sabkha with rough surface
- Bright salt crusts
- Mixture of dry, rough and moist, fine-textured sabkha



1: 250 000

Interpretation: D. LINNE

Cartography and Reproduction by Technische Fachhochschule Berlin 1987

LIST, LINNE & MEISSNER

Color Plate 2

Sabkha Deposits of the Western Qattara Depression
 Re-Interpretation of Digital Classification of Landsat-TM Data



Moghra Formation (Miocene)



Dry, very rough salt crusts



Moist sabkha with fine-textured salt crusts



Marginal sabkha transitional to bed rock



(Unclassified partly comprising wet, rough sabkha)



Bright salt crusts



Very dark, wet salt crusts



Silty to sandy surface topping porous salt crusts



approx. 1:250 000

Digital Classification: J. POHLMANN

Interpretation: D. LINNE

(Cartography and reproduction by Technische Fachhochschule Berlin 1987)

6. References

- Ball J. 1933: The Qattara Depression of the Libyan Desert and the possibility of its utilization for power-production. *Geogr. J.*, 82, 4., p. 289-314, London.
- Bates R.L. & Jackson J.A. eds. 1980: *Glossary of geology*. - 2. ed., 749 pp., Falls Church (AGI).
- Biniki R.M., Hulstrom R.L., Muhm J.R., Stadjuhar S.A. & Worman K.E. 1971a: Bonanza. Application of remote sensor data to geologic analysis of the Bonanza test site, Colorado. - *Sec. year Summ. Rep.* - *Rep. MCR80*, unpag., Martin Marietta Denver Div., Denver.
- Biniki R.M., Hulstrom R.L., Muhm J.R. & Worman K.E. 1971b: Ground instrumentation applicable to remote sensing. - *Rep. R-71-48680-005*, 30 pp., Martin Marietta Denver Div., Denver.
- Klitzsch E. & List F.K. eds. 1979: *Southwest Egypt 1 : 500 000* - Geological interpretation map, preliminary edition: Sheet 2527 Farafra, Sheet 2827 El Minya. - Berlin (TFH).
- Klitzsch E., List F.K., Pöhlmann G., Handley R., Hermina M. & Meissner B. eds. 1986: *Geological map of Egypt 1 : 500 000*, Sheets NH 25 NW Salum, NH 35 NE Alexandria, NH 35 SW Siwa, NH 35 SE Bahariya. - Cairo (Conoco/E.G.P.C.).
- Klitzsch E. & Schrank E. eds. 1987: Research in Egypt and Sudan. Results of the Special Research Project arid areas, period 1984-1987. - *Berliner geowiss. Abh.*, A, 75.1: p. 1-330; 75.2, p. 331-628; 75.3, p. 629-968, Berlin.
- Köhler U. 1982: Messung der richtungsabhängigen spektralen Reflexion von natürlichen Gesteinsoberflächen. *Berliner geowiss. Abh.*, A, 41, p. 167-252, Berlin.
- Köhler U. 1983: Radiometrische Beleuchtungs- und Reflexionskorrekturen. - In: List F.K. & Meissner B. eds.: Beiträge zur Fernerkundung der Erde an der Freien Universität Berlin; *Berliner geowiss. Abh.*, A, 47, S. 121-140, Berlin.
- Linne D. & Meissner B. 1983: Zur Interpretation von Grundwasseraustritten in ariden Gebieten mit Hilfe von Landsat-Daten. - In: List F. K. & Meissner B. eds.: Beiträge zur Fernerkundung der Erde an der Freien Universität Berlin; *Berliner geowiss. Abh.*, A, 47, p. 63-74, Berlin 1983.
- List F.K. & Meissner B. eds. 1983: Beiträge zur Fernerkundung der Erde an der Freien Universität Berlin. - *Berliner geowiss. Abh.*, A, 47, 196 pp., Berlin 1983.
- List F.K., Burger H., Klitzsch E., Meissner B., Pöhlmann G. & Schmitz H. 1982: Application of visual interpretation and digital processing of Landsat data for the preparation of a Geological Interpretation Map of Southwestern Egypt at a scale of 1 : 500 000. - *Proc. internat. Symp. Remote Sensing Environment, Remote Sensing in arid semi-arid Lands*, 2, p. 849-858, Cairo.
- List F.K., Meissner B. & Endriszewits M. 1987: Operational remote sensing for thematic mapping in Egypt and Sudan. - In: Klitzsch, E. & Schrank, E., eds.: Research in Egypt and Sudan. Results of the Special Research Project arid areas, period 1984-1987. *Berliner geowiss. Abh.*, A, 75.3, p. 907-926, Berlin.
- List F.K., Meissner B. & Pöhlmann G. 1986: Landsat-MSS remote sensing and satellite cartography - an integrated approach to the preparation of a new Geological Map of Egypt at a scale of 1 : 500 000. - *Proc. IGARSS'86 Symp.* Zürich, ESA SP-254, p. 1503-1510.
- List F.K., Richter A. & Schoele, R. 1987: Digital image processing and ground reflectance measurements - applications in arid areas. - In: Klitzsch E. & Schrank E., eds.: Research in Egypt and Sudan. Results of the Special Research Project arid areas, period 1984-1987. *Berliner geowiss. Abh.*, A, 75.3, p. 873-906, Berlin.
- Munier C.H. 1983: Verarbeitung von Filmen für das Optonics colourwrite System. - In: List F. K. & Meissner B. eds.: Beiträge zur Fernerkundung der Erde an der Freien Universität Berlin; *Berliner geowiss. Abh.*, A, 47, S. 33-37, Berlin.
- Pertuisot J.P. 1975: De la signification du mot sebkhia en géologie. Exemples tunisiens. - *Ass. sénégal. Et. Quatern. Afr., Bull. liaison*, 44/45, p. 67-75, Dakar.
- Quiel F. 1975: Thermal/IR in geology. - *Photogramm. Eng. remote Sens.*, 41, 3, p. 341-346, Falls Church.
- Richter A. 1983a: Bodengebundene radiometrische Reflexionsmessungen. - In: List F.K. & Meissner B. eds.: Beiträge zur Fernerkundung der Erde an der Freien Universität Berlin; *Berliner geowiss. Abh.*, A, 47, 141-158, Berlin.
- Richter A. 1983b: Ein schwenkbarer Teleskopmast - notwendiges Hilfsmittel für bodengebundene radiometrische Reflexionsmessungen. - In: List F.K. & Meissner B. eds.: Beiträge zur Fernerkundung der Erde an der Freien Universität Berlin; *Berliner geowiss. Abh.*, A, 47, 159-166, Berlin.
- Said R. 1962: *The geology of Egypt*. Elsevier, Amsterdam, 377 p.
- Schmugge T. 1978: Remote sensing of surface soil moisture. *J. appl. Meteor.*, 17, 1549-1557, Washington.
- Schoele R. 1983: Das 'Geowissenschaftliche Multibild Auswerte- und Prozessor-System GEOMAPS'. - In: List F.K. & Meissner B. eds.: Beiträge zur Fernerkundung der Erde an der Freien Universität Berlin; *Berliner geowiss. Abh.*, A, 47, S. 39-47, Berlin.
- Swain P. H. & Davis S. M. 1978: *Remote sensing: The quantitative approach*. Stroudsburg (Dowden, Hutchinson & Ross), 396 p.

Image Processing Strategies for Mineral Exploration in Arid Areas by Use of TM Data

H. Kaufmann

Department of Photogrammetry and Remote Sensing
University of Karlsruhe, FR Germany

Investigations have been carried out in the Wadi Araba – Jordan Graben area, to trace the relationship between diagnostic signals received from Landsat Thematic Mapper data and several mineralised ground districts. To meet the objectives, different approaches, involving ratioing, principal component analysis and IHS-decorrelation processing are used to enhance diagnostic features associated with (hydrothermally) altered areas. Using ratio techniques the best suited approach is given by a colour combination of ratios 5/7, 4/3, 7/4. In principle comparable results can be generated by a combination of PC-2, PC-4 and PC-3 in this order. However the ratio and PC-approach often fail to discriminate clearly between the diagnostic features. The main reasons are attributable to similarities in relative intensities of vegetation and minerals and to disadvantages that arise through the techniques themselves. Decorrelated and filtered colour composites of TM-bands 1, 4, 7 have proved to be more successful for delineation of known and unknown mineralisations via the presence of alteration guide minerals such as iron oxides and phyllosilicates. In addition, the resulting final products of the decorrelation concept can be used for carefully directed field work, as spectral and structural information are enhanced simultaneously.

Keywords: image processing, IHS-decorrelation, hydrothermal alteration, mineral exploration, Wadi-Araba Fault, Jordan.

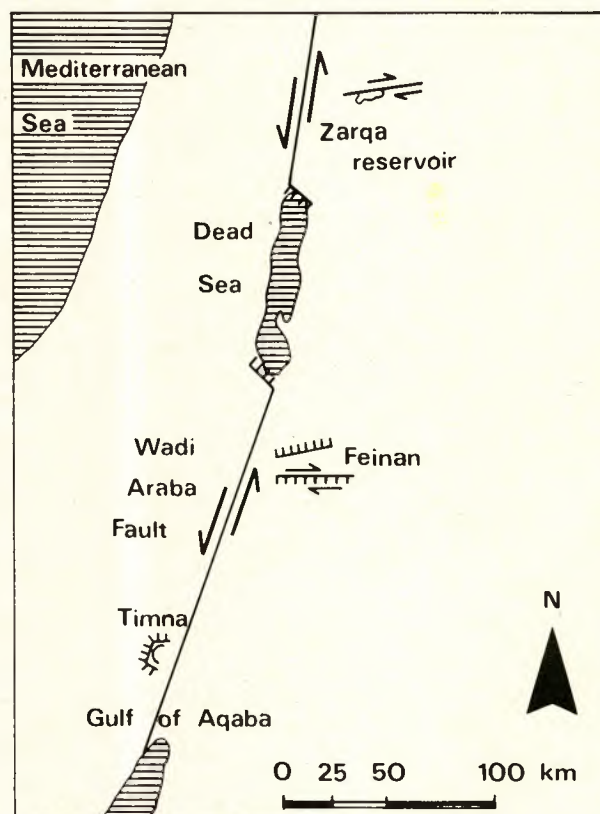
1. Introduction

The purpose of this paper is to evaluate the capabilities and limitations of spaceborne Thematic Mapper data and associated image processing techniques for mineral exploration in the area along the Aqaba-Levant structure in Jordan.

The Wadi Araba region is part of an important plate boundary, where the Arabian plate is in contact with the Sinai-Palestine plate along a sinistral wrench fault system (Fig. 1). Offset along this fault system has been calculated to be in the order of 107 km (Quennell, 1958) during the last 20 Ma b.p. (Garfunkel *et al.* 1981). Recent investigations revealed that the fault was not initiated prior to 14 Ma b.p. (Bayer *et al.*, 1988). One essential element in the assessment of the lateral displacement along this fault is the palinspastic restoration of the dissected copper/manganese deposits of Timna and Feinan.

The Cu/Mn mineralisations occur within Lower to Middle Cambrian alternating layers of shales and siltstones. These sequences of the so-called dolomite-limestone-shale unit are underlain by Lower Cambrian arkoses and overlain by variegated sandstones and shales of Middle Cambrian age. The Precambrian basement underlying the entire area mainly consists of aplitic leucogranites and porphyrites. The Cu/Mn ore deposits can be divided

Figure 1. Sketch map of the Wadi Araba area.



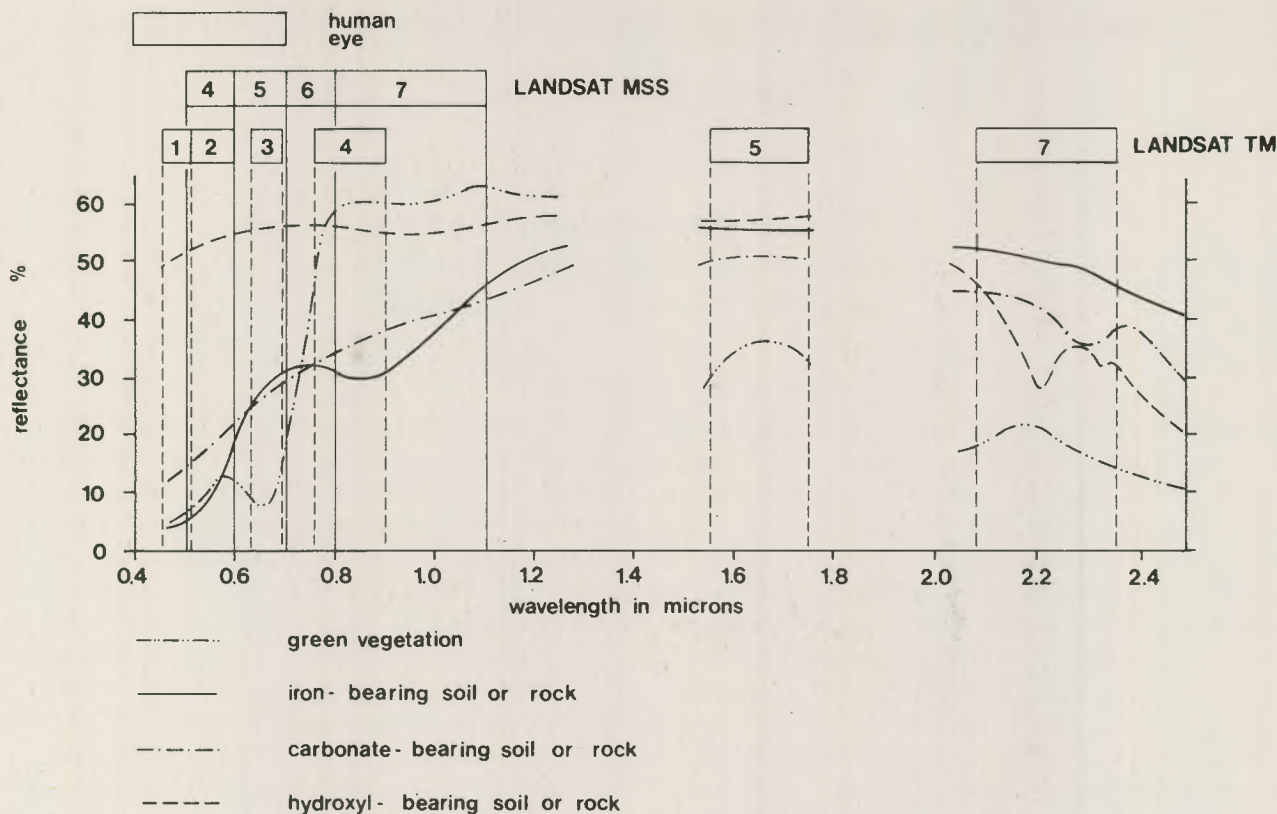


Figure 2. Diagrammatic spectra, illustrating positions of diagnostic iron, clay, carbonate and chlorophyll absorption bands. Also shown are bandpasses of the Landsat MSS and TM sensors.

into two groups. The major part is assumed to be of epigenetic-sedimentary origin containing pyrolusite, psilomelane, malachite and copper silicates. The second group of minor importance is associated with mineralisations in fissures and joints (cuprite, malachite, bornite, covellite, chalcosine). They occur about 100 m above the main sequence and are thought to be of epigenetic to hydrothermal origin.

The potential of TM-data for detecting mineralised zones will be demonstrated by two examples; the Feinan deposit and a previously unknown iron-ore occurrence that was discovered in the framework of this study. This deposit is located near the Zarqa reservoir NNW of Amman. To meet the objectives of remote detection of mineralised zones different processing techniques based on three major concepts have been applied. The concepts aim at the enhancement of increasing presence of alteration guide minerals that may be indicative of mineralised areas.

2. Background

The new shortwave infrared (SWIR) bands of the TM on Landsat 4 and 5 enable one to detect and discriminate minerals which commonly occur in 'hydrothermal' alteration zones. These minerals are mainly iron oxides and phyllosilicates (Fig. 2).

Spectral features, evidenced by bands or changes in slope of spectral curves, appear as a result of either electronic or vibrational processes (Hunt *et al.*, 1971).

The spectral reflectance of minerals in the visible (Vis) and near infrared (NIR) 0.4–1.1 μm is influenced mainly by the wings of charge transfer bands in the ultraviolet, and electronic transitions at longer wavelength, which are caused by transition elements. The most important transition element for terrestrial remote sensing purposes is iron in the bi- and trivalent state. Another range of interest is the short-wave infrared region between 1.1 and 2.5 μm , which provides more diagnostic spectral information about the composition of minerals and rocks than the Vis and NIR range. This region is characterised by high reflectance values of most rock types covered by the 1.6 μm centred band (TM-5) and by strong and relatively sharp absorption features for clays, micas and carbonates covered by the 2.2 μm centred band (TM-7) caused by lattice overtone, bending-stretching vibrations of O-H-bonds resp. C-O-bonds (Goetz & Rowan, 1981).

High-resolution visible and near-infrared laboratory spectra of a large number of minerals published by e.g. Hunt *et al.* (1970, 1971) serve as a guide for detailed examination. However, the relatively broad bands of TM do not allow distinct discrimination among minerals containing bound or unbound water, but enable one to detect almost the whole group of hydroxyl- or water-bearing minerals.

3. Processing Concepts

It is a fact, that all information derived from a seven-band sensor can not conveniently be presented within one single image product. Hence it is generally a problem to select a subset from a multiband image for enhancement by ratioing, PC-analyses or colour compositing. The decisions on which strategy to choose are determined by several different facts, involving the objectives of the particular application, and the choice of bands and algorithms.

In the following sections different approaches will be demonstrated in order to enhance spectral information with special emphasis to accentuate areas characterised by the presence of minerals that are diagnostic of alteration zones resp. ore deposits.

3.1 Ratioing

Figure 3 shows a set of ratios that take the spectral behaviour of iron oxides, hydrous minerals and vegetation into account. Ratio 4/3 displays vegetation in bright tones caused by the high reflectance of mesostructure in the NIR-band in contrast to the steep fall-off of reflectance towards the visible (TM-3) due to an intense chlorophyll absorption.

Carbonates, clay minerals containing bound or unbound water, micas and other OH- resp. H₂O-bearing minerals (e.g. gypsum) are enhanced by the ratio 5/7 (bright

Figure 3. Ratios of Feinan complex: top left TM-4/3, top right TM-5/7; bottom left TM-7/4, bottom right TM-1/7. Area shown is about 15×15 km.



Figure 4a. colour composite of ratios 5/7, 4/3, 7/4, coded blue, green, red resp. Area shown is about 40×30 km.

areas). Most effective signal enhancement related to the ferrous and ferric ion is provided by the ratios 7/4 resp. 7/1 or 5/4 resp. 5/1 due to major electronic transition bands in the NIR at about 0.87 μm resp. the Vis and Ultraviolet and the non-affected SWIR range (bright areas). The common band of the ferrous ion near 1.0 μm is not covered by the TM sensor. The ratio 3/1 used by many authors to enhance ferric iron often fails, as the slope between bands 3/1 is too weak compared with combinations of the SWIR bands with band 1 or 4.

The enhancement of solely spectral variations within two (or more) bands by simultaneously suppressed albedo differences is the major advantage of ratio transformations. However, in our data, non-linearities and non-periodic loss of rows affects band to band registration throughout different bands. Although haze-corrections were applied it was not possible to remove the remaining patterns completely. In addition, the calculation of ratio 5/7 has to be carried out with great care due to overflows in TM-band 5 that occur in desert areas with very high reflectivity at high sun elevations.

The composite in Figure 4a was created by exposing the 5/7 ratio to blue light, the 4/3 ratio to green light and the 7/4 ratio to red light. Absorption features of alteration guide minerals and vegetation are placed in the denominator, and consequently shades of blue should be largely attributable to OH/H₂O- and CO-bearing minerals (rocks and soils), shades of green to vegetated zones and shades of red to minerals (rocks and soils) containing iron ions.

3.2 Principal Component Transformation

The principal component transformation is a widely used method for calculating 'n' new, statistically independent components of 'n' input bands, based on the covariance matrix. It can be applied to any number of bands. Three of the resulting components may be displayed as a colour composite, or the components are used for decorrelation stretching before retransformation (Soha & Schwartz, 1978).



Figure 4b. colour composite of PC-2, PC-4, PC-3, coded blue, green, red resp. Area shown is about 40x30 km.

Figure 4b shows a composite generated of PC-2 depicted in blue, PC-4 depicted in green and PC-3 depicted in red. The calculation is based on all TM-bands, except the thermal band and band 5 (due to overflows in the alluvial fans). Because selection and coding of components for the composite are based on the same considerations as for the ratio-composite, the displayed colours of the diagnostic minerals are relatively similar.

Bright tones indicate OH/H₂O- and CO-bearing minerals in PC-2, vegetated areas in PC-4 and iron oxides in PC-3. PC-1 was not used for compositing as it represents an albedo component containing no spectral information.

The PC-transformation is scene (image contents) dependent, which is a great disadvantage for matching results of separately processed, neighbouring images.

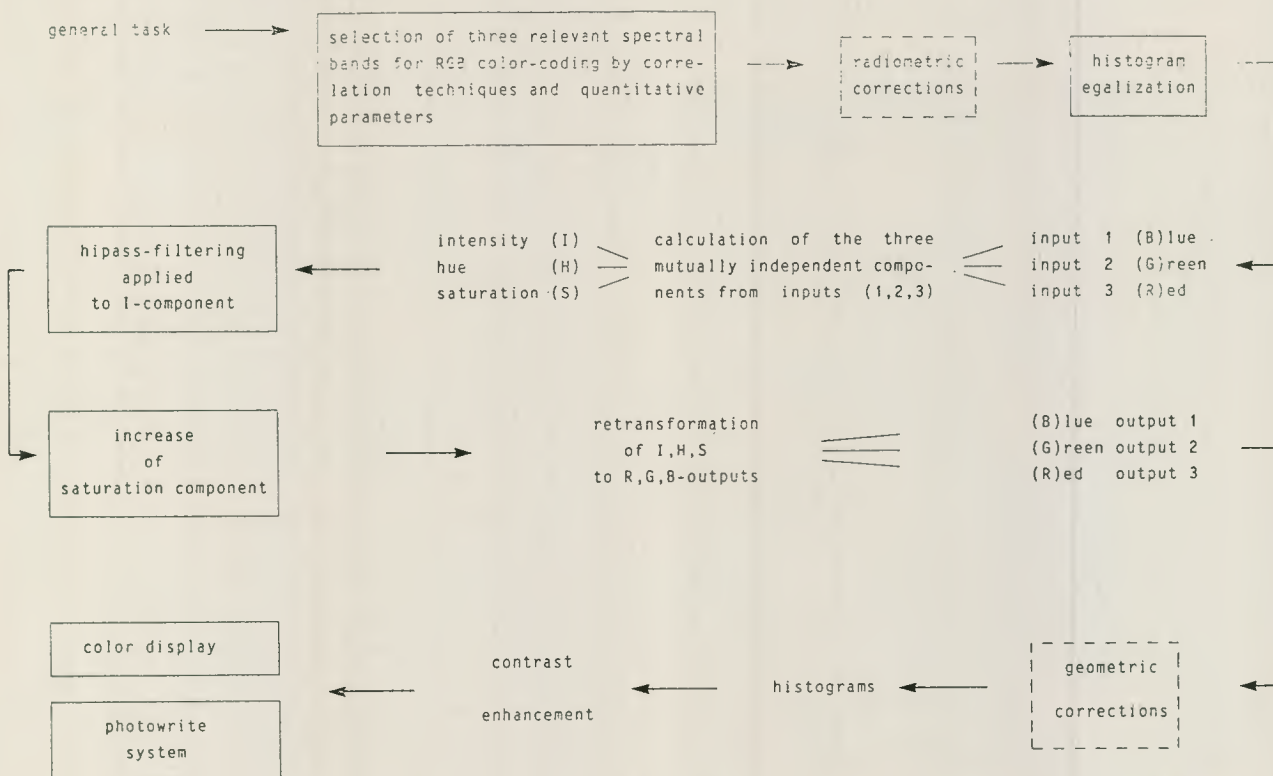
3.3 IHS-Decorrelation Processing

Considering that image products are used to support geoscientists in the planning, execution and completion of field work, both structural and spectral diagnostic enhancement within one image product are required (Kaufmann, 1984; Kaufmann & Schweinfurth, 1986). This is performed by using a reversible transformation to I,H,S-colour coordinates (Haydn *et al.*, 1982; King *et al.*, 1984; Kaufmann & Pfeiffer, 1986; Gillespie *et al.*, 1986).

First of all, based on correlation techniques and known spectral characteristics, three significant bands for additive colour coding are selected. The combination of bands 1, 4, 7 facilitates excellent overall rock discrimination and provides the possibility to enhance the presence of iron oxides (absorptions TM-1, 4), of vegetated areas (absorptions TM-1, 7), and the presence of clay minerals (absorption TM-7), although the latter might be displayed in somewhat varying hues. The presence of iron is indicated by red, vegetation by intense green, and OH/H₂O-bearing minerals exhibit bluish to cyan colours.

Common colour composites generally show a good separability of surface features in brightness (albedo) and

Figure 5. Flow chart of processing concept.



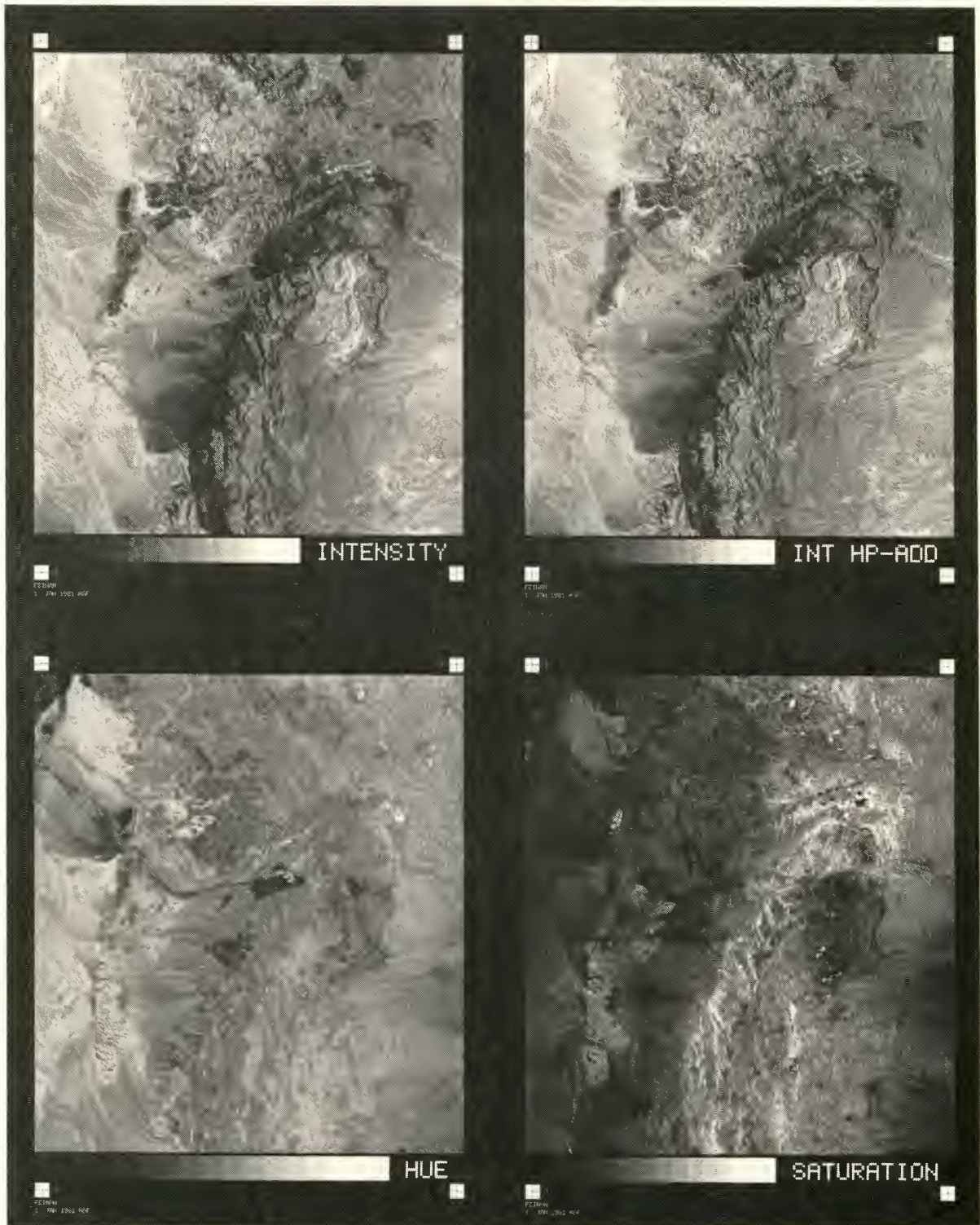


Figure 6. I,H,S components calculated for 1,4,7 (B,G,R) inputs: top left, intensity; top right, intensity + high pass filter 3×3 matrix; bottom left, hue levels; bottom right, saturation levels. Area shown is about 42×46 km.

hues (dominant colour frequencies), however, the interpretability is restricted by low saturation values. This deficiency is caused by relatively well balanced reflectance characteristics, related to the lack of strong absorption bands associated with most rock surfaces, and the broad design of TM-bands. To overcome this problem the enhancement follows a concept which was developed

to satisfy the needs of geologists for one single product with simultaneously optimised spectral and structural image contents (Fig.5).

A precondition is a digital transformation of three selected, equalised, RGB defined bands into three new mutually independent components called Intensity (I),



Figure 7a. Composite TM-1,2,3
(blue, green, red).



Figure 7b. Composite TM-2,3,4
(blue, green, red).

Areas shown in Figures 7a, 7b are about 36×24 km.

Figure 7c. Composite TM-1,4,7 (coded blue, green, red) filtered (3×3 high pass) and IHS-decorrelated. Area shown is about 42×46 km.



Hue (H) and Saturation (S) (Fig. 6). To correct for the low-pass characteristics of the imaging system (Moik, 1980) and in order to enhance subtle variations in structural contrast, highpass-filtering was applied to the I-component using a 3×3 matrix. As the brightness (I) is separated from H and S there is no loss in spectral information, which would occur if filtering were applied to RGB-components. The decorrelation is handled by linear transformation (histogram shift) of the S-component to the high saturation part within the given 8-bit range (Bodechtel & Kaufmann, 1985). Subsequently the modified I and S-components and the original hues are retransformed into RGB-coordinates. In a last step geometric corrections and histogram stretch for display on screen or transmission via photowrite system are applied.

The resulting image (Fig. 7c) displays the same intensities and hues as the unprocessed composite, but is characterised by highly saturated colours and edge-enhanced structural elements. Thus uncertainties in interpretation are now minimised as saturation increase results in actually distinguishable hues. The colour, resp. the spectral information, and the structural patterns exhibited on those calculated products are much more perceptible or recognisable, which is a precondition not only for lithologic and tectonic investigations but even more for any geoscientific application and for economic field work.

4. Case Studies

4.1 Feinan/Khirbet el Nahas Area

The Feinan district in Jordan is located 45 km SSE of the Dead Sea, next to the graben zone that forms the Araba rift valley between the Dead Sea and the Gulf of Aqaba. The centre of Figure 7c shows a Precambrian porphyrite complex that also includes basalts, andesites and propylites in dark blue colours. These porphyrites intruded into aplitic leucogranites, which appear in bluish to brownish colours. These magmatic rocks are bordered by the Wadi Dana normal fault to the north and the Feinan fault to the south which is a dip slip fault with dextral component (compare Fig. 7c and 10). The horst is surrounded by sequences of dolomite-silt-conglomerate-sandstone layers of Cambrian age and Mesozoic to Quaternary sediments.

At the W-segment of the image the N-S trending trace of the Wadi-Araba transform fault is evidenced by pressure ridges, offset wadis and dissected alluvial fans. Additionally fault-line springs are indicated by strong green colours of dense vegetation. East of the fault line there is a triangular shaped horst block (Hamra al Fidan) of aplite granite surrounded by unconsolidated Quaternary sediments of the rift valley. Curvilinear structural elements, mainly dip-slip faults that affiliate this block

with the Feinan horst, and the chemical association and age determination of the occurring intrusiva and the porphyrites are clues that both complexes are outcrops of one larger magmatic stock partly covered by Cambrian sediments.

All volcanic cones east of the Feinan district show the effects of iron oxidation by strong red colours on the composite. This is related to (hydrated) iron oxides that are converted from iron-bearing minerals in lavas and tuffs through weathering or fumarolic steam exhalations. In the field, the iron-bearing areas can be partly distinguished by dark reddish colours, but in TM-composites using NIR and SWIR bands they give an unequivocal signal. A fine, branching-out, similar intensive red signal can be recognised in the Wadi Dana/Khirbet el Nahas (NE) area. Comparative investigations of field data with existing thematic maps and laboratory analysis proved the silt-, sandstone layers of the so-called dolomite-limestone-shale unit (Bender, 1974) and the bedded arkose unit to be responsible for the red signal. In the field, these layers do not show a comparable spectral contrast to their surroundings to that displayed on the processed TM data (see Fig. 7a; real colour composite and Fig. 7b; infrared false colour composite), but can be mapped and characterised via field geological criteria.

Figure 8 shows the stratigraphy and the mineralised sequence. XRF-analyses yielded a slight increase in iron oxide for the arkose, siltstone, sandstone sequences (1.8, 1.2, 0.7% Fe_2O_3 respectively) in contrast to the surrounding sedimentary and magmatic rocks (see also Fig. 9). The signal follows the whole mineralised zone and is also displayed by sections of the Feinan granite and the N-S elongated intrusion on the western border of the complex (Hamra al Fidan).

Within this complex the red coloured section is sharply bordered by N-S and WSW-ENE striking faults, which are partly accompanied by intermediate to basic dykes. It is proposed that these faults acted as barriers to circulating solutions since the western light-blue-coloured section of the granite shows no evidence of alteration.

A vertical zoning is indicated by cyan colours that are exhibited by distinct parts of some layers in the hanging wall of the mineralised strata. This signal, a well balanced mixture of reflectance in the blue and green-coded bands in combination with O-H absorptions in the red-coded band is caused by varying amounts of kaolinite (illite) and traces of dickite. It is displayed by some sections of the leached part (footwall) of the variegated sandstone unit (Lower to Middle Cambrian) and the lower parts of the massive brownish sandstone unit (Middle to Upper Cambrian), both located in the hanging wall of the mineralised zone. Table 1 gives the modal analyses of clays and iron oxides of these formations (Amireh, 1987).

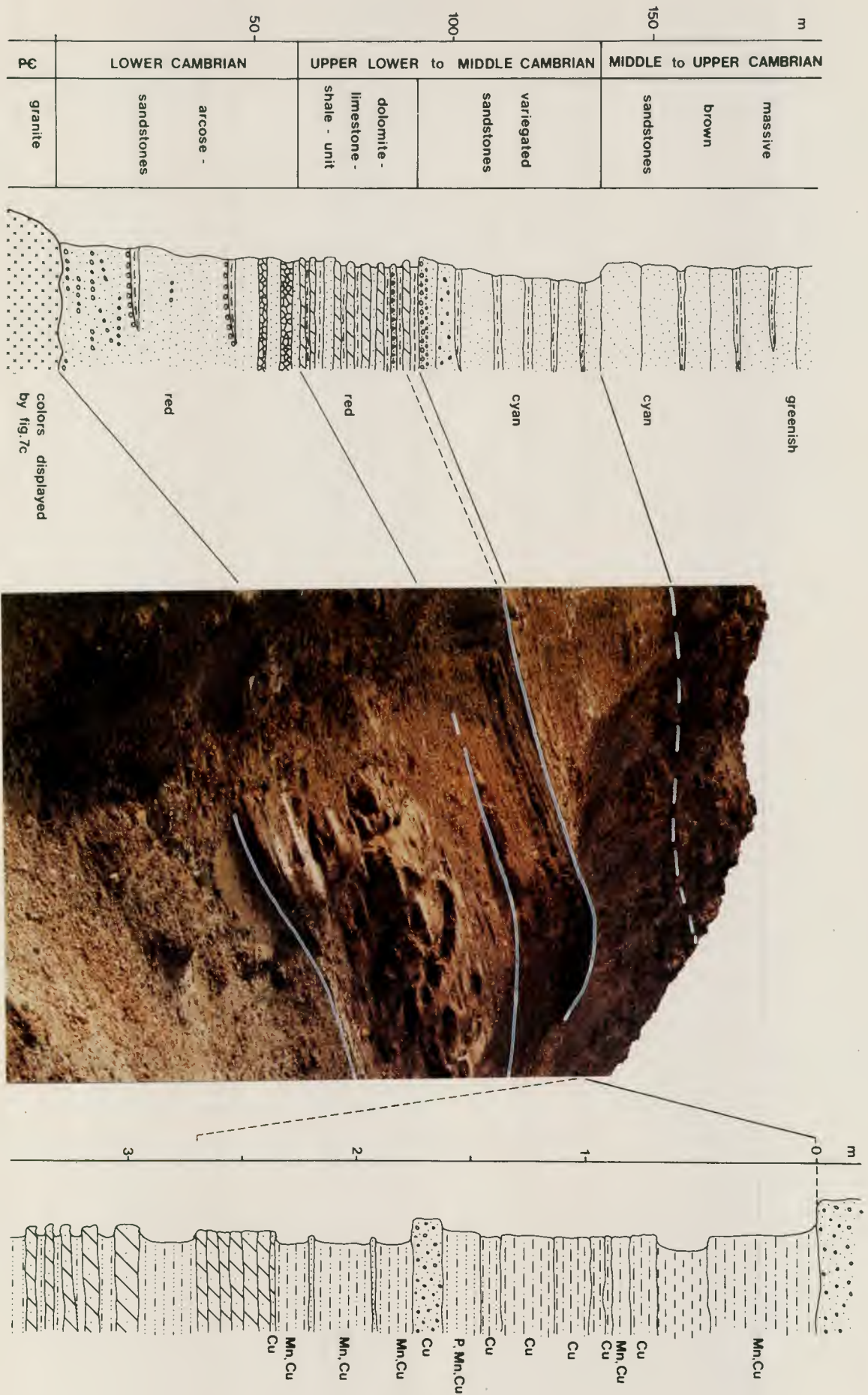


Figure 8. Stratigraphy of Wadi Dana area (Heitkampfer & Hauptmann, 1988).

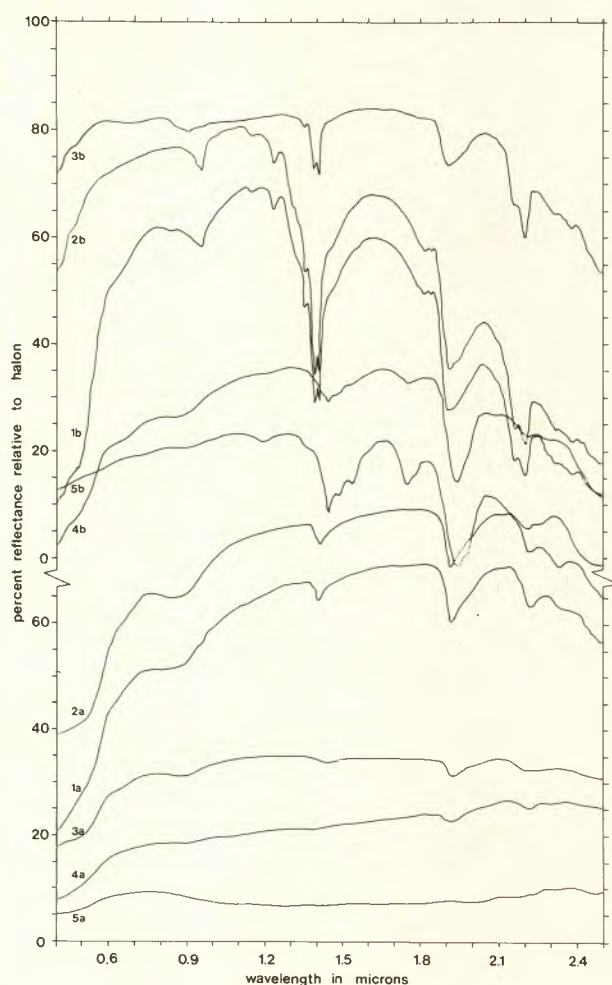


Figure 9. Laboratory spectra of mineralised zone (Feinan).
 1a sandstone weathered 4a dolomite, weathered
 2a sandstone cut surface 5a dolomite, cut surface
 3a arkose-conglomerate

Laboratory spectra of cut and weathered samples
 1b kaolinite, weathered 4b gypsum, weathered (bact.)
 2b kaolinite, cut surface 5b gypsum, cut surface
 3b kaolinite, fractionated
 Spectra are displaced vertically.

Table 1. Modal analyses of clays and iron oxides of Nubian Formations (Vol %). M = average; R = range.

		iron oxides		clay minerals	
Massive brownish weathered sandstone	M	4.4	M	10.1	kaolinite (dickite)
	R	0-24	R	1-22	
Variegated sandstone (fine-white)	M	0.9	M	5.4	kaolinite ill., dick
	R	0-4	R	2-10	
Dolomite-limestone shale unit	M	1.9	M	2.6	illite
	R	0-5	R	0-7	
Conglomerates bedded arkoses	M	8.5	M	9.9	illite kaolinite
	R	0-25	R	0-21	

The main problems in correlating rock analyses and satellite recorded spectral signals result from the selectively diminishing influence of atmospheric gases, from the observed natural surface characteristics in contrast to analyses of cut rock samples and especially from the difficulty of gathering representative samples from highly inhomogeneous strata (see range data of analyses). The latter is not only a severe problem for correlation with a 30 m signal, but a geologic problem as well.

Concerning the modal analysis it can be stated that relative high percentages of clays are present in all stratigraphic units. However, they are only imaged when the ratio of clays and iron oxides is high and kaolinite is dominant. Ongoing investigations on various samples of Jordan, Saudi Arabia and Yemen Arab Republic test sites show that most spectral differences of exposed to cut surfaces are introduced by limonite stain, whereby the influence of Fe^{3+} on the blue range is mostly stronger than that on the NIR. This might be the reason for the hue-shift from blue to cyan for clays and gypsum observed for open pits (cut surface) and exposed surfaces that are weathered and partly inhabited by bacteria, fungi, lichens, etc. (Fig. 9).

The nature and mode of the stratabound Cu/Mn occurrence in this district have been the subject of continued discussions as to whether the mineralisation is of syngenetic, epigenetic or hydrothermal origin. Basta and Sunna (1970) suggested that tuffs and agglomerates provide the pathways for ascending hydrothermal solutions resulting in the alteration of the andesites (horst complex) and their transformation into propylites. This process is possibly associated with the mineralisation occurring in this area. Bender (1974) assumes, that the main Cu/Mn mineralisation took place during the deposition of the host rock (Cambrian sandstone) transported by weathering solutions, and the mineralisation along fissures and joints, e.g. in the dolomite, point to secondary origin by downward migrating weathering solutions.

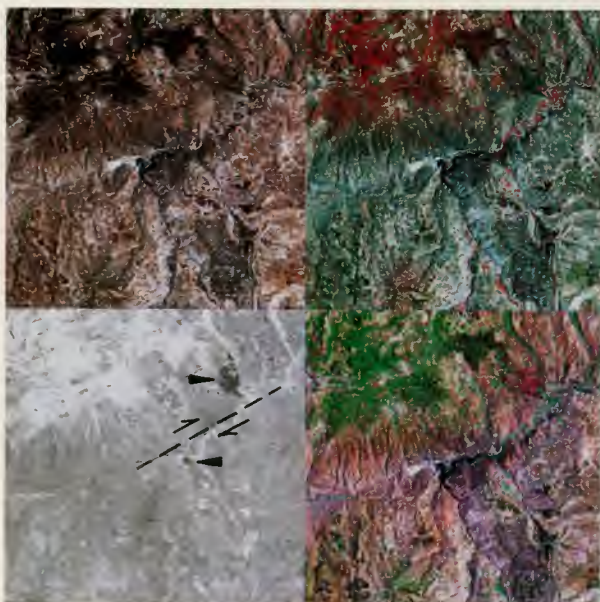
Epigenetic mineralisation is assumed by Khoury (1986). Descending copper and manganese solutions should be controlled by 'shales' and by the alkalinity of the uppermost part of the dolomite-limestone unit. The downward sequence of mineralisation shows iron, manganese and copper rich zones, which may be explained by Eh-pH variations.

The TM signal of the mineralised area can only be interpreted in terms of slightly increasing content of Fe^{2+} and Fe^{3+} ions, in this case Fe-oxides (hematite, goethite) which often occur without 'hydrothermal' alteration. The increase in iron is discernible on the imagery in the mineralised area, in the granites and partly affects the porphyrites (Fig. 7c, 10). Cyan colours displayed by some horizons of the surrounding district are caused mainly by kaolinite, and subordinately by (il-



Figure 10. Map of alteration zones.

Figure 11. Zarqa-reservoir: top left, composite TM-1,2,3 (B,G,R); top right, composite TM-2,3,4 (B,G,R); bottom left, ratio TM-4/7; bottom right, composite TM-1,4,7 (B,G,R) filtered and decorrelated.



lite), dickite and mixed-layer clays. The neo-formation of these clays as well as the observable zoning are not unequivocal clues to 'hydrothermal' alteration. Thin sections of the corresponding layers indicate pressure-solution (diagenesis) and weathering effects. Few sections of different horizons appear to be reformed within the meaning of argillic type of alteration expressed by kaolinisation of feldspars accompanied by sericite and quartz.

The origin of the copper manganese deposits in the Feinan district may be interpreted to be of primary epigenetic character. In addition with the diagnostic signal, observed small-scale mineralisations (bearing baryte and sulphides) occurring along faults, joints and veins, may lead to the conclusion that final enrichment was caused by hydrothermal activities that took place along the major faults during the last epigenetic stage.

4.2 Zarqa-Reservoir

Based on these results, a spectral anomaly north of Amman/Jordan was investigated in the area of the Zarqa-reservoir. The area is about 2.5 km² in extent and it displays a dark reddish colour in the 1,4,7 TM-composite (Fig. 11: bottom right/dark tones bottom left).

Figure 11 top shows the area in band combinations 1, 2, 3 (real colour) and 2, 3, 4 (false colour) and demonstrates

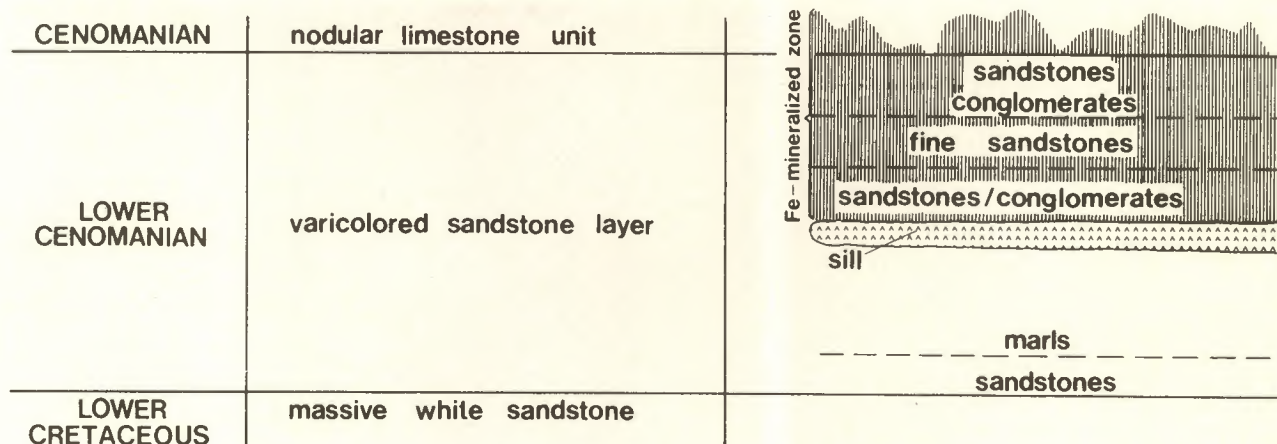


Figure 12. Generalised profile of Fe-deposit at Zarqa reservoir.

that the anomaly is not perceptible using the visible and NIR range for processing. The anomalous region represents a sandstone-conglomerate-limestone layer up to 4 m thick that is cemented by iron oxide minerals (Fig. 12). XRF analyses and polished sections show 30–60% of iron-bearing components (hematite, goethite and siderite). A basic to intermediate sill found in the lower stratum may be the source of temperature which led to the mineralisation.

A second, smaller mineralised area is discernible on the image at the SE-border of the reservoir. It shows similar types of ores in the same strata but no igneous rocks are associated with this mineralisation. This can be seen as additional evidence for an ENE striking dextral transform fault related to rift tectonics (Fig. 11: bottom left). The anomaly shows a clear zoning which is not recognisable on the image due to its small extension. Soils of the outer rim lack iron. The middle zone contains iron and clays (mixed layers). Soils derived from the mineralised area contain only iron oxides, quartz and calcite.

4.3 El Graara area, Morocco

The El Graara area is located in the Anti-Atlas mountains in southern Morocco (Fig. 1b, 13). The ultrabasic rocks of Bou-Azzer belong to an ophiolitic complex (middle or upper Proterozoic), which is 4 to 5 km thick and which includes abundant acid rocks (quartz-diorites and keratophyres). In a vertical sequence it is composed of residual peridotites, ultrabasic cumulates, basic cumulates (layered gabbros), submarine effusive basic lavas (pillow lavas) and associated spilites, keratophyres and quartz-keratophyres, as well as some sediments (graywackes, tuffs, siltstones, limestones and jaspilites). The presence of basic dyke swarms cutting the layered gabbros is further evidence for considering this complex (earlier than 600 Ma b.p.) as a fragment of spreading Precambrian oceanic crust. The ophiolites display a complex magmatic history and have been generated in a shallow, mobile and hydrated environment (Choubert, 1963). Late quartz-diorites intruded syntectonically (major Pan-African phase).

All the ultrabasic rocks are serpentinised. The residual mantle peridotites and ultrabasic cumulates are difficult to distinguish. Serpentinisation occurred in several stages; the development of structures and minerals, particularly the magnetites, allow one to follow some geochemical migration (Co, Fe, Ni, B, As). The abundance of quartz-diorites raises the problem of a calc-alkaline trend in the last stage of the evolution of the ophiolitic complex. The abundant albitophyres are locally of primary origin (spilitic lavas interstratified with tholeiites and keratophyres), but one also notes the presence of post-magmatic secondary albitisation. A last Pan-African phase of folding produced upright folds, accompanied by slaty cleavage, parallel to the border of the craton, and transcurrent faulting (Choubert, 1963).

The area shown in Figure 13 is characterised by a rugged topography and extremely folded geological formations. The various Precambrian magmatic rocks are surrounded by Cambro-Ordovician sequences of sedimentary and metamorphic rocks, all interspersed with quaternary deposits and cut by numerous dykes and faults. Figure 14 shows a sketch-map of the El Graara area including the Bon-Avev mining district. Areas containing anomalous higher amounts of Fe- resp. OH-bearing minerals (in this case mostly serpentinite) and different locations characterised by economical mineralisations are correlated.

5. Discussion and Conclusions

The ratio and PC approach often fail to discriminate clearly among the diagnostic surface features because of the overall similarities in the shape and relative intensities of vegetation, minerals, rock types and soils derived from (Fig. 4a,b). The major disadvantages of both the ratio- and PC-approaches for exploration purposes are the loss of albedo and topographic expression (for this particular application) and a decrease in the signal-to-noise ratio. This diminishes the interpretability of data, even though this problem can be solved by interchanging

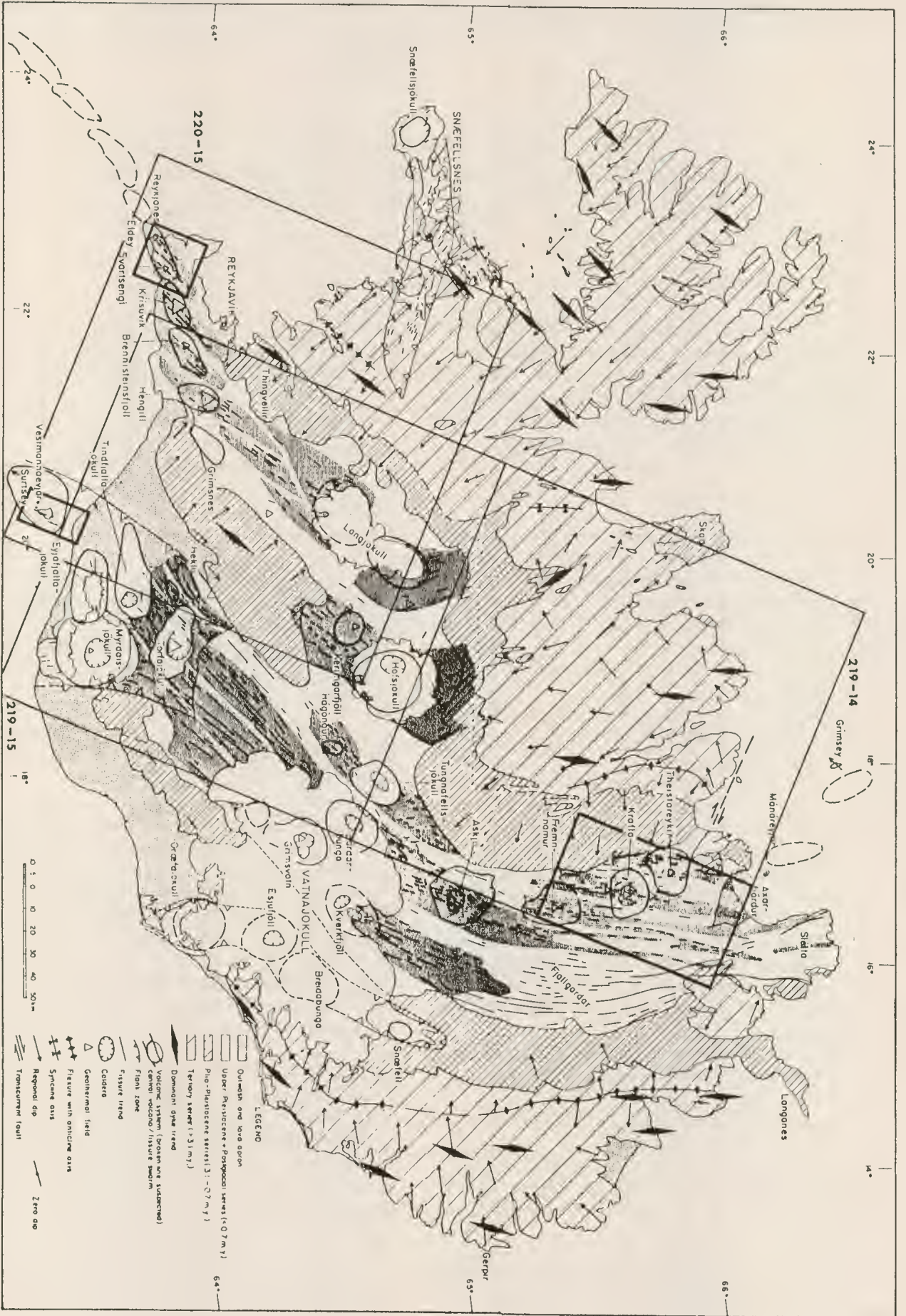


Figure 1. Simplified geological and tectonic map of Iceland. From Saemundsson, 1979. Coverage of TM-scenes 219-14, 219-15, 220-15 and the three test areas Reykjanes, Heimaey (Vestmannaeyjar) and Krafla.

Some 24 volcanic systems have been active in Postglacial time. Their total lava production has been estimated as 400–500 km³ and the lavas cover about 12 000 km², i.e. over 10% of the surface of the island. On average, a volcanic eruption occurs every five years in Iceland.

The soil cover in Iceland is discontinuous and delicate. The interior is more or less barren. Especially in the areas of young volcanism, desert-like conditions prevail as the water soaks into the porous ground. It is not necessary to discuss the geology of Iceland in detail here. For a more comprehensive description the reader is referred to Saemundsson (1979) and Jakobsson (1979). Figure 1 gives an overview of the geology and tectonics of Iceland.

3. Results of the Investigations

The improved capabilities of the Landsat-TM data for the differentiation of geological features are demonstrated in Figure 2, which is a natural colour composite of the Reykjanes peninsula, SW-Iceland. Most of the significant geological elements of the area (like the youngest

lava fields (I), older postglacial lava fields (II), hyaloclastite ridges (III) and table mountains (IV), river (V) and shore sediments (VI) and sediment-laden water (VII)) can easily be distinguished.

Additionally the data, which have been enlarged photographically for interpretation, allow the differentiation of most of the important structures of this area like the strike direction of fissures and faults, previous coastlines and the location of volcanoes and craters. On this basis and in comparison with older Landsat-MSS data and aerial photographs, it can be concluded that Landsat-TM data with their ground resolution of 30 m are advantageous for supporting geological mapping up to scales of 1 : 50 000. Additional aspects of the applicability of Landsat-TM data to geological research in Iceland should, however, be investigated. One of the most interesting applications is regional and local thermal mapping.

The investigations focused on the following test sites:

- Reykjanes Peninsula/SW-Iceland
- Heimaey Island south of Iceland
- Krafla/N-Iceland.

Figure 2. Landsat-TM natural colour composite (bands 1, 2, 3 = blue, green, red) of Reykjanes Peninsula, SW-Iceland.



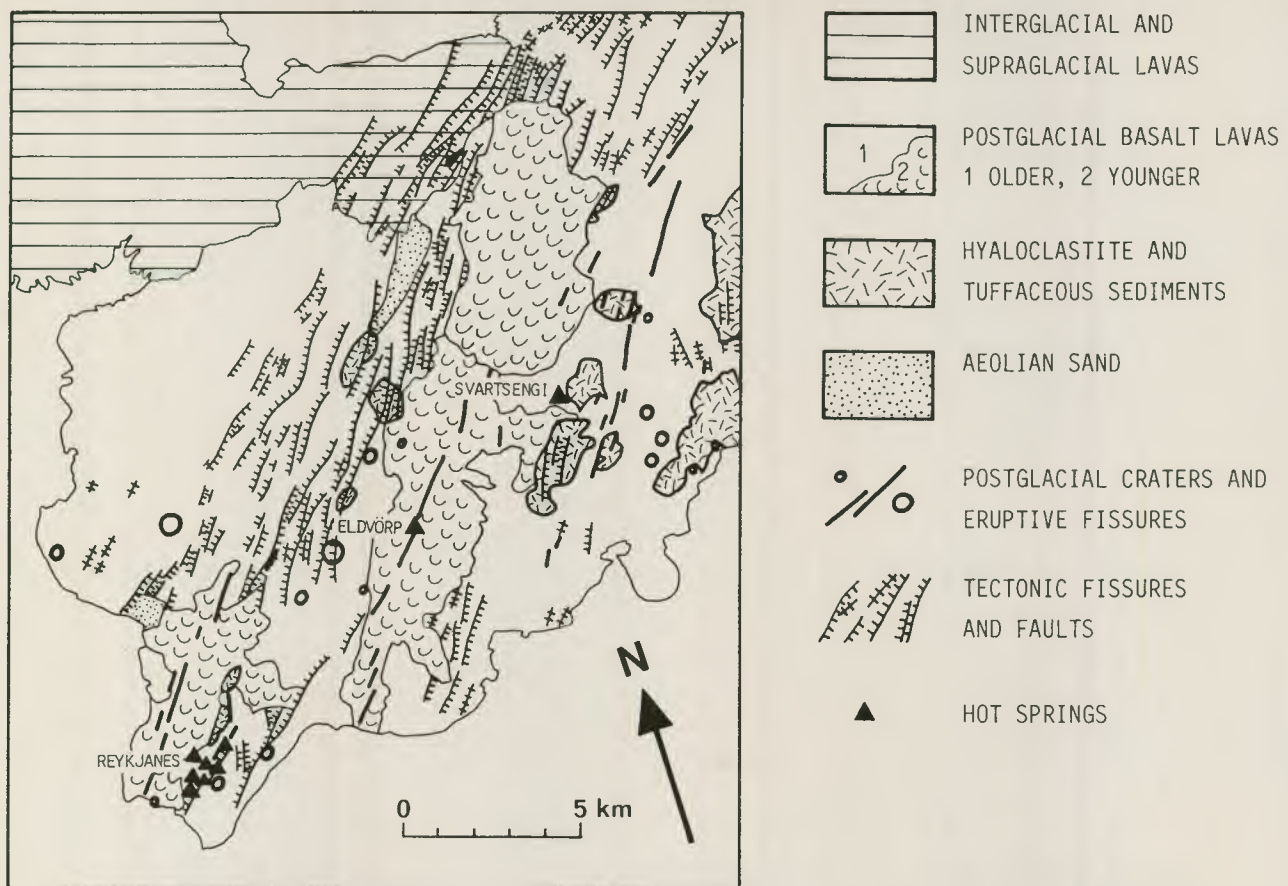


Figure 3. Geological map of Reykjanes test area. After Johnson, 1978.

3.1. Reykjanes Peninsula/SW-Iceland

The first test site is the westernmost part of the Reykjanes Peninsula, where the Neo-Volcanic Zone connects with the submarine Mid-Atlantic Ridge. Its geology is well-known through the investigations of Jonsson (1978). The area is very flat (mean topographic height 30–50 m) and almost completely covered with postglacial lava flows. Occasional hyaloclastite ridges rise above it to a height of 100–200 m. All lithological units except the most recent lava flows (the youngest is dated to 1660 AD) are intensively cut by faults and fissures. Figure 3 is a simplified geological map of the test area.

The Reykjanes Peninsula is an area of high seismicity. The epicentres of the just 1–5 km deep earthquakes are concentrated to a narrow zone (2–3 km), striking in an E-W direction (Einarsson and Björnsson, 1979). This active seismic zone represents the Mid-Atlantic plate boundary. Postglacial eruption sites and fault zones are grouped into swarms, which are arranged en echelon to the plate boundary.

The test area covers the westernmost fissure swarm or volcanic system on Reykjanes Peninsula. Three high-temperature geothermal fields (Reykjanes, Eldvörp, Svartsengi) are located within this fissure swarm where it crosses the plate boundary. Positive magnetic anomalies at each geothermal area may indicate centres

of intrusive activity, which might be the heat sources of the convective geothermal system.

A resistivity survey covering this area revealed a continuous elongated zone of low electrical resistivity containing all three geothermal areas. Relationships between bulk resistivity, temperature, fluid resistivity and porosity, along with data from drill holes, were used to convert the resistivity data to establish a map of the temperature distribution at 600 m depth b.s.l. It shows a 2–6 km wide zone with temperatures exceeding 100°C, stretching from the tip of the Peninsula at least 20–25 km eastwards (Fig. 4). The known geothermal fields are distinguished within the zone as areas where the temperatures exceed 200°C. Outside the anomaly the temperature is 40–50°C, corresponding to a thermal gradient of 70–80°C/km. It is remarkable that north of the Reykjanes geothermal field there appears to be a hot area with temperatures exceeding 150°C at 600 m depth. No geothermal alteration is found at the surface in this region (Georgsson, 1984).

The daytime thermal emission from the test area as registered by Landsat-TM band 6 does not show any obvious correlations with these results (Fig. 5). On the contrary, the radiometric temperatures are closely related to the vegetation distribution and topographic effects. The most conspicuous feature is the relatively high emission

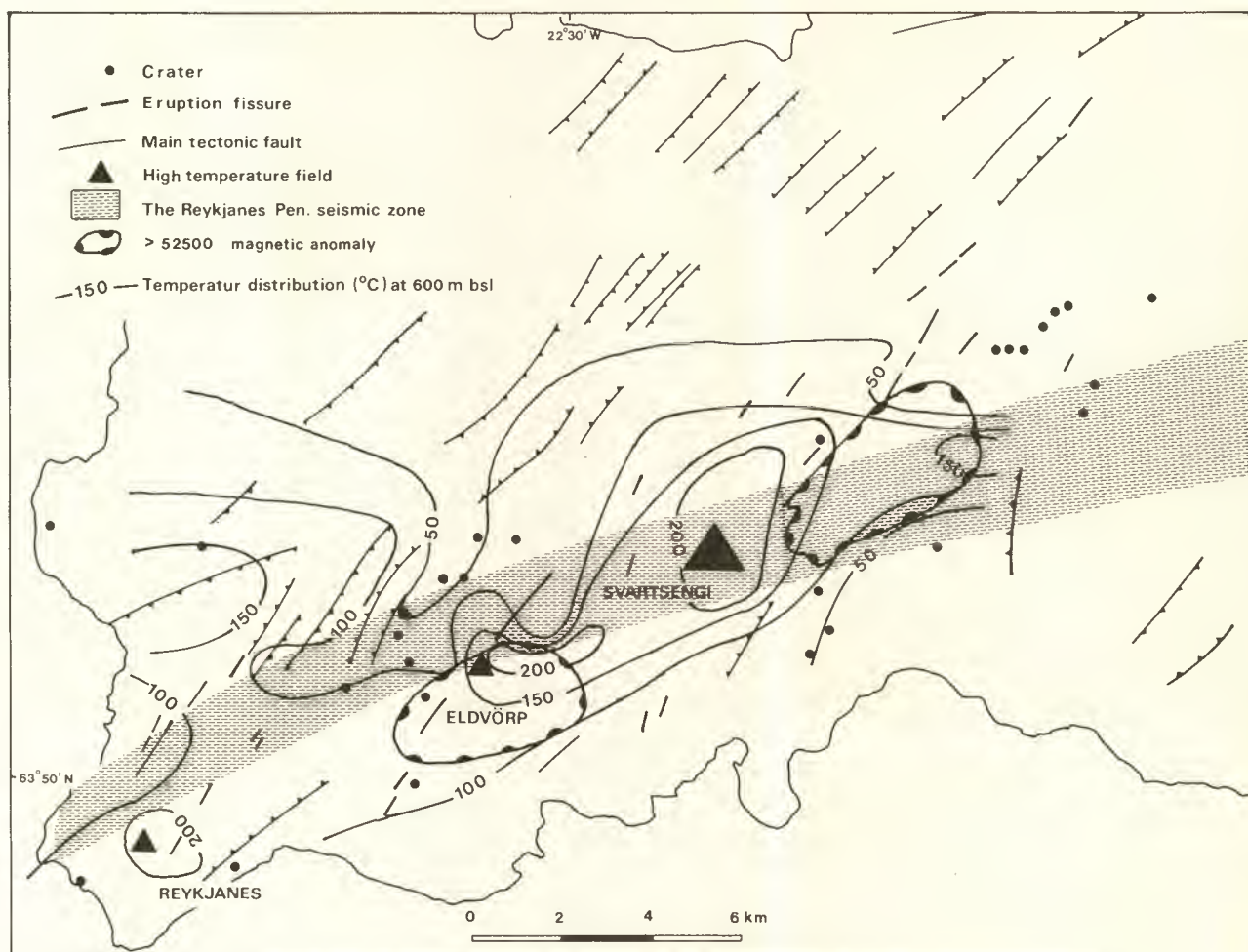
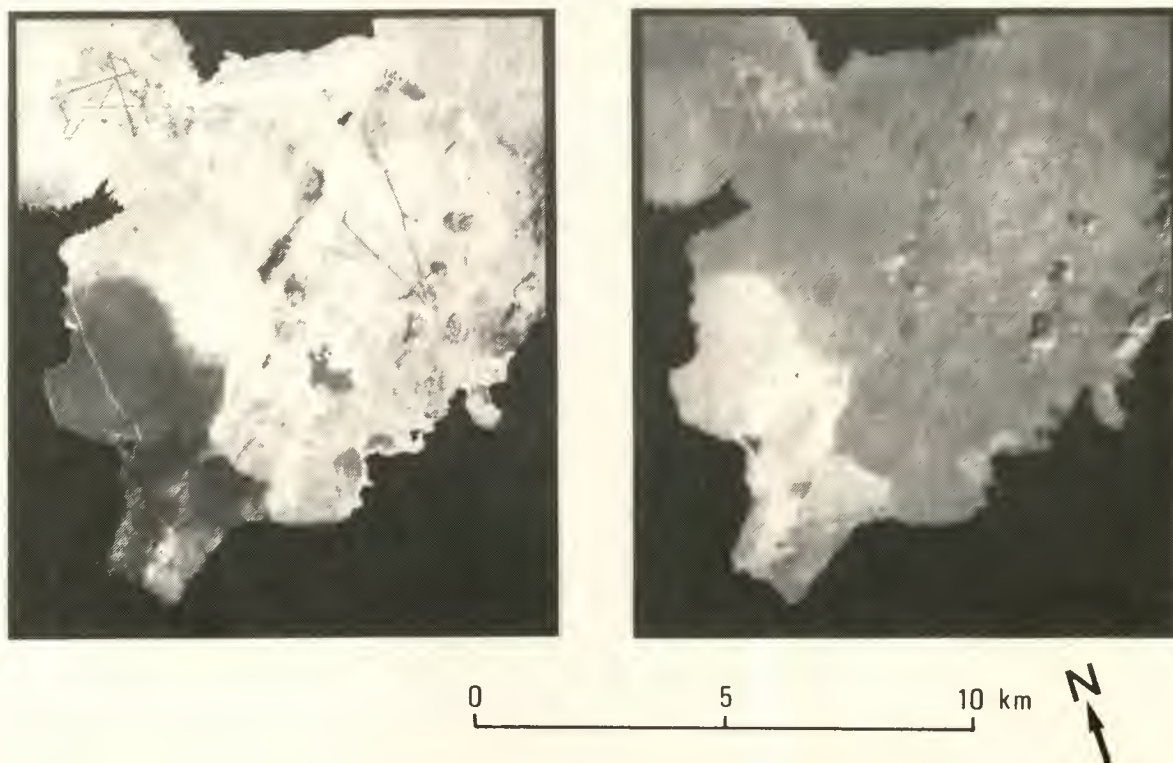


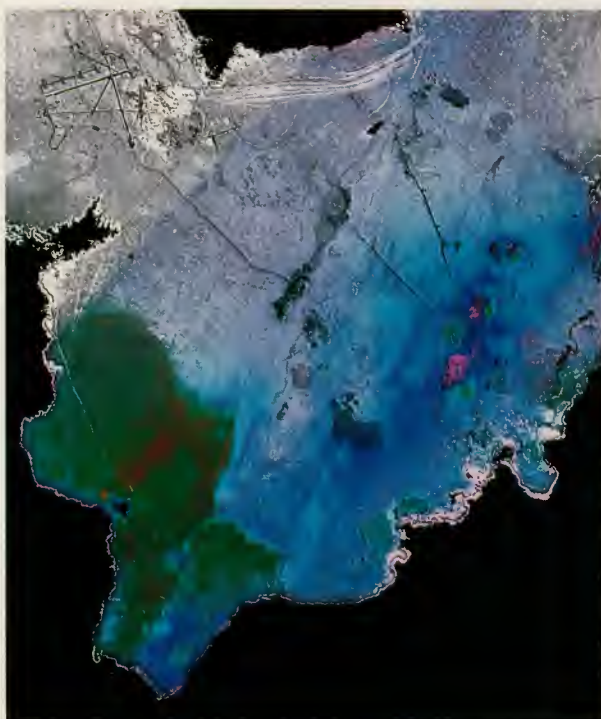
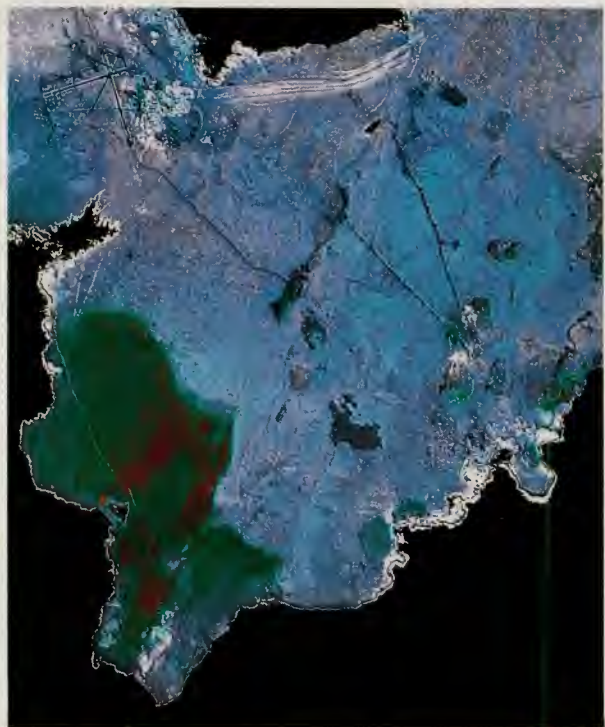
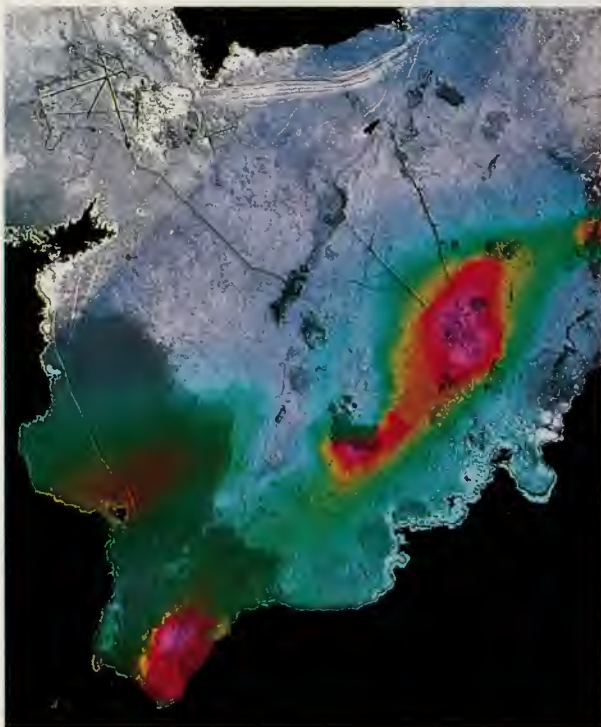
Figure 4. Main geophysical and geologic structures of the outer Reykjanes Peninsula. From Georgsson, 1984.

from the western part of the area in comparison with the eastern part, which is solely due to the absence of vegetation on the former. This becomes obvious when channels

6 and 7 in Figure 5 are compared, the dark barren basalts in channel 7 coincide with the area of high emission in channel 6. Moreover, sunlit south-facing slopes of the

Figure 5. Reykjanes test area. Landsat-TM bands 7 and 6.





Figures 6, 7 & 8. IHS colour composites.

hyaloclastite ridges appear hot, whilst the shaded ones are cool.

The thermal areas of Eldvörp and Svartsengi are not evident on the thermal image; Svartsengi shows up as a tiny hot spot only a few pixels in size and Eldvörp is not distinguishable at all. This may be explained by the complete coverage of these areas with young lava fields, which are entirely without fissures and thus prevent connecting heat transfer to the surface. The areal extent of

hydrothermal alteration is very limited in both areas; in Eldvörp the thermal output is confined to a single volcanic crater and cannot be expected to be detected in this image. Manmade features in the Svartsengi producing field have increased the thermal emission from that area.

In the western part of the test area, quite different conditions prevail. Here the lava series are older and extensively cut by fissures and faults, which may allow heat convection up to the surface. Accordingly, the Reykjanes thermal area is characterised by intensive thermal alteration. Due to the absence of vegetation, the general emission is high in this daytime image, but it is not evenly distributed over the whole area. The most prominent thermal features are two elongated parallel anomalies striking SW-NE. At the SW-end of the southern zone, a patch of increased thermal emission coincides with the northern part of the Reykjanes thermal field. The southern part of the thermal area is not visible on the image, because of different surface conditions here (lower emissivity due to soil and vegetation, see band 7 in Fig. 5). The two SW-NE striking anomalies lie within the area where resistivity soundings indicate temperatures of almost 200°C at 600 m depth and they coincide exactly with two zones of fissure and faults. This correlation makes that area interesting for further thermal investigations.

Figures 6, 7 and 8 are image processing products where the so-called I-H-S transformation has been used (Haydn *et al.*, 1982). The following data combinations are presented:

Figure 6

Intensity: TM band 4 (contrast enhanced);
 Hue: calculated temperature distribution at a depth of 600 m, highest temperatures have magenta and red;
 Saturation: as hue, the highest temperatures have saturated colours, the lowest are unsaturated.

Figure 7

Intensity: TM band 4 (contrast enhanced);
 Hue: radiant temperature of TM band 6 (contrast enhanced), magenta and red highest;
 Saturation: as hue, highest radiometric temperatures have saturated magenta and red, the lowest are unsaturated.

Figure 8

Intensity: TM band 4 (contrast enhanced);
 Hue: radiant temperature of TM band 6 (contrast enhanced), coldest is magenta, hottest is red;
 Saturation: calculated temperature distribution at a depth of 600 m, hottest temperatures saturated, coldest unsaturated.

Accordingly, Figure 8 expresses the correlation of the remotely sensed and geophysical information. The appearance of red, saturated colours indicates high temperatures as well in the underground as well as on the surface. This is the case for the Reykjanes thermal field and the two zones of fissures and faults. The Svartsengi thermal field can be seen as an isolated yellow spot, while Eldvörp cannot be differentiated. Saturated blue appears on the youngest lava flows where the geophysical survey (saturation) reveals high temperatures at depth, but no increased emission is registered by the thematic mapper (hue). The lowest radiometric temperatures, appearing on the the north-facing shaded slopes of the hyaloclastite ridges, are magenta coloured in this image product.

3.2. Heimaey Island

In 1973 a volcanic eruption on the island of Heimaey 10 km off the south coast of Iceland generated a 3.2 km² alkali-andesitic lava, which destroyed a part of the local village. To minimise the damage, over 6 million tons of sea water was pumped on the molten lava to stop the advance of the main flow to the north-west, towards the village. These activities are believed to have saved the main part of the town and its essential fishing harbour. The village is now served by a central heating system which is operated by pumping water through the porous cracked lava to heat it. In 1981 a 40 m thick zone of still molten magma was estimated for the thickest part (some 120-130 m) of the lava (Sigurgeirsson, 1982)

Thermal infrared data for Heimaey are available on quite different scales:

- HCMM data acquired on 23 July 1979 with a pixel size of 600×600 m;
- Landsat-TM data acquired on 22 May 1985 with a pixel size of 120×120 m;
- airborne scanner nighttime image, acquired in April 1985 with a pixel size of 2×2 m.

A comparative evaluation of the interpretations of these data can be summarised as: the sensitivity of the Landsat-TM thermal infrared sensor is sufficient for the differentiation of thermal anomalies – the ground resolution, however, cannot fulfil the requirements for a sensor applied in geothermal research. As massive rock is a very bad thermal conductor, the heat reaches the surface mainly through cracks and fissures by convection. Geothermal areas usually extend over tens of square kilometres, but the spatial extent of the hot sites themselves inside these areas is limited and mostly bound to certain tectonic structures.

The sensor therefore registers an averaged signal of a hot target and its colder surroundings which, depending on the size and temperature of the hot target, might not be unambiguously recognised in a single data set. Low spatial resolution consequently results in a limited radiometric resolution or dynamics of the data.

In Figure 9 TM bands 6 and 4 are compared. It is obvious that a ground resolution of 120 m prevents mapping of relevant features like the detailed areal distribution and strike of faults and fissures. In addition, it has to be considered that the daytime acquisition of Landsat-TM thermal data is very unsatisfactory, as solar heating may completely mask all but the hottest and biggest geothermal phenomena. Unfortunately, no nighttime Landsat-TM data from Iceland exist.

Figure 10 presents again the digital combination of Landsat-TM data via the I-H-S transform:

Intensity: TM band 4 (contrast enhanced),
 Hue: TM band 6, hottest is red, blue is coldest,
 Saturation: as hue, only the hottest areas have saturated colours, the coldest are unsaturated.

The effect of direct solar heating is obvious, for example on the sunlit slopes of the volcano. Also the aeolian sand at the S-coast of Iceland at the top of the image appears warm. These dark (basaltic), dry and loose sediments are considerably heated during sunny days. It is still remarkable that these sediments, which have a very low thermal inertia, are definitely cooler than the hottest part of the lava having much higher thermal inertia. The additional thermal emission from the still hot lava mass is responsible for this difference. The lava surface, which is still without any soil or vegetation and has a uniform emissivity, nevertheless shows distinct temperature differentiation. Its thickest part is hottest; to the northwest

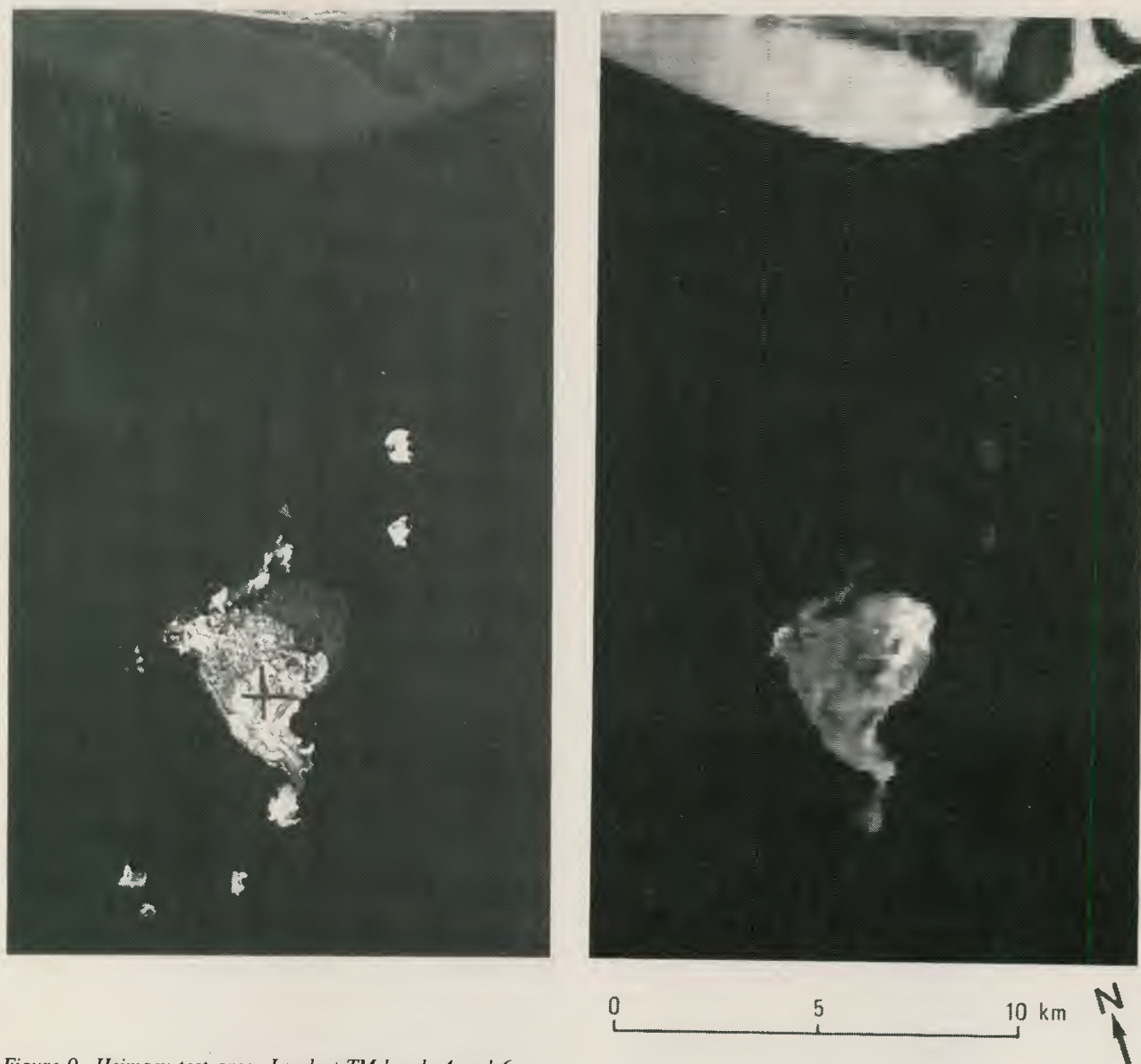


Figure 9. Heimaey test area. Landsat-TM bands 4 and 6.

and south the thermal emission is much lower. The NW-part correlates with the area that was chilled with water during the eruption and in the southern part the thickness of the lava is much more less than elsewhere (only 10–50 m). These regions have therefore lost their original heat energy much sooner than the main part, which still has a molten core.

The airborne thermal scanner image shows good agreement with the Landsat data regarding the gross temperature distribution of the lava surface, but above all it demonstrates the significance of high spatial resolution for geothermal research. It shows linear and curvilinear features of high thermal emission between which the lava surface appears cold. The airborne data consequently demonstrates that the heat loss from the lava is not uniform over its surface, but associated entirely with certain tectonic structures. The simulation of a reduced ground resolution by resampling of these data shows that nighttime thermal-infrared data of 20–30 m spatial

resolution would indeed be very valuable for geothermal mapping.

3.3. Krafla Area/N-Iceland

The tectonic and volcanic activity of the neovolcanic zone is restricted to volcanic systems, i.e. a central volcano and an associate fissure swarm passing through it, and occurs episodically rather than continuously, with a period of 100–150 years. During each active period, which lasts 5–20 years, only one central volcano and fissure swarm is active.

The most recent activity started in 1975 in the Krafla volcanic system in N-Iceland and lasted almost a decade. During this period an E-W rifting of 5–7 m occurred on the 80 km long N-S striking fissure swarm, accompanied by earthquakes, vertical ground movements, changes in geothermal activity and volcanic eruptions. Although the main magma activity was subsurface flows out of a magma chamber horizontally into the fissures to the north



Figure 10. A composite of Landsat-TM bands 4 and 6 with band 6 colour-coded. Highest brightness temperatures have saturated red, lowest temperatures are colourless.

and south, 9 short lava eruptions occurred in this time interval. The extraordinary fluid magma solidified in a 36 km² lava field no more than 7 m thick on average. The last and largest eruption happened in the period 4–18 September 1984 only two to four weeks before the TM-data were acquired (3 Oct.) (Björnsson & *al.* 1979; Einarsson & Grönvold, 1985). In this test area there are four geothermal areas, two in the Krafla volcanic system and two more in the neighbouring systems.

In Figure 11 the TM-bands 4 and 6 of the Krafla area are compared. Regions at a higher altitude than some 450 m are already snow covered. By application of a special image processing technique ('dodging') it was possible to enhance features of the band 4 image both in the snow-covered and the snow-free areas (Fig. 12). The most

striking feature in the thermal image is the hot lava from September 1984. The older parts of the lava field, which are 3 years old or more, have already cooled down completely and are not distinguishable on the image. Unlike the Heimaey lava, this lava flow is just several metres thick and therefore loses its heat content very rapidly. Figure 13 shows the thermal emission of the lava in comparison with the total area of the lava field erupted in 1975–1984.

The detectability of the geothermal fields in this test area is heavily influenced by environmental conditions. The Krafla geothermal area is located approximately at the snow line in a hilly region (I in Fig. 11). Due to combined effects of snow and sunlit south-facing slopes, no definite interpretation of the thermal image is possible. More favourable conditions prevail in the Namafjall field as it lies beneath the snow line in a morphologically rather uniform area. A N-S striking hyaloclastite ridge divides it into a western and an eastern part (II in Fig. 11). The thermal emission from Namafjall area is apparent in the thermal image, especially from the western part, which is characterised by many open fissures, some of which are carrying great quantities of warm ground water. In this producing area, manmade structures have certainly increased the thermal emission.

A further interesting phenomenon is the thermal anomaly at the NE-Shore of the lake Myvatn, which is closely connected with the Namafjall area. Warm ground water flows subsurfaceally into the lake, where it mixes with the cold water along a 2–3 km segment of the shore (III in Fig. 11). A similar feature can be seen at the top of the image, where warm water from a hot spring flows into a small river. Although the water of this river is only about 10°C warmer than its surroundings, its 10–20 m width is enough to make it easily discernible on the thermal image (IV in Fig. 11).

The two remaining geothermal fields in this test area are situated in the neighbouring volcanic systems to the west and east of Krafla. The western one (V in Fig. 11) is not distinguishable on the thermal image although environmental conditions are favourable. This is probably due to disadvantageous distribution of the hot sites with regard to the ground resolution cell. Hydrothermally altered ground is rather scattered in this geothermal area. The eastern one, which is bound to a shield volcano crater, is situated within an entirely snow covered region (VI in Fig. 11). As can be seen in bands 4 or 7 (Figs. 10 and 11) the heat flux has melted the snow off the geothermal field itself. Although the radiometric temperature is not higher than at an arbitrary snow-free spot, the cold surroundings make the thermal area easily detectable. This example may be regarded as an indication of the greatly increased detectability of the constant geothermal emission in night images, where solar heating is absent and the Earth's surface is generally much cooler. Re-

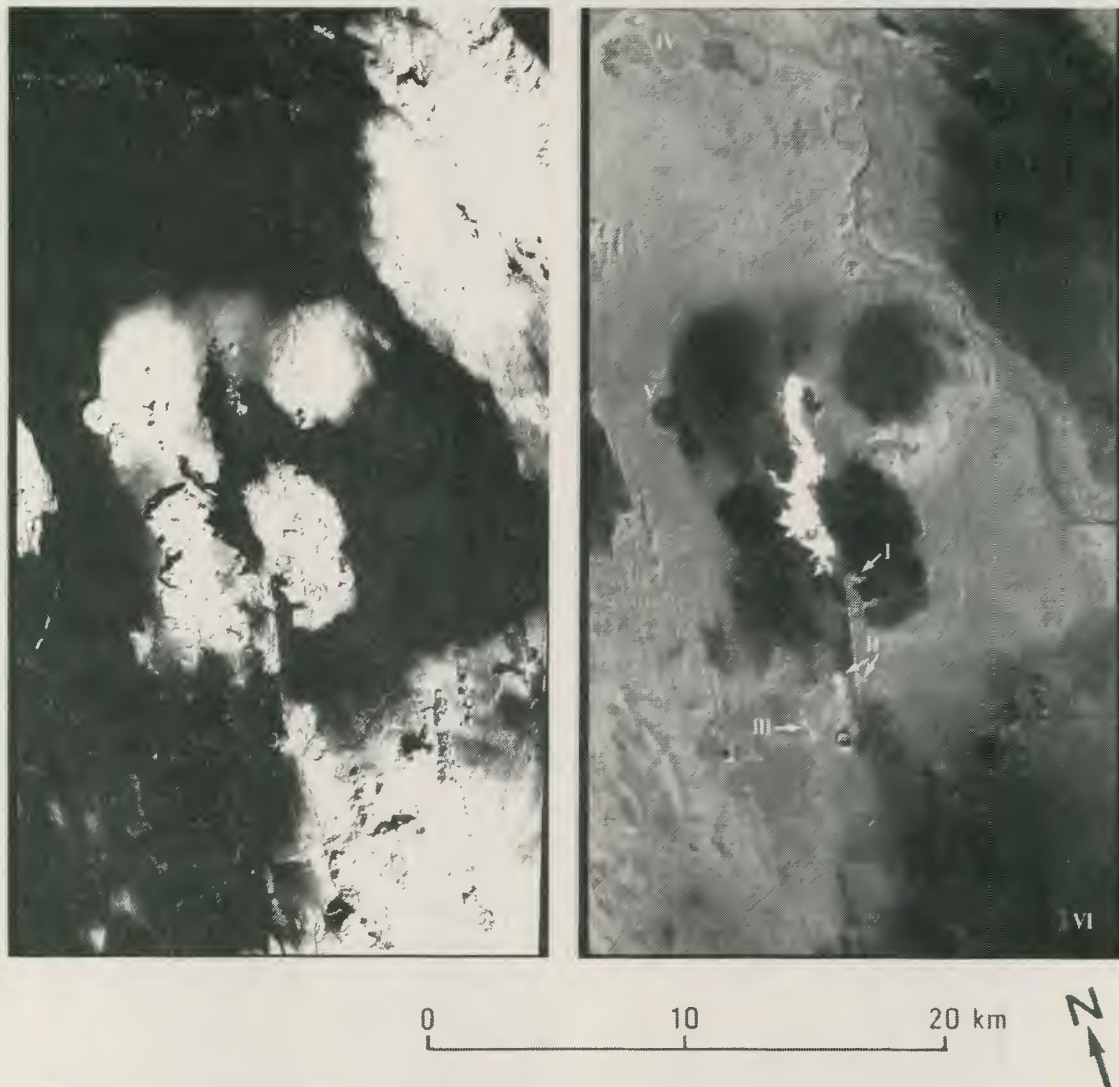


Figure 11. Krafla test area. Landsat-TM bands 4 and 6.

maining thermal structures in the Krafla area are all related to environmental features, mainly emissivity differences and topographic effects, which can be most simply confirmed by comparing the thermal band with bands 4 and 7. Due to the lower position of the Sun the effects of solar heating are however on the whole much less pronounced in this image than in scene 220/15 acquired on 22 May 1985.

The young lava flow from September 1984 represents an interesting test object for a quantitative estimation of the surface temperature by use of Landsat-TM thermal infrared data. Advantageous conditions in the Krafla test area make such an estimation possible:

- The lava is of sufficient size with respect to the ground resolution of the sensor (the most pixels entirely within the lava, i.e. no mixed signatures).
- The lava has a homogenous surface of uniform, known emissivity.
- Kinetic temperatures of at least three homogenous surfaces of known emissivities and of sufficient size to exclude mixed signatures are known in the test area.

These are the ocean water, lake Myvatn and the snow cover.

Concerning the snow temperature, it is known that the spectral reflectance in the short-wave infrared is considerably reduced as the snow begins to melt (O'Brien & Munis, 1975). Band 7 in Figure 12 shows this shift in the snow reflectance at a certain topographic height. Below this height the snow is melting and thus remaining at 0°C. Extrapolating from the three known temperature values and using the form of the grey value/radiometric temperature curve computed after Metzler & Malila (1985), it is possible to estimate the surface temperature of the lava excluding all atmospheric effects. Accordingly the temperature over most of the lava surface varies between 15 and 25°C, its hottest site however being 37°. Of course, this estimation only gives the average temperatures within ground resolution cells of 120×120 m², but it nevertheless demonstrates the potential of satellite-borne thermal infrared data for making a more quantitative approach under favourable conditions.

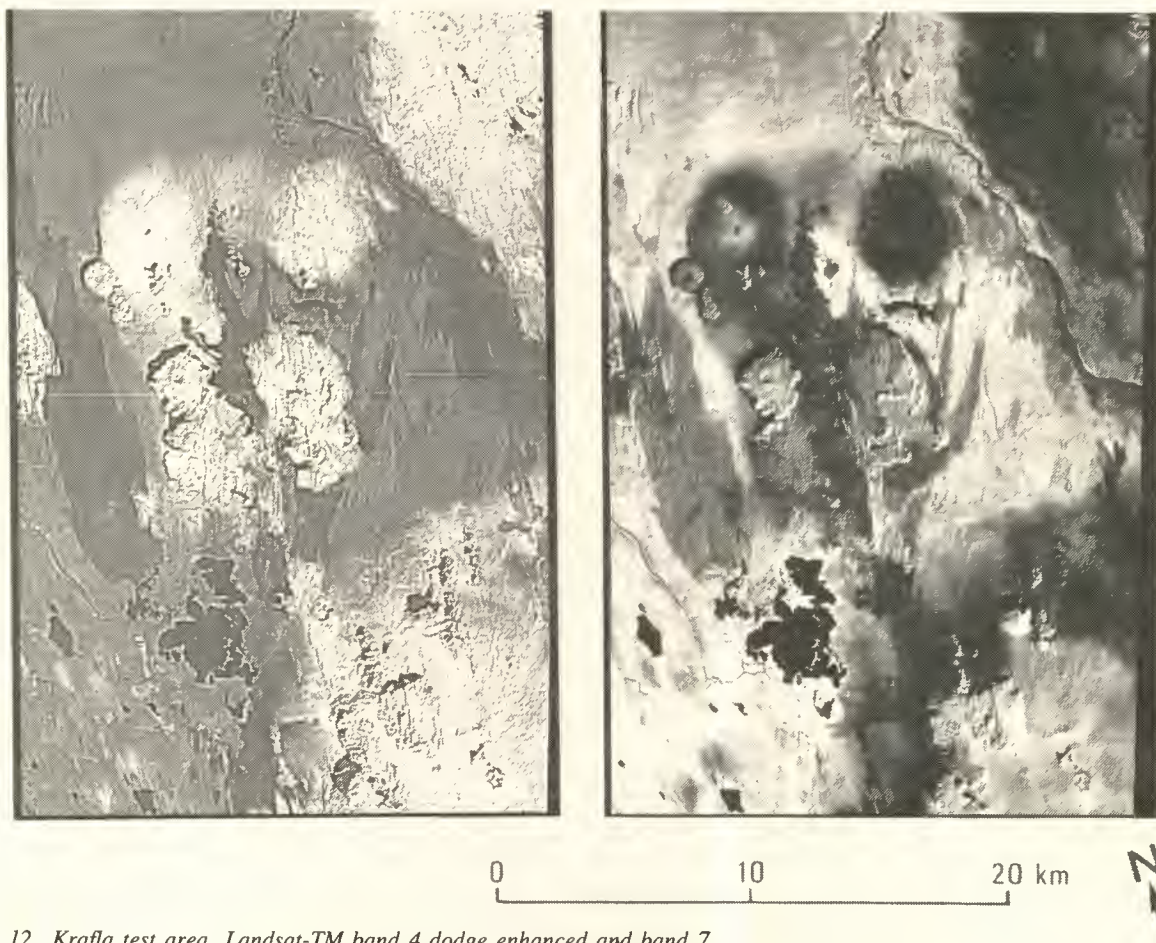


Figure 12. Krafla test area. Landsat-TM band 4 dodge enhanced and band 7.

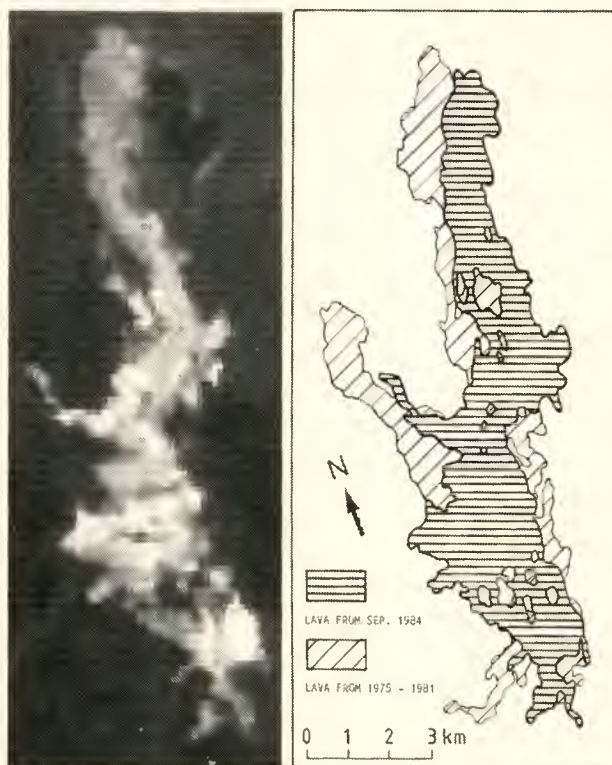
4. Conclusions

Geothermal energy is of major economic importance in Iceland as nearly one third of the net energy consumption of the country is supplied from geothermal resources. This energy is mainly used for space heating (at present almost 80% of all houses in the country) but also for various industrial purposes.

With the launch of Landsat-4 and 5, regional thermal emission data with a relatively high spatial resolution (120 m) became available for Iceland for the first time. Consequently it seemed desirable to examine whether the data might be attractive for future geothermal investigations. ESRIN, Frascati, Italy and DFVLR, Germany provided three complete TM scenes, 219-14 and 219-15 from 3.10.1984 and 220-15 from 22.5.1985 for a study on geothermal anomalies in Iceland. Unfortunately only daytime images of Iceland have been acquired so far, but in spite of this severe restriction and others (partial snow- and cloud-cover of the present data) the investigation of these data has led to several important results:

Overall, the comparison of the Landsat-TM thermal data with the older HCMM-Images (spatial resolution of 600 m) shows an enormous qualitative increase in the information content of the former.

Figure 13. Enhanced image of the thermal emission from the Krafla lava flow as registered by Landsat-TM band 6 on 3.10.1984 compared with the areal extent of the lava field.



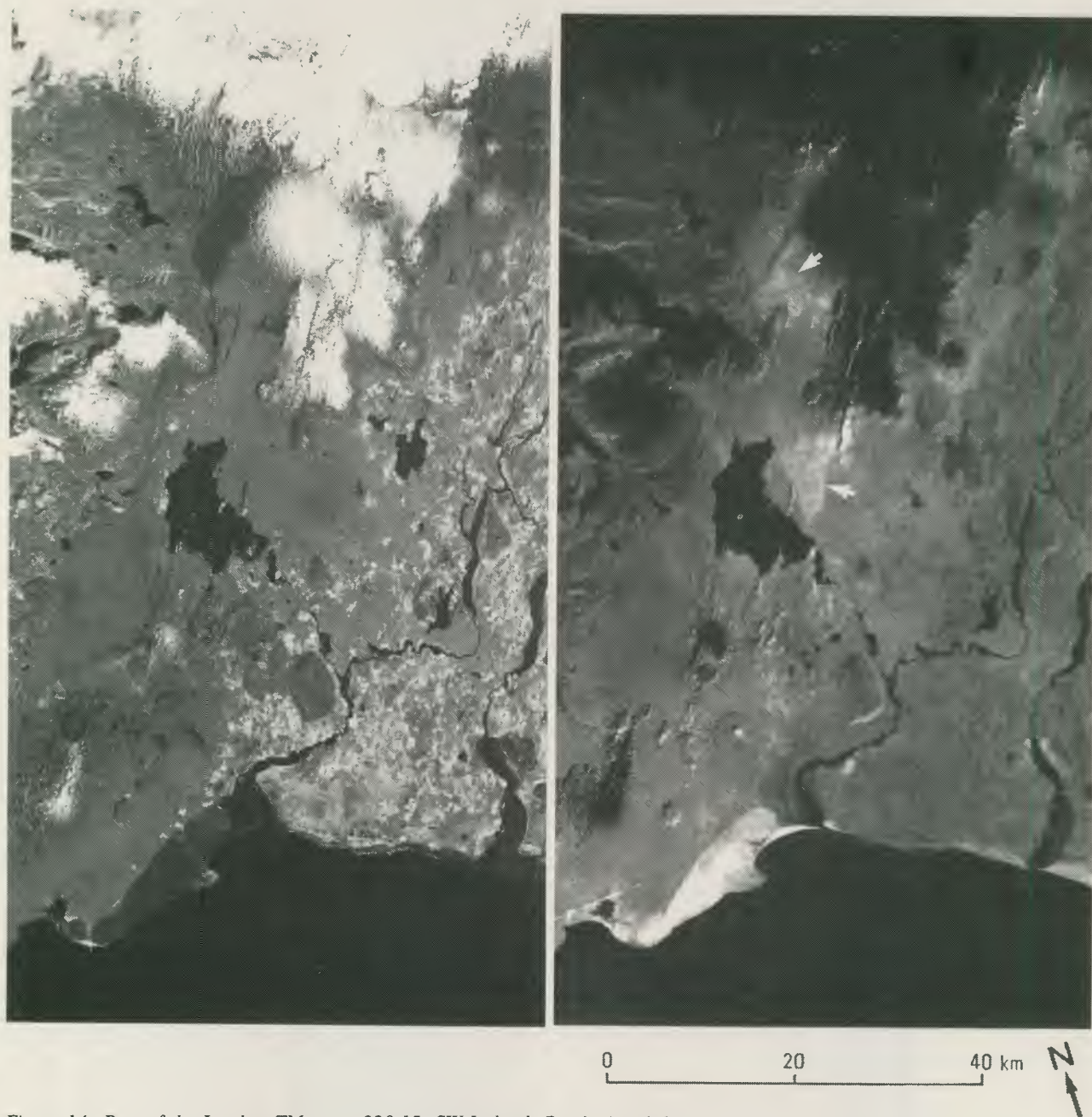


Figure 14. Part of the Landsat-TM scene 220-15, SW-Iceland. Bands 4 and 6.

The spatial variations of the thermal emission as measured by the Landsat-TM are mainly controlled by topographic relief, and differences in vegetation cover. In some localities however, high emission cannot be correlated with these parameters nor known geothermal activity. An example can be seen in Figure 14, where Landsat-TM channels 4 and 6 are compared. Most of the thermal structures of channel 6 can be directly related to certain surface or environmental features, which can be easily recognised in channel 4. Some regional thermal anomalies, however, obviously do not coincide with any features visible in channel 4 (arrows in Fig. 14). These anomalies are probably of meteorological origin, but repetitive Landsat-TM coverage and/or more ground truth data are needed for a definitive interpretation.

Investigations of four high-temperature areas inside the active volcanic zone show that under favourable circumstances, i.e. low relief and even vegetation cover (or absence of vegetation), the thermal emission from geothermal fields may definitely be recognised on the TM-daytime images. The spatial resolution of the Landsat-TM band is, however, still too poor to allow any detailed interpretation of thermal structures in these areas. In regions of rugged topography and varying vegetation density, the geothermal emission may be totally masked on the TM images by surface effects.

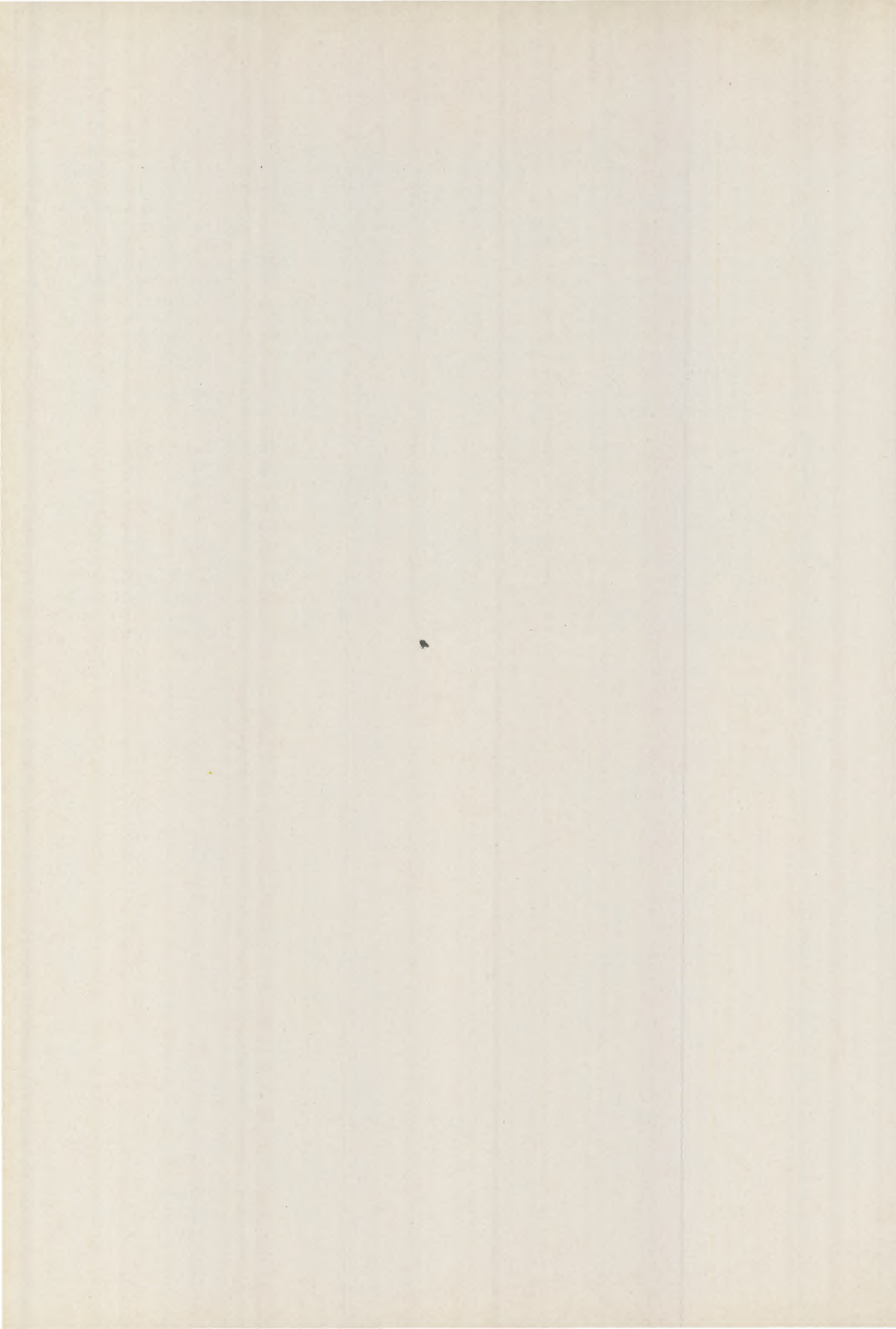
The comparison of the Landsat-TM data with airborne thermal-scanner data clearly shows the importance of high spatial resolution for geothermal investigations (as

the geothermal flux reaches the surface of the Earth mainly along (narrow) fissures and faults while the surrounding area remains relatively cool, high ground resolution is a necessary requirement for a detailed geothermal study). It appears that improvements in the spatial resolution of the Landsat-TM thermal band to, for example, 20 m would make use of the data feasible for geothermal surveys together with higher spectral resolution (two or more bands in TIR) and the availability of images acquired during the night. The availability of nighttime thermal images is of course assumed for reasonable use of this data, whilst the daytime images of the remaining spectral bands give valuable information for the interpretation of the thermal band (lithology, vegetation distribution, topography, etc.).

The TM data is extremely valuable for the registration of the temperature distribution of large homogeneous surfaces (constant emissivity) such as those of the ocean and great lakes. The capability of the satellite to register subtle changes in thermal anomalies of the ocean is of particular interest as these changes are coupled with climatic variations, which often have great impacts on fishery and farming.

5. References

- Björnsson A., Johnsen G., Sigurdsson S., Thorbergsson G. & Tryggvason E. 1979: Rifting of the plate boundary in north Iceland 1975-1978. *J. Geoph. Res.* **84**, B6, 3029-3038.
- Einarsson P. & Björnsson S. 1979. Earthquakes in Iceland. *Jökull*, 27, Special issue: *Geology of Iceland*. Reykjavik; 37-43.
- Einarsson P. & Grönvold K. 1984. Eldgosid a Kröflusvaedi i september 1984 og addragandi thess. *Skjalftabref*, 59. Reykjavik, 7-10.
- Georgsson L.S. 1984: Resistivity and temperature distribution of the outer Reykjanes peninsula, southwest Iceland. Society of Exploration Geophysicists, *54th Annual International SEG Meeting*, Dec 2-6, 1984/Atlanta, Georgia, 81-84.
- Haydn R., Dahlke G.W., Henkel J., Bare J.P. 1982. Application of IHS colour transform for processing of multispectral data and image enhancement. *Int. Symp. on Remote Sensing of Arid and Semi-Arid Lands*, Cairo, Egypt, 19-25. Jan., **1**, 599-616.
- Jakobsson S.P. 1979. Outline of the petrology of Iceland. *Jökull*, 29, Special issue: *Geology of Iceland*. Reykjavik, 57-73.
- Jonsson J. 1978. *Jardfraedikort af Reykjanesskaga*. I. Skyringar vid jardfraedikort. - Orkustofnun, OSJHD 7831, 303 pp, Reykjavik.
- Metzler M.D. & Malila W.A. 1985. Characterisation and comparison of Landsat-4 and Landsat-5 Thematic Mapper data. *Photogrammetric Engineering and Remote Sensing*. **51**, 9, 1315-1330.
- O'Brian H.W. & Munis R.H. 1975. Red and near-infrared spectral reflectance of snow. Cold Regions Research and Engineering Laboratory, Research report 332, Hanover, New Hampshire, 18 pp.
- Saemundsson K. 1979. Outline of the geology of Iceland. *Jökull*, 29, Special issue: *Geology of Iceland*. Reykjavik, 7-28.
- Sigurgeirsson Th. 1982. Hagnyting hraunhita. In: *Eldur er i nordri - Afmaelisrit helgad Sigurdi Thorarinssyni sjötugum 8. januar 1982*. Sögufelag, Reykjavik, 437-441.



Karst Drainage in the Peloponnesus Area: A Case Study for Application of TM Data in Hydrogeology

B. Reichert & H. Hötzl

Lehrstuhl für Angewandte Geologie, Universität Karlsruhe, FR Germany

H. Kaufmann

Institut für Photogrammetrie und Fernerkundung, Universität Karlsruhe

For the water resources management of the Peloponnesus (Greece) the subsurface drainage is of decisive importance. Increasing industrialisation, stepping up of agricultural production and a continuously expanding tourist industry result in increasing water requirements. 'The International Working Group on Tracer Methods in Hydrology' investigated the karst drainage in the central and eastern Peloponnesus for a period of several years.

At the NW coast of the Gulf of Argos big fresh water springs have been known since antiquity. These springs are typical karst springs, characterised by irregular, unstable discharge and even temporary absence. For the water recharge carbonatic catchment areas in form of a polje step in the backland may be relevant.

One main objective was to investigate the drainage system between the catchment areas and the various springs on the coast and to elaborate possible ways of collecting the fresh water before its submarine discharge. This paper will show how far high-resolution satellite data (TM) can be used to support and complement hydrogeological research.

The use of special band combinations of the reflective data made a separation of the main hydrogeological units possible. Furthermore, a fracture pattern could be derived which, separated into strike-slip faults and joints by field check and combined with already known karst caves and tracer experiments, permits new conclusions on possible underground paths of the water. The submarine springs are detectable by the thermal band of TM. Band 6 shows the discharging freshwater of several karst springs in the Gulf of Argos in an impressive way.

Introduction

In the framework of a five-year international research programme the hydrogeological conditions of the karst drainage system prevailing in the central and north-eastern Peloponnesus were investigated. As most parts of the Mediterranean area, southern Greece experiences problems with the water supply, mainly caused by the climate. A recharge of the ground water reservoirs is only possible during the wet winter season. Growing industrialisation, increasing agricultural utilisation and a continuously expanding tourist industry are responsible for the sharply increased water consumption during recent years. Apart from other prolific aquifers the karst water is of greatest importance as a ground water reservoir in the mediterranean area. In order to plan optimal exploitation of the karst water reservoirs the 'Internation-

Working Group on Tracer Methods in Hydrology' carried out an interdisciplinary research programme — a pilot project in the central and NE Peloponnesus — from 1982 to 1986. In September 1986 the results of the investigations were published during an international symposium in Athens (Morfis & Zojer, 1986).

Apart from looking for solutions to various problems and carrying out experiments in connection with the research programme, one purpose of the investigations was to examine the possibilities of applying highly resolving satellite data for hydrological purposes. The main aims were:

- separation of the main hydrogeological units
- evaluation of the structure pattern

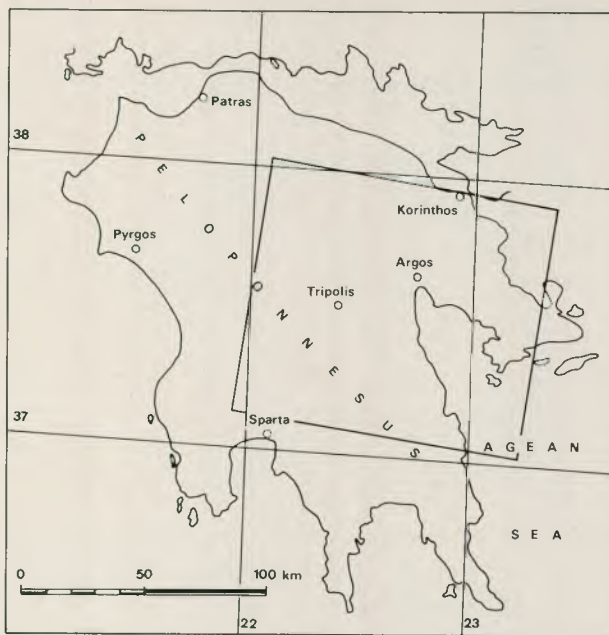


Figure 1. Investigation area

- localisation of submarine spring outlets
- correlation of remote sensing evaluations and interpretations with data of other participating disciplines for the explanation of the results and for the development of an overall model of the subsurface drainage system in the investigated area.

Area of Investigation

The area of investigation is located NW of the Gulf of Argos and includes an area of about 3000 km². It is characterised by a nearly exclusive subsurface drainage system in form of a polje step. The catchment area of the whole system reaches up to 2000 m above sea level in the north. The receiving watercourse in the western part is formed by the Ladona river. In the eastern and southeastern part the sea in the area of the Gulf of Argos forms the receiving watercourse with productive karst springs. Two of the springs are located inland only a few hundred meters away from the coast. Kiveri and Anavalos are submarine springs, whereby a coastal spring belongs to the spring group of the Kiveri besides other submarine spring outlets.

Geologically the investigated area can be subdivided into five different stratigraphic-tectonic units (Fig. 2). The deepest unit is the allochthonous phyllite-quartzite unit (PQ-unit). It is located as a nappe over the presumably autochthonous Plattenkalk series which is not exposed in the investigated area. The phyllite-quartzite unit is formed by palaeozoic to triassic phyllites with intercalated volcanic rocks and carbonates. The Tripolis nappe (Nor to Lower Miocene), a unit of thick-bedded neritic limestones up to 1300 m thick and flysch deposits up to 300 m thick, is thrust over the PQ-unit. The uppermost

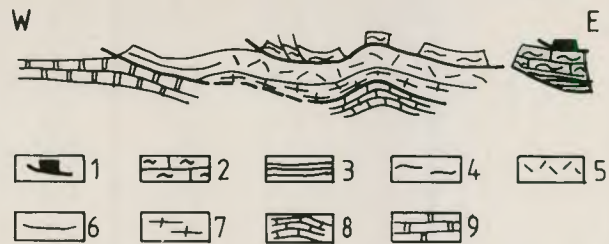


Figure 2: Schematic nappe profile of the Peloponnese (Jacobshagen et al. 1978). 1-3 Units of the Argolicum, 4 Olonos-Pindos nappe, 5 Tripolis nappe, 6 Ionian series, 7 Phyllite-Quartzite unit, 8 Plattenkalk series, 9 preapulian series

alpidic unit in the area of investigation is the Olonos-Pindos nappe. It is formed by pelagic sediments (carbonates and flysch deposits of Jurassic to Eocene age) of up to 500 m thickness. Neogene sediments which can be divided into two lithological units (marls and conglomerates) are located unconformably over the alpidically folded nappe pile. The Quaternary consists of debris and polje fillings, which are made up by thick lake clays and debris fans.

After the alpidic thrust tectonics the area of investigation was exposed to intensive fracturing in the Plio- and Pleistocene. Some of the older structures like the fracture pattern of the deeper nappe units, developed before the overthrusting of the uppermost tectonic unit, were reactivated. So the structure pattern cannot be referred to one simple stress model.

Data Evaluation

For the synoptic evaluation of the described lithological units and associated structural elements a colour composite was calculated of a TM-quarter scene of 7 October 1984 using a concept described in Kaufmann & Pfeiffer (1987). Figure 3 shows a satellite image of the investigated area in the band combination 1, 7, 4 (coded blue, green, red). In spite of the dense vegetation cover up to 1100 m above sea level (red color variations caused by alteration of vegetation reflexion in the red coded infrared band TM-4) it was possible to separate different lithological units on the basis of distinct textures and a varying vegetation density.

Figure 4 shows the distribution of the main lithological units derived from satellite data and proved by field checks for the investigated area in the Peloponnese. A schematic geological cross section is added in Figure 5. In the color composite the Olonos Pindos limestones show a fine texture characterised by numerous erosional channels in contrast to the Tripolis limestones which can be differentiated by slight texture, coarse dissection and even spectrally by dense vegetation cover. The conclusion that there is a higher surface runoff and a lower resistance to weathering of the Olonos Pindos limestone

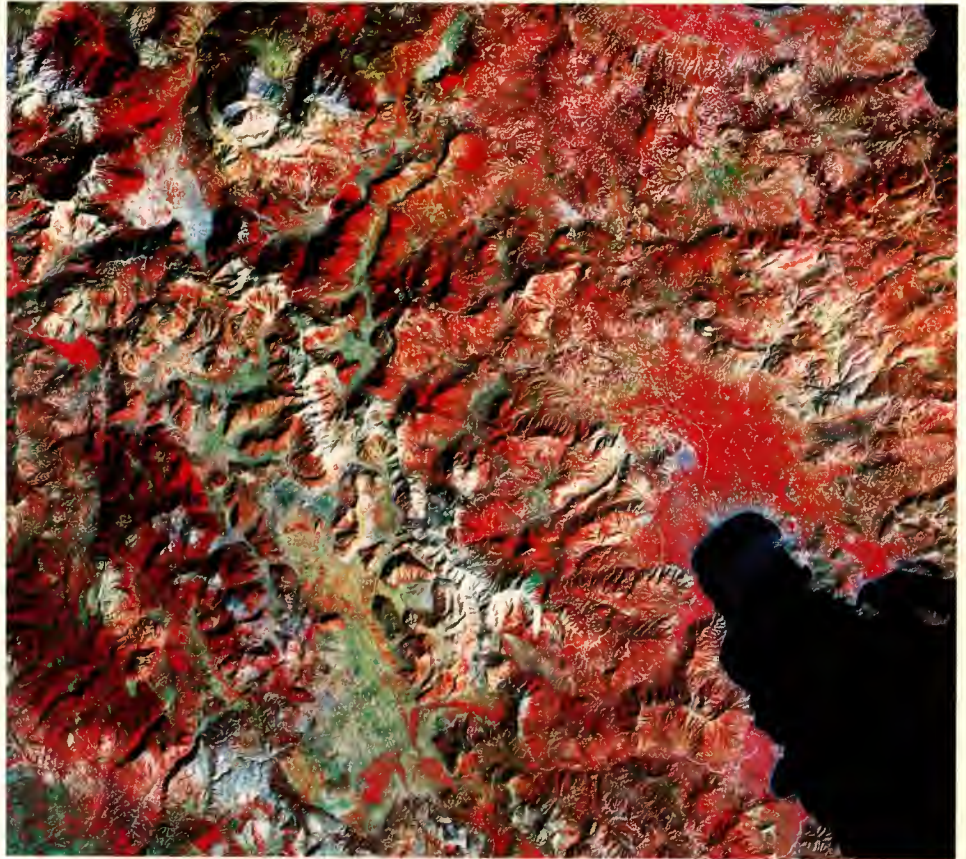


Figure 3: Colour composite of the central and northeastern Peloponnese. Band combination 1, 7, 4 (coded blue, green, red)

compared with the Tripolis limestone was confirmed by field work as well as by exploitation of satellite images which show a stronger folding of the Olonos-Pindos nappe compared with the fracture tectonics of the Tripolis nappe. The Neogene marls and conglomerates are exhibited by strongly spotted textures. The Quaternary polje sediments differ from their surroundings structurally because of the absence of relief formation and by spectral appearance because of their greenish colours.

The registration of the geological structure inventory in the area of investigation was achieved by the colour composite (Fig. 3). A comparison of the structural evaluations derived from TM-data with the structure pattern derived from conventional aerial photographs (Bayer, 1986) shows that the highly resolving satellite imagery is more suitable for the mapping of larger structural elements and the geological structure context resulting from it. Figure 3 shows the main lineaments in the investigated area derived from satellite images and geologic mapping.

For the registration and localisation of the spring outlets in the Gulf of Argos the thermal band and the short wave blue part of the visible spectrum were used. Lower temperatures of the freshwater compared with the sea water lead to the expectation that the discharges of submarine springs can be localised within the thermal band. An extremely contrast-enhanced display of the thermal band of the Gulf of Argos is shown in Figure 6. While

Anavalos shows no signal, the springs Kroe and Kiveri can easily be identified by their wide cold trail along the coast. At a given radiometric resolution of 0.4 K for band 6 the temperature of the spring origin is lower by 2 K at the sea surface. In the range of the trail it is by 0.4-0.8 K lower than the temperature of the surrounding sea water. The numerical values in the contrast enhanced record of Figure 6 represent pixel values with a geometrical resolution of 120×120 m. Every integer step of 1 marks a relative change of temperature of 0.4 K.

A registration of spring outlets by their suspension load carried is possible with the higher energetic short-wave part of the visible spectrum due to their depth of penetration. But Figure 7 shows clearly that the karst springs in the Gulf of Argos were characterised by a very small suspension load in October 1984. A detection of the springs with TM-band 1 alone was impossible. In the enhanced display of the short wave band (Fig. 6) only the shallow water regions of the Gulf and the pollution proceeding from the docks of Nauplia in the north can be recognised.

Interpretation

The Kiveri spring is curbed by a concrete construction. The idea is to use the water for irrigation of the total coastline up to Nauplia; yet up to now only about $2500 \text{ m}^3/\text{h}$ can be produced. The thermal record (Fig. 6)

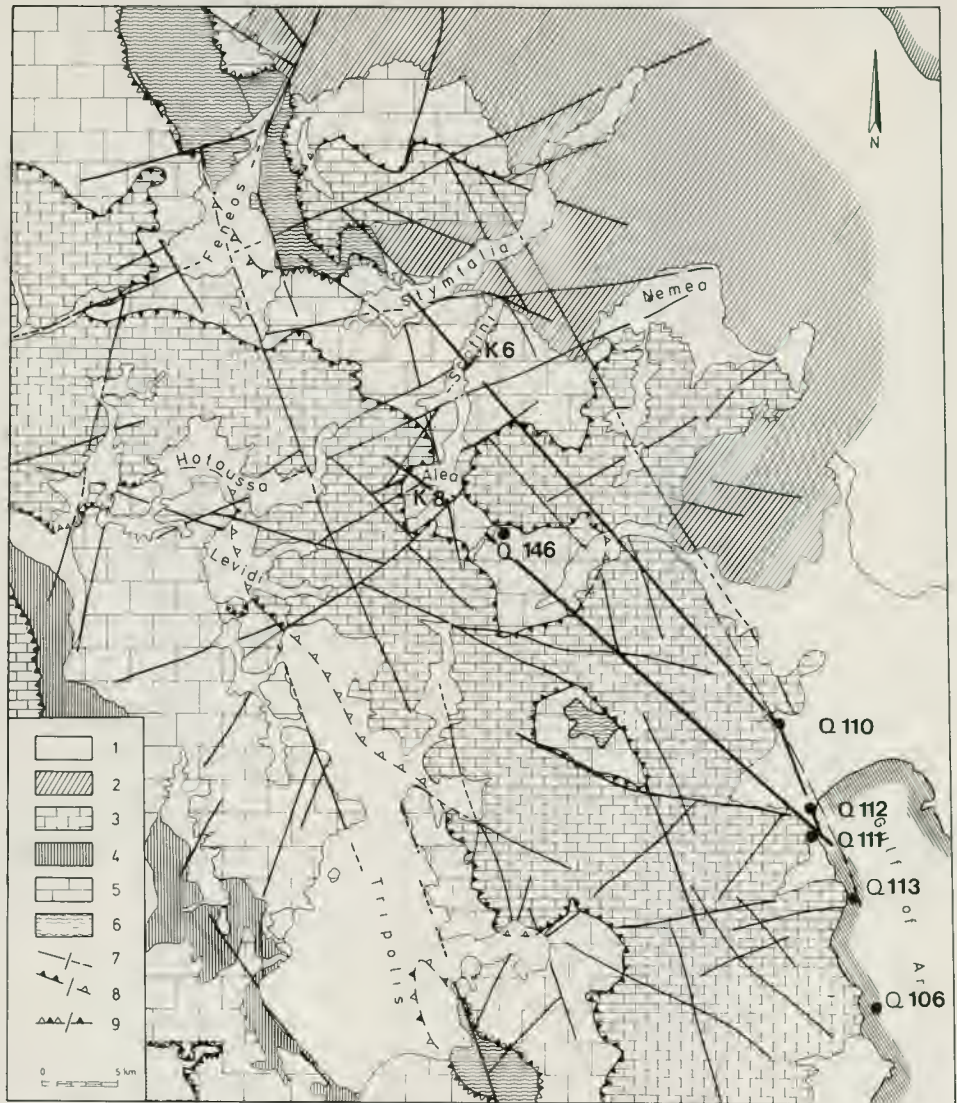


Figure 4: Tectonic-geological map of the karst area of the central and NE Peloponnese derived from satellite data and geological mapping. 1 Quaternary, 2 Neogene, 3 Olonos-Pindos nappe, 4 Tripolis Flysch, 5 Tripolis limestone, 6 metamorphic basis, 7 fault lines, 8 over-thrust of the Olonos-Pindos nappe, 9 overthrust of the Tripolis nappe (A-A' profile section of Fig. 5); Q: springs; K: sinkholes.

Figure 5. Schematic geological profiles through the karst area of the NE Peloponnese. 1 Quaternary, 2 Olonos-Pindos flysch, 3 Olonos-Pindos limestones, 4 Tripolis Flysch, 5 Tripolis limestone, 6 Metamorphic basement, 7 faults, 8 sinkholes, 9 springs (110 Kefalari, 112 Kroe, 111 Leri, 113 Kiveri; 106 Anavalos).

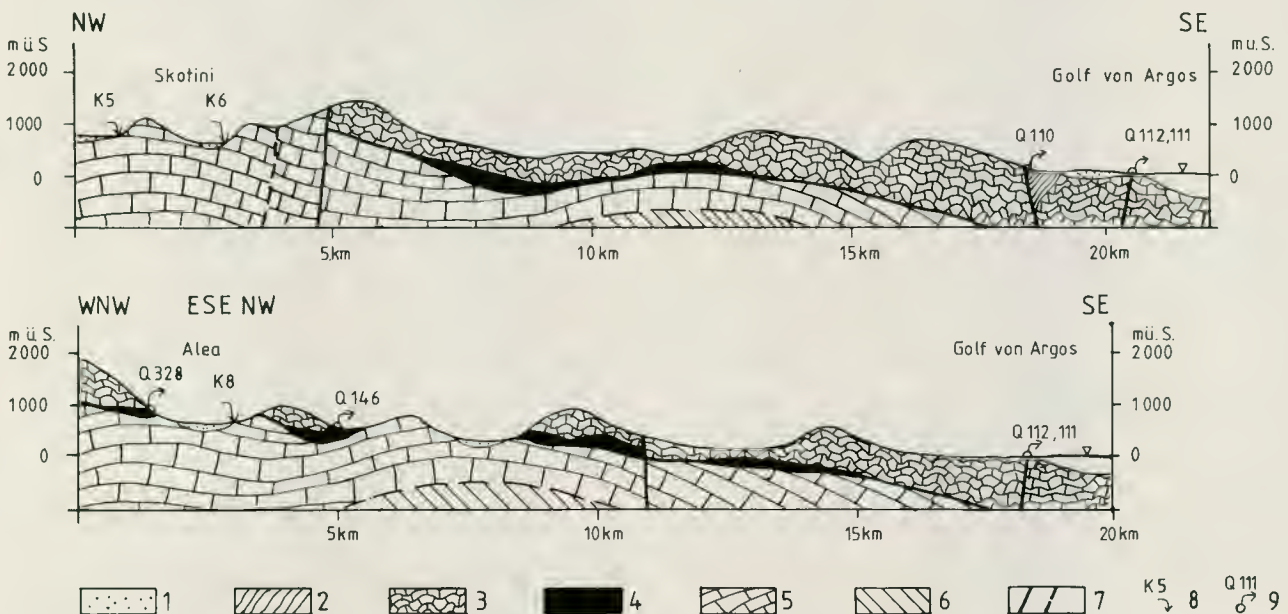




Figure 6. TM-band 6 (thermal infrared). Numeric description of surface temperature differences in the Gulf of Argos expressed in grey values, whereby every integer step of 1 marks a relative change of water temperature of 0,4 K.

Figure 7: TM-band 1 (blue part of the visible spectrum). The shallow water regions in the N and NE of the Gulf of Argos can clearly be recognised as well as the pollution trail of the docks of Nauplia.



confirms to a certain extent a leakage in the 20-year old concrete curb that has been suspected for a long time. On the other hand the centre of the temperature anomaly is located 300 m off the coast. It remains to be investigated to which extent the signal can be traced back to a permeability of the curb resp. to additional karst water outlets outside the curb. A displacement of the main discharge of the Kiveri spring is also possible. The latter could be explained by changed pressure conditions due to the curbing and structure controlled karst water channels running perpendicularly to the coast. The Anavalos of Astros, its position is south of the Kiveri, was not detectable in the processed TM-scene, due to a low outflow rate of the spring in the dry season, a seasonal minimum of temperature difference between the two water mediums and by a 90% mixture with saline water. But south of the Anavalos a few small fresh water springs were recognisable.

One main task of the case study was to establish a relation between the catchment areas (poljes) and the discharge areas (sea), i.d. to register the subsurface drainage system of the aquifer or at least to estimate it. Based mainly on the results of geological mapping in the northern part of the investigated area (Reichert & Hötzl, 1986; Röckel & Hötzl, 1986) the structure pattern shown in Figure 4 can be explained as follows. The structure pattern is characterised by two dominant conjugated

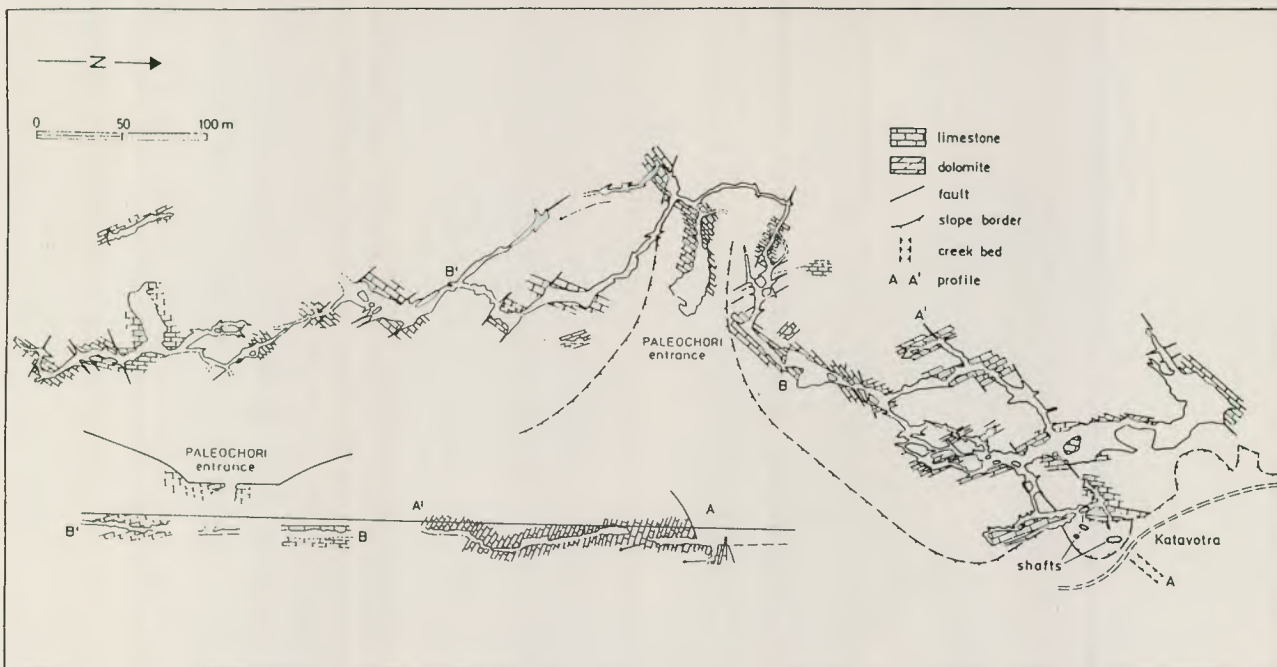


Figure 8: Kapsia-Paleochori cave system in the Tripolis polje (simplified after the cave plan from Gospodaric & Habic, 1986)

systems. With regard to the geologic limitations of the blocks the NNW-SSE direction has a high priority, for example documented by the orientation of the Gulf of Argos. Several faults in the perpendicular, interlocked ENE-WSW direction can be traced over long distances, too. The second system of conjugated faults shows a NW-SE resp. NNE-SSW direction. The faults of this system are not as well developed and their extension is not as continuous as that of the faults of the first system. The second system seems to be the older one. It corresponds with the tensional stress release after the first folding and before the overthrusting of the uppermost nappe of the nappe pile in the Peloponnesus. The faults represent the S- and Q-joints of the old fold system. The postorogenic evolution can be separated into three phases. After the overthrusting of the Olonos-Pindos nappe and the simultaneous folding of the whole nappe pile a second stage of block faulting occurred. In comparison with the first folding the fold axes were slightly rotated. Therefore the NNW-SSE direction represents the longitudinal joints and the ENE-WSW direction the cross joints of the folding phase. The extensional deformation in the Pliocene was cut off by a short phase of compressional tectonics, as wrench faults acted mainly the ENE-WSW direction. The shearing in the 70° direction caused an additional opening of the 110° and 160° joints. Since then a compressional phase with strong vertical displacements has predominated causing an uplift in the northern Peloponnesus and subsidence in the southern part of the investigated area.

From the development of the fault pattern we obtain important indications for a possible underground discharge system. Coming up with the recent strong uplifting in the northern part and the subsidence of large blocks in the

south of the investigated area the drainage systems have orientated themselves to the Gulf of Argos as decisive base level. Preferred draining courses exist in the 110° and 160° , partly deviating to 140° , directions. The occurring strike slip fault systems form barriers that lead to changes in direction within the drainage system. At the intersection points corrosion and mechanically widening occur for example in the Kapsia-Paleochori cave system which is shown in Fig. 8.

Tracing experiments where several types of tracers, for example salts, dyes, spores, isotopes and bacteria were fed into the different sinkholes of the poljes, confirm the drainage system given by the described structural pattern (Fig. 8). The division of the catchment areas of the Kefalari, Kroe and Lerni in the northern part of the Gulf area and the Kiveri in the southern part which had to be postulated by an increased occurrence of strike slip faults could also be verified by the tracing tests.

Conclusions

The case study 'Karst Drainage in the Peloponnesus Area' is an impressive demonstration of the successful application of Thematic Mapper data for hydrogeological purposes. The results can be listed as follows:

- the freshwater influx in regions near the sea surface can be recognised by thermal infrared records of TM-band 6;
- pollution trails in the water can be recognised in their distribution and intensity by the blue part of the visible spectrum (TM-1);
- a synoptic evaluation of lithological units and associated structural elements is possible by filtered

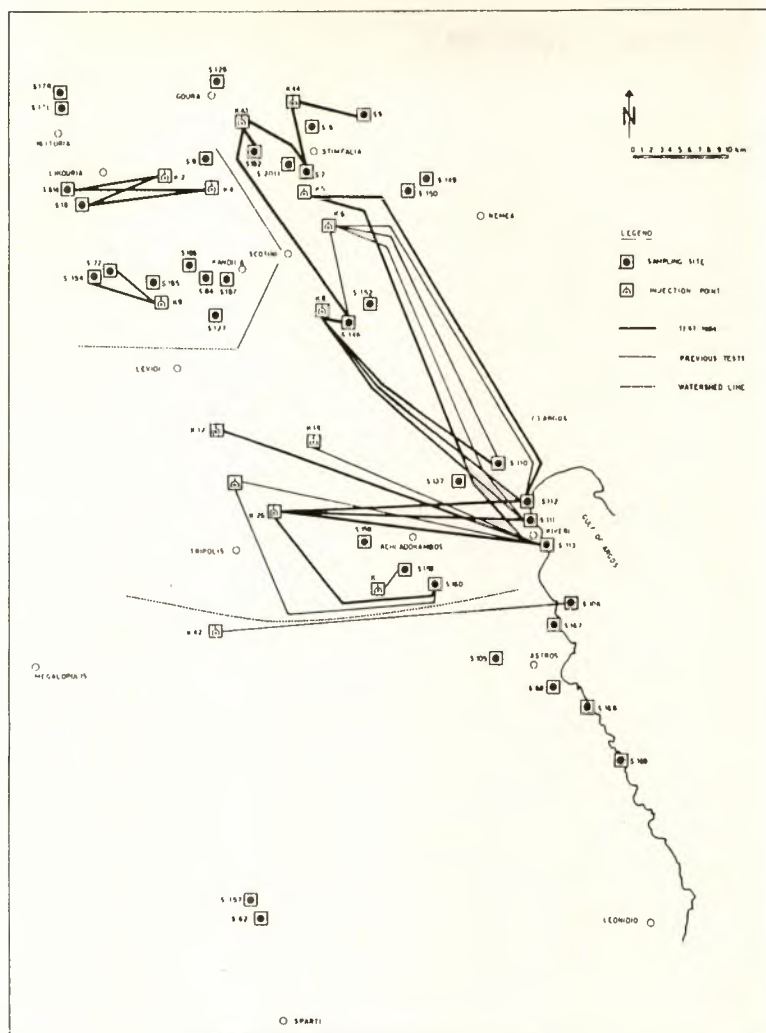


Figure 9: Underground water connections between the sinkholes (katavothres) in the different karst poljes and the springs in the investigation area (Gospodaric & Leibundgut, 1986).

and decorrelated colour composites and give useful clues for the underground discharge system.

In the framework of the described international research programme it could be demonstrated that remote sensing can make an important interdisciplinary contribution to the solution of hydrogeological problems.

Acknowledgement

The authors wish to thank ESA/DFVLR for providing system corrected data free of charge in the framework of a pilot study, and Prof. Dr. J. Bodechtel, University Munich for providing the facilities for data transfer.

References

- Angelier J. 1979: *Néotectonique de l'arc égéen*. Soc. Géol. du Nord, 3, 175 p.; Villeneuve.
- Burdon D.J. 1963: Handbook of Karst Hydrogeology with special References of the Carbonate Aquifers of the Mediterranean Region. *Inst. Geol. subsurface Res.*, VIII, 276 p.
- FAO (Food & Agricultural Organization of the UNO) 1964: *Karst groundwater Investigations Greece*. 99 p, 8 Abb., 26 Tab., 1Kt.; Rom.
- Gospodaric R. & Habic P. 1986: Poljes of Hotoussa, Levidi and Northern Tripolis. *Steir. Beitr. z. Hydrogeologie*, 37, 38: 169-185; Graz.
- Gospodaric R. & Leibundgut C.H. 1986: Evaluation and interpretation of the tracing data. *Steir. Beitr. z. Hydrogeologie*, 37, 38: 276-287; Graz.
- Haydn R. 1983: A Concept for the Processing and Display of Thematic Mapper Data. *Proc. Landsat-4 Science Characterization*, NASA Publ., 2355, GSFC, Greenbelt, MA.
- Hötzl H., Reichert B. & Röckel T. 1986: Hydrogeological characteristics of structural elements. *Steir. Beitr. z. Hydrogeologie*, 37, 38: 24-27; Graz.
- Jacobshagen V., Makris J., Richter D., Bachmann G.H., Doert U., Giese P. & Risch H. 1976: Alpidischer Gebirgsbau und Krustenstruktur des Peloponnes. *Z. dt. Geol. Ges.*, 127: 337-363, 7 Abb.; Hannover.
- Kaufmann H. 1984: A Multiple Approach in Remote Sensing For Structural and Lithological Mapping by Use of MOMS/Landsat/HCM Data. *EARSeL-ESA Symp.*, ESA SP-214: 337-347; Guildford, UK.

- Kaufmann H. & Pfeiffer B. 1986: Image Optimization versus Classification - An Application Oriented Comparison of Different Methods by Use of Thematic Mapper Data. *Proc. 7th Int. Symp. Rem.Sens. for Res., Devel. and Environ. Management*, ISPRS Conf. VII, Enschede, 25-29 Aug., p: 31-35.
- Kowalczyk G., Richter D., Risch H. & Winter K.P. 1977: Zur zeitlichen Einstufung der tektogenetischen Ereignisse auf dem Peloponnes (Griechenland). *N. Jb. Geol. Paläont. Mb.*, 1977, H. 9: 549-564, 2 Abb.; Stuttgart.
- Le Pichon, X. & Angelieur, J. 1981: The Aegean Sea. *Phil. Trans. R. Soc. London*, A 300-82-357-372, 12 Abb.; London.
- Morfis A. & Zojer H. (ed.) 1986: Hydrogeological Investigations in the Karst area of the Northern Peloponnesus, 1982-86. *Steir. Beitr. z. Hydrogeologie*, 37, 38; Graz.
- Reichert B. & Hötzl H. 1986: Polje of Alea Skotini. *Steir. Beitr. z Hydrogeologie*, 37, 38: 153-169; Graz.
- Röckel T. & Hötzl H. 1986: Polje of Stimfalia. *Steir. Beitr. z. Hydrogeologie*, 37, 38: 127-152; Graz.

Detection of Short-Term Changes in Tidal Flat Geomorphology

J. Ehlers

Geologisches Landesamt, Hamburg, FR Germany

F. Böker

Bundesanstalt für Geowissenschaften und Rohstoffe, Hannover, FR Germany

The Wadden Sea is an area of rapid geomorphological changes. Especially the shoals of the so-called 'ebb tidal deltas' which form the seaward border of the tidal inlets are re-modelled and displaced within short periods of time (hundreds of metres per year). To track these changes is important for coastal protection and navigation purposes.

Due to coast-parallel and coast-normal sand transport the barrier island beaches are often exposed to negative sand budgets. These are traditionally countered by either massive constructions (sea walls, groyne) or by beach nourishment. In order to avoid unnecessary coastal engineering measures it is important to know if natural beach replenishment can be anticipated or not.

The migration of shoals causes displacement of the main channels used for Wadden Sea navigation. Therefore charts have to be altered at short intervals and in addition to ground surveys, overview satellite images would be welcome in order to detect critical areas in time.

The changes of coastal geomorphology were traditionally observed by repeated mapping (Homeier & Kramer, 1957) or by aerial photograph evaluation (Luck & Witte, 1979). However, major landform changes occur at a much faster rate (Ehlers, 1984). As monthly surveying by aerial photography would be impossible for technical and financial reasons, other possibilities should be explored.

Hoppe (1976) did demonstrate that Landsat MSS images could be used to track large-scale changes of the tidal flat morphology. Much better results could be expected from Landsat-5 TM imagery. The aim of the recent study was to investigate, how far Landsat-5 TM images can be used to monitor the tidal flat landforms. We have focused our attention on three main topics:

- large-scale features formed by wind-induced drift currents*
- tidal current flow patterns*
- morphological changes in the Wangerooge and Mellum areas.*

The data processing was done at the Bundesanstalt für Geowissenschaften und Rohstoffe, Hannover.

1. Introduction

The Wadden Sea is an area of rapid geomorphological changes. Hoppe (1976) demonstrated that Landsat MSS images could be used to track large-scale changes of the tidal flat morphology. Much better results could be expected from Landsat-5 TM imagery. In the recent study we have focused our attention on three main topics:

- large scale features formed by wind-induced drift currents on the tidal flats,*
- tidal current flow patterns,*

- the application of satellite imagery for tracing morphological changes in the Wangerooge and Mellum areas.*

The Wadden Sea island barrier (Fig. 1) is maintained by a predominantly landward directed sand transport. Coast-normal sand transport is simultaneously overlain by coast-parallel sediment movement. In the West and East Frisian Islands this is directed from west to east, leading

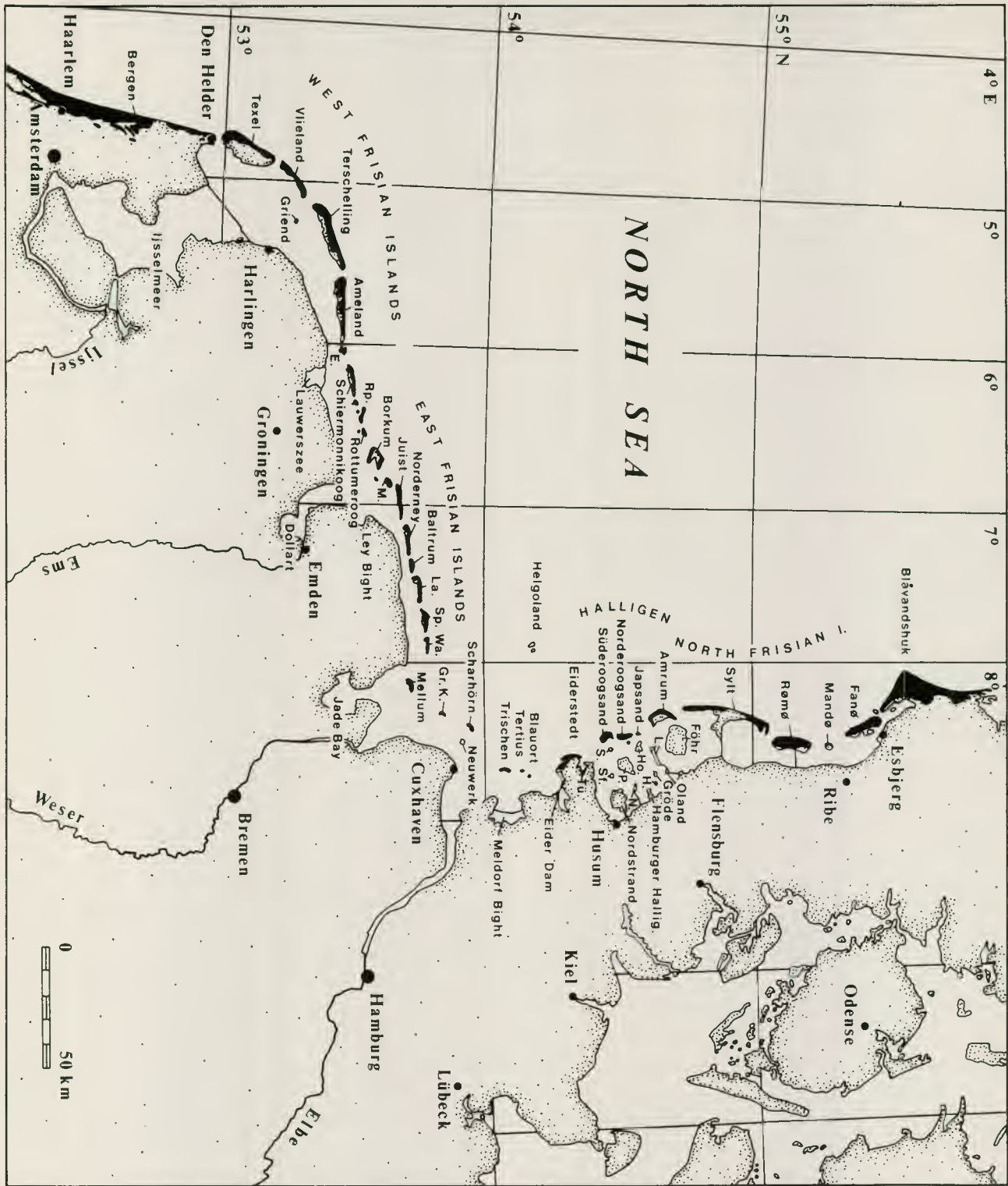


Figure 1. Location map. The coastal dunes are shown in black. L. =Langeneß, H. =Habel, Ho. =Hooge, N. =Nordstrandischmoor, P. =Pellworm, S. =Süderoog, Sf. =Südfall, Tü. =Tümmmlauer Bucht, Gr.-K. =Großer Knechtsand, Wa. =Wangerooge, Sp. =Spiekeroog, La. =Langeoog, M. =Memmert, Rp. =Rottumerplaat, E. =Engelsmanplaat.

on most islands to erosion along the western ends and accretion at the eastern ends.

The island barrier adjusts itself to the respective sea-level stages. A rising sea level results in landward migration of the barrier. Under natural conditions this is achieved

by dune erosion and landward aeolian sand transport or by the breaching of the dune ridges and washover processes. Both these processes are largely prevented at present by coastal engineering countermeasures and the most exposed parts of the islands have been fixed and fortified against erosion. This has resulted in both under-

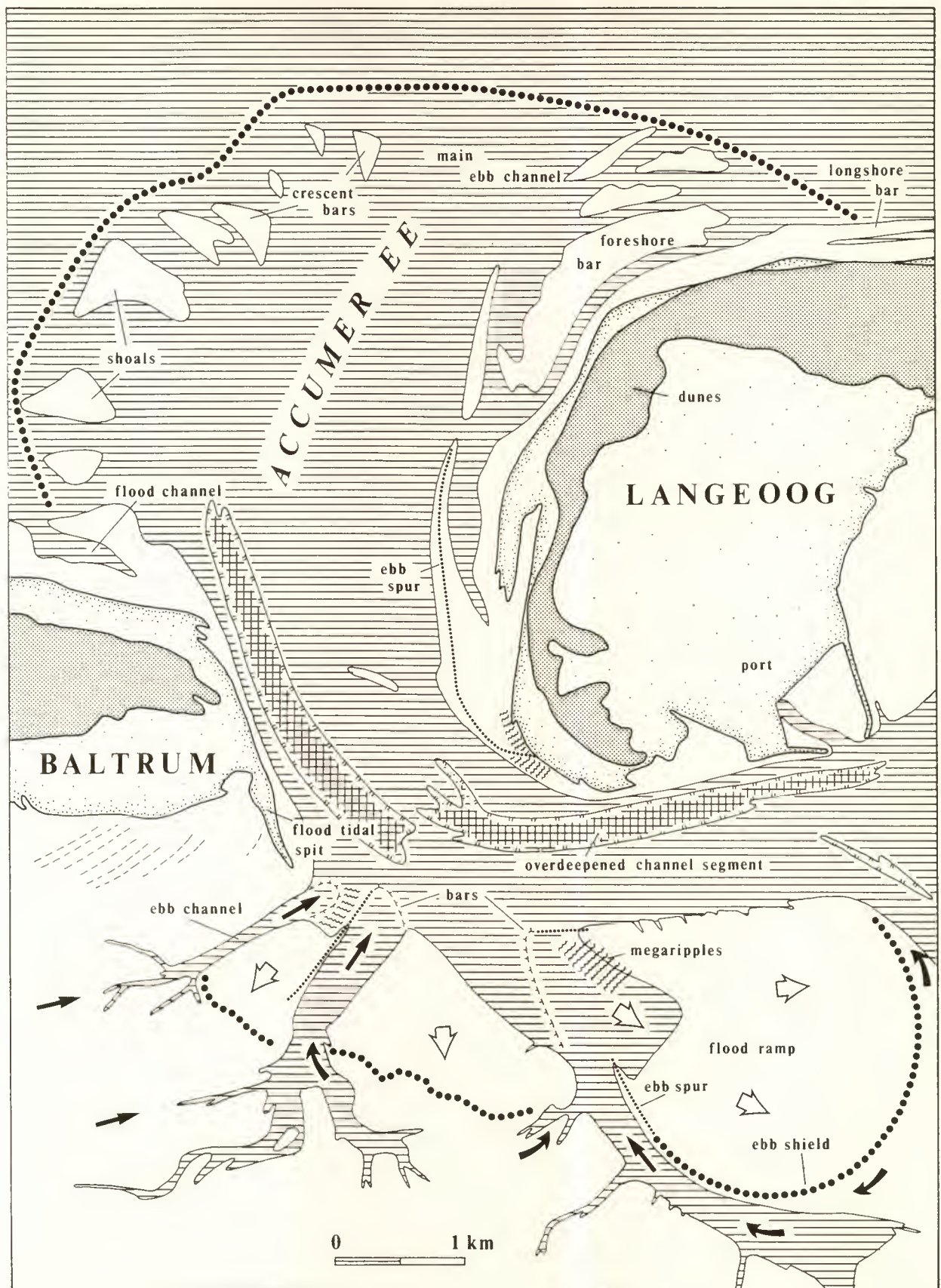


Figure 2. Landforms of a tidal inlet exemplified by the Accumer Ee (between Baltrum and Langeoog). The arrows indicate current directions in the flood delta area during the rising tide. Open arrows: flood current, dark arrows: flow direction of remaining water draining from the higher tidal flats (Sources; Küstenkarte 1 : 25 000, Sheet 2210 K Langeoog and Sh. 2310 K Accumersiel; aerial photographs of the Niedersächsisches Landesverwaltungsamt, Landesvermessung).

nourished beaches and lack of sediment on the tidal-flat facing sides of the islands. This tendency has had to be offset by extensive coastal protection in order to prevent an 'in-situ drowning' of the barrier, as envisaged by Leatherman (1982).

2. Tidal inlet morphodynamics

The morphologically most active parts of the system are the tidal inlets. Tidal inlets between the barrier islands are influenced twice daily, both by flood and by ebb currents. The large water volumes that are forced through these inlets during short periods cause a strong current to develop, the so-called 'tidal jet', which has considerable erosive power. The resulting, overdeepened channel segments occasionally are eroded to depths much greater than the adjoining sea floor (Fig. 2).

Shoal arcs, linking adjoining islands, are found at the mouths of the tidal inlets. Comparison of aerial photographs taken at different times reveals that the shoal arcs are not stable features but undergo rapid changes.

The discharge of a tidal current into the sea is morphodynamically comparable to the discharge of a major river. As a result of its high velocity the ebb current transports large volumes of sediment out towards the sea. At the inlet mouth this sediment load is quickly deposited as the current velocity rapidly decreases. The sand accumulation created in this way is called a 'tidal delta' (van Veen, 1950). As this tidal delta is formed by the ebb current, it can also be called the 'ebb delta'.

The ebb delta of a tidal inlet is not only shaped by the ebb current but also by marine processes and sediment migration in the foreshore area. The extent to which the ebb current can prevail against the coast parallel tidal current depends on the tidal range and the size of the drainage basin. Where the ebb current dominates a large ebb delta is formed, extending far out to the sea; where surf and coast-parallel currents dominate only a small ebb delta can be sustained (Boothroyd, 1985).

Major groups of swash bars become detached from the island ends at the updrift end of the shoal arc. Marginal flood channels are often found at this point as well as at the downdrift end of the arc (cf. Hayes, 1975; Boothroyd, 1985). In the seaward parts of the arc, small isolated crescent-shaped bars are often found, commonly referred to as crescent bars. There is a major gap in the shoal arc at the mouth of the main ebb channel. Downdrift of the main ebb channel largely elongated swash bars are found which slowly move towards the beach of the adjoining island.

The flood current also creates a tidal delta. As a result of the relatively high lying tidal flats of the Wadden Sea

area the tidal inlet flood deltas are not prominent landforms. On aerial photographs and satellite images, however, the brighter sandy shoals of the flood deltas can often be easily distinguished from the darker silty tidal flats. Moreover, the flood deltas have a specific form assemblage which helps to distinguish them from the surrounding areas.

The morphodynamics of a flood delta differ considerably from those of an ebb delta. The influence of the surf, for instance, is much less. Since most parts of the flood deltas are emergent during low tide they provide an excellent opportunity to study the coexistence of ebb- and flood-orientated landforms.

The major channels predominantly are ebb channels. These are usually narrow and deep, and their mouths are blocked by seaward facing shallow bars or 'shield deltas' (van Veen, 1950). The channels used by the flood current are broader and open towards the sea. Their course is normally straighter than that of the ebb channels (Jakobsen, 1962; 1964).

The flood current creates broad flood ramps on the flood delta, which are protected against the ebb current by an ebb shield (cf. Hayes, 1975). The flood ramps are often covered with megaripple fields and sand waves. Elongated, levée-like ebb spurs, often several hundreds of metres in length, are found at the margins.

The areas which remain submerged at low tide are called subtidal, whereas those parts of the Wadden Sea which fall dry during the ebb are referred to as intertidal. Only the intertidal zone is readily accessible to direct field studies. Under favourable conditions, however, aerial photographs and satellite images permit a limited insight into the subtidal area.

3. Tidal currents

Our present knowledge of current movements in the Wadden Sea is based mainly on data gathered by automatic current measurement devices. One of their drawbacks is that measurements are always taken at a fixed height above the seabed, neglecting both currents at the bottom and at the surface. The direction of the currents at the surface, however, can be detected on aerial photographs and satellite images.

Figure 3 shows the tidal flats between Jade and Weser estuaries. In the southern part of the picture ebb has already started (high tide at Alte Mellum gauge: 8.57 AM). The ebb current direction is clearly visible from stream lines in the water, created by differences in wave pattern and sediment concentration. In general the currents follow the major topographical features of the sea bed, the run-off being concentrated in the tidal



Figure 3. Tidal flat area between Jade and Elbe estuaries, falling tide; major parts of the tidal flats are still covered with water. Stream lines indicate the current directions (Landsat-5-TM image of 25.4.1984, Bands 1, 2 and 3, taken at 9.37 AM. High tide at Alte Mellum gauge: 8.57 AM).

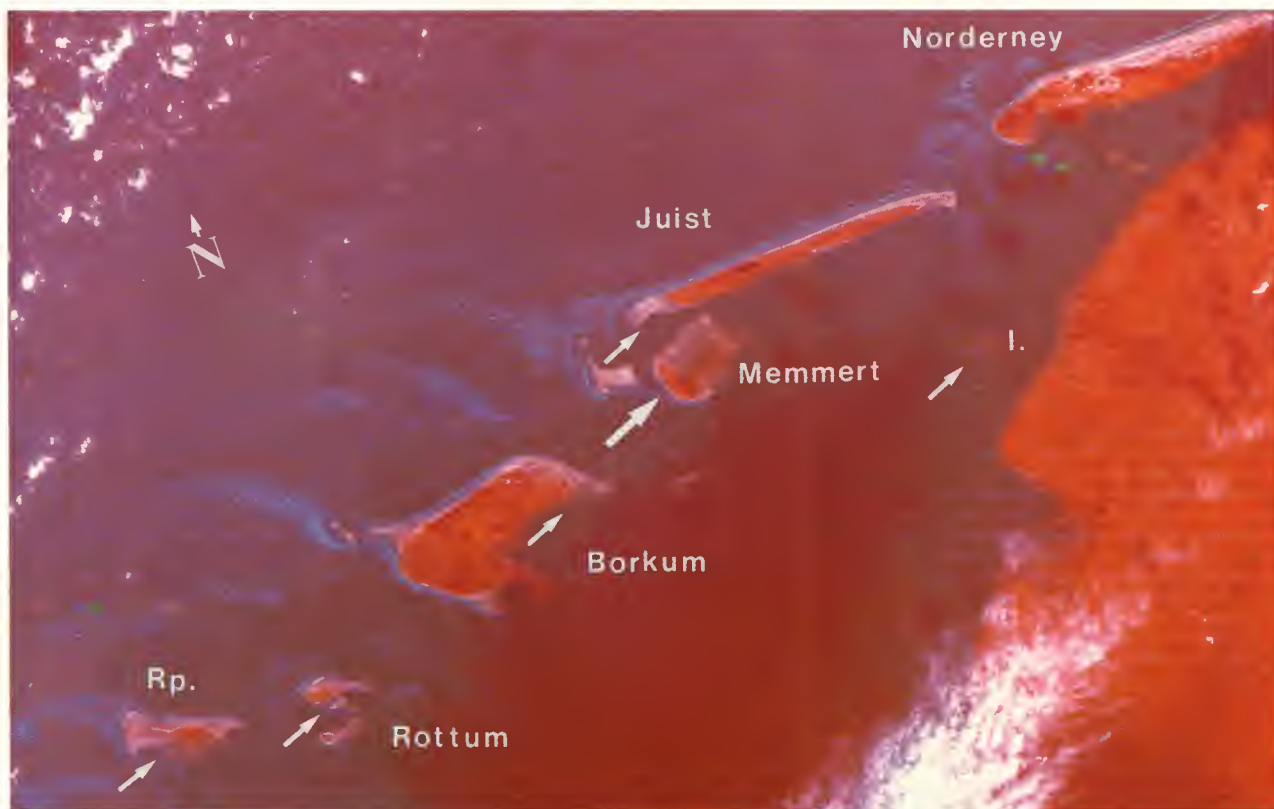
creeks. However, during sufficiently high tides they tend to straighten their routes. The lee-side effect of the ebb shields is clearly visible. In the north and at the mainland coast ebb has not yet started (high tide at Cuxhaven gauge: 9.36 AM).

4. Wind streaks

The formation of currents in the Wadden Sea is dependent not only on the tides but also on the wind. The wind therefore plays a significant part in the shaping of the tidal flats and islands. Whereas the tide-induced currents are primarily controlled by the configuration of the tidal creeks, the wind is not subject to this limitation and can act areally and unidirectionally over large parts of the Wadden Sea.

The prevailing wind direction strongly influences the intensity and direction of sediment movement. The satellite image of 1.2.1983 demonstrates this (Fig. 4). The image was taken at 9.56 AM during stormy weather (8 Bft, in gales 9-10 Bft). Low tide had been at 7.58 AM (Borkum, Fischerbalje). Due to the storm the tidal flats were almost completely submerged when the image was recorded, but the positions of the shoal arcs and longshore bars are indicated by the lines of breakers.

Figure 4. Large-scale wind streaks on the tidal flats between Rottumerplaat and Norderney; Rp. = Rottumerplaat, I. = Itzendorplate (Landsat-4-TM image of 1.2.1983, Bands 1, 2 and 5).



Large parts of the tidal flat surface, and especially those areas which are not juxtaposed to drains, remain covered by a shallow film of water during most of the low tide. This water film is only a few centimetres thick but as a result of the shallow gradient is unable to run off. This residual water can contribute considerably to the sculpturing of the small-scale relief on the tidal flats and the beach. Strong winds create wind-parallel streaks on the tidal flats which are well displayed on aerial photographs (Ehlers, 1988).

Under stormy conditions, re-shaping of the tidal flat surfaces is further enhanced. The satellite image reveals large-scale wind streaks, not visible on fair weather images, on dry parts of the tidal flats of Rottumerplaat, Rottum, Borkum, Memmert, Juist and Itzendorplate. The features have a length of up to 2.5 km and a width of about 200 metres. The wind direction was from the WSW (240°), as recorded on Borkum, Norderney and Borkumriff lightship.

5. Landform changes

The elevations of the tidal flat surfaces are subject to continual change. There have been repeated attempts to quantify this change by measuring height differences over a period of time (e.g. Knop, 1963). The sediment budget measured in this way provides an interesting insight into the mass balance of the tidal flats, but does not explain the morphodynamic processes operating. In order to do this it is necessary to investigate the landforms of the tidal flats and their changes through time.

The aim of this study was to find out, if satellite imagery could be used for such a purpose.

5.1 Harle Inlet (between Wangerooge and Spiekeroog)

Figures 5 and 6 show the eastern part of the East Frisian Islands from Langeoog to Wangerooge. East of Wangerooge the uninhabited sand bank of Minsener Oog is visible, which borders against the Jade estuary. On the 1984 image (Fig. 6) the water level is higher than on the 1976 image (Fig. 5), but it can be easily seen that the tidal flat areas in the west have experienced little change. The only striking difference between the two pictures is the man-made channel connecting the new port on the Isle of Spiekeroog with the Schillbalje channel.

However, considerable changes have taken place in the tidal flat area between Wangerooge and the mainland over the last few years. These have been caused mainly by the sagging of the westernmost section of the over 1 km long Groyne H at the western end of Wangerooge, resulting in an enlarged cross section of the Harle Inlet and in an eastward shift of the inlet axis.

Comparison of the satellite images with charts and aerial photographs reveal the extent of the changes (Fig. 7). A number of technical differences militate against direct comparison of aerial photographs and satellite images, however:

1. The different scale and resolution of the aerial photographs (1 : 28 000) compared with the satellite images (1 : 100 000) permit comparisons of only the larger forms.

Figure 5. Tidal flat area between Langeoog and Wangerooge (Landsat-2 MSS image of 19.4.1976, bands 4, 5 & 6, taken at 9.43 am. Low tide at Wangerooge West gauge: 9.41 am).



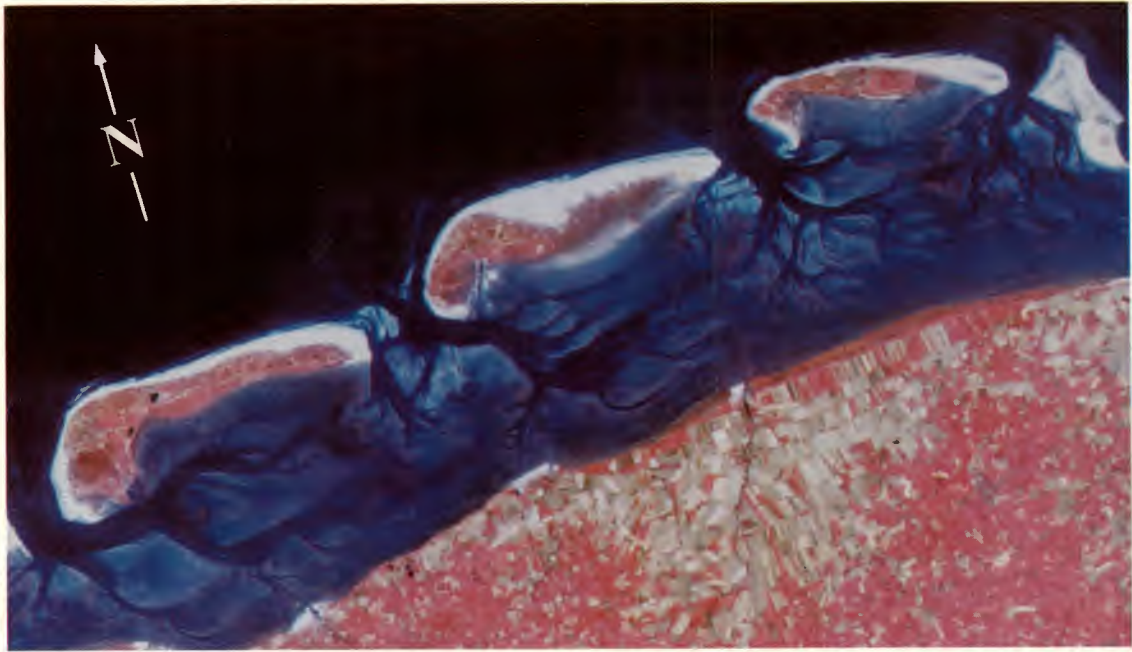


Figure 6. Tidal flat area between Langeoog and Wangerooge (Landsat-5 TM image of 22.8.1984, bands 2, 3 & 5, taken at 9.57 am. High tide at Wangerooge West gauge: 7.32 am).

2. The aerial photographs were taken at low tide whereas one of the satellite images was recorded at half tide when major parts of the flats were still submerged. Only the positions of the steep edges of bars and channels can therefore be regarded as equivalent; these forms only are shown in Figure 7

Despite these problems, the satellite image can be used to identify the major changes of the Harle Inlet morphology:

1. During the last ten years the Hullplate bar has migrated 600 m towards the SE (1). It built a spur of about the same length that extended eastward over the Hoher Rücken flat. However, the enclosing boundary of the Hoher Rücken remained essentially in the same position.
2. Over the same period the Muschelbank bar north of the Hoher Rücken has migrated about 200 m towards the SE.
3. The bar SW of the Harlehörn peninsula (3), which in 1974 was part of the Harle flood delta, now forms part of the ebb delta of the Telegraphenbalje.
4. The Breite Legde (4) has merged with the adjoining channel to the north forming a single main drainage channel; the Eversand bar has disappeared. In the process the mainland flats (Festlandwatt) north of Harlesiel have extended over 500 m towards the NE.
5. One branch of the Carolinensieler Balje channel (5), the tidal creeks west and east of the Langer Jan bar (6) and the creeks at the western margin of the Südersand flat (7) have moved markedly towards the east.

All these changes suggest a recent easterly extension of the Harle drainage basin. The adjoining drainage area of the Blaue Balje inlet appears to have been restricted by

sand replenishment south of Minsener Oog (Figs. 5 and 6). The Minsener Oog area was used as a dumping ground for dredged sediment from the Jade navigation channel in 1980/81, and in the process an area of 220 ha was accumulated beyond high-water level.

5.2 Mellum

Where the tidal range exceeds 2.90 m, barrier islands are absent. The open tidal flats between the Jade mouth and Eiderstedt peninsula show a landform inventory slightly different from that of the barrier island coast. However, the underlying morphodynamic principle is largely the same. Instead of the limiting shoal arcs the seaward ends of the tidal channels in this area are only limited by relatively low-lying bars. These, like the shoals, undergo rapid modification (cf. Ehlers, 1988).

Like Scharhörn and Trischen the Isle of Mellum must be regarded as a young island (Hartung, 1975). It is situated at the outer end of the Hoher Weg tidal flats between the Jade and Weser estuaries. The island is mentioned as a high sand bank on a map of 1792 (Schäfer, 1941). It was only in 1903, however, that Schütte (1905) recorded the development of vegetation. This had allegedly occurred after 1870 (Schütte, 1924; *op. cit.* in Schäfer, 1941).

The formation of Mellum has to be seen in connection with the shoals approaching from the sea, from the Jade bar, as can be seen on the satellite images (Figs. 8 and 9). This system of high sands has shifted landwards through the centuries, at a rate of roughly 15 m/year according to Homeier (1974). The development of Mellum between 1908 and 1952 has been documented by Schäfer (1954). During this period it continued to migrate steadily. Between 1962 and 1978 Mellum had migrated an additional 250 m towards the SE, i.e. approximately 15.6 m/year (Wunderlich, 1979).

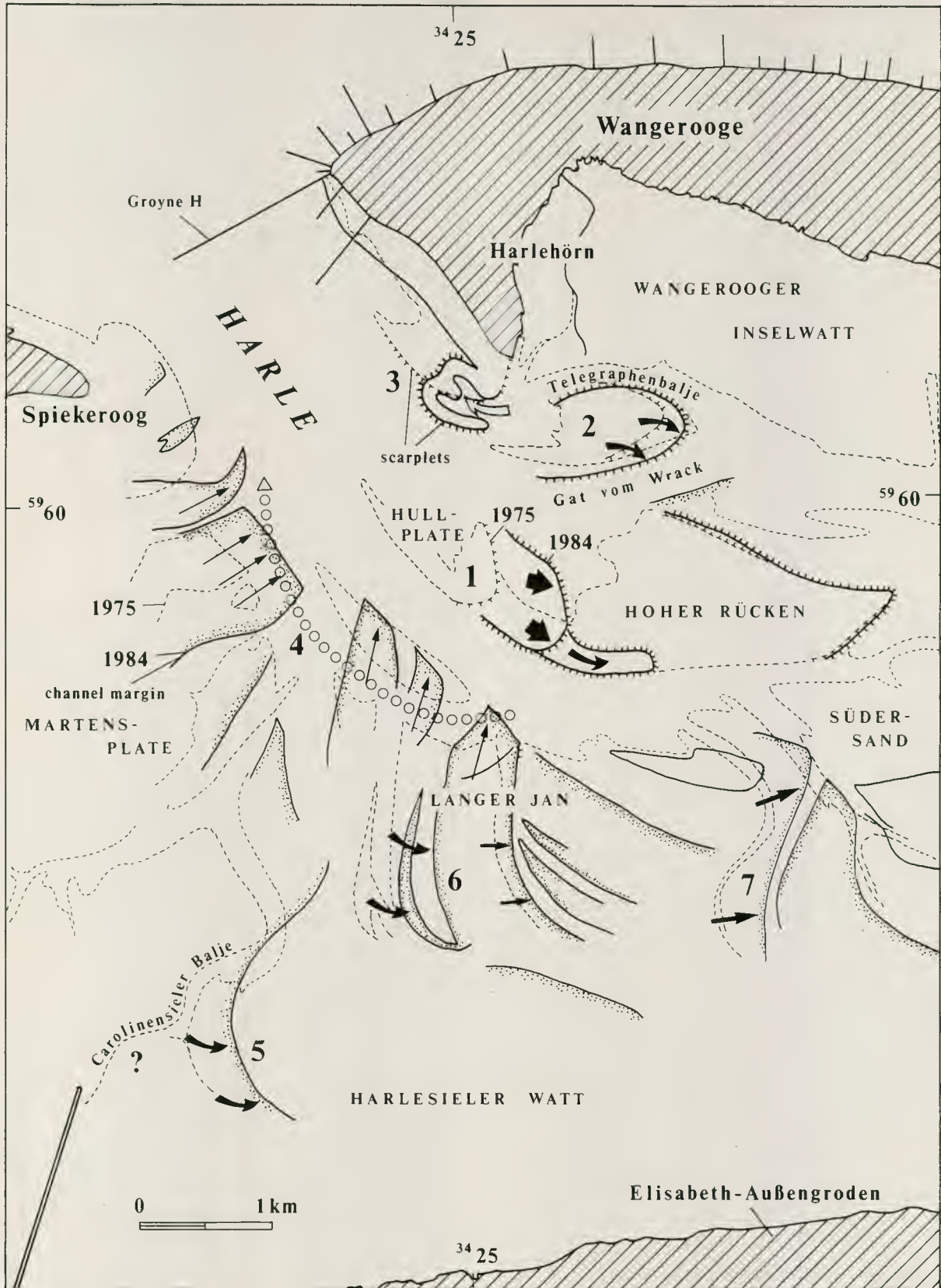


Figure 7. Morphological changes in the tidal flat area southwest of Wangerooge, between 1975 and 1984. Dotted line; former course of main drainage channel. Sources: Landsat-5 TM image of 1984; aerial photographs of the Niedersächsisches Landesverwaltungsamt Landesvermessung; Küstenkarte 1 : 25,000, Sheet 2212 K Wangerooge; Geomorphological Map 1 : 25 000 in Ehlers & Mensching, 1982.

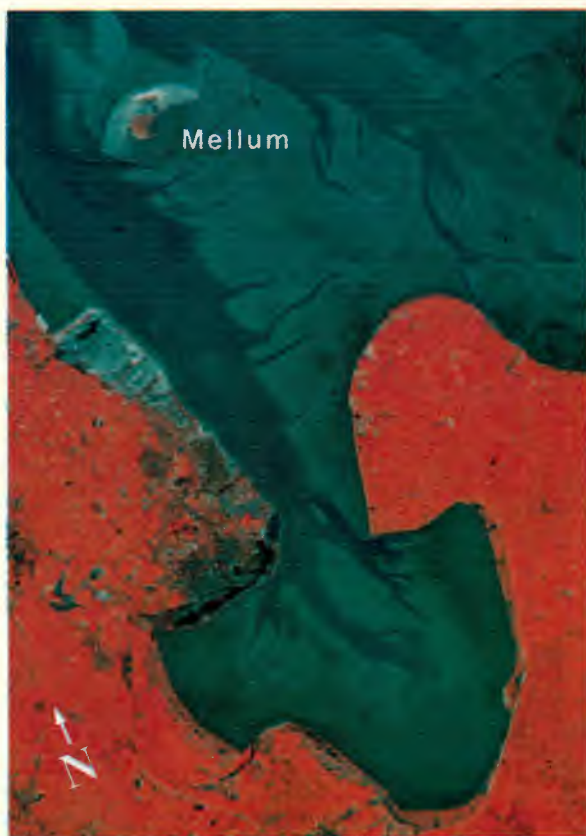


Figure 8. Jade Bay and tidal flats between Jade and Weser estuaries (Landsat-2-MSS image of 19.4.1976, bands 4, 5 & 7, taken at 9.43 am. Low tide at Wilhelmshaven gauge; 10.26 am).

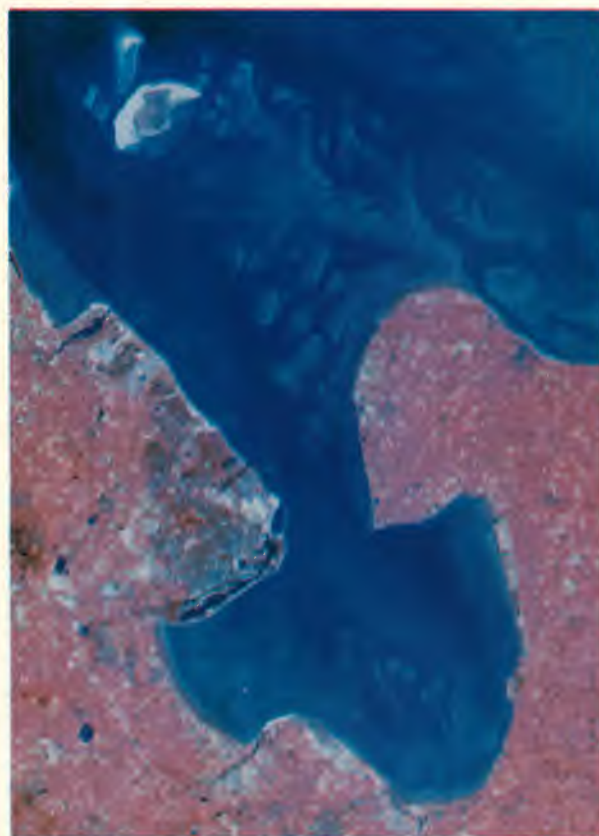


Figure 9. Jade Bay and tidal flats between Jade and Weser estuaries (Landsat-5 TM image of 22.8.1984, bands 2, 3 & 5, taken at 9.57 am. High tide at Wilhelmshaven gauge: 8.34 am).

Evaluation of the available satellite images reveals that the migration of the island has continued. Seaward of the island, however, approaching shoals have supplied the island beach with additional sand (Figs. 8, 9 and 10).

6. Conclusions

Small landforms on the tidal flats (sand waves and bars) undergo rapid replacement and reshaping; in some cases these may even occur within one tidal cycle. The larger landforms (flats and major tidal creeks) undergo only minor alterations, and the general drainage pattern may be maintained for many decades.

Satellite imagery so far has only been used experimentally in coastal geomorphological research at the German North Sea coast (Hoppe, 1976). Although the investigations had to be based on the relatively few images of Landsat-1 and 2 available at that time (4 scenes, of which one was taken during high tide) the result was encouraging and new image processing technologies and the availability of TM images enabled us to improve the application of space borne sensors for tidal flat studies.

With the largely improved quality of the present-day Landsat-TM images (Engel, Mauser & Stibig, 1984) and

SPOT images, preconditions are promising for a reinvestigation of the role remote sensing data may play in coastal research. Additional sensors like SAR may help to overcome some of the limitations to the method (cloud cover, daylight). The landforms involved have a size of between several tens and several hundreds of metres, and their migration rates range from near zero to more than one metre per day (Ehlers, 1984). In order to achieve new results, the evaluation of

- a larger quantity of surveys,
- covering a longer period of time

is required. As could be demonstrated above, for that purpose satellite images are well-suited.

The strong recent morphological changes in parts of the Wadden Sea bear considerable consequences for coastal protection and for navigation in those areas. So far the mapping of those changes is incomplete. Charts only record displacements of the most prominent channels, and even the best available map, the 1:25 000 'Küstenkarte' of the KfKI, omits major components of the morphological inventory. Moreover, major parts of the most recent survey of 1980/81 still await publication.

Therefore, the only suitable means of tracking major morphological changes in the Wadden Sea is by remote

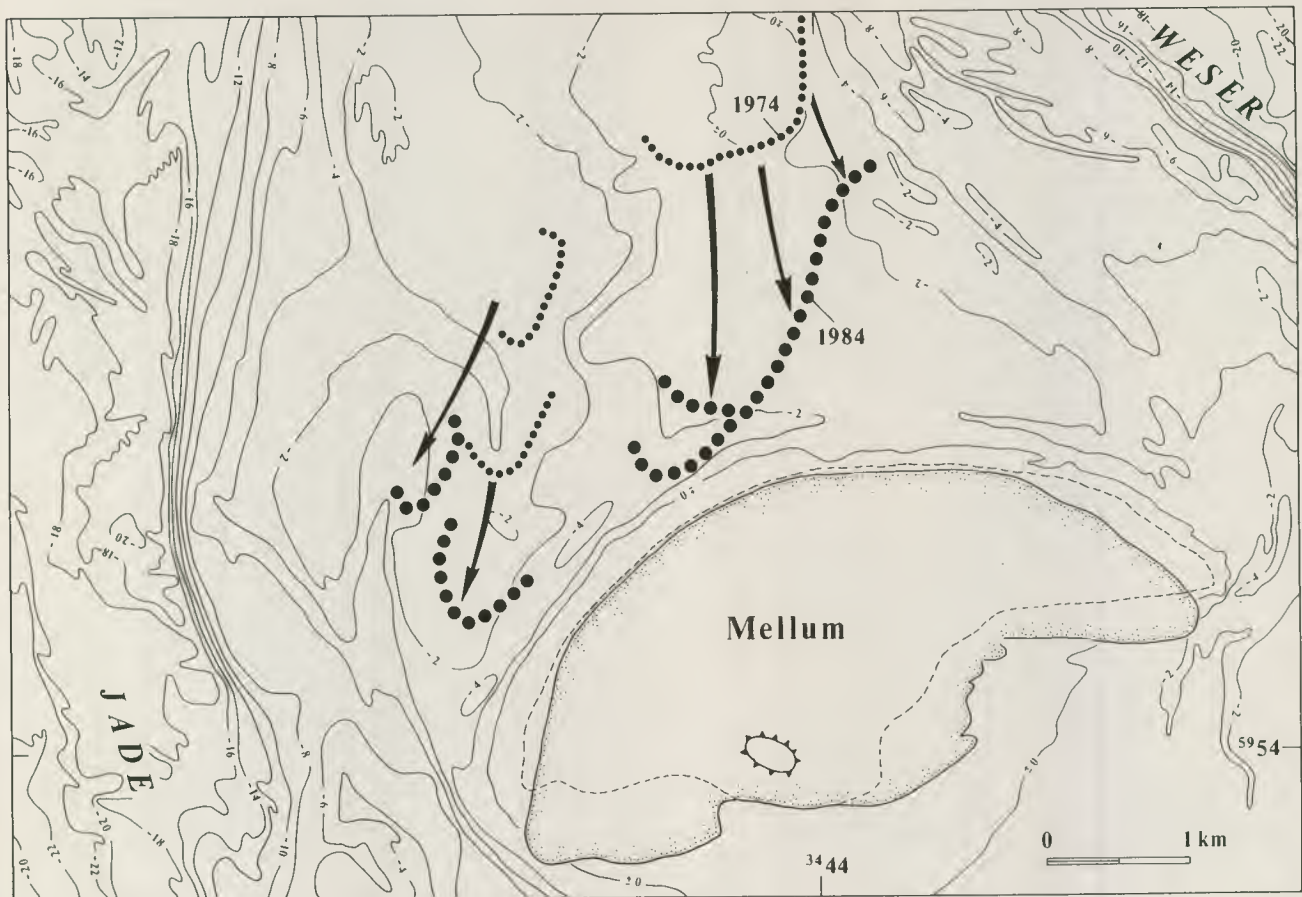


Figure 10. Morphological changes in the Mellum area (Sources; Küstenkarte 1 : 25 000, Sheet 2214 K Alte Mellum).

sensing. As aerial photographic surveys are relatively expensive, they can be conducted only for limited areas of special interest. For a general overview of the area satellite imagery would be almost ideally suited, because it allows for a rapid and complete check of the whole coastal area for signs of possible new morphological developments. Our study has demonstrated that satellite image evaluation is applicable for those purposes.

References

- Boothroyd J.C. 1985. Mesotidal inlets and estuaries. - In R.A. Davis (ed.), *Coastal Sedimentary Environments*, 2nd edition: 445-532.
- Ehlers J. 1984. Platenwanderung an der ostfriesischen Küste? - Ergebnisse der Luftbildauswertung von zwei Befliegungen der Wichter Ee (zwischen Norderney und Baltrum) im Sommer 1982. - *Mitteilungen aus dem Geologisch-Paläontologischen Institut der Universität Hamburg* 57: 123-129.
- Ehlers J. 1988. *The Morphodynamics of the Wadden Sea*. - Rotterdam: Balkema: 395 pp. (in print).
- Ehlers J. & Mensching H. 1982. *Erläuterungen zur Geomorphologischen Karte 1 : 25,000 der Bundesrepublik Deutschland, GMK 25, Blatt 10, 2213 Wangerooge*. Berlin: 55 pp.
- Engel, H., Mauser W. & Stibig H.-J. 1984. Die neuen 7-Kanal-Satelliten setzen Maßstäbe: Deutschland wird neu entdeckt. - *Bild der Wissenschaft* 21 (10): 48-56.
- Hartung W. 1975. Mellum als werdende Nordseeinsel. - In P. Blaszyk (ed.), *Naturschutzgebiete im Oldenburgerland*: 11-27.
- Hayes M.O. 1975. Morphology of sand accumulations in estuaries. - In L.E. Cronin (ed.), *Estuarine Research, Vol.2*: 3-22.
- Homeier H. 1974. *Beiheft zu: Niedersächsische Küste. Historische Karte 1 : 50,000 Nr. 8*: 20 pp. Norderney: Forschungsstelle für Insel- und Küstenschutz.
- Homeier H. & Kramer J. 1957. Verlagerung der Platen im Riffbogen vor Norderney und ihre Anlandung an den Strand. - *Forschungsstelle Norderney, Jahresbericht 1956, VIII*: 37-60.
- Hoppe P. 1976. Die Verfolgung küstendynamischer Prozesse an der deutschen Nordseeküste mit Hilfe von Satellitenbildern. - *Geologisches Jahrbuch A* 33: 49-87.
- Jakobsen B. 1962. Morfologiske og hydrografiske undersøgelser af flod- og ebbeskar i tidevandsrender. - *Geografisk Tidsskrift* 61: 119-141.
- Jakobsen B. 1964. Vadehavets Morfologi. En geografisk analyse af vadelandskabets formudvikling med særlig hensyntagen til Juvre-Dybs tidevandsområde. - *Folia Geographica Danica XI* (1): 176 pp.
- Knop F. 1963. Küsten- und Wattveränderungen Nord-

- frieslands - Methoden und Ergebnisse ihrer Überwachung. - *Die Küste* 11: 1-33.
- Leatherman, S.P., 1982. *Barrier Island Handbook*, 2nd edition: 109 pp.
- Schäfer W. 1941. Mellum, eine Düneninsel an der deutschen Nordsee-Küste. - *Abhandlungen der Senckenbergischen Naturforschenden Gesellschaft* 457: 34-54.
- Schäfer W. 1954. Mellum: Inselentwicklung und Biotopwandel. - *Abhandlungen des naturwissenschaftlichen Vereins zu Bremen* 33 (3): 391-406.
- Schütte H. 1905. Ein neu entstandenes Düneneiland zwischen Aussenjade und Aussenweser. - *Jahrbuch des Vereins für Naturkunde an der Unterweser* 1903/1904: 31-42.
- Veen J. van 1950. Eb- en Vloedschaar systemen in de Nederlandsche Getijwateren. - *Tijdschrift van het Koninklijk Nederlandsch Aardrijkskundig Genootschap, Tweede Reeks* LXVII: 303-325.
- Wunderlich F. 1979. Die Insel Mellum (Südliche Nordsee): Dynamische Prozesse und Sedimentgefüge. I. Südwatt, Übergangszone und Hochfläche. - *Senckenbergiana maritima* 11 (1/2): 59-113.

Methodical and Structural MSS and TM Investigations in the Swabian Alb, SW Germany

R. Stellrecht & A. Hoydem
Geological Institute, Karlsruhe

H. Kaufmann & W. Weisbrich
Institute of Photogrammetry and Remote Sensing, Karlsruhe, FR Germany

Synchronous records of MSS and TM data of the middle Swabian Alb are compared with each other and with geological field data; the structural features known from field investigations are also presented in both satellite data direction roses. TM images give better details than MSS. Geodynamic statements in the investigated area are scarcely possible. In future, comparative work will have to be done with data of different seasons and from sensors with higher ground resolution and a data acquisition suitable for stereoscopic evaluation.

Introduction

For comparative structural and geological setting analysis of different resolving satellite data and field measurements, a section of the Middle Swabian Alb (SW-Germany) and the foreland adjacent to the North has been chosen (Fig. 1), which in the last years has been worked on by a number of field investigations of the Geological Institute of the University of Karlsruhe. These recent papers (Schimmel 1984; Hoydem 1985; Prestel 1985; Spangenberg 1986; Holler-Kracht 1987) examined especially the microtectonic structural inventory in this region. The results are therefore suitable very well for comparing field and satellite data. A similar comparison for the Eastern Swabian Alb is given by Bayer (1982).

The foreland of the Swabian Alb is built up by predominantly incompetent series of claystones of Lower to Middle Jurassic age which intercalate with limestone and sandstone sequences of low thickness. In the range of the Swabian Alb itself morphology is determined by competent limestones with intercalated marls and clays of Upper Jurassic age.

Structurally the investigated area belongs to the so-called South German Block, which was postjurassically subjected to a highly differentiated strain evolution, especially by the collision of the African and Eurasian plates. Thus, for example, a stress field under 120° (Schramm 1967; Hoydem 1985) of Cretaceous age is followed by a horizontal strain directed 20° in the Lower Tertiary which lead to the formation of the Upper Rhine graben.

As in situ stress measurements (Greiner 1978) and investigations of fault plain solutions of earthquakes (Schneider 1980) have indicated, the recent stress field has been directed 140° since the Upper Pliocene (Illies 1978). The rejuvenation of old motion courses complicates the interpretation of the structural pattern found in field and in the satellite data.

Several regional mega-structures lattice in the region of the 'Uracher depression' which is known for geothermal and seismic anomalies, e.g. the Swabian lineament, the Filder graben and the so-called Teck fault. Moreover the area is cut by more than 350 volcanic dikes and pipes of Upper Miocene age (Mäussnest 1974).

Processing and Elaboration Method

The investigations were carried out on the basis of multispectral data of the Landsat-5 sensors. Synchronous records of the Multispectral Scanner (MSS) and Thematic Mapper (TM) from 7 July 1984 were available. For elaboration a section of about 1800×2200 pixels in the southwestern Stuttgart region (Fig. 1) was taken from the whole scene (path 195; row 26).

A sensible, methodic comparison in respect to the explorability of structural geologic phenomena with the given different ground resolution (MSS - 80 m; TM - 30 m) seemed to be granted only by the use of almost similarly centred channels. For this reason the spectral

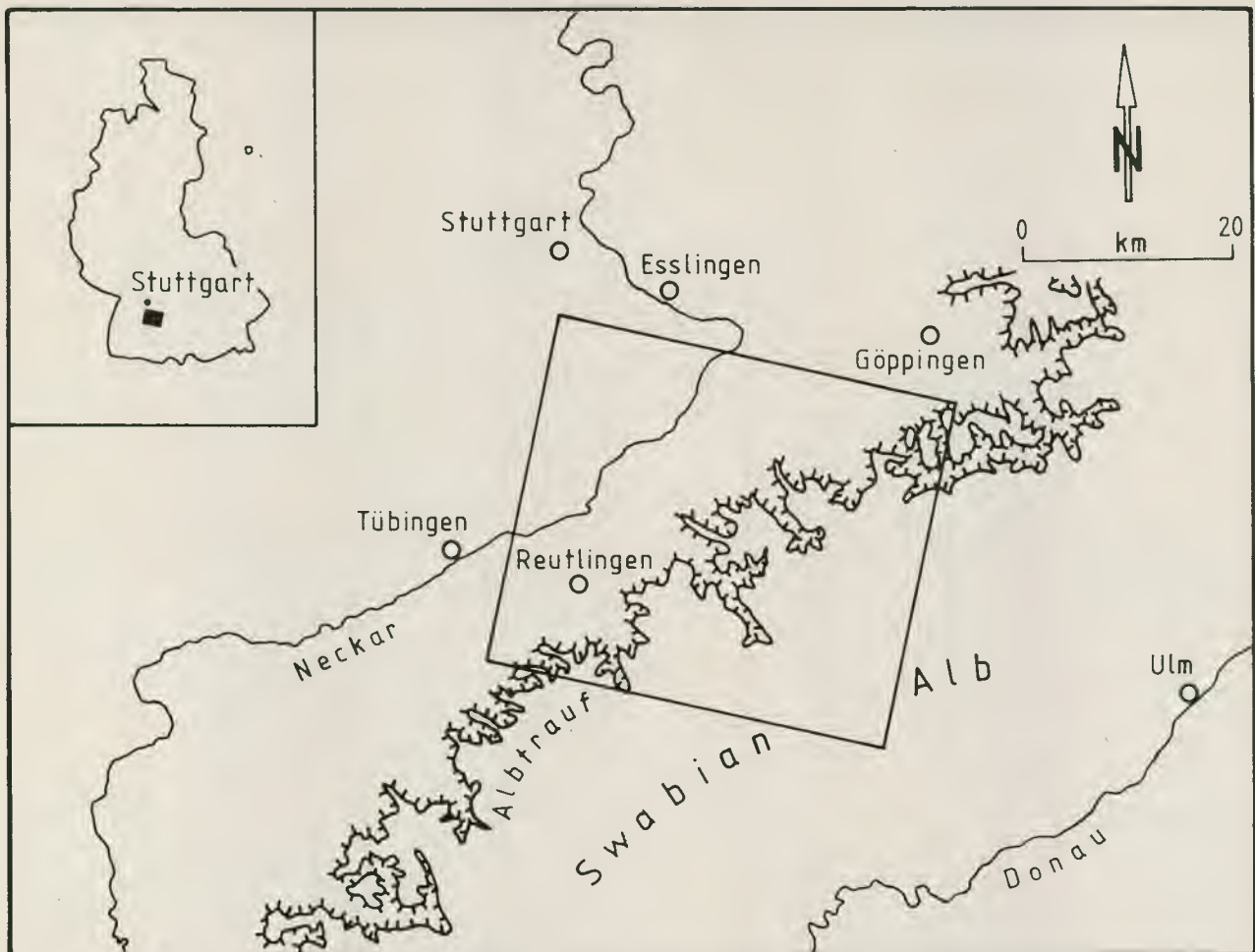
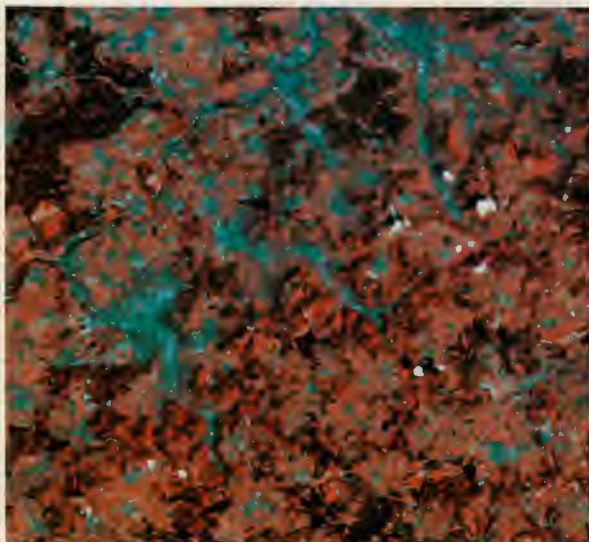


Figure 1. Area of investigations (framed) SW of Stuttgart.

ranges green, red and near infrared (NIR) (MSS-4, 5, 7 / TM-2, 3, 4) have been used for the colour composites of Figures 2 and 3.

Before normalising the histograms of the single colour extracts, filter procedures (Box-can filter) had been used.

Figure 2. MSS scene of the framed area of Figure 1.



The local frequency filtering is a computing operation which makes it possible to separate the frequencies of a scene with its complex light-dark variations into high-pass and low-pass characteristics (Chavez *et al.* 1977). With the spatial filtering each pixel element is brought into relation to its neighbouring values. With a filter matrix

Figure 3. TM scene of the framed area of Figure 1.

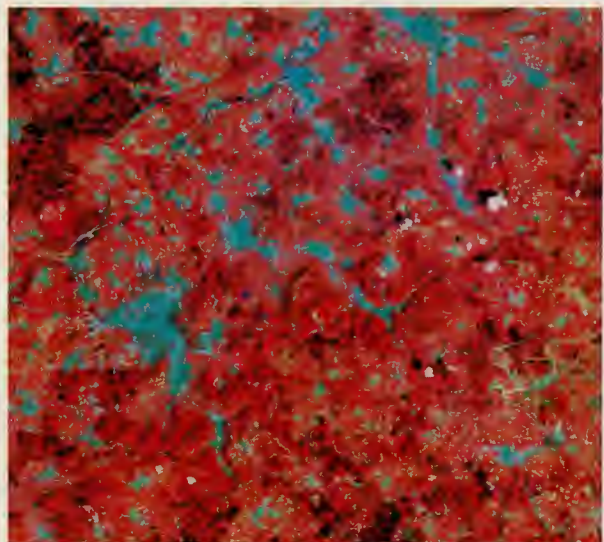




Figure 4. MSS band 7 original.

of 3×3 pixels the central pixel value is replaced by the mean value (low-pass), computed from all nine image points and is subtracted from its corresponding value in the original scene (high-pass). To enhance the spatial contrast of the original scene (Fig. 4) the high-pass values were added to the original scene (Fig. 5).

The choice of filter size enables structures of different extent to be suppressed or enhanced (Fig. 6a, b, c). In the case in question, a small filter matrix (3×3) was used for two reasons. Smaller structures are suppressed by the low-pass characterization of the sensors and bigger structures can also be recognized well even without filtering. On the other hand, when bigger filter matrices are used, the albedo properties of the different surfaces occur increasingly besides the wanted effects, which are displayed by 'light-shadow zones' along their borders (Kaufmann 1985).

Figure 6a. MSS band 7, hipass 7×7 matrix.

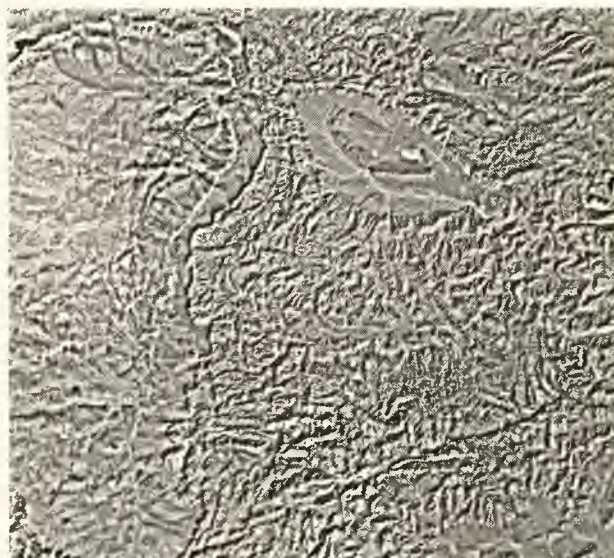


Figure 5. MSS band 7+hipass. Date of acquisition: 15.11 Zenaga/Anti-Atlas, Morocco (Kaufmann, 1985).

An edge-enhancement can also be achieved by the use of direction filtering methods. Depending on the direction, artefacts occur which strongly falsify a complete lineament mapping (Sabins 1986). The position of the sun at the acquisition time has an important influence on the recognisability and on the evaluation and interpretation of structural geological phenomena.

As can clearly be seen from Figures 6c and d, lineaments parallel to the incoming radiation direction are under-represented, those perpendicular to the sun azimuth can be seen especially in November, a fact, which essentially can be traced back to an interrelation between the azimuth and the sun elevation. With a statistical delineation of structural elements (lineaments) from data, which were recorded in different seasons, the maxima agree with each other to a large extent, yet their intensity varies according to the radiation angle.

Figure 6b. MSS band 7, hipass 15×15 matrix.



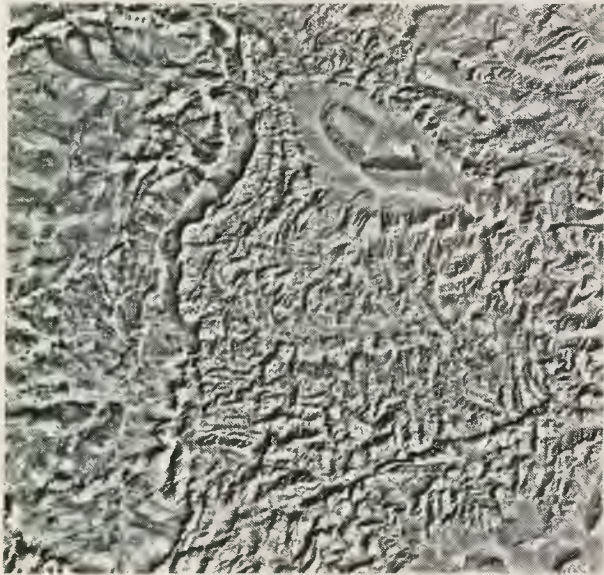


Figure 6c. MSS band 7, hipass 31×31 matrix. Nov., elev. 33°, azim. 144°.

For the investigations, ESA/Earthnet provided a data set of summer time (el: 56°/az: 131°). The evaluation of the different pixels was carried out visually with respect to structural geological and lithological units separately. All lineaments delineated after O'Leary's definition were digitised and printed in roses according to number and total length. The field data necessary for the comparison were taken three-dimensionally, digitalised and converted to three- and two-dimensional presentation by the GELI-program.

Interpretation

For the area of investigation (Fig. 1), lineaments were

Figure 7. Direction rose from 1943 lineaments, MSS, complete research region.

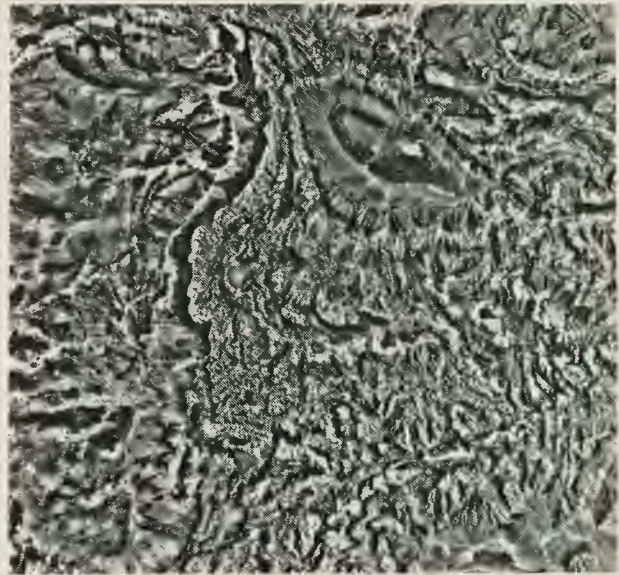
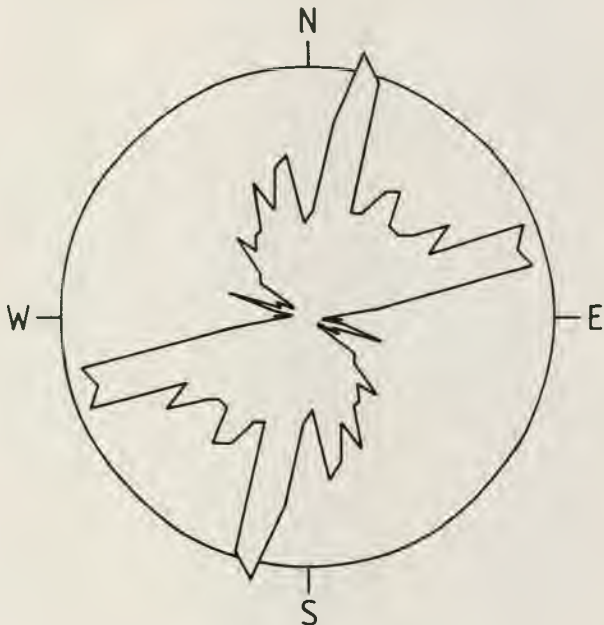
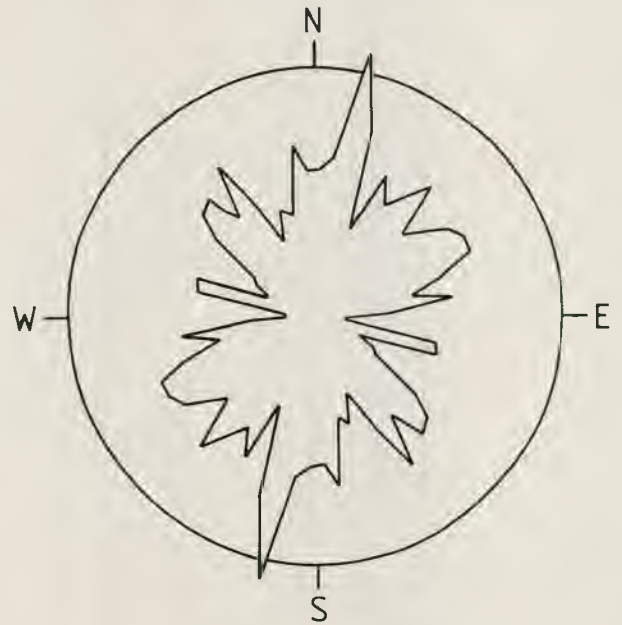


Figure 6d. MSS band 7, hipass 31×31 matrix. Jul., elev. 55°, azim. 94°.

presented as rose diagrams from a MSS and a TM scene; lineament diagrams of the whole area (Figs. 7-8), of interpreted lineaments (Fig. 9), of the foreland area (Figs. 10-11) and the Swabian Alb itself (Figs. 12-13).

Rose diagrams of lineaments from the southern part of the Filder graben (homogenous area at the northern rim of the scene), interpreted from TM data, were evaluated according to their number and length (Figs. 14-15). The lineaments derived from MSS and TM scenes took roughly the same amount of time to determine. In general the number of structural elements shows that the higher-resolution TM data are superior to the MSS data for this kind of structural-tectonic evaluation. The lineament roses of MSS and TM data of the whole area (Figs. 7-8)

Figure 8. Direction rose from 2513 lineaments, TM, complete research region.



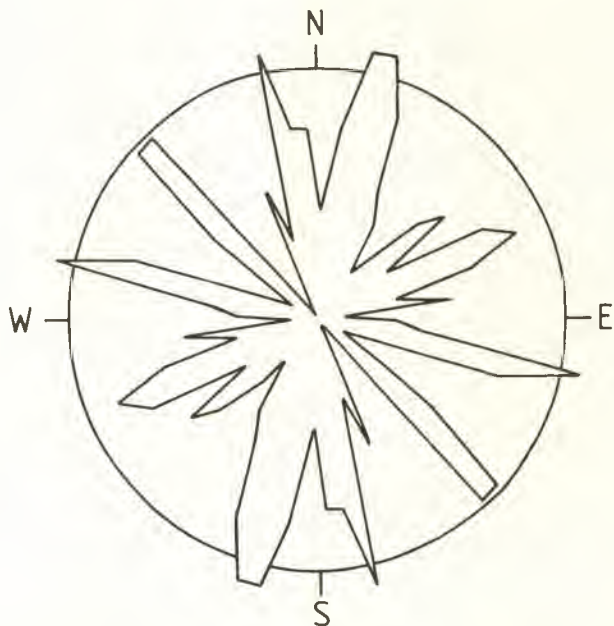


Figure 9. Direction rose from 183 interpreted lineaments from the TM scene.

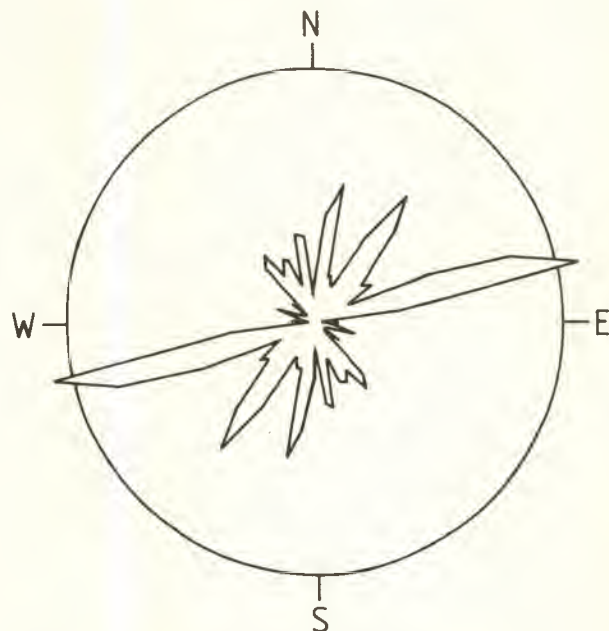


Figure 10. Direction rose from 609 lineaments, MSS, pre-Swabian Alb region.

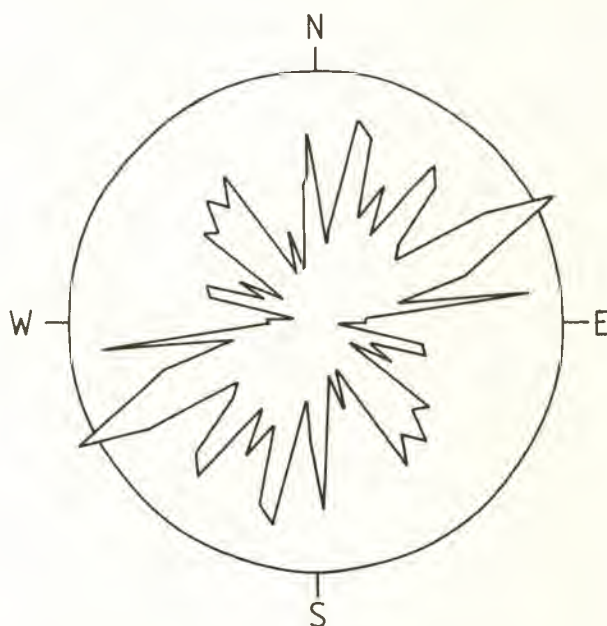


Figure 11. Direction rose from 771 lineaments, TM, pre-Swabian Alb region.

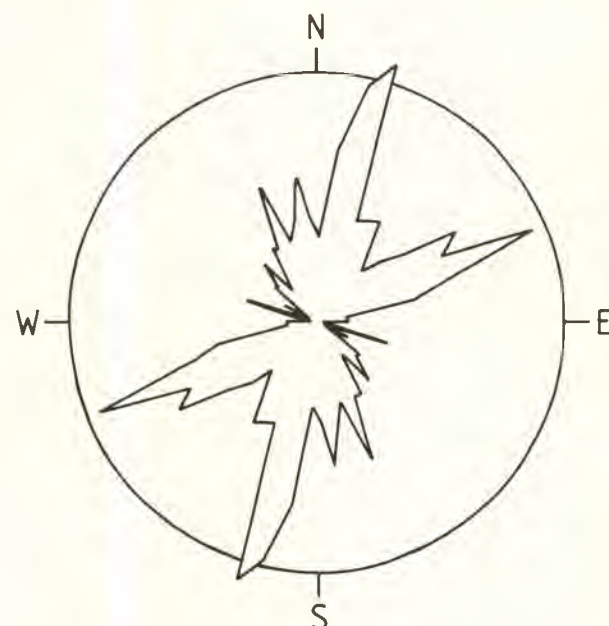


Figure 12. Direction rose from 1190 lineaments, MSS, Swabian Alb region.

show the maxima of all important tectonic directions known from our geological field investigations in this area.

Comparisons of the MSS and TM data

A comparative evaluation of the MSS and TM data of the whole area (Figs. 7-8) clearly shows the higher content of information of the TM data. In the method of evaluation

used which depended on the length of the lineaments, the maxima mostly contrast more clearly than in comparable

evaluations which involved the number of lineaments. Especially mega-structures around 15° , 45° , 70° and 170° become distinct in the MSS scenes. The emphasis of maxima for 15° in the MSS data (Fig. 12) in contrast to the TM data (Fig. 13) is probably caused by the coarser resolution of MSS-data which can lead to an overemphasis of directions ('pixel lineation'). In general the distribution of the direction maxima is more regular in TM lineation analysis. Analysis of MSS data leads to less lineaments which seem to be longer due to the coarse resolution. An interpretative analysis of TM data is important for the determination of main directions of lineaments; the rose diagram constructed from long

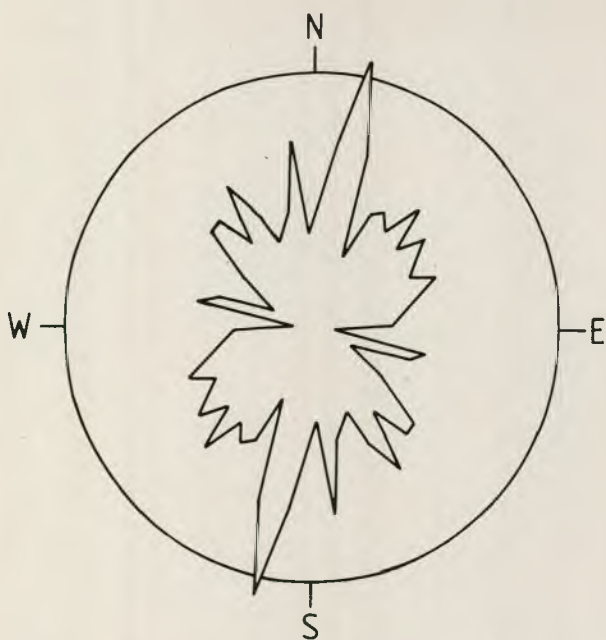


Figure 13. Direction rose from 1674 lineaments, TM, Swabian Alb region.

lineaments only (Fig. 9) shows all structural directions strongly emphasized which are also of importance in field.

Comparison of satellite data with field investigations

In contrast to its foreland the Swabian Alb itself offers good possibilities of comparing satellite lineaments with field indications due to its good exposures. More than 50 000 structural values have been measured and analysed in the area of investigation. The analysis of all normal faults, strike-slip faults and horizontal stylolites found in the field was especially emphasised. Due to the mutual superposition of the single tectonic elements a multi-phase relative age succession of the structural evolution of the Swabian Alb could be detected with the help of stylolites as paleostress indicators (Bergerat 1985; Hoydem 1985).

The satellite data were evaluated section by section both on the basis of petrographic competence (Figs. 10-13) and of structural properties (Figs. 14-15). In general the TM presentation results in a more complex image of directions. The broader mean error of less important maxima in the TM roses (e.g. Figs. 10-11) can be attributed to the higher resolution of the TM data. With it more and smaller structural details can be detected and the lineament-roses become more vivid. The possibility of correlating lineament frequency with the maxima of microstructures recognised in the field is significant. The structural field data in the papers cited are presented in three-dimensional diagrams. Analysis of these data had

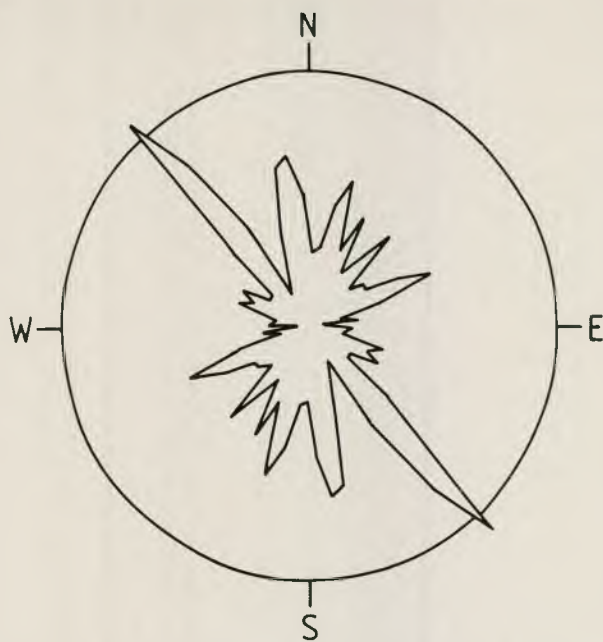


Figure 14. Direction rose from 534 lineaments (in regard of their length), TM, Fildergraben region.

been incorporated in these investigations, but they are not shown here.

In the Swabian Alb the MSS analysis (Fig. 12) emphasises lineaments directed NNE and ENE, the TM analysis also contrasts maxima in 45° , 100° and 130° direction. Regional mega-structures like the Swabian lineament in 70° direction are emphasized out of proportion by the small resolution of the MSS scenes. The discrepancy of maxima directed ENE in the MSS-rose diagram with 77° and in the TM-rose diagram with 62° measured in the pre-Swabian Alb region remains unsolved (Figs. 10-11).

By means of field investigations the following relative age sequence of stress field direction was found: $120-130^\circ$ (post-Tithonian) - 20° - 45° - 70° - 140° (Recent).

Directions of $120^\circ-130^\circ$ are clearly visible both in the satellite scene and in the field. In the field they are mostly represented by relatively large normal faults with shallow dip. In the example of the so-called Jusi fault (southwestern marginal fault of the Filder graben) especially accompanying loosening zones draw attention in the TM scene, but the fault itself cannot be recognised clearly in the TM data. Older faults can simply be recognized in the satellite data if they have been reactivated by younger horizontal superpositions. In this case a geodynamic interpretation without field investigations is not possible.

Structures directed 10° to 20° are the most frequent both in the field and in the satellite scenes. Bundles of NNE-joints which appear as maxima of first or second order

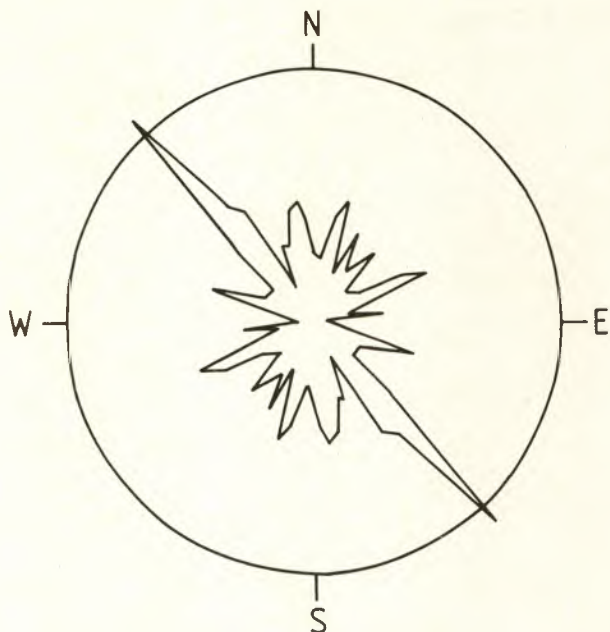


Figure 15. Direction rose from 534 lineaments (in regard of their number), TM, Fildergraben region.

form an important maximum of satellite image lineaments. Moreover a number of larger normal faults are found in 10° – 20° directions with fault throws of up to 40 m (e.g. Neuffener and Teck fault). These old faults which presumably were active in Eocene times have been used several times as shear planes, most recently in the Upper Pliocene.

The 45° direction which is not so emphasized in the TM scene is represented in the field mainly by horizontal stylolites with direction maxima of first or second order, normal faults in 45° are rare and have only small amounts of throw.

The Swabian lineament striking about 70° is one of the most important structural elements in this area. It consists of a system of normal faults which in places are horizontally superimposed.

The Swabian lineament, which is located geographically in the foreland of the Swabian Alb, is characterized in the TM data (Fig. 11) by the strong maximum in 70° . In the TM rose of the Swabian Alb (Fig. 13) this direction is underrepresented. This fact is an important hint to the importance of limiting the test areas.

The maximum of lower order in the 70° direction which can be recognised in the region of the Swabian Alb can occasionally be attributed to newly found accompanying faults with low throw (e.g. the Bauerloch fault). NNE-lineaments around 80° can be recognized locally as strike-slip zones in field. The stopping of normal faults directed ENE along faults striking about N in field (e.g. along the Teck fault) as well as in the satellite scene suggests that the 70° faults are older.

In the TM satellite scene the 140° direction contrasts clearly in the area of the Filder graben (Figs. 14-15). Normal faults running SE are numerous, but of old structure. A young reactivation could only be proved in the form of horizontal shifts.

Critical review and prospects

The structural analysis of satellite images seems to be promising if the satellite data can be compared with field measurements. The synopsis of motion to high resolving imagery gives a better overview of strike, length and general patterns of structural elements, which however in most cases could only be characterised in detail (e.g. slickensides) by field measurements. Due to the smaller ground pixel size of TM, these data could be used for delineation of especially fine structural elements. To elaborate small-scale features over large areas, the MSS data will be sufficient. In future, stereoscopic data as provided by the French SPOT system will be investigated. Although one can expect improvements in elaboration of structural elements, geodynamic conclusions can be drawn in only a very limited way from satellite data. The low amounts of displacement along the faults in the investigated area allow a statement on the course of motion and an age succession of fault systems in only a few places; normally such geodynamic statements can only be made on the basis of field investigation.

In the investigation discussed here, the whole area was subdivided into parts whose different lithologic and structural behaviour was known from field experience. Additional work will aim to filter ranges of uniform structure by lineament direction roses by aimed subdivision of a bigger region of unknown structure, to work with different remote sensing data and with data from different seasons.

Literature

- Bayer H.-J. 1982: *Bruchtektonische Bestandsaufnahme der Schwäbischen Ostalb (Geländeuntersuchung, Luftbild- und Satellitenbildauswertung)*. Thesis Univ. Clausthal, 235 p., 88 fig., supplement., Clausthal.
- Bergerat F. 1985: *Déformations cassantes et champs de contrainte tertiaires dans la plate-forme européenne*. *Mém. Sci. de la Terre*, Univ. M. Curie, Paris, 317 p., Paris.
- Chavez P.S. Jr, Berlin G.L. & Acosta A.V. 1977: Computer processing of Landsat MSS digital data for linear enhancement. Mapping with remote sensing data. *Proc. Sec. An. Pecora Mem. Symp.*, Sioux Falls, South Dakota, 235-250.
- Greiner G. 1978: *Spannungen in der Erdkruste: Bestimmung und Interpretation am Beispiel von in-situ Messungen im süddeutschen Raum*. Thesis Univ. Karlsruhe, 191 p.

- Holler-Kracht P. 1987: *Geologische und tektonische Gelände aufnahme südwestlich von Erkenbrechtsweiler (mittlere Schwäbische Alb)*. Diploma thesis, Geol. Inst. Univ. Karlsruhe, 104 p.
- Hoydem A. 1985: *Geologie und Tektonik des mittleren Lenninger Tals (Schwäbische Alb)*. Diploma thesis, Geol. Inst. Univ. Karlsruhe, 259 p.
- Illies J. H. 1978: Two stages Rhinegraben rifting. In: Ramberg & Neumann (Eds.): *Tectonics and geophysics of continental rifts*, 63-71, Reidel, Dordrecht.
- Kaufmann H. 1985: *Rechnergestützte methodische Untersuchungen multispektraler und multitemporaler Satellitenbilddaten (Landsat/HCMM) für geologische Fragestellungen am Beispiel Anti-Atlas, Marokko*. Thesis Univ. München, 158 p.
- Mäussnest O. 1974: Die Eruptionspunkte des Schwäbische Vulkans. *Z. dt. geol. Ges.*, 125: 23-54; 277-352, Hannover.
- O'Leary D.W., Friedman J.D. & Pohn H.A. 1976: Lineament, linear, lineation: some proposed new standards for old terms. *Geol. Soc. Am. Bull.*, 87: 1463-1469.
- Prestel R. 1984: *Stratigraphie, Vulkanismus und Tektonik nördlich von Bad Urach (Schwäbische Alb) mit einem Anhang über Laevaptychen*. Diploma thesis, Geol. Inst. Univ. Karlsruhe, 212 p.
- Sabins F.F. Jr. 1987: *Remote sensing*. 2nd ed., 449 p., Freeman, New York.
- Schimmel A.I. 1984: *Bruchtektonisch-vulkanologische Bestandsaufnahme SE Grabenstetten (Schwäbische Alb)*. Diploma thesis, Geol. Inst. Univ. Karlsruhe, 167 p.,
- Schneider G. 1980: Das Beben vom 3. Sept. 1978 auf der Schwäbischen Alb als Ausdruck der seismotektonischen Beweglichkeit Südwestdeutschlands. *Jber. Mitt. oberrhein. geol. Ver.*, 62: 143-166, Stuttgart.
- Schramm S. 1967: *Klüfte und Horizontalstylolithen in der südlichen Frankenalb und ihre Stellung in der jüngeren Tektonik Süddeutschlands*. Thesis Univ. Würzburg, 87 p
- Spangenberg H. 1986: *Die Geologie des Südteils von Blatt 7422 Lenningen unter besonderer Berücksichtigung der Tektonik*. Diploma thesis, Geol. Inst. Univ. Karlsruhe, 533 p.

Landsat TM Data Used in the Mapping of Large-Scale Geological Structures in Coastal Areas of Trøndelag, Central Norway

Bjørn Rindstad & Arne Grønlie

Geological Survey of Norway, Trondheim, Norway

Landsat-5 Thematic Mapper data have been used to map linear structures in coastal areas of Trøndelag, Central Norway. Both standard B/W photographs and digital data were employed. Digital image processing of TM data gives more information than with B/W photographs, especially in areas with extensive soil cover. The image processing utilised consists of linear stretching of individual TM channels and generation of colour composites. TM imagery has proved useful for detailed interpretation of geological structures. Compared with MSS-data, the TM data yields more information about structures less than 5 km in length, which means that TM can provide considerably more information about bedrock foliation than MSS, and this makes it a lot easier to distinguish foliations from fracture/fault related lineaments. For structures with a length of 1 km or more, TM provides nearly as much information as high-altitude aerial photographs. When interpreting large geological structures from TM data, using every second or third pixel is an advantage when employing image-processing systems with colour monitors limited to 512×512 pixels. This gives a synoptic view of larger areas, which is the major advantage of using satellite remote-sensing imagery. An image-processing system suitable for TM data should at least be able to display 1024×1024 pixels on a colour monitor.

Introduction

Satellite remote sensing is a widely used and potentially powerful tool in the mapping of large-scale geological structures. The Multispectral Scanner (MSS) (Sabins 1978; Lillesand & Kiefer 1979) onboard the Landsat satellite series is familiar to many geologists but, unfortunately, the poor resolution of the scanner has minimised its use. Beginning with the Landsat-4, however, the Thematic Mapper (TM) (Longdon 1984) instrument delivered data with improved resolution, thus allowing for better identification of both large-scale and small-scale structural features not previously detectable. The TM sensor onboard Landsat-4 failed in 1983 after less than one year of operation, having recorded only a few hundred scenes.

Landsat-5 was launched in March 1984 and is still operative, recording almost 150 scenes per day. The orbit of Landsat-5 is quasi-polar, at an altitude of 705 km, and global coverage is completed in 16 days.

The amount of data has increased considerably from MSS to TM, because of an increase in the number of spectral bands (4-7 channels), in radiometric resolution (64-256 digital levels) and in geometric resolution (80-30 m). Compared to a MSS scene that contains ca. 180 Mbits of information, a TM scene contains ca. 2000 Mbits and covers the same area.

Compared with the MSS instrument, TM has two additional channels in the reflected infrared area and one channel in the thermal infrared area (Fig. 2). The thermal channel has a resolution of 120×120 m. The geometric resolution or pixel size of TM is 30×30 m compared to 56×79 m (Sabins 1978, 233) for MSS. The TM sensor has a swath width of 185 km. The principal use of TM is in the mapping of vegetation, soil, bedrock and water quality.

This paper presents the results of a remote sensing investigation based on digital image processing of Landsat TM-data. The study started in 1985 and has previously been described in two NGU reports by Rindstad *et al.* (1985) and Rindstad & Grønlie (1986). The aim of the study was to evaluate the benefit of digital Landsat TM data used in the mapping of geological structures. In particular, the work aimed to compare TM data with older Landsat MSS data from the same area, and to compare the results of a digital approach with an interpretation based on standard B/W photoproducts from the same Landsat scene.

Three test areas within the same TM scene (Fig. 1) were chosen for trying out the TM sensor's suitability for structural mapping, with special emphasis on fracture-related lineaments, and also its suitability for

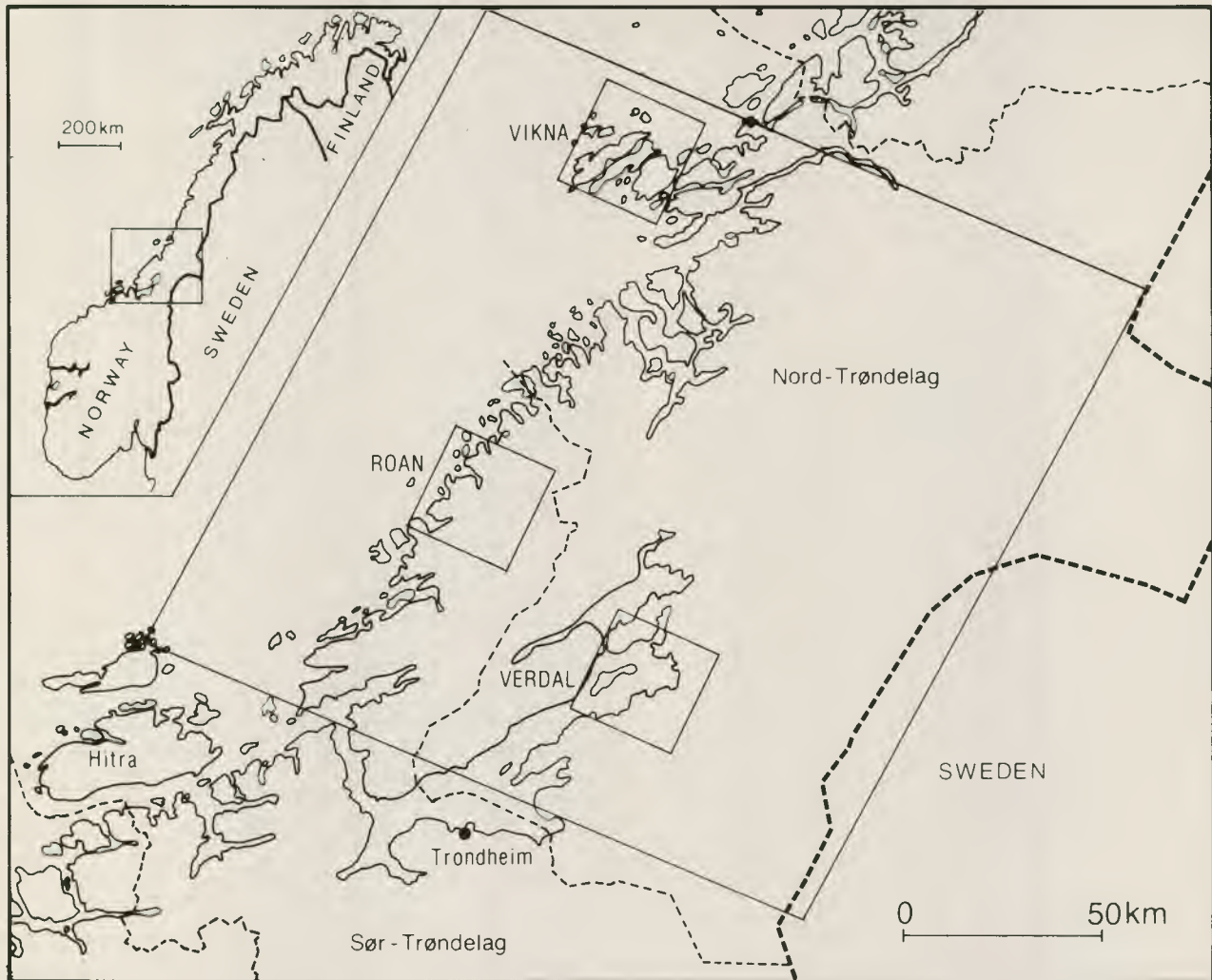


Figure 1. The subareas Vikna, Roan and Verdal, discussed in the text, area indicated. Each subarea is 30×30 km. Location map showing the area covered by Landsat TM scene 50204-10063, taken 21. Sept. 1984.

distinguishing bedrock foliation from other lineaments. Two of the test areas, Vikna (Fig. 3a) and Roan (Fig. 3b), are located on the coast of Trøndelag, in a region of comparatively poorly known geology covered only by reconnaissance mapping in connection with the compilation of the 1 : 1 000 000 bedrock map of Norway (Sigmond *et al.* 1984; see also Roberts 1986). The third area, Verdal (Fig. 3c), situated inland in Nord-Trøndelag, is geologically better known and was chosen as a reference area. Subsequently a lineament interpretation, based on a black-and-white image has been attempted for the entire TM scene, covering the coastal areas of Sør- and Nord-Trøndelag from Ørlandet to Vikna (Fig. 6).

Digital image processing

Data from one TM scene is stored on seven 2400-ft magnetic tapes and their administration is quite time-consuming, especially the reading of data from tape to disc. The investigated scene has reference number 50204-10063 and was recorded on 21 September 1984.

It has a low radiometric quality because of the low sun angle (24°). The best radiometric quality was found on channels 4 and 5 followed by channels 1 and 7, whereas channels 2 and 3 had the lowest radiometric quality. For geological applications, channel 4 was found most suitable, but channels 3, 5 and 7 were also useful. The eastern half of the TM scene is generally cloud-covered, but the western part is devoid of atmospheric haze.

As the TM has quadric pixels, there was no need for any geometric rectification of the data prior to the geological evaluation as is the case for the MSS.

During the digital image processing several techniques for image enhancement were used. These techniques have been described by several authors (among them Sabins 1978 and Lillesand & Kiefer 1979). Most of the techniques were performed on an image of 512×512 pixels, which for TM data covers an area of ca. 15×15 km on Earth. This area, however, is too small for detection of the largest lineaments. To be able to view larger areas, a reduction in the number of pixels was necessary. Two methods of data reduction were tried; pixel averaging and

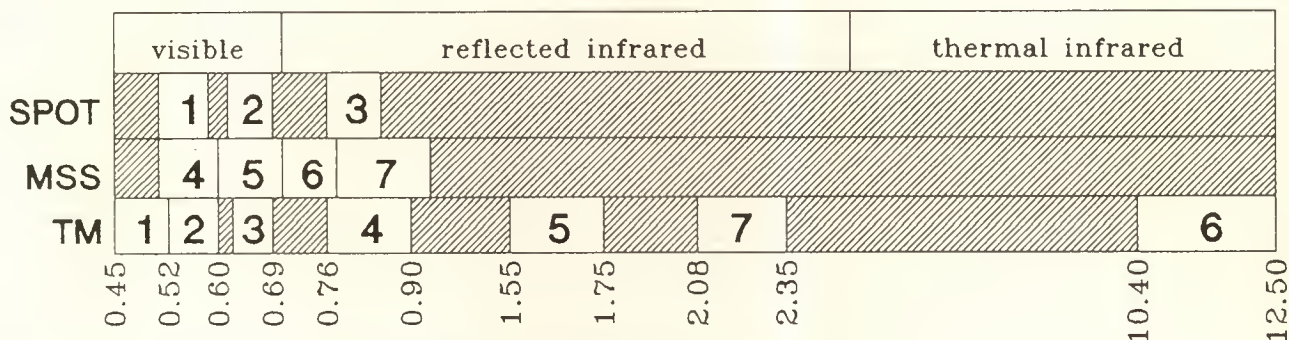


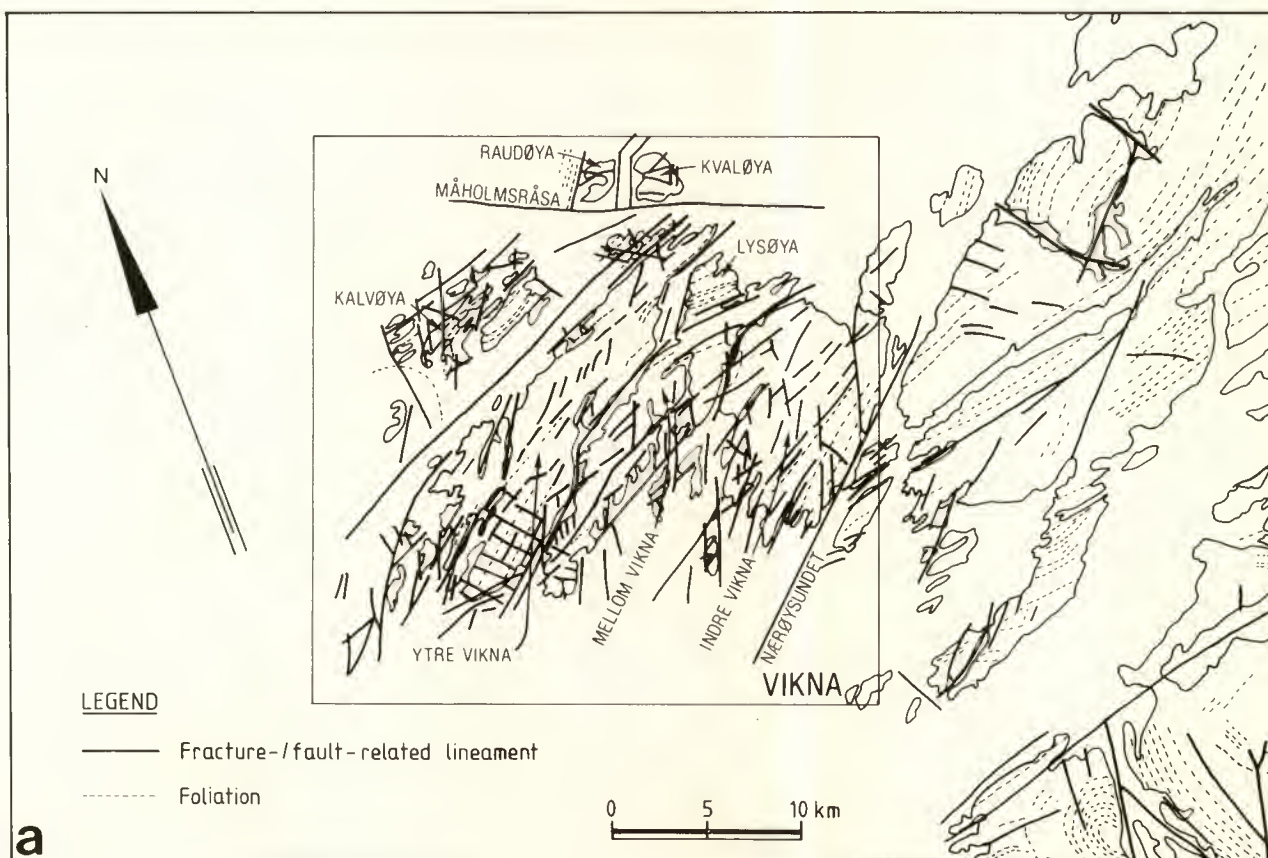
Figure 2. The spectral bands of SPOT and Landsat MSS and TM (wavelength in micrometres).

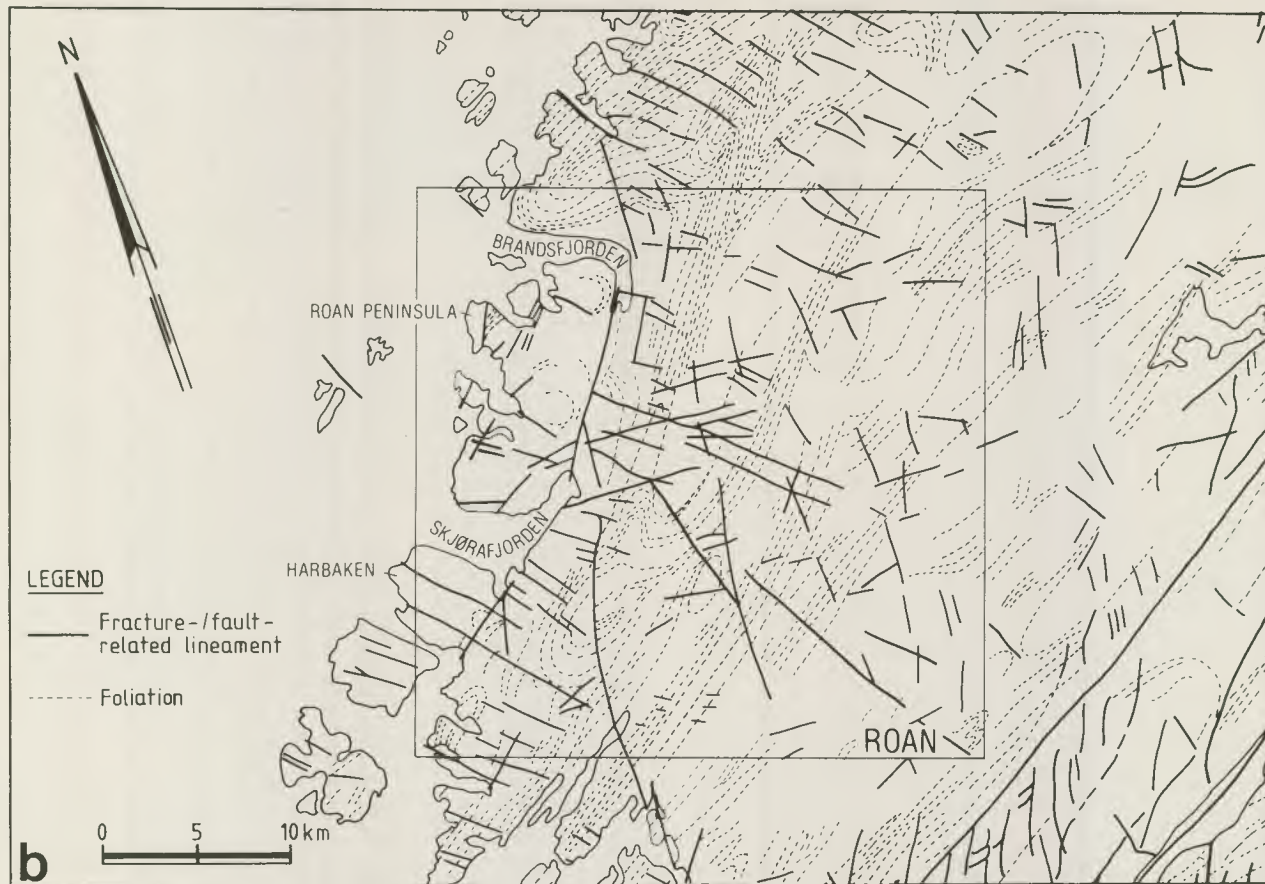
pixel skipping (Gonzalez & Wintz 1977). Pixel averaging allows, for example, 2x2 pixels to be represented by the average value, while in pixel skipping these same 2x2 pixels are represented by just one of the pixels. The latter method is the faster of the two and as the result is as good as without data reduction, this method was therefore chosen for this investigation. The resolution of the pixel is still 30 x 30 m, even though each pixel represents an area of 60 x 60 cm.

Thus, an area of 30x30 km could be displayed without losing too much information on the structural features in the image area. This was checked by analysing a few parallel full-resolution images, but these images did not yield much more structural information than the half-

resolution images. In fact, we found that by using only every third or fourth pixel, we could obtain a synoptic view of very large areas; which favoured the recognition of large geological structures. When working with single band images, using pseudocolours (Gonzalez & Wintz, 1977) was a great improvement over shades of grey. The combination of pixels from three TM-channels into one colour composite gave an image which is superior to that of the individual bands. Three input channels were coded in shades of red, green and blue, thus creating a false colour composite. This was a rather efficient way of utilising the multi-spectral data, and more suitable for lineament mapping than more sophisticated methods such as principal component analysis. Various combinations of channels 1, 2, 3, 4, 5 and 7 were used, but the most

Figures 3a, b, c. Interpreted bedrock foliation and fracture/fault-related lineaments in the (a) Vikna, (b) Roan and (c) Verdal sub-areas. Each sub-area is approximately 30x30 km (1024x1024 pixels).





useful combinations all contained channel 4. The only necessary treatment prior to colour composite generation was linear stretching of each of the three input channels; this helped to improve the contrast of the image (Sabins, 1978; Lillesand & Kiefer, 1979).

A colour composite based on ratios between 4 input channels (Sabins, 1978) contained much information on thematic variations, e.g. differences in vegetation, bedrock, etc., but is less useful for detecting linear features. This is due to the fact that ratios remove topographic features, thus erasing linear structures. If the input channels 2, 3, 4 and 7 are used, the colour composite would be: $R=2/3$, $G=3/4$; $B=4/7$.

Interchanging the colour coding of the various colour composites was useful for detecting certain features in the image. This method is described among others by Gonzalez & Wintz (1977). Interpretation of the images was carried out by visual inspection of the colour monitor and plotting of the linear features on a base map, usually a black-and-white print of the TM scene at 1 : 250 000 scale. The colour composites with the most information were then reproduced on positive colour film by using a Matrix-3000 video-tube.

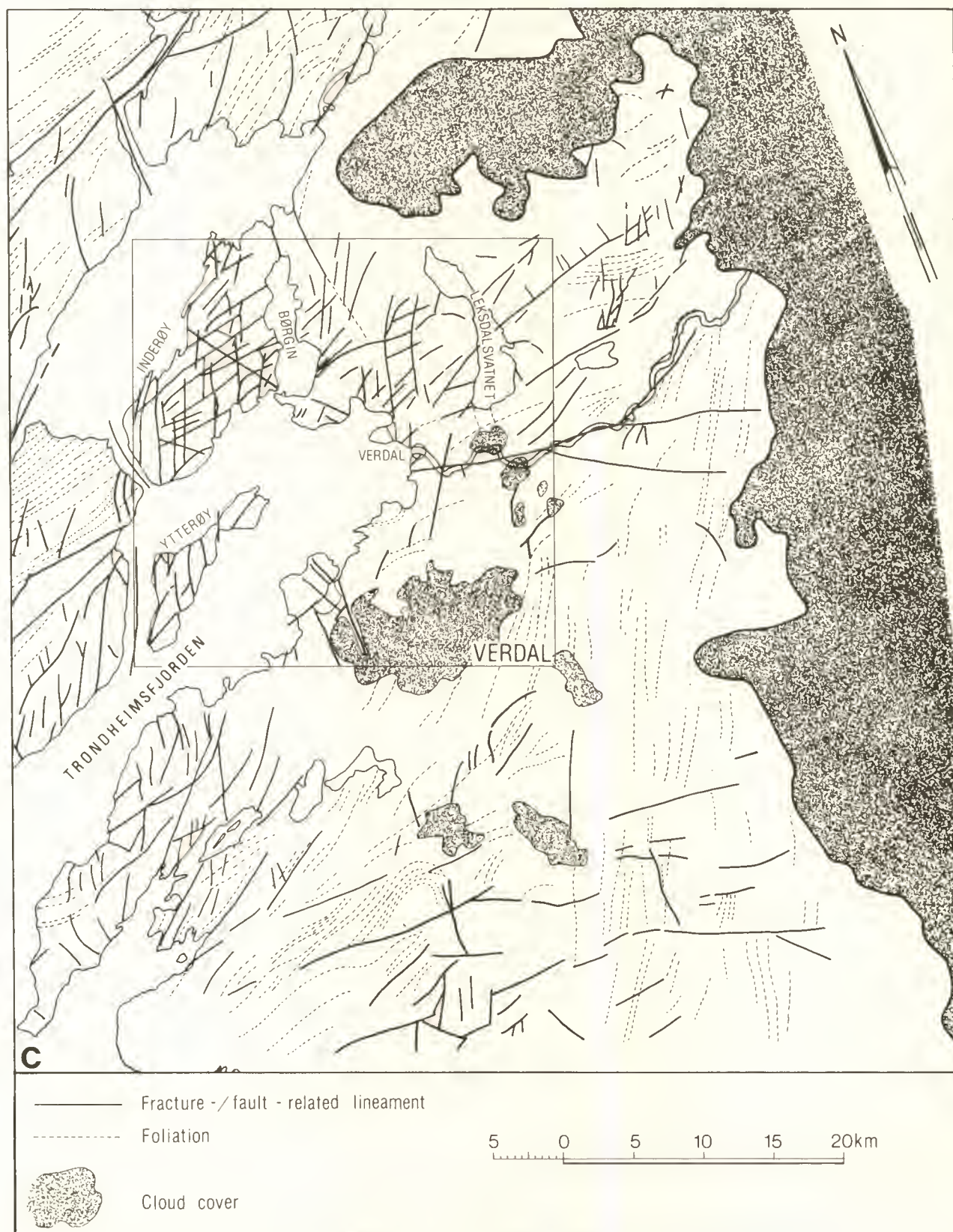
A synoptic view of large areas is the major advantage of using satellite remote-sensing techniques. A Landsat TM scene gives the same view as a Landsat MSS-scene, but TM's improved geometric resolution makes it possible to

detect objects about one fifth the size of those detectable by MSS. As most image-processing systems can display 512×512 pixels on a colour monitor, this means that with MSS-data with a pixel size of 80×80 m one can display an area of 40×40 km, and with TM an area of 15×15 km. The conclusion from this is that an image-processing system suitable for TM data should at least be able to display 1024×1024 pixels on a colour monitor. Thus, one can also take full advantage of the TM's high resolution and at the same time have the same synoptic view of large areas as with Landsat MSS.

Structural geology

Introduction

A lineament can be defined as a linear feature visible on the Earth's surface or seen on a satellite image. The lineaments may be surface expressions of geological structures such as faults, bedrock boundaries, bedrock foliation, crush zones, etc. which are of great importance for the geologist. The mapped lineaments from the three test areas were digitised and analysed on a Hewlett Packard 3000 computer at the Geological Survey of Norway (NGU). The software system for handling the lineaments was developed at NGU (Rindstad & Follestad, 1982) and can produce a variety of discrimination diagrams including histograms, rose diagrams, sector maps and gridded maps.



The Trøndelag area has received attention in a number of regional Landsat MSS lineament studies some of which have also attempted to integrate their interpretation with published geophysical, magnetic and gravity data. Among the principal contributors are Ramberg *et al.*

(1977), Gabrielsen & Ramberg (1979), Gabrielsen *et al.* (1981), Aanstad *et al.* (1981) and Offield *et al.* (1982). Most of these studies have shown that many MSS lineaments can be correlated with fracture or fault zones. The relatively low resolution of the MSS sensor,

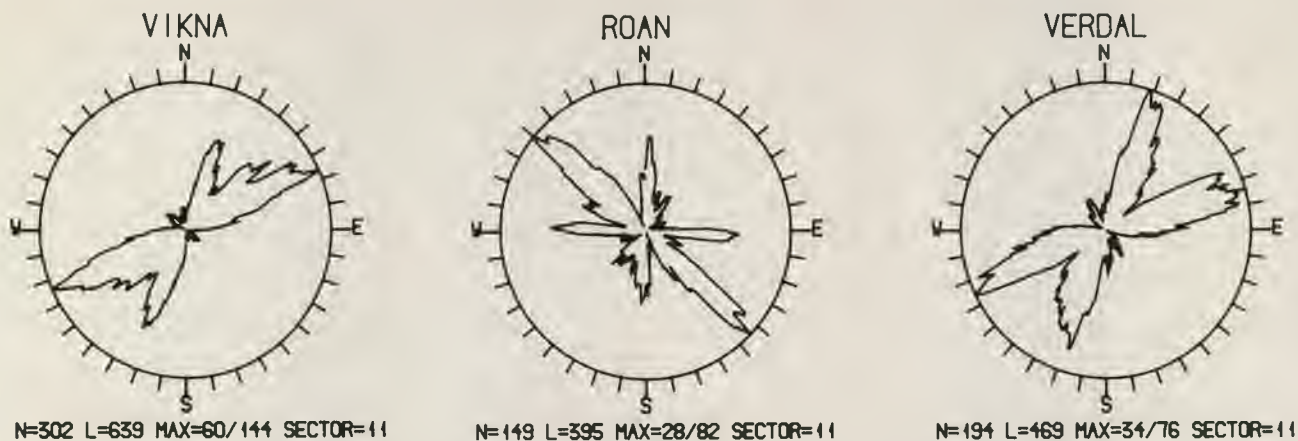


Figure 4. Lineament frequency/length diagrams for lineaments of the Vikna, Roan and Verdal subareas. The left-half of each diagram signifies frequency and the right-half, length. N=number of lineaments. L=length of lineaments in km. MAX=radius in number/km. Sector=filter size.

Figure 5. Lineament interpretation map of coastal Trøndelag based on Landsat MSS-data (channel 5 B/W image). Western square is the Roan sub-area; eastern square is the Verdal sub-area. The Vikna sub-area is only partly covered by this MSS-image.



fracture-related lineaments from bedrock foliation. In the area of southern Fosen the problem arising from a pronounced parallelism of strike-lines, fold axes, fractures and faults, noted by Aanstad *et al.* (1981), has been given special attention.

On the basis of MSS imagery and ground-based geological studies Norway has been divided into five major tectonic intensity zones, some of which are still seismically active (Gabrielsen & Ramberg, 1979). The Verdal area is situated within the so-called Møre-Trøndelag fault zone, one of the most active earthquake zones in the country.

In addition to establishing the fracture pattern of the region, Landsat imagery analysis has detected a province of major basement domes in central and northern Nord-Trøndelag north of a line drawn from Namsfjorden to Namdalseid (Offield *et al.*, 1982). Southwest of this basement dome province, between Namsfjorden and Ørland, the basement rocks of this area are characterised by a uniform, NE-SW strike which is parallel or sub-parallel to the strike of the Møre-Trøndelag fault zone (Gabrielsen & Ramberg, 1979). The basement rocks of these two areas, separated by the Namsfjorden-Namdalseid line, also have different patterns of magnetic anomalies, the southern area being characterised by alternating bands of high and low magnetisation. In the northern province, areas of strong magnetisation are mostly limited to downfolded cover sequences. A set of NW-SE trending magnetic dislocations indicate the presence of a megafault in the Namdalseid area (Bering *et al.*, 1986).

The geology of the Vestranden- Namsos region can be divided into a dominating complex of migmatitic gneisses with associated orthogneisses varying in composition from granite to tonalite and supracrustal cover sequences of metasediments, ortho-amphibolites and paragneisses (Roberts, 1986). A Middle Proterozoic formation age has been suggested for the basement gneisses with deformation, metamorphism and migmatisation occurring in the Svecofennian orogenic phase. That Caledonian deformation has later affected the Precambrian gneisses in the Fosen district is seen in tight to isoclinal folding and refolding of the allochthonous supracrustal rock and their gneissic substrate. According to Roberts (1986) most of the folds and thrusts that deform the tectono-stratigraphy are generally thought to be of Scandian (late Silurian) age apart from the late, upright NE-SW trending folds which are probably Late Devonian structures.

Main structural features

In a companion article in this volume, Roberts has presented a more detailed air-photo compilation of foliation trajectories than that of the TM interpretation. Ideally, the TM study should have been done before the air-photo interpretation, but as the TM image was not available until 1984 this was not possible.

For detailed study of bedrock foliation, air-photo interpretation is far better than TM imagery because of the higher resolution and also as one can study the photos stereoscopically. The main advantage of TM imagery over air-photos is that the TM image gives a synoptic view of a very large area, thereby facilitating detection of large-scale faults and fracture systems, as well as revealing rock structures such as large basement domes that are easily missed when using the multitude of air-photos required to cover the same area. As shown in the TM lineament and foliation interpretation (Fig. 6), this sensor also enables us to pick out the main foliation trends. Especially in the coastal areas from Ørland to Vikna, facilitated by good exposure and steeply dipping foliation, TM gives a fairly detailed picture of bedrock foliation trends.

Foliation interpretation

Looking at the coastal region from Ørland to Namsfjorden (Fig. 6), the general structural grain trends NE-SW coinciding with the main lineament trend in this area as described by Ramberg *et al.* (1977), Aanstad *et al.* (1981) and Offield *et al.* (1982). On the whole the TM interpretation in this area gives a picture which corresponds fairly well with the air-photo interpretation. A good example of this can be seen in the interpretation of the patterns of fold interference from Skjrafjorden to Namsfjorden.

The TM interpretation shows that the prominent NE-SW trend of the southern Fosen area is broken by the Namsfjord-Namdalseid line (Fig. 6), northeast of which the foliation trajectories are more variable. The TM image does not, however, provide as much information on foliation in this area as in the coastal areas to the southwest. This is due to a combination of factors such as flat-lying foliation, subdued relief and poor exposure, all of which make stereoscopic viewing a major advantage. As shown by Roberts (1986), the air-photo interpretation in this area of intricate folding gives a far better and more detailed picture than the TM interpretation.

Doming on various scales has been described by Offield *et al.* (1982) and Roberts (1986). Unfortunately most of the area of their megadomes is cloud covered on the available TM image. The smaller domes or megalenses depicted by Roberts generally do not show up very well on the TM image, although the Roan peninsula could be interpreted as a dome structure of intermediate size (Johansson, 1986). A medium-size lens (3.5 × 1.25 km) just east of the Skjrafjorden fold (Roberts, 1986) (Fig. 6) is discernible on the colour composite (Fig. 7). The smaller Granholvatnet lens north of Brandsfjorden (Johansson, 1986) is also visible.

Lineament interpretation

MSS-based lineament interpretations (Ramberg *et al.*, 1977; Gabrielsen & Ramberg, 1979) led to the definition

of the ESE-WSW trending Møre-Trøndelag fault-zone, which includes the prominent Hitra and Verran faults (Oftedahl, 1972, 1975). The Verran fault, with a vertical displacement of at least 1500 m in the Beitstadfjord area (Oftedahl, 1975) was probably active in the Middle Jurassic. Aanstad *et al.* (1981) found evidence for dextral strike-slip movements along some of the ENE-WSW trending faults of the Møre-Trøndelag fault-zone. Price & Rattey (1984) also considered that there was dextral strike-slip movement along this fault trend, and in particular during Cretaceous time. The pattern of en echelon fractures between the Hitra and Verran faults (Fig. 6) does seem to support the dextral strike-slip interpretation of Aanstad *et al.* (1981). Another feature which is indicative of the deep-seated nature of the Verran fault is the extensive crushing and intense hydrothermal alteration of the gneissic rocks exposed in road-cuts in Verabotn.

Oftedahl (1975) described the NE-SW trending running Tarva fault, limiting the Frohavet basin to the southeast, as bending eastwards in the north and continuing onshore from Osen to Namsos. The TM image and air-photos do show a prominent valley running parallel to the bedrock foliation. There are no structures indicative of strike-slip motion (Fig. 6), as is the case with the Hitra and Verran faults and if the Tarva fault does extend onshore towards Namsos this would point to a purely vertical movement.

With regard to N-S trending lineaments, the prominent Åfjord lineament (Fig. 6) was noted by Oftedahl (1975) and classified as a possible fault. This lineament has the same trend as the Fosdalen fault, which has a downthrow to the east of 600 m (Oftedahl, 1975). Recent fieldwork along the northern, curved segment of the Åfjord lineament (Fig. 6) indicates a considerable downthrow to the east. This fault cuts upright fold structures of assumed Late Devonian age (Roberts, 1986), and as it runs parallel with the supposedly Permian Fosdalen fault (Oftedahl, 1975) an age correlation is thus possible. Arguing against a Permian age is the fact that the fjord lineament does not appear to be offset by the Hitra fault, with its supposedly Middle Cretaceous strike-slip movement (Price & Rattey, 1984). It is therefore conceivable that these N-S trending faults are of Cretaceous or post-Cretaceous origin.

Aanstad *et al.* (1981) recorded a NW-SE, MSS lineament trend in the Trøndelag area. Offshore, this trend has not been found in the seismic data, perhaps because most seismic profiles have been run in the same general trend, but the NW-SE trend is obvious from the magnetic and gravimetric lineament maps. The Jan Mayen fracture zone also runs parallel to this trend (Aanstad *et al.*, 1981). According to Bering *et al.* (1986) this trend is an important magnetic dislocation trend onshore in southern parts of Nord-Trøndelag. As is evident both from the TM

interpretation (Fig. 6) and from the air-photo compilation, this NW-SE trend is particularly prominent between Ørland and Knottfjorden. Fieldwork in the Åfjord-Skjørafjord area has shown that most NW-SE lineaments represent master joints, and that only a few show evidence of minor normal faulting.

Description of three subareas

The Vikna Archipelago

The Vikna archipelago is located in the northern part of coastal Nord-Trøndelag. The bedrock on the main islands of Indre, Mellom and Ytre Vikna consists mainly of Precambrian granodioritic gneisses and migmatites that vary in their degree of deformation (Bering *et al.* 1986). The westernmost island, Kalvøya, exposes mainly high-grade metasediments (Fig. 3a).

Spectral information on the colour composite (Fig. 7) was used to map the amount and types of vegetation in the area. This information can be a subtle indicator of rock-type. The meadows of lowland areas, for example, stand out in light green because of the high response in channel 2, corresponding to the vegetation reflectance peak, between the two chlorophyll absorption bands. Similarly, nonvegetated granodioritic gneisses show a bluish tint on sunlit rock surfaces and a reddish tint elsewhere, because of the chlorophyll absorption in channel 3. Vegetation is usually sparse on granodioritic gneisses, mainly moss and heather, whereas metasedimentary rocks on Kalvøya and Lysøya, Mellom Vikna, and amphibolite gneisses on the Vikna islands are more heavily vegetated and appear dark green.

On eastern Kalvøya (Fig. 3a and Fig. 7) a synform in granodiorite is easily discernible from high-grade metasediments (Bering *et al.* 1986) due to these reflectance characteristics. The granitic rocks of the pluton on Kvaløya, north of Måholmsråsa, show a response close to that of the granodiorite-gneiss areas, but the low-lying Raudøya is heavily vegetated and gives a high channel 2 response.

A major tectonic zone, the Måholmsråsa fracture-zone (Fig. 3a and Fig. 7), separates the Vikna islands from young granitic plutons (Raudøya, Kvaløya) and a supposedly younger, low-grade, NNE-SSW trending sequence of metasedimentary rocks to the north (Bering *et al.* 1986). The Måholmsråsa fracture-zone can be seen to trend ESE-WNW on the colour composite (Fig. 7). Another important tectonic lineament, the Naerøysundet fracture-zone (Bering *et al.* 1986), can be seen running SW-NE in the eastern part of this subarea.

The bedrock in this area is deformed by tight to isoclinal upright folds with axial planes generally striking NE-SW and dipping steeply NW or SE. The strike of a set of ma-

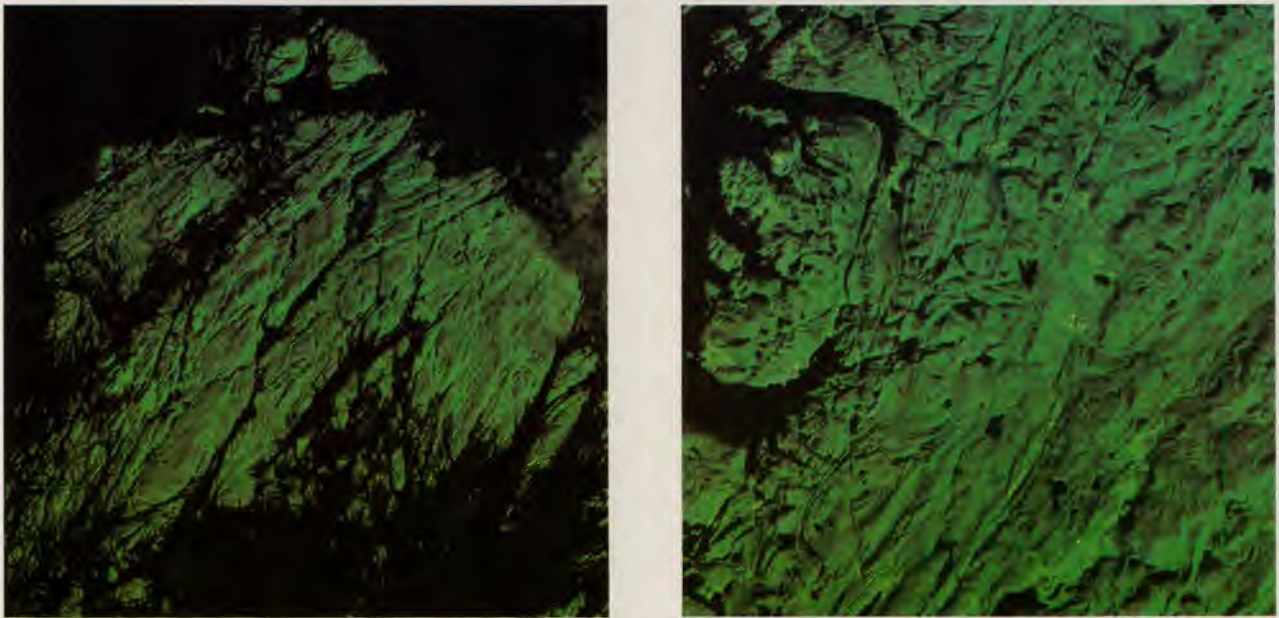


Figure 7. The sub-areas Vikna (left) and Roan (right), each of 30×30 km. TM-channels 3, 2 and 1 coded in red, green and blue gives these simulated natural colour composites.

major fracture planes in this area is parallel or subparallel to this trend, which is also the main trend of nearby fjords and sounds (Bering *et al.* 1986). Another set of major fracture planes trends NNE-SSW (Fig. 4a), which is the strike of the Rana Fault Complex in this region (Gabrielsen *et al.* 1984) and also the trend of a few of the minor fjords. The Rana Fault Complex is located just west of the Vikna islands, and separates the Mesozoic and Cenozoic strata in the shelf areas from the Precambrian and Lower Palaeozoic crystalline rocks that crop out on the sea-bottom to the east.

A lineament interpretation based on colour aerial photographs (1 : 40 000) gives the same major lineament trends as the TM interpretation, considering lineaments with a length of 1 km or more (Bering *et al.* 1986).

Folding is best seen in the metasedimentary rocks on Kalvøya and in the gneisses southwest of the island. Major folds in the gneisses and metasediments on Mellom and Indre Vikna are also evident on the TM colour composite. The major strike trend of the gneisses stands out clearly (Fig. 3a), but it is difficult to discern foliation pattern from fractures.

The Roan Area

This area is situated along the coast of Sør-Trøndelag about 75 km north of Trondheim. The area contains both basement gneisses and infolded metasedimentary rocks. The basement gneisses are a heterogeneous suite of granulite-facies dioritic, granodioritic and granitic gneisses and migmatites. The metasedimentary rocks are mainly biotite gneisses and schists including minor marble and amphibolite gneisses (Johansson 1986; Roberts 1986).

The colour composite (Fig. 7) is excellent for distinguishing different types of vegetation, and exposed rocks from vegetation. There is, however, not much lithological information to be gained, owing to the fact that much of the upland areas in this region are covered by bogs regardless of rock type. Due to chlorophyll absorption in the channel 3 wavelength band, the few exposed rock surfaces show a reddish tint.

The basement can be subdivided into two units. A western area, including the Roan peninsula, consists of partly granulite-facies rocks which are generally, but not always, retrograded to amphibolite facies (C. Møller, pers. comm., 1985). The eastern basement area is characterised by granodioritic and migmatitic gneisses with deeply infolded and polydeformed metasedimentary rocks which show a dominant NE-SW strike trend (Roberts, 1986).

The trace of one such spectacular synform trends NE-SW, diagonally across the image (Fig. 3b and Fig. 7). The southwestern part of this synform is transected by the curved Å fjord lineament which can be traced south to the Verran fault (Ofstedahl 1972, 1975). The TM image (Fig. 7) clearly shows that bedrock structures are not continuous across this lineament, but because the structures have no marked lateral displacement, the lineament represents a dip-slip fault, and as mentioned previously, fieldwork has proved a considerable downthrow to the east. The rose diagram of lineaments (Fig. 4b) in this region illustrates the prominent NW-SE lineament trend in the area Ørland-Namdalseid; a trend which is also the most important magnetic dislocation set in this area (Bering *et al.* 1986). This NW-SE lineament trend is not prominent on the Roan peninsula. The fold structures in the

rocks northeast of Brandsfjorden (Fig. 6), depicted in more detail by Roberts (1986), are clearly seen on the TM image. Comparing this with the MSS-based lineament interpretation map (Fig. 5), the folds in this area are not discernible on the MSS interpretation. It is, however, possible to discern the major fold closure east of Skjørafjorden.

Comparing the lineament interpretation of MSS channel 5 (Fig. 5) with that of TM (Fig. 3b), the TM gives substantially more information on lineaments shorter than ca. 5 km and the ability to distinguish foliation from fracture/fault-related lineaments is greatly improved. The steeply dipping foliation in this region facilitates this distinction.

The Verdal Area

This area is located approximately 70 km northeast of Trondheim, in the inner part of Trondheimsfjorden. Bedrock exposure is comparatively poor with agriculture restricted to the valleys below the marine limit and dense spruce forest above. The quarternary cover in areas below the marine limit is mostly clay. The colour composite readily distinguishes corn fields, meadows and forest, but in this region it is not possible to define rock types on the basis of this classification.

The bedrock consists mainly of metasediments and metavolcanic rocks in nappes emplaced during the Caledonian orogeny (Wolff 1979). Within the area (Fig. 3c) there are rock-units from the Middle and Upper Allochthons, including the Leksdal, the Skjøtingen, the Levanger and Støren Nappes (Wolff 1979, 1984). The rock types include metasandstone, amphibolite, metagraywacke, phyllite and greenstone.

The bedrock in this region is penetrated by hydrothermal alteration zones that contain thorium minerals and fluorite (Hembre & Grønlie 1984, Grønlie 1984). These planar alteration zones represent a comparatively late stage in the geological history of the Trondheimsfjord area. The zones are too narrow to be shown directly on the TM image, but several NE-SW trending lineaments and curvilineaments probably correspond to such zones (Fig. 3c).

Pronounced lineament trends within the image window are NNE-SSW and ENE-WSW; curvilineaments generally trend NE-SW (Figs. 3c and 4c). The shape of inner Trondheimsfjord, as well as Børgin and Leksdalsvatnet, has been influenced by these sets of lineaments. The TM image does not reveal as much about the bedrock structures here as compared with the Vikna and Roan areas, but it does show the presence of flat-lying rocks in the northern part of the Verdal area and the NE-SW strike of bedrock units on Ytterøy and southeast of Levanger.

As illustrated in the Roan area, TM gives substantially

more information on lineaments shorter than ca. 5 km. Because of the extensive marine clay cover and gently dipping bedrock, foliation structures are not as evident here as in the Vikna and Roan areas.

TM versus MSS

The superiority of TM-analysis over conventional MSS-analysis is evident when applied to large-scale geological examples. TM-analysis is especially helpful in distinguishing foliation from fracture/fault-related lineaments. Figure 5 shows a one-channel MSS-based lineament interpretation. Comparison with the TM image (e.g. Roan area, Fig. 3b) shows the superiority of TM in foliation mapping. The MSS image resolution is so low that it is impossible, in many cases, to distinguish between valleys eroded along foliation zones and valleys developed along fractures or faults.

Steeply dipping foliation is more readily discernible than flat-lying foliation which needs some topographic expression to be visible. The combination of steeply dipping foliation, good rock exposure and indented topographic relief is excellent for the interpretation of the Roan area (Fig. 3b and Fig. 7). The Verdal area, on the other hand, has flat-lying bedding and foliation, partly marine clay cover and gentle relief, resulting in less difference between the MSS (Fig. 5) and the TM interpretations (Fig. 3c).

The fact that TM has more spectral bands than MSS means that certain structural features are more easily detected than by conventional MSS-analysis. Spectral information from TM-channel 7 can be useful in the mapping of large-scale hydrothermal zones or of large regions of hydrothermally altered rocks; such uses, however, are likely to be of limited value in Norway.

Conclusion

Data from the TM-instrument onboard the Landsat-5 satellite has proved very useful for detailed interpretation of geological structures. For structures with a length of 1 km or more, TM provides nearly as much information as high-altitude aerial photographs.

Compared with MSS-data, the TM-data gives more information about structures less than 5 km in length. This means that TM can provide considerably more information about foliation than MSS.

Digital image processing of TM data gives more information than the use of standard black-and-white photographs, especially in areas with extensive soil cover. Image processing consists of linear stretching of individual TM-channels and generation of colour composites. Four combinations of TM-channels were found to be useful, and each of them contains channel 4. These combinations are: 2/3/4, 1/4/7, 3/4/7 and 4/5/7.

The spectral quality of the actual TM scene is not always impressive, in part because of the low sun angle of only 24 degrees. This low sun angle is, however, an advantage in the mapping of topographic lineaments, because the shadows enhance subtle linear features.

For the thermal infrared channel 6, the pixel values lie within 8 digital levels, which make it difficult to use the data. Channel 6 can have considerable geological application, however, and should be used in Norway when interpreting TM-data from the months of June, July or August.

When interpreting large geological structures from TM-data, using every second or third pixel is an advantage when employing image processing systems with colour monitors limited to 512×512 pixels. This gives a synoptic view of larger areas, which is the major advantage of using satellite remote-sensing imagery. Ideally, an image-processing system suitable for TM-data should at least be able to display 1024×1024 pixels on a color monitor.

Acknowledgements

This study was made possible by ESA/Earthnet Programme Office which generously gave us the digital TM data free of charge, and by the Technical Research Council of Norway (NTNF) which funded our digital image processing work at Tromsø Telemetry-station (TT). Our thanks go to the staff at TT who gave us a hand when mounting of the tapes was necessary, and especially to Victor Nilsen who introduced us to the International Imaging System (IIS) image-processing system. Bob Tucker and Ron Boyd critically read an early version of the manuscript and improved both the content and the language. Arne Solli, Geoff Milnes and Roy Gabrielsen made valuable and constructive comments on the manuscript and are hereby thanked for their helpful criticisms. David Roberts corrected the final manuscript.

References

- Aanstad K.M., Gabrielsen R.H., Hagevang T., Ramberg I.B. & Torvanger O. 1981: Correlation of offshore and onshore structural features between 62°N and 68°N, Norway. *Proc. Norwegian Symp. on Exploration*, Bergen, *NSE/11*, 11-25.
- Bering D., Boyd R., Grønlie A., Solli A., Atakan K., Bryhni I., Gautneb H., Krill A., Lynum R., Olesen O. & Rindstad B.I. 1986: Berggrunnsgeologisk rekognosering av fire områder på kysten av Møre og Trøndelag. *NGU report 86.027*, 96 pp.
- Gabrielsen R.H. & Ramberg I.B. 1979: Fracture patterns in Norway from Landsat imagery: results and potential use. *Proc. Norwegian Sea Symp.*, Tromsø, Norwegian Petroleum Society, *NSS/23*, 1-28.
- Gabrielsen R.H., Ramberg, I.B. Mørk M.B.E. & Tveiten B. 1981: Regional Geological, Tectonic and Geophysical Features of Nordland, Norway. *Earth Evolution Sciences 1*, 14-26.
- Gabrielsen R.H., Faerseth R., Hamar G. & Rønnevik H. 1983: Nomenclature of the main structural features on the Norwegian Continental Shelf north of the 62nd parallel. *Petroleum Geology of the North European Margin*, Norwegian Petroleum Society, 41-60.
- Gonzalez R.C. & Wintz P. 1977: *Digital Image Processing*. Addison-Wesley Publishing Company Inc., 431 pp.
- Grønlie A. 1984: Naturlig stråling fra beggrunnen i Nord-Trøndelag fylke. *NGU report 84.100*. 10 pp.
- Hembre O.S. & Grønlie A. 1984: Ny malmgeologisk provins i Nord-Trøndelag? *BVLI Malmgeologisk Symposium 'Nye malmtyper i Norge'*, 110-123.
- Johansson L. 1986: *Basement and cover relationships in the Vestranden-Grong-Olden region, Central Scandinavian Caledonides: Petrology, age relationships, structures and regional correlation*. Ph D. thesis, Univ. of Lund, 142 pp.
- Lillesand T.M. & Kiefer R.W. 1979: *Remote Sensing and Image Interpretation*. J. Wiley & Sons 612 pp.
- Longdon N. (ed.) 1984: *Earthnet - A story of Images*. ESA BR-18, 59 pp.
- Offield T.W., Miller G.B. & Petterson B.A. 1982: Regional setting and uranium occurrence, Olden-Hotagen District of Sweden and adjacent Norway: Preliminary Landsat interpretation. *US Geol. Surv. (unpubl. manus.)*, 25 pp.
- Oftedahl C. 1972: A sideritic ironstone of Jurassic age in Beitstadfjorden, Trøndelag. *Nor. Geol. Tidsskr.* 52, 123-134.
- Oftedahl C. 1975: Middle Jurassic graben tectonics in Mid-Norway. *Proc. Jurassic North Sea Symp.*, Stavanger, *JNSS/21*, 1-13.
- Price I. & Rattey R.B. 1984: Cretaceous tectonics off mid-Norway; implications for the Rockall and Faeroe-Shetland Troughs. *J. Geol. Soc. London*, 141, 985-992.
- Ramberg I., Gabrielsen R.H., Larsen B. & Solli A. 1977: Analysis of fracture patterns in southern Norway. *Geol. en Mijnbouw* 56, 295-310.
- Rindstad B.I. & Follestad B. 1982: Digital methods for lineament analysis. In Longdon N. & Levy G. (eds.): *Satellite Remote Sensing for Developing Countries*. ESA SP-175, 211-214.
- Rindstad B.I., Grønlie A. & Nilsen V. 1985: Landsat TM data anvendt innenfor geologisk strukturkartlegging. *NGU report 85.229*, 27 pp.
- Rindstad B.I. & Grønlie A. 1986: Digital Landsat TM data used in the mapping of large-scale geological structures on the coast of Central Norway. *NGU rep. 86.113*, 21 p.
- Roberts D. 1986: Structural-photogeological and general tectonic features of the Fosen-Namsos Western

- Gneiss Region of Central Norway. *Nor. geol. unders. Bull.* 407, 13-25.
- Sabins F.F. jr. 1978: *Remote Sensing, Principles and Interpretation*. W.H. Freeman & Co., 426 p.
- Sigmond E., Gustavson M. & Roberts D. 1984: Bedrock Map of Norway - M 1:1 mill. *Nor. geol. unders.*
- Wolff F.C. 1979: Beskrivelse til de berggrunnsgesologiske kart Trondheim og Østersund, 1:250 000. *Nor. geol. unders.* 353, 76 pp.
- Wolff F.C. 1984: Regional geophysics of the central Norwegian Caledonides. *Norges. geol. unders. Bull.* 397, 1-27.

5. Land Use

Evaluation des potentialités du satellite Landsat TM en milieu urbain – Application au cas de Bruxelles (Belgique)

M.L. De Keersmaecker

Assistant U.C.L.

Laboratoire de Télédétection, Louvain-la-Neuve, Belgique.

L'étude présentée est fondée sur les trois hypothèses suivantes:

- *la télédétection: un outil de classification des affectations du sol en milieu urbain*
- *la télédétection: un outil d'étude des quartiers en milieu urbain*
- *la télédétection: un outil de modélisation du milieu urbain.*

Elle présente donc les résultats de différentes méthodes d'analyse du milieu urbain mises en oeuvre pour atteindre les objectifs présentés.

This study is based on the three following assumptions:

- *remote sensing is an aid to the land-use classification in an urban area*
- *remote sensing is an aid to the study of homogeneous wards in an urban system*
- *remote sensing is an aid to model the spatial distribution of the components of the urban system.*

The study is concerned with the results according to different analysis methods of the urban areas. These methods are used to achieve the presented aims.

Introduction

La télédétection, pour être utilisée à des fins thématiques appliquées, doit être divisée en quatre étapes:

1. la cartographie des affectations du sol. Cette opération s'effectue à l'aide d'une composition colorée;
2. l'inventaire des affectations du sol qui doit être précédé par un processus de classification de l'image en catégories préalablement définies;
3. la modélisation du comportement spatial des affectations du sol;
4. l'introduction de la composante temporelle (De Keersmaecker & Lambin, 1987).

Les deux premières étapes apparaissent dans toutes les études de télédétection; elles sont de toute évidence indispensables pour la réalisation des troisième et quatrième étapes qui sont moins présentes dans la littérature (bibliographie dans De Keersmaecker & Lambin, 1987).

Cette étude, dans une optique d'évaluation des potentialités du satellite Landsat TM en milieu urbain, sera orien-

tée vers les possibilités de réalisation de l'étape de modélisation spatiale du milieu urbain, sans néanmoins passer sous silence les performances du processus de classification, base de toute autre approche.

Aire d'étude et documents utilisés

Le milieu urbain analysé est celui de l'agglomération morphologique de Bruxelles (Belgique) définie par l'Institut National Belge de Statistiques. L'image étudiée a été enregistrée par le satellite Landsat TM le 23 janvier 1983. Des photographies aériennes au 1/15 000 de 1981 ont servi de supports à l'étude.

Problématique

Ce que le satellite enregistre, c'est le paysage urbain. Complexe d'interrelations entre les espaces bâtis ou non,

le paysage urbain peut donc être considéré comme un système (De Keersmaecker & Lambin, 1987). La théorie systémique (Morin, 1977) présente deux méthodes d'étude des systèmes. La première basée sur une vision holistique, considère le système comme un tout tandis que la deuxième, d'inspiration réductionniste, abstrait, séparément, les dimensions du paysage avant d'en rechercher les interrelations et de les réintégrer dans leur ensemble initial. C'est cette dernière méthodologie qui sera appliquée ici.

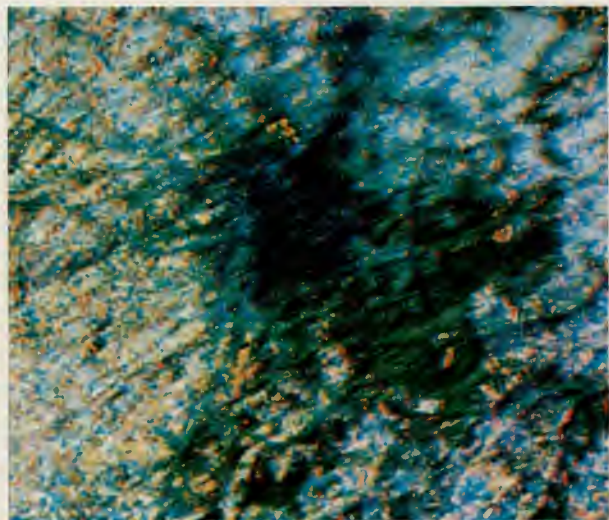
Etape de classification des affectations du sol

Préalablement à tout processus de classification, deux approches doivent être envisagées.

- Tout d'abord, l'utilisation de la technique statistique classique de classification par maximum de vraisemblance nécessite que les données soient caractérisées par une distribution normale. A partir d'échantillons aléatoires de valeurs de radiance dans les différents canaux, un test d'adéquation à la loi normale est réalisé et s'est révélé significatif (De Keersmaecker, 1987 a).
- Ensuite, il faut effectuer une sélection performante de 3 canaux d'étude parmi les sept de Landsat TM (justification: De Keersmaecker, 1987 a). Différentes méthodes existant dans la littérature (Swain & Davis, 1978; Sheffield, 1985) ont été testées aux données analysées et ont conduit au choix de la combinaison 3, 4, 5 qui semble être la plus adaptée à une étude du milieu urbain (De Keersmaecker, 1987 a). Une composition colorée (Fig. 1) est réalisée, présentant ainsi l'image de base de l'étude envisagée.

Dans un premier temps, en fonction des objectifs de la modélisation et des contraintes spectrales, une classification à quatre classes est conduite sur les données: les

Figure 1. Composition colorée Landsat TM, canaux 3, 4, 5



espaces bâtis, les espaces verts, les sols nus (champs) et les prairies.

Pourquoi ce choix? Le paysage urbain peut être considéré comme un complexe d'interrelations entre le bâti, le rural et la verdurisation. Introduire les surfaces aquatiques dans ce schéma est nécessaire mais n'est pas aisé. En effet, les valeurs de radiance de l'eau sont identiques à celles du bâti du centre de Bruxelles (De Keersmaecker, 1987 a) et ne peuvent donc pas être classées séparément. Pour pallier ce problème, une classification par hypercubes sur les surfaces aquatiques est réalisée sur l'aire totale diminuée de la zone centrale de la ville. Les deux classifications sont fusionnées pour obtenir le résultat suivant (Fig. 2). La validité de la classification est testée au moyen de plusieurs indices utilisés dans la littérature (De Keersmaecker, 1987 a). Globalement, ces indicateurs convergent vers une mesure de précision voisinant 85%. Les erreurs concernent essentiellement des problèmes de différenciation entre champs et prairies; cela en raison de la période de prise de vue. Ce n'est donc pas fondamental dans une étude des configurations urbaines.

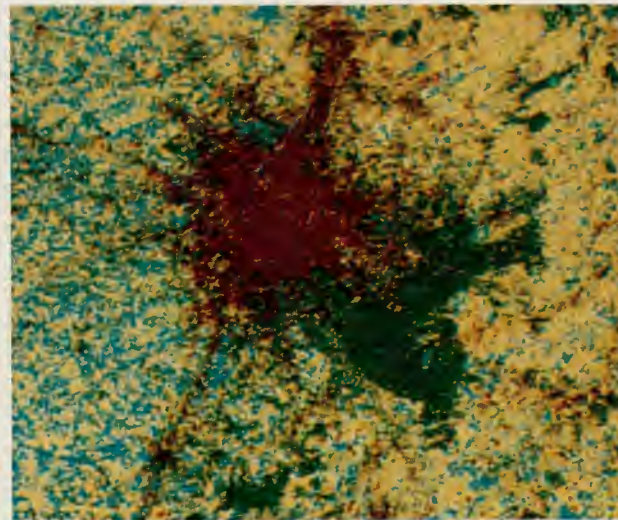
Enfin, il est possible, à l'aide de masques sur les affectations non-urbaines, d'isoler les industries du reste de l'espace bâti (De Keersmaecker, 1987 c).

Etape de modélisation de l'espace urbain

Deux parties essentielles du système urbain peuvent être isolées: les espaces verts et les espaces bâtis. Le problème d'étude de la configuration spatiale des espaces verts et de son rôle comme indicateur socio-économique

Figure 2. Classification par maximum de vraisemblance

- Rouge : bâti
- Vert : espaces verts
- Jaune : sols nus
- Cyan : prairies
- Bleu : surfaces aquatiques.



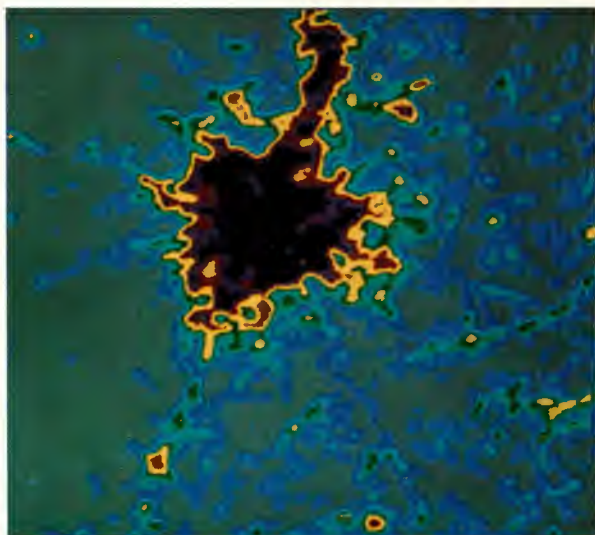


Figure 3. Image de densité de bâti (fenêtre 33×33)
Blanc --> Noir: densité de 0% à 100%.

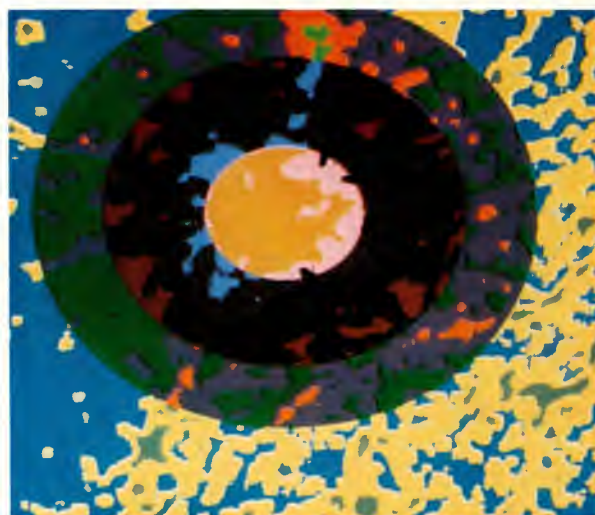


Figure 4. Comparaison du modèle $Densité = \exp(\alpha - \beta * distance)$ (4 classes) à la réalité (4 classes): 16 catégories

a déjà été amplement discuté (De Keersmaecker, 1987 b et c). Il ne sera plus envisagé ici. Cette étude se bornera à extraire une des dimensions particulières de l'espace urbain à savoir le bâti et à en modéliser le comportement spatial. Pour atteindre cet objectif, il sera question d'estimation de la densité des espaces bâtis à partir de l'image classifiée.

Algorithme utilisé pour l'extraction des densités de bâti

L'algorithme repose sur une méthode de fenêtre mobile. Cette méthode consiste à définir une zone carrée de pixels, dans laquelle on détermine la proportion de pixels

dits 'bâtis'. Cette proportion est ensuite convertie en un nombre compris entre 0 et 255 qui est affecté au pixel central de la fenêtre. Le processus est réitéré en déplaçant la fenêtre successivement d'une colonne puis d'une ligne de sorte que chaque pixel reçoit ainsi une nouvelle valeur définissant la proportion d'espaces bâtis qui l'entourent directement. En affectant des couleurs de plus en plus intenses aux valeurs maximales de densité de bâti, on obtient ainsi une 'image-léopard' (Fig. 3) dans laquelle les centres des taches correspondent à des zones dont les caractéristiques de densité s'écartent de manière maximale du continuum du fond de l'image (De Keersmaecker, 1987a).

Un problème est le choix de la taille de la fenêtre. Plusieurs considérations empiriques peuvent être réalisées qui conduisent au choix d'une taille égale à la superficie moyenne des secteurs statistiques en milieu urbain dense (De Keersmaecker, 1987 a); ce qui correspond à une surface de (33×33) pixels.

Approche quantitative de la modélisation

En 1951, Clark a établi, à partir de résultats empiriques, une relation entre la densité de population – estimée dans le cas présent par la densité de bâti – et la distance au centre de la ville. Cette relation basée par la suite sur des fondements théoriques (Mills, 1972, théorie de l'utilité) se formule:

$$D = \exp(\alpha - \beta d) + e$$

- avec D = densité d'espaces bâtis
- d = distance euclidienne au centre
- α, β = paramètres à estimer
- e $\text{II D N}(0, \sigma^2)$

Une analyse de régression est conduite sur un échantillon de 400 pixels sondés aléatoirement sur l'image-densité en vue d'estimer les valeurs des paramètres. Les résultats sont les suivants et sont significatifs au seuil $\alpha=0.0001$

	Estimation	erreur standard	t (H ₀)
α	4,6973	0,1668	28,168
β	0,0039	0,0004	-9,636

La relation de Clark (1951) dont les paramètres ont été estimés par la méthode des moindres carrés ordinaires est à la base de la création d'une nouvelle image. Le principe, analogue au principe désormais classique des images de synthèse, repose sur le calcul, pour chaque pixel, d'une valeur de densité théorique, résultat de la formule présentée, de la conversion de ce nombre en un nombre compris entre 0 et 255 et de l'affectation de cette valeur au pixel concerné. La nouvelle image est une 'image-modèle', fonction de la relation testée.

Pour comparer l'image-léopard à l'image-modèle, on effectue une classification non-supervisée à 16 catégories, correspondant à toutes les combinaisons possibles issues du découpage de chacune des images en 4 catégories. Les résultats sont présentés en Figure 4 et sont conformes à la mauvaise adéquation prévue par le modèle ($R^2=0,1892$). Les causes en sont multiples; parmi elles, citons:

- l'anisotropie de la ville: si l'on introduit dans l'analyse de régression une nouvelle variable d'appartenance régionale, on obtient alors des résultats plus performants ($R^2=0,40$) issus de la mise en place de deux relations, l'une pour l'Est, l'autre pour l'Ouest de la ville;
- la meilleure adéquation d'un autre modèle comme par exemple, la fonction de Bessel (Amson, 1972; $R^2=0,63$);
- la présence de centres secondaires qui sont, deux aussi, caractérisés par un schéma similaire de gradient de densité. Cette particularité peut être introduite dans le modèle par la création d'une nouvelle image. Celle-ci est la somme d'"images-modèles" fabriqués autour de chacun des centres secondaires. Les paramètres de chacune des équations du modèle ont été estimés par analyse de régression à partir d'un échantillon de pixels localisés autour de chacun des centres considérés.

A nouveau, l'image-modèle est comparée à l'image-léopard pour déceler les concordances et les dissimilarités. Le résultat (Fig. 5) paraît plus concluant pour l'agglomération bruxelloise prise globalement même si des surestimations du modèle apparaissent à proximité des centres secondaires; celles-ci sont dues à leur développement irrégulier le long de voies de communication. Les développements de modèles urbains sont multiples; ainsi le sont aussi les considérations d'ordre géographique qui s'ensuivent nécessairement. Le but de cet article est surtout d'en démontrer l'existence ainsi que de prouver l'utilité de l'imagerie satellitaire à des fins purement géographiques (plus de détail dans De Keersmaecker, 1988).

Analyse des interactions des dimensions du paysage urbain

Les interactions des densités de bâti et d'espaces verts sont à la base de la formation de quartiers urbains homogènes. Plusieurs méthodes de discrimination existent et ont été testées (De Keersmaecker, 1986; 1987 a); parmi elles, la méthode de classification d'images-léopard (bâti et espaces verts), la méthode des densités des modifications entre images classifiées lissées ou non et la méthode des paysages (Bruneau & Killian, 1984). Leurs résultats, concluants, permettent un découpage utile de l'espace urbain aux fins de modélisation et d'aménagement du territoire.

D'autres applications...

Dans le même ordre d'idées, des approches similaires de modélisation peuvent être appliquées au milieu rural. Dans un but appliqué de l'étude des zones défavorisées en Europe (projet européen dénommé 'Less-favoured areas'), cette même optique intervient aussi. Wilmet (1987) a démontré, mesures de performance à l'appui, les potentialités du satellite Landsat TM pour la discrimination des affectations du sol dans les Hautes Fagnes et surtout pour la mise en évidence de critères de sous-développement. Ces mêmes indicateurs ont été étudiés dans d'autres recherches: la modélisation du comportement spatial des friches en Ardenne belge (Bottieau & De Keersmaecker, 1987), les degrés d'humidité des sols dans les Hautes Fagnes (Brutsaert, 1987), l'adéquation de la localisation des prairies aux potentialités des sols et les mécanismes de la distribution spatiale des prairies en Lorraine belge (Massart, 1987).

C'est ainsi que l'on remarque les potentialités et surtout les promesses d'avenir, dans le domaine des études de modélisation spatiale, de l'image satellitaire et plus précisément des documents enregistrés par le capteur TM de Landsat.

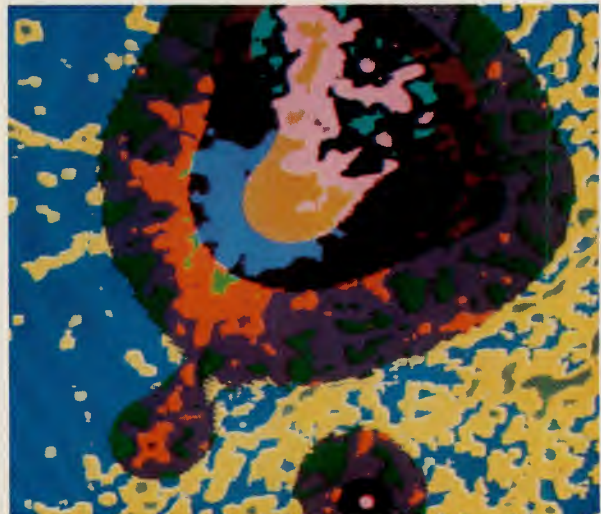
Remerciements

Mes remerciements les plus sincères s'adressent à l'Institut Géographique National Belge qui m'a encouragé dans ce projet-pilote, au Professeur J. Wilmet qui a suivi mes travaux, à M. P. Jacques qui a réalisé expressément certains logiciels, et au Fonds National de la Recherche Scientifique dont les crédits m'ont permis d'acquérir un écran de photographie des images.

Figure 5. Comparaison du modèle Densité =

$$\sum_{i=1}^n \exp(\alpha_i - \beta_i * \text{distance}_i) \quad (4 \text{ classes})$$

avec n = nombre de centres secondaires à la réalité (4 classes): 16 catégories.



Bibliographie

- Amson J.C., 1973, Equilibrium models of cities: single-species cities, *Environment and Planning A.*, 5, 295-338.
- Bottieau V. et De Keersmaecker M.L., 1987, Vers une modélisation du comportement spatial des zones de déprise agricole en Ardenne belge, *Société Belge d'Etudes Géographiques*, 1, pg 59-74.
- Bruneau M. et Killian J., 1984, Inventaires agro-écologiques, paysages et télédétection en milieu tropical: essai méthodologique, *L'Espace Géographique*, 3, 215-224.
- Brutsaert V., 1987, *Etude par télédétection des Hautes-Fagnes*, mémoire inédit, Institut d'Agronomie et d'Aménagement du Territoire, UCL, Louvain-la-Neuve.
- Clark C., 1951, Urban population densities, *Journal of the Royal Statistical Society*, A, 114, 490-496.
- De Keersmaecker M.L., 1986, Etude des paysages urbains à l'aide d'une image Landsat TM, *Photo-Interprétation*, 86-5, 2, pg 13-20.
- De Keersmaecker M.L., 1987a, *Evaluation des potentialités du satellite Landsat-Thematic Mapper en milieu urbain - Une application au cas de Bruxelles (Belgique)*, rapport remis à l'IGN dans le cadre du projet européen Pilote TM, 90 pg.
- De Keersmaecker M.L., 1987b, Etude par télédétection des quartiers résidentiels en milieu urbain: la détermination de leurs caractéristiques socio-économiques, *Actes du Colloque International de l'Information et de l'Instrumentation Géographique*, 517-528.
- De Keersmaecker M.L., 1987c, Vers une modélisation du comportement spatial des quartiers résidentiels en milieu urbain (aire d'étude: Bruxelles), *Actes de la Journée FNRS*, 27 mai 1987, Liège (à paraître).
- De Keersmaecker M.L. et Lambin E., 1987, Quelques réflexions sur l'utilisation de l'imagerie satellitaire à des fins thématiques, *International Journal of Remote Sensing*, Vol. 8, Nr 9, 1277-1288.
- De Keersmaecker M.L., 1988, Approche de modélisation de l'espace urbain par télédétection, *L'Espace Géographique* (en préparation).
- Massart M., 1987, *Contribution à l'étude par télédétection de la Lorraine belge*, mémoire inédit, Institut de Géographie, UCL, Louvain-la-Neuve.
- Mills E., 1972, *Studies in the structure of the Urban Economy*, Hopkins, Baltimore.
- Morin E., 1977, *La Méthode - La Nature de la Nature*, Seuil, Paris.
- Sheffield C., 1985, Selecting Band Combinations from Multispectral Data, *Photogrammetric Engineering and Remote Sensing*, 51, 681-688.
- Swain P.H. et Davis S.M., 1978, *Remote Sensing: the Quantitative Approach*, Mc. Graw Hill International, New York.
- Wilmet J., 1987, *Evaluation des potentialités du satellite Landsat - Thematic Mapper en milieu rural - Une application au cas des Hautes Fagnes (Belgique)*, rapport remis à l'IGN dans le cadre du projet européen Pilote TM.

Agricultural Land-Use Classification in the Upper Rhine Valley using Multitemporal TM Data

Wolfram Mauser

*Institute for Physical Geography, Department of Hydrology
University of Freiburg, FR Germany*

Within the frame of the ESA TM Pilot Project, three Landsat-5 TM quater scenes were geometrically registered to fit for subsequent multitemporal analysis of the separability of agricultural plant species. Eight different maximum-likelihood classifications of different combinations of spectral bands and dates were compared in their accuracy in separating the different plant species. The band combinations include data from 18 April, 7 & 23 July 1984 and the first four principal components of a principal component analysis of 15 bands of the three dates. 44 training areas were chosen to cover different varieties of forest, corn, wheat, barley, sugarbeet, potatoes, grassland, built-up areas and water.

After an analysis of the temporal change of the reflection of different cover types during the observation period, the co-occurrence matrices were determined and compared to give a first overview of the expected classification accuracy. The classified images were then compared. The following first conclusions can be drawn from the classification results:

- *the resolution of TM data is sufficient to recognise the major fields in the study area;*
- *the use of multi-temporal data improves the classification accuracy, especially when moving from spring to summer;*
- *the band-combination 3 (red), 4 (near-IR) and 5 (medium-IR) contains most information on agricultural crops;*
- *the enhanced spectral resolution of TM data causes problems in the classification of major land use categories because a differentiation between varieties and row directions is possible and necessary;*
- *the best classification result is obtained when using the first four principal components calculated from the principal components analysis of 15 bands from the 3 dates as real numbers. In this case it is possible to distinguish between 44 classes without having the problem, that the co-occurrence matrix shows excellent results but the occurrence of the different classes in the whole image is unbalanced.*

1. The Study Area

The study area is situated approx. 20 km West of the City of Freiburg in the Upper Rhine Valley. It is an area of intensive agricultural production with the main crops being wheat, corn, barley, potatoes, sugar-beet and vine. The average field size of approx. 1.5 ha is pretty small causing problems with the spatial resolution of the MSS sensor. Figure 1 shows the study area in a colour composite of the TM-scene 195/27 of July 23, 1984 in the band combination 2, 4, 5. The River Rhine and the French Channel can be seen in the left part of the image, a highway crosses the image from SW to NE and the small villages can be seen in pink colour. In the upper centre of the image a mountain can be seen, which is mainly covered with vineyards, in the upper right corner a part of the City of Freiburg is shown and in the lower

right part of the image the first hills of the Black Forest are seen.

Three TM quater-scenes of the frame 195/27 with the following dates were delivered by DFVLR:

S1	18 April
S2	7 July
S3	23 July

The dates correspond to the following phenology of the different crop types:

- *corn: in S1 no vegetation; in S2 height approx. 20 cm; in S3 height approx. 70 cm;*
- *cereals: in S1 total cover (approx. 20 cm (winter-cereals) and 10 cm (summer-cereals) plant height); in S2 maturity; in S3 harvested;*

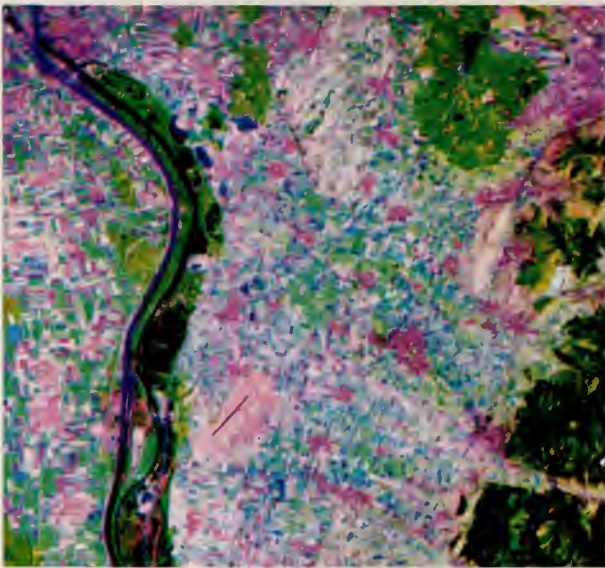


Figure 1. The study area as seen from Landsat-5 TM on 23 July 1984. Band combination: 2=blue, 4=green, 5=red.

- sugar-beet: in S1 no vegetation; in S2 partial coverage; in S3 total coverage;
- grass: in S1 total coverage, active assimilation; in S2 partially dry vegetation or harvested; in S3 either harvested or dried out;
- forest: deciduous: in S1 no leaves; in S2 and S3 almost no change with full leaves; conifers: in S1 old needles; in S2 and S3 no change, new needles.

2. TM Data Preprocessing

To be able to use the different TM-scenes for multitemporal analysis the three images have to be registered onto each others. This enables a pixel-by-pixel comparison of the change in reflectance of the surface cover during the

time period of the study. Since the ground track of the satellite changes slightly with time a co-registration is necessary. The procedure of the co-registration was as follows:

- selection of identical subimages in the three different scenes;
- selection of 14 ground control points in the S1 and S3 scene taking the S2-scene as a reference; the ground control points for S3 are listed in Table 1;
- conducting the geometric transformation.

Table 1. Ground control points for the geometrical registration of S3 onto S2

S2 (7/7/84)		S3(23/7/84)		delta row	delta col
row	col	row	col		
329	178	328	177	-1	-1
539	232	538	230	-1	-2
558	527	558	525	0	-2
611	491	610	489	-1	-2
345	620	345	619	0	-1
40	560	39	558	-1	-2
87	525	86	523	-1	-2
89	85	88	82	-1	-2
26	78	25	76	-1	-2
219	207	218	205	-1	-2
347	229	347	227	0	-2
479	304	478	302	-1	-2
488	307	488	306	0	-1
302	353	301	351	-1	-2

Astonishingly the differences in rows and columns between S2 and S3 are constant to within less than one pixel. This suggests that a geometric correction with first-order or second-order polynomials is not necessary to reach a subpixel registration accuracy. The accuracy reached through a simple linear transposition is 0 pixels in row- and 0.4 pixels in column-direction for the S1-scene and

Figure 2. Colour-composite of band 3 on 18 April, 7 July, and 23 July 1984.



0.28 pixels in row- and 0.21 pixels in column-direction for the S3-scene. This was assumed to be sufficient for the subsequent combined analysis of the three images. Analysis of later scenes, although, especially of 1986, show that this procedure is not possible in any case and that the satellite track has been comparatively stable during the period of 1984. Figure 2 shows a part of the scene (an airfield) in band 3 for all dates, which demonstrates the high accuracy of the geometric co-registration. The one-pixel shelters on the air-field (positioned in three circles) in this multitemporal colour-composite fit onto each others.

3. Analysis of the Spectral Temporal Behaviour of Different Land Covers

The following analysis of the data as well as the subsequent classification were performed at the Institute for Physical Geography at the University of Freiburg on its image processing system. It consists of a DEC-PDP 11/73 with 2 Mbyte of memory, approx. 0.5 Gbyte of disk resources and a 1024 × 1024 VTE-image processing system with a 100 Hz refresh video display and 8 Mbyte of video-buffer, which because of its excellent display quality proved to be of major help in the following analysis. The software consists of the image-processing software package FAP written by the author (1987).

On 7 July 1984 ground thruth was gathered in a sub-area of the image determining the cover type of different fields. This enabled a selection of known fields with known cover type for the subsequent analysis of its spectral behaviour with time. The problem of a comparison of the reflectance values of the cover types for the three different dates is the difference of the sun's illumination angle, which causes different irradiance and a difference in atmospheric conditions, which cause different absorption and scattering in the atmosphere. To circumvent these problems a two-step correction was applied:

- 1) Normalisation of the solar irradiance of the three dates on the S2 scene (7/7/84). This was done using a Standard-Clear-Sky atmosphere model implemented on the image processing system (Mauser, 1986).
- 2) Selection of an area, wich is assumed not to change its reflectance over the year. This enables a check of the accuracy of the calculations of the atmosphere model. As this area of constant reflectance a densely covered industrial area in the City of Freiburg was chosen.

The following correction parameters were determined for the solar angle, the incident solar radiation on a plane (not tilted) at 220 m above sea level, the ratio between the irradiances of S1 and S2 and S3 and S2 and the ratio determined from an irradiance-corrected, densely covered industrial area.

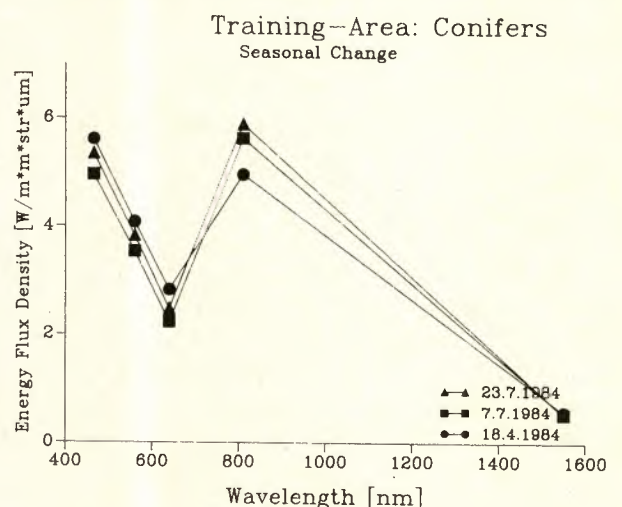
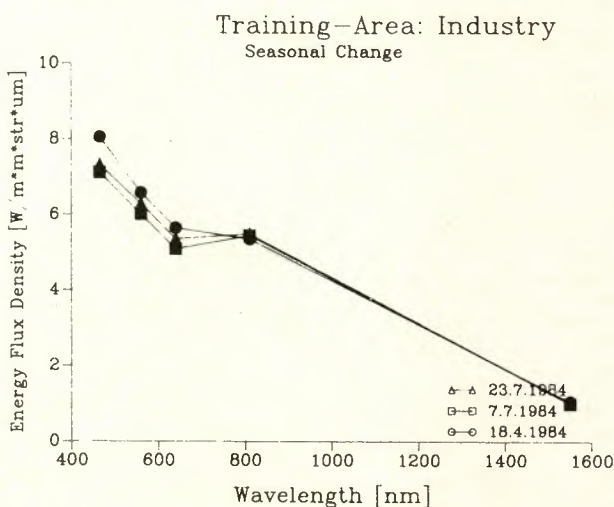
Table 2. Solar angle, incident, solar radiation (short wave) and ratios for dates S1, S2, S3

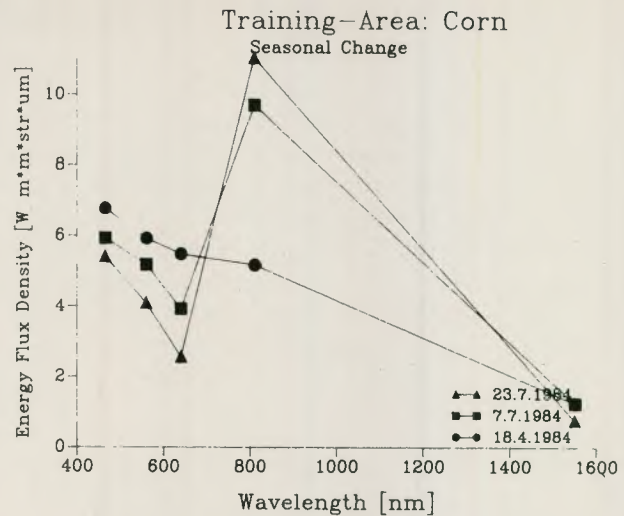
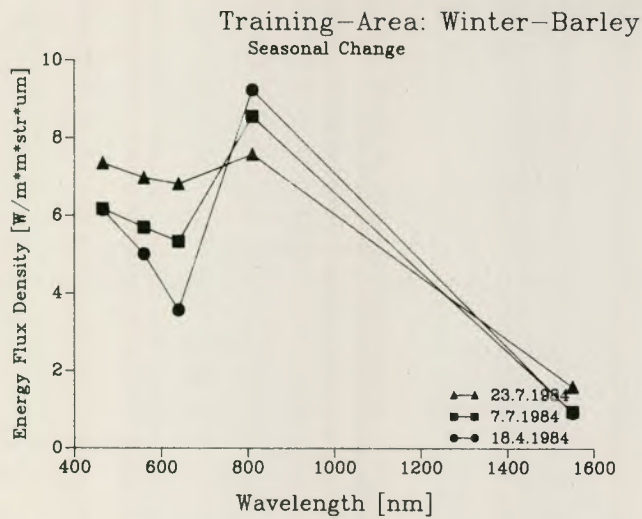
Date	Solar Ang. (Deg)	Inc. Solar Rad. (W/m ²)	Ratio	Ratio (Ind)
18/4/84	38	0.82	0.861	0.859
7/7/84	46	0.95	1.000	1.000
23/7/84	45	0.92	0.959	0.977

Table 2 shows a close correspondence between the calculated and the measured irradiances of the industrial area in band 1 (blue). Band 1 was chosen because it reacts most sensitive to differences in the atmospheric conditions. The energy flux density values were determined from the grey-values of the image using TM preflight calibration data (NASA, 1983).

Figures 3-6 show the reflectance curves for the cover types industry, conifers, winter-barley and corn. As can be seen clearly the industrial area does not show major changes in its spectral behaviour over the period; the conifer trees show a slight increase between spring and sum-

Figures 3 and 4. Energy flux density measured at the satellite in the first 5 TM bands for industry and conifers for three different dates.





Figures 5 and 6. Energy flux density measured at the satellite in the first 5 TM bands for winter-barley and corn for three different dates.

mer and remain stable over the month of July; winter barley shows a decrease in reflectance in the near-IR which corresponds to a decrease in physiological activity of the plants from spring development over maturity to harvest (the decrease in reflectance in the near-IR is combined with an increase in reflectance in the blue and red bands caused by the deterioration of the plants' chlorophyll); corn shows a strong increase in reflectance in the near-IR together with a strong decrease in the blue and red bands in July caused by its very rapid growth during this time of the year (Fig. 6). It can be assumed that the information, which can be gathered on the different plant species is greatly enhanced through multitemporal images.

4. Multitemporal Classification of Image

44 training areas were chosen for the multitemporal classification of the images, assuming that all the relevant land uses in the area should be covered. The start-point for the selection of the training areas was a set of 14, which was supposed to represent the following major land use categories:

Water	Forest	Corn
Wheat	Barley	Oats
Potatoes	Sugar-Beet	Vineyards
Grassland	Low-Density Resid.	Medium-Density Resid.
Industry	Gravel	

For each major category one training and one test area was selected. The first test classification showed that only one of the test areas was recognised by the maximum-likelihood classifier. The reason for this was that the great spectral resolution of the sensor makes a distinction between different varieties within one major land-use class possible and necessary. The inclusion of a seed-corn field in an area where no ground truth was gathered

enabled the recognition of a major corn area (the seed-corn area) in the image. Since, as this example shows, the collection of ground truth at the time of the overflight was not sufficient, interviews of farmers in the area enabled the inclusion of more training fields in the classification. A distinction between deciduous and conifer forests and different forest types enabled the distinction between forested and non forested areas. The vineyards proved to be a problem because of their very inhomogeneous treatment practices. They cause extremely inhomogeneous reflection from these areas. Another problem is, that vine in the area is favourably grown on hill slopes, which causes different illumination conditions for the exposed and non-exposed slopes. This led to a minimum of 4 training areas for vine. Oats was left out of the final classification because it is only grown on very few fields.

The sizes of the different training areas are shown in Table 3.

Table 3. Size of the training areas in pixel

Water	238	Forest 1	77	Forest 2	31
Forest 3	46	Forest 4	84	Forest 5	93
Forest 6	91	Forest 7	136	Corn 1	118
Corn 2	17	Corn 3	99	Corn 4	16
Corn 5	25	Corn 6	67	Corn 7	49
Corn 8	15	Corn 9	39	Sugar-Beet 1	17
Sugar-Beet 2	34	Sugar-Beet 3	24	Potatoes 1	42
Wheat 1	24	Wheat 2	16	Wheat 3	51
Wheat 4	17	Barley 1	17	Barley 2	16
Barley 3	29	Barley 4	22	Barley 5	56
Vine 1	44	Vine 2	24	Vine 3	15
Vine 4	48	Industry	56	Med.-dens.Res.	19
Low-dens.Res	20	Gravel 1	50	Gravel 2	28
Fallow 1	18	Grassland 1	66	Grassland 2	17
Grassland 3	27	Grassland 4	16		

From the multiple classification runs with different band combinations and rejection thresholds 8 classification runs were selected to show the effects of the different parameters on the classification result. The classification accuracy was determined using a ranking procedure, which is based on the co-occurrence matrix between the true and classified pixels in the different training areas. The percentage of right decisions within each class and within each of the 11 major land-use categories was determined and the band-combinations were ranked according to these percentage values. The first value gives a measure to what extent the different classes (training areas) were classified right, that means to what extent they are spectrally separable. The second value gives a measure to what extent the major categories in the image can be distinguished. Clearly the second measure is the weaker, though for practical purposes it is assumed to be more realistic. Table 4 shows the result of this ranking procedure together with the percentage of unclassified pixels.

Table 4. Results of the statistical analysis of the co-occurrence matrices for different band combinations

Band Combination	% true class	% true categ.	Number pixels	unclass.
4, 5 dates: S1, S2, S3	94.3	99.4	2138	7
3, 4 dates: S1, S2, S3	93.1	97.0	2138	10
3, 4, 5 dates: S2, S3	92.9	96.9	2138	6
HPT 1-4 dates: S1, S2, S3	91.8	95.7	2138	1
HPT 1-4 dates: S2, S3	90.8	95.7	2138	1
1, 2, 3, 4, 5 dates: S3	85.9	94.9	2138	12
1, 2, 3, 4, 5 dates: S2, S3	83.1	91.0	2138	17
1, 2, 3, 4, 5 dates: S2	82.7	86.7	2138	20
1, 2, 3, 4, 5 dates: S1	63.0	76.8	2138	0

The classifications denoted with HPT 1-4 need some further explanation. These classifications were carried out on principal component data, which had been calculated on the basis of bands 1-5 of the dates S1, S2, S3 and S2, S3 respectively. The principal components calculation is usually done in the way, that a set of *n* 8-bit bands is



Figure 7. First three principal components of the 18 April, 7 July, and 23 July data (3 dates, bands 1, 2, 3, 4, 5). Blue: second component - Green: third component - Red: first component.

transformed into another set of *n* 8-bit bands of different grey-value distribution through an optimised rotation of the coordinate system. This, though, can lead to a loss of information, especially in the first and second component, since scaling of the data is necessary to fit the data in the 0..255 interval. Since most of the information is concentrated in the first transformed bands their variance is increased and the variance of the last transformed bands, which belong to the smallest eigenvalues of the covariance matrix, is decreased.

Therefore it is dangerous to use the 8-bit transforms for classification purposes, since the loss of information is usually not known. A way out is to store the results of the principal component transformation as a Real-image. Through this the full dynamic range of the transformation is preserved and the transformed data can be input to the classification program. The HPT 1-4 classifications have been carried out on Real-images. Figure 7 shows an image of the first 3 principal components of the 3-date transformation. To be able to display the bands on the screen they have been scaled to a Byte-image.

The rejection threshold has been set to 4 standard deviations after confirmation for the in-orbit data by Kirchhoff *et al.* (1986), who have shown that a rejection threshold of 4 standard deviations is optimal for TM-simulation data.

Table 4 shows some interesting results. The first thing that can be seen is the very small number of unclassified pixels. This indicates that all the training areas are pure and homogeneous.

Obviously, the worst results are obtained when using only one date. This is not surprising in the case of the April

data since most of the fields are not defined yet in their use and the inhomogeneities of the soil colours are different from those of the plants, that will be on these fields. More surprising is the relatively bad result of the S2 (7 July) data. There the differentiation of the surface is at a maximum since the cereals are still standing, though already mature, and the corn, potatoes, sugar beet and forests are all growing. The better result of the classification of the S3 (23 July) date may be in relation to the bad result of the S2 date in that the complexity of the surface is diminished by the fact that the cereals are harvested and there is not that much difference in the spectral reflectance between the stubbles of the different fields. It has to be pointed out that if there were only the S3 scene available it would have been impossible to distinguish between the cereals because there would have been no chance to get adequate ground truth.

The bad result of the 10-band classification of the dates S2 and S3 is astonishing since one would assume that an increase in information would result in an increase in separability of the different classes. This is not the case.

By far the best results in the percentages of the co-occurrence matrix were obtained when using 2 bands at all three dates. Two bands two combinations of bands 3, 4 and 5, which contain most information on agricultural areas (Kirchhof 1985), were chosen. The band combinations are 3+4 and 4+5. The co-occurrence-matrix results of the combination 4+5 are slightly better than those of the combination 3+4 reaching almost a 100% accuracy in recognising the major land use categories in the training areas. If they were a truly representative sample of the whole image this accuracy would also hold for the whole image.

The classification of the principal-component images lies, when looking at the co-occurrence-matrix, between the excellent results of the 2-band-3-date classifications and the 5-band-1-date classifications.

This easy way of ranking the quality of the classification would result in the following conclusions:

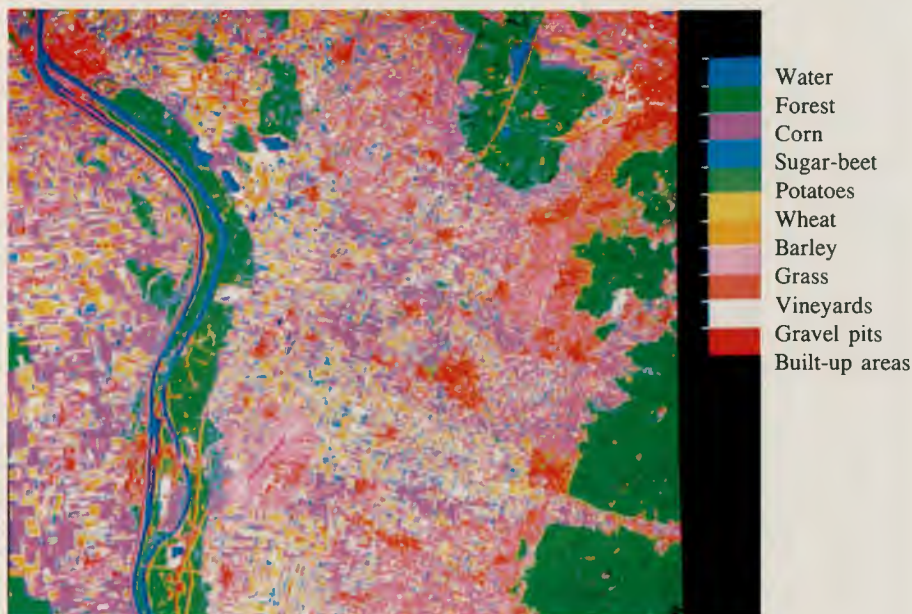
- 1) adding data from different dates to the classification of land use categories greatly improves the classification accuracy;
- 2) the classification of only one date can at best reach an accuracy of around 90%;
- 3) different summer dates can improve the classification accuracy to more than 95%;
- 4) best results are obtained using non-transformed data in bands 4 and 5.

Figures 8-10 show the classified images for the following classifications:

- bands: 1, 2, 3, 4, 5 date: S3 (23 July 1984)
- bands: 4, 5 date: S1, S2, S3
- bands: HPT 1-4 date: S1, S2, S3

Figure 8 shows the best single-date result. It also shows some errors in the classification. The first obvious error is the scattering of sugar-beet, which is all together a pretty rare plant (approx. 2.0% of the cultivated area), into forest. In addition there is a considerable scatter of very small corn fields in the area south of the City of Freiburg (upper right corner) and at the edge of the Black Forest (forest in the lower right corner). Since corn is usually planted on larger fields in the area this is a misclassification. The percentage of wheat (7.5%) is estimated much too low. This percentage is estimated to be 15% by the agricultural administrations. One can con-

Figure 8. Classification results of band combination 1, 2, 3, 4, 5 of 23 July 1984 using 44 training areas.



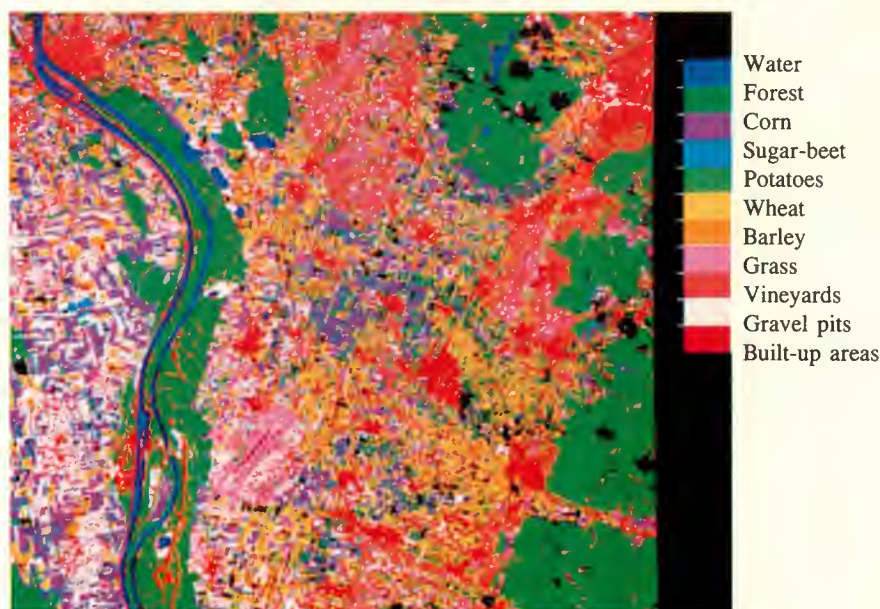


Figure 9. Classification results of band combination 4, 5 of 18 April, 7 July and 23 July 1984 using 44 training areas.

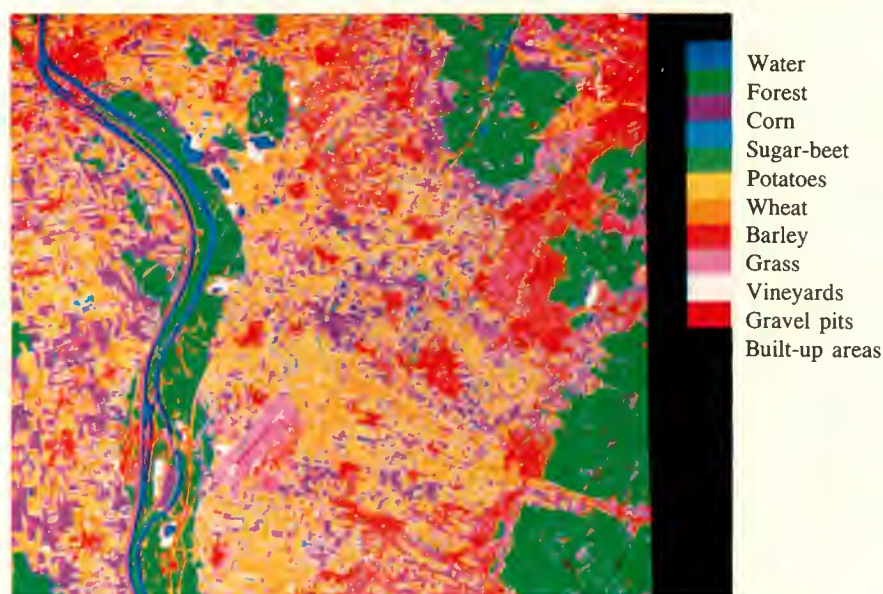


Figure 10. Classification results of first four principal components of the 18 April, 7 July and 23 July data using 44 training areas.

clude that when using the information available as ground truth (gathered directly during the over-flight and additionally through interviews of farmers), this classification result of the whole image is far behind what can be expected from an 95% accuracy of the co-occurrence matrix.

Figure 9 shows the classified image of the band combination of 4+5 and all three dates. The problem of the distinction between forest and sugar-beet fields is gone, the corn fields are in the right order of magnitude for the area and cereals have gained much area. Problems arise with scattered forested areas in the Rhine valley, large gravel pits in France (left of the River Rhine) and around

the air-field and villages, that are too big. There are also black spots in the image indicating unclassified pixels due to clouds and their shadows in the S1 scene. In conclusion, this classification is much closer to reality although it is difficult to quantify objectively what the real land-use has been, because for the whole area there are no exact statistics of the percentages of the different crops. For one land-cover, which is vineyards, this percentage can be estimated pretty accurately because they do not change from year to year. This area (approx. 15%, measured from the 1:2500 topo-map) has been overestimated by a factor of 1.5.

Figure 10 shows the result of the classification of the

principal component image of the area. The problems arisen in Figures 8 and 9 have disappeared, leading to an image where the different centres for corn, cereals, grassland and vine can clearly be distinguished. The areal statistics of the whole image are listed in Table 10. The percentages for wheat and vineyards now correspond to those gathered from maps and estimates.

Table 10. Fractional major land-use categories in the study area (%)

Forest	20.99	Corn	11.53
Wheat	15.84	Barley	18.02
Sugar-Beet	0.75	Potatoes	0.14
Vineyards	14.49	Gravel	0.57
Built-Up	7.07	Grassland	5.05
Water	2.04	Unclassified	0.60

6. Conclusions

It has been shown that a major improvement of a maximum-likelihood classification can be achieved through the inclusion of multiple dates. Most information for the recognition of agricultural areas is contained in bands 3, 4 and 5 and is gathered in the time between the beginning and the end of July. When using multitemporal data the discrepancy between the estimation of the classification accuracy using co-occurrence matrices and the actual classification result shown in the classified image is becoming obvious. This leads to the conclusion that the co-occurrence matrix is only a very coarse measure for the expected classification accuracy. In the case where there are only limited resources for the collection of ground truth (usually) the verification of the classification results becomes the major problem in areas with very inhomogeneous ground cover, like the area

under investigation. Four major conclusions can be drawn:

- 1) The spatial resolution of TM data is sufficient for the classification of the major agricultural fields in a very inhomogeneous area like the Upper Rhine Valley, which can be considered representative for large parts of Central Europe.
- 2) Classification accuracy increases when combining multitemporal data.
- 3) The best results on an overall basis (although not exactly quantifiable to date) is achieved with the first four principal components of all three dates. This is due presumably to the fact that original TM data is not normally distributed, the PC-transformation brings it closer to a normal distribution and therefore makes it more suitable for the maximum-likelihood classifier.
- 4) Ground-data collection is becoming one of the main problems when using TM data. New methods have to be developed to permit more exact statements on the classification accuracy before new classification algorithms can be tested.

7. References

- Kirchhof, W., Mauser, W., Stibig, H.J.: Investigation of the Information Content of Landsat Thematic Mapper and Spot Multiband Image Data Using Simulated Multispectral Image Data of the Freiburg Region, *ESA Technical Translation n° 975*, April 1986
- Mauser, W.: Multitemporal Analysis of the Pehological Stage of Vegetation Using TM-Data in the Southern Black Forest, *Proc. IGARSS'86*, Vol. III, p. 1461
- Mauser, W.: FAP – Nutzerhandbuch, Institut für Physische Geographie, Universität Freiburg, 1987
- NASA: *TM-Data User' Handbook*, NASA Goddard Space Flight Center, Greenbelt, Md, 1983

Mapping Winter Grazing Areas for Reindeer on Svalbard Using Landsat Thematic Mapper Data

Sigmund Spjelkavik & Arve Elvebakk

Institute of Biology and Geology, University of Tromsø, Norway

*In this study Landsat-TM data have been used to detect potential winter grazing areas for the reindeer (*Rangifer tarandus platyrhynchus* Vrolik) in the mountain in Bünsow Land, Svalbard. A vegetation map was made on panchromatic aerial photos in a limited area and later compared with enhanced and classified TM images. Moss communities dominated by *Drepanocladus uncinatus*, *Schistidium apocarpum* and *Cyrtomnium hymenophyllum* together with the bareground community *Papaverion dahliani* were recognised on the mountain plateaus. Faeces counting was used as an indication of reindeer grazing.*

Introduction

The accessibility of food during winter is considered to be the main factor regulating the reindeer (*Rangifer tarandus platyrhynchus* Vrolik) populations in the Svalbard archipelago, arctic Norway, 77–80°N (Fig. 1), as in many other reindeer/caribou herds in arctic and subarctic environments (Punsvik & al. 1980, Gates & al. 1986). Recent research suggests that winter forage plays a more substantial role in meeting the energy requirement during winter than the large reserves of fat accumulated in the reindeer during summer and autumn indicates (Tyler 1986, 1987). Therefore evaluation and mapping of winter grazing areas is important for the monitoring of the reindeer population.

Some of the most important winter grazing areas are found on ridges and in windswept areas with little or no snow cover during winter (Gates & al. 1986, Reimers 1983). The negative effect of the snow cover is intensified by the lack of erect stems from trees or bushes that could penetrate and ventilate the snow and make it easier for the reindeer to smell appropriate forage plants (Bergerud 1974). The amount of snow will fluctuate between some extremes from one winter to another, but the distribution is more or less constant. The snow cover is one of the main factor controlling the distribution of the different plant communities in arctic and alpine environments (Gjærevoll 1956).

Snow accumulates in valleys, therefore grazing areas on mountain ridges and plateaux are probably more important for the reindeer during the winter months than in the summer. With few exceptions, however, vegetation mapping and grazing studies on Svalbard have dealt with areas below altitudes of 200 m (Brattbakk 1985).

Landsat/MSS data have been used for evaluating carrying capacity for reindeer on Svalbard (Øritsland & Ødegaard 1980), and for related topics like caribou habitat studies in Canada (Thompson & al., 1980), moose habitat studies in Alaska (La Pierre & al., 1980) and a lot of other range and habitat mapping purposes (e.g. Carneggie & al., 1983). The coarse spatial resolution in Landsat/MSS data is, however, a major limiting

Figure 1. Svalbard. In circle: Bünsow Land. Redrawn from maps from Norwegian Polar Research Institute.

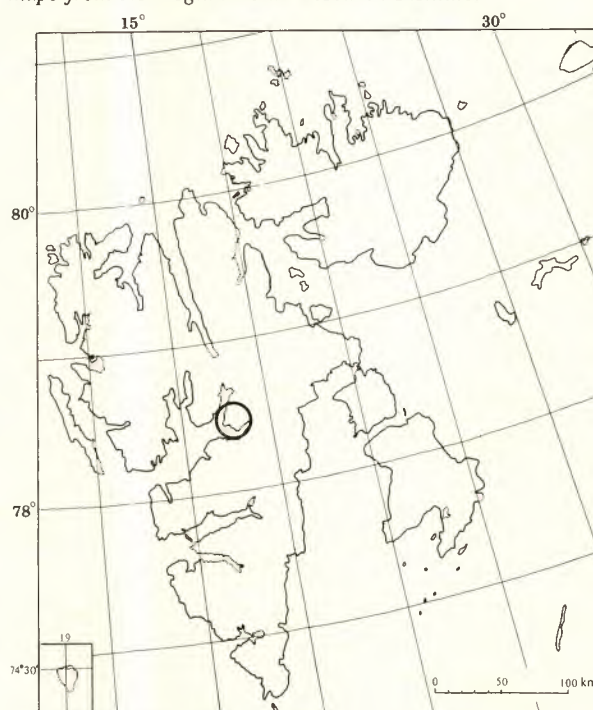




Figure 2. Bünsow Land, equidistance 50 m. From map C8, Billefjorden 1 : 100 000, Norwegian Polar Research Institute.

problem, especially in a topographically varied region like Svalbard.

Landsat-Thematic Mapper (TM) data partly meet the requirements of better spatial and spectral resolution and have recently been used in a series of rangeland investigation and wildlife habitat mapping (e.g. Thomson & al., 1985, Tømmervik & Lauknes, 1986,).

The objective of the present study was to evaluate the use of Landsat-TM data for estimating the potential winter foraging locations and acreage utilized by reindeer in the Bünsow Land area.

Investigated Area

The investigated area is located on Bünsow Land (Fig. 1) by the mountain Gipshuken (726 m.a.s.l., Fig. 2).

The study area comprises the mountain plateaux and ridges of Bünsow Land peninsula in central Spitsbergen, Svalbard. The lowland areas are classified within the middle arctic tundra zone, but the mountain areas belong to an altitudinal arctic polar desert zone (Brattbakk 1985, Elvebakk 1985).

Bünsow Land is dominated by more or less horizontal

deposits of Carboniferous and Permian limestones and with several beds of silicified limestone (chert) (Gee & al. 1952, Winsnes 1966). Shale, siltstone, anhydrite/gypsum, dolerite, and quartzite are also found, but their importance to the plant life in the area is small due to the prevalence of limestone soil deposits.

The surficial materials consist mainly of glaciofluvial and fluvial deposits and marine deposits in the lowland and colluvium in the mountain sides (Kristiansen & Sollid 1987a). Weathered deposits mantle the mountain plateaux and slopes 300-800 m asl. Characteristic geomorphological features are beach ridges as far as 5 km from the sea, alluvial fans/sandur in the lowland, and confluent talus cones on the mountain sides (Kristiansen & Sollid 1987b) separated from the mountain plateaux by vertical cliff walls. The cliffs make the plateaux relatively inaccessible.

Methods

A field investigation with vegetation mapping and reindeer faeces counting was conducted on the Gipshuken mountain during the last week of July 1985. In August 1986 a short visit by helicopter on Sindballefjellet (737 m asl, Fig. 2) was made to check whether an assumed grazing area was in fact present.

Vegetation mapping on aerial photos:

A vegetation map was made of the Gipshuken mountain area using conventional mapping on panchromatic aerial photos (1 : 46 000). Due to small scale patterns of ridges and depressions, most vegetation mapping units were a mosaic of several communities in the sense of the European phytosociology. As a documentation of the mapping units, most communities were analysed with 5 relevés in selected stands using percentage cover values.

Faeces counting ('Pelletgroup Count Technique'):

To measure how many times or how long the reindeer visits an area, the 'pelletgroup count technique' was used. It is a commonly accepted method used by several other investigators in zoology: Neff (1968), Punsvik & al. (1980), Staaland & Punsvik (1980), Thompson & al. (1980), and other.

The method is based on the positive correlation between the amount of faeces registered on a site, and the number of animals and/or the length of time the animals spend on that site. Grazing activity is the main factor determining the distribution of Svalbard reindeer, an animal lacking natural enemies.

Reindeer faeces were counted along transects 2 m broad and with a total length of 4.5 km in the mapped area in different vegetation types. The faeces were divided into winter and summer types.

Landsat-TM image processing:

There was no Landsat TM scene from previous summers of acceptable quality available covering the study area, so image processing or classifications before the fieldwork was not possible. A scene from 5 August 1985 was acquired and processed during the following winter.

The digital Landsat-TM (path 217, row 3, Q4) data was analysed on the Tromsø Telemetry Station's I²S image processing system (system 575, International Imaging Systems, 1984), using standard image enhancement processing routines, and an unsupervised classification (cluster analysis). Geometric correction was also performed.

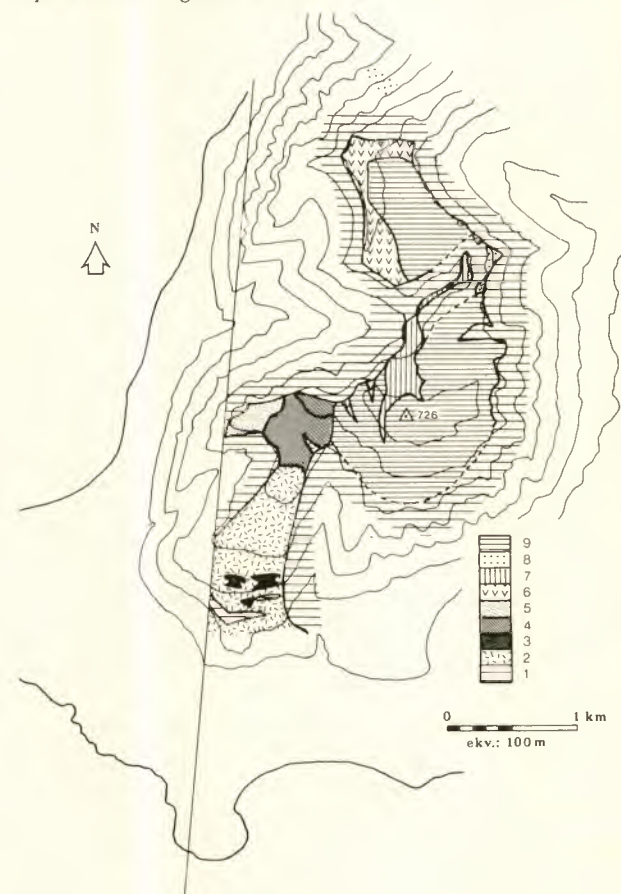
Different combinations of bands were tested in an attempt to reconstruct the vegetation map made during ground truthing. Vegetation indices as ratios between different bands were tried in order to register vegetated areas.

Results

Vegetation map from Gipshuken:

A vegetation map was made covering 5 km² of the Gipshuken mountain above 300 m asl (Fig. 3). The following 9 mapping units were used:

Figure 3. Vegetation map from the upper part of Gipshuken. Explanation to legends in text.



- 1) Mostly sterile limestone deposits below altitudes of 600 m.
- 2) *Parmelia stygia* – *Sporostatia testudinea* community. This is a community characterized by the lack of vascular plants and bryophytes. These chert gravel areas are covered by saxicolous, acidophilous lichens. Crustose lichens like *Sporostatia testudinea* and *Rizocarpon* spp. cover 20–40% of the surface, while fruticose lichens like *Parmelia stygia*, *P. alpicola*, *Umbilicaria proboscidea* and the rare *Hypogymnia austerodes*, *H. oroarctica* and *H. physodes* cover 4–12%. This community has a dominant position on the plateau and the gentle slopes below 550 m.
- 3) A vegetation complex comprising four communities covering small areas in the lowermost part of the mapped area:
 - a) *Papaverion dahliani* Hoffm. 68. em. Elvebakk 85. This is a polar desert community with 0.1–1% cover of vascular plants and terricolous lichens and bryophytes. *Saxifraga oppositifolia* is the most common plant along with the lichens *Thamnolia vermicularis*, *Cetraria nivalis* and *Ochrolechia frigida*. The community is rather rich in species, but is dominated by limestone and chert debris.
 - b) Like 2.
 - c) *Kobresio*–*Dryadion* Nordh. 36. A very common community on Svalbard, 20–50% vegetation cover.
 - d) *Luzulion arcticae* (Nordh. 36) Gjaerev. 56. This is a moderate snowbed community on limestone substrate rich in species. Bryophytes like *Homalothecium nitens*, *Timmia austriaca* and *Drepanocladus uncinatus* dominates with a total of 50–80% cover. Vascular plant cover is 20–30% with *Salix polaris* as the dominant species.
- 4) A vegetation complex comprising four communities covering a rather large area 550–620 m asl on a mixture of limestone, siliceous sandstone and chert. Figure 4 illustrates the relative area of this community within the mapping unit.
 - a) *Papaverion dahliani*. This is a community on unstable ridges, but it is more vegetated than the related 3a, with 4–10% cover of vascular plants and 5–10% cover of lichens and bryophytes.
 - b) *Schistidium apocarpum*. This is a community on loose gravel with good drainage and lack of fine textured soils. Vascular plants are sparse, except for *Saxifraga cernua* and *S. hyperborea* constantly occurring in very small quantities. The bryophyte *Schistidium apocarpum* dominates with a cover of 50–80%, with other bryophytes like *Disticum flexicaule* and *Drepanocladus uncinatus* and the lichen *Ochrolechia frigida* making up 5–15%.
 - c) *Drepanocladus uncinatus* community. This is a well-drained moderate snowbed possibly manured by reindeer. *Drepanocladus uncinatus* is the dominant species with cover values ranging from 30–70%. Other bryophytes, especially *Pohlia cruda*, make up 5–30%. Very few vascular plants are present, except for a number of the small *Saxifraga hyperborea* (2–10%).
- d) *Cyrtomnium hymenophyllum* community. This is a wet moss community along drainage systems. *Cyrtomnium hymenophyllum* is dominant (30–80%); other characteristic bryophytes includes *Brachytechium turgidum*, *Plagiomnium ellipticum*, and *Bryum cryophilum*.
- 5) A vegetation mosaic including *Papaver dahlianum* and *Poa alpina* communities. This unit was not studied in detail.
- 6) Vegetation complexes on mixtures on limestones and chert gravel at altitudes above 600 m.
 - a) *Dicranoweisia crispula* community (cf. Elvebakk, 1984) growing on chert gravel and stones in slight depressions, while *Cetraria delisei* is found between stones.
 - b) *Cetraria nivalis* communities on exposed sites associated with *Alectoria nigricans*. This community covers small areas.
 - c) *Papaver dahlianum*/*Cladonia pocillum* community on small spots of fine-textured soils. This community covers only small areas.
- 7) Glaciers.
- 8) A vegetation complex found once in the northern part of the investigated area with a varied topography. The mapped unit is intermediate between 4 and 6.
 - a) Like 4a.
 - b) Like 6b.
 - c) Siliceous gravel or stony slopes with *Cetraria hepatizon*. The community is less humid than the *Dicranoweisia crispula* community and less dry and thermophilic than the *Parmelia stygia*/*Sporostatia testudinea* community.
- 9) Sterile 'limestone desert' on the top plateau above 550 m asl. The area is practically devoid of plants; even crustaceous lichens are lacking.

Faeces distribution

The results of the reindeer faeces counting on Gipshuken is shown in Figures 4 & 5.

The transect in Figure 4 shows that mapping units 3 and 4 are the only ones with any number of reindeer droppings. This coincides well with their vegetation cover, which was more than 50% in two of the communities of mapping units 3 and three of the communities of mapping unit 4.

Figure 5 illustrates the distribution of faeces over the different communities within mapping unit 3 and 4. This shows that there is a positive correlation between amount of faeces and vegetation cover. There is also a higher proportion of winter faeces in the ridge communities (3a, 3c, 4a) that are accepted to be more easily accessible to the animals during winter. There is an increase in faeces as one moves to the depression communities. The highest

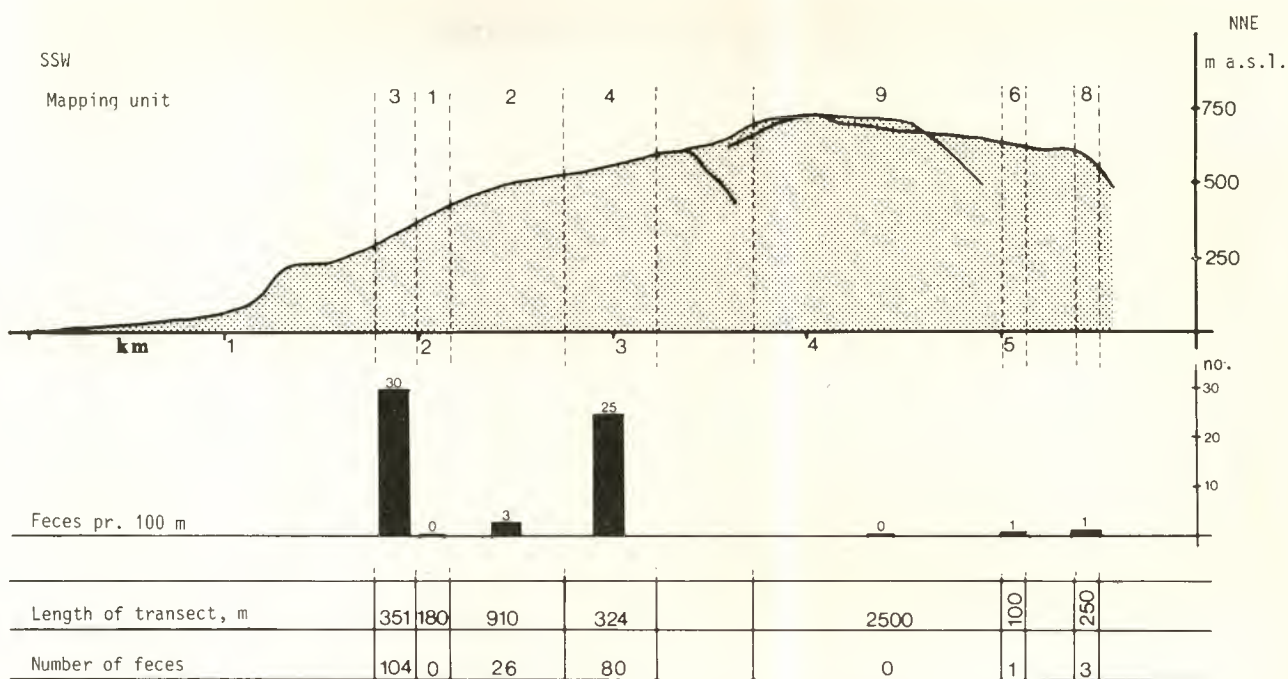


Figure 4. Distribution of faeces along a transect on Gipshuken. The vegetation units are the same as on the vegetation map in Fig. 3.

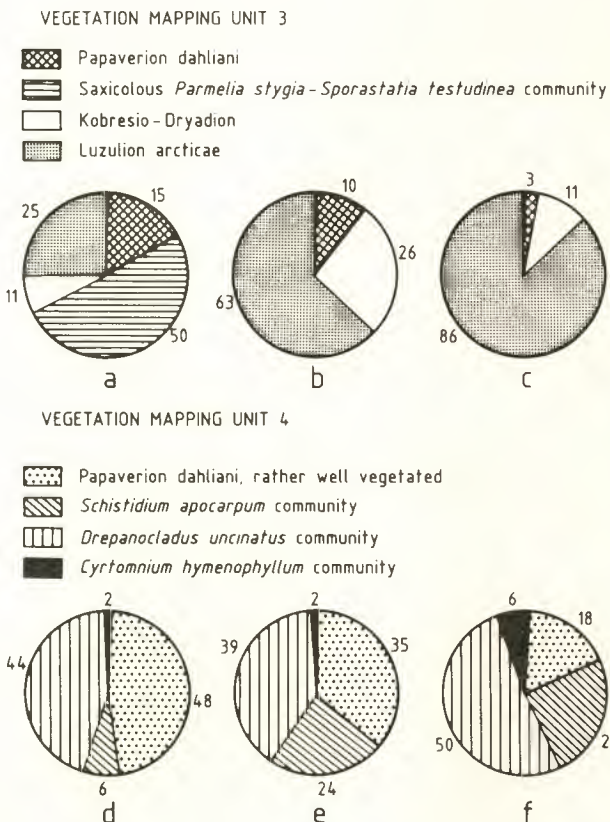
Figure 5. Relative distribution of communities and results of faeces counting in vegetation complexes 3 and 4.

Complex 3: a) distribution of communities

- b) winter faeces
- c) summer faeces

Complex 4: a) distribution of communities

- b) winter faeces
- c) summer faeces



proportion of summer faeces is found in the wettest community: 4d.

Sindballefjellet:

The short visit on Sindballefjellet in 1986, confirmed that the plateau 650 m asl, clearly distinguished on the satellite image, was vegetated in contrast to the surrounding fields (Fig. 6). The terrain was undulating and slightly tilting SW. The vegetation was similiar to the vegetation complex mapped as unit 4 on the Gipshuken map and consists of *Drepanucladus uncinatus* communities in mosaic with *Phippsia algida* communities with *Saxifraga hyperborea*, *Stereocaulon arcticum* and *Peltigera canina* in addition to *Phippsia*.

The amount of reindeer faeces was higher on Sindballefjellet than on Gipshuken. The numbers from the com-

Figure 6. Sindballefjellet with the vegetated area in the middle of the picture. Photo: K. Sollid/Polar Press, Tromsø.





Figure 7. Standard false-colour composite (TM-bands 2, 3 & 4) of Bünsow Land.

pared vegetation complex were 50 faeces/100 m on Sindballefjellet and 25 faeces/100 m on Gipshuken. In the desert-like surrounding areas on Sindballefjellet, no faecal droppings were observed.

Image processing

A good quality image for visual interpretation resulted from standard enhancement of the satellite scene achieved by contrast stretching of a composite of bands 4, 3 and 2; a standard false colour composite (Fig. 7).

An unsupervised classification using bands 7, 4 and 3 gave a result with 27 classes and one group of rejected pixels. Nine classes could be related to different vegetation types. In this classified image, vegetation unit 4 in the vegetation map from Gipshuken, was recognised on Sindballefjellet. Some of the vegetated classes are shown in green and yellow together with the topographic map in Figure 8.

In addition to the localities on Gipshuken and Sindballefjellet, this class was common below the compound alluvial fans on lower elevations.

To distinguish vegetated areas from bare soil and water, a vegetation index was obtained by dividing the near infrared band (NIR) by the red band (R). Then by thresholding the ratio vegetated areas were separated from nonvegetated areas (Fig. 9).

Conclusions

With the combination of bands 3, 4 and 7, and with the ratio NIR/R, the sparsely vegetated areas on Gipshuken



Figure 8. Some of the vegetated classes shown in green and yellow together with the topographic map. Dark green: moist meadow, green: moss communities on Gipshuken and Sindballefjellet together with moss communities in the lowland and birdcliff vegetation, yellow: mesic meadow/heath, greenish grey: mixed vegetation.

Figure 9. Vegetated areas. Result of thresholding the vegetation indices NIR/R.



and Sindballefjellet were detected. They could not be recognised on the black and white aerial photos. These vegetated areas were the only possible grazing areas in the mountain in the investigated part of Bünsow Land.

The correlations between faeces distribution and vegetation cover, and also the ridge snowbed gradient indicates that the faeces group counting technique is a satisfactory

method for evaluating grazing areas of the Svalbard reindeer.

This investigation also concludes that mountains with bedrock of limestone in areas with little precipitation are of low value as range for reindeer.

A traditional field examination of all mountain plateaux of Bünsow Land, would involve a high investment of time, money and personnel. Examination of test sites in a limited geographical area and extrapolations to a larger region with Landsat TM data seem to be a viable alternative.

The spatial and spectral resolution of the Thematic Mapper system seems to be sufficient for rangeland mapping in this arctic region. But for future vegetation mapping and classification with satellite data on Svalbard, associated digital terrain data with information about elevation, slope and aspect would be of great value.

Acknowledgements

This study was supported by ESA/Earthnet in the framework of the Pilot Project Campaign. The authors want to thank Earthnet, the NPOC R.T. Enoksen, Tromsø Telemetry Station and The Royal Norwegian Council for Scientific & Industrial Research for their help and support and the Norwegian Polar Research Institute for their funding of the field work. Special thanks are conveyed to Dr. A.M. Odasz for revising the English text.

References

- Brattbakk I., 1985. Flora og vegetasjon. p. 10-34, in N.A. Øritsland (red.): Svalbardreinen og dens livsgrunnlag. *Avslutningsrapport før MAB-prosjektet 1975-1985*. Norsk Polarinstitutt, Oslo, 278 p.
- Bergerud A.T., 1974. Relative abundance of food in winter for Newfoundland caribou. *Oikos* 25 (3): 379-387
- Carnegie D.M., Schrumph B.J. & Mouat D.A., 1983. Rangeland Applications. p. 2325-2384, in Colwell, R.N. (ed.): *Manual of Remote Sensing*, Second Edition, Virginia, 2440 p.
- Elvebakk A., 1984. Vegetation Pattern and Ecology of Siliceous Boulder Snow Beds on Svalbard. *Polarforschung* 54(1): 9-20.
- Elvebakk A., 1985. Higher phytosociological syntaxa on Svalbard and their use in subdivision of the Arctic. *Nord. J. Bot.* 5(3): 273-284, Geobot 014.
- La Perrier A.J., Lent P.C., Gassaway W.C. & Nodler F.A., 1980. Use of Landsat data for moose-habitat analyses in Alaska. *J. Wildl. Manage.* 44(4): 881-887.
- Gates C.C., Adamczewski J. & Mulders R., 1986. Population Dynamics, Winter Ecology and Social Organization of Coats Island Caribou. *Arctic* 39(3): 216-222.
- Gee E.R., Harland W.B. & McWhae J.R.H., 1952. Geology of Central Vestspitsbergen: Part I. Review of the Geology of Spitsbergen, with special reference to Central Vestspitsbergen; Part II. Carboniferous to Lower Permian of Billefjorden. *Trans. Roy. Soc. Edin.* 62(9): 299-356.
- Gjærevoll O., 1956. The plant communities of the Scandinavian alpine snowbeds. *Det kgl. norske. vidensk. selsk. skr. 1956: 1*. Trondheim, 405 p.
- Kristiansen K.J. & Sollid J.L., 1987. Svalbard. Jordartskart. Map of surficial materials 1 : 1000 000. *Nasjonaltlas for Norge*. Geografisk Institutt Universitetet i Oslo.
- Kristiansen K.J. & Sollid J.L., 1987. Svalbard. Glacialgeologi og geomorfologi. Glacial Geology and Geomorphology. 1 : 1000 000. *Nasjonaltlas for Norge*. Geografisk Institutt Universitetet i Oslo.
- Neff D.J., 1968. The Pellet-group Count Technique for Big Game Trend, Census, and Distribution: A Review. *J. Wildl. Manage.* 32(3): 597-614.
- Punsvik T., Syvertsen A. & Staaland H., 1980. Reindeer grazing in Advendtdalen, Svalbard. s. 115-123 in Reimers E., Gaare E. & Skjenneberg S. (eds.): *Proc. 2nd. Int. Reindeer/Caribou Symp., Røros, Norway 1979*. Direktoratet før vilt og ferskvannsfisk, Trondheim. 799 p.
- Reimers E., 1983. Mortality in Svalbard reindeer. *Holarctic Ecology*. 6(2): 141-149.
- Staaland H., 1985. Svalbardreinenens ernæring. p. 97-128, in N.A. Øritsland (red.): *Svalbardreinen og dens livsgrunnlag. Avslutningsrapport før MAB-prosjektet 1975-1985*. Norsk Polarinstitutt, Oslo, 278 p.
- Summerhayes V.S. & Elton C.S., 1928. Further contribution to the ecology of Spitsbergen. *J. Ecol.* 16(2): 193-268.
- Tyler N., 1986. The relationship between the fat content of Svalbard reindeer in autumn and their death from starvation in winter. *Rangifer*, Special Issue No. 1.
- Tyler N., 1987. Estimating the daily dry matter intake of Svalbard reindeer in late winter. *Rangifer* 7(1): 29-32.
- Thompson D.C., Klassen G.H. & Cihlar J., 1980. Caribou habitat mapping in the southern district of Keewatin, N.W.T.: An application of digital Landsat data. *J. Appl. Ecol.* 17: 125-138.
- Thomson K.P.B., Gosselin C., Adams B.W. & Sutherland I., 1985. Thematic Mapper Data used for Rangeland Management in Rough Fescue Grasslands in Western Canada. *Canadian Journal of Remote Sensing*, 11(2): 162-176.
- Tømmervik H., Lauknes I., 1986. Noen erfaringer med bruk av satellittdata i kartlegging av reinbeiter, Dividal, Kautokeino og Pasvik. Third Nordic

substratum with a predominance of gypsiferous materials, abundant in the southeast of the province.

The soils developing in this pilot zone can be classified as Entisols (Xerofluvents) to those formed over the lower terrace of the River Tajo, the profile of which shows little development. Evolution of the soil profile is greater in the higher terraces, and the illuvial horizons being of clay, these are classified as Alfisols (Haploxeralfs and Palixeralfs).

Evolution of the types of soils developed in gypsiferous formations is of little consequence, due principally to the intense erosion process to which they are submitted, and these soils are classified as Entisols (Xerorthents), no diagnostic horizons being observed.

3.1. Interpretation of June Image

Four areas were selected from within this pilot zone of Fuentidueña de Tajo: two of them (1 and 2) correspond to gypsiferous soil landscapes and the others (3 and 4) to the irrigated farmland soils of the River Tajo terraces.

3.1.1. Composition of Bands

Bands 2, 3 and 4 were combined in this image taken on

15 June 1984, the blue, green and red filters being assigned in all cases to obtain the most used false-colour composition (Fig. 1).

The image obtained by the TM sensor shows the patterns of drainage characteristic of gypsiferous material. These patterns are clearly visualised in Band 2, while in the image corresponding to Band 4 the presence of water is even more clearly in evidence.

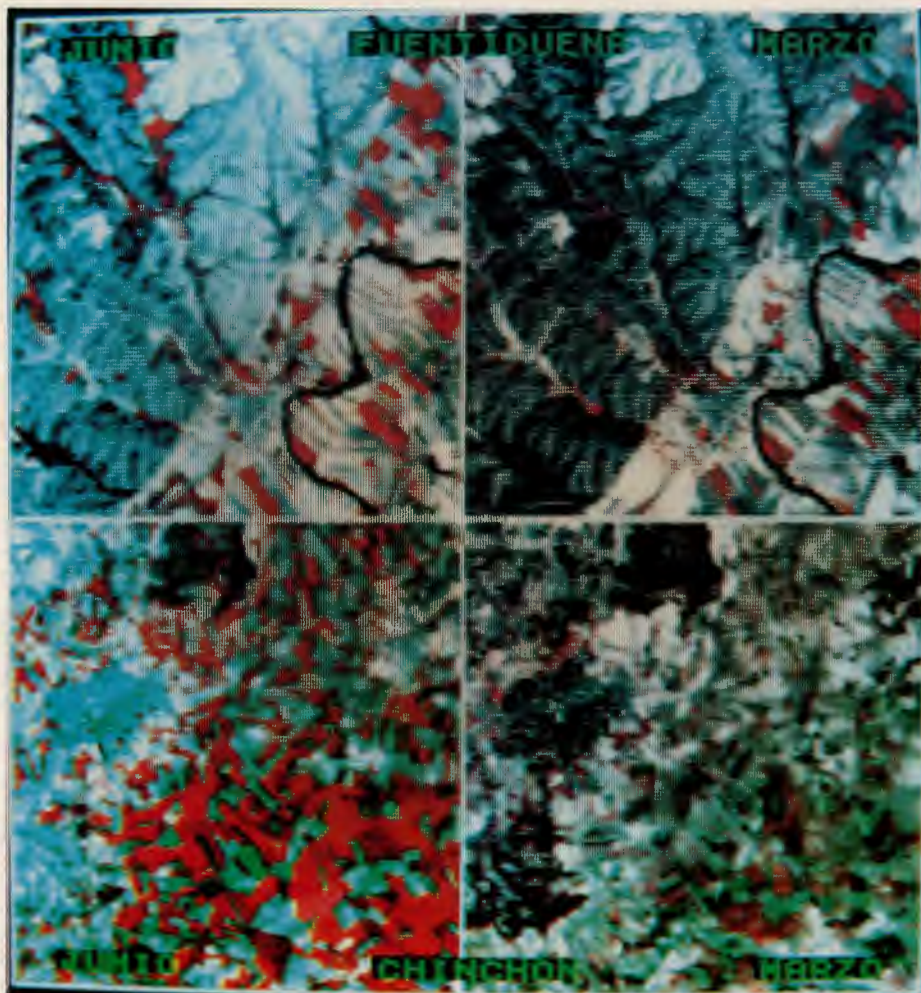
The perfect separation between gypsiferous materials and the River Tajo terraces is made conspicuous by the patterns of erosion and the uses given to the soils. The white tones correspond to bare soils in flat gypsiferous areas and terraced areas.

3.1.2. Vegetation Indices

The ratio of difference to sum of bands gives the indices of vegetation, making it possible to observe the separation between areas with and without green vegetation.

Bands 4 and 3 would seem more useful than bands 4 and 2 in obtaining indices of vegetation, the red and green outlines being more easily distinguishable.

Figure 1. Composite image. Pilot zone of Fuentidueña de Tajo and Chinchón.



3.2. Interpretation of March Image

The height of the sun at this date accentuates relief in the areas of gypsum lithology and visualisation of the drainage system in comparison with June is considerably improved.

3.2.1. Composition of Bands

The combination of Bands 7, 5 and 4 accentuates the eroded areas of gypsum and the network of roads. The natural colour obtained with Bands 1, 2 and 3 serves to separate the deeper soils which develop over the terraces, and practically the same result is attained with Bands 1, 5 and 7 as well as detection of throughways. (Fig. 1).

In the coloured compositions of the different bands the deeper, more fertile and more intensely cultivated soils can be separated with precision from the associated soils composing the cartographic unit of the River Tajo terraces.

4. Ecosystem Related to Calcareous Materials

The pilot zone of Chinchón is representative of the landscape which extends between the valleys of the River Tajo and the River Tajuña. It is composed of a succession of plateaux cut by steep slopes caused by erosion.

The area of this pilot zone is a square of somewhat more than 7 km×7 km with three outstanding land elements, i.e. 1) two residential areas (Chinchón and Colmenar de Oreja) forming an urban landscape; 2) the lands given over to cereal crops and vineyards on soils developed over the surface of the paramo, 3) and the slopes of the paramo produced by the incidence of fluvial erosion on the primitive calcareous surface which has cut through the geological materials.

The presence of calcium carbonate in the soil is a predominant character in the development and evolution of soil profiles. The soils which develop over the calcareous formation are known as Inceptisols (Xerochrepts), of medium evolution and with the presence of cambic horizon; in very specific areas 'Alfisols' (Haploxeralfs and Palexeralfs) associated with the aforementioned area are also to be found. Above the gypsiferous marls the most frequent associations of soils are Aridisols, with gypseous horizons and Entisols (Xerorthents).

4.1. Interpretation of June Image

Analysis of the most outstanding land elements of this image was carried out by choosing five test fields, two of them on the surface of the paramo, a third representative of the slope of the paramo facing south, and the other two considered typical landscape of urban settlements in the south east of the province. Discrimination between urban

landscapes, composed of villages of a size and structure clearly visible in all bands of the TM image, and the rural landscapes devoted to farming is simple and easy.

4.1.1. Composition of Bands

The false colour obtained when assigning blue, green and red to Bands 2, 3 and 4 is much more adequate for the study of soil coverings. The breaches in the gradient at the edges of the paramo and the severe erosion processes are sufficiently well differentiated (Fig. 1).

From a pedological point of view, the intensity of colour is in direct relation to the depth of soils, a more intense red indicating greater depth.

Colours light in tone show up in the image where gypsiferous materials have made their appearance bordering the surface of the paramo (affected by severe erosion), and the limestone quarries are also distinguishable in white. Dark colouring coincides with eroded areas, with steep gradients and sparse thickets.

Natural colour 1, 2, 3 facilitates localisation of the deep soils found over the surface of the paramo, and great precision in the visualisation of urban district limits is obtained with the combination of Bands 1, 5, 7.

4.2. Interpretation of March Image

Analysis of the seven bands of the TM sensor in this image showed that Bands 1, 2 and 7 were of little or no interest since the land elements were not in evidence. The surface area of the paramo could be observed in Band 3; Band 4 emphasized the contours of the parcelled lands; Band 5 provided information with regard to highways and the contours or urban districts and the thermic band marked the lower areas (which coincide with the darker tones) and the higher (represented by light tones).

4.2.1. Composition of Bands

The most characteristic and important detail to note about this false-colour 2, 3, 4 image is the clear delimitation of the deep and less deep soils within the same landscape unit of the paramo. The deeper soils, having greater capacity for the retention of water, are used to a greater degree, crop rotation by the agriculturist being carried out without fallowing; this is the reason for the presence of redder tones. The darker tones corresponding to deeper soils can be observed in the centre of the image (Fig. 1).

In the image in natural colour all the aforementioned characteristics are even more outstanding, and this image is of special interest from a pedological point of view, the cartographic units of the soils being much more clearly identified.

5. Characterisation of Land Elements

Analysis and spectral interpretation of these two pilot zones of the Autonomous Community of Madrid, situated in the south and southeast of its territory, have served as a starting point in establishing the most outstanding characteristics of the land element of major influence in the composition of the ecosystems studied.

The spectral characteristics of each of these land elements (considered test samples), of the pilot zones are defined by the following radiance values in the seven bands obtained by the TM sensors, through the Landsat 5 image (15-June-1984).

Land elements	TM Bands						
	1	2	3	4	5	6	7
Gypsum landscape	133	68	82	95	143	157	63
Paramo	90	47	61	96	128	149	64
Paramo scarps	110	58	72	100	146	147	72
Urban districts	114	55	68	71	127	152	78
Vegetal cover	76	34	30	125	96	135	31

The patterns of the gypsum landscape can be easily differentiated.

A second land element discernible is that denominated paramo. An effort has been made to diminish the slight variations caused by the diversity of soil and the uses to which the soil is put in order to obtain a fair evaluation of these variations.

The ruptures originated by fluvial currents of varying strength found on the surface of the paramo are converted into scarps of different gradient, topographical positions and different vegetation. The spectral curve presents a very high value in Band 5 (1.55–1.75 μm), and this circumstance should be taken into account in spectral discrimination.

The vegetal coverings present a typical spectral curve cutting through those without green vegetal mass. The relation between the values of Bands 2, 3, 4 and 5 also gives indices of discrimination of great significance.

The rural urban districts whose values pertain to the villages of Chinchón and Colmenar de Oreja are clearly characterised and classification of same could only induce errors if Band 5 were not eliminated.

Taking into account the data obtained from the TM sensor in March, detection of the land elements would apparently seem more difficult but, in fact, as has been indicated in the analysis of images, from a geological and pedological point of view, the images at this date contain considerable valid information.

The spectral characteristics of each of these land elements (14-March-1985) are defined by the following radiance values:

Land elements	TM Bands						
	1	2	3	4	5	6	7
Gypsum landscape	93	45	53	59	99	109	43
Paramo	80	40	52	58	112	115	61
Paramo scarps	86	42	53	63	114	112	58
Urban districts	86	39	47	47	88	108	53
Vegetal cover	85	41	50	65	108	110	54

Landsat TM data have been used in conjunction with other sources of information in order to analyse and interpret the spectral characteristics of the most significant land elements in two pilot zones in the south east of the Community of Madrid. Fig. 1 is a composite of images at both dates of the pilot zones of Fuentidueña de Tajo and Chinchon showing the large landscape units.

The radiance values in the seven bands, the configuration of the spectral curve and the composition of bands constitute information made available by the Landsat TM images, analysis of which complements knowledge of the land elements, adding valuable data to classic sources of information in order to better understand the ecosystems in existence. Multispectral data has been found of great assistance in the control of degradation in these particular areas, which should be protected at all cost.

6. Conclusions

Analysis of Landsat TM images with a view to knowledge of land elements from a different perspective provides additional information to that obtained from other sources, and can be of available assistance with regard to the following:

1. The combination of Bands 2, 3 and 4 is the most adequate for a study of soil coverings. Red indicates green vegetation, and is related to a greater depth and development of the soil profile.
2. The coloured composition of Bands 1, 2, 3 greatly emphasises the soil landscape, the topographical forms, the eroded areas, the eroded developed soils of the River Tajo's terraces (Haploxeralfs) and the cartographic units of the soils.
3. Spectral characterisation of a gypsum landscape where soils of little evolution (Xerorthents) develop is made possible with data from the Landsat TM. The characteristics patterns of gypsiferous material are clearly observed in Band 4.
4. The alluvial and terrace soils can be distinguished where occupied by crops. It is not possible to dif-

ferentiate the levels of the terraces except at definite points, due to a change in the parcelling and use of the soil.

5. Discrimination of the different landscapes in a summer image is best when using the Thematic Mapper bands 2, 3 and 5.
6. Bands 4 and 5 permit a clear separation of the 'Urban' classes.
7. The 'scarp' class of the paramo, affected by severe erosion processes, presents characteristics of a mixed class and difficulty in discrimination.
8. Band 4 and 3 are the most apt for obtaining vegetation indices.
9. Bands 5 (1.55–1.75 μm) was found to be best for the differentiation of land elements.
10. Soils are better detected in the March image, and natural colours 1, 2, 3 enhances the presence and localisation of deep soils (Haploxeralfs and Palexeralfs) developed over the surface of the paramo.

7. Bibliography

- American Society of Photogrammetry (1983). 'Manual of Remote Sensing' Volume I and II. Falls Church Virginia. Second Edition.
- Carrol D.M., Evans R. & Bendelow V.C. (1977). 'Air Photo-interpretation for Soil Mapping'. *Soil Survey Technical Monograph*, n° 8. Harpenden, UK, 85 p.
- Centro de Investigacion U.A.M-I.B.M. (1981). 'Tratamiento digital de imágenes y sus aplicaciones'. Madrid, 352 p.
- Labradero J.L. (1978). 'Aplicación de Métodos Digitales al Reconocimiento de Suelos mediante Sensores Remotos'. Tesis Doctoral. Universidad Autónoma de Madrid, 455 p.
- Scanvic, J.I. (1983). 'Utilisation de la Télédétection dans les Sciences de la terre'. Bureau de recherches géologiques et minières. *Manuels & Méthodes*, 7, 159 p.
- Westing F.C. & Frazee C.J. (1976). 'Landsat data, its use in a soil survey program'. *Soil Science Society of America Journal*, 40 (1): 81-89.

Comparison of the Classification Results Obtained with TM and MSS Data in the Land Uses Identification of the 'Comunidad Autónoma de Cantabria'

Federico Gonzalez Alonso

*Proyecto de Teledetección, Sección de Proceso de Datos I.N.I.A
Madrid*

José Mara Ureña Francés

*Departamento de Urbanismo y Medio Natural
Universidad de Cantabria, Santander, Spain*

The different sensors now operative (MSS, TM, HRV, AVHRR) make it possible to determine the normalised vegetation index for the monitoring and discrimination of several types of vegetal canopies with different frequency and degree of spatial resolution.

With the aim of making the indices obtained from the TM and MSS data more easily comparable several radiometric corrections are made.

Subsequently, training areas for the different types of canopy are delimited, and the study zone is classified using the intervals obtained for the normalised vegetation index in each class. The results obtained are compared in a pilot zone of the Comunidad Autónoma de Cantabria.

1. Introduction

One of the major advantages shown by remote sensing, and more specifically, the use of digital images obtained from the earth observation satellites (Landsat, Spot, NOAA, etc) is the frequency of the observations that, as indicated in Table 1, ranges from 8760 images yearly from Meteosat to 14 from Spot, which is due to the very great differences in their spatial and spectral resolution.

In the future, this continuity of the information flow will make it possible to control and monitor the land uses and vegetation cover in larger or smaller areas of the territory. The scale of work depends on the spatial resolution of the sensor employed.

In this work we try to compare the utility and viability of the different land-use classifications obtained from vegetation indices.

These indices were calculated using TM and MSS data from a pilot zone of the Comunidad Autónoma of Cantabria.

The main objective of this project was to establish a methodology that makes it easy to monitor and update the different land uses in the above-mentioned region.

This project was performed in cooperation with the Catedra de urbanismo y medio natural of the Cantabria University. The material support of the project was provided by Earthnet through the Spanish National Point of Contact.

2. Radiometric Correction of the Images

The standard use of the digital images as provided to the users by the distribution centers can sometimes produce incorrect or inaccurate results. The reason is that the digital values of the CCTs do not quantitatively represent real physical values and are used only for convenience in computer processing of the data (Robinove, 1982).

Table 1. Earth observation satellites

Satellite and sensor	Band	Wavelength (μm)	Spatial resolution	Frequency
Landsat MSS	1(4)	.5- .6	80×80 m	16 days
	2(5)	.6- .7	„	„
	3(6)	.7- .8	„	„
	4(7)	.8- 1.1	„	„
Landsat TM	1	.45- .52	30×30 m	16 days
	2	.52- .60	„	„
	3	.63- .69	„	„
	4	.76- .90	„	„
	5	1.55- 1.75	„	„
	6	10.40-12.50	120×120 m	„
	7	2.08- 2.35	30× 30 m	„
Spot HRV	1	.50-.59	20×20 m	26 days
	2	.61-.68	„	„
	3	.79-.89	„	„
Panchromatic	1	.51-.73	10×10 m	„
NOAA/ AVHRR	1	.58- .68	3.3×4.0 km	12 hours
	2	.72- 1.10	„	„
	3	3.55- 3.93	„	„
	4	10.30-11.30	„	„
	5	11.50-12.50	„	„
Meteosat	1	.4- 1.1	2.5×2.5 km	1 hour
	2	5.7- 7.1	5×5 km	.5 hour
	3	10.5-12.5	„	1 hour

To facilitate comparison among images taken at different dates by different sensors, the effects of differently calibrated sensors and different angles of solar illumination have been corrected.

In the case of the MSS sensor of the Landsat-4 satellite, the radiance ($\text{mW}/\text{cm}^2/\text{sr}$) and the reflectance at the top of the atmosphere were calculated using the formulas indicated by Robinove (1982).

$$\text{Radiance} = D_n (L_{\max} - L_{\min}) / D_{\max} + L_{\min}$$

where:

D_n = the digital value of a pixel from the CCT.

D_{\max} = the maximum digital number recorded on the CCT.

L_{\max} = radiance measured at detector saturation in $\text{mW}/\text{cm}^2/\text{sr}$.

L_{\min} = lowest radiance measured by the detector in $\text{mW}/\text{cm}^2/\text{sr}$.

The values corresponding to L_{\max} and L_{\min} are in Robinove (1982) and Nelson (1985).

Reflectance in a single band for a Lambertian surface is calculated by:

$$\text{Reflectance} = \text{Radiance } 3.1416 / E \sin(\alpha)$$

where:

E = irradiance in $\text{mW}/\text{cm}^2/\text{sr}$ at the top of the atmosphere. For the MSS sensor the values are (mW/cm^2):

$$\text{Band 4} = 17.70$$

$$\text{Band 5} = 15.15$$

$$\text{Band 6} = 12.37$$

$$\text{Band 7} = 24.91$$

α = solar elevation, measured from the horizontal, as annotated on Landsat images.

In this study, the corrections for bands 4 (previously 7) and 2 (previously 5) of MSS Landsat image 4-202-30 of the date 14 June 1984 were:

$$R_4 = 1.5772 + 0.2412 \times D_4$$

$$R_2 = 1.0362 + 0.1788 \times D_2$$

In the case of TM sensor of Landsat 5 the digital values were transformed into radiances using the expression indicated by Lopez-Garcia *et al.* (1985).

$$\text{Radiance} = a_0 + a_1 \times D \text{ (W}/\text{m}^2/\text{sr)}$$

were:

D = digital value of a pixel from the CCT.

a_0 and a_1 = calibration coefficients for each TM band.

Reflectances were calculated in a form similar to the MSS data, but in this case the irradiance values (W/m^2) at the top of the atmosphere were:

$$\text{TM band 1} = 138.25$$

$$\text{TM band 2} = 139.44$$

$$\text{TM band 3} = 89.10$$

$$\text{TM band 4} = 147.70$$

$$\text{TM band 5} = 44.60$$

$$\text{TM band 7} = 21.33$$

In this project the corrections for the TM band 4 and band 3 corresponding to the TM Landsat image 5-202-030-2 of the date 25 June 1985 were:

$$R_4 = -0.6178 + 0.3105 \times D_4$$

$$R_3 = -0.4955 + 0.2858 \times D_3$$

After the radiometric corrections we can consider that the MSS data of 84/Jun/14 and the TM data of 85/Jun/25 are actually comparable.

3. The Normalised Difference Vegetation Index NDVI

All photosynthetic organisms contain one or more pigments capable of absorbing visible radiation which will initiate the photochemical reactions of photosynthesis. The most widespread pigments are the chlorophylls which give most green plants two radiation absorption maxima: one in the blue region of the spectrum (0.43 μm) and one in the red region (0.66 μm). In contrast, the spongy mesophyll in healthy green plants is highly reflective to incident near-infrared radiation (0.75–1.1 μm) (Lloyd and Barrett, 1986).

The spectral response of green and healthy vegetation is characterized by a strong absorption in the red region together with a strong reflection of near-infrared radiation. These responses are very different from those of other surfaces, such as soils, rocks, water, snow, etc.

It has also been observed that diseased or senescent vegetation has increased reflection of visible radiation and increased absorption of near-infrared radiation.

Numerous vegetation indices have been developed to reduce the multispectral data, particularly red and near-infrared reflectance data, to one-dimensional scales for the assessment of vegetation characteristics such as cover type, leaf area, plant stress and phytomass (Tucker, 1979; Perry *et al.*, 1984).

Hayes (1985) suggested the existence of a general agreement on the various near-infrared and red combinations that are able to provide useful indicators of biotic properties of vegetation.

In fact the following indices:

IR/R = Infrared/Red ratio
 EVI = Environmental Vegetation Index
 NDVI = (NIR-RED)/(NIR+RED)
 Normalised Difference Vegetation Index
 TVI = (NDVI+0.5) * 0.5 Transformed Vegetation Index

have been found to be sensitive to the amount of photosynthetically active vegetation present in plant canopy. One of the most popular 'Vegetation Indices' is the Normalized Difference Vegetation Index, previously defined.

Hayes (1985) has suggested that the NDVI correlates very strongly with the leaf-area index, net primary productivity and biomass.

By definition the NDVI has a nominal range of -1 to +1. In general terms, water, snow and clouds have negative values because they reflect more red than near-

infrared radiation; rocks and bare soil have NDVI values around zero since they have similar reflectances in both wavebands; only green vegetation has positive NDVI values, higher values being associated with higher densities of green and healthy phytomass. Normally the range of NDVI for vegetation is from 0 to +0.6.

It is necessary to emphasize that many investigators are making extensive use of NDVI in the global monitoring of vegetation on the basis of the NOAA-AVHRR data. (Justice *et al.*, 1985; Hayes, 1985; Tucker & Sellers, 1986; Townshend & Justice, 1986).

Finally, as can be seen in the Table 1, if we consider the situation in the electromagnetic spectrum of spectral bands of the different sensors operating so far, the NDVI calculus will be:

NDVI(TM) = (TM4 - TM3)/(TM4 + TM3)
 NDVI(MSS) = (MSS7 - MSS5)/(MSS7 + MSS5)
 NDVI(Spot) = (Spot3 - Spot2)/(Spot3 + Spot2)
 NDVI(AVHRR) = (AVHRR2 - AVHRR1)/(AVHRR2 + AVHRR1)

An interesting aspect to be considered is the different frequency and resolution of the satellites that will make it possible to select in each case the vegetation index that is most suitable for the monitoring of vegetal cover.

4. Classification of Comillas Area Using NDVI

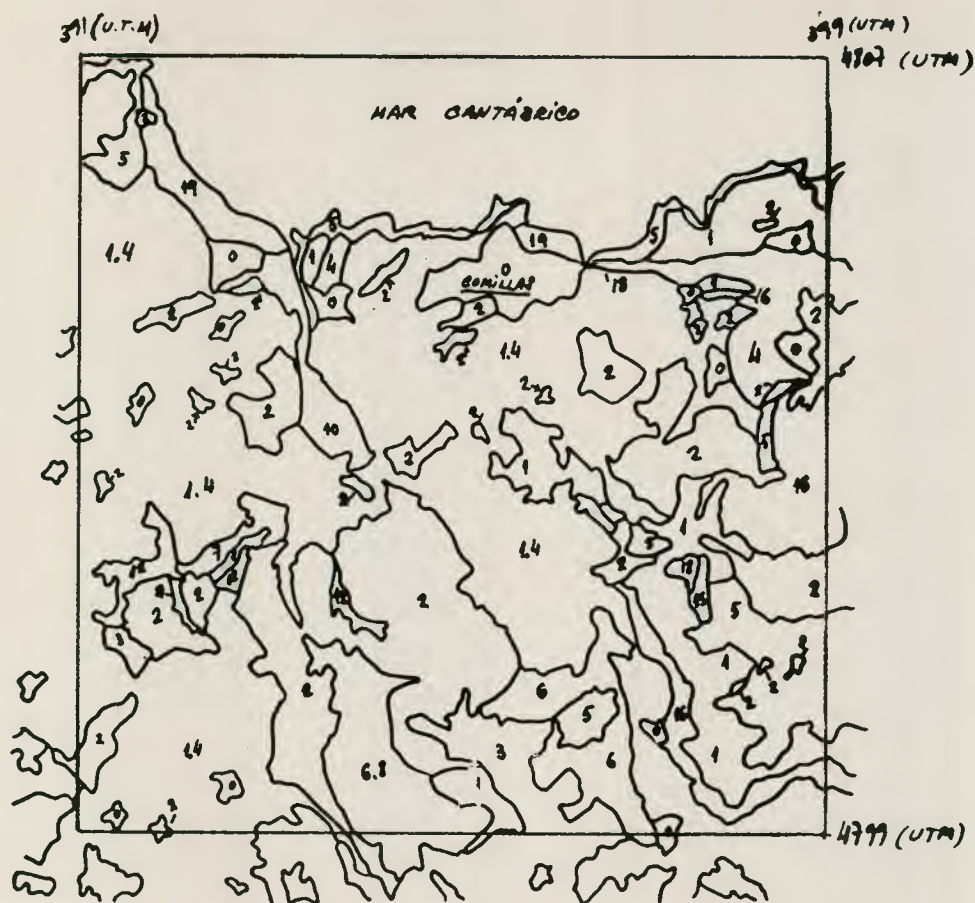
The main goal of this project was to investigate the possibility of performing the classification of the vegetal cover in those areas distinguished by the presence and persistence of vegetation (as is the case of the Cominidad autonoma de Cantabria) using to accomplish this task the NDVI derived from different sensors of high spatial resolution (as TM and MSS).

For this study a pilot zone was selected approximately centered in the village of Comillas and delimited by the U.T.M. coordinates 391, 399 in the west-east direction and the U.T.M. coordinates 4799, 4807 in the south-north direction.

Figure 1 shows a diagram of the study zone at the 1/50 000 scale. Also included is a thematic cartography related to the different types of vegetation cover performed by the Centro de Investigacion y Desarrollo (Diputacion de Cantabria).

The main steps of the employed methodology were:

1. Radiometric correction of the TM and MSS images.
2. NDVI determination in both images.
3. Training areas selection and determination of statistical parameters.



0	Villages	10	Marshes
1	Pastures	12	Mixed forest
2	Eucalyptus	11	Oaks
3	Pinus radiata	15	Rocks
4	Crops	16	Rocks and shrub
5	Shrub	17	Rocks and trees
6	Oak	18	Dump
7	Deciduous	19	Beaches
8	Beech	21	Poplars
1.4	Pastures and crops	6.8	Oak and beech

Figure 1. Comillas area: map of vegetation cover

4. Classification of the TM and MSS images based in the NDVI values.

The first step was to locate the study area in the TM (5-202-030-2, 25 June 85) and MSS (4-202-030, 14 June 84) images, generating the appropriate work files.

Figure 2 shows a false-colour combination of bands 2, 3, 4 of TM sensor relative to the pilot zone.

Figure 3 shows a false colour combination of bands 4, 5, 7 of MSS sensor relative also to the pilot zone.

The radiometric correction of the images was performed following the procedure and using the formulas previously described.

The normalised difference vegetation index for the TM and MSS data was calculated with the NDVI(TM) and NDVI(MSS) formulas mentioned in point 3. After these steps, a data 'scaling' was done to allow their colour representation in the Pericolor-1000 image processor of the Spanish NPOC.

In both cases the training areas were selected on the corresponding NDVI image, with the help of the topographic map and the thematic map of cover types of vegetation. This selection was conditioned by the spatial resolution of the sensors.

In Figures 4 and 5 the NDVI corresponding to the TM and MSS images are represented.

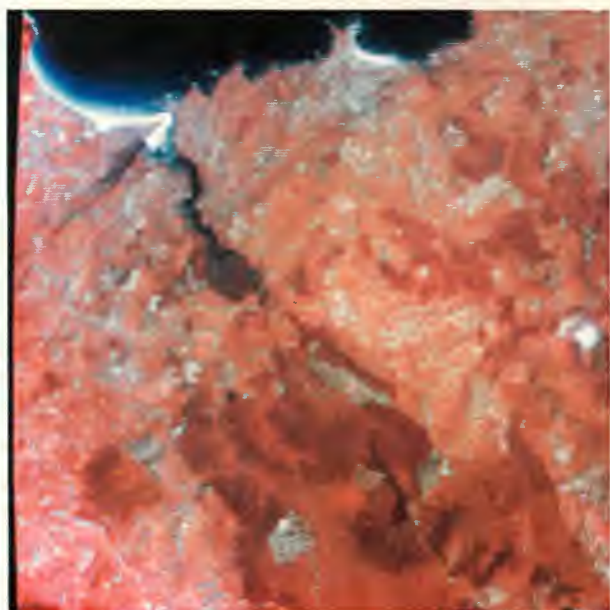


Figure 2. Comillas area: false-colour combination of TM bands 2, 3, 4.



Figure 3. Comillas area: false-colour combination of MSS bands 4, 5, 7.

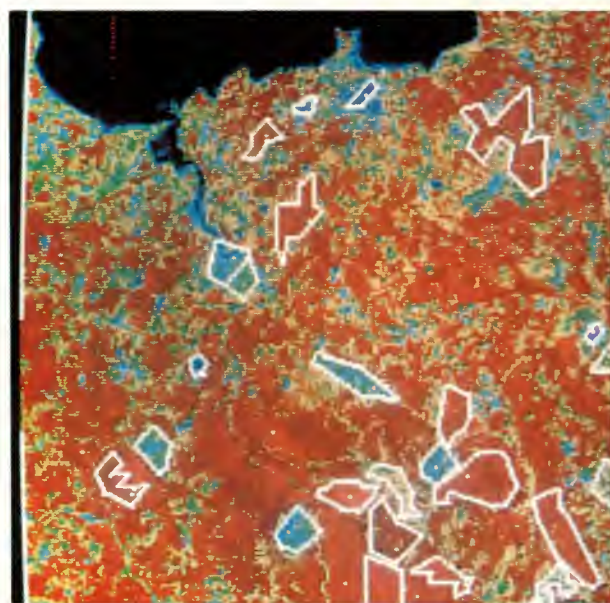


Figure 4. Comillas area: representation of NDVI(TM) image and situation of the training areas.

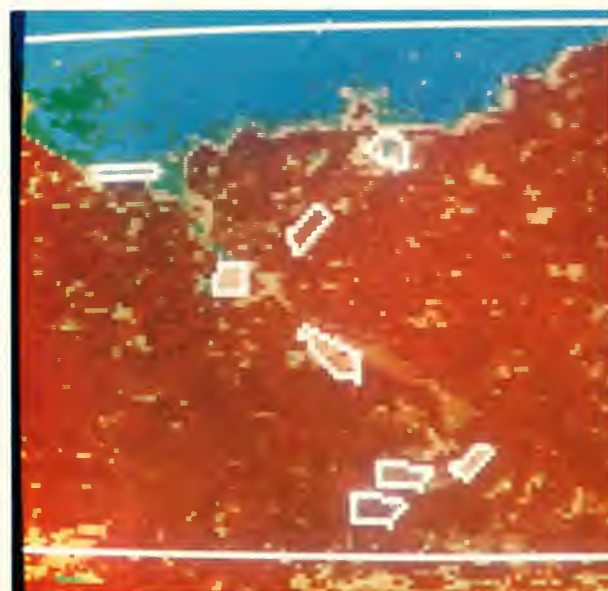


Figure 5. Comillas area: representation of the NDVI(MSS) image and situation of the training areas.

Tables 2 and 3 show the interval of NDVI values defined for each class based on the training areas for the TM and MSS data respectively.

Finally Figures 6 and 7 show the classification results of the study zone based in the NDVI values for the TM and MSS data respectively.

Table 2. TM data. Classification of Comillas area

Class	Digital value	NDVI (TM)
1. Water	< 130	< .0156
2. Urban dense and dump	131–150	.0156–.1718
3. Urban sparse and beach	151–165	.1718–.2890
4. Cutting and marsh	166–185	.2890–.4453
5. Pastures and crops and Pinus radiata	186–208	.4453–.6250
6. Eucalyptus, oaks, pastures	209–222	.6250–.7343
7. Oak and beech	> 223	> .7343



Figure 6. Comillas area: classification results obtained from the NDVI(TM) values.

Blue = Water. Brown = Urban dense and dump. Pink = Urban sparse and beach. Red = Cutting and marsh. Yellow = Pastures and crops, Pinus radiata. Light green = Eucalyptus, oaks and pastures. Dark green = Oak and beech.



Figure 7. Comillas area: classification results obtained from the NDVI(MSS) values.

Dark blue = Water. Light blue = Urban, beach and dump.. Red = Marsh, urban sparse. Yellow = Pinus radiata and cutting. Light green = Pastures and eucalyptus. Dark green = Oak and beech.

Table 3. MSS data. Classification of Comillas area

Class	Digital Value	NDVI (MSS)
1. Water	< 130	< .0156
2. Urban, beach, dump	131-165	.0156-.2890
3. Marsh, urban sparse	166-185	.2890-.4453
4. Pinus radiata, cutting	186-197	.4453-.5390
5. Pasture and eucalyptus	198-218	.5390-.7031
6. Oak and beech	> 218	> .7031

5. Conclusions

The radiometric correction of the digital values on the CCT is a useful technique to attenuate the different calibration of the sensors. As a consequence, the normalised difference vegetation indices deduced from the TM and MSS images at different dates are more readily comparable.

The NDVI values obtained are more or less similar for both sensors for the majority of vegetation class cover analysed. This fact confirms the consistency of this parameter for monitoring the vegetal cover from different satellites.

The selection of training areas for the MSS image with respect to the TM image was very difficult. For this

reason the NDVI(MSS) data are less representative than the NDVI(TM) data.

The values for NDVI obtained make it possible to establish a gradation among the different types of vegetal cover. This gradation seemingly is associated to the intensity of chlorophyllic function.

It is necessary to show up the high value of NDVI for the class 'Oak and beech' that confirms the high ecological value of this class compared with the other classes.

The cover-type classification obtained in this study zone is not completely satisfactory in both cases and the TM classification is better than the MSS classification. Probably a multitemporal analysis of the NDVI parameter will make it possible to discriminate more accurately among the different types of vegetal covers and also to establish a phenological profile for each vegetation type.

Finally, while the NDVI parameter is insufficiently well-known, the systematic cartography of NDVI can be a useful help to the physical planning and management of natural resources at regional level, specially in those areas with a high productivity in the agricultural, cattle and forestry sectors, as is the case of the Comunidad Autonoma de Cantabria.

6. Acknowledgements

This project was supported by the Spanish NPOC as an Earthnet-ESA pilot project in the year 1985.

The authors wish to thank to all the technical personnel of Spanish NPOC for the high level of co-operation demonstrated during the development of this project, specially for their advice and also for the use of the Pericolor-1000 image processor.

7. References

- Hayes L., 1985. The current use of TIROS-N series of meteorological satellites for land-cover studies. *Intl. Jl. of Remote Sensing*, 1985, vol 6, no. 1, 35-45.
- Justice C.O., Townshend J.R., Holben B.N., Tucker C.J., 1985. Analysis of the phenology of global vegetation using meteorological satellite data. *Intl. Jl. of Remote Sensing*, 1985, vol. 6, no. 8.
- Lopez Garcia M., Caselles V. & Melia J., 1985. Following the Microclimatic Alterations produced by Forest Fires by means of the Landsat 5 (TM) sensor. *3rd Int. Coll. Spectral Signatures of objects in Remote Sensing*, Les Arcs, Dec. 1985 (ESA SP-247).
- Lloyd D. & Barrett E.C., 1986. Mapping and monitoring vegetation over the Iberian peninsula using small scale radiometric data from NOAA satellites. *Jl. Brit. Interplan. Soc.*, 1986, vol. 39, 535-541.
- Nelson R.F., 1985. Sensor-Induced Temporal Variability of Landsat MSS data. *Remote Sensing of Environment* 18: 35-48.
- Perry C.R. & Lautenschlager L.F., 1984. Functional Equivalence of Spectral Vegetation Indices. *Remote Sensing of Environment* 14: 169-182.
- Robinove C.J., 1982. Computation with Physical Values from Landsat Digital Data. *Photogrammetric Engineering & Remote Sensing*, May 1982, vol. 48, no. 5, 781-784.
- Townshend J.R.G. & Justice C.O., 1986. Analysis of the dynamics of African vegetations using the normalised difference vegetation index. *Intl. Jl. of Remote Sensing*, 1986, vol. 7, no. 11.
- Tucker C.J., 1979. Red and Photographic Infrared Linear Combination for Monitoring Vegetation. *Remote Sensing of Environment* 1979, 8: 127-150.
- Tucker C.J. & Sellers P.I. 1986. Satellite remote sensing of primary production. *Intl. Jl. of Remote Sensing*, 1986, vol. 7, no. 11.

6. *Forestry*

Forest Damage Mapping in Austria with the Aid of Landsat TM Image Data

W. Schneider

*Institut für Vermessungswesen und Fernerkundung
Universität für Bodenkultur, Vienna, Austria*

Landsat TM temporal/spectral signatures of forest stands of different species composition, age class, crown closure and crown condition were analysed. It was confirmed that channels 5 and/or 7 (mid-infrared) are most important and valuable for separating forest categories. Different crown condition classes as defined in the Austrian 'Waldzustandsinventur' (forest condition inventory) could be separated. There is, however, a certain correlation between crown condition and crown closure in the area studied in this project. It could not be decided whether it is the 'crown condition' proper or the crown closure which is sensed by Landsat TM.

1. Introduction

Alarming symptoms of forest dieback are being observed in many European countries in the last years. Reliable, detailed and periodically updated information on the forest condition is urgently needed as a basis for preventive and curing measures against this phenomenon of forest decline.

At present, forest damage assessment in Austria is based on terrestrial methods including visual classification of morphological crown condition and defoliation of individual trees in five 'crown condition categories'. It is planned to augment and, ultimately, to replace (as far as possible) terrestrial assessment by colour infrared aerial photo interpretation. These methods are, in any case, time consuming and expensive as well as subjective.

It would therefore be advantageous if satellite remote sensing techniques could be used for forest damage mapping. This can conceivably be done at different levels:

(a) Satellite remote-sensing data can provide fundamental information on forest cover, tree species distribution etc. These data may then be used for planning damage assessment strategies based on terrestrial methods and/or aerial photo interpretation.

(b) Satellite remote sensing data may provide information on the damage situation proper. For this application, it must be possible to differentiate, with a certain reliability, between the five crown condition categories under the typical conditions prevailing in central Europe, i.e. in the case of small, inhomogeneous forest stands, intensive management practices etc.

The potential of satellite remote-sensing techniques for forestry applications including forest damage assessment is being evaluated by various research groups all over the world (Spanner *et al* 1984, Cihlar 1986, Franklin 1986, Horler & Ahern 1986, Vogelmann & Rock 1986). It is the aim of this project to explore the usefulness of multitemporal Landsat TM data for forest damage assessment in Austria, to find out to which extent information on forest condition relevant for measures against forest decline can be derived from Landsat TM data, and to determine the (potential) role of Landsat TM data in a comprehensive forest inventory system comprising terrestrial, airborne and spaceborne techniques of data acquisition.

2. Test Site and Reference Data

The test site for this study is an area in Upper Austria where extensive reference data are available from terrestrial surveys and CIR aerial photo interpretation. The site is located at 48° 13'N latitude and 13° 2'E longitude, close to the river Inn (which is the border to the Federal Republic of Germany) in the vicinity of the aluminium plant 'Ranshofen'. The forest stands mainly contain the tree species spruce (52%), pine (39%), and beech (6%).

The site is characterised by a pronounced spatial pattern of forest damage (obviously due to emissions from the nearby aluminum plant), which makes it particularly suited for this project. The size of the forest area studied in detail is 2000 ha or 20 km².

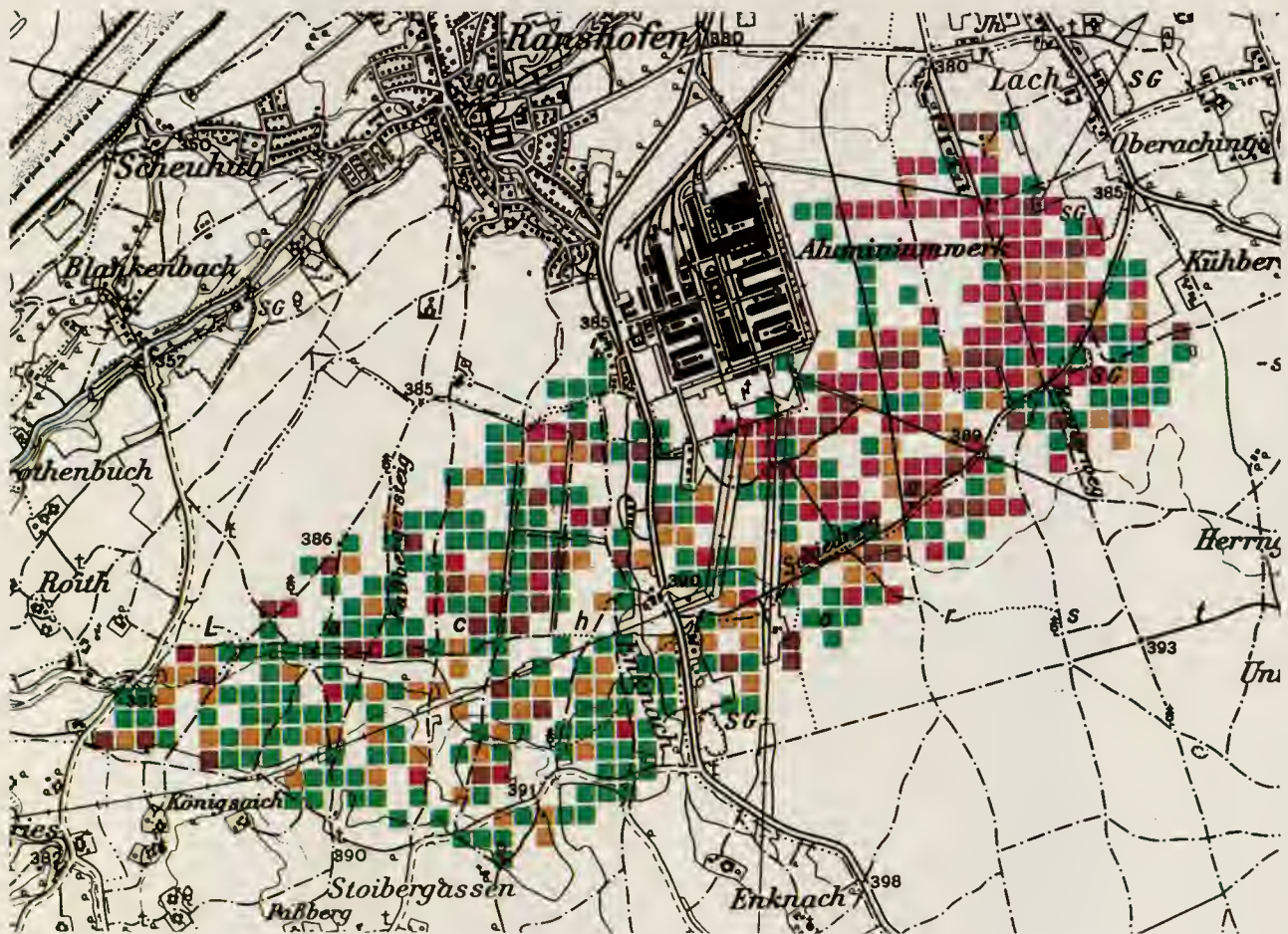


Figure 1. Crown condition map with 100 m raster cells, prepared by visual interpretation of CIR aerial photos of scale 1 : 8000. Crown condition of individual trees is categorized in 5 classes (1..healthy tree, 5..dead tree). Green: average crown condition 1.0 to 2.2 - Yellow: average crown condition 2.3 to 2.4 - Brown: average crown condition 2.5 to 2.6 - Red: average crown condition 2.7 to 5.0

Colour infrared aerial photos of image scales between 1 : 4000 and 1 : 32 000 acquired in April 1984 and in August 1984 are available. Ground truth data, particularly on tree crown condition, have been collected at a number of sample plots during photo acquisition.

On the basis of these ground truth data, the colour infrared photos were interpreted according to the following guidelines:

- a) Homogeneous forest stands were delineated on the photos of scale 1 : 16 000. The following data were collected for each stand:
 - gross species composition (coniferous - mixed - broad-leaved)
 - crown closure (in tens of percent)
 - age (young crops - thicket - pole stands - timber stands)
- b) A detailed inventory of crown condition was performed in a part of the test area by interpreting a sample of approximately eight tree crowns per hectare on CIR photos of scale 1 : 8000. The tree species interpreted were spruce, fir, larch, pine and beech. Crown condition was categorised in five 'crown condition classes' according to the specifications of the Austrian

'Waldzustandsinventur' (forest condition inventory). The result of this crown condition inventory is illustrated in Figure 1, which shows the 'average crown condition number' per 100 m-cell (ha). Due to the high variability of crown condition (from tree to tree, but also from raster cell to raster cell), it does not seem appropriate to use these high-resolution data directly as reference information for analysing Landsat TM pixels, as one cannot expect to have exactly the same trees interpreted on the photos and observed in a certain pixel of the TM scene. On the other hand, there is a distinct coarse spatial pattern of tree crown condition. The data of Figure 1 were therefore averaged over coarser cells of 500 m raster size, as shown in Figure 2.

These data represent the reference information for the evaluation of Landsat TM images.

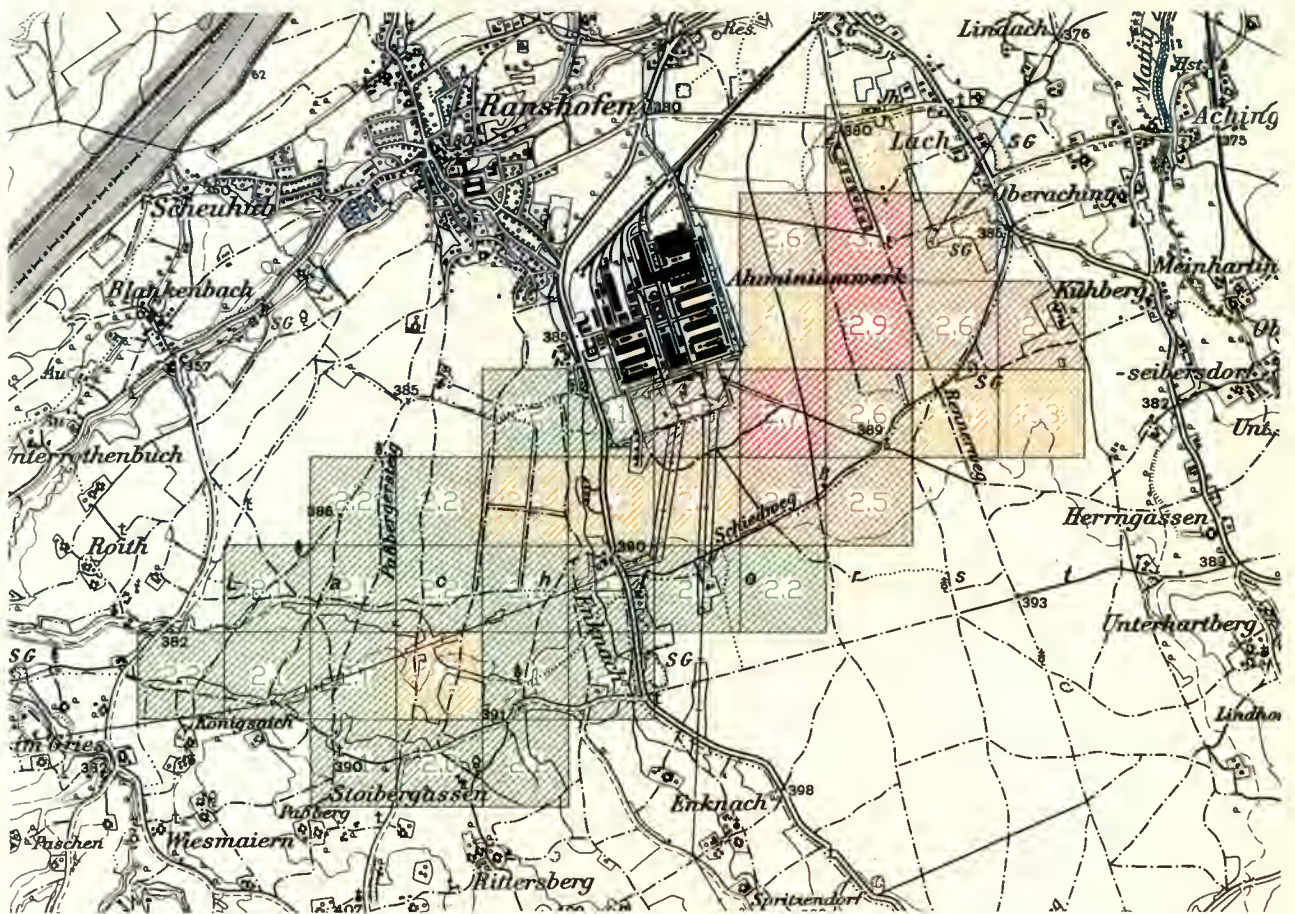


Figure 2. Crown condition map with 500 m raster cells, prepared from Figure 1.

3. Digital Analysis of TM Image Data

3.1. Method

To obtain the optimum information on forest condition, it was planned to analyse three different Landsat scenes acquired in August 1984 (just before leaf fall), in October 1984 (after leaf fall) and in April 1984 (just before leafing). Unfortunately, there was no suitable cloud-free scene acquired in spring. The project was therefore carried out with scenes of orbit 192, frame 26, quarter 4, of the following acquisition dates:

3 August 1984, 22 October 1984 and 22 August 1985.

The data were supplied in 'system-corrected' form. Further processing and analysis was done at the processing facilities of the Institut für Vermessungswesen und Fernerkundung - IVF (minicomputer HP 1000 A 900, images processing and display system Frinnell GMR 275, software developed at the IVF).

In Figure 3, a true-colour composite of channels 1, 2 and 3 of the August 1984 test scene is reproduced. The dynamic range of forest pixels is seen to be very small: All forest areas appear in black. Figure 4 shows an enlargement of a false-colour composite of channels 2, 3 and 4. The contrast is enhanced for maximum differentiation of coniferous forest stands. Due to the small dynamic

range of forest pixels, the signal-to-noise ratio is low. System noise becomes visible.

Figure 3. True-colour composite of channels 1, 2 and 3 of the August 1984 scene. The dynamic range of forest pixels is seen to be very small: all coniferous forest areas appear in black.



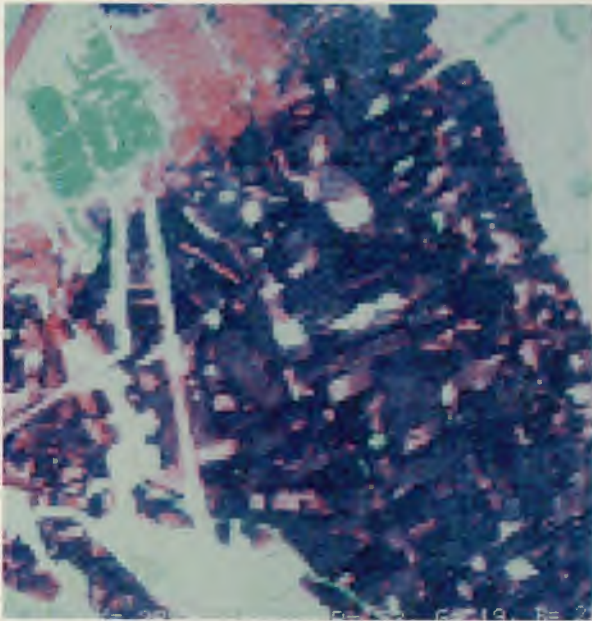


Figure 4. False-colour composite of channels 2, 3 and 4 of the August 1984 test scene. Contrast is enhanced for maximum differentiation of coniferous forest stands. System noise becomes visible.

To facilitate multitemporal evaluation, the scenes of Oct. 84 and of Aug. 85 were geometrically rectified relative to the Aug. 84 scene (nearest neighbour resampling). The three images were then combined, resulting in an image of $3 \times 7 = 21$ temporal/spectral channels.

150 sample areas of homogeneous forest stands were selected. The areas were localised visually on the TM multitemporal image, on the CIR aerial photos (with superimposed forest stand information) and on the crown condition map. The size of these sample areas is 3×3 pixels and, in some cases (for small stands), 1 pixel on the TM image.

For every sample area, the following reference data are available:

- species composition in 3 categories (coniferous - mixed - broad-leaved)
- crown closure (in tens of percent)
- age class in 4 categories (young crops - thicket - pole stands - timber stands)
- average crown condition number (in tenths on a 5-category-scale)
- intensity of haze/smoke at the 3 acquisition dates (in 3 categories for each date, as assessed visually from real-colour composites of the individual Landsat scenes: no visible haze - light haze - strong haze).

In Figure 5, the temporal/spectral spectra of coniferous and of deciduous forest sample areas are reproduced to illustrate the dynamic range of TM forest pixels.

The diagrams as shown in Figures. 6 to 9 were prepared in order to visualise how the pixel values in the different

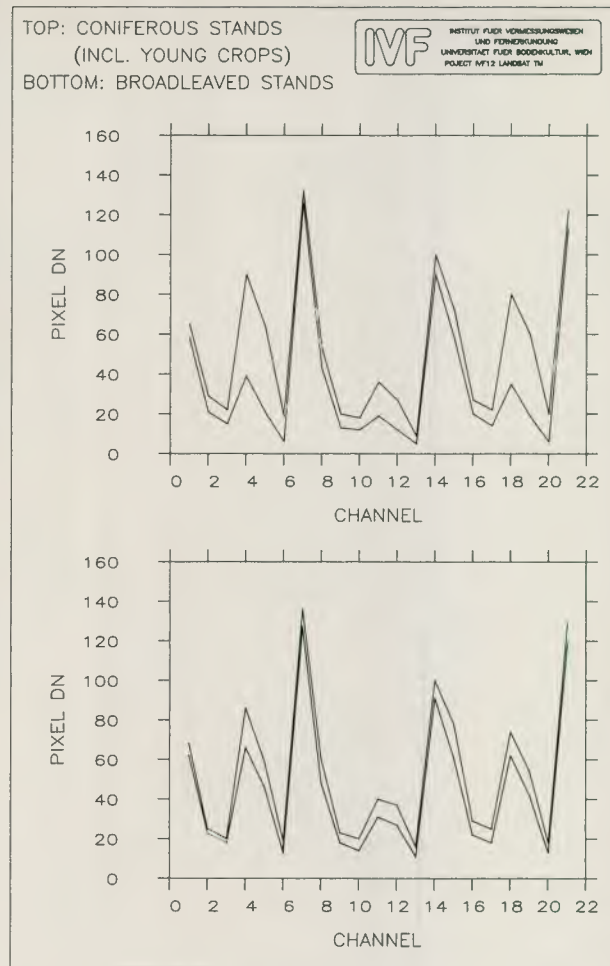


Figure 5. Dynamic range of temporal/spectral Landsat TM data of forest areas. Channels 1 to 7 in this figure represent the TM channels of the August 1984 scene, channels 8 to 14 are the TM channels of the October 1984 scene, and channels 15 to 21 are the TM channels of the August 1985 scene. Channels 6 and 7 (13 and 14, 20 and 21) are interchanged here so as to show the channels in their true order of succession in the electromagnetic spectrum.

spectral and temporal channels depend on the various forest stand parameters.

Finally, attempts were made to automatically classify the multitemporal/multispectral Landsat scene and to prepare thematic maps showing the different forest stand categories. A modified hyper-box classification based on up to 15 channels and ratios of channels as well as a maximum likelihood classification based on up to 8 channels were employed for this purpose.

3.2. Spectral characteristics of forest stands

In Figure 6, the range of the pixel values (intervals between one-sigma-boundaries) are indicated for the categories

- broad-leaved forest stands
- mixed forest stands
- coniferous forest stands - young crops
- coniferous forest stands - thicket

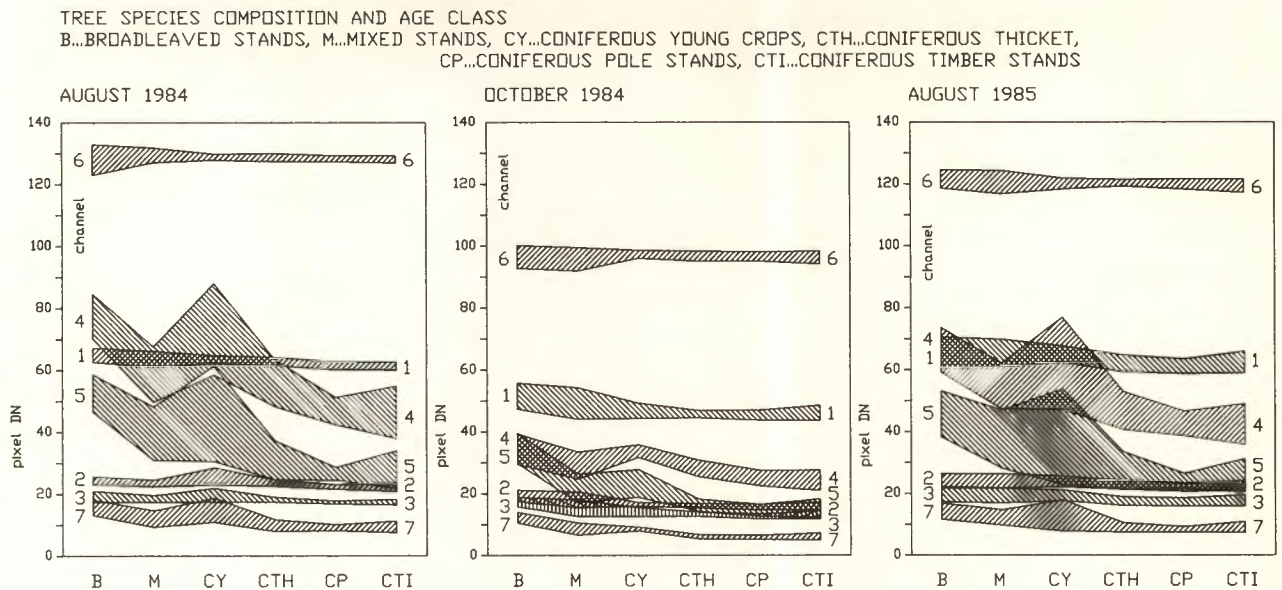


Figure 6. One-sigma-intervals of pixel values in the 7 TM channels at 3 acquisition dates for different species composition and stand age.

coniferous forest stands - pole stands
 coniferous forest stands - timber stands.

Channels 1 ($0.45-0.52 \mu\text{m}$), 2 ($0.52-0.60 \mu\text{m}$) and 3 ($0.63-0.69 \mu\text{m}$) in general carry little information on the stand category, although there is a slight decrease of the pixel values from broad-leaved forest to coniferous timber forest. (The darker appearance of coniferous forest certainly is partly due to the geometry of the vegetation canopy, i.e. due to the narrow, conical crowns resulting in a higher amount of shadow seen by the sensor). In the October scene, however, channels 2 and 3 allow a clear separation between (defoliated) broad-leaved stands on the one hand and older coniferous stands (thicket, pole stands, timber stands) on the other hand.

In channel 4 ($0.76-0.90 \mu\text{m}$), broad-leaved stands can be clearly separated from older coniferous stands in the August scenes (due to the higher near-infrared reflectance of leaves and leaf canopies as compared to needles and needle canopies), while there is less separation in October. The pixel values of coniferous young forest vary considerably. They overlap with those of broad-leaved forest, which is due to the contribution of herbaceous vegetation on the ground.

Channel 5 ($1.55-1.75 \mu\text{m}$) behaves in a similar way as channel 4; there is, however, a clear difference between broad-leaved stands and coniferous stands of any age (including *young forest!*) in the October scene.

Channel 6 ($10.3-12.5 \mu\text{m}$) exhibits a slight decrease from broad-leaved stands to coniferous timber stands, which again may be due to the rougher surface of the coniferous forest canopy, casting shadow and causing a lower average surface temperature. Also, radiation emit-

ted from the cooler inner parts of the conifer crowns may reach the sensor.

Channel 7 ($2.08-2.35 \mu\text{m}$) shows a similar behaviour as channel 5.

In Figure 7, the one-sigma-boundaries of the pixel values for coniferous timber stands are plotted as a function of average *tree crown condition*. Although, for individual tree crowns, the 'crown condition number' may vary between 1 (fully developed, 'normal' tree crown) and 5 (dead tree), the average crown condition number for larger areas ($500 \text{ m} \times 500 \text{ m}$) varies only between 2.0 and 3.0. The most remarkable feature to be seen in these diagrams is the trend of channels 4 and 5, going in opposite directions: With increasing stress of vegetation, the reflectance in the near infrared slightly decreases, while the reflectance in the mid-infrared increase (due to the reduced moisture content and due to the increase of the area of bark - branches and twigs - seen by the sensor?).

A very similar pattern of reflectance trends is seen in Figure 8, which shows the pixel values as a function of *crown closure* for coniferous timber stands. The similarity between Figure 10 and Figure 11 is explained by a certain (negative) correlation between tree crown condition number and crown closure, which is weak ($r=0.58$) but statistically significant. As a consequence, it is not quite clear whether Figure 7 really indicates that the average crown condition of forest stands can be deduced from Landsat TM signatures. The observed relationship between crown condition number and spectral signature may be a secondary one, caused by the correlation between crown condition number and crown closure on the one hand and between crown closure and spectral signature on the other hand.

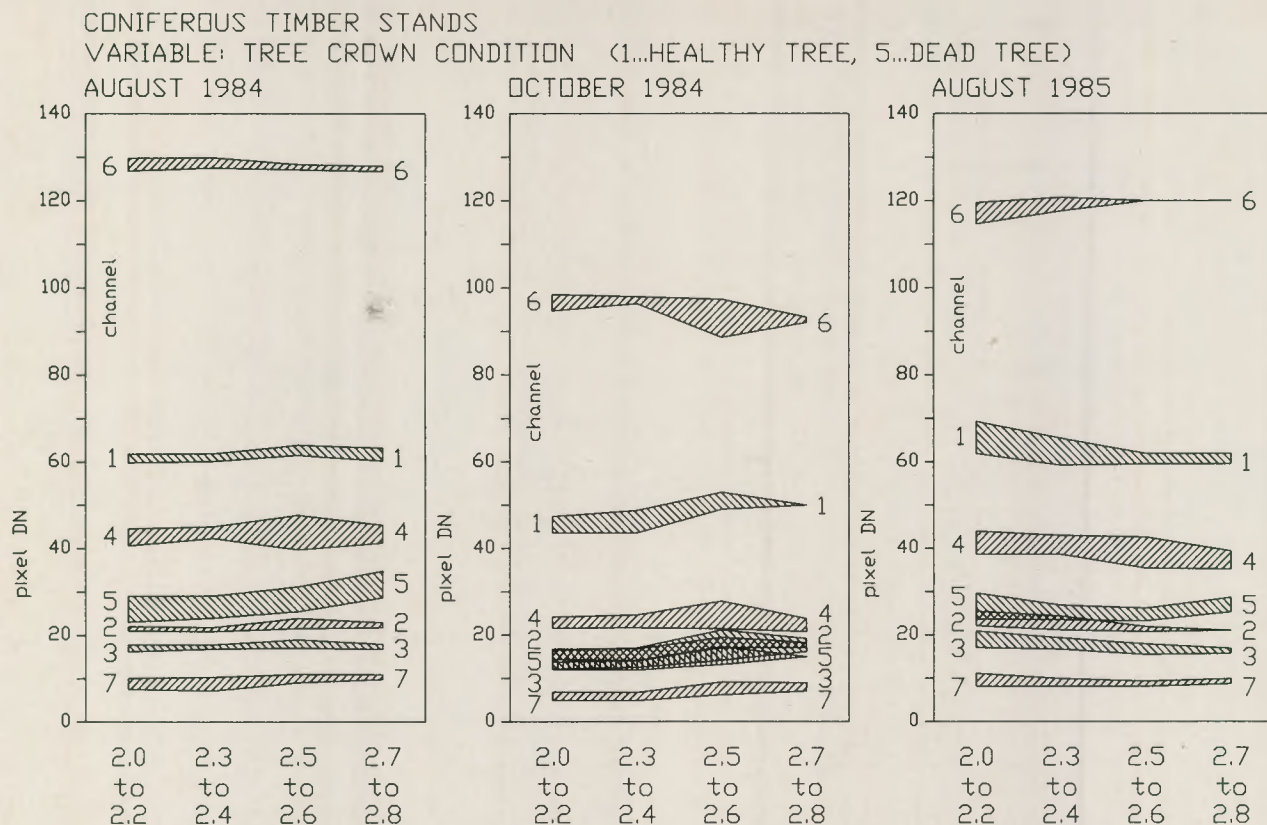


Figure 7. One-sigma-intervals of pixel values in the 7 TM channels at 3 acquisition dates for different average tree crown condition of coniferous timber stands.

TM pixel values are strongly influenced by haze and smoke. Several patches of haze and/or smoke are visible on contrast-enhanced true-colour composites (channels 1, 2, 3) of the analysed scenes. Figure 9 illustrates the

functional relationship between the (visually assessed) intensity of haze and the pixel values of coniferous timber stands. The pixel values of reflective channels are seen to increase (scattering of sun radiation in the haze layers

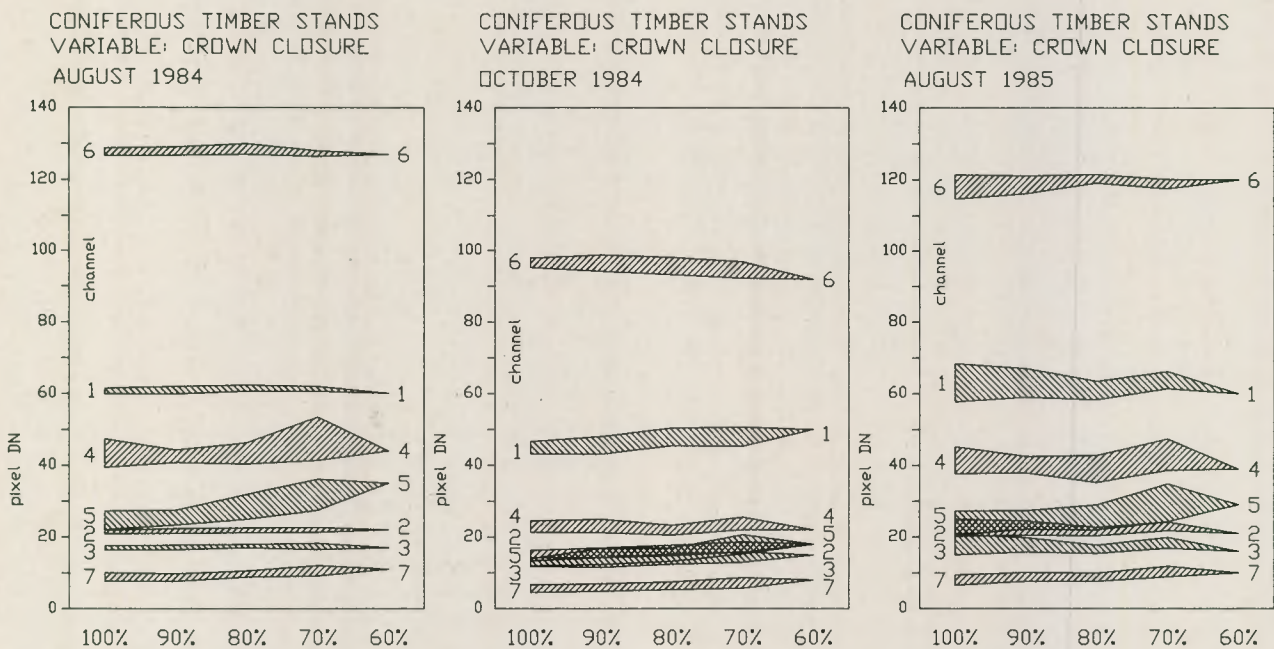


Figure 8. One-sigma-intervals of pixel values in the 7 TM channels at 3 acquisition dates for different crown closure of coniferous timber stands.

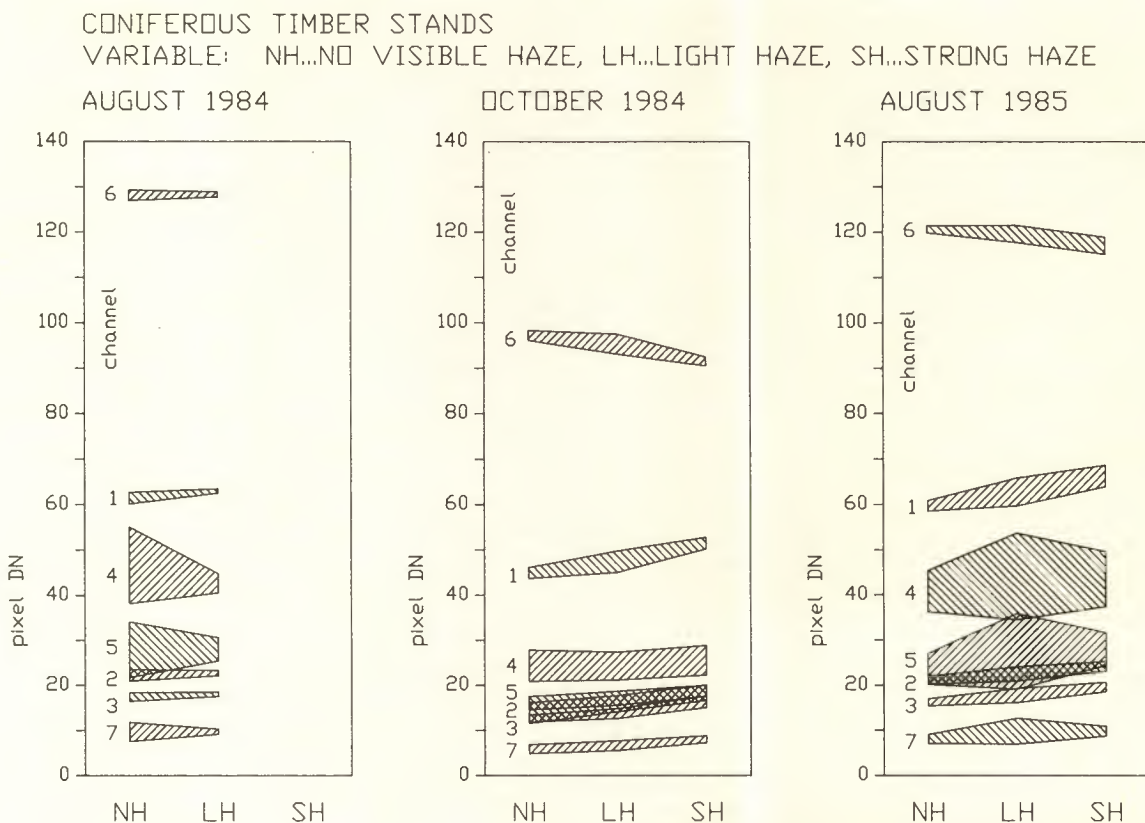


Figure 9. One-sigma-intervals of pixel values of coniferous timber stands in the 7 TM channels at 3 acquisition dates for different (visually assessed) haze intensity.

towards the sensor), while the pixel values of channel 6 decrease (weaker emission from colder canopies, absorption of radiation from the ground in the haze layers, weaker emission from colder haze layers) with increasing haze intensity. The amount of change is considerable, indicating that haze and smoke may cause severe problems in multispectral classification.

3.3. Digital classification

Thematic maps of the area under investigation were prepared, differentiating between the following categories:

a) *broad-leaved stands - mixed stands - coniferous stands - nonforest area:*

The main problem is the differentiation between broad-leaved trees and young coniferous crops, as mentioned already in 3.2. In agreement with the findings discussed there, a satisfactory classification is possible only if channels (in particular, channel 5) of the October scene are utilised. The exclusive use of October channels, however, gave problems with haze, as there are local patches of very strong haze in the October scene. The most satisfactory result was obtained by classification based on 15 channels from all 3 acquisition dates (channels 2, 3, 4, 5, 7 from every date). The main benefit of the multispectral approach obviously is the suppression of haze effects, which are different at different acquisition dates. Figure 10 renders the classification result.

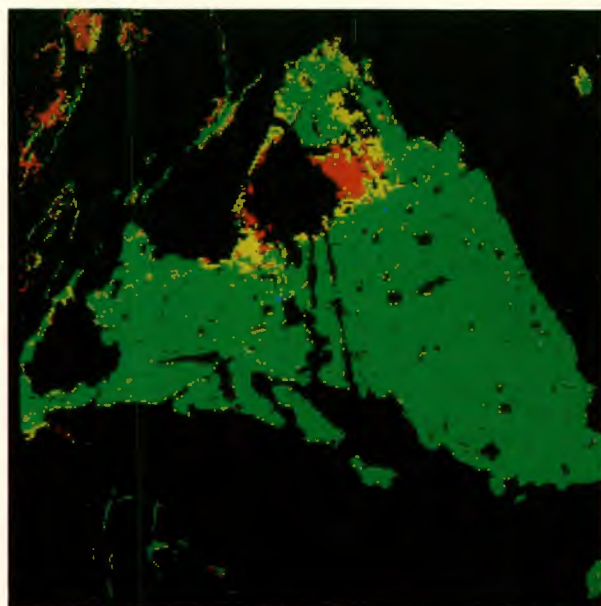


Figure 10. Result of classification of species composition: red: broad-leaved stands - yellow: mixed stands green: coniferous stands - black: nonforest area.

b) *coniferous forest: young crops - thicket - pole stands - timber stands:*

Here again the main difficulty lies in the differentiation between broad-leaved stands and young coniferous

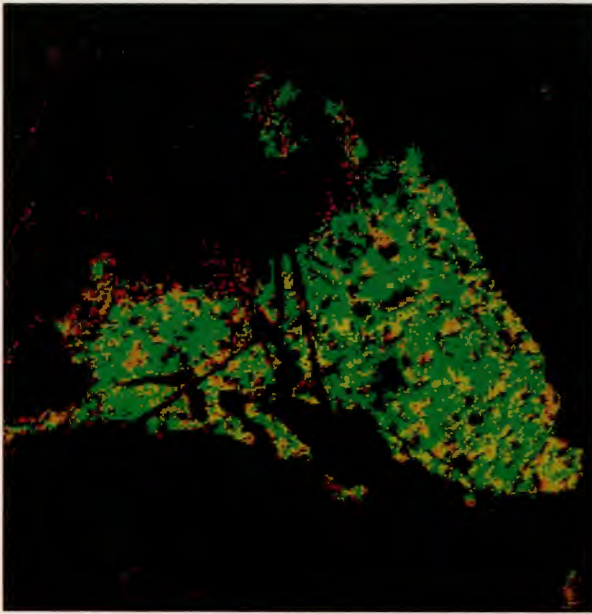


Figure 11. Result of classification of coniferous forest stand age:

red: young crops - range: thicket
yellow: pole stands - green: timber stands

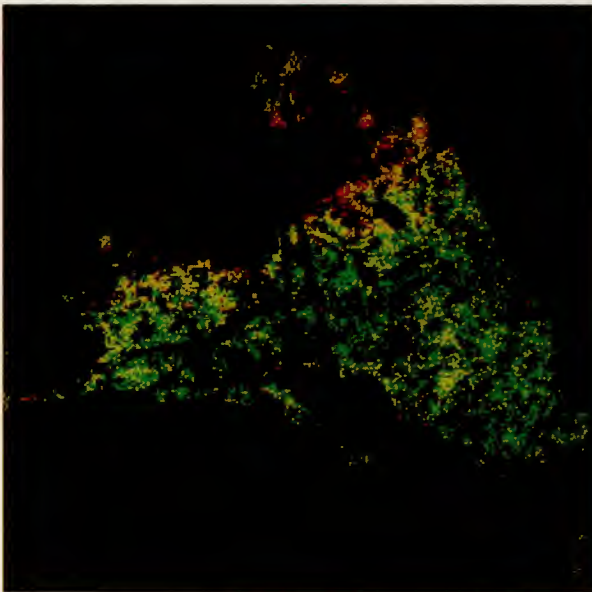


Figure 12. Result of classification of crown condition of coniferous timber:

green: average crown condition number below 2.3
yellow: average crown condition number 2.3 to 2.4
orange: average crown condition number 2.5 to 2.6
red: average crown condition number above 2.

crops. Classification of August scenes produces results, in which broad-leaved stands are mis-identified as coniferous young crops. Classification of the October scene is severely affected by haze. Multitemporal classification with channels 2, 3, 4, 5, 7 from 3 acquisition dates (15 channels in total) gave the best result; however, due to haze, certain coniferous forest areas are classified as non-forest. The classification result is shown in Figure 11.

c) coniferous timber forest: crown condition classification:

Due to the small overall dynamic range of coniferous timber pixels, classification results are heavily affected by haze as well as system noise (especially in channel 6). For this reason, single-date-classification does not produce any useful results at all. Multitemporal classification based on 15 single TM channels from 3 acquisition dates yields improvements. The best results, however, were obtained by multitemporal classification using the 3 ratios (channel 5/channel 4) from the 3 acquisition dates, together with the classification result of coniferous timber forest (see b) above. This result is reproduced in Figure 12.

In any automatic classification based on the evaluation of individual pixels, border pixels are misclassified with a certain probability, due to the mixing of different signatures. This fault may be corrected in a post-processing step, eliminating isolated single-pixel areas, at the expense of a certain degradation of spatial resolution.

4. Conclusions

The limitations in the use of Landsat TM data for forest damage mapping are not only determined by the finite spatial resolution of the sensor: The dynamic range of the pixels of forest areas, especially of coniferous forest, is very small in most TM channels. As a consequence, environmental noise (e.g. haze) as well as system noise may dominate and may impede a reliable separation of forest stands of different attributes.

On the other hand, it has been confirmed in this project that channels 5 and 7 (mid-infrared) are most important and valuable for separating forest categories.

The findings of this project indicate that, *on flat terrain*, the following forest categories may be discriminated and mapped by classification of *multitemporal* Landsat TM data:

Coarse species composition:

- broad-leaved stands
- mixed stands (possibly subdivided into 2 to 3 categories)
- coniferous stands

Age class: young crops
thicket
pole stands
timber stands.

Different crown condition classes as defined in the Austrian 'Waldzustandsinventur' (forest condition inventory) could be separated. There is, however, a certain

correlation between crown condition and crown closure in the area studied in this project. It could not be decided whether it is the 'crown condition' proper or the crown closure which is sensed by Landsat TM.

Another major difficulty arises in this context: In a well-managed forest, damaged trees are removed before cutting healthy ones. Forest monitoring by spectral analysis of satellite remote sensing data therefore will provide information on the forest management practices rather than on the dynamics of the damage situation, if cutting of individual trees is not taken into account. This problem could be solved if crown condition and crown closure could be sensed independently of each other. At the moment we have no indication that this is possible.

Further investigations are necessary to study the Landsat TM signatures of different tree species as well as the information content of Landsat TM data in mountainous terrain. If it can be proved that forest categories as identified in this project can also be differentiated in mountainous country, it might be of advantage to use Landsat TM data for national forest inventory purposes.

Acknowledgements

The data for this project were supplied at a reduced rate within the framework of the ESA Earthnet programme.

The project was financed in part by the Austrian Ministry of Science and Research (BMWF) (order no. 37.007/1-25/85) and is based on work supported by the Austrian 'Fonds zur Förderung der wissenschaftlichen Forschung', projects no. 4489 and S38/2. The CIR aerial photos used as reference information were interpreted under the guidance of M. Gärtner. The software used has been developed under the supervision of A. Pinz.

References

- Spanner M.A., Brass J.A., Peterson D.L., 1984, Feature Selection and the Information Content of Thematic Mapper Simulator Data for Forest Structural Assessment. *IEEE Transact. GE-22*(6), 482-489.
- Cihlar J. (ed.), 1986, The Use of Landsat Data in Forestry. *Remote Sensing Reviews* Vol. 2, Part 1.
- Horler D.N.H. & Ahern F.J., 1986, Forestry Information Content of Thematic Mapper Data. *Int. J. Remote Sensing* 7(3), 405-428.
- Franklin J., Thematic Mapper Analysis of Coniferous Forest Structure and Composition. *Int. J. Remote Sensing* 7(10), 1287-1301.
- Vogelmann J.E. & Rock B.N., Assessing Forest Decline in Coniferous Forests of Vermont Using NS-001 Thematic Mapper Simulator Data. *Int. J. Remote Sensing* 7(10), 1303-1321.

Discrimination of Geobotanical Anomalies in Coniferous Forests from Landsat TM Data

C. Banninger

*Institute for Image Processing and Computer Graphics
Graz Research Centre, Graz, Austria*

Low levels of heavy metal stress in coniferous trees are detectable using the Landsat TM sensor system, thereby supporting its employment in the search for orebodies lying within the coniferous-forested regions of the world. A statistical analysis of multitemporal Thematic Mapper data from a test site in Austria established a strong relationship between soil metal content, canopy leaf density, and canopy reflectance, and defined the TM bands and transformations best suited for distinguishing geobotanical anomalies in forest stands – particularly those related to changes in canopy structure. The results of the study indicate that incipient or subtle levels of heavy metal stress are most likely manifested by morphological rather than physiological changes in a canopy, which has implications for the selection of TM bands and transformations to be employed in a geobotanical survey.

Keywords: Geobotany, Landsat Thematic Mapper, Heavy Metal Stress, Coniferous Forest, Leaf Area Index

1. Introduction

Plants are frequently good indicators for the presence of subsurface mineralisation and will respond to toxic concentrations of metals in the soil substrate by undergoing physiological and morphological changes to their systems. These changes commonly alter the spectral properties of plants in a manner that is detectable by air- and spaceborne optical sensor systems, such as the Landsat TM.

The primary designed function of the Thematic Mapper is to monitor vegetation, which makes it particularly applicable to the task of discerning geobotanical anomalies associated with heavy metal stress. With almost two thirds of the world's land surface moderately to heavily covered in vegetation, the employment of TM data in the search for concealed orebodies in vegetated terrain offers the feasibility to survey large, vegetation-covered areas for geobotanical targets in a rapid and cost effective manner.

The manner in which symptoms of metal stress manifest themselves in plants has important implications in the selection of TM bands and transformations for geobotanical prospecting. The study reported herein, therefore, had two principal objectives: to establish the viability of using TM data for geobotanical prospecting, and to determine which TM spectral bands and transformations are most suited to performing this task. A

coniferous-forested area in Austria underlain by mineralised country rock provided a suitable setting in which to assess these capabilities of TM data.

Although this study focused on the utilisation of TM data for mineral exploration, the same techniques and methodology applied to this purpose are equally applicable to the detection of toxic waste deposits in forested areas and to the larger problem of forest damage in connection with air pollutants.

2. Heavy Metal Toxicity in Plants

Plants respond to the presence of toxic amounts of heavy metals in the environment by undergoing physiological and morphological changes that result in a reduction in plant vitality and growth. These effects can range from previsual impairment of plant functions related to photosynthesis to a pronounced decrease in leaf and plant density. Unless there is a complete breakdown in a plant's regulatory mechanism, however, most plants suffering from heavy metal toxicity will normally display only subtle symptoms of stress.

Plants exhibit a strong biological absorption for zinc, moderate for copper, and only weak for lead (Perel'man, 1967), which mirror the moderate, moderately severe,

(Fig. 2). Forest understory consists of variable, but small amounts of forbs, grasses, and low-lying bushes, except where openings in the forest canopy permit a more luxurious undergrowth. A residual soil layer covers the test site to a depth in excess of one metre in places, although it normally varies between 40 and 80 cm in thickness.

7. Ground Data Collection and Analysis

All procedures employed in the collection of ground data from the test site utilised a survey grid with 50 m line and station intervals. A total of 51 grid stations covered the test site and served as the reference base for collecting data on soil geochemistry and canopy structure. Together, these data provided information on the type, nature, and extent of stress in the forest stand occupying the test site.

Soil samples obtained from the base of the B-horizon at each grid station and analysed for total copper, lead and zinc content by the atomic-absorption spectrophotometry method show a large geochemical anomaly present at the test site. Copper values range from 20 to 940 ppm, lead values from 10 to 10 800 ppm, and zinc values from 60 to 6300 ppm, with the metal values at the higher end of the range associated with probable waste material derived from former mining activity. Because of their common genesis and mode of emplacement, there is a close, although not an exact correspondence between the copper, lead and zinc anomalies.

Leaf area index (LAI) determinations give a measure of the amount of foliage contained in a canopy and can be used to map changes in canopy density caused by the toxic effects of heavy metals in the underlying soil. Calculations of leaf area indices involve the measurement of tree stem diameters at breast height (DBH) level and their transformation to leaf area values using appropriate allometric equations. Tree measurements are based on fixed-size sample plots placed in undisturbed areas of a forest stand. Locations near the edge of clearings were excluded from the data collection to avoid any bias in stand growth that may have resulted from a greater exposure to sunlight of exterior versus interior stand trees.

The procedure employed in collecting the DBH measurements involved first the establishment of 5 m-radius sample plots at or in close proximity to 31 of the 51 grid stations, and the subsequent measurement of all trees within a sample plot having trunk diameters greater than 5 cm. LAI values were obtained for each sample plot by first determining the leaf areas of the enclosed trees, using allometric equations derived by Whittaker & Woodwell (1968), Whittaker *et al.* (1974), and Gholz *et al.* (1979), and then dividing their summation by the sample plot area.

Before a comparison of the soil and LAI data sets could be made with the TM data sets, they had to be first transformed from their discrete or point source representation to an isopleth or areal distribution format to permit their integration with the TM canopy radiance data sets.

8. Thematic Mapper Scene Data

Thematic Mapper scenes from 2 June and 5 August 1984 provided the canopy radiance data for the test site used in the study. Both scenes are, for the most part, free of clouds and excessive haze. Radiance values employed in any numerical analysis were first corrected for atmospheric haze, employing the darkest object subtraction method of Crane (1971).

9. Evaluation of Ground and TM Data Sets

The approach employed in the establishment of relationships between the soil, LAI, and TM spectral data involved first merging the different data sets with each other and then applying statistical analysis to the combined data sets. The average ground coverage of a TM pixel served as the unit cell for the integration of the various ground data sets to their corresponding TM data set. Each TM pixel array is first co-registered with its corresponding soil metal and LAI isopleth maps and the average soil metal and LAI values then calculated for each pixel representing 95% or more canopy cover, using a 36-point dot grid scaled to the dimensions of the nominal 30×30 m instantaneous field of view of the TM sensor system. Linear combinations of the derived pixel metal values increased the data set to seven variables (see Table 2).

Table 3 lists the thirty single and transformed TM spectral bands used in the statistical comparison with the ground data sets from the test site. The TM bands and transformations employed in the analysis are specifically chosen for their ability to reinforce and emphasise changes (especially subtle ones) in the forest canopy-solar radiation relationships, as defined by the TM spectral bandwidths.

Statistical analysis of the combined soil geochemical (pixel metal values), canopy density (pixel LAI values), and canopy reflectance (pixel radiance values) data sets involved the regressing of the various data sets against each other and subjecting the results to an analysis of variance. Correlation coefficients (*r*-values) and variance ratios (*F*-test values) provided the statistical basis for assessing the relationships between the various sets of variables. For the seven metal values, thirty TM bands and transformations, and two TM scene dates used in the study, the regression analysis involved a total of 420 data sets.

Table 2. Soil metals and combinations used in statistical analysis

Lead	(Pb)
Zinc	(Zn)
Copper	(Cu)
Lead + Zinc	(Pb + Zn)
Lead + Copper	(Pb + Cu)
Zinc + Copper	(Zn + Cu)
Lead + Zinc + Copper	(Pb + Zn + Cu)

10. Results of Statistical Analysis

The correlation coefficients and variance ratios derived for the 420 pairwise combinations employed in the regression analysis indicate an overall consistency in the

ability of certain TM bands and transformations to discriminate metal stress in the test site forest stand. The normalised difference (ND1) yielded the highest correlation values for all scene dates with respect to the soil metal data sets from the test site. The simple band ratio (R41), band difference (BD1), and, in the case of the August TM scene, normalised difference (ND3) produced slightly lower but comparable correlation values, followed closely by the greenness index (TMG), band difference (BD3), and, again for only the August TM scene, the first principal component (PC1). The remaining TM bands and transformations display progressively weaker relationships with respect to the soil metal data. For all seven metal data sets examined, the strongest statistical relationships are shown with respect to lead and its various combinations with copper and zinc, and the weakest relationships with respect to copper.

Table 3. Landsat TM bands and transformations used in statistical analysis

Band 1	(TM1)	Landsat TM Band
Band 2	(TM2)	
Band 3	(TM3)	
Band 4	(TM4)	
Band 5	(TM5)	
Band 7	(TM7)	
Band 4 - Band 1	(BD1)	Band Difference
Band 4 - Band 2	(BD2)	
Band 4 - Band 3	(BD3)	
Band 4 - Band 5	(BD5)	
Band 4 - Band 7	(BD7)	
Band 4/Band 1	(R41)	Simple Band Ratio
Band 4/Band 2	(R42)	
Band 4/Band 3	(R43)	
Band 4/Band 5	(R45)	
Band 4/Band 7	(R47)	
Band 2/Band 3	(R23)	
Band 3/Band 1	(R31)	
Band 5/Band 7	(R57)	
(Band 4 - Band 1)/(Band 4 + Band 1)	(ND1)	Normalised Difference
(Band 4 - Band 2)/(Band 4 + Band 2)	(ND2)	
(Band 4 - Band 3)/(Band 4 + Band 3)	(ND3)	
(Band 4 - Band 5)/(Band 4 + Band 5)	(ND5)	
(Band 4 - Band 7)/(Band 4 + Band 7)	(ND7)	
0.3037 (TM1) + 0.2793 (TM2) + 0.4743 (TM3) +0.5585 (TM4) + 0.5082 (TM5) + 0.1863 (TM7)	(TMB)	Brightness Index*
-0.2848 (TM1) + 0.2435 (TM2) - 0.5436 (TM3) +0.7243 (TM4) + 0.0840 (TM5) - 0.1800 (TM7)	(TMG)	Greenness Index*
0.1509 (TM1) + 0.1973 (TM2) + 0.3279 (TM3) +0.3406 (TM4) - 0.7112 (TM5) - 0.4572 (TM7)	(TMW)	Wetness Index*
First Principal Component	(PC1)	
Second Principal Component	(PC2)	
Third Principal Component	(PC3)	

* Source: Crist (1983)

Statistical results obtained using radiance data from the August TM scene are, overall, slightly better than for the June scene data. Table 4 gives a ranking of the thirty TM bands and transformations employed in the analysis as to their usefulness in detecting heavy metal stress in the spruce tree stand of the test site.

The regression of canopy LAI against soil metal content produced moderately strong to strong negative correlations with respect to all seven metal variables. Correlation coefficients range from $r = -0.64$ to -0.75 , with all values significant at greater than the 99% probability level.

Similarly ranked, but positively correlated relationships exist between TM canopy radiance values and canopy LAI. The normalised difference (ND1), band difference (BD1 and BD3), simple band ratio (R41), and greenness index (TMG) yielded the highest correlation coefficients ($r = 0.68$ to 0.77), followed by the first principal component (PC1), band difference (BD2), and TM bands 4 and 5 ($r = 0.60$ to 0.66). These values are also significant at greater than the 99% probability level.

11. Discussion of Results

The results of the study show that a strong relationship exists between soil metal content, canopy structure and canopy reflectance. The strong negative correlation established between canopy LAI and soil metal concentration and the similarly strong, but positive correlation found between canopy LAI and canopy reflectance imply that a reduction in canopy leaf density is related to the presence of toxic concentrations of heavy metals in the underlying soil, and that the resultant changes in canopy structure are detectable using TM spectral data.

Canopy reflectance in the visible, near-infrared, and shortwave infrared spectral regions is closely related to the physiological and morphological properties of the vegetation cover, as described in Table 1. Vegetation under stress would normally be expected to show an increase in visible reflectance in response to a decrease in radiation absorption properties of the foliage, a decrease in near-infrared reflectance as a result of a reduction in leaf or plant density, and an increase in shortwave infrared reflectance related to a loss in foliar water content. The negative relationships exhibited by the TM band transformations with respect to soil metal content are in agreement with an expected decrease in canopy reflectance in the near-infrared band (TM4) and an expected corresponding increase in reflectance in the visible (TM1, TM2 and TM3) and shortwave infrared (TM5 and TM7) bands in response to the effects of metal toxicity on plant vitality. The negative correlation values obtained for all six TM bands indicate that variations in canopy reflectance are associated more with morphological than

with physiological changes in the coniferous tree stands. A decrease in canopy leaf density would result in an increase in the amount of shadow within the tree stand and a consequent decrease in canopy reflectance. This is particularly true for the spectral response of the stand in the visible region (covered by TM1, TM2, and TM3), which is strongly affected by the presence of canopy shadow, and likely accounts for the negative correlations obtained from TM bands 1, 2, 3, 5 and 7. If a reduction in leaf pigment and water content also takes place, one would expect to see an increase in canopy reflectance in the visi-

Table 4. Ranking of TM bands and transformations for usefulness in geobotanical prospecting

Rank	Correlation Coefficient Range* (negatively signed)	Test Site	
		June TM Scene	August TM Scene
Group I	0.70–0.80 (1)	ND1 BD1	ND1 R41 ND3
Group II	0.65–0.70 (1)	R41 TMG BD3	BD1 TMG BD3 PC1
Group III	0.60–0.70 (1)	PC1 BD2 TM4 TM5 TMB BD7 TM7	TMB R43 BD7 TM4 TM5 BD2 TM2
Group IV	0.45–0.55 (1)	ND3 R43 ND2 R42 TMW TM2	TM7 ND2 R42 TMW TM3
Group V	0.30–0.45 (1–2)	PC3 TM3 BD5 R23 R31	R31 BD5 R57 TM1 PC3
Group VI	0.00–0.30 (3)	ND5 R57 TM1 R45 PC2 R47 ND7	R23 R47 ND5 ND7 R45 PC2

* Majority of r-values for all metals and combinations (excluding copper).

Significance Levels: 1 = $p > 0.99$

2 = $0.90 < p < 0.99$

3 = $p < 0.90$

ble and shortwave infrared TM bands, due to an increase in leaf transmittance and reflectance and a corresponding decrease in canopy shadow. This does not appear to happen, at least not in a sufficient amount to negate the increase in canopy shadow caused by morphological changes in the canopy.

The ranking of seven of the TM transformations above the highest ranked TM spectral bands (TM4 and TM5) in ability to detect metal stress in the spruce tree stand demonstrates the capacity of such transformations to enhance weak or difficult to discern changes in a canopy's spectral response to stress conditions, as recorded by the individual TM bands. This is best exemplified by the three top-ranked transformations (ND1, BD1 and R41), which employ TM bands 1 and 4. Correlation coefficients for TM1 regressed against the seven soil metal values are decidedly poor ($r = -0.20$ to -0.27) and for TM4 only fair to good ($r = -0.62$ to -0.68), but increase significantly ($r = -0.65$ to -0.73) when the two single bands are used together in the three transformations.

The August TM scene data produced, overall, slightly stronger statistical results than the data from the June TM scene, which implies an increase in canopy stress conditions as the vegetation progressed into its mid- and late-summer growth phases. This may reflect both an increase in heavy metal uptake (and hence metal stress) by the trees over the two month interval separating the June and August scene acquisition dates and an increase in tree water stress related to the normal increase in temperature (and hence plant evapotranspiration) and decrease in precipitation in going from spring to summer climatic conditions. The presence of plant moisture stress would accentuate any heavy metal stress conditions prevailing in the canopy and induce the needles to droop, thereby changing the structure of the canopy as seen by the TM sensor. The effects of needle droop on canopy shadow content and reflectance would be similar to the effects caused by a reduction in needle density.

The failure to obtain stronger statistical correlations between soil metal and canopy radiance values was not for a lack of correspondence between the soil geochemical anomaly and TM pixels representing anomalous canopy radiance values. A block of twenty odd such pixels coincided well with the soil metal anomaly, even when allowing for possible positioning errors in the registration of the two data sets to each other. A number of pixels that lie outside the soil anomaly zone, however, display radiance values similar to the anomalous pixels associated with the soil anomaly, and, conversely, a number of pixels included within the block of anomalous canopy pixels have radiance values more in agreement with pixels that reside outside the soil anomaly zone. These pixels may represent a discontinuous state of the soil anomaly that is not reflected in the soil metal isopleth maps generated

from the spot soil metal values, or perhaps the uneven response of the tree stand to the toxic effects of the soil substrate metals. In most cases, however, they appear to represent irregularities within the tree stand, such as small, pixel-size or less openings in the canopy, produced by factors unrelated to metal stress. These pixels are commonly associated with areas unsuitable for sustaining tree growth, although they often are able to support lower plant forms, such as forbs and grasses. Depending on whether such openings give rise to a dense herbaceous plant growth or are occupied mainly by canopy litter (needles, leaves and branches), wet areas (bogs, marshes or swamps), or rock outcrops, the spectral response of the corresponding TM pixels will likely be markedly different from those of the surrounding tree pixels.

Although the results of the study employing TM data are similar to those found using MSS data (Banninger, 1986a), the correlation coefficients derived for the former are lower than for the latter. At first, this may seem incongruous, as the 30 m spatial resolution of the TM sensor system results in a greater number of pure pixels and thereby permits a better definition of a geobotanical anomaly than the much coarser 80 m resolution of the MSS system. The smaller TM pixel size, however, also increases the influence of small irregularities in a canopy, such as stand openings, on the radiance values of the corresponding pixel(s), thereby possible militating against the detection of metal-stressed areas within a forest canopy. These 'noisy' pixels should be removed from the data set before any computational work is performed, either by the application of a suitable 'noise removal' operator or a discriminatory function that would flag these anomalous pixels.

12. Summary and Conclusions

The strong correlation established between soil metal content, canopy structure, and canopy reflectance substantiates the utility of canopy reflectance data as a surrogate for detecting the presence of toxic concentrations of heavy metals in the underlying substrate. The results show that small changes in canopy reflectance related to low levels of metal-induced stress in a forest stand can be detected using reflectance data acquired from spaceborne platforms employing rather coarse spatial, spectral, and radiometric resolution sensor systems, such as the Landsat Thematic Mapper.

It is clear from the study that structural changes in a canopy cover are an important, if not a dominant component in the spectral response of a coniferous tree stand experience low levels of metal stress. This signifies that subtle or incipient levels of heavy metal stress are most likely manifested by morphological rather than physiological changes in a canopy, which has implications in the selection of the TM spectral bands and

transformations for employment in a geobotanical survey. It is important that the most common expression(s) of metal stress symptoms occurring in a canopy be recognised, so that the best TM bands and transformations can be selected for maximum discriminatory capability.

The higher ranking of many of the TM transformations over single TM bands shows that simple linear and non-linear transformations of scene data can better detect changes in the status of a plant canopy than can single band data. This is accomplished by the removal of much of the radiometric variability and sensor system noise by the transformation process, and by the enhancement of the vegetation-solar energy relationships measured by the individual TM bands comprising the transformations.

The upper ranking of the normalised difference (ND1), band differences (BD1 and BD3), simple and ratio (R41), greenness index (TMG), and the first principal component (PC1) for both scene dates of the test suggests a possible general applicability in their use in a geobotanical remote sensing survey. Differences, however, in the top ranking of TM bands and transformations attained for a similar study in the Spanish Pyrite Belt (Banninger, 1986b) underscore the difficulty of finding a single spectral band or transformation that can be used universally for this purpose.

Notwithstanding the above stated reservations, the significance of the results of this study for mineral exploration are twofold: canopy reflectance data acquired from space can be used successfully to find concealed orebodies lying beneath a dense coniferous forest cover, and the expression of a geochemical anomaly in an overlying forest canopy need not be manifest to be discerned in Landsat Thematic Mapper data. This increases by many fold the number of soil metal anomalies that can be detected in a geobotanical remote sensing survey employing the TM sensor system.

Acknowledgements

This work was supported by a joint grant from the Austrian Ministry of Science & Research and the Scientific Research Office of the government of Styria. ESA/Earthnet programme provided the Thematic Mapper computer-compatible tapes used in the study.

References

- Ausmus B.S. & Hilty J.W. 1972: Reflectance Studies of Healthy, Maize Dwarf Mosaic Virus-Infected, and Helminthosporium Maydis-Infected Corn Leaves; *Rem. Sen. Environ.*, **2**, 2, pp. 77-81.
- Banninger C. 1986a: Relationship Between Tree Density, Leaf Area Index, Soil Metal Content and Landsat MSS Canopy Radiance Values; *Proc. Int. Geoscience and Rem. Sen. Symp. (IGARSS'86)*, Univ. Zürich, Switzerland, pp. 1401-1404.
- Banninger C. 1986b: Optimal Thematic Mapper Bands and Transformations for Discerning Metal Stress in Coniferous Tree Canopies; *7th Int. Symp. Int. Soc. Photogram. and Rem. Sen. (ISPRS)*, Enschede, The Netherlands, pp. 371-374.
- Bowen H.J.M. 1966: *Trace Elements in Biochemistry*; Macmillan, London, 241 p.
- Brooks R.R. 1972: *Geobotany and Biogeochemistry in Mineral Exploration*; Harper and Row, New York, 290 p.
- Bunnik N.J.J. 1978: *The Multispectral Reflectance of Shortwave Radiation by Agricultural Crops in Relation with their Morphological and Optical Properties*; Ph.D. Thesis, Landbauhogeschool (Agricultural University), Wageningen, The Netherlands, 176 p.
- Crane R.B. 1971: Preprocessing Techniques to Reduce Atmospheric and Sensor Variability in Multispectral Scanner Data; *Proc. 7th Int. Symp. Rem. Sen. Environ.*, Univ. Michigan, Ann Arbor, pp. 1345-1355.
- Crist E.P. 1983: The Thematic Mapper Tasseled Cap — A Preliminary Formulation; *Proc. 9th Int. Symp. Machine Processing Remotely Sensed Data*, Purdue Univ., W. Lafayette, Ind., pp. 357-363.
- Gholz H.L., Grier C.C., Campbell A.G. & Brown A.T. 1971: *Equations for Estimating Biomass and Leaf Area of Plants in the Pacific Northwest*; Research Paper 41, Forest Research Lab., Oregon State Univ., 40 p.
- Hawkes H.E. & Webb J.S. 1962: *Geochemistry in Mineral Exploration*; Harper and Row, New York, 415 p.
- Knipling E.B. 1969: Leaf Reflectance and Image Formation on Colour Infrared Film; in *Remote Sensing in Ecology*, P.L. Johnson (ed.), Univ. Georgia Press, Athens, Ga., 244 p., pp. 17-29.
- Knipling E.B. 1970: Physical and Physiological Basis for the Reflectance of Visible and Near-Infrared Radiation from Vegetation; *Rem. Sen. Environ.*, **1**, 3, 155-159.
- Perel'man A.I. 1967: *Geochemistry of Epigenesis*; N.N. Kohanowski (trans.), Plenum Press, New York, 266 p.
- Tucker C.J. 1978: Are Two Photographic Infrared Sensor Required?; *Photogram. Eng. Rem. Sen.*, **44**, 3, pp. 289-295.
- Whittaker R.H. & Woodwell G.M. 1968: Dimension and Production Relations of Trees and Shrubs in the Brookhaven Forest, New York; *J. Ecol.*, **56**, pp. 1-25.
- Whittaker R.H., Bormann F.H., Likens G.E. & Siccamo, T.G. 1974: The Hubbard Brook Ecosystem Study: Forest Biomass and Production; *Ecological Monography*, **44**, pp. 233-252.

Classification of Small-Scale Forests in Flanders Using Landsat TM Digital Data: Preliminary Results

Robert R. De Wulf & Roland E. Goossens

Laboratory of Remote Sensing and Forest Management
Gent State University, Belgium

The second-generation earth observation satellites of the Landsat programme carry the Thematic Mapper sensor with improved spatial and spectral resolution. The feasibility of the Thematic Mapper for forest classification in Flanders is investigated. Due to the unfortunate recording time of the available test image (1 November), the described results have to be considered as provisional. Two test zones, representative of the small-scale forest situation in Flanders, are selected as study sites. A supervised classification scheme is adopted, with special emphasis on the assessment of classification accuracy on different levels of detail: forest/non-forest, coniferous/deciduous, species and age classes. Channel ratios and linear combinations are tested against single TM channels. It is concluded that the type of classification algorithm does not significantly influence classification results. The Vegetation Index VI43 (ratio of TM4 and TM3) together with TM5 yield the best results. Forest/non-forest distinction is possible with an accuracy ranging between 79% and 92%, assuming a consumer's risk of 5%. Coniferous species can automatically be recognised as such with an accuracy ranging between 60% and 82%. Individual species and age classes cannot be classified satisfactorily. In Flanders forest classification using digital satellite data is unlikely to replace visual interpretation of high quality colour infrared orthophotomaps, which is being applied in a 10-yearly regional inventory cycle. However, due to its repetitiveness, satellite data can be used for monitoring purposes during the interim period. The low chance to obtain cloud free imagery during the growing season is not limited to Landsat Thematic Mapper, but affects all sensors operating in the visible and optical infrared wavebands.

1. Introduction

Synoptic view, repetitive coverage and image uniformity make satellite imagery a potentially powerful tool for forest resources assessment. However if satellite imagery is to be used in an operational framework for forest management and inventory and damage assessment regular availability of cloud-free images is required. Large parts of North America, Canada, North and Northwest Europe and the humid tropics have high cloud cover. For forestry the recording time is also of paramount importance. Winter images are only useful for coniferous forest.

In Flanders an operational methodology for mapping and inventory of the region's forest resources (115 000 ha, 70% privately owned) has been developed. A 10-yearly inventory using 1:30 000 colour infrared aerial photographs replaced the antiquated method using questionnaires. Visual interpretation and field checks produce base maps with high planimetric accuracy. The creation of a forest management data bank is put into effect (Coppin *et al.*, 1987). Orthophotomaps are relatively easily ac-

cepted as a new information medium for forest managers who until recently received limited remote sensing training. Satellite imagery is not yet used in an operational framework for forest management in Belgium. Landsat MSS images have proved their usefulness in other countries but due to the coarse 80 m resolution operational application in the small scale forestry situation in Belgium is unlikely to succeed. The spatial resolution of second-generation spaceborne sensors (Spot-1, TM) has significantly improved and is thought to be usable for the Belgian forestry situation.

The discussed pilot study, coordinated and sponsored by the National Science Policy Office, and executed by the Laboratory of Remote Sensing and Forest Management, envisaged a research programme to assess the usefulness of Thematic Mapper images for forestry purposes in Flanders. In particular the following questions were to be answered:

1. What is the classification accuracy on the following levels of detail: forest/non-forest, coniferous/

deciduous, species and age class (for conifers) identification?

2. Can channel ratios and linear combinations improve classification accuracy?
3. Is a 30 m spatial resolution sufficient for relatively small forests stands in Flanders?

2. Important Steps in a DIP Exercise: a Short Review

Available hardware and software and final classification objectives strongly influence the adopted digital image processing (DIP) procedure. For the study under consideration special attention was paid to class labeling, classification procedure and error analysis.

2.1. Class Labeling

Classification based on phytosociologic foundations or economic considerations cannot serve as a model for visual interpretation or digital processing of satellite images. Thematic maps should feature information classes which are relevant to the end user (e.g. production classes or species classes). The main difficulty is to relate spectral classes, which usually are not information classes to useful information for the forest manager. For example it is not always possible to distinguish between small agricultural areas and recently logged stands. Many forest classification studies feature rather simple level I classification schemes involving also a number of non-forest classes such as agriculture and urban areas.

There is obviously a much larger amount of reports on the use of MSS images for forestry purposes as compared to TM images. Classification results do not show a general trend and should be appreciated case by case. However most authors agree that with MSS data only general vegetation type mapping exercises do yield satisfying results (Wacharakitti 1975, Driscoll and Spencer, 1972). Lillesand *et al* (1985) report that, using TM data it is possible to obtain 98% accuracy for forest/non-forest classification, and 94% for softwood/hardwood distinction. The most detailed forest-type classification, involving both species and mixed species classes, scores an average accuracy of 69%. Mueller-Dombois (1984) states that even with the improved 30 m resolution of TM only broad vegetation types can be identified.

2.2. Classification procedure

A supervised approach is adopted when sufficient ground truth is collected to sustain a reliable training process. Sampling, training class statistics calculation and feature extraction precede the actual classification stage. Pixel per pixel classifications are comprehensive and easy to implement. Numerous authors agree that improved spectral and spatial resolution of second-generation sensors will necessarily result in different approaches (Jaakkola *et al* 1984, Megier *et al* 1984, Acevedo *et al*, 1984). Im-

proved spatial resolution will not necessarily lead to higher accuracy in spectral classification: in forests more spectrally overlapping classes are to be expected (Irons *et al*, 1985). Auxiliary data sources should be incorporated with spectral radiance. For instance Beaubien (1979) concluded that percentage and aspect of slopes have a significant influence on the spectral signature of forest classes.

A number of authors compared MSS with TM for forest classification purposes. MSS features a lower spectral and radiometric resolution. The selection of optimum TM bands is a function of the target classes of interest (Teillet *et al*, 1981). The improved spatial resolution of TM also allows for a more easy location of training samples to represent a spectrally pure resource type.

2.3. Error analysis

Dittel (1976) distinguishes two main types of classification errors. The first type is related to natural spectral characteristics. Different terrain classes can have similar spectral signatures in certain wavebands. This problem cannot be tackled. However the variability of the object class and the mixed pixel problem can be solved in the sampling stage. Unreliable ground truthing can ruin an otherwise carefully designed classification procedure. The second type of errors are called 'processing-induced'. Main causes are redundancy of spectral information and an 'overcrowded' discrimination space. These problems can be solved by the use of feature extraction algorithms.

Development of more or less standardised test methods for classification and map accuracy assessment are needed for comparison of image processing techniques. The following conditions are to be fulfilled whatever test method is applied:

1. ground truth should be available, preferable in digital format
2. test samples should be selected at random
3. the amount of test samples should be limited.

The most widely used tool for classification accuracy assessment is the confusion matrix. Its advantages are obvious: easy to interpret and fast to calculate. However, measures such as average accuracy, even if obtained from an independent set of test data, lack statistical background. Confusion matrices can give general indications.

The acceptance sampling theory as worked out by Aronoff (1982) and Ginevan (1979) is based upon the adoption of a sampling distribution model, which can be normal, or more appropriately, binomial. Classified samples are compared with ground truth and a probabilistic evaluation is formulated.

A third method for classification accuracy assessment, involves comparison of error matrices by using discrete

multivariate analysis (DMA). With this method classification 'treatment effects' such as channel choice, weight factors and algorithms can be evaluated. Classification data are discrete and multinomially distributed. DMA does not assume that the categories are independent nor does it require any transformation of data. A statistical measure named KHAT is computed along with the large sample variance (Bishop *et al* 1975). These parameters allow calculation of the Z-statistic. This measure is then used to conduct pairwise tests of significance. Values larger than 1.96 indicate a difference significant at the 5% level of confidence.

3. Materials and Methods

3.1. Study area

Landsat TM frames 198/24 and 198/25 cover the majority of the forest resources in the Flemish region. Ravels and Pynven, both state-owned forests, were selected as study sites. They are representative of average forest unit size in Flanders and are dominated by coniferous species. Considering the image recording date (1 November 1984) the selection of deciduous forests was out of the question.

Ravels forests, 810.94 ha, is located between 51°21'N and 51°24'N latitude and 4°59'E and 5°04'E longitude. The relief is flat and ranges between 30 m and 35 m above sea level. The sandy soil fraction dominates and the presence of a podsol layer indicates poor growing conditions for production forest. Homogeneous coniferous forest (54.2%) dominates Ravels. *Pinus nigra* ARN. var. *Calabrica* SCHN. and *Pinus sylvestris* L. are the most important species constituting 75% of the coniferous stands. Mixed deciduous/coniferous forest occupies 18.5% of Ravels, with a mixture of *Quercus robur* L. and *Larix leptolepis* GORD. being the main type. The colour-infrared aerial photograph (recording date 5 September 1986, © Eurosense-Belfotop, Wemmel, Belgium) clearly shows the group-wise mixture of tree species in Ravels.

The Pynven/Eksel test area is geographically located between 51°09'N and 51°12'N latitude and 5°17'E and 5°24'E longitude. Pynven state forest covers 741.07 ha and the adjacent communal forest of Eksel has a surface of 382.27 ha. Soils are generally dry to very dry with a sandy or loam-sandy, usually of the podsol type. Scots pine (about 55%) and Corsican pine (38%) are the most important timber species. The rest of the surface is covered by larch (1%) and deciduous species (2%).

3.2. Field work

A detailed stand description (1985) of Ravels was made available to the research team. As ground data for this document were probably collected much earlier than the image recording date it was necessary to make detailed

field checks (18 man-days). In practice only cover changes due to management operations such as clear cuts and reforestations made up significant differences. Colour-infrared aerial photography (recording date 23.09.83, scale 1:10 000) was the main source of ancillary data for the Pijnven/Eksel forest. This area was the subject of a number of other studies by CEVA (Centre for Remote Sensing of Vegetation), resulting in an abundance of ground data. It was found that especially in mixed species stands it was difficult to obtain an exact idea of the forest canopy condition in terms of spatial distribution of species and crown condition. The use of a remotely piloted aircraft equipped with a motor-driven camera, such as that tested out by CEVA in August 1986 offers new perspectives for individual crown mapping and examination.

3.3. Image processing

Two sections of 512 × 512 pixels of the fourth quarter of image 198/24 were selected and labeled TMRAVELS and TMPYNVEN respectively.

The spectral information content of the selected images was evaluated using level slicing and histogram generation. Channels 1 and 2 featured a low dynamic range for forest classes, while channel 6 did not contain relevant spectral and spatial information at all. The latter channel was excluded from further analysis.

3.3.1. Sampling

A supervised per-point classification scheme was envisaged. The choice of the terrain classes was determined by the finest level possible for automatic feature discrimination, i.e. tree species (Table 1). Discrimination between broader classes such as coniferous/deciduous and forest/non-forest were to be tested through regrouping of classification results in the confusion matrix. In some cases important species mixture were

Table 1. Choice of terrain classes for supervised forest classification

TMRAVELS	TMPYNVEN
Corsican pine	Corsican pine 1 (0–25 years)
Spruce	Corsican pine 2 (25–50 years)
Scots pine	Corsican pine 3 (50–75 years)
Cupressaceae	Scots pine 1 (0–25 years)
Larch	Scots pine 2 (25–50 years)
Douglas fir	Scots pine 3 (50–75 years)
Fagaceae	Scots + Corsican pine
Oak + Larch ('oakx')	Douglas fir
Grass	Oak species
Bare soil	Heather
Water	Grass
Crops	Crops
	Concrete features
	Bare soil
	Water

singled out as a separate class. 'Cupressaceae' is a mixture of *Thuja sp.* and *Chamaecyparis sp.*, while 'Fagaceae' includes oak and beech (TMRAVELS). 'Oak species' are *Quercus borealis* MICHX. and *Q. robur* L. (TMPYNVEN). The Pijnven/Eksel forest features relatively homogeneous stands of even aged Scots and Corsican pine, justifying an attempt to distinguish between age classes (steps of 25 years).

3.3.2. Training class statistics

In the sampling stage it became already clear that the 30 m resolution of TM is still relatively coarse with reference to the average stand size. For training class statistics calculations one 10×10 pixel sample was selected whenever possible.

Arithmetic mean and standard deviation make a first evaluation of spectral separability possible if plotted out as in figure 1. The low information content of channels 1 and 2 is confirmed. Channels 3 and 4 are more promising with regard to spectral separability whereas channels 5 and 7 offer the best spectral discrimination. The arithmetic means of the different age classes of Scots and Corsican pine are very close to each other. Based on these data a clear distinction cannot be expected.

3.3.3. Image transformations

It was decided to investigate the possibilities of channel ratios and linear combinations as single channel input in digital forest classification. Relatively few authors attempted to use these image transformations in digital forest classification schemes. Senoo *et al* (1984) used MSS 7/5 ratio to evaluate forest regeneration and found that this ratio was superior to the single channels. Berg (1981) used the same ratio to lessen considerably the confusion between beech, chestnut and other broad-leaved species. From both TMRAVELS and TMPYNVEN the VI images with channels 4 and 3 and 5 and 3 were generated as well as the Normalised Difference versions. Tasseled Cap transformations (Kauth & Thomas 1976) were computed with omission of TM channel 6 for reasons already mentioned.

3.3.4. Feature extraction

The selection of features should ideally be based upon classification accuracy, which, however, is information only available after the fact. Most feature extraction processes reduce the original feature space by removing noise and redundancy. Principal Components Analysis has the capability to reduce the feature space, but it has been experienced that important information can be hidden in higher components which are usually deleted. Other methods are based upon information and distance measure with the main goal being a selection of a subset of channels without significantly degrading the performance of the recognition system (Swain and Davis 1978). An in-house developed feature extraction algorithm labeled CAE-index (IWONL 1984) is based upon the

divergence principle and tests for each terrain class its separability from all other terrain classes. The channels with the best CAE-index are retained in the classification scheme. The number of times that each channel is selected is automatically the weight factor to be included in the classification algorithm. For the TMRAVELS image the CAE procedure selected only channels 4 and 5. For TMPYNVEN only channel 7 was excluded. For both images Brightness, Greenness and Yellowness were selected out of all Tasseled Cap transformations.

3.3.5. Classification procedures

The Minimum Distance algorithm, further referred to as MINDIS, is the fastest and most simple classification algorithm. Its major drawback is the exclusion of any measure of dispersion around the mean. The Maximum Likelihood algorithm is widely used but assumes a normal distribution of the image data. Though this assumption is usually violated it can yield results superior to those obtained by MINDIS. The software used allowed for the application of two adaptations of the Maximum Likelihood rule, both with the constraint of the covariance equalling zero. This constraint was necessary due to frequent occurrence of singular matrices. The available software did not allow for inversion of singular matrices. MAXL1 attaches the weight factors to the log standard deviation rather than to the distance factor itself. MAXL2 is the classical Maximum Likelihood distance measure. For all MAXL classifications equal a priori probabilities were assumed. The last algorithm used was an adaptation of the Mahalanobis distance (MAHDIS) with the same constraint as mentioned above. Schowengerdt (1983) proved that the Mahalanobis distance is a special case of the Maximum Likelihood rule.

An extensive classification schedule has been worked out of which, for conciseness, only the salient points will be discussed. Individual channels as well as ratios and Tasseled Cap transformations were tested on classification power. Parallel tests to assess the influence of weight factors were included. Samples used for training (TR) were reclassified. It is well known that accuracies obtained from such an exercise are far from representative of complete image classification accuracy. To assess classification in a more realistic way a complete set of independent samples (TS) was selected with sample sizes similar to those used for training. This set was submitted to exactly the same classification schedule as TR.

3.3.6. Classification results

3.3.6.1. Examination of confusion matrices

Table 2 lists the best average TS classification per algorithm and per image. The best classified images were labeled and used during the acceptance sampling tests. Figure 2 shows a colour plot of the four best classifications for TMRAVELS. The effect of classification algorithm is statistically lower than the pictures actually show (see further).

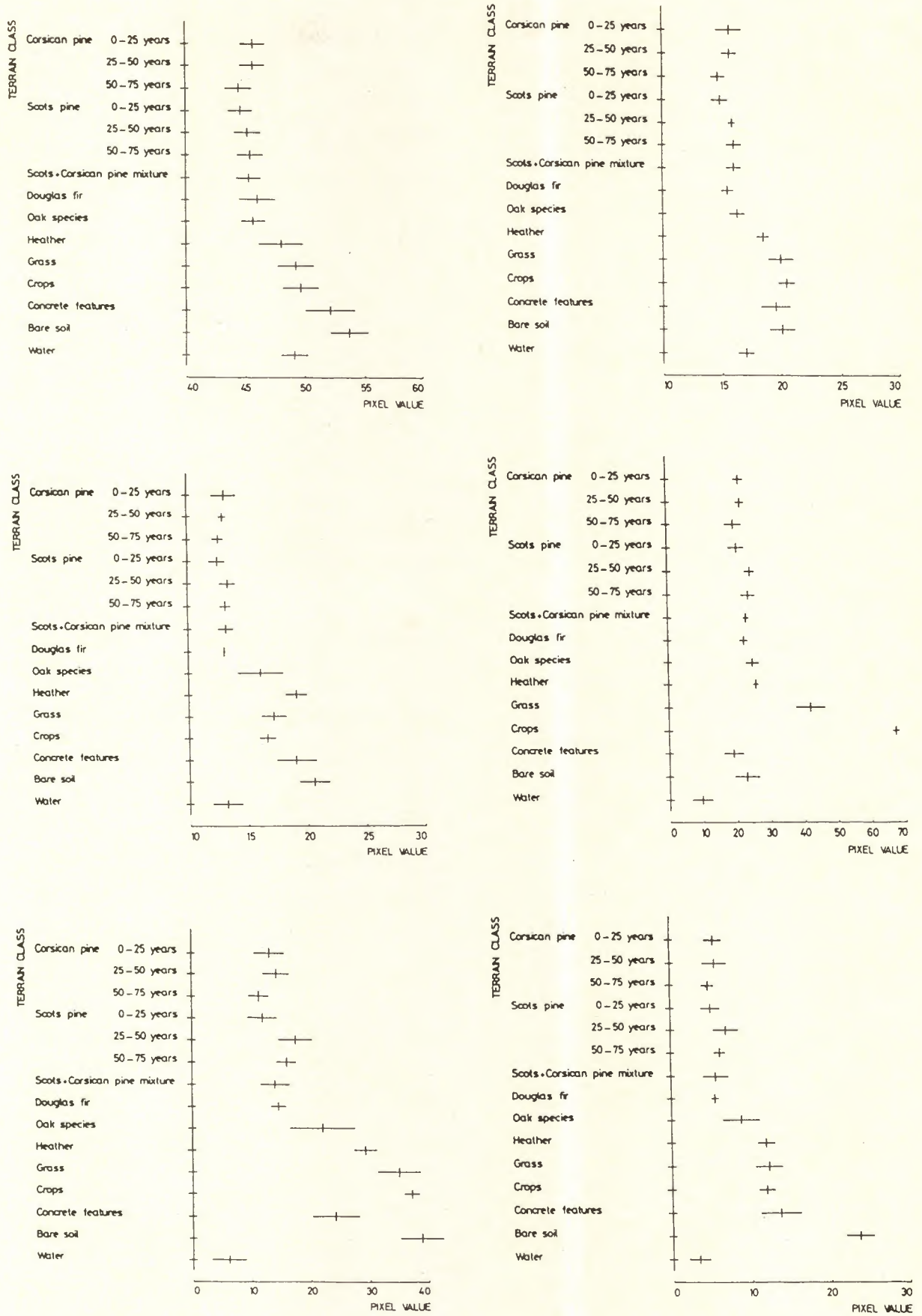
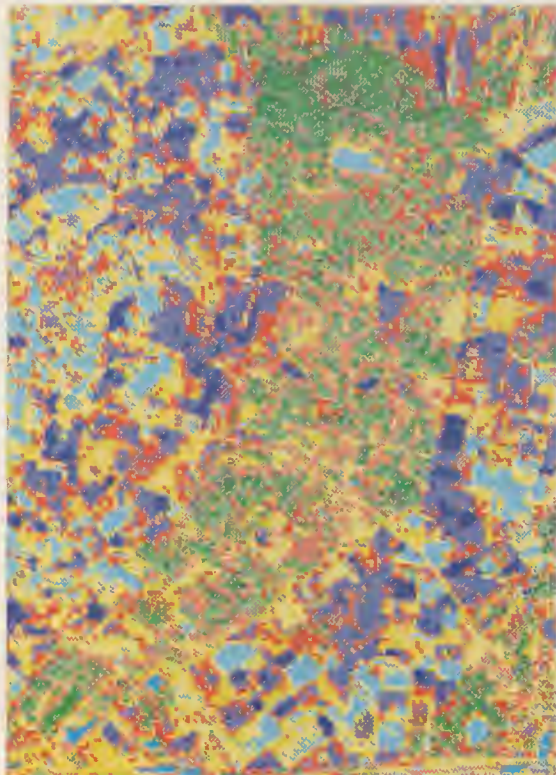
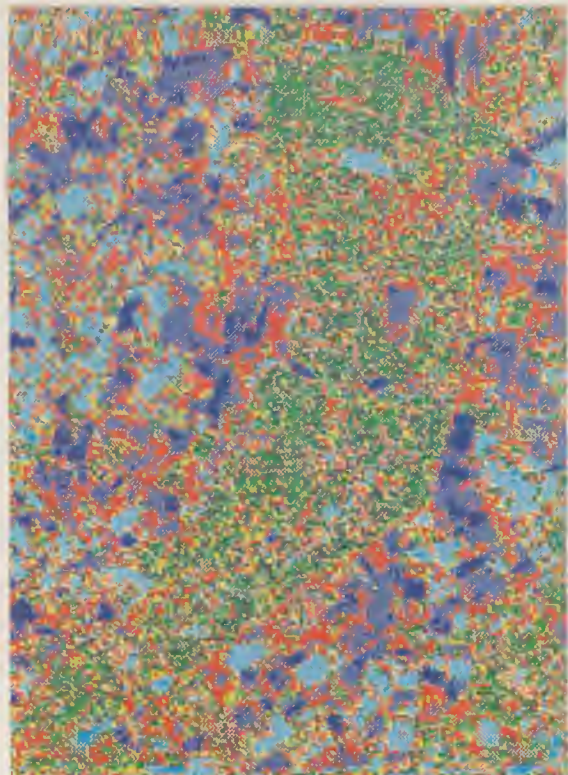


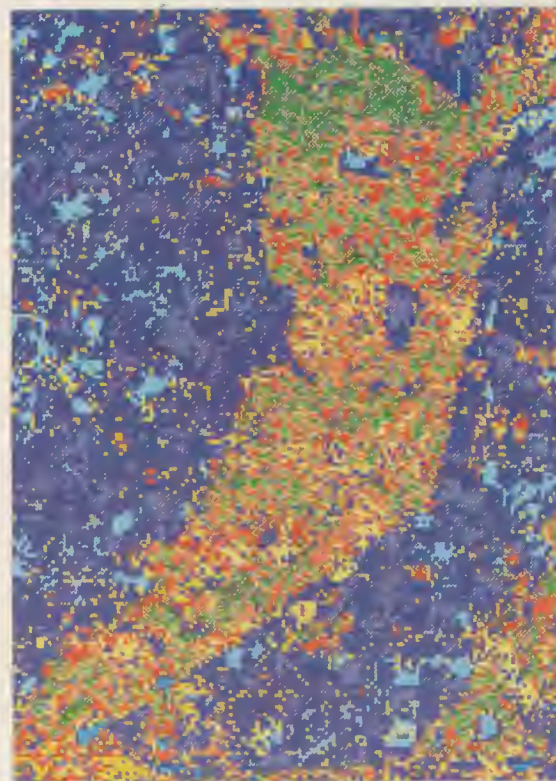
Figure 1. TMPYNVEN: Spectral separability of training classes ($\mu \pm s$)



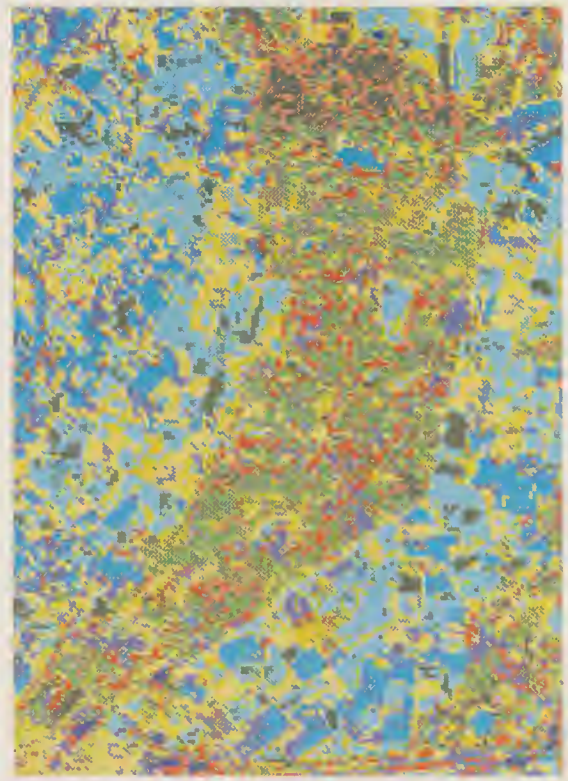
rava



ravb



ravc



ravd

SPRUCE	CROPS	CORS	WATER	DOUG	FAG
CUPR	GRASS	SYLV	BARE	LARCH	DAKX

Figure 2. Classified images of TMRAVELS.



Figure 3. Aerial IR photo of the test area (Flanders).

Copyright Eurosense, Wommel, Belgium.

Table 2: Best average classification accuracies of TS samples

Algorithm	TMRAVELS		Class. label	TMPYNVEN		Class. label
	Channels	%		Channels	%	
MINDIS	VI+5	63.7	RAVA	VI+5	39.7	PYNA
MAHDIS	ND43	58.9	RAVB	VI+5	40.5	PYNB
MAXL1	2,3,4	62.3	RAVC	VI+5	41.2	PYNC
MAXL2	2,3,4	61.8	RAVD	VI+5	42.9	PYND

Furthermore, following general conclusions, based upon examination of confusion matrices could be drawn:

1. Classification accuracies based on TR samples can be twice as good as those based on TS samples
2. Broad (Level I) classes are better classified than narrow (Level III) classes
3. The use of all available channels does not guarantee the best classification results. This is especially the case with Level III classes.
4. The effect of weights assigned to certain channels appears to be negligible. In fact, best results were obtained without weights.
5. Scots pine and Corsican pine are difficult to separate.
6. Deciduous trees cannot be classified with

reasonable results at this time of the year (1 November).

7. Classification accuracies are problem-dependent: worse results with TMPYNVEN are caused by the choice of classes: age classes are difficult to distinguish.

3.3.6.2. Acceptance sampling tests

Accuracy tests based on the acceptance sampling theory and applied to the best classified images yielded the following results:

1. Classification accuracy for the FOREST class, with a desired consumers risk of 5%, ranges between 79% and 92%, dependent upon the applied algorithms. The widely accepted requirement of 90% accuracy is only met in Pynven/Eksel.
2. The CONIFEROUS class can be classified with an accuracy ranging between 60% and 82%, with the MINDIS algorithm yielding the best results, especially in Ravels.
3. Attempts to classify DECIDUOUS yielded completely unsatisfactory results. In view of the less advantageous recording date this was not unexpected.
4. Classification of species classes yields equally disappointing results. DOUGLAS, for instance, was always misclassified.
5. Age classes of Scots and Corsican pine cannot be distinguished.

3.3.6.3. Discrete multivariate error matrix analysis

Based on the extensive classification exercise a huge amount of tests using discrete multivariate error matrix analysis could be executed. Only a few results can be mentioned here.

1. The use of VI43 and ND43 as single channels for classification yield equal results. This is to be expected since there is no inherent spectral information difference between VI and ND.
2. ND43 yields significantly better results than ND53 using all available classification algorithms for the FOREST/NON-FOREST distinction as well as for the complete confusion matrix.
3. In half of the investigated cases the application of weight factors decrease classification accuracy. This is mostly the case with the MAXL algorithms (test with Tasseled Cap transformations as single channels).
4. No single classification algorithm stands out as the best one to distinguish FOREST from NON FOREST. The faster MINDIS algorithm was equal to the more complicated ones. The frequent occurrence of mixed pixels can explain the similar results for all algorithms.

4. Conclusions

FOREST/NON FOREST distinction is possible with an accuracy ranging between 79% and 92%, assuming a consumers risk of 5%. This compares with results reported by other authors. The spectral differences between both Level I classes are obvious, which means that a minimum accuracy requirement of 90% is not unreasonable. Due to the lack of sufficient DECIDUOUS terrain classes for sampling, discrimination from CONIFEROUS cannot yield conclusive results. DECIDUOUS species were almost all defoliated resulting in a non-descript spectral signature. CONIFEROUS species can be recognised as such with an accuracy between 60% and 82%. Species recognition is still a problem. The best results are obtained for the Pynven/Eksel area for Scots pine (66%). Age classes could not be recognised accurately: for Scots pine the accuracies ranged between 1% and 42%, for Corsican pine between 1% and 21%. These poor results might be explained by the fact that the age classes are very much user classes and not spectral classes.

The CAE feature extractor yields good results. Its performance could only be judged by the average accuracies obtained from the original, complete confusion matrices. It could be concluded that the use of all available TM channels (with the exclusion of TM6) did not yield significantly better results than the subset obtained by the feature extraction algorithm.

The use of weight factors decreases classification accuracy.

Channel combinations and ratios can be considered as an alternative to original TM channels.

In particular the combination of VI43 and TM5 as a two-channel input yielded the best results.

Among the used classification algorithms there is no best one to discern. It is remarkable how well the simple MINDIS algorithm performs.

Though a 30-m resolution is a considerable improvement over the 80-m resolution of MSS, an area of 900 m² can contain different tree species in Flanders. Parcels are small and forest roads cannot be detected satisfactorily.

Clearly the spatial resolution of TM limits the successful application of TM images for forestry in Flanders. Most bad classifications can be traced back to insufficient or inadequate training samples.

For general land cover studies TM images can be useful and can yield results that are close to ground observations. On the other hand it should be noted that little information exists on the accuracy of land cover studies using traditional methods. In addition, the recording date was unfortunate, and better results are to be expected within the growing season.

The orthophotomaps presently in use in the regional forest service is without doubt the best document available, and is unlikely to be replaced by present generation space imagery. However, as aerial photography is very costly, space imagery such as TM data can play a useful role for periodical updating in between the 10-yearly photo missions.

References

- Acevedo W., Buis J.S. & Wrigley R.C. (1984) Changes in classification accuracy due to varying Thematic Mapper and Multispectral Scanner spatial, spectral and radiometric resolution, *Proc. 18th International Symp. Remote Sensing of Environment*, Ann Arbor, Michigan, pp. 21-44.
- Aronoff S. (1982) Classification accuracy: a user approach, *Photogrammetric Engineering and Remote Sensing*, 48(8), pp. 1299-1307.
- Beaubien J. (1979) Forest type mapping from Landsat digital data, *Photogrammetric Engineering and Remote Sensing*, 45(8), pp. 1135-1144.
- Berg A. General results of a European remote sensing project (AGRESTE). Agronomic considerations and needs of society. In: *Applications of Remote Sensing to agricultural production forecasting*. Ed. A. Berg, Balkema, Rotterdam.
- Bishop Y.M., Fienberg S.E. & Holland P.W. (1975) *Discrete Multivariate analysis: Theory and practice*, MIT Press, Cambridge

- Coppin P., Goossens R. & Dewispelaere W. (1986) Thematic mapping of the Flemish forest cover using aerial photography, *Sylva Gandavensis*, 51, pp. 123-149.
- Driscoll R. & Spencer M.M. (1972) Multispectral scanner imagery for plant community classification, *Proc. 8th Int. Symp. Remote Sensing of Environment*, Ann Arbor, Michigan, pp. 1259-1278.
- Ginevan M.E. (1979) Testing land use map accuracy: another look, *Photogrammetric Engineering and Remote Sensing*, 45(10), pp. 1371-1373.
- Irons J.R., Markham B.L., Nelson R.F., Toll D.L., Williams D.L., Latty R.S. & Staufer M.L. (1985) The effects of spatial resolution on the classification of Thematic Mapper data, *International Journal of Remote Sensing*, 6(8), pp. 1385-1403.
- Jaakkola S., Rosenholm D. & Isakson L. (1974) SPOT simulation: An evaluation for forest inventory and mapping purposes, *Proc. 18th Int. Symp. Remote Sensing of Environment*, Ann Arbor, Michigan, pp. 521-528.
- Kauth R.J. & Thomas G.S. (1976) The Tasseled Cap. A graphic description of the spectral temporal development of agricultural crops as seen by Landsat. *Proc. Symp. Machine Processing of Remotely Sensed Data*, Purdue University, pp. 41-51.
- Lillesand T.M., Hopkins P.F., Buchheim M.P. & Maclean A.L. (1985) The potential impact of Thematic Mapper, SPOT and microprocessor technology on forest type mapping under Lake State conditions, In: *PECORA 10, Remote Sensing in Forest and Range Resource Management*, Colorado State University, Fort Collins, Colorado, pp. 43-57.
- Megier J., Mehl W. & Ruppelt R. (1984) Per-field classification and application to SPOT-simulated, SAR and combined SAR-MSS data, *Proc. 15th Symp. Remote Sensing of Environment*, Ann Arbor, Michigan, pp. 1011-1017.
- Mueller-Dombois D. (1984) Classification and mapping of plant communities: a review with emphasis on tropical vegetation. In: *The role of terrestrial vegetation in the global carbon cycle: measurements by remote sensing*, Ed. G.M. Woodwell, SCOPE 23, Wiley, pp. 21-90.
- Schowengerdt R.A. (1983) *Techniques for image processing and classification in remote sensing*, Academic Press, New York.
- Senoo T., Iwanami E., Hoshino K., Tanaka S. & Sugimura T. (1984) Diagnosis of forest recovery in the East Region of Kyoto using Landsat data, *Proc. 15th International Symposium on Remote Sensing of Environment*, Ann Arbor, Michigan, pp. 1019-1023.
- Swain P. & Davis S. (1987) *Remote Sensing: The quantitative approach*, McGraw Hill, New York.
- Teillet P.M., Guindon B. & Goodenough D.G. (1981) Forest classification using simulated Landsat-D TM data, *Canadian Journal of Remote Sensing*, 7(1), pp. 51-61.
- Wacharakitti S. (1975) *Automatic analysis of remote sensing data*. Research note No. 18, Kasetsart University, Faculty of Forestry, Bangkok, Thailand.

Acknowledgements

This report presents research results of the Belgian scientific research programme in the field of remote sensing from space (Services of the Prime Minister - Science Policy Office). The scientific responsibility is assumed by its authors. Research team members Dirk Tietens and Peter Haelvoet are gratefully acknowledged for their assistance in the field. The computer infrastructure of CEVA was used throughout this research project. Luc Vandekerckove, system analyst with CEVA, was very helpful to solve hardware and software problems. Marc Vereecken (TELSAT/04) wrote the program that enabled screen dumps from the Toshiba PC to a colour ink jet printer. Special thanks are due to ir. Adri Verstuylen, senior forestry officer in Turnhout, for support in the field and for providing maps and the management plan for Ravels. Computer Compatible Tapes of TM frames 198/24 and 198/25 were provided free of charge by Earthnet on 06.06.1986 through the Science Policy Office. The authors also gratefully acknowledge N.V. Eurosense-Belfotop, Wommel, for the use of colour-infrared aerial photographs of the test areas.

Forest Classification with TM Data in the Area of Freiburg, Federal Republic of Germany

M. Schardt

*German Aerospace Research Establishment, Oberpfaffenhofen
and Albert-Ludwigs-Universität, Freiburg, FR Germany*

In this investigation, Landsat-5/TM data pertaining to forest cover in a part of the Rhine valley near Freiburg has been digitally classified to delineate its information content according to forest inventories. Data from two different seasons were used:

First, an April scene was evaluated for the separation of deciduous and coniferous forests and for the general separation of forested and agricultural areas. In the July scene, it was possible to distinguish three natural age classes of trees with an accuracy of 80% to 90%. It is found that within the deciduous forest stands, pure poplar stands could be clearly separated from mixed deciduous forest stands using the amplitude differences in band TM5, the middle infrared band. From the data of band TM4, the near infrared band, one observes that within the coniferous stands, pine could be differentiated from stands of douglas fir. The tree species classified in this investigation could be separated with an accuracy of over 90%.

To avoid misclassifications caused by the influence of topography differences between the forest of the Rhine plain and the higher areas of the Kaiserstuhl, the additional information of a digital terrain model was integrated.

Keywords: Digital Classification, Maximum-Likelihood Method, Tree Species, Age Classes, Divergence Analysis, Median Filter, Digital Terrain Model, Verification.

1. Introduction

Previously, in tropical and subtropical areas, digital classification using optical remote sensing data has quickly and successfully produced helpful information on the development and condition of vegetation. In countries with temperate climates and very intensive forest and agricultural usage, such as the Federal Republic of Germany, the only type of remote sensing data used to aid in the production of forest inventories is that obtained operationally from air photos.

In the Federal Republic of Germany, detailed forest maps of state, community, and larger private forest holdings are available at a large scale of 1:10 000.

With the exception of small scale forest maps that simply denote the boundaries of the various types of forest holdings, no small scale forest maps exist. This means that there is a need for small scale maps depicting areas of specific tree species. This need could be filled by maps made with optical remote sensing data with a low geometric resolution, such as, for example, Thematic

Mapper data. The disadvantage of using these less detailed inventories is outweighed by the advantage of having a small scale forest map. This paper shows the information content of Thematic Mapper data that is applicable to an inventory of tree species and natural age classes.

This paper focuses on results obtained from one test area in the 'Oberer Rheingraben' growth zone in the Baden-Württemberg area. Two additional investigations, each covering a different zone in this same area, are currently in progress.

The results of this investigation will also be published in the proceedings of the Willi Nordberg Symposium, Graz, 1987 (Ref. 1).

2. Description of Test Site

The 'Oberer Rheingraben' test site is bordered on the north by the 'Taubergießen' nature reserve and on the

training areas / verification areas:

	culture thicket low pole wood	pole wood high pole wood	low timber old timber	poplar
culture thicket low pole wood	89.8 %	9.9 %	0.3 %	
pole wood high pole wood	4.3 %	84.7 %	10.8 %	0.2 %
low timber old timber	0.3 %	13.6 %	84.3 %	1.8 %

Classification accuracy weighted by area size: 85.7%

Table 6. Confusion matrix of age classes of deciduous

training areas:

	culture thicket low pole wood	pole wood high pole wood	low timber old timber	poplar
culture thicket low pole wood	88.3 %	11.7 %	0.0 %	
pole wood high pole wood	4.1 %	84.8 %	10.9 %	0.2 %
low timber old timber	0.1 %	9.0 %	90.3 %	0.6 %

Classification accuracy weighted by area size: 88.7 %

Table 7. Confusion matrix of age classes of deciduous

	douglas fir		mixed deciduous	poplar
	culture	pole timber		
culture	75.3 %	9.1 %	2.6 %	13.0 %
pole timber	12.4 %	81.9 %	2.4 %	3.3 %

Classification accuracy weighted by area size: 77.7 %

Table 8. Confusion matrix of age classes of douglas fir

a higher percentage of accuracy than the confusion matrix obtained by using training areas and verification areas (Table 6). This comparison shows that it is important to choose verification areas in addition to training areas. This should be done so that one achieves a more objective verification result, because the selected training areas are not necessarily representative of all the spectral features occurring in forests.

The verification was broken down into three steps:

1. Separation of forest and nonforest. The overlapping of the two datasets creates mistakes due to the imperfect geometric alignment of both scenes. The degree of the mistake depends on the size and shape of the forest areas. Large complex areas cause fewer mistakes than

small irregularly shaped units. In this investigation, about 3% of the forested areas were incorrectly eliminated due to this overlapping error.

2. The separation of tree species. The accuracy of the tree species classification was 90% to 100% (Table 4). Despite the multitemporal analysis, the lowest accuracy was found for the douglas fir (culture). Thirteen percent was misclassified as poplar. The absolute accuracy of 100% of the forest of the Kaiserstuhl is not due to reflectance differences, but to the additional information of height provided by the digital terrain model.
3. The separation of natural age classes. For the classification, the different tree species were divided into many narrow age classes, narrow with respect to their spectral variance. These narrow age classes were later joined together into spectrally larger and more accurate classes. Table 5 shows that the many smaller age classes of deciduous forest with an accuracy of 36% to 86% can be joined into a few larger classes with an acceptable accuracy of about 80% to 90% (Table 6). The classification accuracy of the two natural age classes of douglas fir was 75% to 80% (Table 8).

6. Areal Statistics

Table 9 shows areal sizes of the various classes. Combining the classification result with the digital terrain model makes it possible to create additional statistics.

deciduous
Rhine plain 3656.4 ha

culture thicket low pole wood	847.7 ha
----------------------------------	----------

pole timber high pole timber	1111.0 ha
---------------------------------	-----------

low timber old timber	1697.7 ha
--------------------------	-----------

poplar	680.3 ha
douglas fir	131.2 ha
culture / thicket	82.6 ha
pole timber	48.6 ha

pine 36.9 ha

total area 4504.8 ha

Table 9. Areal statistics of the Rhine plain forest

Tables 10 and 11 show the percentage of forest associated with different heights and expositions determined by the digital terrain model. In Table 10 one can see the increased percentage of the forest area that is associated with the increasing elevation.

height	forest	nonforest	total area size
200 m - 300 m	205.4 ha (3.4%)	5811.7 ha (96.6%)	6017.1 ha
300 m - 400 m	937.6 ha (39.9%)	1409.5 ha (61.1%)	2347.1 ha
400 m - 500 m	632.7 ha (84.1%)	119.8 ha (15.9%)	752.5 ha
500 m - 600 m	24.7 ha (100.0%)	-	24.7 ha
total	1800.4 ha (19.7%)	7341.0 ha (80.3%)	9141.4 ha

Table 10. Tree percentage for the different heights in the Kaiserstuhl

exposition	forest	nonforest
west (135° - 224°)	691.9 ha (29.5%)	1656.9 ha (70.5%)
north (315° - 44°)	332.8 ha (18.8%)	1422.7 ha (81.2%)
east (45° - 134°)	467.9 ha (18.0%)	2135.2 ha (82.0%)
south (215° - 314°)	307.8 ha (12.6%)	2126.2 ha (87.4%)

Table 11. Tree percentage for the different expositions in the Kaiserstuhl

7. Conclusion

This investigation is appropriate only for a small area and, therefore, shows a high accuracy of classification of natural age classes and tree species. An extrapolation of these training areas to a larger area will not be as accurate because of atmospheric influences and the effect of different types of stands.

Therefore, it is important that, when attempting to enlarge the classification area, that one chooses additional training areas representative of the new areas.

The additional information from a digital terrain model and data from different seasons improves the classification result.

8. References

1. Schardt M 1987, Forest classification with TM data in the area of Freiburg, Federal Republic of Germany, *Willi Nordberg Symposium*, Graz (in print).
2. Stiebig H J & Schardt M 1986, Digital classification of forested areas using simulated TM- and Spot- and Landsat 5/TM data, *Symp. on Remote Sensing for Resources Development and Environmental Management*, Enschede.
3. Hildebrandt G 1976, Die spektralen Reflexionseigenschaften der Vegetation, *Proc. Symp. Remote Sensing in Forestry*, Freiburg, XVI IUFRO World Congr, 9-22.
4. Fehlert G P 1984, Kalibrierung von MSS-Satellitenbilddaten zur Auswertung zeitlicher Reflexionsänderungen an Fichtenbeständen, *DFVLR Forschungsbericht* 84-44, Oberpfaffenhofen.
5. Haberäcker P 1985, *Digitale Bildverarbeitung*, Carl Hanser, München.

Use of Landsat-TM Data for Forest Damage Inventory

A. Kadro

*Abt. Luftbildmessung und Fernerkundung der
Universität Freiburg, FR Germany*

The use of Landsat-TM data for the monitoring and survey of forest decline became a proposition because of rapidly increasing forest decline in middle and western Europe, due to acid rain and air pollution.

An important point of this pilot project is, among others, the involvement of Landsat-TM data. First encouraging results have been achieved by TM simulations from different flight altitudes. For such studies test sites have been established which are located in damaged areas in middle and southern parts of the Black Forest. These sites are under permanent control. The dominant tree species here are spruce and fir which are stocked on different slopes and expositions. To achieve optimal results, well investigated sites (ground truth, IRC 1 : 5000) have been selected for the purpose of training the use of TM simulation data. The same sites were used for the later Landsat-TM evaluations. Ground truth and visual IRC photo interpretation results were the data base for the verification of the computer-aided classifications.

Several investigations on spectral signatures of different TM bands have been performed. The main point of investigation there was the degree of stand damage. Spectral signature investigations resulted in clear separability of different degrees of damages by using different spectral TM bands. Bands 5 and 7 (middle IR), which are not yet sufficiently evaluated as to their applicability for forest damage investigation, demonstrate practicability. Additional signature investigation of the other forest types (deciduous, coniferous, mixed forest) present also separability on TM data.

Computer-aided classifications in form of ratioing (B5/B4) show first positive results as separation of damaged and healthy sites is concerned. In addition the ratio RVI B4/B3 (vegetation index) shows the separability of classes and even subclasses.

Computer-aided classifications for different test sites on Landsat-TM data have been evaluated. In this computer classification a supervised classification according to maximum likelihood methods has been used.

The verification of computer-aided results in correlation with the result of TM simulation data and with direct comparison with ground truth and IR photo interpretation presents an acceptable output. But some very few classes are overlapping each other. This can happen because of the relatively large TM pixel size of 30×30 m.

Abstract

TM-simulation data were acquired from different altitudes within the scope of a project for forest damage inventory in the Black Forest in Germany. The evaluation of the TM simulation data will be the base for the analysis and the computer-aided classification of Landsat-TM data. Different investigations of the spectral signatures, computer-aided classification (supervised) and ratio image analysis on different TM bands have been carried out. Thereby it was possible to classify different degrees of forest decline and also different types

of vegetations. Ground truth and the results of IRC photo interpretation were the basis for the verification of the results of the computer-aided classification.

1. Introduction

Since the forest decline has been increasing for the last ten years in Middle and Western Europe, the need for detailed information on the actual situation of the forest

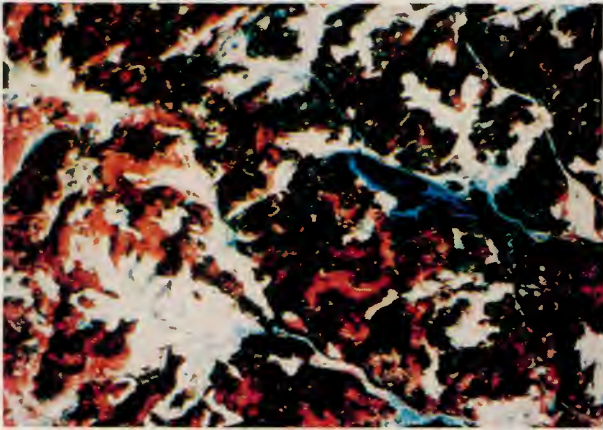


Photo 1: Landsat-TM imagery, IR colour composite from bands 2, 3 and 4, showing the test site St. Blasien - South Black Forest, acquired on 12 September 1985, covering approximately 15x21 km.

in Germany has proved to be of vital interest. Therefore remote sensing appears to be the most convenient tool for the monitoring and quantification of the forest decline. Ground and aerial survey methods are time-consuming and expensive. That is why a project started at the Department of photo interpretation and Remote Sensing at the University of Freiburg to evaluate multispectral data for forest damage inventory. This project is dealing with research as regards the application of the Landsat-TM data for the monitoring and survey of forest decline after encouraging results achieved through TM simulation (Hildebrandt, Kadro *et al.* 1987; Kadro *et al.* 1986).

2. Test Sites

The same test sites already covered by TM simulation during the ongoing project conducted at the department, have also remained the subject of analysis with TM-data. These test sites are located in the Black Forest (South-West-Germany).

They differ in morphology, forest types and the degree of the actual forest damage to simulate all possible survey problems. The sites contain mostly coniferous trees (spruce mixed with fir) and some smaller stands of deciduous trees (mostly beech). The main interest in this project is the monitoring of coniferous trees. The damage classes differ according to age, altitude exposure in the different test strips. The damage symptoms mainly consist of needle loss and chlorosis, at times both symptoms

Table 1

healthy	D0 = 0-10% needle loss
sickly	D1 = 10-25% needle loss
damaged	D2 = 26-60% needle loss
severely damaged	D3 = >60% needle loss

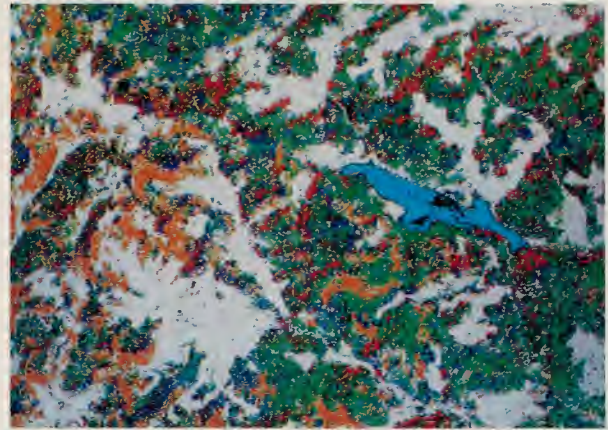


Photo 2: Computer classification of the area in Photo 1 (supervised classification, bands 2, 3, 4, 5 have been used).

Identification key

colour	vegetation/terrain type
green:	healthy conifer
dark blue:	damaged conifer
red:	severely damaged forest
light blue:	water surface
white:	meadow, agriculture, roads

appear together. According to the percentage of the needle loss the damage classes are being determined in the following classes (Table 1).

3. Available Basic Information

The data and information available about the test strips are the following:

3.1. TM Simulation Data

TM simulation data were acquired in July 1984 and August 1985 from different altitudes: 300, 1000 and 3000 m above ground. The Landsat-TM data (scene 195/27 and 195/26) were acquired at approximately the same time as the TM simulation: 7.07.1984, 12.09.1985.

The differences as to the dates of acquisition between the data obtained being so slight a comparison between TM-Simulation and Landsat-TM data is made possible. The different altitudes have the following ground resolution (pixel size) Table 2.

Table 2

Altitude	Resolution (m)
300 m	0.75x0.75 (aircraft TMS)
1000 m	2.5 x2.5 (aircraft TMS)
3000 m	7.5 x7.5 (aircraft TMS)
705 km	30x30 (Landsat 5)

3.2. Ground Truth

A lot of test areas have been established alongside the test strips (Photo 5). The respective size of each test area is

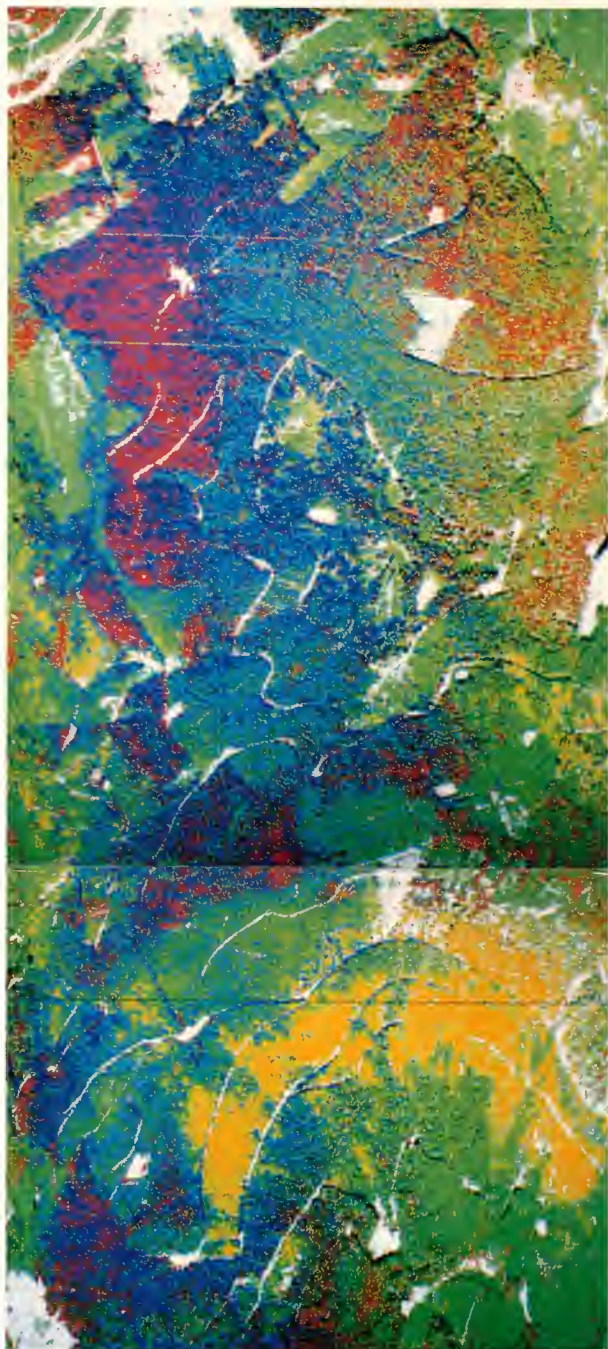


Photo 3: Computer classification (supervised), TM simulator (TMS), aircraft scanner data for the test site St. Blasien. Data are acquired from 1000 m altitude above ground on 22 Aug. 1985, covering approximately 1.75×5 km, colour coding as in Photo 2.

between 2 and 40 ha. Information on the vitality of the trees in each test area has been collected through ground check by means of line samples along the test area.

3.3. IRC Photo Interpretation

IRC photography in scale 1:5000 was also available for the test strips; these photographs were taken at approximately the same time as TM-simulation and Landsat-TM data. The vitality of the trees in each test area has also been determined by photointerpretation and also by



Photo 4: Computer classification (supervised), TMS data also for the test site St. Blasien. Data are acquired from 3000 m altitude above ground on 22 Aug. 1985, covering approximately 4.5×4.5 km, colour coding as in Photo 2.



Photo 5: Test areas on the IR colour composite. The information in these test areas will be used for the verification of the computer-classification results (see chapter 3.2).

means of line samples. An interpretation key has been developed for the photo interpretation.

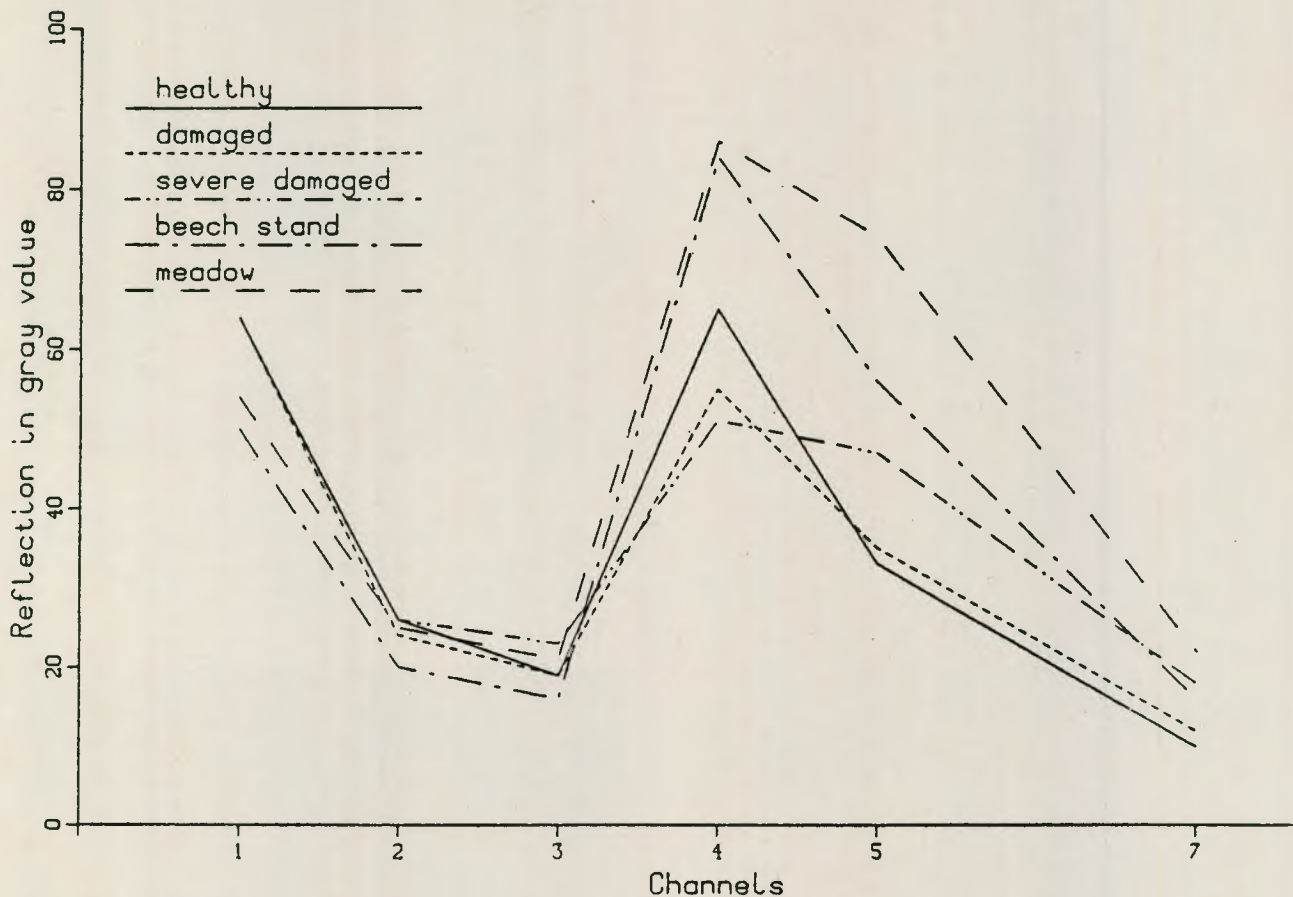


Figure 1. Forest stands.

4. Results of Spectral Signature Analysis

The advantage of the TM data is that they have additional to the other bands in the visible and near infrared two spectral bands in the middle infrared. Till now they have not been investigated and proved to analyse the spectral signature of different forest damage classes.

Figure 1 illustrates clearly that not only in the near infrared, but also in the middle infrared there is information about the reflection properties of different vegetation types. This could be an additional advantage for the computer-aided classification.

For the selection of a certain TM band for computer

Figure 2.

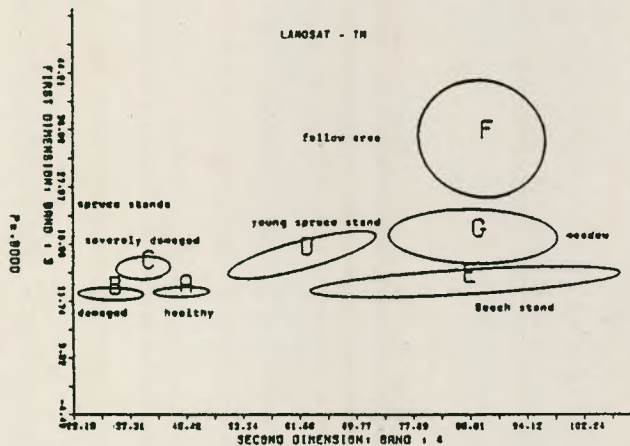
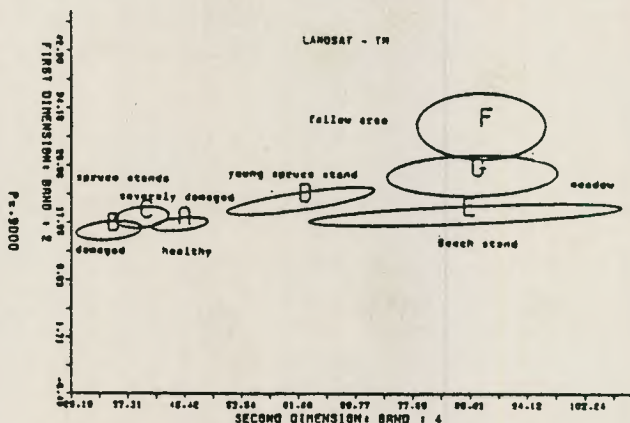


Figure 3.



classification certain investigations should be carried out in a two-dimensional feature. Figures 2 and 3 show such kinds of investigation. Each cluster in the figures contains the middle grey value and the standard deviation for different vegetation types.

The reflection intensity in the visible bands is too small for all levels, but on the other hand the different vegetation types have a low reflection in the visible bands (Kadro 1985, Kadro 1986, Wastenson *et al.* 1987).

5. Results of Computer-aided Classification

TM simulation data and Landsat-TM data were evaluated simultaneously in this pilot project in order to test the practicability of Landsat-TM data for forest decline survey. The data, having been acquired during ideal weather conditions, consequently have not been atmospherically corrected.

The main difference between the data acquired is the pixel size (ground resolution) Table 2. It is only possible to investigate single trees from low altitudes; but data from other altitudes allow for the investigation of groups of trees or stands. As a consequence the grey value of the pixel does not present a single crown, but represents the reflection of all the components in the pixel size; thus resulting in the formation of mixed signatures. It is decisive for computer-aided classification which component is dominant in a pixel, thus determining the allocation of the pixels.

The spectral properties of the stands are being influenced by the following aspects (Kadro 1981):

- the phenological and physiological situation of the trees
- the vertical structure of the canopy and the relation between illuminated and unilluminated portions of the crowns
- species composition
- crown density and ground cover.

The problem with the mixed pixel is obvious at Landsat-TM data; although Landsat TM has a high ground resolution each pixel covers an area of 900 m². In this case only large areas can be investigated and sensed. To achieve an appropriate computer-aided classification the area to be classified should be homogeneous. For the more inhomogeneous the reflection characteristics of an area may be, the more difficult will be the unequivocal allocation to a specific class by the computer.

5.1. Determination of the Training Area for the Supervised Classification

Determination of the training area on the digital images occur by the user and with already available information through ground truth, IRC photo interpretation and the interpretation of the colour composition directly on the screen. Determination of the training area for deciduous trees, coniferous trees, grass land, water surface etc. . . . is not so difficult, but to determine the training area for different damage classes among the coniferous trees is not so easy for the user.

The experience and the knowledge of the spectral signatures, interpretation of the digital images of the different forest types and damage levels by the user is a basic essential for the handling with digital image analysis in remote sensing.

Photo 6: Landsat-TM image from the middle in Photo 1, showing a ratio image TM4/TM3 near IR band/red band (vegetation index).

Identification key

colour	vegetation type
green:	conifer forest
dark blue:	deciduous forest
light blue:	agricultural/grassland

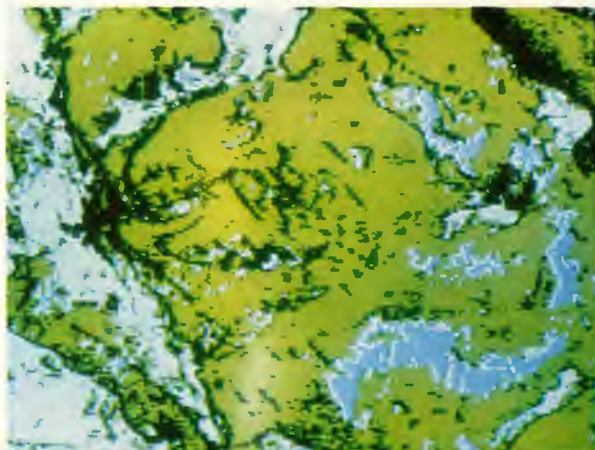
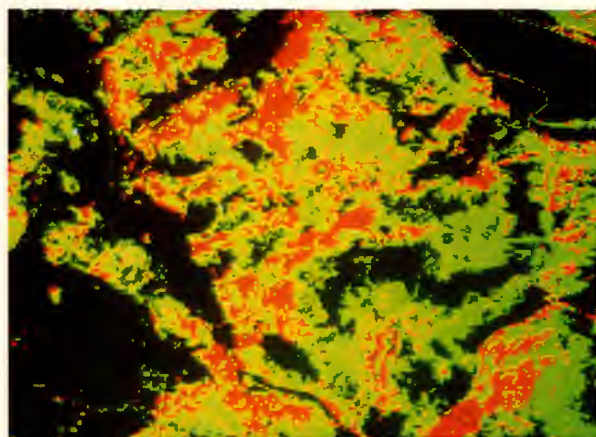


Photo 7: Landsat-TM ratio image B5/B4 for the area in Photo 6.

Identification key:

colour	vegetation type
green:	healthy conifer forest
red:	damaged conifer forest
black:	non-conifer forest area



5.2. Results of the Ratio Image Analysis

The first simple handling of the TM bands for the reconnaissance of the damaged area is the analysis of the ratio $TM5/TM4$. By this method it is possible to separate the damaged areas from non-damaged ones because the damaged areas have a high grey value in this ratio, due to a higher reflection in $TM5$ and lower reflection in $TM4$ than the healthy ones (Photo 7).

This kind of ratio does not differentiate between the damage levels, but at least differentiates between healthy and damaged in addition to severely damaged stands. The advantage of this method is that it is easy and not time-consuming, presenting and indicating in general the distribution of the decline.

Apart from the method already described there is still another ratio, and that is the ratio of the vegetation index. This will be obtained through ratio $TM4/TM3$ (Photo 6).

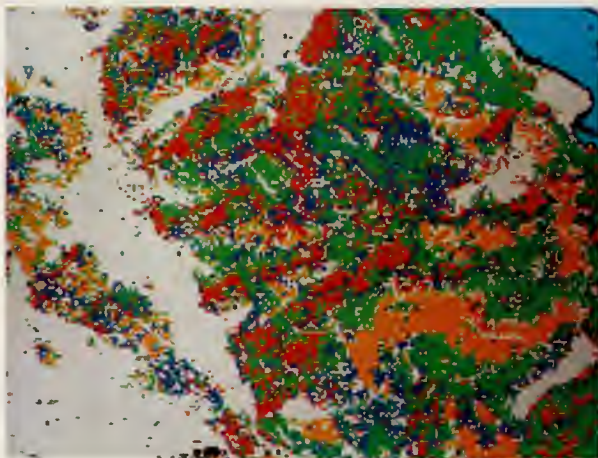
This ratio allows not only for the separation of vegetation areas from non-vegetation areas, but for the distinction even between deciduous and coniferous trees, grassland or agricultural areas.

It is possible to use this vegetation index ratio as an auxiliary band in addition to the Landsat-TM band set. In this case there is a facility to do a computer-aided classification with different TM bands, but in dependence on the auxiliary bands (ratio of vegetation index) and on certain vegetation types. In this way the misclassified pixels could be reduced by this method.

5.3. Results of the Supervised Classification

The main evaluation method in this pilot project is a supervised classification according to the maximum likelihood method. All investigated data sets from different altitudes have been classified with this

Photo 8: Computer classification (supervised) of Landsat-TM data for St. Blasien test site, bands 2, 3, 4 and 5 have been used. The area is the same as Photos 6 and 7 and covering the area in Photos 3 and 4.



methodology. The most important step in this method is to determine an exact training area for forest damage levels and to select different spectral TM bands for the calculation with the computer; at the evaluation of different data sets the fact has been taken into consideration that the data sets should cover the same area. Therefore the comparison of the data from different altitudes is made possible.

The main task of the user was to classify the different forest damage levels among the coniferous trees but other classes in the data sets have also been classified such as

Photo 9: Computer classification (supervised) of TMS data for a test site Bad Peterstal/North Black Forest, acquired on 21 July 1984 at 3000 m altitude above ground. Identification key as in Photo 2.

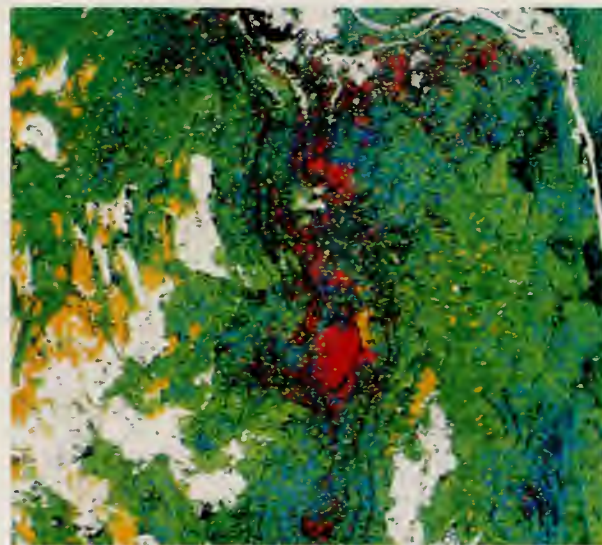


Photo 10: Computer classification (supervised) at Landsat-TM data, acquired on 7 July 1984. The image covers the area in Photo 9. Identification key as in Photo 2, in addition light blue = settlements, black = shadow on west slope.

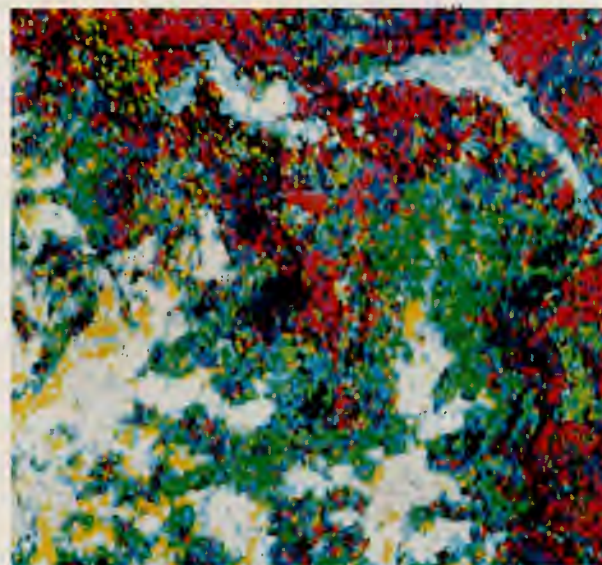




Photo 11: Computer classification (supervised) of TMS data for a test site in Baden Weiler/South Black Forest. Data acquired on 21 July 1984 at 3000 m altitude above ground. Identification key as in photo 2.

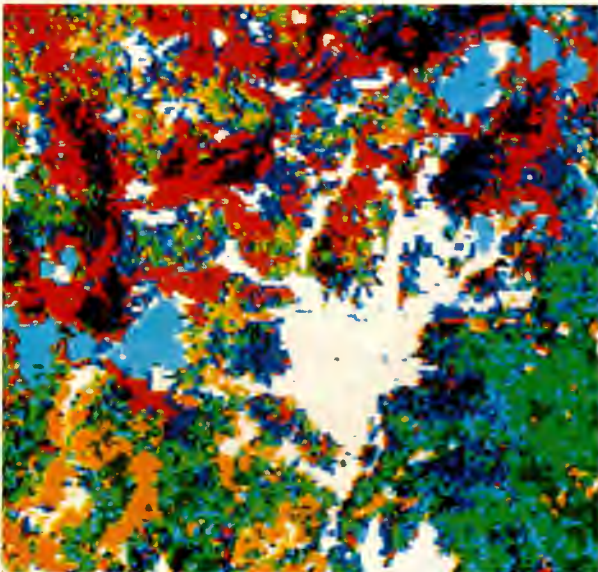


Photo 12: Computer classification (supervised) of Landsat-TM data acquired on 7 July 1984. The image covers the area in photo 11. Identification key as in photo 2 and in addition light blue = clouds, black = shadow on west slope.

deciduous trees, roads, bar soil etc. in order to render it possible for the forest departments to compare with their own available forest maps. The photos (2, 3, 4, 8, 9, 10,

11, 12) illustrate the results of examples of some test sites which have been classified through a supervised computer-aided classification method.

5.4. Analysis of the Results of the Supervised Computer-Aided Classification

The results obtained from different data sets have been analysed by comparison with information obtained through ground truth or with results of IRC photo interpretation. All the trees in each test area have been counted according to different damage levels, and their respective numbers in percentage have been calculated. As regards the case of the classified data sets however, the pixels have also been counted in each test area also according to different damage classes, and their respective numbers in percentage have been calculated. Both figures of percentage (photo interpretation and classification results) have been set off against and compared with each other. The verification of the computer-classified results is illustrated for some test areas in form of histogrammes (Figs. 4, 5). Actually that is respective to the distribution of damage degrees and different data sets according to the differing acquisition of the data sets from different altitudes.

6. Discussion of the Computer-Aided Classification

On the basis of the results achieved by means of the evaluation of Landsat-TM data sets, it has been possible to come to a decision as regards the use of Landsat-TM for the monitoring and survey of the forest decline. It can be concluded that it will only be possible to identify and quantify forest decline for three damage levels (D0-1, D2, D3: healthy/slightly damaged, damaged and severely damaged stands) on the TM data images. The following remarks will illustrate the potential and the difficulties of the Landsat-TM data as a tool for forest damage survey:

1. Homogeneous canopies can be classified and distinguished without any restriction.
2. Vigorous stands with a low density of trees will be classified in dependence of the ground cover type. Green vegetation between the trees promote the classification of the pixels to the low damage class. Dry vegetation ground cover favours the shift of the pixels to the highly damaged class.
3. Generally the shadows between the trees in the old stands, independent of the dominant class, favour the classification of the pixels into a highly damaged class.
4. It is difficult to classify stands on a steep western slope because of the shadows cast during the flight of Landsat in the morning.
5. Use of Landsat-TM data is practicable to survey the forest decline in different levels only for large stands due to the ground resolution (pixel size).

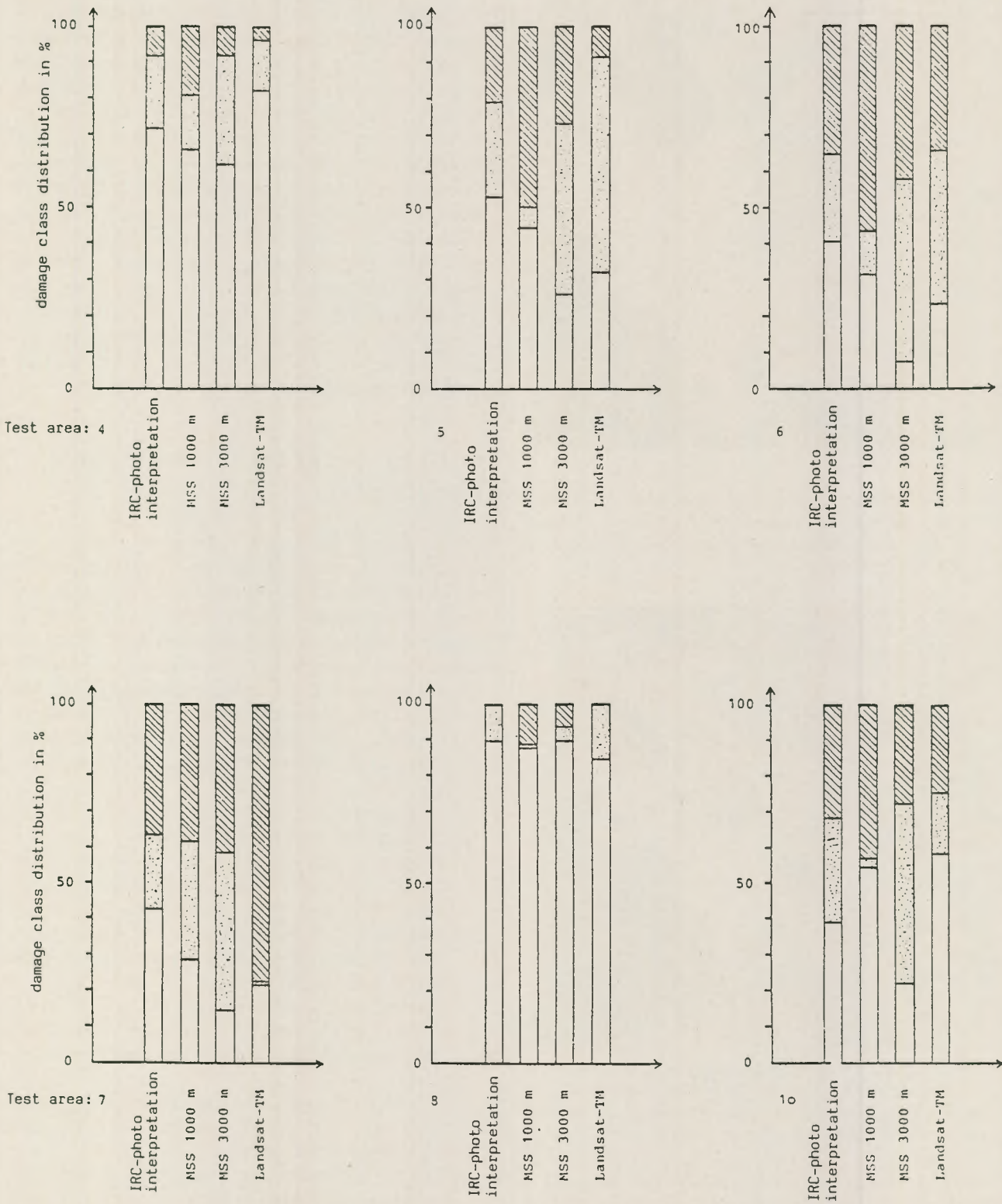
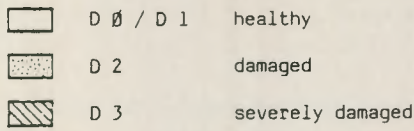


Figure 4.

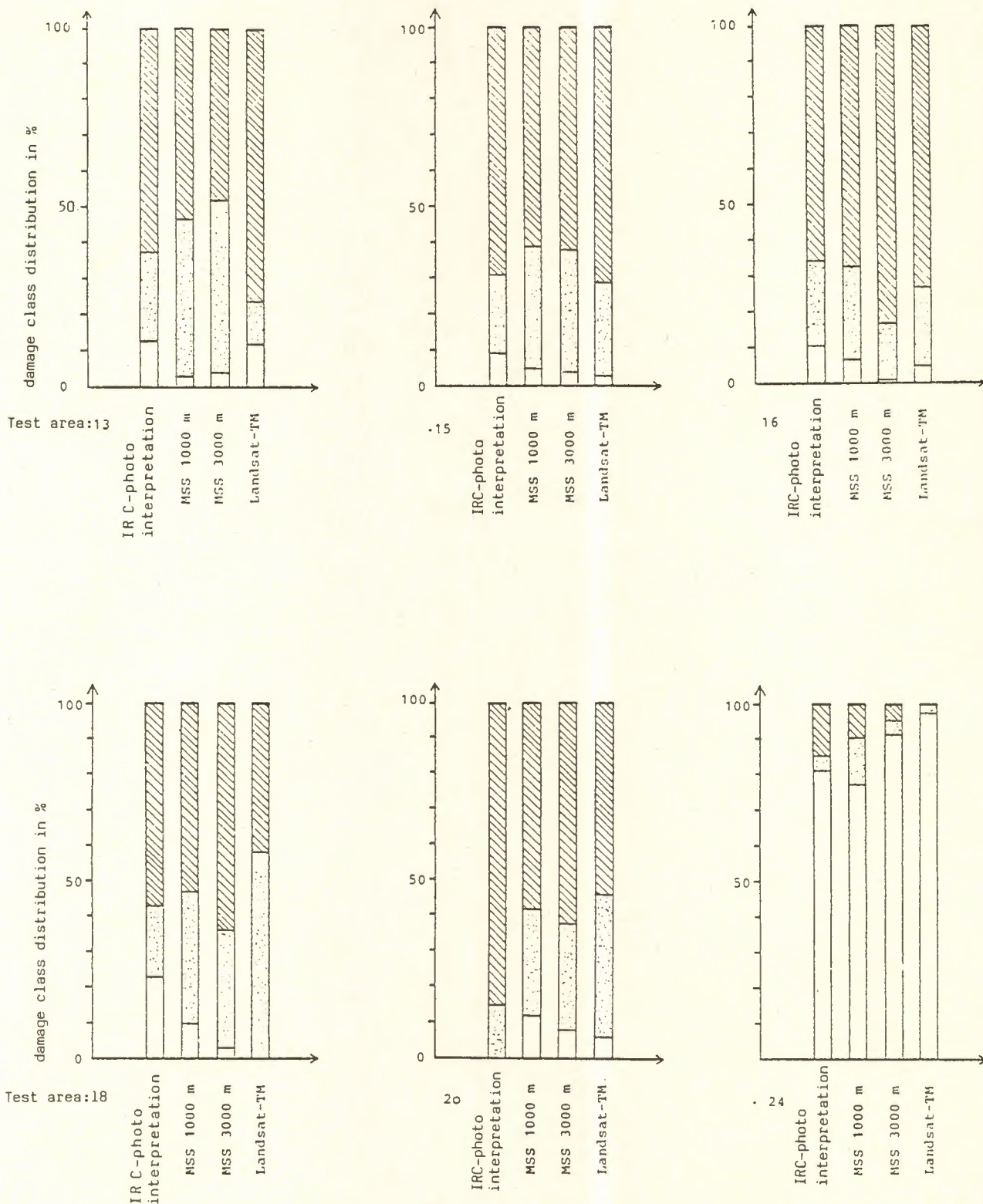
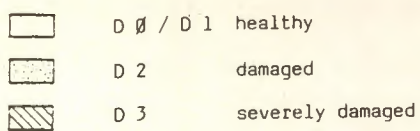


Figure 5.

6. Before the application of results achieved with TM-data, a confirmation of the result should be carried out by another survey method like ground truth or IR photo interpretation, before any operational steps will be taken.
7. Finally it is important for the Forest Department to have information about the location of the damages and therefore it is not necessary to know whether one single tree or small group of trees in the stands have been correctly classified or not.
8. Simultaneously to the classification of the damage levels in one test site the distribution, quantification and monitoring of other classes should also be classified to achieve a high utility of Landsat-TM data.
9. Landsat-TM data can be obtained regularly and continuously for different purposes for monitoring and surveillance of forest developments.
10. Structure and texture parameters of the level of forest decline cannot be investigated and determined on TM data due to the pixel size. In this situation a detailed investigation of the spectral signatures of different decline levels is a fundamental step for the analysis and application of the Landsat-TM data for forest monitoring as an important tool for remote sensing.

Reference

- Hildebrandt G., Kadro A., Kuntz S. & Kim, C. 1987: Entwicklung eines Verfahrens zur Waldschadeninventur durch multispektrale Fernerkundung. Bericht, *Projekt Europäisches Forschungszentrum für*

Maßnahmen zur Luftreinhaltung. KFK-PEF 25. März 1987.

Hildebrandt G. 1987: Toy or tool. Fernerkundung aus dem Weltraum: Spiel oder Werkzeug für die Forstwirtschaft? *Forstwissenschaftl. Centralblatt*, 106. Jahrgang (1987), Heft 3. S. 141-168. Paul Parey Verlag, Hamburg, Berlin.

Kadro A. 1981: *Untersuchung der spektralen Reflexionseigenschaften verschiedener Vegetationsbestände*. Diss. 215 S. Universität Freiburg.

Kadro A. 1986: Determination of spectral signatures of different forest damages from varying altitudes of multispectral scanner data. *Proc. 7th Int. Symp. Remote Sensing for Resources Development and Environmental Management*, ISPRS Commission VII, Enschede, 25-29 Aug. 1986.

Kadro A. & Kuntz S. 1986: Experiences in application of multispectral scanner-data for forest damage inventory. *Proc. 7th Int. Symp. Remote Sensing for Resources Development and Environmental Management*, ISPRS Commission VII, Enschede, 25-29 Aug. 1986.

Wastenson, Alm, Kleman & Wastenson 1987: Swedish experiences on forest damage inventory by remote sensing methods. *Int. J. IMAG, Rem. Sens.* IGS 1987, 1, I, 43-52.

Acknowledgement

The author thanks H.P. Kienzle, H. Schneider, G. Lang and P. Lösche for developing special software, R. Winter (DFVLR) for providing Landsat-TM data and V. Amann (DFVLR) for acquiring the TM-simulation data.

Use of Remote Sensing in Mapping of Vegetation in the Dividalen Area, Central Troms, Northern Norway

Hans Tømmervik

University of Tromsø, Norway

(Presently with Sami Reindeer Herders' Association of Norway)

The aim of this study was to evaluate how different vegetation cover types may be identified from Landsat-5 TM data. This will improve the very scattered vegetation mapping in the northern Norway. The test area is located in the largest valley system, Dividalen, in central Troms, and has a fairly wide variation in ecological niches and comprises both forest vegetation and mountain vegetation. The ground truth programme did include a traditional vegetation mapping programme and a test site programme.

Digital image processing (supervised classification) done on the imagery showed that it was possible to classify the most phenological developed vegetation cover types with an overall accuracy of 90% or more, in spite of the unfortunate fact that the scene were taken too early in the spring season. Visual interpretation on both the spring scene and the autumn scene combined with digital classification done on several band combinations was a good tool to improve the interpretation of each imagery.

The study included a comparison of SPOT-simulated and Landsat-5 TM imagery for vegetation mapping purposes. This investigation has shown that the Landsat-5 TM scene from the spring season almost had the same accuracy by supervised classification as the SPOT simulated imagery from the same season, due to the better radiometric resolution for the TM-sensor compared to the simulated HRV-sensor for the SPOT satellite. Supervised classification done on the SPOT-simulated imagery showed that vegetation cover types within small areas, were better picked out due to the better spatial resolution, compared to the TM sensor on the Landsat-5 satellite. This project was carried out at the Institute for Biology and Geology, University of Tromsø, and Tromsø Telemetry Station (TTS), both institutions situated in Tromsø, Northern Norway. The project was initiated as a study for the Cand. Scient. thesis at the University of Tromsø, Norway.

1. Introduction

In Norway there are very small areas that have been vegetation mapped, and there is in certain areas a very strong need for vegetation cover maps as basis for land use planning. Methods for mapping natural resources have been strongly developed in the last decades, and one of the most used methods is remote sensing. In comparison with personal intensive and conventional methods, remote sensing from satellites give a good ability for mapping and monitoring the natural resources, as a result of the great coverage in area and the ability for repetitive passes. The aim of this study was to evaluate how different vegetation cover types may be identified from Landsat-5 TM data.

2. The Study Area

In this present study I have selected one of the test areas which was included in the SPOT-simulation programme

in Norway 1982. This area called Habafjell-Skrubben (Cavarre in lappish) is situated in the largest valley system in Central Troms, Northern Norway, and comprises parts of the Rostadalen and Dividalen valleys (Figs. 1 and 2). This area has a fairly wide variation in ecological niches and most of the common vegetation cover types in the central part of Troms are represented in this study area. Forests covers about 60% and alpine vegetation 30% of the land area (Elven & Vorren 1980). Spontaneous spruce (*Picea abies*) is absent in the forest of Troms, and the maritime climate limits the distribution of pine (*Pinus Silvestris*). Grey alder (*Alnus incana*) forms large stands in the plant community *Alno Prunetum* up to 350 m a.s.l. in the easternmost parts of Troms Fylke, and up to 100–200 m a.s.l. at the outer coast. Many of the thermo-ophilous plant species in Troms are confined to this plant association (Fremstad & Øvstedal 1978).

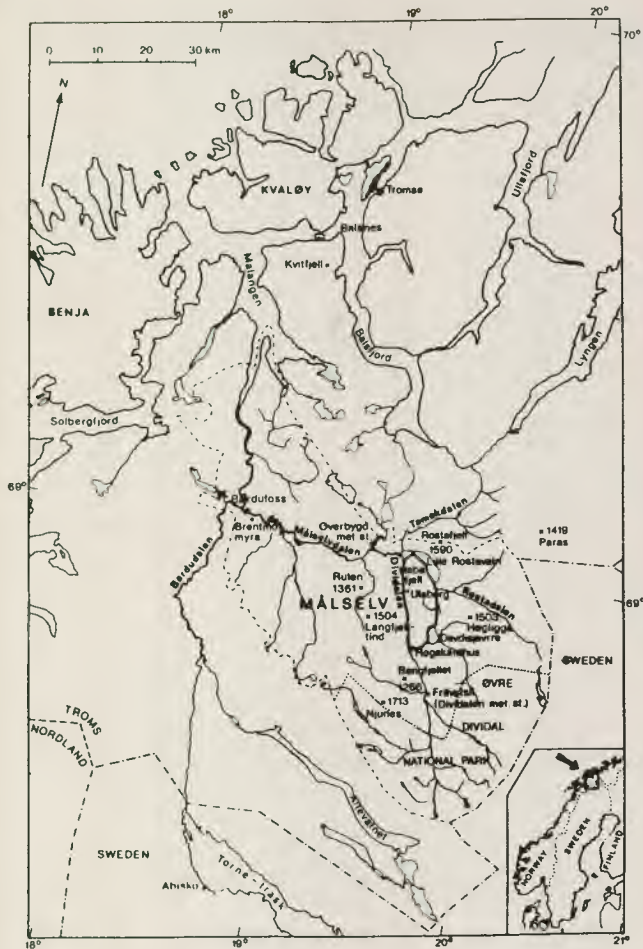


Figure 1. The position of the study area, and the most important geographical names mentioned in the text. (Based on Cap-pelen's map 9-10, 1 : 400 000).

2.1 Ground Truth Programme

The ground truth programme did include:

1. 'Traditional vegetation mapping' of the whole study area based both on IR-aerial and BW-aerial photographs.
2. A special training-site programme.
3. Phytosociological investigation of the several vegetation types within the study area.

2.2 Fieldwork

The fieldwork was carried out during June to September 1983 with some supplementary visits to the area in 1984. A traditional mapping programme based both on IR-photographs and BW-photographs.

2.3 Cluster Analysis

In order to facilitate comparison with the phytosociological classification system of vegetation-types, the phyto-sociological data were subjected to hierarchic, agglomerative classification. The group-average method (GA) (Goodall 1973) was elaborated and the Bray & Curtis index (1957) was subjected to the classification.



Figure 2. Landsat-5 TM image (band combination TM 4, 3, 2) over the study area.

2.4 Data Acquisition

Two Landsat-5 TM scenes were ordered, the first from 3 June 1984 and the second from 2 October 1984.

Image data:

Landsat-5 TM Pass 197/11 1984-06-03 Time: 09.50.00 AM
Sun elevation: 42°

Landsat-5 TM Pass 197/11 1984-10-02 Time: 09.46.00 AM
Sun elevation: 17°

Spot Simulation 1982-06-30 Time: 12.32.42 PM

IR Imagery (aerial photo) 1982-06-30 Time: 12.32.42 PM

BW Imagery (aerial photo) 1975 Summer

2.5 Laboratory Work

Digital and visual classification were carried out at the I2S Image Processing System (Model 575) at Tromsø Telemetry Station (TTS).

2.6 Classification

The procedures followed are illustrated in the flow chart (Fig. 3). A supervised classification method has been elaborated using Max-Log-Likelihood classifier with a threshold of 3.00, 4.00 and 5.00.

In addition to this, several band combinations and ratios were used both for digital and visual classification.

2.7 Accuracy Assessment

There are two major types of accuracy assessment procedures: non-site-specific (total areal extent) and site-specific (location). Non-site-specific accuracy is usually expressed as the similarity between the total numbers of

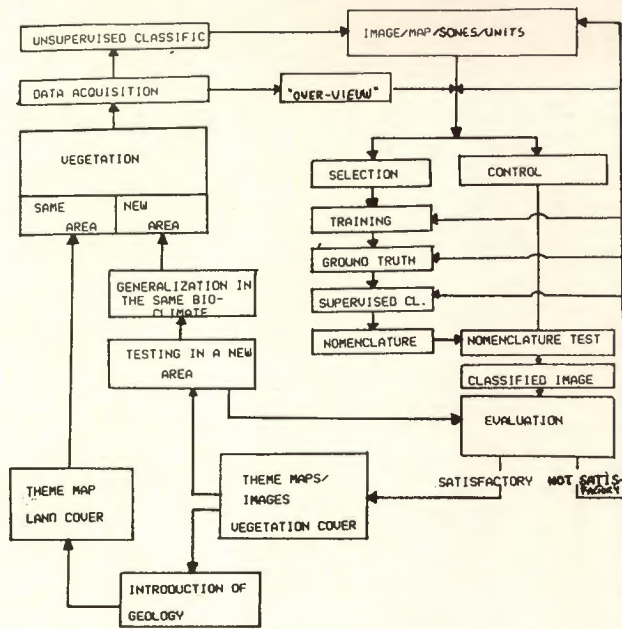


Figure 3. Methodology flow chart for detection of the vegetation cover types.

hectares in each vegetation-cover type as determined by a Landsat or SPOT classification compared to the corresponding total area determined from the digital vegetation map. The non-site-specific method compares only the total area without regard to location. Site-specific accuracy, however, considers the spatial nature of the data when two spatially defined data sets (one ground truth) are registered and compared for the amount of agreement (Reichert & Crown 1984). The chosen method in this study is the non-site-specific method.

3. Results and Discussion

The results of the project are presented and discussed in this chapter. Some of the basic tables and figures in the project are not presented here, but I refer to my thesis-report (Tømmervik 1985a)

3.1 Ground Truth

3.1.1 Floristic

The area is very rich in species, and of the 489 plant taxa at species and sub-species levels encountered in the ground truth programme, 371 were vascular plants, 82 mosses and 36 lichens.

3.1.2 Cluster Analysis of the Phytosociological Data

The phytosociological data consist of 203 releves from 101 localities. The main result of this study that the area is very heterogeneous, and 39 main vegetation-units on several levels in the phytosociological hierarchy were picked out.

3.1.3 Digital Vegetation Map

A digital map has been generated on basis of this ground

truth programme, and the legend consists of 31 vegetational units. The work with the digital vegetation cover map has shown that it is a good tool for resource studies and vegetation mapping purposes, and that it can be updated very easily.

3.2 Digital Image Processing

Digital image processing was done both on 'SPOT-simulated' imagery (82-06-30) and Landsat-5 TM imagery (two quarter-scenes; the first from 84-06-03 and the second from 84-10-02).

Digital classification was based on a supervised method using Max-Log-Likelihood-classifier.

Unfortunately, both the spring-scenes from 1982 and 1984 were taken too early in the spring/summertime due to snowcover, and the autumn-scene was taken too late in the autumn to give a sufficient basis for a good digital classification. The resulting themes left many pixels around vegetation-type boundaries unclassified. Boundary pixels presented a special problem, as they represented portions of different vegetation-type units. Their values were a function of the amount of the area of each vegetation type within the pixel and the relative reflectance of each material as a whole. This was also the result within the resulting themes, and this was a result of the variation in phenology, heterogeneous vegetation and distribution of snowcover.

Figure 4. The spectral signatures of H1 Extremely Dry Shrub, H2 Dry Shrub and H7 Rich Shrub showed a very good separation in the bands 2, 3, 5 and 7.

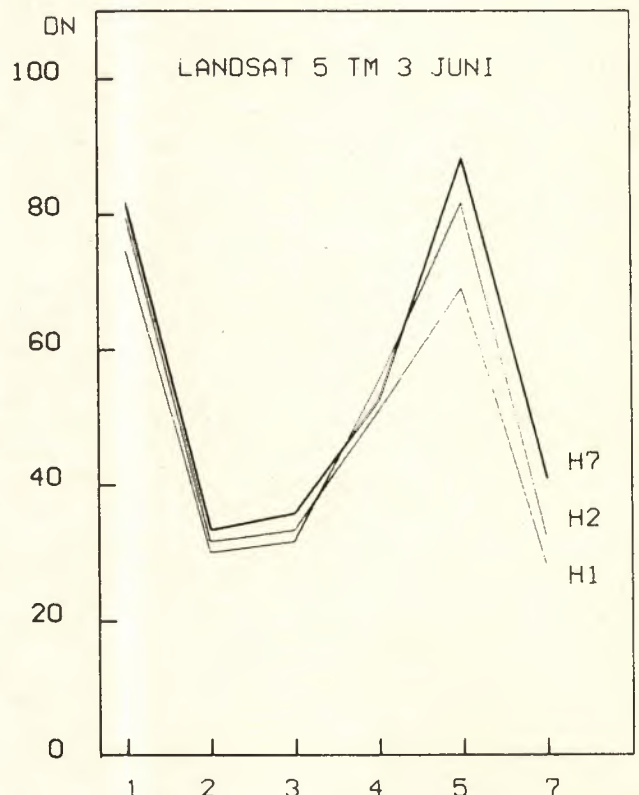


Table 1. Accuracy of the Digital Classification – Dividal - Cavarre

Covertyp	Threshold	Accuracy in percent						Vegetation-map (ha)
		SPOT-simulation			Landsat-5 TM			
		3.0	4.0	5.0	3.0	4.0	5.0	
A4b Birch forests (heath)		7.6 23%	7.8 24%	7.8 24%	7.0 21%	7.6 23%	7.8 23%	31.9
B1 Birch forests (richer heath)		2.1 32%	1.8 28%	1.6 26%	1.6 25%	1.5 23%	1.5 23%	6.4
E5a, c Grey Alder forests (very rich type)		4.8 94%	5.5 84%	5.6 81%	5.2 88%	5.9 78%	5.9 78%	4.6
E5b Grey Alder forests (poorer type)		5.5 29%	5.8 27%	5.6 26%	8.0 20%	8.1 19%	8.1 19%	1.6
G7 Birch forests (meadow type)		1.2 16%	1.2 16%	1.2 16%	11.2 1%	11.6 0.7%	11.9 0.7%	0.2
H1 Extremely dry shrub		24.0 66%	28.0 56%	29.8 53%	9.2 58%	10.1 63%	10.4 66%	15.8
H2 Dry shrub		14.4 52%	16.2 59%	17.6 64%	47.9 57%	51.3 53%	51.9 53%	27.6
H7 Rich shrub		6.2 29%	7.2 25%	7.2 25%	1.6 89%	1.4 78%	1.4 78%	1.8
Å1 / Å2 Farmland		0.6 32%	1.0 50%	1.1 55%	0.4 20%	0.3 15%	0.3 15%	2.0
Unclassified pixels		23.6	13.6	10.6	7.4	1.7	0.3	
Snowcover		9.6	11.5	11.0				

The interpretation and classification were checked by comparing the classified imagery with the digital map, and the accuracy of the interpretation was assessed on a quantitative basis. Two areas within the digital map were checked, Dividal-Cavarre and Saratrøa-Habafjell (Tables 1 and 2).

3.2.1 Alpine vegetation (Tables 1 & 2, and Figure 4)

H1 Extremely dry shrub were well mapped by the two sensor systems (Landsat-5 TM and SPOT) with an optimal accuracy of 89% for the SPOT-simulation (threshold: 3.00) and 93% for Landsat-5 TM (threshold: 5.00). For H7 Rich shrub was the Landsat-5 TM-sensor the best sensor for mapping of this vegetation cover type with a accuracy of 89% (threshold: 3.00). H2 Dry shrub were rather bad detected, 36% for SPOT and 66% for Landsat-5 TM (threshold: 5.00), due to the distribution of snowcover.

3.2.2 Mire vegetation (Tables 1 & 2)

Q5 Rich mire and P2' Wet shrub were bad detected and mapped, due to the high amount of watercontent and the distribution of snow cover at these types of vegetation. But Q4 Poor mire (intermediate) showed a very good ac-

curacy of 83% for the SPOT-simulation (threshold: 3.00) and 97% for the Landsat-5 TM (threshold: 5.00), respectively.

3.2.3 Forests (Tables 1 & 2 and Figure 5)

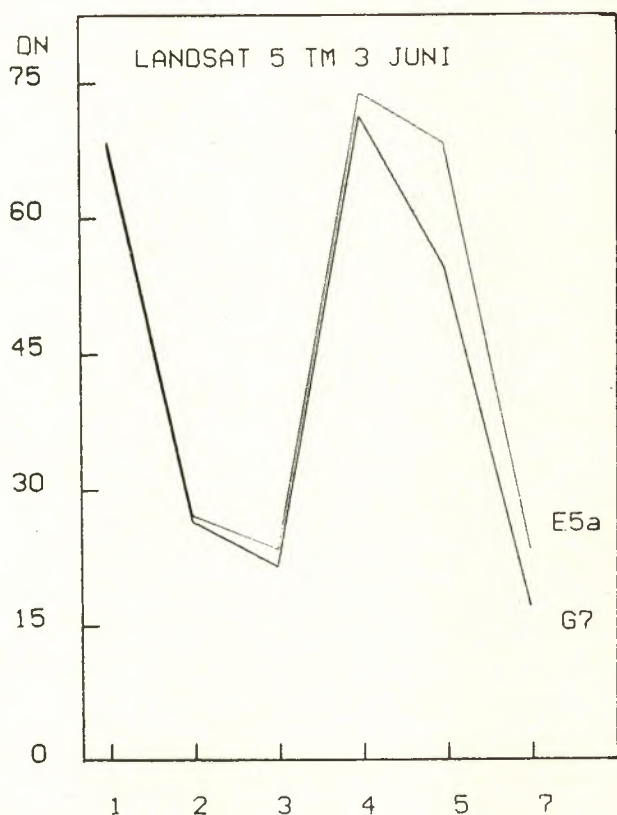
G7' Rich meadow with willow and birch showed a very good accuracy for the SPOT-simulation (accuracy of 91.3%). Concerning G7 Birch forests (meadow type), the accuracy was rather low. The same low percent of accuracy were shown by E5b Grey alder forests (poorer type), B1 Birch forests (richer heath-type) and A4b Birch forests (shrub type) were rather poorly mapped in the area of Dividal-Cavarre by both systems (accuracy up to 24%). In the area of Saratrøa-Habafjell this vegetation cover type was mapped by an accuracy for SPOT of 87% (threshold: 3.00) and 93% for Landsat-5 TM (threshold: 3.00), respectively. E5a and E5c, Grey alder forests were well mapped by both systems, with an accuracy of 94% for SPOT (threshold: 3.00) and 88% for Landsat-5 TM (threshold: 3.00), respectively.

3.2.4 Farmland (Tables 1 & 2)

AA1/AA2 Farmland was poorly detected and mapped by the both sensor systems of SPOT and Landsat-5 TM, due

Table 2. Accuracy of the Digital Classification – Saratrøa - Habafjell

Coverttype	Threshold	Accuracy in percent						Vegetation-map (ha)
		SPOT-simulation			Landsat-5 TM			
		3.0	4.0	5.0	3.0	4.0	5.0	
Va Water (lakes and rivers)		2.4 89%	2.5 92%	2.6 96%	2.5 92%	2.6 96%	2.7 100%	2.7
A4b Birch forests (heath)		27.1 87%	35.0 68%	37.0 64%	25.6 93%	33.0 72%	34.1 69%	23.8
G7' Rich meadow with willow and birch		2.1 91%	2.1 91%	2.1 91%				2.3
H1 Extremely dry shrub		3.5 89%	3.3 76%	3.4 78%	3.0 68%	3.8 86%	4.1 93%	4.4
H2 Dry shrub		8.7 28%	10.0 34%	11.1 36%	11.1 36%	15.3 49%	20.3 66%	30.7
P2 Wet shrub		5.5 62%	6.8 48%	7.5 44%	0.4 12%	0.1 3%	0.1 3%	3.3
Q4 Poor mire (intermediate type)		15.2 83%	16.1 77%	17.3 73%	12.0 94%	11.6 91%	12.4 97%	12.7
Q5 Rich mire		3.2 62%	3.7 54%	4.3 46%	0.7 35%	1.3 65%	1.4 70%	2.0
Unclassified pixels		33.4	16.0	10.8	42.8	30.6	22.5	



to the early phenological stage and the water content in the soil.

3.3 Visual Interpretation and Classification

Visual classification and interpretation was done on the imagery. Ratio methods were elaborated using ratios of the bands 5:3, 4:3, 5:4:3:2 and 4:3:2:1. In addition to this, several band combinations were interpreted in order to detect barely-detectable vegetation cover types by digital classification.

3.3.1 Ratio

Landsat-5 TM 1984-06-03

Ratio 5:3 gave a good delineation of mixed spruce seedling stands (01) from the surrounding deciduous forests. In addition this ratio gave a good delineation between lowland vegetation and alpine vegetation (Tømmervik 1985b.)

Ratio 4:3 gave a good delineation of pine forests (A4a) from other forest types. It shows in addition phenological divergencies in the image, and a good delineation of vegetation on calcarous soil from vegetation on poor soil.

Figure 5. The spectral signatures of E5a Grey Alder Forests and G7 Birch Forests (meadow type) showed good separation in the bands 4, 5 and 7.

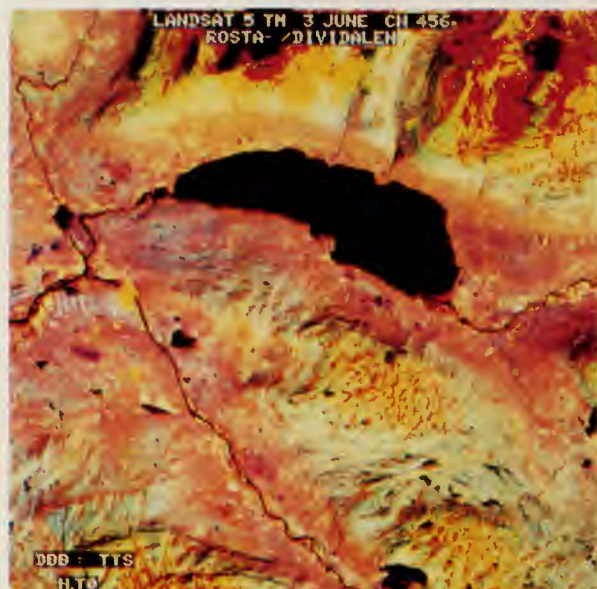


Figure 6. The band combination of TM 4, 5, 6 gave a good result in detection and delineation of mixed spruce seedling stands (see arrow) and pine forests.

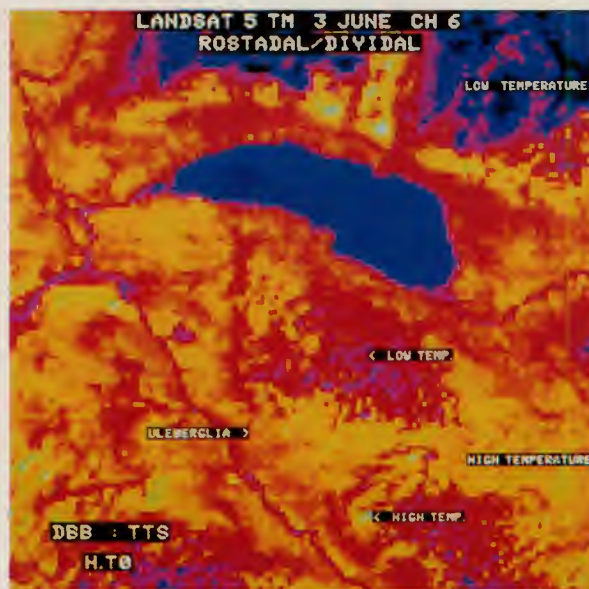


Figure 7. The band TM 6 (thermal band) separated the vegetation cover types (Dry Shrub complex and Pine Forests) from the vegetation cover types with lower temperatures (mires, swamp forests, snow beds). This is also correlated with exposition and phenological stage.

Ratio 4:3:2:1 shows the same relation as the ratio 4:3.

Ratio 5:4:3:2 gave a good delineation of mixed spruces seedling stands from the surrounding deciduous forests.

3.3.2 Band combinations

Landsat-5 TM 1984-06-03

The band combinations of CH 456 (Fig. 6), CH 532 and CH 754 gave a good delineation of the mixed spruce seedling stands from the surrounding deciduous forests, but not as good as the ratio 5:3. These combinations gave a good delineation of G7 Birch-forests of meadow type and E5a/E5c Grey alder forests (rich type) from poorer forest cover types. Pine forests were also well detected.

Band 6: An image of band 6 (thermal band) was generated and this band separated the vegetation cover types with high thermal temperatures (Dry shrub complex and pine forests) from the vegetation cover types with lower temperatures (mires, swamp forests, snow beds). This is correlated with exposition and phenological stage (Fig. 7).

Landsat-5 TM 1984-10-02

Band combinations: The band combinations of CH 432, CH 456 and CH 543 gave a good result in detection and delineation of C5 Swamp forests at the riverbanks and E5a/E5c Grey alder forests at the hillsides, due to the litter.

The band combination of CH 432 was a good basis for interpretation of H7 Rich shrub and snowbeds (K2, K6 and K6').

The band combination of CH 456 gave a good delineation of pine forests (A4a), spruce seedling stands (01), Snowbeds (K2,K6), and Farmland (AA1/AA2).

3.4 General Comments and Discussion

The number of unclassified pixels was rather great, due to the early phenological stage with wide variation within the vegetation cover types and the distribution of snow cover.

The investigation has shown that the Landsat-5 TM scene from the springtime almost had the same accuracy by supervised classification as the SPOT-simulated imagery, due to the better radiometric resolution for the TM-sensor compared to the simulated HRV-sensor on the SPOT-satellite. For some vegetation cover types the Landsat-5 TM sensor was even better than the simulated HRV sensor on the SPOT-satellite, for mapping purposes.

By comparing the classification results with the 'ground truth'-digital map, the main trend was that the vegetation cover types which were most phenologically developed, showed the best accuracy in the supervised classification. This is due to the very early phenological stage and the distribution of snow cover in the mountain areas. But even the classification of the vegetation cover types H1 Extremely dry shrub and Q4 Poor mire (intermediate type) in the mountain area was successful, with an overall classification accuracy of 90% or more. Classification of the SPOT-simulated imagery showed that the vegetation cover types within small areas, were better detected and mapped, due to the better spatial resolution compared to the TM-sensor on the Landsat-5 satellite.

The autumn scene taken by the Landsat-5 TM sensor could not be used as a basis for a supervised digital classification, due to the very low sun elevation and to the very late phenological stage.

Several authors have discussed the possibilities of using SPOT-images and Landsat TM images as a basis for mapping of vegetation.

Teillet *et al.* (1981) compared MSS data with simulated TM data, and stated that the accuracy of classification was improved by using TM data instead of MSS data (MSS: 67% - TM: 83% of accuracy) in classification of forest cover types. This improvement was a result of the better radiometric and spatial resolution for the TM sensor. In addition they found no significant improvement as a result of improvement in spatial resolution alone. This is also my experience.

Jaakkola (1985) stated that forest cover type classification into six classes was successful with an overall classification accuracy of 90% or more. For some of the forest cover types and even other vegetation cover types I got a successful result with an overall classification accuracy of 90% or more. Especially forest cover types that were in an optimal phenological stage (summer) got such a good classification accuracy.

Lannelongue & Saint (1981) investigated simulated SPOT-data, and stated that 'the geometry is not representative of the SPOT- system'. I do hope that real SPOT-data will give us a possibility of improved detection and mapping of forest cover types, but I don't expect the optimal use of the SPOT-satellite system for vegetation mapping purposes before the HRV-sensor get an additional band in the MIR-area of 1.5–1.7 μm . This is also the area where the vegetation cover types with lichen-cover is best detectable and mapped (Ref: M. Byström, Satimage, Kiruna, Sweden 1985).

Hame (1984) has stated that the best results in delineation of mixed spruce seedling stands and other very hardly detectable vegetation cover types, were obtained using parallelepiped classifications with the first two principal components calculated of Landsat MSS-imagery. Jaakkola (1985) has done a similar study on SPOT-simulated imagery and stated that the best results of the classifications of the imagery were obtained by using multipoint (contextual) classification techniques. I have shown by simple ratio methods and band combinations elaborated on TM-imagery, that we can delineate very heterogeneous forest- and vegetation cover types easily.

4. Conclusions

Second-generation satellites such as Landsat-5 TM and SPOT HRV, providing high spatial resolution between

10 m and 30 m and in the case of TM, new spectral bands, will increase the level and accuracy of digital classification. This study has shown that it was possible to classify the vegetation cover types which were furthest developed, what phenology concern, with an overall accuracy of 90% or more, in spite of the unfortunate fact that the scenes were taken too early in the spring season.

In addition to this the digital classification even went good in an area with a fairly wide variation in ecological niches and a heterogeneous vegetation.

Visual interpretation and classification based on ratio-techniques and band combinations was a very good tool to improve the interpretation of imagery. The best results in this case were obtained by the TM-sensor on the Landsat-5 satellite.

The middle infrared (MIR) bands of TM were useful for vegetation classification especially for delineation of heterogeneous forest cover types.

Comparison between the Landsat TM-sensor and the simulated SPOT-HRV-sensor has shown that the two-sensor systems have almost the same ability to detect and map vegetation cover types within this area, due to the higher radiometric resolution for the TM-sensor compared to the simulated HRV-sensor. Classification of the SPOT-simulated imagery showed that vegetation units within small areas, texture and patterns were better detected, due to the higher spatial resolution for the HRV sensor compared to the TM sensor.

I expect, on the basis of this study, that the second-generation satellites and multilayer classification systems will improve the capability of satellite data to serve as a first stage in multistage land use and vegetation inventory and monitoring systems.

Acknowledgement

This present study started as a study for the Cand. Scient. thesis at the Institute for Biology and Geology at the University of Troms, Northern Norway. I wish to thank my advisors Amanuensis Dag Olav Øvstedal and Professor Karl Dag Vorren for their support during initial phases of this study. Furthermore, thanks are due to my advisor in Digital Image Processing Victor Nilsen at Troms Telemetry Station (TTS). Finally, I will give my thanks to all other people, including NPOC Rolf T. Enoksen at TTS, who have supported the work in some way.

5. Literature

- Elven & Vorren. 1980. Flora and phytogeography of the Habafjell-Skrubben area of central Troms, Northern Norway. *Tromsura, Naturv.* 9: 1-64. Tromsø.
- Fremstad E. & D.O. Øvstedal. 1978 The phytosociology and ecology of grey alder (*Alnus incana*) forests in Central Troms. *Astarte* 11: 93-112.
- Goodall D.W. 1973. Sample similarity and species correlation. Pp. 105-156 in: R.H. Wittacker (ed.). *Ordination and classification of plant communities*. Dr. W. Junk. den Haag. 737 pp.
- Hame T. 1984. Interpretation of deciduous trees and shrubs in conifer seedling stands from Landsat imagery. Technical Research Center of Finland. Laboratory of Landuse. Helsinki, Finland. *XV Congress of the ISPRS*, Commission VII, 84-91.
- Jaakkola S. 1985. Possibilities for using satellite imagery (including SPOT) in forest inventory and management. *Seminar on the practical application of remote sensing in forestry*. ECE - FAO - UN. 28-31 May 1985. Jönköping, Sweden.
- Lannelongue N. & G. Saint. 1981. Radiometric approach. Sheet F2, Technical Appendix. SPOT Imagery Simulation. Dep. des Public. Paris.
- Reichert G.C. & P.H. Crown 1984. Identification of Winter Wheat Using Landsat MSS Data. *Can. J. Remote Sens.* 10 (2): 111-120.
- Teillet P.M., B. Quindon & D.G. Goodenough. 1981. Forest classification using simulated Landsat-D Thematic Mapper data. - *Can. J. Remote Sens.* 7(1): 51-60.
- Tømmervik H.T. 1985a. Bruk av fjernanalyse i vegetasjonskartlegging anvendt på et område i Indre Troms, Nord-Norge. *Cand. Scient. thesis*. University of Tromsø, Norway. 234 pp.
- Tømmervik H.T. 1985b. Use of Landsat-5 TM Imagery in Detection of Mixed Spruce Seedling Stands in the Dividalen Area of Central Troms, Northern Norway. - *Seminar on the Practical Application of Remote Sensing in Forestry*. ECE - FAO - UN. 28-31 May 1985. Jönköping, Sweden. 5 pp.
- Tømmervik H.T. 1986. Comparison of SPOT-simulated and Landsat-5 TM imagery in vegetation mapping. International Society for Photogrammetry and Remote Sensing, Com. VII, 'International Symposium on Remote Sensing Resources Development and Environmental Management', 25.-29. August 1986, Enschede, The Netherlands.

Multitemporal Analysis of TM Images: Application to Forest Fire Mapping and Inventory in a Mediterranean Environment

Emilio Chuvieco

Department of Geography, University of Alcalá de Henares, Madrid

The aim of this project is to study the performance of multitemporal analysis of TM images for forest fire mapping and inventory. A test area on the mediterranean coast of Spain is employed in the present report.

This area was disturbed by a big conflagration in August, 1985. Two TM images (before and after the fire) were selected for multitemporal comparison. To avoid modifying the original data, the classification was performed independently on both images, prior to registration.

Cluster analysis was employed to group supervised and unsupervised training statistics, while discriminant analysis tested the strength of the grouping process. Then, the resulting cluster statistics were input to the classification algorithm, yielding 4% and 13% better overall accuracy than supervised and unsupervised approaches, respectively. Normalisation and Kappa statistics were used to assess the accuracy of the final classification.

The same process was applied to the image before and after the fire. Registration of both maps allowed a detailed overlaying necessary for the change detection study.

Masking of the burned surface was useful for a more detailed study of those zones, as well as to facilitate their inventory. Statistics about the disturbed area as a whole and by previous species coverage were also generated.

1. Introduction

The objective of this project was to evaluate the performance of multitemporal analysis of TM images for vegetation assessment. An application to forest fire mapping and inventory was chosen because it represented one of the most important environmental disasters in Spain.

2. Multitemporal Remote Sensing

Multitemporal land satellite data represents one of the most fruitful informational sources available from spaceborne sensors. Thanks to the design of Landsat, it is possible to acquire periodic images on the same area with similar conditions of observation (sensor, time, scale, angle, etc. . . .)

These characteristics explain the great amount of work performed using multitemporal Landsat images. Generally this work can be divided in two broad categories: using the temporal dimension to improve the discrimination of vegetation or agricultural categories

(seasonal approach), and employing it to detect landscape dynamism (change detection approach). In spite of its convenience, the multitemporal approach to Landsat classification raises several problems. It requires high accuracy in the registration of the images, which is a difficult task especially when there are not clear landmarks in the scene for the selection of control points. If we assume that further analysis usually involves a pixel per pixel comparison, this possible misalignment may negate the improvements expected by the temporal dimension (Gordon, 1980; Nelson & Grebowsky, 1982).

Therefore the error accepted in the registration process should not be greater than 0.5–0.7 pixels. Otherwise we would have a high probability to deduce inadequate conclusions. This effect would increase according to the number of images simultaneously processed.

Another important problem regards to the differences introduced by atmospheric and environmental characteristics of the several images processed. Various

solar altitudes, atmospheric scattering, or soil moisture conditions affect the spectral response of a particular land cover type causing frequent errors in the multitemporal classifier. This problem can be solved in different ways in relation to the purpose of a particular study.

In the case of multiseasonal analysis we should isolate the changes in the spectral radiance due only to different growing conditions. Those originated by other variables (soil moisture, scattering, solar altitude, calibration of the sensors, etc.) must be extracted prior to other analyses. Respecting the change detection approach, all the alterations in the scene are assumed to be dependent on land cover changes. Then, to minimise the effect of the seasonal growth, images of the same period of the year are selected. In any case, the homogenisation of radiance levels due to extraneous factors is required to detect the areas of real changes from those surfaces.

In both cases the radiance adjustment is usually undertaken by the identification of sample areas which are assumed to be constant between the images analysed (roads, airports). The differences in the mean spectral radiance of these areas with respect to the referenced image are used for the spectral standardisation (Bronsveld & Luderus, 1982; Lo *et al.*, 1986).

The third factor to consider in multitemporal classification is the increased volume of data to process. Additional data increases the time and cost required for the project. For this reason several feature selection and compression techniques have been developed (Lo *et al.*, 1986; Jensen, 1986).

These methods are aimed at reducing the number of bands to classify without a significant loss of the original information. Ratios, principal component and discriminant analysis are the most widespread techniques used for that purpose (Byrne *et al.*, 1980; Hall *et al.*, 1984).

Once these difficulties have been solved, the final step involves the combined analysis of the images considered in the study. The techniques for image comparison are numerous and varied. These range from simple image subtracting and image ratioing techniques (Schowengerdt, 1983; Renz, 1985), to post-classified map analysis and complex transformations such as Tasseled Cap, canonical and principal component analysis or temporal profiles fitting (Townshend, 1981; Jensen, 1983; Jensen, 1986; Lo *et al.*, 1986). On the other hand, studies based on visual analysis are also greatly improved with the aid of multitemporal information (Chuvieco, 1987).

3. Remote Sensing as a Technique in Forest Fire Research

The periodic and systematic observation carried out by Landsat satellites has been shown to be especially effec-

tive for monitoring environmental disasters. Floods, volcano eruptions or intense droughts can be well analyzed on these images. Also in studies of this type, the multitemporal approach represents a crucial source of information, because it is possible to follow the dynamics of the event, to detect its consequences, and to prevent its repetition.

The multitemporal capacities of space-borne sensors have been broadly used in forest fire research. Most of the studies have been performed from MSS images. They can be classified according to their orientation in two broad groups:

- a) Mapping of burned areas, with an assessment of the ecological responses of the original species to the fire. The multitemporal dimension is employed either to inventory the species burned (Isaacson *et al.*, 1982; Arbiol *et al.*, 1987) or to study the revegetation stages of the scorched area (Hitchcock & Hoffer, 1974; Hall *et al.*, 1980).
- b) Fire fuel models. In this approach, Landsat images have been used for mapping natural vegetation which is classified according to some fire danger rating system. Typically, the images are combined with other variables, like topography, soils or fire history. Digital elevation data has been used to improve the classification results (Rabii, 1979; Shasby *et al.*, 1981) as well as to create risk models (Yool *et al.*, 1981; Cosentino *et al.*, 1981). In those models, additional information is also employed, like weather data, soil maps, insolation and so on (Burgan *et al.*, 1984; Gum, 1985; Agee & Pickford, 1985).

4. Method and Results

4.1. Geographical Characteristics of the Test Area

It is generally accepted that the mediterranean climate presents one of the best situations for natural forest fire (Folch, 1976; Calabri, 1984). The summer drought causes the presence of a xerophilic vegetation, adapted to that lack of humidity by reducing the water lost through evapotranspiration.

These species have small and resistant leaves and usually high resin or essential oil content. For this reason these species have a high rate of flammability (evergreen oaks, Aleppo pine, Maritime pine and Black pine).

On other hand, the thermal differences between sea and land are extreme during the summer period, causing strong coastal winds which both increase the evapotranspiration and aid the spread of the fire once it starts.

Another main factor affecting forest fires, topography, is also clearly present in the mediterranean region. The Alpine deformations during the Tertiary Age affected the



Figure 1. Location map

southern part of Europe. Hence, it is more likely to find in these areas rough terrain with steep slopes, even in areas very close to the coast.

Given these reasons, we decided to select a test area in the Spanish mediterranean region. The coast of Castellón, traditionally affected by forest fires was selected, in order to take advantage of the experience gained in previous studies (Sancho and Chuvieco, 1986).

Our specific area corresponds to sheets #616 and #617 of the National Topographic Map (scale 1:50 000) centered upon the towns of Villafams and Oropesa del Mar (Fig. 1). The zone exhibits the typical characteristics of a coastal mediterranean climate, with cool winters and warm summers. The annual rainfall ranges from 400 to 800 mm, mainly concentrated during fall and spring, with a very dry summer. The annual water budget exhibits a mean deficit of 250 mm.

The topography of the area is complex with a continuous succession of different slopes, which are especially steep in the interior 'sierras'. Only in the vicinity of the shoreline has a littoral plain been developed, which is used for agricultural production, mainly citrus trees and orchards. There are also some agricultural zones in the interior uplands where the almond trees and vineyards are located. Forest lands cover the higher areas (Sierra del Desierto de las Palmas, Montes de Villafamés). Aleppo pine (*Pinus Halepensis*) and Maritime pine (*Pinus Pinaster*) are the principal species. Scrub covers many transitional areas, for example the southern face of Sierra de las Palmas, Montes de Cabanes and Sierra de Oropesa. The species are typical of the mediterranean environment with a big proportion of igneous components (*Genista Scorpius*, *Rosmarinus Officinalis* and *Quercus Coccifera*).

The agricultural, as well as the natural land cover, shows

an extreme fragmentation in the area analysed. The traditional cultural practices in this zone have lead to a very complex parcel structure. Many of the agricultural properties, especially the irrigated crops, are less than 1 ha in size. This complexity complicates the classification task by introducing in many pixels a mixed signature as a result of the boundary effect. In the forest land the problem is not less important, although in this case it is caused by a frequent mixture between forest and scrub with various densities and stand heights.

4.2. Analysis of the data

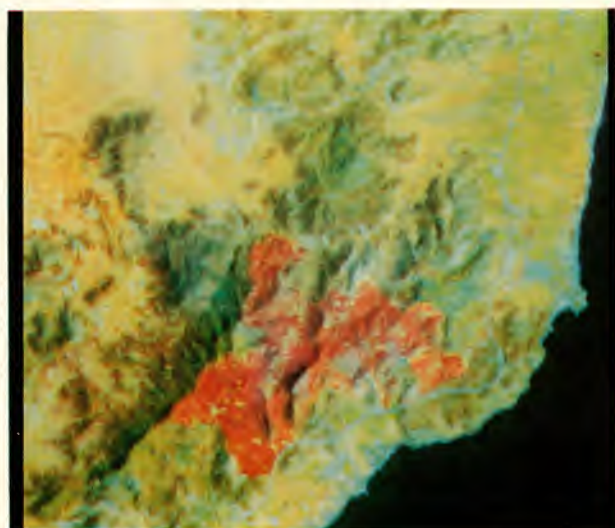
This complex landscape was disturbed by an important forest fire in the first days of August, 1985. That event is used in this study to demonstrate the use of multitemporal analysis of Landsat data.

The images selected for analysis were 26 June 1984 (before the fire) and 7 August 1985 (shortly after the fire). As soon as we received the image data set we performed an initial analysis to explore their spectral characteristics. The 26 June scene showed a slight striping, especially visible in the Mediterranean Sea. The scene corresponding to August offered high scattering due to the presence of smoke in areas affected in that particular moment by the fire. Fortunately this effect is only serious in the shorter bands, especially in band 1, more sensitive to this kind of dispersion. For future studies in the same subject, it is recommended to select a date distant enough from the start of the fire not to be directly affected by the smoke.

The 6/4/2 colour composite seemed to be one of the most suitable to monitor the area disturbed by the fire (Fig. 2). The true colour composite 3/2/1 facilitates the location of smoke sources.

These visual displays were used to isolate the area affected by the fire on the August image. This masking pro-

Figure 2. 6/4/2 Colour Composite



cess allowed the performance of a more detailed study on the affected zone. Using the GIS capacities of the software employed in this study, the scorched surface was digitised and that polygon employed to mask the original image. Then, histograms of that area were obtained for the seven original bands.

As several authors have noted (Castelman, 1978; Jensen, 1986), the analysis of the histogram is a very convenient way to deduce the spectral characteristics of a specific target. Not much effort has been devoted to the spectral definition of an area destroyed by a forest fire, perhaps due to the fact that most of the studies analyse the affected surfaces without making further distinctions in the burned area. Partial information has been reported on the spectral regions covered by MSS bands (Tanaka *et al.*, 1983).

All the visible bands show a reduction in the reflectance values with respect to the non disturbed vegetation. The lack of pigments (especially chlorophyll a and b) can be the cause of that decreasing. Band 1, shows even higher values, as a consequence of the scattering produced by the smoke.

Near infrared (band 4) is a region especially sensitive to chlorophyll function. As a consequence of the fire, the scorched areas shows severe reduction of reflectance in this band, while there is an increasing in the blue and red region (Murtha, 1978). The histogram is centered on 36 (digital value) with some overlaps with water among the lower half of the histogram.

The middle and thermal infrared are especially significant for forest fire mapping because they are able to sense the thermal characteristic of the scorched surfaces. Wien's displacement law determines the wavelength at which the maximum amount of energy is radiated for a particular temperature ($\lambda = 2897 \mu\text{m K}/T \text{ rad K}$). If we assume the flame combustion temperature to be in the range between 275°C and 420°C (Artsybashev, 1983; Calabri, 1984), we can specify the wavelength of maximum spectral radiance to be between 5.28 μm and 4.30 μm . Unfortunately, there is no TM band in that particular window. Band 7 (2.08–2.35 μm) and band 5 (1.55–1.75 μm) provide the best approach for detection of burning surfaces. Actually it is possible in band 7, for instance, to monitor the areas active in the particular time of acquisition of the image. As said before, band 1 provides complementary information about the surfaces affected by smoke.

Although some of the areas were burned even a week before the acquisition of the image, band 6 still shows a clear thermal anomaly on this zone. The mean for the whole image is 151 in this band, while the average of the burned surface is 162. Unfortunately there are some other categories with high radiant temperature (wine-

almond trees), so it is not possible to isolate clearly the burned surfaces by a simple density slicing of this band. In any case, it is extremely helpful for making further divisions on them.

4.3. Multitemporal Techniques

As we discussed previously, the change detection studies start from a multitemporal set of Landsat images corresponding to a date before and after the target phenomenon. Most of the projects employ images acquired in the same season to reduce the atmospheric and environmental variations between the scenes. The images used in this study were acquired on 26 June and 7 August, close enough in time to expect homogeneity, although they correspond to different years.

Typically, most of the change detection studies perform a equalisation of radiances between the scenes was involved in the analysis. This task is done after the registration of the images to a common grid (usually U.T.M.) or to one of the images which is used as reference. In both cases, a large amount of computer time is required to resample the images to obtain a high accuracy in the registration. Otherwise, the further analysis made in a pixel per pixel basis will contain an unexpected rate of error. Even more important than this problem, however is the fact that the resampling process, assumed to be correct, always involves a change in the original information. In the case of bilinear or cubic interpolation, an averaging effect is introduced in the original data by relating the radiance value of each pixel with the neighbors. Although this effect has not been properly evaluated (Smith and Kovalick, 1985), it seems more advisable to postpone the registration for the classified image. Therefore, the change detection algorithms employed are based in the comparison of the maps produced on different dates, and as a result, the previous homologation between scenes becomes unnecessary.

This was the strategy we followed. The analysis was performed individually on the two images, and after that classification results were compared. The processing of both dates was based on a mixed supervised and unsupervised technique. Two unsupervised analyses were performed on both images modifying the control parameters (distance and number of elements to sample). This stage yielded finally two sets of training classes for each image which are supposed to be a good representation of the natural spectral variability in the scenes. Supervised training categories were also selected, as a way to introduce a definition of the informational categories.

After the training phase was completed, a cluster analysis was employed to combine the supervised and unsupervised training statistics generated from the same image. The aim was to combine the information given by the two approaches. Hierarchical clustering using complete linkage and standardised variables, yielded the best results of our

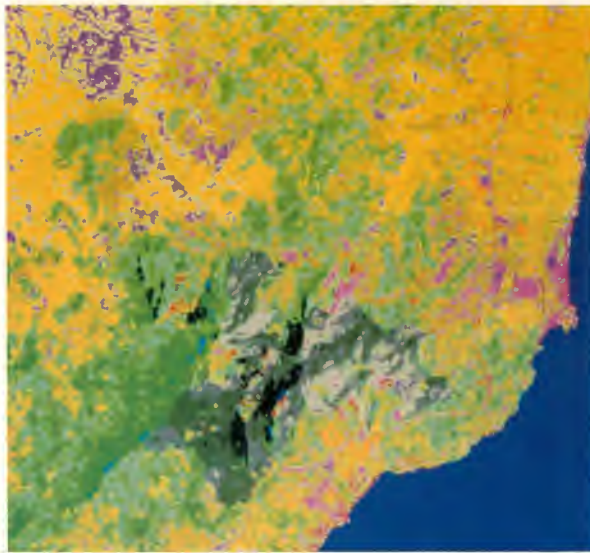


Figure 3. Classification map (August Image)

trials. To improve the definition of some of these categories, discriminant analysis was also employed, allowing a test of the strength and stability of the grouping.

After all the training groups were included in any cluster the mean values of each group were used as input to the classification (Fig. 3). Several accuracy assessment procedures confirmed the interest of this method. The overall accuracy of the image before the fire was evaluated at 60.5% using a post-clustering approach while standard supervised training yielded 57.5% and unsupervised training gave 48.12%. Normalisation of the matrices (Congalton *et al.*, 1983) emphasizes these differences: 63.62%, 60.36% and 48.34% respectively. Application of the KHAT statistic to the same image confirmed these differences, although they did not satisfy the significance threshold.

Once both classified maps were obtained, a polynomial registration procedure was used to overlay them in order to perform a change detection analysis. Seventeen points were selected to compute the coefficients of the regression model and a nearest neighbor algorithm was used to accomplish the resampling process.

Then, the polygon previously used to isolate the burned area was applied for masking the image obtained before the fire. This provided a new image with the land cover previous to the conflagration (Fig. 4). Statistics on the area disturbed by the fire were easily obtained as well (Table I). In summary the whole process required the classification of two images (before and after the fire), overlaying them, extraction of all the polygons that define the area affected by the fire, and masking the classified images from before the fire using those polygons. This methodology might be used in larger surveys improving the evaluation, and leading to the prevention of these catastrophic events.

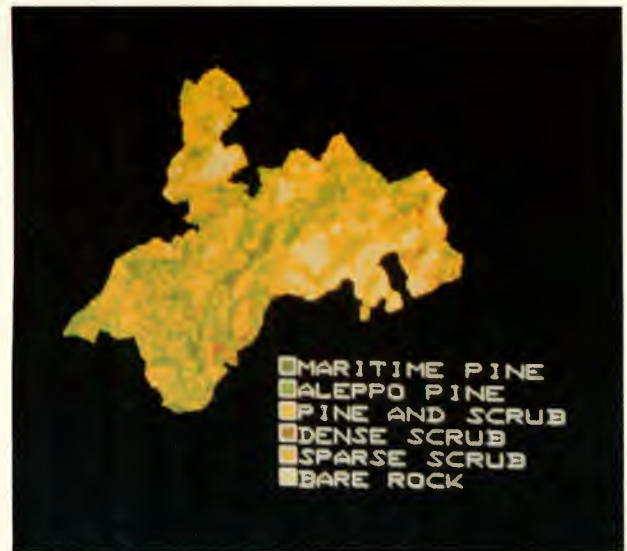


Figure 4. Cover Species disturbed by the fire

Category	Has	%
1. Maritime pine	399.15	19.15
2. Aleppo pine	400.41	19.21
3. Pine and Scrub	608.13	29.18
4. Dense scrub	218.79	10.50
5. Sparse scrub	207.27	9.94
6. Bare rock	250.65	12.02
Total	2084.04	100.00

Table I. Evaluation of the area burned by land cover types

The whole area affected by the fire was estimated to be 2084.04 ha. Considering that in Spain the average area burned in each forest fire is 51 ha. (Velez, 1982), this conflagration can be considered as a large forest fire in our country.

The two categories of pine (aleppo and maritime) are affected in similar terms by the fire. Both sum up 40% of the burned area. Scrub of different densities occupied the rest of the disturbed zone.

A small amount of residential area also affected is not shown in the table as a consequence of its dense forest cover. Bare rock category should be referred to very sparse scrub on limestone, occupying the southern slopes of Sierra del Desierto de las Palmas.

4.4. Summary and recommendations

During our work we have applied multitemporal analysis of Landsat images to the detection of forest fire damage, as an example of the possibilities of this method to monitor the dynamism of the environment. Special emphasis has been put on the selection of training statistics for the classification, showing the convenience of employing multivariate statistical techniques in this phase. Regarding the detection of forest fires, the

multitemporal approach was basic for mapping and inventory of the area burned, as well as to quantifying the area of different land cover types affected by the fire.

The next step will be to complete our model of evaluation by introducing auxiliary variables such as topographic or climatological descriptors. This information will be combined to obtain a model of risk associated with specific parameters (vegetation, humidity, slope, etc.) mapped mainly from satellite data and using the new techniques of Geographic Information System processing for their combined analysis. A great amount of the work already analysed in this report tries to organise conveniently the information for a model of fire risk.

4.5. Acknowledgements

Most of this work has been performed in the Department of Forestry and Resource Management and the Space Science Laboratory of the University of California at Berkeley. The author is very grateful to the authorities for the facilities used during the last months. Prof. Congalton and Cathy Travlos made a significant contribution to the results reported here. Randall Thomas had a great deal of patience in the reviewing of this manuscript.

The TM data were provided by Earthnet through the Spanish NPOC – INTA.

5. Bibliography

- Agee, J.K. and Pickford, S.G. (1985): *Vegetation and fuel mapping of North Cascades National Park Service Complex, Final Report*, NPS Cooperative Park Studies Unit, Seattle, College of Forest Resources.
- Arbiol, R. *et al*, (1987): 'Detecció i evaluació de las superfícies forestals cremades durant l'any 1984 a Catalunya, mitjançant tècniques de Teledetecció', *Revista Catalana de Geografia*, vol. 2(4), pp. 21-46.
- Artsybashev, E.S. (1983): *Forest fires and their control*, New Delhi, Oxonian (1st. Edition in Russian, 1974).
- Bronsveld, M.C. y Luderus, F.J.D. (1982): *Analysis of multi-temporal data for the identification of land use and crops (Case Study on the Merida Region in the province of Badajoz, SW Spain)*, Madrid, ITC-IBM Scientific Center.
- Burgan, R.E. *et al* (1984): 'Mapping broad-area fire potential from digital fuel, terrain and weather data', *Journal of Forestry*, vol. 82 (4), pp. 228-31.
- Byrne, G.F. *et al* (1980): 'Monitoring land-cover change by principal component analysis of multitemporal Landsat data', *Remote Sensing of Environment*, vol. 10 (3), pp. 175-84.
- Calabri, G. (1984): *La Prevenzione degli Incendi Boschivi. I problemi e le tecniche della difesa*, Bologna, Edagricole.
- Castelman, K.E. (1978): 'The gray level histogram', chapter 5 in *Digital Image Processing*, Englewood Cliffs, Prentice-Hall, pp. 68-84.
- Chuvieco, E. (1987): 'An essay of land cover map from visual analysis of multitemporal TM images', *Proc. American Society of Photogrammetry and Remote Sensing, Annual Convention*, Baltimore, vol. 2, pp. 113-21.
- Congalton, R.G. *et al* (1983): 'Assessing Landsat Classification Accuracy Using Discrete Multivariate Analysis Statistical Techniques', *Photogrammetric Engineering and Remote Sensing*, vol. 49 (12), pp. 1671-78.
- Cosentino, M.J. *et al* (1981): 'Scene analysis for Wildland Fire-Fuel Characteristics in a mediterranean climate', *Proc. 15th Int. Symp. on Remote Sensing of Environment*, Ann Arbor, pp. 635-646.
- Folch, R. (1976): 'El incendio forestal, fenomeno biológico', *Cuadernos de Ecología Aplicada*, vol. 1, pp. 7-32.
- Gordon, S.I. (1980): 'Utilizing Landsat imagery to monitor land use change: a case study in Ohio', *Remote Sensing of Environment*, vol. 9 (3), pp. 189-96.
- Gum, P.W. (1985): 'Computerization of fire dispatch utilizing satellite imagery Okanogan Project', *Pecora X Symposium*, Fort Collins, pp. 315-325.
- Hall, D.K. *et al* (1980): 'Landsat digital analysis of the initial recovery of burned tundra at Kokolik river, Alaska', *Remote Sensing of Environment*, vol. 10, pp. 263-72.
- Hall, R.J. *et al* (1984): 'Change detection methodology for aspen defoliation with Landsat MSS digital data', *Canadian Journal of Remote Sensing*, vol. 10 (2), pp. 135-42.
- Hitchcock, H.C. and Hoffer, R.M. (1974): *Mapping a recent forest fire with ERTS-1 MSS Data*, West Lafayette, LARS Information Note 032674.
- Isaacson, D.L. *et al* (1982): 'Erosion hazard reduction in a wildfire damaged area', in Johansen and Sanders (eds): *Remote Sensing for Resource Management*, Ankeny, Soil Conservation Society of America, pp. 179-90.
- Jensen, J.R. (Ed): 'Urban/Suburban land use analysis', in Colwell (ed): *Manual of Remote Sensing*, 2nd Edition, Falls Church, American Society of Photogrammetry, pp. 1571-1666.
- Jensen, J.R. (1986): *Introductory Digital Image Processing. A Remote Sensing Perspective*, Englewood Cliffs, Prentice-Hall.
- Lo, T.H.C. *et al* (1986): 'Use of multitemporal spectral profiles in agricultural land-cover classification', *Photogrammetric Engineering and Remote Sensing*, Vol. 52 (4), pp. 535-44.
- Murtha, P.A. (1978): 'Remote sensing and vegetation damage: a theory for detection and assessment', *Photogrammetric Engineering and Remote Sensing*, vol. 44, pp. 1147-58.
- Nelson, R. and Grebowsky, G. (1982): 'Evaluation of temporal registration of Landsat scenes', *International Journal of Remote Sensing*, vol. 3 (1), pp. 45-50.

- Rabii, H.A. (1979): *An Investigation of the utility of Landsat-2 MSS data to the fire-danger rating area, and forest fuel analysis within Crater Lake National Park*, Oregon, Ph.D. dissertation, Oregon State University.
- Renz, A.N. (1985): 'Multitemporal analysis of Landsat imagery for monitoring forest cutovers in Nova Scotia', *Canadian Journal of Remote Sensing*, vol. 11 (2), pp. 189-94.
- Sancho, J. and Chuvieco, E. (1986): *Castellón desde el espacio*, Castellón, Caja de Ahorros de Castellón de la Plana.
- Schowengerdt, R.A. (1983): *Techniques for Image Processing and Classification in Remote Sensing*, New York, Academic Press.
- Shasby, M.B. *et al* (1981): 'Broad area forest fuels and topography mapping using digital Landsat and terrain data', *Proc. Seventh Int. Symposium on Machine Processing of Remotely Sensed Data*, Purdue University, pp. 529-37.
- Smith, J.L. and Kovalik, B. (1985): 'A comparison of the effects of resampling before and after classification on the accuracy of a Landsat derived cover type map', *Advanced Technology for Monitoring and Processing Global Environmental Data*, London, pp. 391-99.
- Tanaka, S.; Kimura, H. and Suga, Y. (1983): 'Preparation of a 1:25 000 Landsat map for assessment of burnt area on Etajima Island', *International Journal of Remote Sensing*, vol. 4(1), pp. 17-31.
- Townshend, J.R.G. (Ed.) (1981): *Terrain Analysis and Remote Sensing*, London, George Allen and Unwin Ltd.
- Velez, R. (1982): 'Forest Fires in the Mediterranean Region', in Van Nao (Ed): *Forest Fire Prevention and Control*, New York, Martinus Nijhoff/DrW.Junk Publs.
- Yool, S.R. *et al* (1984): 'A Geographic Information System approach to quantitative assessment of wildlife fuels', *ASP-ACSM Convention. Technical Papers*, Washington, D.C., vol. 2, pp. 792-801.

Large-Scale Forest Management Using Landsat Thematic Mapper Data

R. Caloz

Physician

Institute of Rural Engineering, Lausanne, Switzerland

T. Blaser

Rural Engineer

Swiss Federal Institute of Technology of Lausanne, Switzerland

Abstract

A lot of information is required from public services for good forest management. Which of this information can be drawn out in an operational way by a TM-Landsat images? By studying two typical small forests of the Swiss 'Plateau', we show that it is possible at a municipal scale to give:

- 1. Physical limits actualisation of the forestal area at a scale of 1:25 000.*
- 2. The inventory and spatial distribution of the species.*

Résumé

La gestion des forêts requiert de la part des services publics de nombreuses informations. Quelles sont celles qui peuvent aujourd'hui être extraites, de manière opérationnelle, d'une image TM-Landsat? Par l'étude de deux forêts de taille relativement faible, représentatives de celles que l'on rencontre fréquemment sur le Plateau suisse, on montre qu'il est possible aujourd'hui de fournir, à l'échelle communale:

- 1. la mise à jour des contours de la forêt pour la carte 1:25 000;*
- 2. l'inventaire des peuplements avec leurs répartitions spatiales.*

Introduction

Contrary to the alpine regions, the forests of the Swiss 'Plateau' are relatively small in extension, i.e. a few hundreds to a few thousands of hectares. Situated in areas of agricultural and farming activities, they form large islands of forests protecting the soil. They are submitted to rigorous observation and permanent maintainance by public services. In general these forests are exploited. Their management belongs to the municipal authority. Today forest inventories are presented statistically, after analysing adjacent areas of one hectare each, called 'placette'. All of this information is updated within the same time period as the National topographic maps.

Such a procedure may be satisfactory at the cantonal or federal scale, but is not for management purposes inside the municipal administration unity. More rigorous observation of forest contours and more detailed information about geographical distribution and surface statistics for

the different kinds of forest populations are needed at that scale. To what extent may this information be extracted from a Landsat thematic mapper scene? This study, which takes into account a large number of theoretical works already published in the international scientific press, deals with this question.

A traditional approach has been chosen. Firstly, an inventory of the information collected today by forest services is presented. Then, we analyse them under the spectral aspect with the objective of determining those which are likely to be detected in the image through their spectral manifestation. The following step directly concerns the application: after a short presentation of the test sites, the sequences used for image processing are analysed.

Data Collecting and Actual Management

Forest services today principally use two methods for data collecting. The first one is of statistical nature. It consists in inventorying the characteristics of a 'placette' in the field (forest cell of 30 m diameter). For each cell, the state of five categories of parameters is periodically examined: species composition, stand size classes, damage, density of stocking and topography. There are about 600 possible combinations when permuting these categories! A 'placette' is selected per hectare in a way to guarantee the statistical signification when extrapolating the results to the entity of the forest.

Aerial infrared false colour photographs form the second source of information. Based on the methods of photo-interpretation, they are used to complete the information obtained by the first method. General forest supervision is assumed through federal and cantonal services while forest management is of municipal competence. This fact implies that the information must be adjusted to a geographic entity at municipal scale.

Test Areas

The two test areas chosen for this study are representative for the Swiss 'Plateau' forest types. They are located ten kilometers north of the city of Lausanne. The principal characteristics are presented below:

Forest no. 1 'Romanel'

Area: about 320 hectares
 Species composition: conifer (in majority spruces and pines) deciduous (in majority beeches, with the presence of oaks and poplars)
 Topography: flat

Forest no. 2 'Jorat'

Area: about 2700 hectares
 Species composition: conifer (spruces and pines) deciduous (in majority beeches, with the presence of oaks and ashes)
 Topography: mild slopes

Analysis of Collected Information

The descriptive parameters of a 'placette' allowed us to choose 12 classes. The two examples below help to illustrate them:

- class 1: conifer - medium size or age - healthy - medium stocked - flat
 class 2: deciduous - full size or old - ill - poorly stocked - mild slope

Obviously, radiometric significations are different from one class to the other. For instance age cannot be observed directly. Without any other information, it may be correlated to the degree of covering. J. Franklin recommended this method as reliable for large, relatively homogeneous areas. On the other hand, the distinction between deciduous and conifer depends directly on their spectral differences. In spite of the complexity and number of classes within a 'placette', a supervised classification has been attempted. On the whole, the results obtained were poor: the percentage of correctly classified pixels was lower than 50%. This situation reflects the heterogeneity of the forests in the test areas very well. Consequently, these results limited our choice of information when using remote sensing. The information retained concerning the evolution of forest contours and the geographic distribution of tree species may be considered as simple, but are paradoxically little known at a municipal scale.

Data Characteristics

1. Landsat 5 thematic mapper image of 26 July 1985, frame 195/028.
2. Aerial infrared false colour photographs of June 1986 at the scale of 1:25 000.

Analysis of Forest Contours and Updating of Topographic Maps at the Scale of 1:25 000.

Many studies have confirmed the advantages in forest discrimination of Landsat TM bands 4, 5 and 7. They have largely been used in our study. A classic processing scheme has been applied:

1. Geometric image rectification using 22 control points, identified upon topographical map at the scale of 1:25 000. The planimetric precision achieved by geometric rectification is within a pixel, i.e. about 30 m.
2. Supervised forest classification (minimum distance classifier using a threshold of 4 standard deviations) and high-pass filtering.
3. Extraction of forest maskings, computing and printing of the forest contours upon a transparent sheet. The computed contours superimposed to the corresponding topographic map lined out the contour differences.
4. Verification of contradictions on aerial infrared false colour photographs.

Figure 1 shows the differences observed.

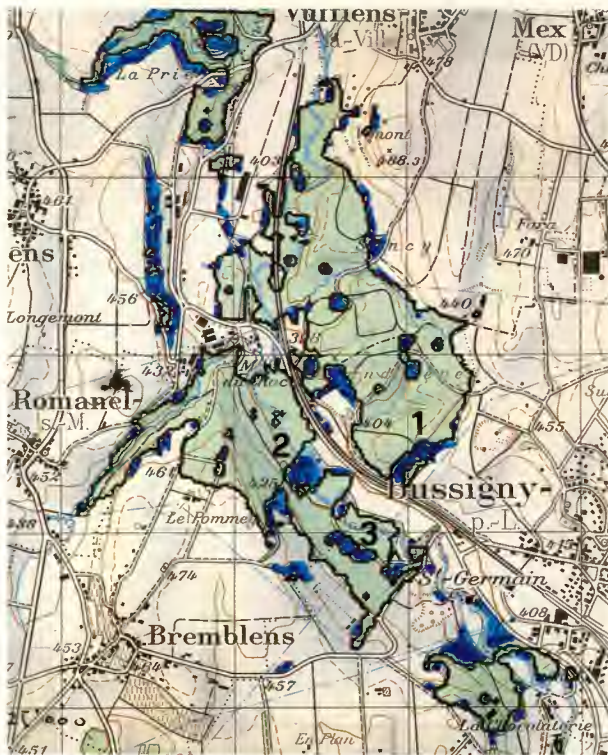


Figure 1. Forest contours on topographic map and after image classification.

Analysis of contour differences

On the whole, the forest contours extracted from the satellite image have the same shape as those on the topographic map shown in Figure 1. For page-setting reasons, the scale of Figure 1 is 1:50 000, but the result remain similar at the 1:25 000 scale. The differences observed in Figure 1 at points 1, 2 and 3 result of clear-cuttings (all the trees were cleared) followed by reforestation. In the following paragraphs, the principal aspects of the relatively complex problems resulting from these areas for remote sensing applications, will be discussed. During the first years after the clear-cut, the soil is recovered by grass. It is impossible to discriminate these plots from prairies. To remove this obstacle, there are hardly any other means than the use of information from a geographic information system (GIS) which covers the forest area concerned and in which all changes in soil assignment are updated. In case of doubt, priority is given to GIS.

This same identification problems remain in afforested areas even with trees 2 to 3 m in size. The degree of soil covering is still too small to significantly modify the spectral signature. Classification using a perpendicular vegetation index has not improved the results. The advantages obtained through texture analysis cannot be qualified definitively yet.

The natural extension of forest over abandoned agricultural surfaces has not been observed in our two

test areas. Cutting and reforestation are radiometrically similar. Only a multitemporal analysis would reveal ground covering modifications.

Determination of Forest Populations

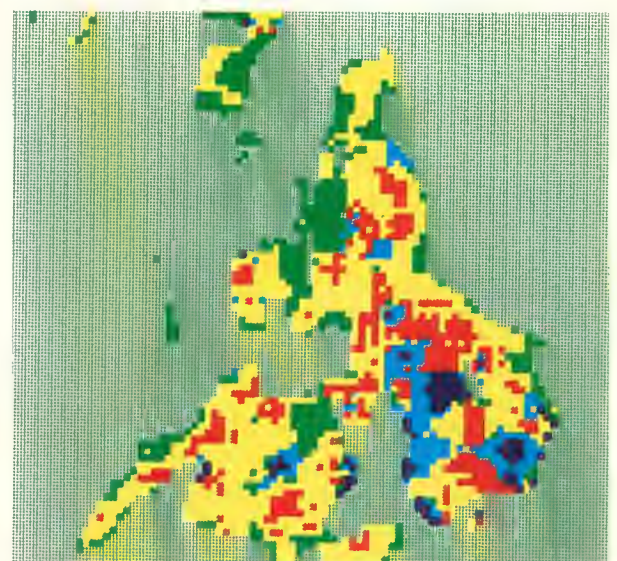
Both test areas are characterised by the presence of deciduous and conifer forests. In some cases, these two types are fairly well separated and form homogeneous areas with relatively important extensions, but with random boundary forms; sometimes deciduous and coniferous trees are intimately mixed together.

Which is the potential information inside a Landsat TM image above such forest populations? Our still traditional approach led us to the following steps:

- Histogram analysis of each spectral band to detect those with the largest variances (cf. Table 1).
- Application of diverse supervised classification techniques to determine the algorithm whose results are nearest to ground truth.
- Classification has been realised in two steps. Firstly, the homogeneous areas of deciduous, conifer and mixed forests have been extracted separately. Then, using successively the three maskings obtained, classification is applied inside each class.
- Verification of classification results is realised by applying a grid sampling technique to the aerial infrared photograph: tree species and tree numbers are identified, respectively added up using grid cells of 15 m side.

The red band offers little discrimination capacity for forest analysis. Therefore the red band statistics do not figure in the table above. As shown in Table 1, band 5 is the most discriminant for conifer and deciduous separation.

Figure 2. Forest of 'Romanel'. Classification by perpendicular vegetation index.



FOREST Band	ROMANEL			JORAT		
	conifers	deciduous	mixed	conifers	deciduous	mixed
TM2	28.1±0.8	30.2±0.7	29.2±0.8	25.1±0.8	28.0±1.4	26.3±1.0
TM4	61.3±3.6	102.7±3.4	79.5±6.9	55.5±6.7	88.5±8.2	80.2±7.8
TM5	44.7±3.5	68.0±3.1	54.3±5.6	34.6±4.8	45.4±6.2	53.2±5.4
TM7	15.0±1.0	20.4±0.9	17.0±1.8	11.5±1.7	13.6±2.3	16.4±1.6

Table 1. Mean radiance and standard deviations in training areas

Results are presented in Table 1

The processing method described above led us to the discrimination of five classes:

Class 1: conifer with a homogeneity rate greater than 90% (magenta).

Class 2: conifer with a homogeneity rate between 60% and 90% (blue).

Class 3: deciduous with a homogeneity rate greater than 90% (green).

Class 4: deciduous with a homogeneity rate between 60% and 90% (yellow).

Class 5: mixed compositions of conifer and deciduous between 40% and 60% (red).

Comments

The 'minimum distance' classifier has been applied using a threshold of four standard deviations. Training areas were identified upon a false colour composition 'red-green-blue' of Landsat thematic mapper bands 4, 5 and 7.

Classification results may be qualified as good considering the heterogeneity of the forest in the test areas. Classification accuracy is estimated at 90%.

Species separation inside conifer or deciduous classes could not be realised, the spectral signature not being discriminative enough.

The same problems as in the identification of forest contours occurred with species discrimination in the presence of recent plantations: deciduous and conifer appeared to be too similar in spectral signature for discrimination. This fact suggested that, as in the situation of forest contours, we use multitemporal analysis or a geographical information system.

Surface Computation per Municipality

Municipal borders have been digitalised from topographic map at the scale of 1:25 000. Again with masking, areas of the different forest populations have been computed for each municipality. Table 2 represents forest surfaces for six municipalities which are adjacent to the Romanel forest.

Table 2. Forest of 'Romanel'. Forest populations and surfaces for 6 municipalities

Populations Municipalities	Conifers (ha)	Deciduous (ha)	Mixed (ha)	Total (ha)
Bremblens	2.34	9.44	36.80	48.58
Romanel S/Morges	—	4.05	11.25	15.30
Aclens	1.44	15.21	29.79	46.44
Echandens	0.72	12.60	25.38	38.70
Bussigny	13.41	9.09	44.28	66.78
Vufflens-la-Ville	5.58	27.63	67.32	100.53
Total	23.49	78.02	214.82	316.33

Conclusions

According to the nature of certain information required by forest services, and according to the actual capacity of spatial and spectral resolution, we may hope that space-borne remote sensing will take the place of conventional data acquisition methods. In the meantime, the two methods will be complementary, as demonstrated in this study. In the case of applications such as those presented in this paper, Landsat-5 thematic mapper data offer information which is very expensive to obtain by traditional means. Associated to a geographic information system, they considerably increase the reliability of the data required for supervision and integrated forest management.

Bibliography

- J. Franklin *et al*, Coniferous forest classification and inventory using Landsat and digital terrain data, *IEEE Trans. on Geosc. and Remote Sensing*, Vol. GE-24 no.1, 1986, pp. 139-149.
- L. Wastenson *et al*, Swedish experiences on forest damage inventory by remote sensing methods, *Imaging Remote Sensing*. Vol 1 no.1, 1987, pp. 43-52.
- V. Felten, Contribution à la cartographie forestière en zone fortement morcelée à l'aide de l'imagerie SPOT, *Colloque SPOT*, nov. 1987.
- W.D. Hudson & D.P. Lush, Spectral response curve models applied to forest cover-type discrimination,

Proceedings of Machine processing of Remotely Sensed Data Symposium, Purdue 1984, pp. 175-179.

Jian-Kang Wu *et al*, A forest inventory using Landsat imagery in the Moo-shan area of China. *Int. Journal of Remote Sensing*, Vol 6 no.12, 1985, pp. 1783-1795.

La télédétection par satellites de 2ème génération - un nouvel outil pour l'aménagement et la foresterie, Institut d'aménagement et d'urbanisme de la région d'Ile-de-France (IAURIF), septembre 1986, 140 p.

Multitemporal Analysis of Forest Areas in the Surroundings of Innsbruck, Austria

Franz H. Berger*

Institut für Meteorologie, Freie Universität Berlin, FR Germany

(* formerly with Institut für Meteorologie und Geophysik, Universität Innsbruck, Austria)

Using Thematic Mapper (TM) data from Landsat-5, the seasonal variation in 1984-85 of directional vegetation reflectance was analysed for various forested areas (mainly coniferous forests) near Innsbruck, Austria. For such an analysis the influence of the atmosphere has to be taken into account. Therefore a simple radiative transfer model was applied to correct for atmospheric effects. This resulted in spectral surface reflectances of each TM-band. For testing this method of atmospheric correction, it was applied to the radiances of a lake surface (Achensee in Tirol, Austria). The results of the evaluation of the TM data were also validated by means of spectral albedo measurements for selected homogeneous surfaces.

The correlation and the multiple correlation between the different TM-channels were computed. Channel 4 (760-900 nm) is least correlated to all other channels and its combination with any of them results in a maximum of information about the seasonal variability of the forest reflectances. From two- and three-dimensional plots of the calculated reflectances it seems possible to extract a seasonal variation of the growth of vegetation. The correlation of this variability with biological parameters (biomass production) requires further investigations.

1. Introduction

The purpose of this investigation is an analysis of the spectral reflectances of various forested areas during the vegetation period. Seven cloudfree Thematic Mapper (TM) scenes from Landsat-5 were selected for different dates within a vegetation period. Unfortunately, it was not possible to obtain all scenes from the same year. Consequently, the following dates had to be used: 20 April 1984; 6 May 1984; 9 July 1984; 28 July 1985; 3 August 1985; 30 September 1985 and 25 October 1985.

For the multitemporal analysis some forest areas (mainly coniferous forests) in the surroundings of Innsbruck, Austria were selected.

In order to compare and to 'calibrate' the method of atmospheric correction, some invariable test areas without any seasonal variation in the reflectance were selected. For some of these areas, the spectral reflectance was measured with a radiometer and a spectral albedometer in summer 1985 (1).

2. Atmospheric correction

To relate the radiance L_{sat} measured at the satellite to the surface reflectances, a simple radiative transfer model

(Fig. 1) was applied following a proposal by Bolle (2). This model is based upon the following simplifications:

1. The atmosphere is plan-parallel and horizontally homogeneous.
2. All computations are made monochromatically.
3. No polarization effect is considered, neither for the measurements nor for the computations.

The radiance L_{sat} at the top of the atmosphere can be described according to Figure 1 by:

$$L_{sat} = L_0 [1 - \tau(z, \zeta)]b + L_0 \{ \tau(z, \zeta) + [1 - \tau(z, \zeta)] f \}$$

$$\frac{\rho' \tau'(z, \zeta) + [1 - \tau'(z, \zeta)] f' \bar{\rho}}{1 - [1 - \tau(z, \zeta)] b \bar{\rho}} \quad [1]$$

where L_0 is the solar spectral irradiance at a horizontal surface at the top of the atmosphere divided by π ; $\tau(z, \zeta)$ is the transmittance for a given altitude and a given solar zenith angle; f and b are the fractions of the forward and the backward scattering, respectively. The symbols with an apostrophe represent the quantities in the direction to the satellite. The fractions f and b are calculated by applying the Mie theory (3). Because of the lack of information about the optical properties of the aerosols,

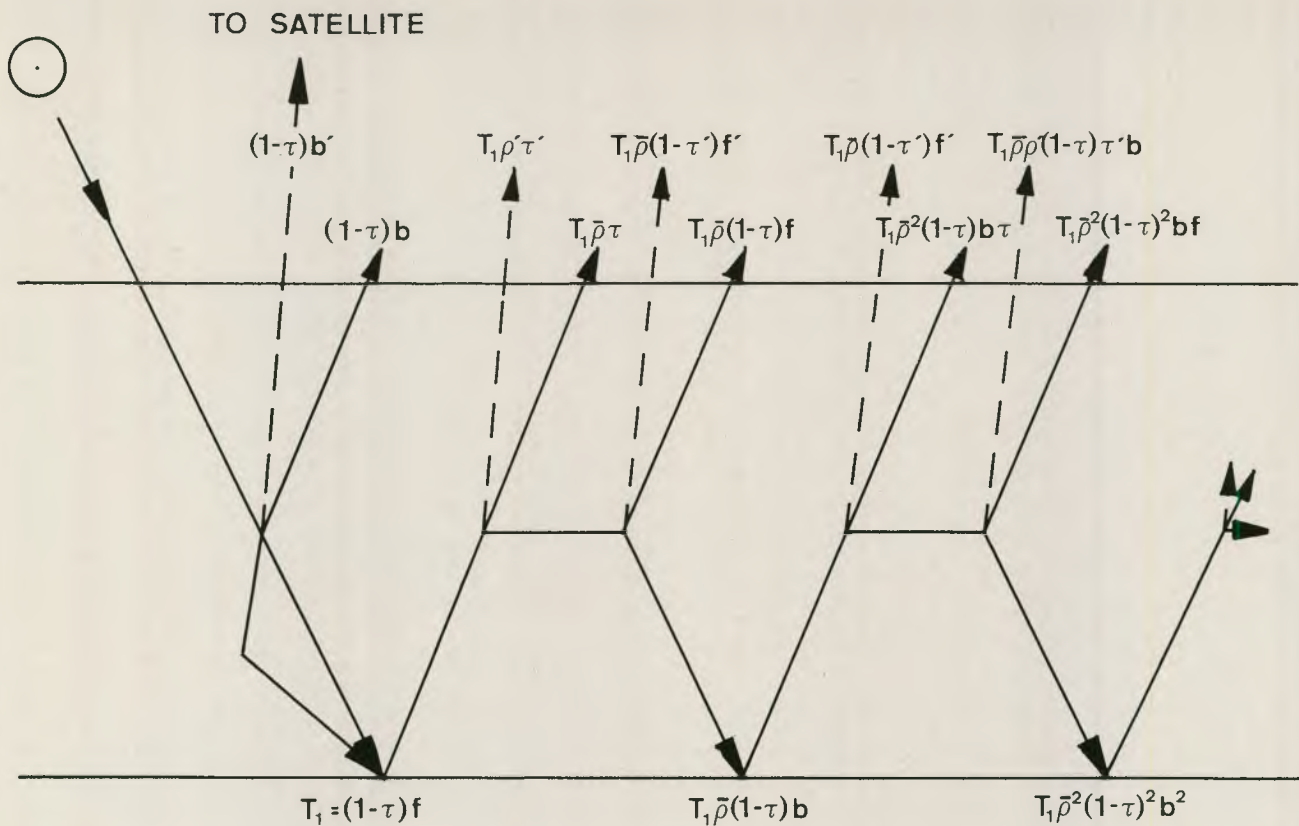
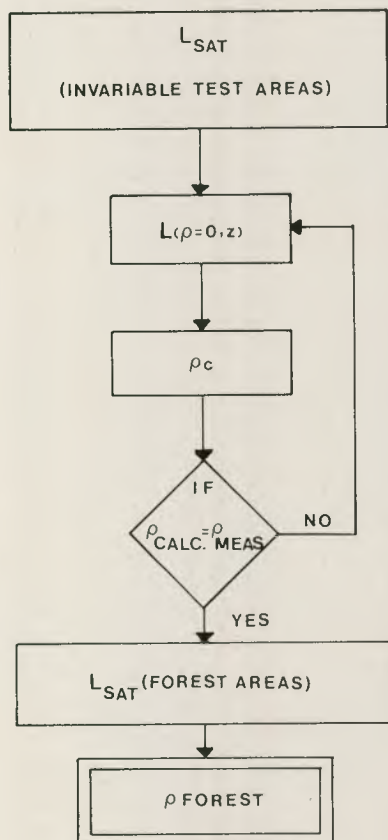


Figure 1. Scheme of the atmospheric radiative transfer model [after Bolle (2)]

Figure 2. Outline of the algorithm applied to the calculation of the surface reflectances



climatological values had to be used (4). $\bar{\rho}$ is the albedo of the surface.

The first term on the right-hand side of equation [1] represents the backscattered solar radiation of the atmosphere, when the ground is nonreflecting and it can be considered as the atmospheric planetary albedo. This term is especially important if the surface reflectance is small. With increasing albedo of the surface, the second term in [1] becomes more important, which stands for the radiation reflected at the ground to the satellite including multiple scattering.

The following scheme is applied to compute the spectral reflectances (Fig. 2):

- I. Transformation of digital signals of invariable test areas into radiances.
- II. Approximation of the path radiance $L(\rho=0, z)$.
- III. Iterative solution of equation [1] in order to determine the critical albedo ρ_c at which the signal becomes independent of the atmospheric properties.
- IV. Comparison of the calculated reflectances with the measured reflectances on top of the invariable test areas.
- V. Transformation of digital signals of forested areas into radiances and calculation of spectral reflectances of forest areas.

ad I.) The 8-bit digital signal transmitted from the Thematic Mapper can be converted to calibrated radiances L_{sat} using published calibration constants (5).

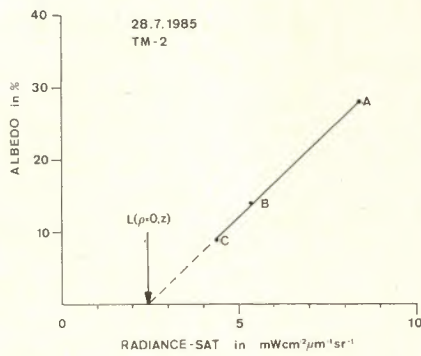


Figure 3. Regression line of TM-band 2 for the approximation of the path radiance $L(\rho=0, z)$ (28 July 1985); the arrow shows the path radiance. The test areas are: the concrete surface at the Innsbruck Airport (A), a shopping center (B) and the railway station (C).

ad II.) With the knowledge of the spectral surface reflectances of invariable test areas and the related radiances measured at the satellite, it is possible to estimate the path radiance in a first approximation. A linear dependence between the spectral surface reflectances and the radiances measured at the satellite can be assumed. If the ground is nonreflecting, the path radiance (the first term in the right-hand side of [1]) is determined by an extrapolation to $\rho=0$ (Fig. 3).

ad III.) The value of the surface reflectance for which the loss of the outgoing radiation will be compensated by the path radiances, is called the critical albedo ρ_c . For example, if the surface reflectance is very small, the path radiance makes the observed area appearing brighter. And if the surface reflectance exceeds the critical albedo ρ_c the observed area appears darker.

Because the path radiance compensates the loss of the outgoing radiation, one must modify equation [1] and one obtains a quadratic equation [2] to calculate the surface reflectance (6):

$$\begin{aligned} \bar{\rho}_2 \left\{ \frac{L(\rho=0, z)}{L_0} \frac{b[1-\tau(z, \zeta)]}{\rho_c} \right\} + \bar{\rho} \left\{ \frac{L_{sat}}{L_0} b[1-\tau(z, \zeta)] \right. \\ \left. + T_1 T_2 - \frac{L(\rho=0, z)}{L_0} b[1-\tau(z, \zeta)] - \frac{L(\rho=0, z)}{L_0} \right\} \\ + \left\{ \frac{L(\rho=0, z)}{L_0} - \frac{L_{sat}}{L_0} \right\} = 0 \end{aligned} \quad [2]$$

where

$$T_1 = [1-\tau(z, \zeta)] f + \tau(z, \zeta)$$

and

$$T_2 = [1-\tau'(z, \zeta_s)] f + \tau'(z, \zeta_s).$$

In this equation another unknown quantity is the critical albedo ρ_c . With the extrapolated (Fig. 3) path radiance

for each channel and with any accepted critical albedo, it is possible to calculate the surface reflectance of one invariable test area. To get the critical albedo in a first approximation, the calculated reflectance was compared with the measured reflectance with an iterative approach to the critical albedo.

ad IV.) If the calculated and the measured reflectances differ, the critical albedo is calculated again with another path radiance (back to II). By this iterative method it is possible to obtain the critical albedo and the path radiance. From the approximated path radiance for each channel one obtains for each date the atmospheric transmittance and the optical depth.

ad V.) Now the quadratic equation [2] can be solved and one obtains the spectral reflectance of each test area for each date and channel.

If the surface reflectance is unknown, it is possible to determine the critical albedo by means of the method of Fraser & Kaufman (7). This method compares the normalised upward radiance on a clear day with the normalised upward radiance on a hazy day assuming constant reflectances. But the following problems arose with the application of this method in the structured, inhomogeneous area around Innsbruck:

1. The time-interval between two observed scenes was too long so that it was impossible to construct a two-dimensional histogram from two observed scenes, because the influence of the seasonal variation of the spectral reflectances especially of the vegetations was too large.
2. In this alpine valley, another disadvantage is the dependence on the altitude of the test areas.

3. Applications

In summer 1985, the spectral reflectances of two test sites (1) were measured with a radiometer and a spectral albedometer. These were a concrete surface and a grass area at the Innsbruck airport. Because of their seasonal variability, the reflectances of the grass area had to be replaced by the calculated reflectances of the railway station and shopping center (Table 1). From the

Table 1. Calculated spectral reflectance of the railway station and of a shopping center in Innsbruck; center wavelength in brackets

	Railway Station	Shopping Center
TM-1 (483 nm)	0.065	0.110
TM-2 (568 nm)	0.090	0.140
TM-3 (656 nm)	0.090	0.145
TM-4 (829 nm)	0.100	0.200
TM-5 (1653 nm)	0.150	0.275
TM-7 (2180 nm)	0.150	0.250

measurements made of the two test sites the spectral reflectances were calculated by means of the presented method of atmospheric correction of the TM data for the railway station and for the shopping center for 28 July 1985 and 3 August 1984.

To test this method of atmospheric correction, it was applied to the radiances of a lake (Achensee in Tirol/Austria). At two dates (3 August 1984; 25 October 1985) a good agreement with expected values was achieved within 1% (8). The results are shown in Table 2.

Table 2. Calculated spectral reflectance of Achensee in Tirol, Austria

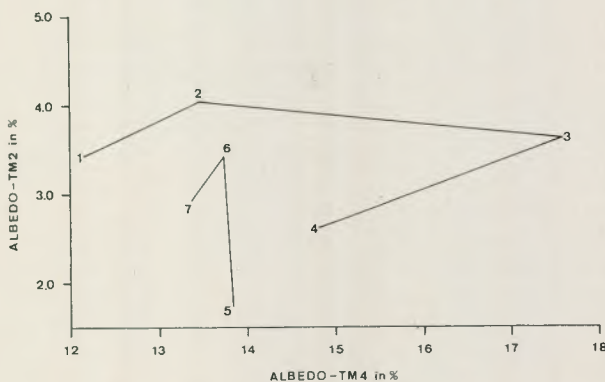
	3 August 1984	25 October 1985
TM-1	0.025	0.019
TM-2	0.017	0.016
TM-3	0.014	0.015
TM-4	0.012	0.002
TM-5	-0.004	-0.007
TM-7	-0.002	-0.005

Table 3. Correlation matrix and mean values of calculated reflectances in % in the diagonal (averaged over all forest areas)

	TM-1	TM-2	TM-3	TM-4	TM-5	TM-7
TM-1	2.9	0.835	0.757	0.311	0.502	0.672
TM-2		3.1	0.846	0.351	0.588	0.723
TM-3			1.4	0.297	0.480	0.704
TM-4				13.6	0.725	0.496
TM-5					6.7	0.842
TM-7						3.0

Using the approximated quantities (critical albedo, path radiance) for solving the quadratic equation [2], it was

Figure 4. Variation of spectral reflectance of a forest in channels 2 and 4; (1 - 20 April 1984; 2 - 6 May 1984; 3 - 9 July 1984; 4 - 3 August 1984; 5 - 28 July 1985; 6 - 30 September 1985; 7 - 25 October 1985).

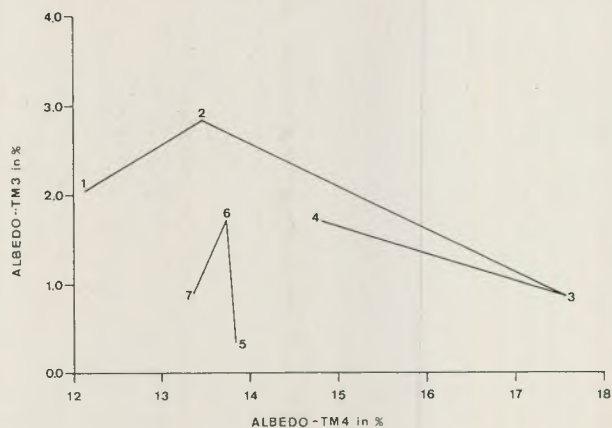


possible to calculate the spectral reflectances of the forest areas. With these values, the correlation between the different TM-channels were computed. The correlation matrix (Table 3) shows that the channel 4 (near-infrared) is least correlated to all other channels. Its combination with any of them results in a maximum of information about the seasonal variability of the forest reflectances. This result is in good agreement with similar investigations. For example, Horler and Ahern (9) applied an atmospheric correction, too. Their result was that the best forest cover-type discrimination is between the TM-band 3, 4 and 5. Xu (10) investigated TM-data with regard to their applicability to forest classification, and he found that channel 4 is the best.

Two examples of the seasonal variation of the spectral reflectances of one forest area are given in Figures 4 & 5. Here the spectral reflectance of channel 4 (760-900 nm) was plotted as a function of the spectral reflectances of channel 2 (520-600 nm) (Fig. 4) and of channel 3 (630-690 nm) (Fig. 5). These figures show that the forest reflectances increase in all three TM-bands from 20 April (1) to 6 May (2). These increases indicate the beginning of the vegetation period between April and May. While the reflectance in the near-infrared increases in the following vegetation period, the reflectances in the visible (channel 2 and channel 3) decrease (2-3). Considering the variation in channel 3 alone, one can see the strong chlorophyll-absorption in this period (3). It shows a use of the radiant energy for the photosynthesis. From data point 3 to 4, the spectral reflectances in channel 2 and 4 decrease, but the spectral reflectance in channel 3 increases. This seems to be the sign that the maximum of the vegetation growth has been passed.

The second fraction (5 to 7) in these plots shows the variation of the reflectances in 1985. In order to compare the reflectances of 28 July 1985 (4) with the reflectances of 3 August 1984 (5), the weather situation of the pro-

Figure 5. Variation of spectral reflectance of a forest in channels 3 and 4; (1 - 20 April 1984; 2 - 6 May 1984; 3 - 9 July 1984; 4 - 3 August 1984; 5 - 28 July 1985; 6 - 30 September 1985; 7 - 25 October 1985).



	Jan	Feb	Mar	Apr	May	Jun	Jul	Aug	Sep	Okt	Nov	Dec
1984	32.1	87.9	31.9	38.1	62.9	75.8	73.5	104.3	173.1	56.0	20.3	33.5
1985	22.6	32.7	22.5	67.0	59.2	103.9	120.6	229.2	41.3	22.9	40.4	32.9
\bar{N}	59.0	46.0	45.0	63.0	83.0	115.0	136.0	122.0	85.0	68.0	60.0	58.0

Table 4. Monthly precipitation in 1984 and 1985 in Innsbruck, Austria; \bar{N} is the mean monthly precipitation (1906–1965).

ceeding days has to be taken into account. Table 4 shows the monthly precipitation in 1984 and 1985 in comparison to the mean monthly precipitation \bar{N} (1906–1965).

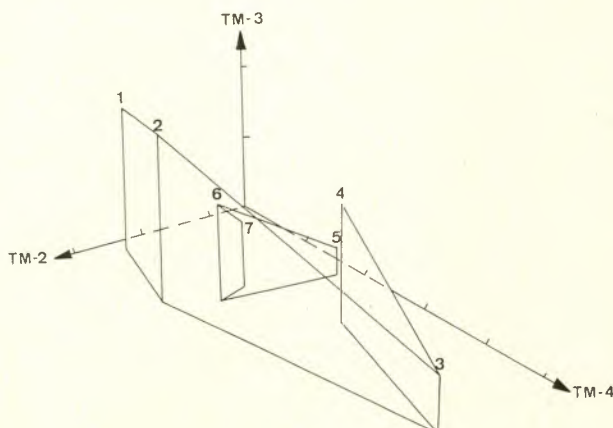
Table 5. State of the surface during the observation dates

observed date	state of the surface
20 April 1984	wet
6 May 1984	dry
9 July 1984	dry
3 August 1984	dry
28 July 1985	wet
30 September 1985	dry
25 October 1985	wet

With the knowledge of the precipitation conditions and the state of the surface, it seems possible to explain the difference between these two observed dates. As an example, the reflectance of wet surfaces is smaller than of dry surfaces (11). At the end of the vegetation period, the plots show a small decrease in all investigated channels.

The next step in this investigation was to calculate the multiple correlation between all channels. The channels 4, 2, 3 and 4, 2, 7 turned out to be least correlated. The multiple correlation coefficients (averaged over all forested areas) are: $R_{4,23}=0.500$ and $R_{4,27}=0.608$. After the F-test (12) the three channels were significantly dif-

Figure 6. Variation of spectral reflectance of a forest in channels 2, 3 and 4; (1 - 20 April 1984; 2 - 6 May 1984; 3 - 9 July 1984; 4 - 3 August 1984; 5 - 28 July 1985; 6 - 30 September 1985; 7 - 25 October 1985).



ferent to 95% from zero, if the multiple correlation coefficient is larger than $R_{x,yz}=0.93$.

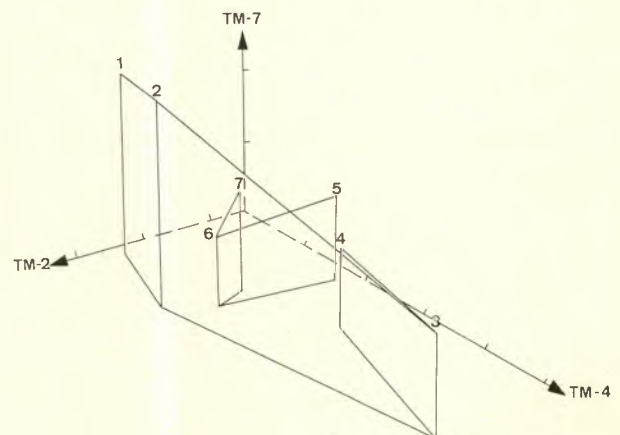
Figures 6 & 7 describe results of the reflectances in the channels 4, 2, 3 and 4, 2, 7. The variations in channel 2, 3 and 4 are discussed above. But the seasonal variation in channel 7 (2.08–2.35 μm) shows a small increase in the beginning of the vegetation growth (1 to 2) and a decrease thereafter (2-3). In summer and in autumn, it is very difficult to analyse a variation in the middle-infrared, because of the small variation.

4. Conclusions

For forested areas in structured terrain it is not a straight forward task to identify the seasonal variation of the growth of vegetation and to understand differences that occur from year to year. Large scatter of the date is obviously introduced by the optical depth that varies over the scene, especially in valley atmospheres. Also the weather situation of preceding days has to be taken into account (e.g. precipitation). For the analysis it turned out that the near-infrared band 4 in combination with the other bands gives a possibility to analyse the multitemporal variation of vegetation reflectances.

Further studies will have to address the improvement of atmospheric correction including the directional dependence of scattering by air particles and aerosols. Furthermore the angular dependence of directional

Figure 7. Variation of spectral reflectance of a forest in channels 2, 4 and 7; (1 - 20 April 1984; 2 - 6 May 1984; 3 - 9 July 1984; 4 - 3 August 1984; 5 - 28 July 1985; 6 - 30 September 1985; 7 - 25 October 1985).



reflectance of test areas must be considered. Since for most applications the optical depth of the atmosphere is not known, the method of Fraser and Kaufman (7) or the method demonstrated in this paper should further be explored to determine the optical properties of the atmosphere from images itself or with a minimum of additional information about the characteristics of the observed land surface.

Acknowledgements

The author would like to thank Prof. H.-J. Bolle of the Institut of Meteorology, Free University of Berlin for stimulating discussions and comments. This work was supported by the Austrian Solar and Space Agency and the BMWF.

References

1. Bolle H.-J., Berger F.H.: Spektrale Albedo- und Reflexionseigenschaften von Pflanzen. in: Mondre E.; Pollanschütz J.: Zweites österreichisches Symposium Fernerkundung. *Mitteil. forst. Bundesversuchsanstalt*, Heft 157, Wien 1986.
2. Bolle H.-J.: Personal Communication, 1985.
3. Van de Hulst H.C.: Multiple Light Sattering, Tables, Formulas and Applications. Vol. 1 and 2, Academic Press, New York, 1980.
4. McClatchey R.A.; Bolle H.-J.; Kondratyev K.Ya.: A preliminary cloudless standard atmosphere for radiation computation. *WCP-112, WMO/TD-No. 24*, March 1986.
5. Barker J.: Relative radiometric calibration of Landsat-TM reflective bands. *Landsat-4 Investigations Summary*, NASA conference publication 2355, 1985.
6. Berger F.H.: Multitemporale Analyse von Vegetationsflächen aus Landsat-Daten. Diplomarbeit, Inst. f. Meteorologie und Geophysik der Universität Innsbruck, Feb. 1987.
7. Fraser R.S.; Kaufman Y.J.: The Relative Importance of Aerosol Scattering and Absorption in Remote Sensing. *IEEE Transactions on Geoscience and Remote Sensing*, Vol. GE-23, No. 5, Sept. 1985.
8. Koepke P.: Bestimmung der atmosphärischen Trübung mittels geostationärem Satelliten. Münch. Univ. Schriften, Fachbereich Physik, Met. Inst., Wiss. Mitt. Nr. 30, München 1977.
9. Horler D.N.H.; Ahern F.J.: Forestry information content of Thematic Mapper. *Int. J. Rem. Sens.*, Vol. 7, No. 3, 1986.
10. Xu G.Q.: Forstklassifikation mit Landsat-Daten, Eine Fallstudie in der Steiermark, in: Mondre E.; Pollanschütz J.: Zweites österreichisches Symposium Fernerkundung. *Mitteil. forst. Bundesversuchsanstalt*, Heft 157, Wien 1986.
11. Twomey S.A. et al.: Reflectance and albedo differences between wet and dry surfaces. *Applied Optics*, Vol. 25, No. 3, Feb. 1986.
12. Taubenheim J.: Statistische Auswertung geophysikalischer und meteorologischer Daten. *Geogr. Monographien*, Akad. Verlagsgesellschaft, Leipzig, 1969.

7. *Cartography*

Comparaison des données Landsat MSS et TM pour la cartographie des formations superficielles en zone aride (Tunisie méridionale)

R. Escadafal et J. Pouget

Atelier de Télédétection, Centre ORSTOM, Bondy, France

In a previous study the Landsat MSS data were found to be a useful tool for the surveying of arid soils in Tunisia. The data of the 'visible' channels 4 and 5 are correlated with the roughness and the colour saturation of the soil surfaces. Based on these properties a first 'soil-surface condition' map has been produced and interpreted. This map contained pedological information but was not sufficient in itself to determine all the soil types. For instance, the loamy and the gypsiferous soils, both light coloured, were difficult to separate.

Considering this background, the Thematic Mapper image that has been evaluated in this TM-Earthnet pilot project represents a considerable progress. Firstly the 30×30 m ground resolution allows to recognise and describe precisely the physiographic units, and also to locate accurately the ground sampling sites. Secondly, the new visible channel (TM1), forming a trichromatic system with the two others, gives a more precise characterisation of the soil colour. Last but not least, the data of the medium-infrared channel (TM7) are strongly correlated with the mineralogical content of the soil surface in the studied area. This enables to distinguish easily gypsum from carbonate- and quartz-dominated soils. These results are illustrated by a plate showing the 'soil-surface types' map produced by classifying this Landsat TM image. The promising use of this kind of schematic maps in arid land studies is discussed.

Keywords: remote sensing / Landsat MSS / Landsat TM / arid zone / soil surface / soil colour / gypsum.

Au cours d'un précédent travail nous avons utilisé les données Landsat MSS comme aide à la cartographie pédologique de reconnaissance en Tunisie. En se basant sur des données de terrain précises et adaptées, il a été montré que les luminances spectrales mesurées dans les canaux MSS4 et MSS5 permettent de discriminer différents milieux par la rugosité et la couleur de la surface des sols. Mais des confusions existent en particulier entre les sols clairs limoneux et gypseux.

Les données du détecteur 'Thematic Mapper' permettent d'aller beaucoup plus loin dans la caractérisation de l'état et de la nature des surfaces. Ainsi, avec la résolution de 30×30 m, la morphologie est beaucoup mieux cernée et le repérage facilité. Le canal 1, combiné aux deux autres canaux visibles classiques, permet une meilleure distinction des couleurs. Le rapport entre canal 7 et canaux visibles varie avec la nature minéralogique des matériaux de surface; le gypse, notamment, est discriminé sans ambiguïté. Un exemple de carte des types de surfaces obtenu par traitement des données TM illustre ces résultats. Ce type de document, où s'expriment à la fois des ressources et des contraintes, apporte une nouvelle vision des problèmes de mise en valeur des milieux arides.

Mots-clés: télédétection / Landsat MSS / Landsat TM / zones arides / surface du sol / couleur des sols / gypse.

Introduction

L'inventaire des ressources naturelles des milieux arides est une tâche qui est encore loin d'être achevée. Pourtant avec l'augmentation croissante de leur utilisation, il devient urgent de disposer de ces inventaires pour pou-

voir proposer des schémas de mise en valeur qui tiennent compte de la spécificité de ces milieux, et en particulier de leur fragilité.

La télédétection, en apportant une vue synoptique, actualisée et répétitive de ces paysages, est apparue dès ses débuts comme une solution prometteuse face à ce besoin. De fait, en Afrique du Nord, les données Landsat MSS ont été disponibles en assez grand nombre à partir de 1973, grâce à la faible fréquence de la couverture nuageuse sur ces régions et à la proximité de la station de réception de Fucino (Italie).

En Tunisie, la Direction des Sols du Ministère de l'Agriculture a entrepris en 1979 la constitution d'un atlas des ressources en sols à l'échelle du 1/200 000. Dans la partie méridionale du pays, les données disponibles étaient rares et bien des zones difficiles d'accès. Un programme de cartographie de reconnaissance des sols assistée par télédétection spatiale a été alors mis sur pied en 1981 (Pouget *et al.*, 1984).

Ces travaux ont montré que l'on peut obtenir par traitement des données Landsat MSS des informations sur la surface des sols. En effet, dans ces paysages présahariens la végétation steppique est très lâche et généralement peu active. Le capteur du satellite mesure donc des luminances qui dépendent essentiellement de la composition et de l'état de la surface des sols. Elles varient peu à une échelle pluriannuelle dans ces régions arides exploitées par un pastoralisme extensif.

Une analyse fine des relations entre sols, composition de leur surface, végétation et données radiométriques a mis en évidence l'intérêt des canaux visibles du MSS (Escadafal & Pouget, 1986). Les valeurs des canaux 4 et 5 croissent simultanément en fonction de la brillance de la surface, mais celle-ci est souvent réduite par l'effet d'ombrage dû aux cailloux et aux blocs ou encore aux touffes de végétation sèche (rugosité au sens large).

Parallèlement, le rapport entre MSS4 et 5 diminue assez sensiblement lorsque la couleur de la surface des sols est plus saturée (c.à d. plus rougeâtre pour le cas des sols observés).

En se basant sur ces constatations, il a été possible de discriminer 16 types d'états de surface différents d'après leur rugosité et leur couleur. La carte infographique représentant ces états de surface s'est révélée être un outil d'aide à la prospection très efficace, elle peut être également utilisée pour étudier les problèmes de bilan hydrique (aptitude des sols à l'infiltration) et de désertification, par exemple.

Cependant cette étude a aussi montré les limitations inhérentes à la nature des données. En premier lieu, la résolution au sol du capteur MSS ne permet pas de se repérer sur les images sur lesquelles on ne peut reconnaître les pistes, maisons et autres constructions utilisées habituellement à cette fin.

Il a donc fallu constamment recalculer sur les images la position des observations au sol repérées par d'autres méthodes (triangulation à la boussole, notamment). Cette mauvaise résolution est également gênante lorsque l'on veut identifier des formes de relief assez fines, or l'analyse géomorphologique est indispensable pour aborder l'étude de ces paysages arides.

Un deuxième point concerne la difficulté à distinguer les surfaces gypseuses des autres matériaux peu colorés (limons battants, sables grossiers...), dont le comportement radiométrique dans le visible est souvent très voisin. Les informations contenues dans les cartes géologiques permettent de trancher dans les cas des roches affleurantes, mais ceci est insuffisant pour lever toutes les confusions possibles.

Cette expérience a montré à la fois l'intérêt d'avoir facilement et sur de grandes étendues des informations sur la surface des sols grâce aux satellites et les difficultés rencontrées dans certains cas avec MSS. Elle nous a incité à tester sur la même région les possibilités offertes par la nouvelle génération de capteurs en abordant l'étude des données Thematic Mapper, dont l'intérêt pour les zones arides a été récemment souligné (Mulders & Epema, 1986).

Méthodologie

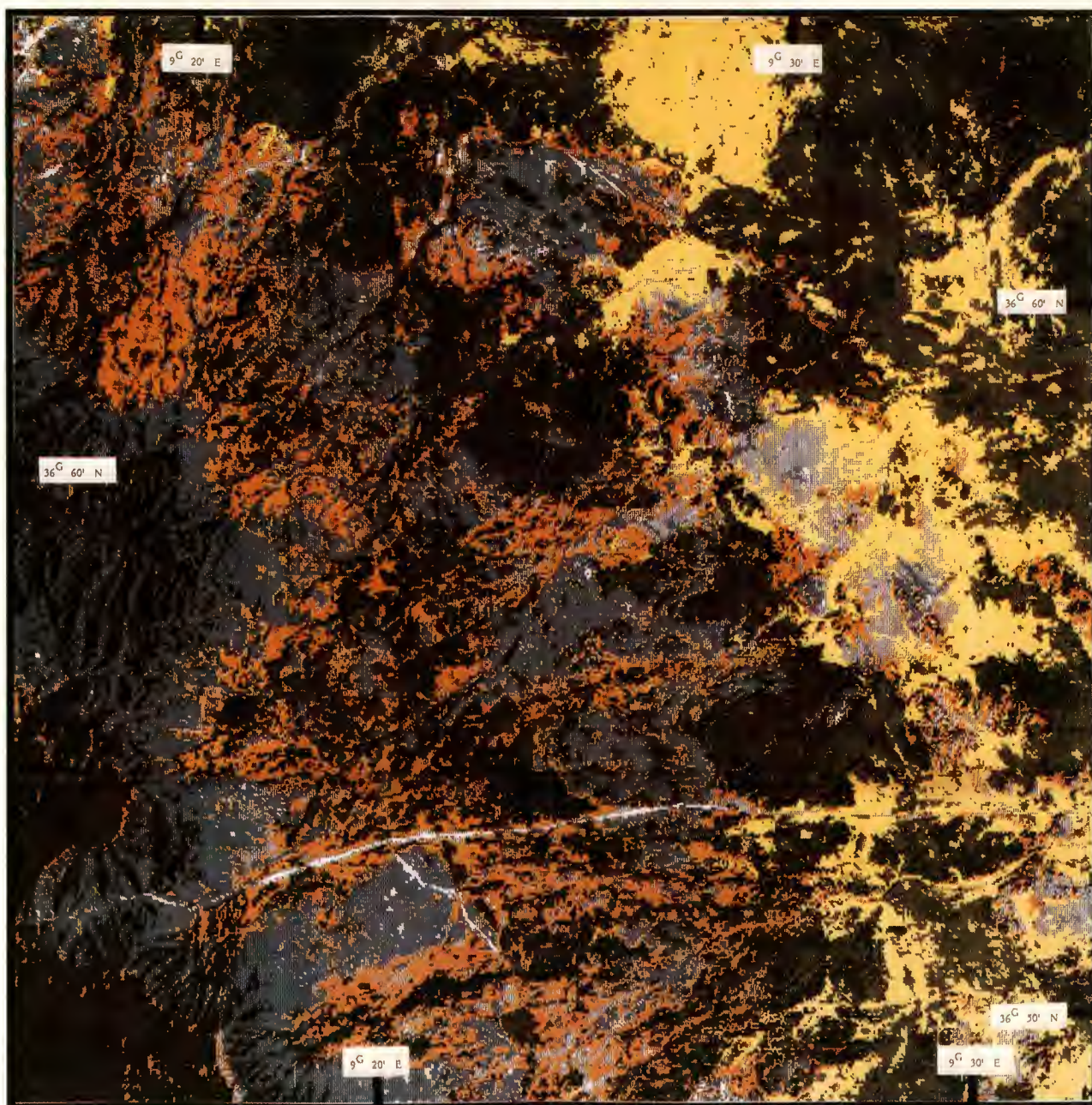
Pour tester dans notre milieu d'étude l'apport du nouveau capteur de Landsat, nous avons choisi, à l'est de la ville de Tataouine, une zone test présentant une forte hétérogénéité.

Elle est composée de reliefs et glacis façonnés dans des formations triasiques où dominent les gypses avec des intercalations de calcaires dolomitiques. Ce paysage est creusé localement de petites dépressions (dollines) le plus souvent cultivées au printemps, il est envahi par des sables éoliens. Il en résulte une juxtaposition de matériaux de couleur, de faciès et de nature très variés (gypse, calcaire et quartz).

Observations de terrain

Suivant la méthode développée et appliquée lors de l'étude des données MSS, nous avons repéré très précisément au sol un ensemble de 48 sites tests constituant un échantillon représentatif des différents ensembles sol-surface-végétation caractéristiques de la zone.

Chaque site test est défini par sa position (unité morphologique), la nature de son sol et l'organisation de sa surface (au sens large). Celle-ci est décrite en mesurant le pourcentage en recouvrement occupé par les différents composants: sol nu, sables, graviers, cailloux et pierres, débris, végétation. Chaque composant est décrit séparément: nature, couleur, état. Des photographies des fosses



(Méridien origine Paris)



LEGENDE

- | | |
|---|---|
| <ul style="list-style-type: none"> 1 Ombres 2 Surfaces très rugueuses :
- roches calcaires
- végétation dense sèche 3 Surfaces caillouteuses calcaires 4 Surfaces caillouteuses calcaires
à recouvrement de sable quartzéux | <ul style="list-style-type: none"> 5 Surfaces limoneuses calcaires 6 Surfaces gypseuses (? caillouteuses) 7 Surfaces gypseuses
à recouvrement de sable quartzéux 8 Surfaces sableuses (sable quartzéux) 9 Surfaces très brillantes
(pistes, gypse érodé) |
|---|---|

Image Landsat Thematic Mapper
190/37.3 du 5 août 1984

PROJET PILOTE TM/EARTHNET
Classification supervisée des canaux 1, 3, 7
[Méthode barycentrique]

R.B. CADAFAL et M. POUGET - 1986 -
Atelier de Télédétection de l'ORSTOM - Bondy (France)

Figure 1. Carte schématique des types de surface de sols – Région de Tataouine-Est (Tunisie).

pédologiques et des échantillons de surface complètent ces relevés.

On obtient ainsi une caractérisation du milieu tel qu'il apparaît vu à la verticale et en particulier par les satell-

tes. En choisissant des sites tests suffisamment étendus et homogènes, ils correspondent à un nombre assez important de pixels pour étudier les relations entre données terrain et luminances spectrales sous un angle statistique.

Traitement des données Landsat TM

L'image utilisée a été acquise le 5 août 1984 dans le cadre du projet pilote TM-Earthnet (Fig. 1). Notons qu'à cette période de l'année la végétation est à l'état sec et peu abondante après avoir été pâturée au printemps.

Une première *visualisation globale* a été faite sous la forme de compositions colorées en réalisant sur une console vidéo couleur interactive (Périscolor 1000) différentes combinaisons de canaux.

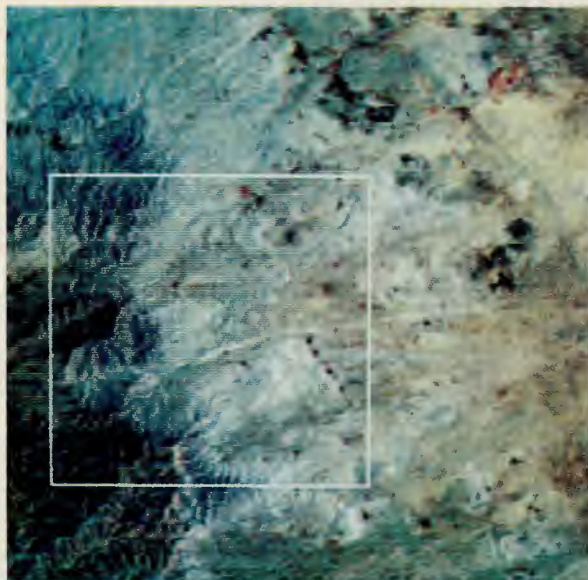
Deux modes principaux ont été utilisés, le mode 'standard' ou 'fausses couleurs' associant les canaux 2, 3 et 4 (équivalents aux canaux MSS 4, 5 et 7) et le mode associant les canaux visibles 1 et 3 au canal 7 (infrarouge moyen). Les limites des sites tests y ont été repérées et intégrées à ces images.

L'*analyse statistique générale* de la distribution des valeurs dans les six canaux étudiés a eu pour but de cerner la qualité de l'information contenue dans chacun d'eux: dynamique et corrélations entre canaux (le canal 6, dans l'infrarouge thermique, n'a pas été pris en considération).

L'*analyse statistique détaillée* des valeurs de luminance observées dans les sites tests a été conduite en comparant les sites entre eux par les méthodes multivariées, puis les relations entre ces valeurs et la composition de chaque type de sites.

Suite à ces analyses, l'interprétation de la distribution relative des différents thèmes dans l'espace des données TM a permis de définir les centres des classes qui leur correspondent. Utilisant une *classification* basée sur la

Figure 2a. Landsat MSS - 4 avril 1981: composition colorée standard (256×256 pixels): MSS4 en bleu, MSS5 en vert, MSS7 en rouge. En jaune: les surfaces sableuses (sable quartzeux).



méthode barycentrique, nous avons enfin tracé une carte des principaux types de surface de la partie de l'image couvrant la zone test (512×512 pixels soit 15×15 km environ).

Résultats

L'observation des compositions colorées standard fait apparaître immédiatement le saut qualitatif apporté par la résolution de 30×30 m (Fig. 2a-b). Contrairement à l'image MSS, on reconnaît sur l'image TM les pistes principales et secondaires (grâce à leur fort contraste avec leur contexte), le cours précis des oueds, les formes de relief remarquables (petites buttes témoins, p.ex.).

Nous avons donc parfaitement pu nous y repérer, positionner les sites tests avec précision et identifier les formes caractéristiques du modelé comme on peut le faire sur une photographie aérienne à l'échelle du 1/50 000.

L'étude des relations entre canaux a montré que, comme dans le cas des données MSS, les valeurs des canaux rouge (3) et proche infrarouge (4) sont très corrélées; ceci est lié à l'absence de végétation verte. Les canaux 1 et 3 sont par contre nettement moins redondants. Les valeurs du canal 5 présentant une troncature par saturation n'ont pas pu être prises en compte. Le canal 7 enfin, apporte une information très différente de celles des autres canaux, comme en témoigne la composition colorée combinant les canaux 1, 3 et 7 (Fig. 3) où l'on voit notamment apparaître en cyan les formations gypseuses.

L'analyse statistique détaillée a montré que pour les canaux 2, 3 et 4 on retrouve exactement les mêmes rela-

Figure 2b. Landsat TM - 5 août 1984: composition colorée standard (256×256) couvrant la zone encadrée de blanc sur la Figure 2a. Remarquer la netteté des formes de relief. TM2 en bleu, TM3 en vert, TM4 en rouge.



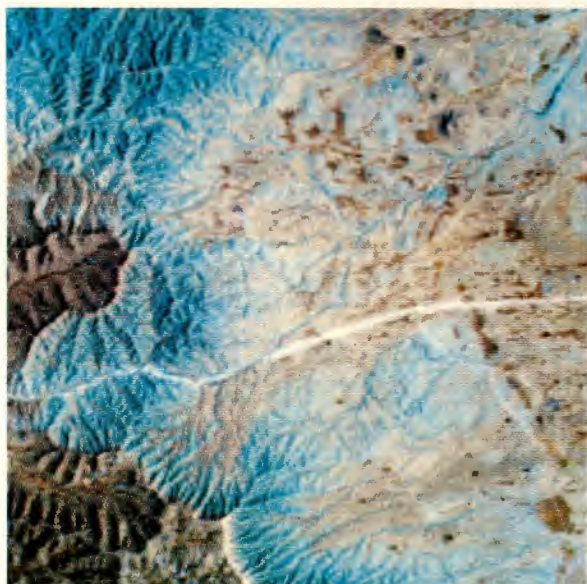


Figure 3. Landsat TM du 5 août 1984: composition colorée avec TM1 en bleu, TM3 en vert et TM7 en rouge. Remarquer en cyan les surfaces gypseuses.

tions entre composition des surfaces et luminance spectrale que dans le cas des canaux MSS 4, 5 et 7. Les mesures enregistrées dans ces canaux sont directement en relation avec la brillance, la rugosité et surtout la couleur des surfaces.

Grâce au nouveau canal TM1, dont la bande spectrale est centrée sur le bleu vert et donc complémentaire des deux autres (jaune orangé et rouge), cette perception des couleurs est fortement améliorée. Suivant le principe de la trichromie, il devient en effet théoriquement possible de distinguer une gamme de couleurs variées.

En ce qui concerne les sols, leur couleur de surface ne varie ici que dans la gamme des bruns jaunes aux bruns rouges (10 YR à 5 YR du système Munsell). Cependant, on constate que le contraste entre ceux dont la couleur est assez saturée (chroma ou pureté relativement élevée) et les autres apparaît encore plus nettement dans le rapport TM1/TM3 que dans celui précédemment utilisé (MSS4/MSS5). Il est ainsi possible de distinguer aisément les surfaces des sols d'après leur couleur suivant qu'elle est plus ou moins saturée, des teintes rougeâtres aux grises, en passant par les beiges.

La couleur des sols étant un des critères de diagnostic les plus spontanément et le plus couramment utilisé par les pédologues, on perçoit bien ici tout l'intérêt de cette nouvelle bande spectrale. Ces relations entre couleurs et réponses spectrales dans les trois premiers canaux de TM sont d'ailleurs un des axes de recherches actuellement poursuivis par notre équipe.

Compte tenu des remarques faites sur le canal proche infra-rouge (4), nous ne l'avons pas sélectionné pour la suite du travail. Le canal 7 par contre, spécialement

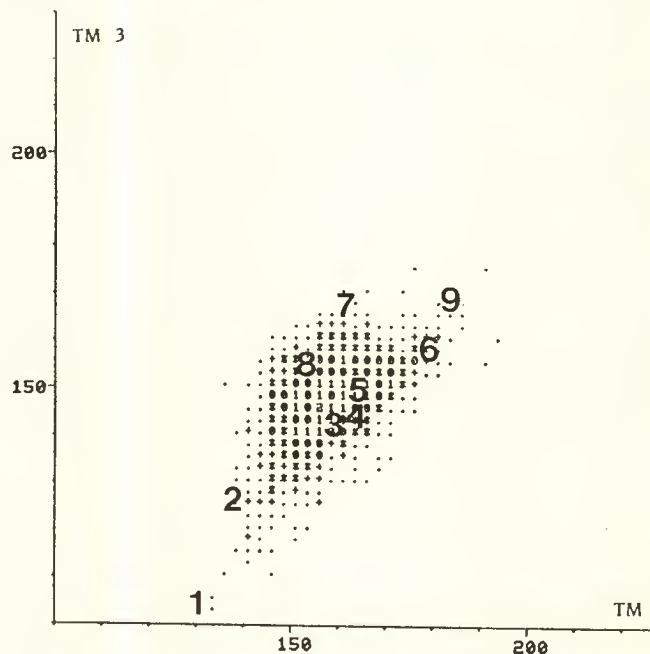
conçu pour répondre à des préoccupations de géologues, s'est révélé apporter des informations sur la nature minéralogique des surfaces. Les relations suivantes ont été observées:

- luminance moyenne à forte dans le visible et faible dans le canal 7: surfaces à dominante gypseuse;
- luminance faible à moyenne dans le visible et moyenne dans le canal 7: surfaces à dominante calcaire;
- luminance moyenne à forte dans le visible et forte dans le canal 7: surfaces à dominante quartzreuse (sables éoliens).

Le choix de la fenêtre spectrale de ce canal 7 (2080 à 2350 nm) n'est pas étranger à cet intéressant résultat, puisqu'elle correspond à la bande d'absorption des groupements hydroxyles. La présence de ces groupements diminue considérablement des sulfates hydratés (gypse), aux carbonates (calcaires et dolomies) puis à la silice (quartz), ce qui explique les variations observées.

En résumé, cet ensemble de résultats a montré que les canaux 1, 3 et 7 sont les plus intéressants pour notre étude. Pour chaque groupe de sites tests correspondant à un thème bien individualisé, nous avons identifié les valeurs radiométriques caractéristiques dans chacun de ces trois canaux, pour définir une classification multispectrale de l'image (méthode barycentrique). Elle a permis la visualisation de 9 types de surfaces dans la zone d'étude, sous la forme d'une carte schématique de la région de Tataouine-est (Fig. 1).

Figure 4. Position des centres des classes sur l'histogramme bidimensionnel TM1-TM3. Les surfaces se répartissent en fonction de leur 'brillance'. Noter la position des thèmes 7 et 8.



La distribution des centres de ces classes dans l'espace des données exprime bien les relations entre radiométrie et types de surfaces.

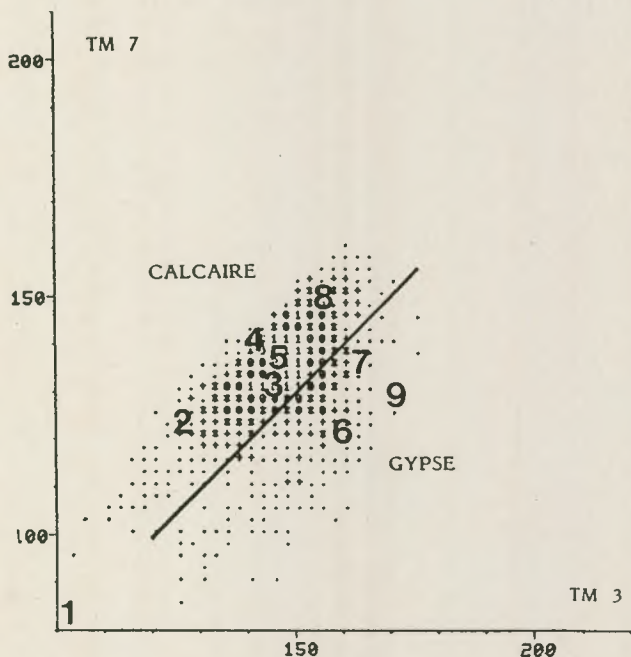
Ainsi sur l'histogramme bidimensionnel TM1/TM3 (Fig. 4), leur position le long de l'axe principal d'allongement du nuage de points dépend de leur brillance dans le visible.

Près de l'origine se trouvent les zones à l'ombre des reliefs (thème 1). En s'éloignant de cette origine on rencontre les roches affleurantes en cailloux et blocs et les zones de végétation dense sèche des bas-fonds. Ce thème 2 regroupe donc les surfaces de forte rugosité créant un taux d'auto-ombrage élevé.

En suivant toujours l'axe principal, les surfaces brillantes et très brillantes sont dans la partie opposée du plan. On remarque que les thèmes 6 et 8 se trouvent de part et d'autre du nuage de points, les surfaces gypseuses (6) étant grisâtres et proches des limons de couleur beige (5), alors que les sables quartzueux (8) sont rougeâtres (ils présentent des traces d'oxydes de fer).

Sur l'histogramme TM3/TM7 (Fig. 5), le phénomène le plus marquant est la distribution des thèmes perpendiculairement à l'axe principal, qui illustre bien l'apport du canal 7. Ainsi, les surfaces gypseuses sont les plus décalées vers TM3, puis les surfaces calcaires se trouvent vers le centre.

Figure 5. Position des centres des classes sur l'histogramme bidimensionnel TM3-TM7. Les domaines calcaire et gypse s'individualisent très nettement.



Conclusion

La première génération des satellites Landsat a fait la preuve de l'utilité des images fournies par son détecteur à balayage multispectral (MSS) pour l'étude des milieux arides. Dans le domaine des inventaires pédologiques, nous avons déjà utilisé ce type de données comme aide à la cartographie. Elles sont insuffisantes en elles-mêmes, mais en les associant aux autres sources d'informations, telles les photographies aériennes pour l'étude de formes de relief, les cartes géologiques pour l'étude de la lithologie et, bien sûr, les travaux de terrain, nous avons réalisé la carte de reconnaissance des ressources en sols de la région de Tataouine (Escadafal, 1985).

Au cours du présent travail, concernant la même région, nous avons montré que les données TM apportent des informations beaucoup plus complètes sur la morphologie des unités de terrain, leur couleur et leur lithologie. Une simple classification des données des canaux 1, 3 et 7 a permis de tracer une carte des principaux types de surfaces, déterminant autant de types de sols et de potentialités différentes.

Compte tenu de la saison à laquelle l'image utilisée a été enregistrée (août), nous n'avons pu aborder le thème végétation. Il ne fait pas de doute qu'une image prise au printemps permettra de délimiter, beaucoup plus précisément qu'avec MSS, les zones où se développe la végétation à cette saison (zones naturelles ou aménagées suivant les techniques d'aridoculture traditionnelle). Dans ce cas encore, cela constitue des informations précieuses, difficiles à obtenir par d'autres moyens.

Le traitement des données TM est donc un outil puissant permettant de produire des cartes détaillées de l'état et de la nature de la surface des sols (au sens large).

Ces cartes permettent une nouvelle ap, roche des milieux arides en exprimant des potentialités (ressources en sols et propriétés hydrodynamiques, ressources végétales), mais aussi des contraintes (traces de phénomènes de dégradation en cours, sensibilité à l'érosion éolienne ou hydrique).

Ceci correspond précisément aux préoccupations des spécialistes de l'étude et de l'aménagement de ces milieux, où la télédétection semble donc pouvoir répondre de mieux en mieux à leurs besoins.

Références

- Escadafal R. 1985. *Carte des ressources en sols de la Tunisie au 1/200 000. Feuille de Tataouine*. Direction des sols, Tunis, notice 37 p., 1 carte coul. h.t.
- Escadafal R. & Pouget M. 1986. Luminance spectrale et caractères de la surface des sols en région aride méditerranéenne. *I.T.C. Journal*, p. 19-23.

- Mulders M.A. & Epema G.F. 1986. The Thematic Mapper: a new tool for soil mapping in arid areas. *I.T.C. Journal*, p. 24-29.
- Pouget M., B. Lortic, A. Souissi, R. Escadafal & A. Mtimet. 1984. Contribution of Landsat data to mapping of land resources in arid regions. *18th Int. Symp. Rem. Sens. Env.*, Paris, 1-5/10/1984.
- Thompson D.R., K.R. Henderson, A.G. Houston & D.E. Pitts, 1984. Variations in alluvial derived soils as measured by Landsat Thematic Mapper. *Soil Sci. Soc. Am. Jl.*, 48(1), p. 137-142.

Processing and Interpretation of Thematic Mapper Images in the Province of Piacenza

Alessandro Annoni & Enrico Zini

RSDE, Milan

Rita Arcozzi

Ufficio Cartografico, Regione Emilia-Romagna, Bologna, Italy

This paper deals with the use of Landsat TM data to obtain soil maps of parts of the Po plain following the methodology used by the Cartographical Office of Regione Emilia Romagna. Through variations in tone and colour, satellite images show different levels of water retention depending on the variations in the physical characteristics of soil. Of the available images, two were tested: the first taken after a long dry spell (20/1/83) and the second after several rainy days (20/4/84). In this paper we describe and discuss the image processing methods available and the one best suited to our purposes.

The area studied, near to the town of Piacenza, was well known pedologically and field data were available. The spring image was considered to be the most interesting, the best image processing being colour composite of bands 4, 5, 3 simply enhanced by contrast stretching.

In order to investigate urban land cover, we selected composite bands of 4, 5, 1 to make it possible to compare Landsat-TM data and aerial photographs taken during 1985 at a scale of approximately 1:3500. We noted that 80% of the built-up areas visible on the aerial photographs were also visible on Landsat-TM data when photointerpretation was used.

Objectives

In 1985 the Statistics and Information Service of the Region of Emilia-Romagna decided to undertake a series of experiments that had been started by using data relayed by Landsat satellites 4 and 5, and which in the near future would also include data received from the SPOT satellite.

This interest shown by the Region coincided with the time when the European Space Agency were granting Thematic Mapper images free of charge to anyone who might want any, as a promotional policy towards the development of new methodologies.

Initial investment enabled some minimum objectives to be reached, and these, in turn, afforded glimpses of definite ways of dealing with both the analysis of more complex problems and with the integration of such problems into those systems then in operation or in the act of being acquired by the Regional Informations System.

The research themes were landscape unit reconnaissance and mapping in order to obtain correct pedological car-

tography and territorial evolution as a result of anthropical intervention.

Processing of the images was entrusted to the R.S.D.E. srl company of Milan, whereas the results were analysed with the help of CNUCE CNR of Pisa who have considerable experience in this field.

In the light of the themes that had been chosen, the Val d'Arda and Val d'Ongina (about 43 000 ha) in the province of Piacenza were selected as research territory, mainly on account of the large amount of pedological data already available; also of considerable use were the agrometeorological archives of the Provincial Administration of Piacenza, which supplied data on rainfall, which was of fundamental importance in distinguishing which images were most suited to our aims.

Both research topics only covered the plain area of the province of Piacenza, as a digital model of the terrain is needed to make correct geometric use of satellite images of uneven surfaces.

Landscape Units for Pedological Cartography

Our first theme concerned the way that thematic mapping was carried out: in other words it was a question of deciding what contribution suitably selected and processed satellite images might make towards the identification of landscape units, a basic requirement in soil cartography.

At this point an explanation has to be given of the pedological mapping methods used by the Cartography Office experts. After extensive bibliographical research of all existing evidence, directed mainly at historical maps and data, aerial photography is analysed for identification and mapping of landscape units according to Pattern Analysis and Physiographic Analysis Methods (FAO 1967). The former method is based on the strict correlation between the pattern in the sense of the appearance of determined territorial features such as morphology, drainage and soil type or association of soil types, whereas the latter method is based on extensive knowledge of physiographical units such as sedimentary processes that have determined the present landscape (here, too, a particular type of soil association corresponds to a certain landscape unit).

Areas marked in this way formed the basis for field survey aimed at checking just how accurate any hypotheses were that had been put forward while photographs were still being interpreted, thus also offering a quantitative aspect to pedological data.

It was a case of identifying areas within which geological-environmental, genetic processes were either correlated to the physiographical features of the territory or to the pattern of its photographic or multispectral image: to put it more simply such phenomena that could be directly or indirectly observed were correlated to the processes that had generated them. Before correct use could be made of the information acquired from these observations, a sound knowledge of sedimentary processes was obviously needed so as to make good analysis of the photographs for the pedological survey. The future prospects of this research theme were obviously reflected in the fact that the Region opted for pedological cartography of the entire plain areas within its territory. In the future they might not only use aerial photography for this purpose (in this case usually at a scale varying from 1:30 000 to 1:50 000), but also, and perhaps even exclusively, images that have been received from space.

The theoretical advantages gained from using satellite images as opposed to aerial photography for this particular research were:

- 1) it was possible to benefit from images received during moments of particularly favourable climatic conditions;
- 2) increased radiometric resolution was acquired both in terms of the number of spectral bands and of quality of acquired data, thus optimising the possibilities of differentiation between data types;
- 3) global shots of the entire territory were available with the subsequent possibility of objective comparisons being made of areas that were far away from each other;
- 4) the sensors of these images were insensitive to human factors, i.e. the possibility of obtaining the absolute radiance values of objects, as opposed to aerial photography where exposure times, different photographic emulsion, developing, etc. did not enable quantitative analysis of the image;
- 5) there was the possibility of multi-temporal analysis.

The first advantage was derived from the possibility of choosing two images, one from 20 January, 1983 after a long period of drought, and the other from 20 April, 1984 after a period of diametrically opposed meteorological conditions, i.e. three days after rainfall involving about 30 mm of precipitation.

In this case the existing pedological map of the Val d'Arda and Val d'Ongina territory had been used as a model of the ground truth and panchromatic photographs at a scale of about 1:33 000 that had been taken in 1954 were interpreted for analysis.

Description of Processing

A detailed description of processing follows. We aimed to examine the possibilities and limitations of communications relayed by satellite as an aid to studying Landscape Units and controlling urban area evolution. The processing of Thematic Mapper Images used during the course of this research may be summed up as:

- 1 - (3, 2, 1) colour synthesis
- 2 - (4, 3, 2) colour synthesis
- 3 - (4, 5, 7) colour synthesis
- 4 - (4, 5, 3) and (4, 7, 3) colour synthesis
- 5 - (4, 5, 1) and (4, 5, 2) colour synthesis

N.B.: The order in which Thematic Mapper bands are arranged in colour syntheses, indicates their implicit association with conventional red, green and dark-blue colours.

(3, 2, 1) Colour Synthesis

The presence of band 1 in blue, a region of the spectrum highly sensitive to atmospheric diffusion, did not contribute to the sharpness of the image, and the resulting effect was like that of a colour photograph taken at high altitude.

It was noted that the effect of moisture in the terrain caused scarcely perceivable chromatic variations.

(4, 3, 2) Colour Synthesis

Near-infrared, red and green colour synthesis was particularly suited to differentiating areas with vegetation from those without any, and it was generally useful in preliminary evaluation of the type or extent of classes of land cover present in a given territory. All classification procedures should be preceded and guided by this kind of evaluation.

Near infrared was highly sensitive to the amount of assimilative biomass. What was more, in this region of the spectrum, vegetation had a higher spectral response than bare soils did.

Yet red was a region of chlorophyll absorption, so land that had vegetation was less reflecting in red than bare land. Thus in the presence of vegetation the red and near infrared bands were inversely correlated, whereas in the absence of vegetation correlation was direct. This justified the combined use of these two bands for the study of cover classification.

It should not, however, be forgotten that the spectral response of vegetation does not depend solely upon the density of biomass. It also depends upon the particular species of vegetation, so comparisons of biomass density are only valid when made between areas that were covered with the same kind of vegetation.

Within the same class of vegetation colour variations ranging from dark-brown to orange and brilliant red could denote increasing levels of biomass density.

When a comparison was made of the colours associated with different classes of vegetation with consistent terrain cover and contour it was noted that the red colour attributed to conifers, broad-leaved vegetation and meadow or pastureland became increasingly bright.

Bare soils were characterised by varying degrees of greens and bluish greens.

Near-infrared depended slightly upon soil moisture content. In fact variations between loamy and sandy soils were scarcely perceivable in this band.

Within the range of consistent vegetation cover and contour, two types of chromatic anomaly were encountered.

The former was in areas that tended to be a darker red, which indicated structural alteration to foliage or a loss of leaves caused by water stress, disease or chemical agents.

The latter type of anomaly was represented by dark-brown areas signalling a decrease in chlorophyll content (chlorosis).

Cultivated terrains offered considerable chromatic variation which was linked not only to the vegetation species but also to the complexity of different kinds of cultivation practised.

Water courses were noticeable on account of their substantial lack of colour, whereas bare rocks, quarries and scree stood out in shades of brilliant white.

Urban areas were mainly a bluish colour, and if this blue colour was subjected to more detailed analysis it revealed tremendous spectral variation according to the different kinds of construction materials used and the presence of vegetation.

(4, 5, 7) Colour Synthesis

This was a particularly interesting synthesis as it involved three bands entirely within infrared, i.e. within a region of the spectrum to which the human eye was totally insensitive.

Referring to the example of spectral response curves shown by green vegetation and also by soils it was noticeable that the bands in near and middle infrared displayed contrasting variations during the shift from vegetation to non-vegetation areas.

Reflectance in the near-infrared band 4 closely linked to the quantity of biomass, dropped sharply, whereas in bands 5 and 7 in middle infrared it varied according to soil type and moisture content.

On account of these possibly contrasting tendencies, two images, one selected in near infrared and the other in middle infrared, would at first sight appear to be complementary.

The combined use, therefore, of these bands in one colour synthesis placed considerable emphasis upon variations in vegetation cover in any situation where the pedology and moisture conditions of the terrain did not undergo further variations to the side.

So the presence of different terrain types may not be immediately obvious because of this enormous contradiction regarding surface variations.

(4, 5, 3) and (4, 7, 3) Colour Synthesis

The presence of the near infrared band associated with the colour red in these two syntheses guaranteed partial analytical continuity as regards the (4, 3, 2) synthesis. Similarly, hues of orange and red signalled the presence of vegetation. Rivers, and rocks were also shown in this way.

Before analysing differences in the meaning of specific chromatisms we noted that the image itself had clear definition. Good image legibility was made possible by

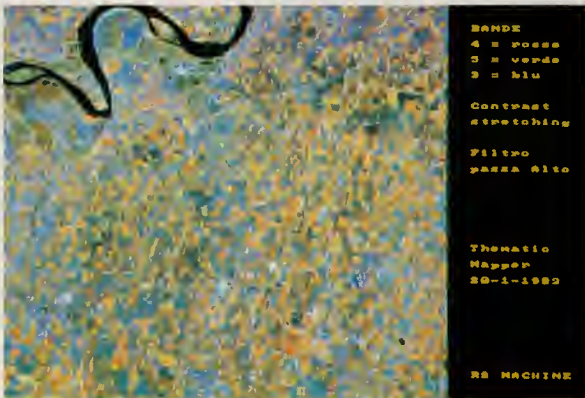


Figure 1. TM bands 4, 5 and 3 displayed in red, green and blue. The image was acquired on 20 April 1984 in the Po plain near Piacenza.

the prevailing presence of two infrared bands whose influence could be perceived on two accounts. Firstly there was good transmittance of the air in this region of the spectrum.

Secondly almost all of the bodies within the visible region offered good reflectance, and this favoured increased signal/noise ratio.

Once this consideration had been made, the only thing left for examination was the effect that the high sensitivi-

Figure 2. TM bands 4, 5 and 1 acquired on 20 January 1983. This image shows the town of Piacenza in the far west of Emilia-Romagna (Italy).



ty of the middle infrared bands to the presence of moisture in both soils and vegetation tissues might have upon the image.

In both syntheses, (4, 5, 3) and (4, 7, 3), the presence of moisture in both bare and vegetation land was indicated by bluish stains which faded at the edges.

The structure and layout of these stains would often appear to be quite irrespective of agricultural parcels and this made them stand out all the more and gave the impression that they had little to do with surface structures. Areas marked in the darkest blue were characterised by scarce drainage capability and should therefore indicate land that tended to be finely textured.

Whereas bare soils that were blue or light-green-bluish should have consisted of geo-pedological units that tended to be more loamy.

The differences between syntheses using band 5 and those using band 7 were not absolute, but they deserve some mention. Both vegetation and bare soils showed greater response in band 5 than they did in band 7. In fact the moist areas stood out in the (4, 5, 3) synthesis in a more brilliant blue and were easier to identify than they were in the (4, 7, 3) one.

Yet band 5 was slightly correlated to band 4 in near infrared, which meant that it carried two different sets of

information. The first set, the dominant one, was to do with moisture content, the second set was associated with foliar structure and quantity of biomass. Thus the surest pedological analysis could only be made in band 5 in areas where there was scarcely any vegetation cover.

(4, 5, 1) and (4, 5, 2) Colour Synthesis

(4, 5, 1) synthesis in near-infrared, middle infrared and blue infrared and (4, 5, 2) synthesis using green instead of blue were chosen for the study of urban areas.

It has already been pointed out that urban areas presented a wide range of spectral response. If one were to examine a dispersion diagram in bands 4 and 2, for example, it would be noticeable that the classification 'urban area' had maximum dispersion and its edges were easily superimposed onto those of other classes such as bare land, rocks and grasslands.

If, therefore, on the one hand, it was possible within an urban context to easily differentiate between different subclasses such as the historical centre, areas under completion or expansion and industrial ones, it could, on the other hand, often be difficult to differentiate urban areas from other classes upon a purely spectral basis.

Consequently the study of urban areas by satellite images cannot, as a rule, manage without some contribution from human or computer-assisted interpretation of photographs in order to identify and select urban areas upon the basis of structural and textural considerations.

Once this problem has been resolved, spectral information may have a valid contribution to make, both to a description of urban classification, and to a dynamic monitoring of areas of expansion identified by clearly-defined geographical growth poles.

In our research, buildings and other minor urban constructions usually presented increased spectral response in the visible region. For this reason, two syntheses were produced that could only be distinguished from one another by their different spectral band, in order to check which was the more efficient of the two.

The blue band and the green one were quite well correlated. But the former was more sensitive to different kinds of buildings, thus enabling differentiation between various urban classes and causing road networks to stand out in particular.

Band 4 in near-infrared made vegetation areas stand out particularly well. The validity of the combined use of bands 1 and 4 with band 5 had already been ascertained several times.

Analysis was made of dispersion per band pair in various parts of the territory around Piacenza. Indeed this

analysis confirmed how difficult it was to differentiate the spectral class of the urban area as a whole from the remaining ones. Yet the individual, thematic features of the urban areas stood out very well.

In spectral terms the historical centre appeared to be a clearly defined cluster standing out from the slightly more faded one associated with the residential and expansion areas.

The concentration of colour in the spectral class of the historical centre could largely be explained by the homogeneity of the materials formerly used in buildings, but also by the lack of vegetation as well as the generally small size of the roads.

Maximum spectral definition of urban themes was to be found particularly in the area around Fiorenzuola. The dispersion diagram of bands 1 and 4 showed increased spectral separation between the historical centre, the areas being completed and undergoing residential expansion and the industrial estates.

Final Considerations Regarding Processing

Initial, visual analysis of the use of (4, 5, 3) and (4, 7, 3) colour syntheses had already provided optimum comparison with the Landscape Unit Map. More accurate analysis was, however, required and this was obtained by digitising the limits of the Landscape Units on the map and superimposing them on the satellite image.

This superimposing operation was carried out by distorting the limits of the Landscape Units, through polynomial transformation, through a series of control points that were based mainly on crossroads that could be easily identified both on the map and on the image.

The only alternative to superimposing both these sets of information would have been to distort the image, but this would not really have been an appropriate solution since we only had qualitative information.

Furthermore it should be noted that the preliminary version of the Landscape Unit Map used was on a non-distortable support, so intrinsic inaccuracies in cartographical data would not have justified laborious superimposing methods.

As has already been mentioned, of all the colour syntheses carried out, the one most suited to our pre-established aims was the 4/5/3 band combination and it was processed according to a simple emphasising process, such as contrast stretching.

Of the two sets of images taken in January and April the spring one was preferred for this use. This went against

were acquired in 1986 and cover mainly the oasis region and the belt of sand dunes. A section of the map Baris 1:250 000 is presented as an appendix to this paper (Fig. 4).

During the preparatory work for the mapping projects useful experience was made which is summarized in the following subsections.

3.1 Geometrical Rectification

The experimental map of Berlin in scale 1:100 000 consists of four TM subscenes that had to be mosaicked and rectified. This was achieved by means of nine control points. Moreover, more than 40 check points were used to determine the accuracy of the result. These control and check points have been picked up from actual topographic maps within West-Berlin. However, for the surrounding area only more than 40 years old topographic maps in scale 1:25 000 were available. Although significant changes of the landscape had occurred in the meantime, a sufficient number of points could be selected, mainly man-made topographical features. Planimetric accuracy of the rectified image was determined to be ± 20.4 m or 0.68 pixels (original TM pixel size). This result corresponds to the experience reported by other investigators (Welch *et al.* 1985).

For the mapping projects in the Western Desert in Egypt no suitable maps were available. This is why surveying methods mainly based on Doppler techniques were applied to establish ground control. In addition to this, stereophotogrammetric point densification could be achieved by means of Large Format Camera images. The map Baris 1:250 000, which is a mosaic of MSS and TM data, is based on 15 control points, nine of them being determined by Doppler measurements and six by stereophotogrammetry. The map Baris 1:100 000 is based on six Doppler points and three additional control points determined photogrammetrically. In both cases the accuracy achieved in the rectified images is estimated to be around ± 0.2 mm in the map scales.

3.2 Spectral Band Selection and Enhancement Techniques

It became apparent that satellite image map production requires also some special enhancement techniques depending on the cartographic concept and on the properties of the geographical region concerned.

In the case of the Berlin map where a close-to-natural colour rendition was desired the TM-channels 1, 2 and 3 were selected for the production process and enhanced by suitable algorithms. But it turned out, that in these bands water areas could hardly be distinguished from neighbouring forest areas. Furthermore, the differentiation between deciduous and coniferous forests was insufficient. In order to solve these problems a special masking technique was applied.

Water areas as well as forest areas were separated in the data by means of multispectral classification using the near infrared TM band. But it is general experience, that such algorithms do not work without misclassification. Therefore interactive control at the monitor of the image processing system and revision of the errors was necessary. This procedure resulted in two digital masks, one containing the water areas, the other one covering the forests. Both masks could separately be used to manipulate the data of the main bands 1, 2 and 3. For the water areas the original data were completely replaced by an artificial set of data, so that these areas got a continuous blue colour. For the forest areas the data from the infrared channel were weighted by coefficients and added to the green spectral information in order to create differentiated forest regions.

In the desert area in Egypt the situation is completely different. A pleasing image rendition is achieved if the data are assigned to colours in the following combination:

MSS 4 and TM 2 in blue
 MSS 5 and TM 3 in green
 MSS 6 and TM 4 in red

However, this combination yields red colour for the vegetated areas of the oases. In order to convert these areas to the desired green colour again a masking technique was applied. The vegetation mask was derived by contrast stretching from TM band 4 and was used for partial changing the data from TM band 4 to TM band 3. The data of both spectral bands were added using weight coefficients in such a way that the vegetated regions in the oasis appeared in green.

The example of the map Baris 1:250 000 demonstrates evidently the potential of the radiometrical mosaicking approach. The oasis region itself is covered by TM data whereas the adjacent mountainous region in the east and the sandy plain in the west are imaged by MSS data. It is worth mentioning that the radiometrical mosaicking approach is flexible enough to combine the spectral bands applied from MSS and TM data to a mosaic without any residual colour discrepancies at the border lines.

3.3 Filtering Techniques

For the production of the Berlin map no spatial filtering techniques have been applied. However, recent experiments demonstrated a significant improvement of the interpretability of smaller topographical features if filters for gradient enhancement are used. This applies to the TM data of Berlin as well as to the data from Egypt. The combination of the resampling techniques described above and such filter operations seems to optimise the data for the purpose of image map production, so that even small geomorphological features become recognisable in the image map as one can see in the map Baris 1:250 000.

3.4 Reproduction and Printing

Image processing ends up with colour-separated files of image data which have to be prepared for printing. Multicolour satellite image maps are usually printed in the subtractive primary colours yellow, magenta and cyan in respective order of the primary additive colours blue, green and red.

The problem is that a harmonised colour rendition at the monitor is not a guarantee to achieve an equivalent result on paper. Some physical limitations of the materials and the equipment involved affect the fidelity of the reproduction and should be taken into account. The radiometrical transfer characteristics from the digital data to the screened film as well as to the paper of the map must be carefully considered. It is not before the first printed copies are available that colour effects, image clearness and interaction of graphical elements can be evaluated. Therefore, the standardisation of all relevant procedures is of great practical importance for this task.

4. Conclusions

From the studies and experiments carried out so far the following conclusions can be drawn.

Thematic Mapper (TM) data are very well suited for the production of image maps in the scale 1:100 000. The visibility of small topographical features can be optimised if improved resampling algorithms as well as filter techniques are applied. As compared with the MSS sensor the spectral bands, that are available from TM, offer more flexibility for the design of image maps and the application of masking techniques for enhancement.

Although SPOT data are acquired with higher spatial resolution, the application is limited by the smaller number of spectral bands. Therefore the combination of data from both sensors is a very promising approach for the purpose of image map production.

5. References

- Albertz J., M. Kähler, B. Kugler & A. Mehlbreuer (1987): A Digital Approach to Satellite Image Map Production. *Berliner Geowissenschaftliche Abhandlungen*, Reihe A, Band 75.3, pp. 833-872.
- Colvocoresses A.P. (1986): Image Mapping with the Thematic Mapper. *Photogrammetric Engineering and Remote Sensing*, 52 (1986) pp. 1499-1505.
- Gossmann H. (1984): Satelliten-Thermalbilder - Ein neues Hilfsmittel für die Umweltforschung. *Fernerkundung in Raumordnung und Städtebau*, No.16, 117 pp., Bonn.
- Kähler M. & I. Milkus: Berlin from Space - A Digitally Produced Satellite Image Map. In: *Mapping from Modern Imagery. Proceedings of the Symposium of Commission IV of ISPRS*, Edinburgh 1986, pp.85-92.
- Milkus I. (1984): Geometrische Entzerrung von Satellitenbilddaten zur Herstellung von Bildkarten arider Gebiete. *International Archives of Photogrammetry and Remote Sensing*, Vol. XXV, Part A 3b, pp. 713-720.
- Welch R., T.R. Jordan & M. Ehlers (1985): Comparative Evaluations of the Geodetic Accuracy and Cartographic Potential of Landsat-4 and Landsat-5 Thematic Mapper Image Data. *Photogrammetric Engineering and Remote Sensing*, 51 (1985) pp. 1249-1262.

Acknowledgements

The satellite image mapping project was sponsored by the German Research Foundation (Deutsche Forschungsgemeinschaft) within the framework of the Special Research Project 69 'Geoscientific Problems in Arid Areas'.

The project group received valuable assistance from many colleagues in Egypt and Germany. Especially the efforts of the General Petroleum Company (GPC) in Cairo must be mentioned. This cooperation is gratefully acknowledged.

Integrating TM and Cartographic Data

P. Mogorovich

CNUCE Institute, CNR, Pisa, Italy

The aim of the study was to investigate the type of problems arising from the integration of Landsat TM data with cartographic data and to evaluate the benefits of this exercise. As both types of data give complementary information, their integration is particularly interesting.

The results of our experience are expected to be of interest for administrative and technical operators working for local government. The average size of these local authorities (approximately 15 000 km² with a population varying between 1 and 6 million inhabitants) means that the different operations involved in town and country planning are performed using cartographic documents with a scale of between 1 : 10 000 and 1 : 200 000. Some of these documents could use TM data as an information source.

1. Objectives

The integration of TM and cartographic data has the following main objectives:

- to superimpose TM and cartographic data so that similar features, documented and updated at different times, can be compared visually;
- to superimpose TM and cartographic data so that different types of features can be compared visually;
- to employ TM data to update basic or thematic maps and documents.

The following organisations participated in the project:

- Telespazio contributed equipment and experts, in particular for the experience described in section 5;
- CNUCE-CNR contributed equipment and experts, in particular for the experience described in section 6;
- the 'Regione Toscana' local authorities supplied all the cartographic material, additional data on magnetic supports, and competence in the sectors of cartography and photo-interpretation;
- ESA/Earthnet supplied the promotional material for the project.

2. Technical Premises

The first decision to be made concerned the type of cartographic data to be superimposed on the TM data. At this stage of the project, our choice was determined by the data available and by technical requirements.

We had a series of cartographic data in digital format; as a sufficiently powerful geographic information system was not available to obtain derived data, we were obliged to limit our efforts to the primary data. Certain territorial

information (administrative boundaries with associated thematic values) and linear data (communication networks) was of particular interest.

The integration of data provides two types of information: (i) information from thematic or cartographic documents, which for the operator is direct and quantified information; (ii) information associated to photo-interpreted remote-sensing data.

The extraction of information from remote-sensing images by means of photo-interpretation is interesting for a series of reasons, namely:

- the improvement in the geometric resolution which makes the images appear as high-altitude aerial photos;
- the partial success of automatic classification and its cost in terms of computing resources and competence;
- the speed with which a result can be obtained by photo-interpretation;
- the fact that specialised expertise in photo-interpretation is now available in a number of different sectors.

The integrated management of TM and cartographic data requires highly complex computing tools because of the functions to be performed; a 'user-friendly' interactive system is necessary since the user normally is not a computer expert. Such a system will be divided into two parts, one for image processing and the other for the analysis of cartographic data. Presently two types of tools are available: the first generally implies an expert, the second is relatively new, little known, technically complex, and often oriented only towards pure cartography. There

are very few tools currently available which integrate the two aspects of image processing and cartographic data management.

3. Defining the Problem

In order to obtain the best possible results from the integration of cartographic and remote-sensing information, the data must be superimposed with the maximum of precision. The degree of precision will influence the final product and in particular will determine the largest scale at which it is possible to operate. This will normally be between 1 : 50 000 and 1 : 100 000. In view of the average dimensions of the areas regulated by the local government authorities, it is important to obtain the largest possible scale. Our efforts were concentrated on this problem.

The cartographic data were taken from official cartographic documents and maps with a scale of 1 : 25 000, using UTM projection. According to cartographic standards, this means that the coordinates of a point identified on the map can be verified to a maximum error of 5 m. The data was digitised using criteria which tolerate a further increase in error within 0.5 mm on the map, which corresponds to 12 m. Summing the two errors, we assumed that the numerical coordinates attributed to a point will be equal to the true coordinates, with an error which will not exceed 20 m.

For the remote-sensing data, the matrix coordinates of a pixel cannot be immediately translated into its geographic coordinates but a number of parameters must first be considered. These include the asset of the satellite at the moment of acquisition, differences in projection, the presence of reliefs, atmospheric conditions, and also unpredictable situations such as, for example, the 'a posteriori' generation of a scanning line when there is loss in synchronisation during acquisition by the sensor. When integrating remote-sensing and cartographic data, it is possible to superimpose the former on the latter or vice versa. One of the two images must thus be defined as the reference image, leaving the other for eventual modifications.

Our first impression was that it would be better to use the remotely sensed data as the reference image, and to modify the geographical data. In fact, geographical data, which are generally in 'vector form' can be modified (transformed, rotated, etc.) with no loss in quality whereas the deformation of a 'raster'-type image implies a resampling and a consequent quality loss.

However, in the end, the opposite path was chosen, i.e. we decided to take the cartographic image as the reference image and superimpose the remotely sensed image on it. The reasons for this were:

1. having to select a reference image it seemed wise to choose the image with the greatest geometric precision;
2. the opposite choice would have presented an unfamiliar image to the expert in the sector (images which were not oriented towards north, unusual map frames, etc.);
3. when analysing multi-temporal series of images, this choice is more neutral with respect to the different images;
4. merging images coming from two types of data, the geographic view is the most convenient one;
5. some data of cartographic origin are in 'raster' format and a resampling of such data is in any case necessary (e.g. Digital Terrain Model, DTM). Clearly, we always made allowance for deformations caused by resampling and, above all, we tried to avoid further sampling an image which had already been resampled.

It would have been possible to transform a complete 'frame' into an image which could then be superimposed on the cartographic images. However, tests have only been made over small areas. This is because the areas of interest are relatively small (approx. 400 km² compared with almost 6400 km² for the entire 'frame') and because, otherwise, the computing resources involved would have been considerable. Furthermore, it seemed reasonable to test small areas in an attempt to obtain a greater precision.

In order to evaluate the precision of the superimposition of cartographic and remote-sensing data, certain basic parameters must first be defined.

Once the superimposition algorithm and its parameters have been defined, a common method consists in transforming the reference points for which the coordinates are known into the two images and comparing the known coordinates with those that result from the transformation. However, this method gives results which are open to criticism. A more correct method is to divide the ground control points into two subsets: one will be used to compute the parameters for the transformation algorithm and the other, independently, for error evaluation.

Both these methods are influenced by the error, at times considerable, with which we are able to define the coordinates of the ground control points on a remotely sensed image. A better criteria is not to use 'control points' but 'control structures', especially linear-type structures. This method has been adopted to compare linear structures on cartographic documents (roads) with their remotely sensed image. The comparison was visual. It should be noted that the view of the image without applying a zoom (i.e. with a 1 : 1 enlargement) inhibits quantitative measurements, whereas, on the contrary, an

excessive enlargement (more than 4 : 1) makes a precise evaluation of the structure in the remotely sensed image impossible.

As is known, each land point of height h , viewed from the satellite at angle a with respect to nadir, is recorded in a position which is displaced towards the exterior of the path of the orbit by a value dX

$$dX = h \cdot \sin(a)$$

When the value of dX is small with respect to the dimensions of the pixel, the deformation is negligible. Resolutions such as that of the TM can, however, cause macroscopic errors. For example, a point at 60 km from the path of the satellite will be displaced towards the exterior by 85 m for every 1000 m of altitude, equal to 3 pixel. As can be seen, this error is higher than the limits of precision which we had defined, and thus allowance must be made for this effect.

Two different experiments have been performed to evidence different aspects of the problem.

The first consisted in the superimposition of remote-sensing data on cartographic data for a relatively simple zone, i.e. a level area with many roads and fairly regular structures. In this way, it was possible to acquire a large number of control points and thus evaluate the superimposition errors analytically. We refer to this as the Grosseto experiment.

The second experiment was carried out in the Garfagnana area. This is an extremely uneven area, rich in vegetation but with few roads or recognisable structures. There were few identifiable ground control points and even these were relatively uncertain. In addition, the area chosen was on the edge of a frame. In this way, the same scene could be seen from two different points of view (two orbits) and the effect of the reliefs could be better evaluated.

The experiments were conducted using two automatic image processing systems. The first is the Telespazio IIS system, mod M575. This system uses a Digital PDP11/780 system and has an interactive image display station. The software provides all the functions normally used in remotely sensed image processing.

At CNUCE we have used the CIPS system. This system has been designed to permit new functions to be developed easily and to offer very fast data processing response times. It runs on an IBM 3081K with a VDS701 restitution terminal.

According to cartographic precision standards, at a scale of 1 : 25 000, the precision of a point, or the maximum error between a point on the ground and its cartographic

representation will be 5 m. We will call this type of error Eg .

The remotely sensed data are presented as sets of pixels. Each set contains a radiant information and, implicitly, a geographic information. This second information associates each pixel, or better the geometric centre of each pixel, to a pair of geographic coordinates. This association is made within a certain error, which will be called Ep .

The third parameter which we consider is the size of the pixel. It is generally considered that the radiance from a rectangular area is measured and directly connected to the instantaneous field of view. If this area is rectangular, we will call the length of the shortest side R .

Once we have defined these three values, we can analytically define the acceptability criteria for the superimposition of a cartographic point on remotely sensed data. The ideal acceptability condition is that a cartographic point on the ground is included in the field of view of the pixel which is associated to it. This is expressed as follows:

$$Ep + Eg = < R/2 \quad \text{Eq. (1)}$$

It may be convenient to introduce a parameter K defined as

$$K = (Ep + Eg) \cdot 2/R \quad \text{Eq. (2)}$$

It can be easily seen that if $Ep + Eg = R/2$, K will assume the value 1, otherwise it will assume higher values. From a geometric viewpoint, the cartographic point considered is found within the pixel assigned to it if $K \leq 1$. If, on the other hand K is included between 1 and 3, it will be found in the adjacent pixel, if between 3 and 5 two pixels on, and so on.

From Eq. (2) it appears that K can be reduced simply by increasing R , i.e. by using large size pixels. This is only true from an analytical viewpoint. In fact, according to the commonly accepted standards, a restitution is good and suitable for photo-interpretation when the final document has a density of at least 4 pixels per linear mm. Therefore, the value of R is determined by the restitution scale and it is thus necessary to operate on Ep and Eg to reduce the value of K .

4. Analysing the Data

For this study, ESA/Earthnet has provided a total coverage of Tuscany. The images are the following:

Image 191.30/1 (NW) of 11.07.84

Image 192.29/3 (SW) of 03.08.84

Image 192.29/4 (SE) of 03.08.84
 Image 192.30/1 (NW) of 03.08.84
 Image 192.30/2 (NE) of 03.08.84
 Image 192.30/3 (SW) of 03.08.84
 Image 192.30/4 (SE) of 03.08.84
 Image 193.29/3 (SW) of 25.07.84
 Image 193.29/4 (SE) of 25.07.84

The data are of the 'system-corrected' type.

A geometric type error has been declared for band 5 of the TM sensor. Because of this error, linear structures parallel to the satellite path appear curved, and oscillate around the correct position. For this reason, this band was not considered during the geometric considerations. Furthermore, numerical data given by the digitising of maps in scale 1 : 25 000 was used.

The most used data are the lines of communication (railways and roads). They have been digitised using tablets; the maximum tolerance between the map data and the acquired data is 0.5 mm. The basic unit for the communication lines is the 'arc'; an arc is that part of a communication line between two junctions. Furthermore, a value is associated to each arc which identifies the type of road or railway. The roads have not been digitised within the urban centres.

These data are linear structures, easily found on the remotely sensed image; for this reason, they provide excellent elements to verify the validity of the registration.

5. Grosseto

For our first trial we chose a flat area with structures which would permit the ground control points to be chosen easily. The area corresponds to sheet 128 of the official Italian Geographical Military Institute (IGMI) map for Grosseto. The image is 192/30, quadrant four, of 3 August 1984. A subimage of the entire quadrant, 1300 lines by 1600 columns, was processed.

14 ground control points were identified in the image; these were generally crossroads or easily recognisable field boundaries. The same points were then identified in the image and their UTM coordinates were measured on the updated maps of the Tuscan Region at the scale of 1 : 25 000.

Test	Polynomial Degree	Number of GCP	Average Error (m)
1	1	10	18.88
2	2	10	9.83
3	3	14	93.21
4	3	12	56.50
5	3	11	4.17
6	3	11	3.22

The coefficients for an interpolating surface were thus calculated using a least square algorithm. The errors obtained vary according to the polynomial degree and the control points used; they are reported in the table below.

The data for tests 3, 4, 5 and 6 are particularly interesting. It can be seen that by eliminating certain control points, the errors can be greatly reduced and if different combinations of control points are chosen, the errors vary appreciably. As the polynomial degree is high, the adjustment of the interpolating surface is good, but there is the risk that the error outside the control points is high.

In a second experiment, the data for the lines of communication (roads and railways) have been transformed into raster format, giving an image of 800 columns and 720 lines (25 m pixel). All the elements are at zero except for those where the communication lines are present. The remotely sensed image has also been resampled at 25 m and has been superimposed on the image previously described.

This technique has made it possible to select with good precision a sufficiently large number of control points for the superimposition zone. The density has been approximately one control point for each 10 km². Therefore, the coefficients of a transformation polynomial have been calculated under various conditions. The results are given in the following table.

Test	Polynomial Degree	Number of GCP	Average Error (m)
7	1	32	25.14
8	1	27	23.84
9	2	32	22.26
10	3	32	20.05
11	3	31	18.57

In this table, the degree to which the error depends on the choice of control points can be clearly seen.

In these trials no allowance was made for the effect of the deformation caused by reliefs as the area studied was completely level.

From Eq. (1) it can be seen that the required condition was not verified and that the error ($Eg + Ep$) is approximately 30 m.

Considering the use which will be made of these images and the restitution system employed, it can be considered acceptable to contain this error within approximately 5 mm on the output document; thus the scale is implicitly defined as 1 : 60 000.

In any case, this information is to be considered purely indicative as different applications may require a greater precision or accept larger margins of tolerance.

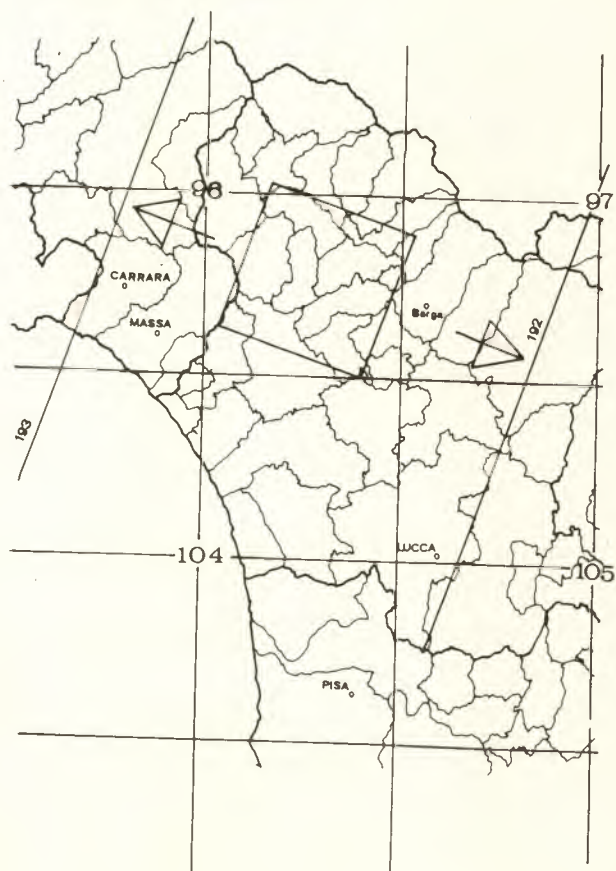
The final product, restituted by an Optronix C4300 has been analysed by cartographic experts of the Tuscan region. The image was judged suitable for a rapid updating of the basic cartographic documents with respect to the communication network, expansions of urban or industrial areas, and changes in quarry sites.

6. Garfagnana

The aim of the experiment performed in this area was to verify the geometric quality of the remote sensing data and the advantages of using these data in areas which are unfavourable from an orographic viewpoint.

In fact, the area examined presented considerable variations in altitude. In addition, these variations are almost perpendicular to the path of the orbit and are relatively distant from it.

Figure 1. The area under test is between tracks 193 and 192. The 'relief effect' may be observed from two different points of view. Here and in the other figures the grid and the numbers 96, 97, 104 and 105 refer to the standard 1 : 100 000 cartography of the Italian Military Geographic Institute. The irregular lines are the boundaries of small local governments, some of which are unidentified.



The images available for this zone are:

192.29/3 (SW) 3.08.84 - (NE side) (S237)

192.30/1 (NW) 3.08.84 - (SE side) (S139)

193.29/4 (SE) 25.07.84 - (W side) (S144)

These three images present a wide area of overlapping. This area is seen from orbit 192 as left marginal and from orbit 193 as right marginal. Consequently, the effect of the reliefs is to produce opposing and therefore more easily observable effects in the images coming from the two different orbits (Fig. 1).

The predominant feature in the area is woodland; other visible structures are roads, some quarries, a number of small urban centres and two medium-size lakes.

The first operation was the geometric recording of the image. To perform this, it was necessary to identify a number of easily recognisable points on the image and on the basic maps.

The procedure to search the GCPs uses the CIPS system and a VDS701 terminal. A number of restrictions caused by the relatively low resolution of the terminal ($512 \times 512 \times 12$) and its connection to the CIPS system (serial port with data compression) oblige the search of the GCPs to be made using a single band. Algorithms to improve the contrast offer a good view of the image, even if it is monochromatic.

However, the characteristics of the area are such that it is difficult to recognise a structure in the image and associate it to the corresponding structure on the maps. For this reason, we have developed a procedure which operates in the following way.

Three GCPs are identified in the image, as far distant from each other as possible. On the basis of these three points, a first geotransformation is performed and an intermediate image is obtained which can be superimposed on cartographic documents, even if there are some errors present. Cartographic data can then be superimposed on this draft image in order to identify linear structures; positioning the cursor on a pixel, its UTM coordinates can be obtained or a pair of coordinates can be entered and the cursor can be moved to the corresponding pixel. These features, together with the zoom functions make the search of GCPs relatively easy in zones where otherwise it would have been extremely difficult.

In order to identify the GCP, the information content of a number of bands has been analysed with reference to objects present in the area under examination. Band 4 was found to be good for the identification of rivers and lakes; however, the roads were not visible and the quarries could only be seen with some difficulty. The visibility of a bridge over a river was also very poor. Bands 1 and 2 were equivalent. The roads and the quarries were

clearly visible and so was the previously mentioned bridge. Band 3 appeared to be generally good; the bridge, quarries and roads were all visible.

The most easily identifiable GCPs were the roads; both surfaced and unsurfaced roads gave a sufficiently high contrast with the environment. Nevertheless, very often, they were covered by the tree tops, particularly leafy at the time the data were acquired. Consequently, even a long road could often be followed only for relatively short segments; at times it was even impossible to match a road to the corresponding road on the map.

Other interesting GCP were given by the rivers and lakes; particular bends were readily recognisable by their shape even if their geometric identification was questionable. In fact, erosion factors and variations in flow rate can cause considerable discrepancies between image points and the corresponding points on the maps. For this reason, the GCP acquired in correspondence with the edges of the rivers or lakes have been chosen where the banks were as steep as possible. This information, retrievable from the cartographic documents, guarantees the stability of a point over time, independently of variations in flow rate and erosion factors.

Despite the care taken, the number of ground control points identified was not high. Furthermore, as we were

Figure 2. The Ground Control Points identified in the S 138 image.

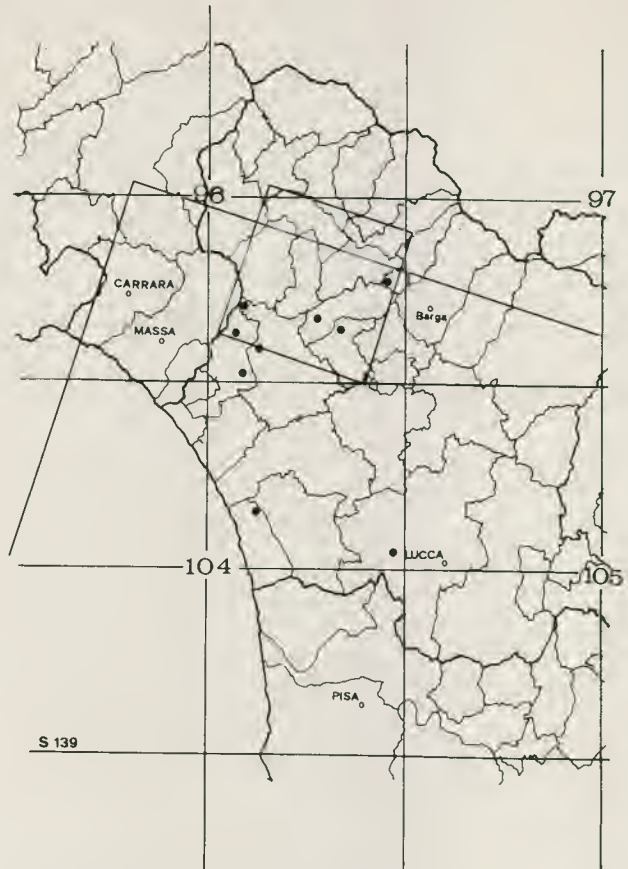
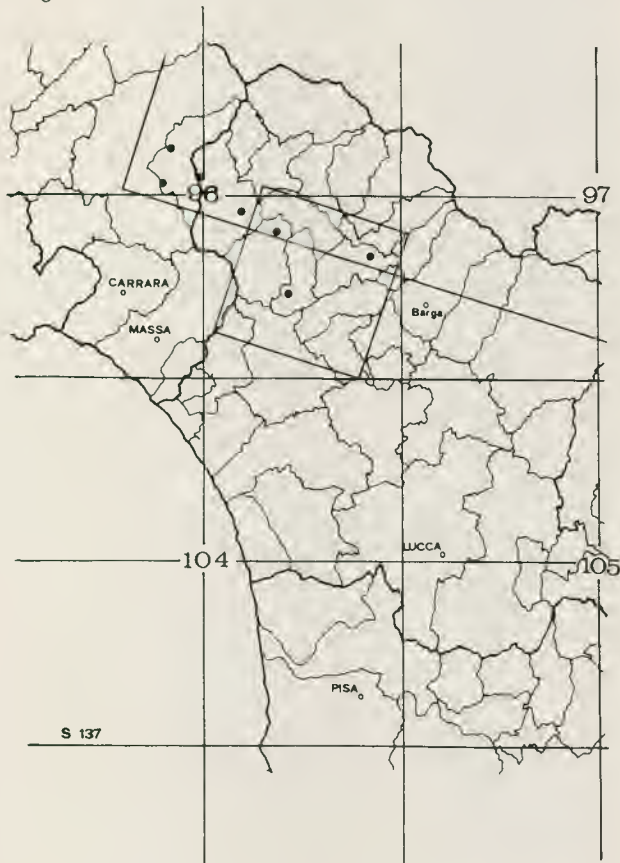
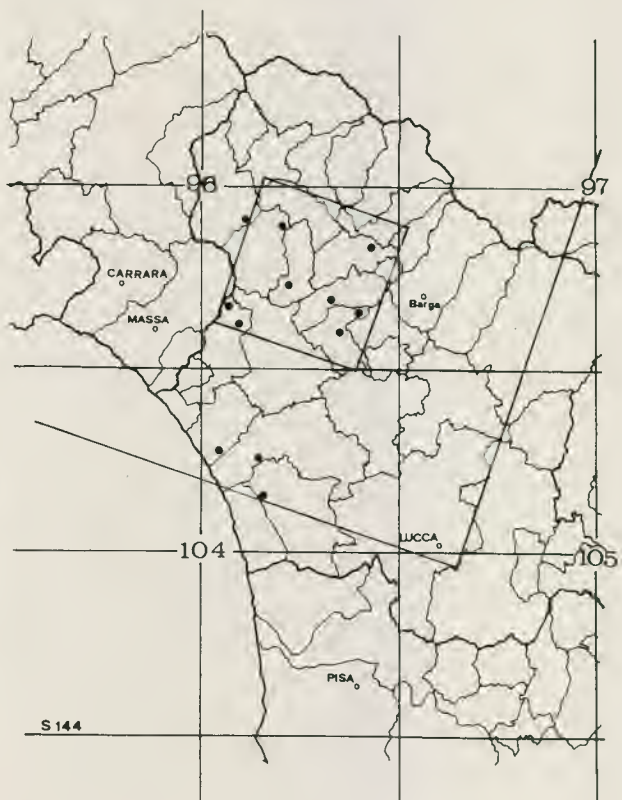


Figure 3. The Ground Control Points identified in the S 139 image.

Figure 4. The Ground Control Points identified in the S 144 image.



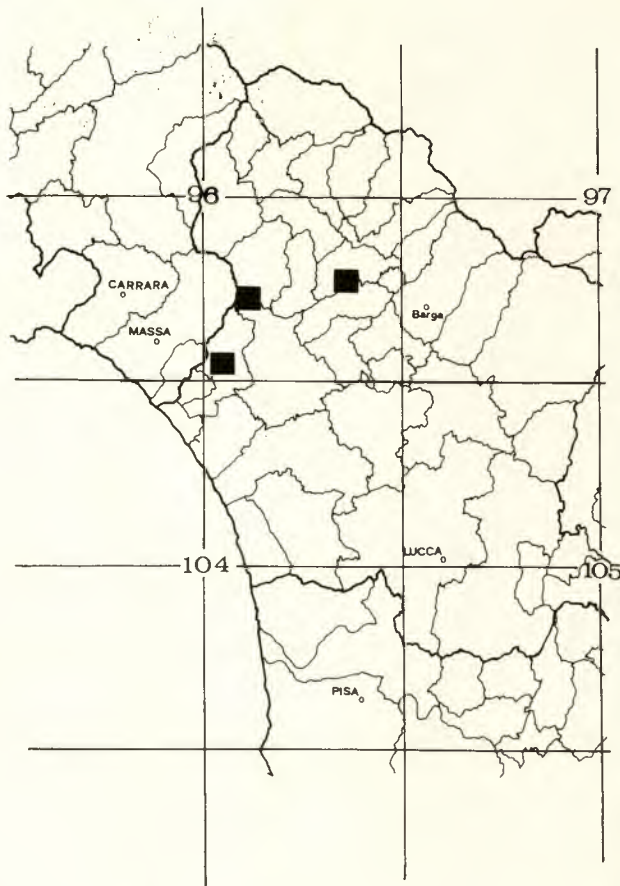


Figure 5. The three black figures identify the test areas used to visually check the registration errors. In these little areas no ground control points have been taken.

at the edge of a quadrant, it was difficult to identify enough points to completely surround the area under examination. The GCP used are reported in Figures 2, 3 and 4.

Three procedures were available for the geometric transformation. Each of these, in turn, required a series of parameters. The first uses a polynomial transformation, the second is based on a triangulation criterion, the third on a vectorial sum of the deformation effects of a number of GCPs on a generic point. It was decided not to use the latter two procedures as the choice of parameters is critical and it is possible to obtain undesirable effects.

The polynomial transformation has been used, with the polynomial degree equal to 1. Given the relatively small area and the small number of control points, it would have been useless to employ high polynomial degrees and it could have produced undesirable local deformations. The cubic convolution resampling technique was used as the image was intended for a purely visual and not a numerical analysis.

In an attempt to evaluate errors in transformation a procedure was developed which can be used to choose two

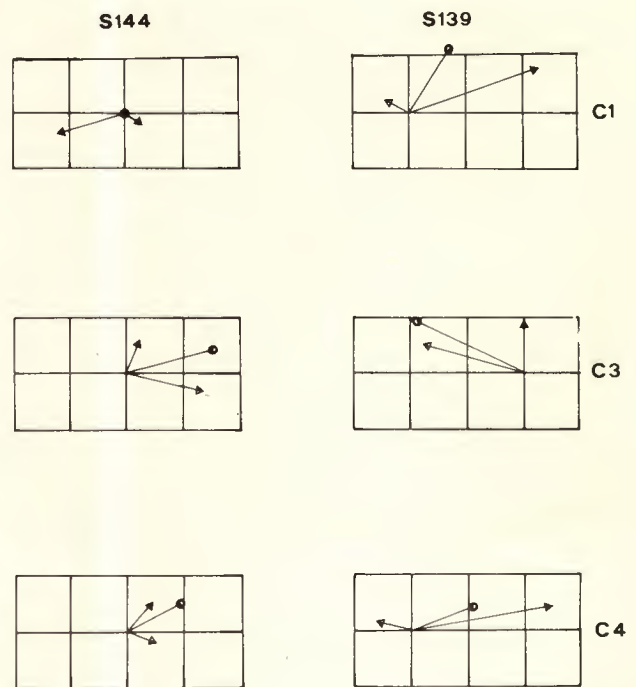


Figure 6. In this figure different vectors point out the registration errors in the three test areas (C1, C3 and C4) in the case of the image taken from the left (S144, left column in the figure) and the image taken from the right side (S139, right column in the figure).

The origin of the vectors identifies the centre of the test area; the 'light triangular' vector describes the error due to the relief, i.e. the point where the test area should be seen due to its elevation. The 'dark triangular' vector indicates where the test area is, in the image, after the transformation has been performed. The 'circular vector' points where the test area is, in the image, after a correction has been performed, considering the elevation of the ground control points.

The distance between the circle and the light triangle represents the final registration error while the distance between the dark triangle and the circle represents the gain due to the ground control point elevation correction.

A pixel in the figure represents two image pixels.

sets of GCPs: (i) to perform the transformations, and (ii) for error evaluation. Each ground control point is defined by its image and geographic coordinates and has two 'flags' associated to it. If the first is 1(0) the point will (not) be used to define the transformation; if the second is 1(0) the point will (not) be considered to evaluate the average error of the transformation. Every combination is permitted. This procedure makes it possible to select rapidly the most suitable points, rejecting those which have been acquired with an obvious error.

The evaluation has been performed by comparing visually structures of the image against structures on the maps, superimposed on the image. These structures were roads with well-defined forms and a good contrast. The displacements were observed separately by two operators, and the values were averaged.



Figure 7. In this figure the final result of the Grosseto experience is shown. The image is a TM, registered and resampled at 25 m. Bands 4, 3 and 2 modulate red, green and blue. Roads are overlaid in white colour and railroads are yellow.

In Figure 5 the three sample areas used for the comparison are shown. In these areas no ground control points have been taken.

Figure 6 gives a graphic representation (direction and width) of the displacement between the cartographic documents and the image. The data are reported on the left for image S144 (193.29/4) and on the right for image S139 (192.30/1), and are represented by the vector with the shaded triangular point.

Nevertheless, in this area, the relief effect causes considerable error. For this reason, a correction which allows for the altitude of the ground control points has been applied. However, a correction over the whole image using a DTM has not been made, as the procedure applied is sufficient for a complete check.

In Figure 6, various information is presented. This information has been encoded using the following criteria. The graph is referred to the maps, and the source point of the vectors represents the centre of the testing area. The vector with the empty triangular point represents the deformation caused by the relief, i.e. the point where it should be possible to observe the structure in the image, once the error caused by the altitude of the GCPs has been corrected, but without having corrected the whole image with a DTM. The vector with the shaded triangular point indicates the position of the structure described on the image after the transformation, but without having applied any correction to the altitude of the ground control points. The vector with the round point indicates the position of the structure described on the image after having applied the correction for the altitude of the known points.

The distance between the circle and the empty triangle represents the final error and the distance between the shaded triangle and the circle represents the improvement resulting from the correction of the altitude of the ground control points.

The average errors before correction are 2.4 pixels for S144 and 4.8 for S139; after correction they are 1.2 for S144 and 2.3 for S139.

7. Conclusions

From the experience gained during this project, the following considerations emerge.

The set of operations has not been found particularly simple or linear to perform; consequently it does not appear advisable to propose the introduction of this system into the public administration without simplifying the procedures and encouraging the creation of suitable competences and expertise.

The geometric precision obtained indicates the scale 1 : 100 000 as the scale at which the remote sensing data of the Thematic Mapper best respects cartographic standards. 1 : 50 000 seems a reasonable scale for small areas while for overall views, the scale would be reduced to 1 : 250 000.

These figures refer to flat areas; in hilly zones more than 40 km from the path of the orbit, the effect of the reliefs is considerable and a DTM correction is necessary.

It would be interesting to propose new criteria for the cartographer. Maps must be accurate not only from the geographic but also from the temporal viewpoint. Perhaps the best solution would be to be able to frequently update existing maps of high geometric precision even if the updates themselves have a lesser degree of accuracy. The simultaneous presence of both factors (accuracy and frequent updates) is contrary to cartographic standards and customs, but would be extremely useful.

From a purely technical point of view, a first geometric correction using a small number of GCPs and a superimposition with linear data would greatly facilitate the identification of further GCPs.

However, the possibility that this system can be adopted by the public authorities in the near future appears very slight unless support structures can be created in public research or industrial organisations, only entrusting the public authorities with the responsibility for the final management of the information.

Acknowledgements

The above experiments were undertaken under the coordinated effort of Telespazio, Regione Toscana and CNUCE. In particular we wish to thank Mrs. Sophie De Vos and Mrs. Lucia Maffei for their technical assistance in performing the geometric corrections.

Tests of Topographic Mapping with Thematic Mapper Images

G. Togliatti, G. Lechi & A. Moriondo
Istituto di Topografia, Fotogrammetria e Geofisica
Politecnico di Milano, Milan, Italy

1. Introduction

In the framework of the ESA Pilot Project Campaign (1985-86), Earthnet has provided this Institute, through the Italian NPOC, with several Thematic Mapper tapes over national areas located in Alto Adige (Bolzano), Piemonte (Turin, Ivrea) and Lombardia (Milan).

The assignment had been made according to a project common to several EARSeL members, within the frame of Working Group n° 9 on 'Satellite Cartography'. Among the many points of such an overall programme, only some were applicable to TM images which do not have stereoscopic performances, that is:

1. Errors in planimetric positions.
2. Comparison with maps in terms of quality and quantity of identifiable details.
3. Analogous comparison with other sensors meant for metric cartography.
4. Patterns of geometrical deformations.
5. Outline of merits and faults for mapping purposes.

The material meant for comparison and evaluation of the TM images included:

1. National maps on the 1 : 50 000 scale (where existing) and on 1 : 25 000 scale (for special purposes).
2. Northern Italy test field (see § 3).
3. Metric Camera images.
4. Large-Format Camera images.

In the following paragraphs an account is given of the various steps of the work, of the difficulties that have been found with consequent changes in the original programme, and of the results obtained.

2. Image processing

The TM images had to be examined at first under three view points:

- which were the most suitable bands to use in order to prepare the positive transparencies on which to perform measures and details identification;
- which types of image enhancement were most suitable for topographic mapping purposes;
- which pixel size in the transparencies would be most acceptable to the operators eyes, given that all obser-

vations were going to be made with 10 × (PK-1 Monocomparator) or 8 × (Planicomp).

The first point has been investigated on the images displayed on the screen by the Ramtek (3 refresh memories 1024 × 1280 × 8 bits). The evaluation was based on the average contents of a 1 : 50 000 map which is mostly made of:

- a) road network (from highways to footpaths);
- b) railways;
- c) hydrological network;
- d) urban settlements;
- e) field boundaries (very few);
- f) altimetry (not applicable to TM).

For each of categories a) to d), five sample areas were chosen in bands 2, 3, 4, 5, 7, and assigned marks according to visual evaluation given by two different operators on the basis of the content of information of the given set. The marks ranged from 0 (not suitable for topographic mapping) to 3 (best of the given set). The criterion may seem too empirical but was coherent with the fact that the subsequent analysis had to be made on instruments based on human photo-interpretation.

On the basis of the marks bands 3, 4, 7 were selected for the analysis (bands 5 and 7 were very correlated in the domain of the targets of a topographical map. The choice between the two was more or less arbitrary).

As far as enhancement was concerned, the full frame system corrected histograms were displayed and then sliced into small ranges (five grey levels each), looking at the type of objects falling in each slide, for each band. The sets covering the objects looked for (e.g. test site Adige Valley, April 1984, Band 3: from 40 to 55 grey levels), have been full-range stretched with linear algorithms and printed on B&W film with Optronix C-4500.

As far as pixel size was concerned for the production of transparencies, several samples were produced with pixel size ranging from 25 to 200 μm and then taken for observation on the Zeiss Monocomparator PK-1 with 10 × and 20 μm measuring mark. It was eventually decided

that the optimum pixel size in the diapositive was $50 \mu\text{m}$. However, the operator stressed the fact that, no matter the size of the pixel, the 'grid-looking images' are a remarkable hindrance to any type of observation with standard photogrammetric equipments, such as mono-comparators and analytical plotters.

Three test areas were therefore prepared in the bands 3, 4, 7, on the 1 : 600 000 scale, for an extension of $\sim 33 \text{ km} \times 33 \text{ km}$, one in the Adige Valley, the second centered on the town of Milan, the third in the Po Valley next to Ivrea. All the three bands were contained in the same film so that the observation could be shifted from one to the other.

3. Geometric accuracy

From the start, the identification of details proved to be the most heavy drawback in the use of TM images for topographic cartography because the position of both isolated points and line features could normally be only 'guessed'. The Adige area presented a narrow flat valley surrounded by woods and only very few points in the valley could be identified, the sample being so small that it was statistically useless. Moreover, since in this case the ground truth was coming from 1 : 50 000 map, these very few points (highway bridges, very large road crossings, etc.) were affected on the map by the overwhelming effects of generalisation, so that their ground coordinates could not constitute a reliable ground truth. Of course, no points could be selected on the mountains for metric evaluation (but no points could have been identified anyway). Therefore, the area was maintained for qualitative evaluation only.

The Milan images were, apparently, much better for the assessment of the planimetric accuracy, in so far as, at first sight, all the urban texture could easily be identified. There was no problem as far as ground truth was concerned because the coordinates could be derived from technical maps on 1 : 2000 or 1 : 5000 scale. However, a more detailed examination has shown that, again, even very large squares could be located only because the operators knew by personal experience where some important through-traffic roads did actually cross. This test area was again dismissed as not being the most suitable for the accuracy tests.

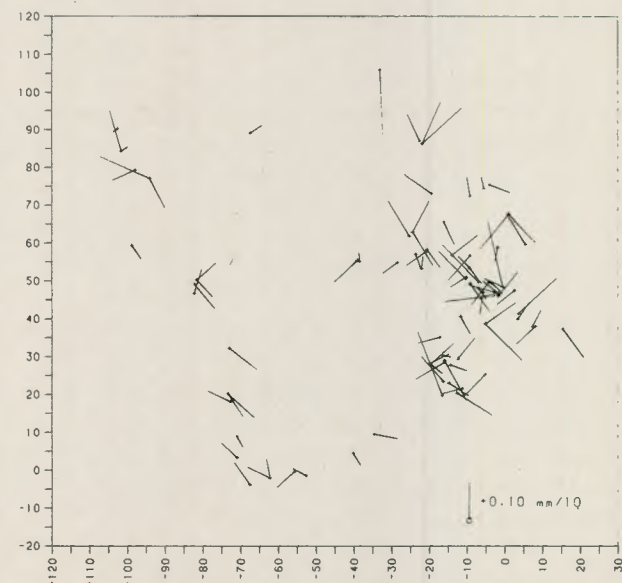
The Ivrea area was then compared with Metric Camera (MC) images taken during the same period (Winter 1982-83) on the scale $\sim 1 : 800 000$. The contemporary observation was made on the two carriages of the analytical plotter Zeiss Planicomp C-100, used, however, as a stereo-comparator rather than as a plotter. One more failure was met, because of the very poor contrast given by the MC in the valleys. The performances of the MC, very good for the accuracy of plano-altimetric

measures, had been previously assessed in (1), and its limits found in the very difficult identification of details. Even though the information contents of TM in that area appeared to be much higher than that of the MC, the difficult identification of topographic details in TM images added to that proper of the MC and to the different responses of the two sensors (e.g. water courses) made it practically impossible to compare MC and TM in a small area such as $33 \text{ km} \times 33 \text{ km}$.

It was quite evident at that point that a suitable ground truth was necessary in order to proceed with the geometrical tests but that, at the same time, a very large extension had to be tested since the density per square km of the sample points was going to be very low.

The best material was found in a colour composite transparency, scale 1 : 500 000, $90 \text{ km} \times 90 \text{ km}$, covering from the Adige Valley to Vicenza, frame 19-28-III, 3 Aug. 1984, bands 345, that we had at our disposal. The image, printed on a Vizir, appeared to be much better than those produced by Optronix, even though the pixel pattern didn't appear as sharp as it should be on a 1 : 500 000 scale. The reference image was coming from the Large-Format Camera and was taken in Oct. 1984. In the same area, a very wide test field of more than 700 points had been established, the coordinates of which had been determined with m.s.e. $\sim 1.5 \text{ m}$, by digitisation of technical regional maps on 1 : 5000 and 1 : 10 000 scales. 687 of those points had been used to test the accuracy of LFC altimetric determinations ($\text{mse.z} = 5 \text{ m}$) and 388 to test the planimetric accuracy ($\text{mse NE} = 5 \text{ m}$) (2). The TM and LFC images were again observed contemporarily on the Planicomp used as a stereocomparator, selecting points that could be identified on both, in flat areas of the ground in order to avoid the x,y

Figure 1. Distribution of discrepancies between TM and LFC (considered as error free). The values, in μm , are at LFC image scale, i.e. 1 : 770 000.



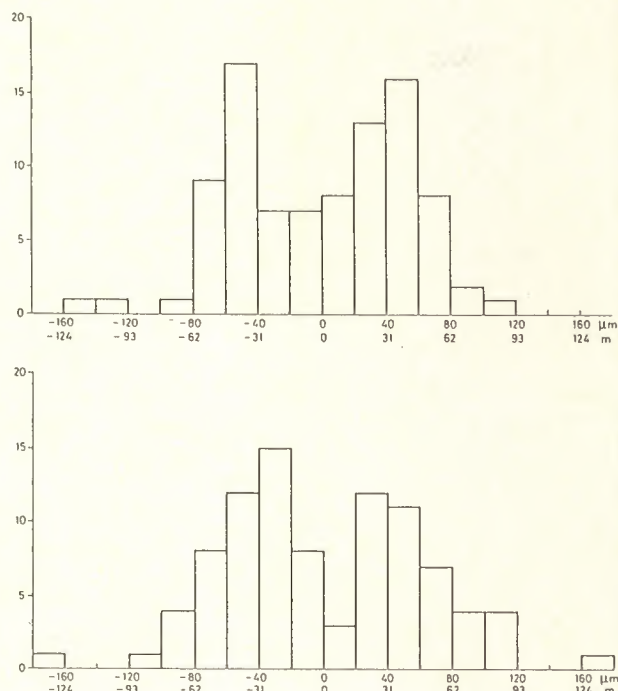


Figure 2. Histograms of Δx and Δy of Figure 1.

displacements due to elevations. The m.s.e. of pointing on LFC ($\sim 6.5 \mu\text{m}$ at image scale) was assumed to be small enough to allow its use as a valid reference for a TM image with pixel size of $60 \mu\text{m}$ at image scale.

With careful examination throughout, 90 points were found, none of which, however, belonging to the test field. The reason of this fact lies in the different response of LFC and TM to road networks and water: the test field, prepared for LFC, included many road crossings and very few bridges, river junctions, etc., the latter, on the contrary, being much more visible on TM than on LFC. The two sets of image coordinates were fitted with an affine transformation, giving rise to the distribution of residuals of Figure 1. The m.s. value is $56 \mu\text{m}$ in x , $64 \mu\text{m}$ in y at LFC scale ($\sim 1 : 770\,000$), equivalent respectively to $\sim 45 \text{ m}$ and $\sim 51 \text{ m}$ at ground scale. No rejection of outliers has been made. The histograms of the x and y discrepancies are shown in Figure 2: they are quite evidently bi-modal with y modal value equal to the pixel size ($40 \mu\text{m} = 30 \text{ m}$), x modal value only slightly higher. The affine transformation shows a figure of 0.3° of lack of orthogonality. So far it has not been possible to investigate further into its meaning.

The set of discrepancies has been filtered with least squares collocation algorithms and only 3% of variability can be assumed to be pseudosystematical. The random distribution of discrepancies is a guarantee that the unusual approach in the use of both images and instruments does not affect the measures and, at the same time, that no relevant pattern deformation is present in the TM images. Even if the already mentioned lack of orthogo-

nality should be due to TM images, its effect would fall within the overall noise.

The accuracy of the TM measures we have found is larger than values given by other authors (3). It must be underlined, however, that the area for points selection is very wide, approx. $70 \text{ km} \times 80 \text{ km}$. We feel, therefore, that the results are consistent with what could be expected from the sensor, from the view point of geometrical performances.

4. Cartographic performances

The tests concerning the extent in which TM images can be used in order to draw or update $1 : 50\,000$ scale maps has been developed along two lines:

- a) autonomous map drawing
- b) identification of elements shown on already existing maps.

The test field for a) was the Adige Valley in the Bolzano area. Three different drawing were made, from bands 3, 4, 7 respectively, enhanced as mentioned in par. 2. The job proved to be very difficult mainly as far as the road network is concerned: even large roads were missing or abruptly disappeared without the operator knowing why: in any case only a small percentage of medium/small roads could be traced on the maps.

Much better information was derived concerning the spreading of urbanisation. For instance, the comparison with a $1 : 50\,000$ scale map based on a 1968 survey shows a remarkable increase in the urbanised areas south and west of the town of Bolzano, quite similar in all the three bands. However, the type of enhancement described in § 2 that had stretched only limited portions of the histogram proved good for drawing the few linear details that could be found (e.g. roads, rivers) but misleading for a sort of thematic mapping such as urban areas. This because too many different grey levels were out of the range and, therefore, had either been turned to black or white. The sketches of bands 3, 4, 7 have been superimposed, giving rise to Figure 3, the contents of which is quite far from that of the corresponding $1 : 50\,000$ map.

The experiment has then been repeated in the area of a large town (Vicenza) on the colour composite of bands 3, 4, 5. The sketch of the urban area is enclosed in Figure 4, and the $1 : 50\,000$ scale map in Figure 5. The changes between the two are evident but just as evident is the lack of fundamental topographical information. The operator's feeling is that he is not able to translate into a line plot the wealth of information contained in the image and that he cannot rely on the continuity of linear features, even large rivers, which, here and there, just disappear.

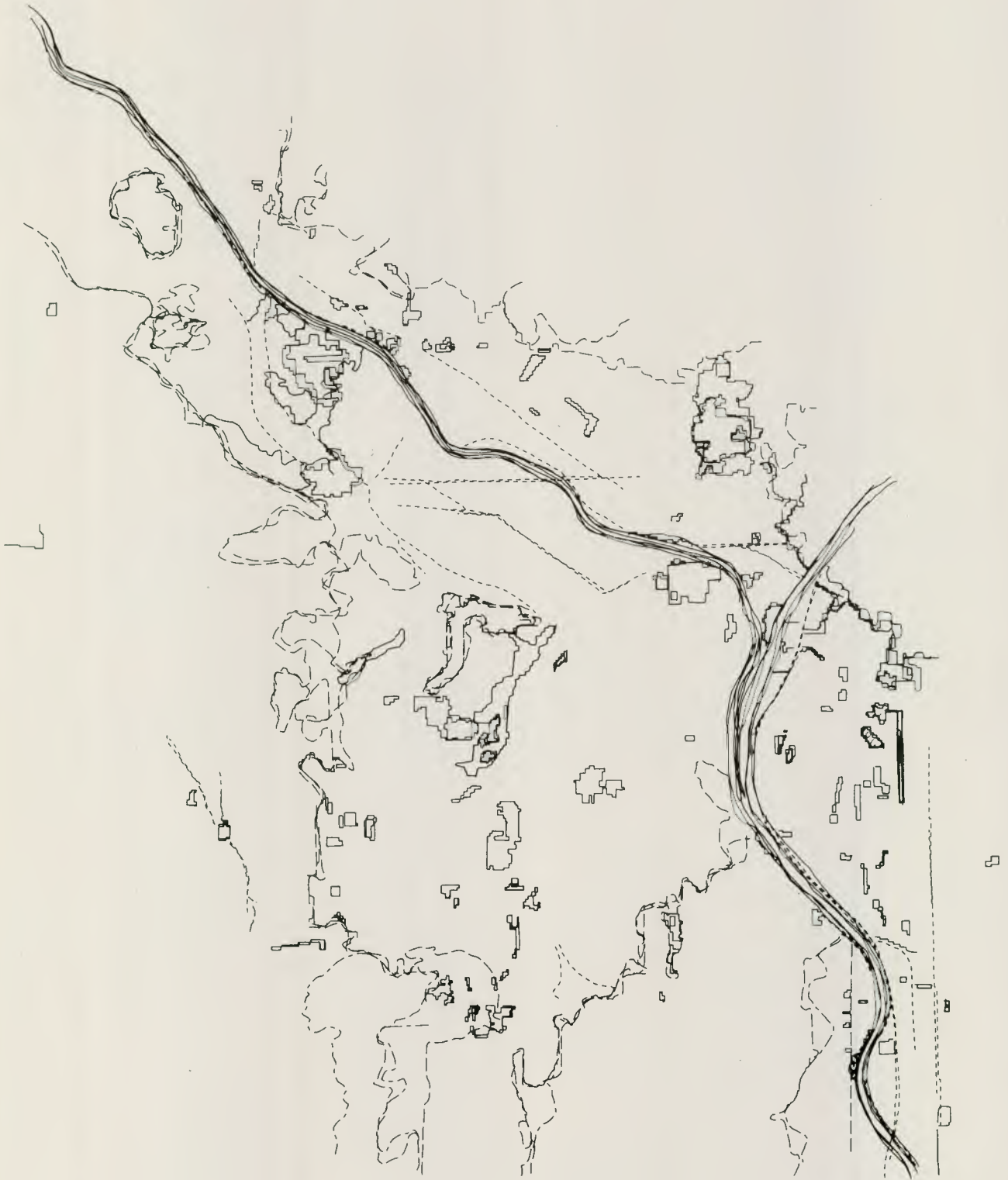


Figure 3. Superimposition of sketches derived from bands 3, 4, 7.

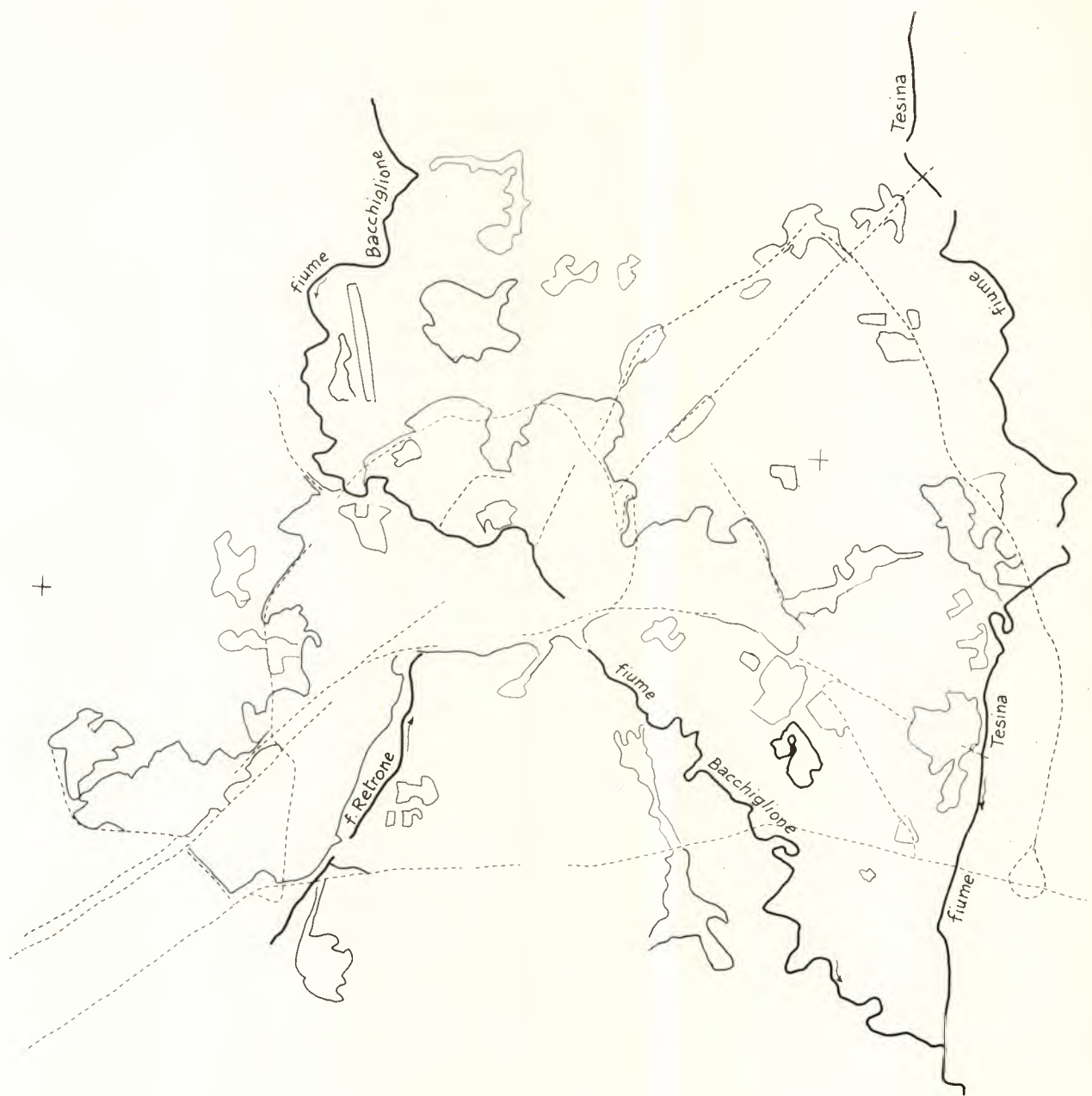


Figure 4. Sample of map drawing from colour composite of bands 3, 4, 5.

The second type of test was made on a sample of four sheets of the 1 : 25 000 map, the smallest scale which is drawn without generalisation. The maps were observed contemporarily to the colour composite transparency put on the monocomparator Zeiss PK-1, 10 \times . The results

confirm all that has previously been said, i.e. that the information appears to be not enough to draw or reliably update a 1 : 50 000 map. On the other hand, we are conscious that we are losing the greatest part of what is shown in the TM image.

List of Keywords

Cartography	Cartography of Arid Areas
Coastal Waters	Sabkha Surfaces
Forestry	Karst Drainage
Geology	Tidal Flat Geomorphology
Hydrology	Comparison of MSS and TM Data
Hydrogeology	Norwegian Coastal Structures
Land Use	
Snow Cover	Urban Areas
Landsat Thematic Mapper	Land-Use Classification
Earthnet Pilot Project	Mapping Winter Grazing Areas
	Ecosystems
Snow & Glacier Monitoring	
Snow Classification	Forest Damage Mapping
Lake Survey	Coniferous Geobotanical Anomalies
Hydrologic Mapping	Small-Scale Forest Classification
Irrigation Water Management	Forest Damage Inventory
Limnological Parameters	Vegetation Mapping
Colour Analysis of Inland Waters	Forest Fire Mapping
	Forest Management
Pollution Characteristics	Multitemporal Analysis
Suspended Sediments	
Norwegian Fjord System	Satellite Image Map Production
	Processing and Interpretation
Peatland Mapping	TM and Cartographic Data Integration
Mineral Exploration	Topographic Mapping with TM Images

List of Participants

J. ALBERTZ

Technische Universität Berlin
Photogrammetrie und Kartographie
Strasse des 17. Juni 135
D-1000 Berlin 12
F R Germany

R. ARCOZZI

Ufficio Cartografico
Regione Emilia Romagna
Viale Silvani 4/3
I-40122 Bologna
Italy

S. AZZALI

Institute for Land & Water Management Res.
Staringgebouw
Marijkeweg 11
NL-6700 AA Wageningen
The Netherlands

C. BANNINGER

Forschungszentrum Graz
Institut für Digitale Bildverarbeitung
Wastiangasse 6
A-8010 Graz
Austria

F. H. BERGER

Institut für Meteorologie
Freie Universität Berlin
Dietrich-Schäfer-Weg 6-10
D-1000 Berlin
F R Germany

R. CALOZ

Institut du Génie Rural
Ecole Polytechnique Fédérale de Lausanne
Dépt. Hydrologie & Aménagements
CH-1015 Lausanne
Suisse

E. CHUVIECO

Department of Geography
University of Alcalá de Henares
Calle de los Colegios, 1
Alcalá de Henares, Madrid
Spain

M. L. DE KEERSMAECKER

Labo. Télédétection & Analyse Régionale
Université Catholique de Louvain
Place Louis-Pasteur 3
B-1348 Louvain-la-Neuve
Belgique

R. E. DE WULF

Lab. of Remote Sensing & Forest Management
Gent State University
Coupure 653
B-9000 Gent
Belgium

J. EHLERS

Geologisches Landesamt
Oberstr. 88
D-2000 Hamburg 13
FR Germany

R. ESCADAFAL

Orstom - Centre de Bondy
70-74, route d'Aulnay
F-93140 Bondy
France

U. GANGKOFNER

Gesellschaft für Angewandte Fernerkundung
Leonrodstr. 68
D-8000 München
FR Germany

F. GONZALEZ-ALONSO

Seccion de Proceso de Datos
I.N.I.A.
Apartado de Correos 8111
E-28080 Madrid
Spain

G. W. HORGAN

Trinity College
5 South Leinster Street
Dublin 2
Ireland

F. JASKOLLA

Inst. f. Allgemeine & Angewandte Geologie
Universität München
Luisenstrasse 37
D-8000 München 2
FR Germany

M. JAQUET

Dépt. de Géologie
Université de Genève
13 rue des Maraîchers
Ch-1211 Genève
Suisse

A. KADRO

Albert-Ludwigs-Universität
Abt. Luftbildmessung & Fernerkundung
Werderring 6
D-7800 Freiburg
FR Germany

H. KAUFMANN

Inst. für Photogrammetrie & Fernerkundung
Universität Karlsruhe
Englerstrasse 7
D-7500 Karlsruhe
FR Germany

J. L. LABRANDERO

Inst. de Edafología y Biología Vegetal
Serrano, 115 dpdo
E-28006 Madrid
Spain

F. K. LIST

Inst. f. Angewandte Geologie & Fernerkundung
Freie Universität Berlin
Malteserstrasse 74-100
D-1000 Berlin 46
FR Germany

B. MASTERSON

Biochemistry Department
University College
Belfield, Dublin 4
Ireland

W. MAUSER

Institut für Physische Geographie
Universität Freiburg
Werderring 4
D-7800 Freiburg
FR Germany

P. MOGOROVICH

Istituto CNUCE
Via S. Maria 36
I-56100 Pisa
Italy

J. H. NILSEN

Norwegian Hydrotechnical Laboratory
N-7034 Trondheim
Norway

J. L. ORTIZ CASAS

Centro de Estudios y Experimentación
de Obras Públicas
Paseo Bajo de la Virgen del Puerto, 3
E-28005 Madrid
Spain

M. POUGET

Orstom - Centre de Bondy
70-74, route d'Aulnay
F-93140 Bondy
France

B. C. REARDON

Department of Computer Science
University College
Belfield, Dublin 4
Ireland

B. REICHERT

Institut für Angewandte Geologie
Universität Karlsruhe
Kaiserstrasse 12
D-7500 Karlsruhe
FR Germany

B. RINDSTAD

Norges Geologiske Undersøkerse
Leiv Eirikssons vei 39
N-7001 Trondheim
Norway

H. ROTT

Institut für Meteorologie & Geophysik
Universität Innsbruck
Schopstrasse 41
A-6020 Innsbruck
Austria

M. SCHARDT
DFVLR – WT-DA
Oberpfaffenhofen
D-8031 Wessling
F R Germany

W. SCHNEIDER
Inst. f. Vermessungswesen & Fernerkundung
Universität für Bodenkultur
Peter Jordan Strasse 82
A-1190 Wien
Austria

R. STELLRECHT
Geologisches Institut
Universität Karlsruhe
Kaiserstrasse 12
D-7500 Karlsruhe
F R Germany

S. SPJELKAVIK
Institute of Biology and Geology
University of Tromso
P.O. Box 3085 Guleng
N-9001 Tromso
Norway

U. STREIT
Institut of Geography
University of Münster
Robert-Koch-Str. 26
D-4400 Münster
F R Germany

G. TOGLIATTI
Istit. Topografia, Fotogrammetria & Geofisica
Politecnico di Milano
Piazza Leonardo da Vinci, 32
I-20133 Milano
Italy

H. TOMMERVIK
Institute of Biology
University of Tromso
P.O. Box 385 Guleng
N-9001 Tromso
Norway

